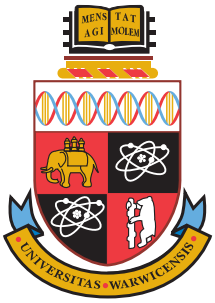

Understanding electronic energy transport in biologically relevant systems: The photochemistry of sunscreens and the photophysics of photosynthesis

by

Lewis A. Baker

Doctoral Thesis

Submitted to the University of Warwick

for the award of

Doctor of Philosophy

in *Mathematical Biology and Biophysical Chemistry*

Supervisors: Dr Scott Habershon and Prof. Vasilios Stavros

Molecular Organisation and Assembly in Cells Doctoral Training Centre.

October 23, 2017.

THE UNIVERSITY OF WARWICK

Contents

Acknowledgements

This thesis is the culmination of three years of PhD research, and marks the end of my formal scientific education. As such, it provides the perfect opportunity to reflect on those who have supported me along the way. Most immediately, I am grateful to my two supervisors, Dr Scott Habershon and Prof. Vasilios Stavros. They have provided me with the guidance, opportunities, and experiences to grow as a scientist, making this PhD an overall success. Both have been indispensable mentors, and I thank them for their unwavering support throughout my PhD.

The research groups with whom I worked with day-to-day are due great gratitude. Mr Maximilian Saller, has been a friend and colleague throughout my PhD, providing as much LaTeX, Python, and UNIX assistance as required. Outside the office, I have enjoyed the outreach activities I usually forced him to join me on, and all of our ridiculous and hilarious DayZ sessions! Mr Samuel Buxton, one half of the Rocket League 'Dream Team', has been a great personality to join the group and I hope that Max and I, being the more 'seasoned' PhDs, have been positive influences on him (although probably not). Finally, I thank our latest Habershon group members, Drs Gareth Richings and Christopher Robertson for their daily useful discussions and distractions. I would also like to thank the members of the Stavros group, with whom I worked with on numerous experimental projects. Specifically, Drs Michael Horbury, Michael Staniforth and Simon Greenough taught me a lot about the experimental techniques, particularly during the early parts of my PhD. I am grateful to Dr Wen-Dong Quan, my fellow MOAC graduate, collaborator, and friend, from whom I learned a lot, and who encouraged me to expand my research horizons. Finally, I would like to thank the undergraduate students I have had the pleasure to help supervise during research projects over the last three years. I have learnt a lot from the perspective of a teacher and have thoroughly enjoyed it, I hope the experience was mutual!

From the many theses I have read over the years, I feel that earlier educational influences are often overlooked, something I wish to avoid here. I have had a number of excellent teachers during my education, but a few have influenced my decisions

regarding the pursuit of further scientific education as much as: Mr Michael Dams, Ms Christine Dams, Dr Shirley Danby, and Mr Michael Wilson. These teachers' enthusiasm was infectious and a lasting influence on me. I credit them with sparking my interest in interdisciplinary science, as well as providing me with an exceptional education.

My friends and family have played an important role in supporting me throughout my life, and not just my education. Mr Daniel Hume has been, and continues to be, one of the greatest friends a person could ask for, I therefore give my sincere thanks to him, and hope I too return in kindness, such support in the future. Last but in no way least, I give my sincerest gratitude to my mother. She has been the biggest influence in my life, and I have learned more from her than she will ever know. I unreservedly thank you for your love and support.

I thank the Engineering and Physical Science Research Council for providing funding through the *Molecular Organisation and Assembly in Cells* (MOAC) doctoral training centre. MOAC has been *the* perfect environment for a budding interdisciplinary physicist to try, discover, and learn. I remain indefinitely grateful for being part of such a great community. To this end, I thank Prof. Alison Rodger, Dr Nikola Chmel, Dr Hugo van den Berg, and Mrs Naomi Grew for creating and encouraging such an interdisciplinary, cohesive, and enjoyable place that MOAC had come to be.

I reserve my final gratitudes to my fiancée Sarah. You are my best friend and my life-partner. I am thankful for your unconditional love and support every day.

Declaration

This thesis is submitted to the University of Warwick in support of my application for the degree of Doctor of Philosophy. It has been composed by myself and has not been submitted in any previous application for any degree. The work presented (including data generated and data analysis) was carried out by me except in the cases outlined below. Parts of this thesis have been published, such cases are outlined at the beginning of the relevant chapters.

Lewis A. Baker
October 23, 2017

Chapter 3:

- The solution-phase transient absorption spectroscopy experimental table was set-up by Dr Simon E. Greenough (University of Warwick, U.K.). The *LabView* program which controls the experimental procedure was written by Dr Simon E. Greenough with contributions from Dr Michael D. Horbury (University of Warwick, U.K.).
- The global fitting script was provided by Dr Adam Chatterly (University of California, Berkeley), which was edited by the author, and used as discussed in Chapters 4 and 5.

Chapter 4:

- In Section 4.1, the transient vibrational absorption spectroscopy measurements were performed in the lab of Prof. Andrew Orr-Ewing FRS, and analysed by Mr Philip M. Coulter and Dr Gareth M. Roberts (University of Bristol, U.K.). The *ab initio* electronic structure calculations were performed by Dr Gareth M. Roberts.

Chapter 5:

- Prof. Florent Allais (AgroParisTech, France) synthesised the methyl sinapate and sinapoyl malate compounds.

List of Figures

List of Tables

List of Publications

1. **Lewis A. Baker**, Michael D. Horbury, Simon E. Greenough, Philip M. Coulter, Tolga N. V. Karsili, Gareth M. Roberts, Andrew J. Orr-Ewing, Michael N. R. Ashfold, and Vasilios G. Stavros. Probing the ultrafast energy dissipation mechanism of the sunscreen oxybenzone after UVA irradiation. *J. Phys. Chem. Lett.*, **2015**, 6(*8*):1363–1368.

2. Michael D. Horbury, **Lewis A. Baker**, Wen-Dong Quan, Jamie D. Young, Michael Staniforth, Simon E. Greenough, and Vasilios G. Stavros. Bridging the gap between the gas and solution phase: Solvent specific photochemistry in 4-*tert*-butylcatechol. *J. Phys. Chem. A*, **2015**, 119(*50*):11989–11996.

3. **Lewis A. Baker**, Michael D. Horbury, Simon E. Greenough, Michael N. R. Ashfold, and Vasilios G. Stavros. Broadband ultrafast photoprotection by oxybenzone across the UVB and UVC spectral regions. *Photochem. Photobiol. Sci.*, **2015**, 14(*10*):1814–1820.

4. **Lewis A. Baker** and Scott Habershon. Robustness, efficiency, and optimality in the Fenna-Matthews-Olson photosynthetic pigment-protein complex. *J. Chem. Phys.*, **2015**, 143(*10*):105101.

5. Wen-Dong Quan, Anaïs Pitto-Barry, **Lewis A. Baker**, Eugen Stulz, Richard Napier, Rachel K. O'Reilly, and Vasilios G. Stavros. Retaining individualities: The photodynamics of self-ordering porphyrin assemblies. *Chem. Commun.*, **2015**, 52(*9*):1938–1941

6. **Lewis A. Baker**, Michael D. Horbury, Simon E. Greenough, Florent Allais, Patrick S. Walsh, Scott Habershon, and Vasilios G. Stavros. Ultrafast photoprotecting sunscreens in natural plants. *J. Phys. Chem. Lett.*, **2016**, 7(*1*):56–61.

7. **Lewis A. Baker**, Michael D. Horbury, and Vasilios G. Stavros. Ultrafast photoprotective properties of the sunscreening agent octocrylene. *Opt. Express*, **2016**,

24(*10*):10700–10709.

8. Michael D. Horbury, **Lewis A. Baker**, Wen-Dong Quan, Simon E. Greenough, and Vasilios G. Stavros. Photodynamics of potent antioxidants: Ferulic and caffeic acids. *Phys. Chem. Chem. Phys.*, **2016**, 18(*26*):17691–17697.

9. **Lewis A. Baker** and Vasilios G. Stavros. Observing and understanding the ultrafast photochemistry in small molecules: Applications to sunscreens. *Sci. Prog.*, **2016**, 99(*3*):282–311

10. Yoann Peperstraete, Michael Staniforth, **Lewis A. Baker**, Natércia D. N. Rodrigues, Neil C. Cole-Filipiak, Wen-Dong Quan, and Vasilios G. Stavros. Bottom-up excited state dynamics of two cinnamate-based sunscreen filter molecules. *Phys. Chem. Chem. Phys.*, **2016**, 18(*40*):28140–28149.

11. **Lewis A. Baker**, Lucy C. Grosvenor, Michael N. R. Ashfold, and Vasilios G. Stavros. Ultrafast photophysical studies of a multicomponent sunscreen: Oxybenzone – titanium dioxide mixtures. *Chem. Phys. Lett.*, **2016**, 664:39–43.

12. **Lewis A. Baker**, Simon E. Greenough, and Vasilios G. Stavros. A perspective on the ultrafast photochemistry of solution-phase sunscreen molecules. *J. Phys. Chem. Lett.*, **2016**, 7(*22*):4655–4665.

13. Michael D. Horbury, **Lewis A. Baker**, Natércia D. N. Rodrigues, Wen-Dong Quan, and Vasilios G. Stavros. Photoisomerization of ethyl ferulate: A solution phase transient absorption study. *Chem. Phys. Lett.*, **2017**, 673:62–67

14. **Lewis A. Baker**, Sarah L. Clark, Scott Habershon, and Vasilios G. Stavros. Ultrafast transient absorption spectroscopy of the sunscreen constituent ethylhexyl triazone. *J. Phys. Chem. Lett.*, **2017**, 8(*10*):2113–2118.

15. **Lewis A. Baker**, Barbara Marchetti, Tolga N. V. Karsili, Vasilios G. Stavros, and Michael N. R. Ashfold. Photoprotection: Extending lessons learned from studying natural sunscreens to the design of artificial sunscreen constituents. *Chem. Soc. Rev.*, **2017**, 46(*12*):3770–3791.

16. **Lewis A. Baker** and Scott Habershon. Photosynthetic pigment-protein complexes as highly-connected networks: Implications for robust energy transport. *Proc. R. Soc. A*, **2017**, 473(*2201*):20170112.

17. Michael Staniforth, Wen-Dong Quan, Tolga N. V. Karsili, **Lewis A. Baker**, Rachel K. O'Reilly, and Vasilios G. Stavros. A first step towards a universal fluorescent probe: Unravelling the photodynamics of an amino-maleimide fluorophore. *J. Phys. Chem. A*, **2017**, 121(*34*):6357–6365.

18. **Lewis A. Baker** and Scott Habershon. Photosynthesis, pigment-protein complexes and electronic energy transport – simple models for complicated processes. *Sci. Prog.*, **2017**, 100(*3*):313–330.

19. Wen-Dong Quan, Michael Staniforth, **Lewis A. Baker**, Rachel K. O'Reilly, and Vasilios G. Stavros. Enhanced charge transfer complex formation of Zn-porphyrin to polymer conjugates. In preparation.

20. **Lewis A. Baker**, Michael Staniforth, Florent Allais, and Vasilios G. Stavros. Gas-solution phase transient absorption study of the plant sunscreen derivative methyl sinapate. In preparation.

Abbreviations

ABP	Absolute Phase
ACN	Acetonitrile
ADC(2)	Second-Order Algebraic Diagrammatic Construction
AOM	Acousto-Optic Modulator
ASE	Asymptotic Standard Error
ATP	Adenosine Triphosphate
Bchl	Bacteriochlorophyll
BO	Born-Oppenhiemer
CASPT2	Complete Active-Space Second-Order Pertubation Theory
CASSCF	Complete Active-Space Self-Consistent Field
CC	Coupled-Cluster
CC2	Second-Order Approximate Coupled-Cluster
CCD	Charge-Coupled Device
CfI	Configuration Interaction
CI	Conical Intersection
COSMO	Conductor-Like Screening Model
CPA	Chirp Regenerative Amplifier
DAS	Decay Associated Spectrum
DFG	Difference Frequency Generation
DFT	Density Functional Theory
DHI	5,6-Dihydroxyindole
DHICA	5,6-Dihydroxyindole-2-Carboxylic Acid
DNA	Deoxyribonucleic Acid
EET	Electronic Energy Transport
EHT	Ethylhexyl Triazone
ENAQT	Environmentally-Assisted Quantum Transport
EOM-CC	Equation-of-Motion Coupled-Cluster
ESA	Excited State Absorption

ESHT	Excited State Hydrogen Atom Transfer
FC	Franck-Condon
FMO	Fenna-Matthews-Olson
fs	femtoseconds
FSSH	Fewest-Switches Surface Hopping
FTIR	Fourier Transform Infrared
FWHM	Full-Width at Half-Maximum
Ga	Giga-annum
GDD	Group Delay Dispersion
GOE	Great Oxidation Event
GrSB	Green Sulphur Bacteria
GSB	Ground State Bleach
GSHT	Ground State Hydrogen Atom Transfer
GTO	Gaussian Type Orbital
GVD	Group Velocity Dispersion
HBT	2-(2'-Hydroxyphenyl)benzothiazole
HF	Hartree-Fock
HF-SCF	Hartree-Fock Self-Consistent Field
HUP	Heisenberg Uncertainty Principle
IC	Internal Conversion
IET	Intermolecular Energy Transfer
IR	Infrared
IRF	Instrument Response Function
ISC	Intersystem Crossing
IVR	Intramolecular Vibrational Energy Transfer
KOALA	Kinetics Observed After Light Absorption
LBO	Lithium Triborate
LCAO	Linear Combination of Atomic Orbitals
LHC-II	Light-Harvesting Complex II
MCSCF	Multiconfigurational Self-Consistent Field
MM	Molecular Mechanics
MP2	Møller-Plesset 2nd-Order Perturbation Theory
MRCI	Multi-Reference Configuration Interaction
MS	Methyl sinapate
ns	nanoseconds
OB	Oxybenzone

OC	Octocrylene
OPA	Optical Parametric Amplifier
OPG	Optical Parametric Generation
OR	Optical Rectification
PAL	Present O_2 Atmosphere Levels
PES	Potential Energy Surface
PPC	Pigment-Protein Complex
ps	picoseconds
PT	Perturbation Theory
PTFE	Polytetrafluoroethylene
QM	Quantum Mechanics
QM/MM	Quantum Mechanics/Molecular Mechanics
RASSCF	Restricted Active-Space SCF
RC	Reaction Centre
RDF	Radial Distribution Function
ROS	Reactive Oxygen Species
SA	Sinapic acid
SCF	Self-Consistent Field
SE	Stimulated Emission
SFG	Sum Frequency Generation
SHG	Second Harmonic Generation
SM	Sinapoyl malate
SMARTS	Simple Model of the Atmospheric Radiative Transfer of Sunshine
SPA	Support Plane Analysis
SPF	Sun Protection Factor
SPM	Self Phase Modulation
STO	Slater Type Orbital
TAS	Transient Absorption Spectra
TD-DFT	Time-Dependent Density Functional Theory
TDSE	Time-Dependent Schrödinger Equation
TEA	Transient Electronic Absorption
TEAS	Transient Electronic Absorption Spectroscopy
TFP	Thin Film Polariser
THG	Third Harmonic Generation
TISE	Time-Independent Schrödinger Equation

TOD	Third-Order Disperion
TR-MS	Time-Resolved Mass-Spectroscopy
TVA	Transient Vibrational Absorption
TVAS	Transient Vibrational Absorption Spectroscopy
UPF	Ultraviolet Protection Factor
UVR	Ultraviolet (UV) Radiation
VET	Vibrational Energy Transfer
WLC	White Light Continuum
WLG	White Light Generation

Abstract

This thesis focusses on two areas. The first is elucidating the ultrafast photoprotective mechanisms exhibited by a number of commercial and natural sunscreening agents, through the use of femtosecond pump-probe transient absorption spectroscopy, coupled with *ab initio* electronic structure calculations. The second is understanding the electronic energy transport properties of pigment-protein complexes found in photosynthetic organisms, through the use of quantum dynamics simulations.

Oxybenzone, titanium dioxide, octocrylene and ethylhexyl triazone are all studied given their prevalence in commercial sunscreen products. We deduce that oxybenzone relaxes through an *enol–keto* isomerism (∼400 fs) followed by back-isomerisation commensurate with vibration energy transfer to the surrounding solvent (∼5–8 ps). Titanium dioxide is then considered in multicomponent suspensions with oxybenzone, where we find that the photodynamics exhibited by each component can be considered independent from one another. Octocrylene is shown to undergo the majority of its photodynamics within ∼2 ps, displaying remarkable efficiency as a ultraviolet light chromophore, relaxing through nonradiative internal conversion pathways. Studies of ethylhexyl triazone are presented, where results suggest this molecule relaxes through a number of ultrafast processes, ranging from ∼400 fs, ∼20 ps and ∼200 ps, involving a large change in nuclear geometry, which couples excited states to the ground state through a conical intersection.

Sinapoyl malate is the predominant sunscreening agent synthesised in *arabidopsis thaliana* which is deposited into the upper epidermis of its leaves. This molecule, along with its biological precursor sinapic acid, are shown to relax through ultrafast pathways (∼10–30 ps), which we suggest is mediated by a *trans–cis* isomerism, in stark contrast to the recent time-resolved gas-phase measurements indicating the solvent environment alters the photodynamics significantly.

Considering the second half of this thesis, we study the Fenna-Matthews-Olson pigment protein complex found in green sulphur bacteria, and the light-harvesting complex II found in the spinach plant. Employing a simple quantum master equation, the Haken-

Strobl model, we highlight a computationally tractable approach for describing these large, complicated systems. To this end, we perform an enormous array of simulations which include a simple description of environmental perturbations and find, for the first time, the full extent of the robustness of these pigment-protein complexes. Most strikingly, for the Fenna-Matthews-Olson complex, we find that up to 50% of the available pigments may be removed, with a small drop of 20% in electronic energy transport, displaying an incredible robustness to network disruption.

Chapter 0

Structure and overview of thesis

Introduction: molecular quantum mechanics. This introductory chapter has been written to provide a concrete, yet concise overview of the fundamental quantum mechanics required to both describe and understand photochemical processes, like those which govern all types of electronic energy transport. *This chapter may be skipped without loss of continuity to the remainder of the thesis.* The first section attempts to lay the foundations of quantum mechanics on a firm basis for describing electrons in atoms and molecules. Key solutions to the Schrödinger equation are derived including: the quantum harmonic oscillator, the Morse potential, and the hydrogen atom. The difficulty in treating multi-electron atoms and molecules is discussed; Hartree-Fock and density functional theory are presented which, with appropriate approximations such as the Born-Oppenheimer approximation, provide a practical route to understanding otherwise computationally impossible molecular systems. The section continues by highlighting the various improvements to *ab initio* methods which increase the accuracy of the quantitative results from these approximations, albeit with an increased computational cost. Finally, the chapter closes with a brief discussion on excited state computational methods, with an extension to quantum dynamics, where explicit temporal information can be extracted which directly correlates with experimentally measured temporal profiles.

Introduction: photochemistry and biological photoprotection. The purpose of this chapter is to first introduce the questions photochemistry tries to answer. Photochemistry is defined as the processes which occur after a molecule transitions to an electronic excited state because of its interaction with electromagnetic radiation. Specifically, this chapter couples the description of electrons in molecules with the perturbative action of radiation within the framework of the molecular dipole moment. Such a treatment naturally leads to the result familiarly known as Fermi's golden rule, and serves to in-

troduce the collection of selection rules which governs electronic, vibrational, and spin transitions. Formally-forbidden transitions are discussed and understood from the conservation of quantum numbers. Predominantly, the coupling of an electron's spin with its orbital angular momentum results in the formally-forbidden transitions met in the photochemistry of organic molecules. From these selection rules, and the higher-order perturbations which lift some of the restrictions on the allows transition, the common photochemical processes which may occur in a photoexcited molecule are summarised. Their typical operational timescales are given and understood using a quantum description of probability. The concept of competing deactivation pathways is brought to attention as a paramount argument for why a molecule will *typically* deactivate in any one particular way. The discussion on photochemistry is brought to a close by connecting the quantum mechanical description of photochemistry to experimentally measurable observables, such as a molecule's extinction coefficient, and the soothing words of the 'Beer-Lambert' law!

The second half of this chapter provides a comprehensive biological context of photoprotection and, ultimately, where sunscreens fit into additional photoprotective measures. Firstly, the evolutionary origins of natural photoprotection as a function of ultraviolet radiation levels over the course of Earth's history are discussed, culminating to the impact of the present-day ultraviolet levels. Specifically, the effects on humans and plants are reviewed (both positive and adverse to survival), and the dominant biochemical pathways which aim to strike a balance of 'too-much' or 'too-little' ultraviolet radiation are discussed. Sunscreens are presented as a widely-used, convenient complement to natural photoprotection, providing additional protection in environments where ultraviolet levels pose an unacceptably large risk of damage to the skin. The mechanisms by which sunscreens provide their photoprotection are described, and the requirement of ultrafast temporal resolution arises naturally given the photochemical processes likely in operation. Finally, a succinct review of the literature for many of the common sunscreen constituents is presented from the perspective of ultrafast transient electronic absorption and transient vibrational absorption spectroscopies, the experimental methodologies used in this thesis, providing a concrete justification for where the work presented in this thesis contributes to the scientific literature.

Experimental methodology. The photophysical and photochemical processes which are likely to be in operation in the deactivation of photoexcited species will require ultrafast (femtosecond-picosecond) resolution to be observed. Furthermore, all the biological systems for photoprotection and electronic energy transport take place in a condensed-phase, which needs to be sensibly replicated if measurements are to be representative

of their natural environment. To that end, solution-phase transient absorption spectroscopy is introduced as the experiment of choice, capable of achieving a resolution of ∼100 fs with condensed-phase (or even solid-phase) samples, making this experiment ideal for observing and understanding the deactivation mechanisms of photoprotective molecules. Indeed, similar techniques have also successfully been applied to observe electronic energy transport in photosynthetic systems, the subject of the last results chapter. To complement these measurements, gas-phase time-resolved measurements can often provide insight and interpretation of the more complicated spectra measured in solution-phase experiments by virtue of removing all environmental perturbations, measuring only the excited state species and nothing more. The complementary nature of this experiment justifies the brief discussion of this technique. More generally, both these techniques require ultrashort laser pulses in a pump-probe set-up; the generation of such pulses and their time-resolution is discussed. The details of how pump-probe spectroscopy is achieved are presented with a focus on how samples in the solution-phase are treated reliably. The measurements of transient absorption spectra are highlighted, and the photophysical origin of common features found in spectra are summarised and explained. Since these measurements require intense laser pulses, there are a number of artefacts which appear in measured spectra, as such, a short description of how measured spectra are corrected (post-experiment) before any kinetics are extracted, is outlined. Finally, the common methods for extracting and analysing the kinetics in each set of spectra are given, with a broad description on the advantages and disadvantages of each method.

Artificial sunscreen constituents. This is the first results chapter in this thesis. It focusses on elucidating the photoprotective mechanisms exhibited by some of the common artificial sunscreen constituents found in commercial products. As given in the introduction, there are myriad possible constituents to consider. Ultimately, the constituents presented in this chapter have been selected for study based on a number of factors including: popularity, sparsity of literature, and availability of purchase, summarised in Figure 0.1. Specifically, we present a comprehensive transient absorption spectroscopy study on UV-A photoexcited oxybenzone, utilising both electronic and vibrational spectroscopies, supported by *ab initio* electronic structure calculations. The transient electronic absorption studies are then extended to include UV-B and UV-C photoexcitation. The phenomenally popular inorganic particulate filter titanium dioxide is investigated at the extreme concentrations likely to be found in commercial products. Given the extensive characterisation of oxybenzone in the previous section, suspensions of titanium dioxide with oxybenzone are considered as a first step in un-

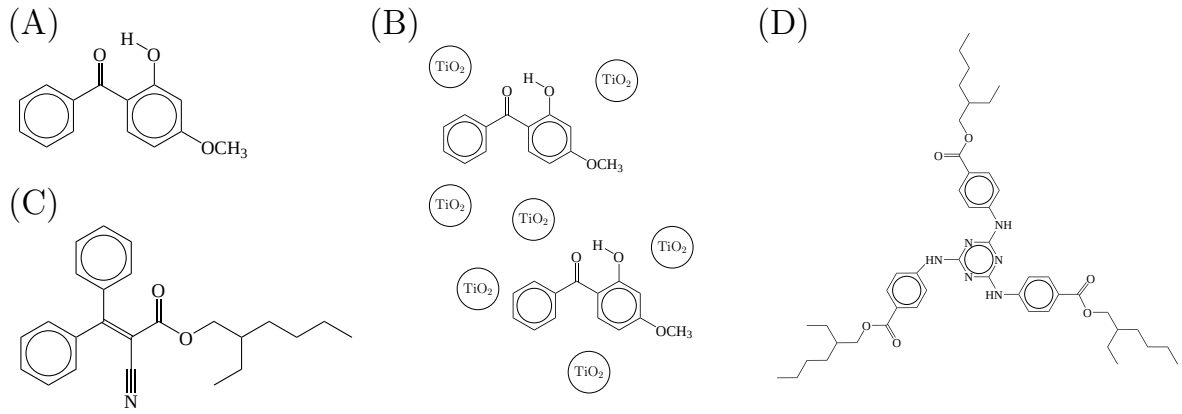

Figure 0.1 | A summary of the artificial sunscreen constituents studied and reported in this thesis. (A) Oxybenzone; (B) titanium dioxide and its suspensions with oxybenzone; (C) octocrylene; (D) ethylhexyl triazone.

derstanding a multicomponent sunscreen, a step closer to the environment these constituents exist as in commercial products. The rest of this chapter focusses on larger organic filters since their large molecular weights may reduce their likelihood of penetrating the skin, making them particularly worthy of further research. To this end, we investigate the photoprotective properties of octocrylene, currently one of the world's most popular sunscreening agents, with support from *ab initio* electronic structure calculations to identify the likely excited states. Finally, ethylhexyl triazone, the largest (by molecular weight) organic filter considered in this thesis, is investigated by transient electronic absorption spectroscopy and a more substantive set of *ab initio* electronic structure calculations of excited molecular states helps to determine the likely excited state absorption signals.

Natural sunscreen constituents. This chapter introduces the biological photoprotective molecule sinapoyl malate and its precursor sinapic acid (Figure 0.2). These molecules are in contrast to those of the previous chapter which are not synthesised within an organism, rather, synthesised 'artificially'. As such, they present themselves as interesting molecules to study given, on some level, these have been biologically selected for, perhaps (in part), their photoprotective properties? Furthermore, the molecules of that chapter (*cf.* Figure 0.1) are used in commercial sunscreen products and applied to the skin; sinapoyl malate (analogously to the melanins in human skin) is synthesised inside the plant leaves and deposited in the path of ultraviolet radiation and sensitive tissues. As such, sinapoyl malate is interesting to consider from a photoprotective perspective where it might find application to general photoprotection (sun-

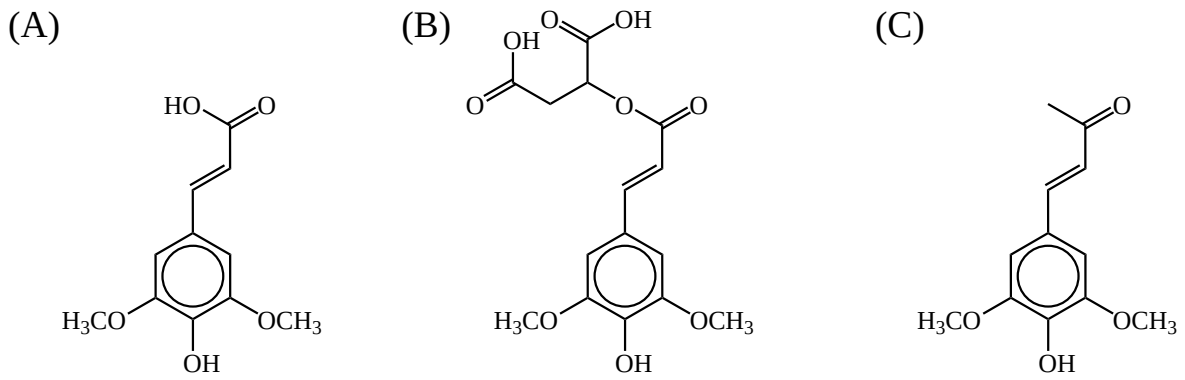

Figure 0.2 | A summary of the natural photoprotective molecules studied and reported in this thesis. (A) Sinapic acid, the biological precursor to sinapoyl malate (B). The simplest chemical derivative of sinapic acid, methyl sinapate is also considered in this thesis (C).

screens, crop protection, ultraviolet inhibition in chemical reactions *etc.*). This chapter begins with an overview of the relevant literature regarding sinapic acid and sinapoyl malate, where a great deal of studies have focused on gas-phase measurements of these molecules. What is presented is an in-depth transient electronic absorption study of these molecules, along with complementary steady-state ultraviolet-visible and infrared spectroscopies.

Network-based analysis of pigment-protein complexes. The third and final results chapter of this thesis focusses on modelling some of the large and complicated photosynthetic machinery responsible for the incredible efficiencies photosynthetic organisms achieve. Such processes may at first appear disjointed from the first two results chapters, which focussed on the photophysics and photochemistry of (small) photoexcited molecules, but they are in fact two sides of the same coin. On the one hand, photoexcited molecules deactivate excess electronic energy through a number of photochemical pathways to achieve energetic stability. On the other hand, the main processes at the heart of photosynthesis is the directed transfer of electronic energy to a reaction centre, where it is converted to chemical energy for storage. Thus both systems are examples of directed energy transport at a fundamental level. This chapter therefore provides an overview of photosynthesis and highlights how electronic energy transport is at the heart of its efficiency. A full quantum-mechanical treatment of these systems along with a representative environment (solvent and protein for example) would be almost impossible with current computing capabilities. Instead, the widely used Haken-Strobl quantum master equation approach provides a viable alternative. This model is presented in the context of electronic energy transport, and the origins of all the parameters used in the

model are discussed. Specifically, a network-based framework of light-absorbing pigments is developed which allows a systematic treatment of network modifications to be explored. Two prototypical pigment-protein complexes are introduced and recast into this network-based framework, namely the Fenna-Matthews-Olson complex from green sulphur bacteria and the light-harvesting complex II from green plants are considered. Each network is disrupted in a series of ways which represent plausible biological disruptions to the operation of these complexes. Specifically, we consider what happens when one or more pigments are lost from the network, or when native electronic transport pathways are blocked. Within the network-based framework, we apply standard graph-theory algorithms to determine the most efficient electronic energy pathways, and how these change upon network disruption. Environmental perturbations, temperature fluctuation, and evolutionary optimality are some of the other questions examined in this work.

The thesis closes with a summary of the main results reported in this thesis and where this work contributes to scientific literature. An open discussion follows of important questions regarding sunscreen use, its safety, and the direction of future studies. An analogous discussion regarding electronic energy transport of photosynthetic pigment-protein complexes is given.

Chapter 1

Introduction: Molecular quantum mechanics

1.1 The foundations of quantum mechanics

The following postulates form the foundations of Quantum Mechanics (QM), and therein form the basis of vast majority of the theory presented in this thesis.[1] *Bra-ket* notation is used throughout this thesis,[1,2] where integrals are written as

$$\langle \Psi | \, \mathrm{H} \, | \Psi \rangle = \int \Psi^* \mathrm{H} \Psi d\tau, \tag{1.1}$$

for arbitrary, integrable functions, Ψ and H, over implied coordinates $d\tau$.

1. All possible information about a system, parametrised by position $\mathbf{r}$, and time t, is fully described by a mathematical function, $\Psi(\mathbf{r}, t)$, referred to as the wavefunction.

2. The wavefunction, $\Psi(\mathbf{r}, t)$, can be expanded as a linear combination of n orthonormal eigenfunctions $\psi_i(\mathbf{r}, t)$, of some operator, with coefficients, c_i, as

$$\Psi(\mathbf{r}, t) = \sum_i^n c_i \psi_i, \tag{1.2}$$

   where $|c_i|^2$ represents the probability of the i^{th} eigenfunction. As such, the expec-

tation value, E, of some operator, $\hat{\mathrm{O}}(\mathbf{r}, t)$, can therefore be expressed as

$$E = \frac{\langle \Psi | \, \hat{\mathrm{O}} \, | \Psi \rangle}{\langle \Psi | \Psi \rangle} = \frac{\sum_i |c_i|^2 \lambda_i}{\sum_i |c_i|^2}, \tag{1.3}$$

where λ_i is the corresponding eigenvalue for eigenfunction ψ_i.

3. Observable quantities, such as q which denotes a spatial coordinate ($\hat{\mathbf{x}}$, $\hat{\mathbf{y}}$ or $\hat{\mathbf{z}}$), and P_q, the corresponding momentum, are represented by linear, Hermitian operators which satisfy the following commutation relations:

$$[q, P_{q'}] = i\hbar\delta_{qq'} \tag{1.4}$$

$$[q, q'] = 0 \tag{1.5}$$

$$[P_q, P_{q'}] = 0, \tag{1.6}$$

where i is the imaginary unit, $\hbar$ is the reduced Planck's constant, and $\delta_{qq'}$ is the Dirac delta function.

4. The probability that a particle is found in a volume element, $d\tau$, at coordinate, $\mathbf{r}$, is $|\Psi(\mathbf{r}, t)|^2 d\tau$ for a normalised wavefunction, *i.e.* $\langle \Psi | \Psi \rangle = 1$.

5. The wavefunction evolves in time according the the Time-Dependent Schrödinger Equation (TDSE),

$$i\hbar \frac{\partial \Psi}{\partial t} = \hat{\mathrm{H}}\Psi, \tag{1.7}$$

where $\hat{\mathrm{H}}$ is the Hamiltonian operator, discussed next.

That is essentially it; the predictions and results of quantum mechanics are derived from these postulates using appropriate approximations for the system in question. The remainder of this section will cover the various systems and approximations which lead to a functioning quantum theory for molecular photophysics and photochemistry.

1.1.1 Direct consequences and results of these postulates

An operator, $\hat{\mathrm{O}}$, is said to be linear if it satisfies[1]

$$\hat{\mathrm{O}}(c_1\Psi_1 + c_2\Psi_2) = c_1\hat{\mathrm{O}}\Psi_1 + c_2\hat{\mathrm{O}}\Psi_2, \tag{1.8}$$

for any function Ψ_1 and Ψ_2 with coefficients c_1 and c_2 respectively. The operator $\hat{\mathrm{O}}$, is Hermitian only if it satisfies

$$\langle\Psi_1|\,\hat{\mathrm{O}}\,|\Psi_2\rangle = \langle\Psi_2|\,\hat{\mathrm{O}}\,|\Psi_1\rangle^*\,. \tag{1.9}$$

Two important consequences arise from the condition of Hermiticity, firstly, *eigenvalues associated with the operator are real*, and secondly, *eigenstates corresponding to different eigenvalues of such an operator are orthogonal*.

Proof of real eigenvalues. This property is quickly deduced by considering some Hermitian operator $\hat{\mathrm{O}}$, acting on a normalised eigenstate $|m\rangle$, which returns the eigenvalue m,

$$\hat{\mathrm{O}}\,|m\rangle = m\,|m\rangle\,. \tag{1.10}$$

Left multiplying Equation 1.10 by $\langle m|$ gives

$$\langle m|\,\hat{\mathrm{O}}\,|m\rangle = m\,\langle m|m\rangle\,. \tag{1.11}$$

Given $|m\rangle$ is normalised, $\langle m|m\rangle = 1$. Taking the complex conjugate of both sides gives

$$\langle m|\,\hat{\mathrm{O}}\,|m\rangle^* = m^*, \tag{1.12}$$

which, given the condition of Hermiticity in Equation 1.9, it follows $m = m^*$ and is hence real.

Proof of orthogonality. In much the same way we consider two eigenvalue equations, where $m \neq m'$ and the states $|m\rangle$ and $|m'\rangle$ are eigenstates of $\hat{\mathrm{O}}$,

$$\hat{\mathrm{O}}\,|m\rangle = m\,|m\rangle\,; \quad \hat{\mathrm{O}}\,|m'\rangle = m'\,|m'\rangle\,. \tag{1.13}$$

Left multiplying the first of these by $\langle m'|$ and the second by $\langle m|$ gives

$$\langle m'|\,\hat{\mathrm{O}}\,|m\rangle = m\,\langle m'|m\rangle\,; \quad \langle m|\,\hat{\mathrm{O}}\,|m'\rangle = m'\,\langle m|m'\rangle\,. \tag{1.14}$$

Taking the complex conjugate of the second of these, then subtracting the result from the first expression, noting $m' = m'^*$ and $\langle m|m'\rangle^* = \langle m'|m\rangle$ gives

$$(m - m')\,\langle m|m'\rangle = \underbrace{\langle m'|\,\hat{\mathrm{O}}\,|m\rangle - \langle m|\,\hat{\mathrm{O}}\,|m'\rangle^*}_{=\,0 \text{ from Equation 1.9}} = 0, \tag{1.15}$$

and since we stipulated $m \neq m'$, $\langle m'|m\rangle = 0$ and thus $|m\rangle$ and $|m'\rangle$ are orthogonal.

Postulate 3 requires that the two operators of position and momentum do not commute for the same spatial coordinate, *i.e.*, $[q, P_{q'}] = i\hbar\delta_{qq'}$. It can be shown however, that this is a general property of simultaneous observables; if two operators commute, then their corresponding eigenvalues are simultaneously observable. Turning this around, two non-commuting operators insists their corresponding eigenvalues cannot be precisely defined simultaneously, which is a statement of the well known Heisenberg Uncertainty Principle (HUP).

Heisenberg Uncertainty Principle.[1] Consider two Hermitian operators, $\hat{\mathrm{A}}$ and $\hat{\mathrm{B}}$, with commutator $\left[\hat{\mathrm{A}}, \hat{\mathrm{B}}\right] = i\hat{\mathrm{C}}$, acting on a normalised, arbitrary function of both operators, $|\psi\rangle$, with the expectation values

$$\left\langle \hat{\mathrm{A}} \right\rangle = \langle\psi| \hat{\mathrm{A}} |\psi\rangle ; \quad \left\langle \hat{\mathrm{B}} \right\rangle = \langle\psi| \hat{\mathrm{B}} |\psi\rangle . \tag{1.16}$$

The corresponding deviation about the mean can be defined as

$$\delta\hat{\mathrm{A}} = \hat{\mathrm{A}} - \left\langle \hat{\mathrm{A}} \right\rangle ; \quad \delta\hat{\mathrm{B}} = \hat{\mathrm{B}} - \left\langle \hat{\mathrm{B}} \right\rangle , \tag{1.17}$$

where the commutator of these deviations can be written as

$$\left[\delta\hat{\mathrm{A}}, \delta\hat{\mathrm{B}}\right] = \left[\hat{\mathrm{A}} - \left\langle \hat{\mathrm{A}} \right\rangle , \hat{\mathrm{B}} - \left\langle \hat{\mathrm{B}} \right\rangle\right] = \left[\hat{\mathrm{A}}, \hat{\mathrm{B}}\right] = i\hat{\mathrm{C}}. \tag{1.18}$$

Leaving this result for a moment, we consider the following integral, I, over some arbitrary dimension τ,

$$\mathrm{I} = \int |\left(\lambda\delta\hat{\mathrm{A}} - i\delta\hat{\mathrm{B}}\right)\psi|^2 \mathrm{d}\tau, \tag{1.19}$$

where λ is a real, arbitrary number. Note that the integrand is positive everywhere, thus $\mathrm{I} \geq 0$, meaning the integrand can be split into the following products:

$$\begin{aligned} \mathrm{I} &= \int \left(\lambda\delta\hat{\mathrm{A}}\psi - i\delta\hat{\mathrm{B}}\psi\right)^* \left(\lambda\delta\hat{\mathrm{A}} - i\delta\hat{\mathrm{B}}\right)\psi \ \mathrm{d}\tau \\ &= \int \psi^* \left(\lambda\delta\hat{\mathrm{A}} + i\delta\hat{\mathrm{B}}\right)\left(\lambda\delta\hat{\mathrm{A}} - i\delta\hat{\mathrm{B}}\right)\psi \ \mathrm{d}\tau \\ &= \left\langle \left(\lambda\delta\hat{\mathrm{A}} + i\delta\hat{\mathrm{B}}\right) \middle| \left(\lambda\delta\hat{\mathrm{A}} - i\delta\hat{\mathrm{B}}\right) \right\rangle . \end{aligned} \tag{1.20}$$

In the first step the squared modulus is rewritten with a complex conjugate, in the second step, the complex conjugate is applied to the bracket and the property of Hermiticity is used. Finally, the integral was written in terms of the corresponding expectation value. Expanding out and simplifying (using Equation 1.18) the resultant quadratic

expression yields

$$\mathrm{I} = \left\langle \delta\hat{\mathrm{A}}^2 \right\rangle \left(\lambda + \frac{\langle C \rangle}{2\left\langle \delta\hat{\mathrm{A}} \right\rangle} \right)^2 + \left\langle \delta\hat{\mathrm{B}}^2 \right\rangle - \frac{\langle C \rangle^2}{4\left\langle \delta\hat{\mathrm{A}}^2 \right\rangle}. \tag{1.21}$$

We now choose $\lambda = -\dfrac{\langle C \rangle}{2\left\langle \delta\hat{\mathrm{A}} \right\rangle}$, which makes the first term zero, leaving,

$$\mathrm{I} = \left\langle \delta\hat{\mathrm{B}}^2 \right\rangle - \frac{\langle C \rangle^2}{4\left\langle \delta\hat{\mathrm{A}}^2 \right\rangle} \geq 0, \tag{1.22}$$

which is rearranged to give

$$\left\langle \delta\hat{\mathrm{A}}^2 \right\rangle \left\langle \delta\hat{\mathrm{B}}^2 \right\rangle \geq \frac{\langle C \rangle^2}{4}. \tag{1.23}$$

The deviations $\delta\hat{\mathrm{A}}$ and $\delta\hat{\mathrm{B}}$ can be written in a convenient way noting they are simply root mean square deviations, *i.e.* $\left\langle \delta\hat{\mathrm{A}} \right\rangle = \sqrt{\left\langle \hat{\mathrm{A}}^2 \right\rangle - \left\langle \hat{\mathrm{A}} \right\rangle^2}$, similarly for $\left\langle \delta\hat{\mathrm{B}} \right\rangle$, which on substitution results in the general statement of the HUP

$$\Delta\hat{\mathrm{A}}\Delta\hat{\mathrm{B}} \geq \frac{1}{2}|\left\langle \left[\hat{\mathrm{A}}, \hat{\mathrm{B}}\right] \right\rangle|, \tag{1.24}$$

where $\Delta\hat{\mathrm{A}}$ and $\Delta\hat{\mathrm{B}}$ represent the deviations from the mean expectation values for operator $\hat{\mathrm{A}}$ and $\hat{\mathrm{B}}$ respectively.

Thus for any two non-commuting operators *i.e.* $\left[\hat{\mathrm{A}}, \hat{\mathrm{B}}\right] \neq 0$, there exists a limit on the precision on the observables, for example, position and parallel momentum *cf.* Equation 1.4. Conversely, two commuting operators allow the corresponding observables to be known to arbitrary precision *cf.* Equation 1.6. This is in stark contrast to classical physics where all 'operators' commute with each other.

Taking the time out of time-dependent. The Hamiltonian, H, named after the Irish physicist William Hamilton, is an expression of a system's total energy as the sum of all energy contributions, *i.e.* all sources of kinetic (T_i) and potential energies (V_j), $\mathrm{H}(\mathbf{r},t) = \sum_i \mathrm{T}_i(\mathbf{r},t) + \sum_j \mathrm{V}_j(\mathbf{r},t)$. The Hamiltonian operator, $\hat{\mathrm{H}}(\mathbf{r},t)$, is the quantum mechanical equivalent, a series of functions which returns the total energy, E, of a system upon acting on the system wavefunction, $\Psi(\mathbf{r},t)$, *cf.* Equation 1.3. In its most general form, the Hamiltonian is a function of space-time as given, however, for a system where the Hamiltonian does not depend on time, then one can simplify the TDSE, postulate 5. Consider a free particle with mass, m, restricted to propagating in the $\hat{\mathbf{x}}$ direction. If

it experiences a potential, $V(x)$, the total Hamiltonian is

$$\hat{\mathrm{H}} = -\frac{\hbar}{2m}\frac{\partial^2}{\partial x^2} + V(x), \tag{1.25}$$

where we have used postulate 3; classical dynamic variables are replaced with linear, Hermitian quantum mechanical operators, in this case[3]

$$\text{Position: } x \longrightarrow x, \tag{1.26}$$

and

$$\text{Momentum: } p(x) \longrightarrow -i\hbar\frac{\partial}{\partial x}, \tag{1.27}$$

where p is the classical momentum of the particle.* Using this Hamiltonian, the TDSE equation is

$$i\hbar\frac{\partial\Psi}{\partial t} = -\frac{\hbar}{2m}\frac{\partial^2\Psi}{\partial x^2} + V(x)\Psi. \tag{1.28}$$

One can suggest a trial solution, $\Psi(x,t) = \psi(x)\phi(t)$, which on substitution, and collating spatial and temporal variables gives

$$i\hbar\frac{1}{\phi}\frac{\mathrm{d}\phi}{\mathrm{d}t} = -\frac{\hbar}{2m}\frac{1}{\psi}\frac{\mathrm{d}^2\psi}{\mathrm{d}x^2} + V(x), \tag{1.29}$$

which, given each side of this equation is dependent only on one of the two parameters (x or t), separates into two differential equations

$$i\hbar\frac{1}{\phi}\frac{\mathrm{d}\phi}{\mathrm{d}t} = E\phi \tag{1.30}$$

and

$$-\frac{\hbar}{2m}\frac{1}{\psi}\frac{\mathrm{d}^2\psi}{\mathrm{d}x^2} + V(x) = E\psi, \tag{1.31}$$

where E is some constant with dimensions of energy. The first of these, Equation 1.30, has a simple solution, $\phi(t) = Ae^{-\frac{iE}{\hbar}t}$, where A is a normalisation constant yet to be determined, and, as will be shown, is not important. Thus, the total wavefunction is $\Psi(x,t) = A\psi(x)e^{-\frac{iE}{\hbar}t}$ and satisfies the second differential equation, Equation 1.31, which is a general eigenvalue equation of the form

$$\hat{\mathrm{H}}\psi = E\psi. \tag{1.32}$$

*Of course, should we lift the propagation restriction to allow movement in general space ($\hat{\mathbf{x}}$, $\hat{\mathbf{y}}$, $\hat{\mathbf{z}}$), momentum is simply the sum of linear momenta, *i.e.*: $p(x,y,z) \longrightarrow -i\hbar\left(\frac{\partial}{\partial x} + \frac{\partial}{\partial y} + \frac{\partial}{\partial z}\right)$.

which is the Time-Independent Schrödinger Equation (TISE), where E can be interpreted as the energy eigenvalue of the Hamiltonian. The solutions to the TISE are plane waves, with a time-dependent phase (of angular frequency $E/\hbar$), importantly, the probability density remains constant in time, *i.e.* $\Psi^*\Psi$ = constant, hence are referred to as *stationary states*.

Time-evolution of an expectation value.[1,3] Consider an operator $\hat{\mathrm{O}}$ with expectation value $\left\langle \hat{\mathrm{O}} \right\rangle$, its time-evolution is

$$\frac{\partial \left\langle \hat{\mathrm{O}} \right\rangle}{\partial t} = \frac{\partial}{\partial t} \langle \Psi | \, \hat{\mathrm{O}} \, | \Psi \rangle = \int \left(\frac{\partial \Psi}{\partial t} \right)^* \hat{\mathrm{O}} \Psi d\tau + \int \Psi^* \hat{\mathrm{O}} \left(\frac{\partial \Psi}{\partial t} \right) d\tau. \tag{1.33}$$

From the TDSE, Equation 1.7, the derivative of the wavefunction is simply $\frac{\partial \Psi}{\partial t} = \frac{1}{i\hbar} \hat{\mathrm{H}} \Psi$, thus upon substitution

$$\frac{\partial \left\langle \hat{\mathrm{O}} \right\rangle}{\partial t} = -\frac{1}{i\hbar} \left(\left\langle \hat{\mathrm{H}} \hat{\mathrm{O}} \right\rangle - \left\langle \hat{\mathrm{O}} \hat{\mathrm{H}} \right\rangle \right) = \frac{i}{\hbar} \left\langle \left[\hat{\mathrm{H}}, \hat{\mathrm{O}} \right] \right\rangle. \tag{1.34}$$

This means that if an operator commutes with the Hamiltonian for a system $\Psi(\mathbf{r}, t)$, the expectation value of that operator does not change over time, in other words, it is conserved. This result provides an important bridge between classical and quantum physics in that the time-evolution of position, x, and linear momentum, p_x, are shown to be equivalent to the average velocity and average force, F, applied to the system (of mass m) from classical mechanics, collectively known as Ehrenfest's theorem,[1]

$$\begin{aligned} \frac{\mathrm{d}}{\mathrm{d}t} \langle x \rangle &= \frac{\langle p_x \rangle}{m}, \\ \frac{\mathrm{d}}{\mathrm{d}t} \langle p_x \rangle &= \langle F \rangle . \end{aligned} \tag{1.35}$$

However, it is important to note that such an equivalence is only exact for harmonic potentials.[4]

Consequences of the Born-interpretation. In Postulate 4, we stated that the probability that a particle is found in a volume element, $\mathrm{d}\tau$, at coordinate, $\mathbf{r}$, is $|\Psi(\mathbf{r}, t)|^2 \, \mathrm{d}\tau$. Whilst the interpretation of the wavefunction itself remains somewhat philosophical, $\Psi^*\Psi$ is clearly a probability density. This places two restrictions on the property of wavefunctions. The first is that a wavefunction must remain finite over a finite region of space otherwise the integral $\langle \Psi | \Psi \rangle$ would be nonsensical. The second is that $\Psi^*\Psi$

must be single valued, otherwise multiple probabilities would exist for a single state. Further restrictions are placed on the wavefunction when one considers it is a solution to a second-order differential equation, *i.e.* it is a solution to the wave equation, *e.g.* Equation 1.31. This requires firstly, that the wavefunction is continuous over all space. It also requires the wavefunction to have a continuous first derivative, with exceptions where discontinuities occur over delta functions of the potential.[†]

So what is left? What remains is to find the functional form of the wavefunction for the system of interest - usually much, much easier said than done. One has to model the system appropriately which requires the consideration of all the contributions to the Hamiltonian. In fact, there are only a few specific cases where the wavefunction can be determined exactly because of the complexity of solving the Schrödinger equation with the Hamiltonian of multi-electron systems. Some of the exactly solvable systems include the one-dimensional 'particle in a box' with infinite and finite potential wells.[1] In this thesis however, we will only cover the standard harmonic oscillator problem, its extension to the Morse potential which provides a good description of the vibrational spectrum of molecules, and finally the the Hydrogen atom, the solutions of which are critical to the development of molecular orbital theory.

1.1.2 The quantum harmonic oscillator

A harmonic oscillator is a system which, when displaced from its equilibrium position, experiences a restoring force, F, proportional to the magnitude of the displacement, x, *i.e.* $F = -kx = -\frac{dV}{dx}$, where k is a force or 'spring' constant and V is the associated potential energy. To a first approximation, this system describes a diatomic molecule vibrating; the bond length between the molecules can compress or extend, *i.e.* a displacement, which experiences a restoring force towards the equilibrium bond length. The Hamiltonian of such a system of masses (m_1 and m_2, have a reduced mass of $\mu = \frac{m_1 m_2}{m_1+m_2}$), under one-dimensional harmonic motion is

$$\hat{\mathrm{H}} = -\frac{\hbar}{2\mu}\frac{\mathrm{d}^2}{\mathrm{d}x^2} + \frac{1}{2}kx^2, \tag{1.36}$$

thus for time-independent solutions, the Schrödinger equation of the system, Ψ, is

$$-\frac{\hbar}{2\mu}\frac{\mathrm{d}^2\Psi}{\mathrm{d}x^2} + \frac{1}{2}kx^2\Psi = E\Psi. \tag{1.37}$$

[†]This is because a property of the delta function is: $\int f(r)\delta(r-r')\mathrm{d}r = f(r')$, for some function $f(r)$.

This differential equation can be solved in a couple of ways such as a Fourier spectral method,[5] or through factorising the Hamiltonian, the latter turns out to be much more elegant. Using the following substitutions:[1,3,6]

$$\lambda = \frac{2E}{\hbar\omega}; \quad y = \left(\frac{\mu\omega}{\hbar}\right)^{\frac{1}{2}}; \quad \omega = \left(\frac{k}{\mu}\right)^{\frac{1}{2}}, \tag{1.38}$$

which allows Equation 1.37 to be written as

$$\left(\frac{\mathrm{d}^2}{\mathrm{d}y^2} - y^2\right)\Psi = -\lambda\Psi. \tag{1.39}$$

We now (with hindsight) introduce the creation operator, $a^\dagger$, and annihilation operator, a, which form a Hermitian conjugate pair *i.e.* $\left[a, a^\dagger\right] = 1$,[6]

$$a^\dagger = \frac{1}{\sqrt{2}}\left(y - \frac{\mathrm{d}}{\mathrm{d}y}\right); \quad a = \frac{1}{\sqrt{2}}\left(y + \frac{\mathrm{d}}{\mathrm{d}y}\right), \tag{1.40}$$

such that

$$1 - 2aa^\dagger = \left(\frac{\mathrm{d}^2}{\mathrm{d}y^2} - y^2\right), \tag{1.41}$$

thus the Schrödinger Equation 1.39 is simply

$$aa^\dagger\Psi_\lambda = \frac{1}{2}(\lambda + 1)\Psi_\lambda \quad \text{or} \quad a^\dagger a\Psi_\lambda = \frac{1}{2}(\lambda - 1)\Psi_\lambda. \tag{1.42}$$

We have introduced the subscript λ on Ψ to track which energy eigenstate we are describing. Applying the annihilation creation operator to the second of these

$$aa^\dagger a\Psi_\lambda = \frac{1}{2}(\lambda - 1)a\Psi_\lambda, \tag{1.43}$$

and using the commutation relation gives

$$a^\dagger aa\Psi_\lambda = \frac{1}{2}(\lambda - 3)a\Psi_\lambda, \tag{1.44}$$

which looks similar to

$$a^\dagger a\Psi_{\lambda-2} = \frac{1}{2}(\lambda - 3)\Psi_{\lambda-2}. \tag{1.45}$$

Hence $a\Psi_\lambda \propto \Psi_{\lambda-1}$. Thus, applying the annihilation operator to the wavefunction lowers the energy eigenstate by one quantum. The limit of this is that annihilating the ground state wavefunction, $\Psi_{\lambda_{min}}$, is zero, hence $a^\dagger a\Psi_{\lambda_{min}} = \frac{1}{2}(\lambda_{min} - 1)\Psi_{\lambda_{min}} = 0$, and as such, $\lambda_{min} = 1$, where λ is allowed to increase in increments of 2. We can redefine

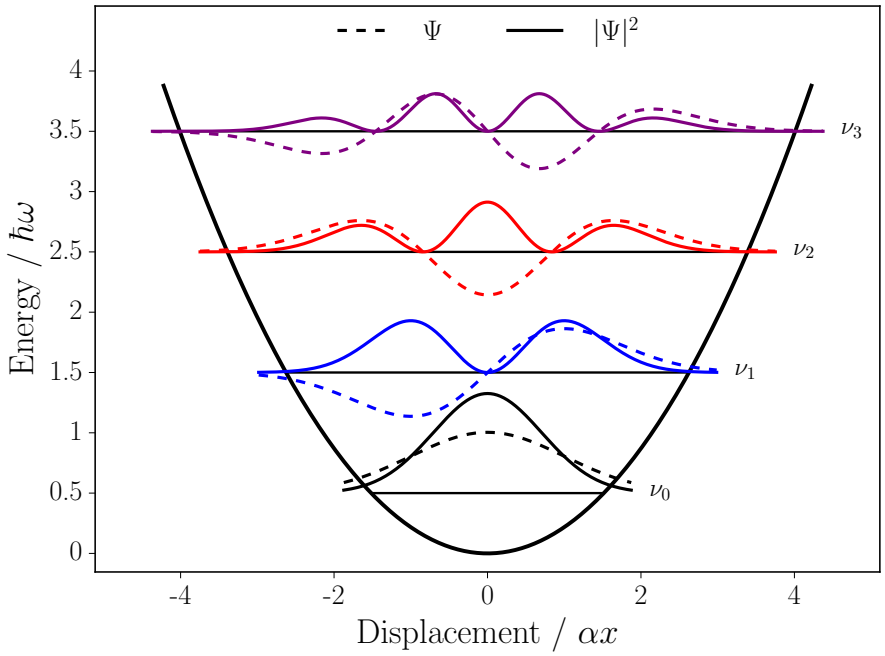

Figure 1.1 | The eigenstates, $\Psi_\nu(x)$ (dashed lines) and their corresponding eigenenergies for vibrational states $\nu = 0, 1, 2, 3$. The probability density of each eigenstate is also given (solid lines). Important observations are that each vibrational state has a quantised energy level, equally spaced by $\hbar\omega$, and is always non-zero, leading to a zero-point energy of $\frac{1}{2}\hbar\omega$ for $\nu = 0$, which can be interpreted as a consequence of the uncertainty principle. Furthermore, each wavefunction has finite amplitude outside the potential well, and thus can tunnel through an otherwise classically forbidden region. The amplitudes of all wavefunctions have been doubled for clarity.

this as, $\lambda = 2\nu + 1$, where $\nu = 0, 1, 2 \ldots$. The energy eigenvalues for the quantum harmonic oscillator (Figure 1.1), of angular frequency ω, are therefore

$$E = \left(\nu + \frac{1}{2}\right)\hbar\omega. \tag{1.46}$$

The corresponding eigenstates are found by applying, $a^\dagger$ n, times to Ψ_0, recovering the nth order eigenstate. Clearly the ground state eigenstate is the solution to $a\Psi_0 = 0$, which, using the definition of the annihilation operator in Equation 1.40 is a first-order differential equation

$$a = \frac{1}{\sqrt{2}}\left(y + \frac{\mathrm{d}}{\mathrm{d}y}\right)\Psi_0 = 0, \tag{1.47}$$

with solution

$$\Psi_0 = A_0 e^{-\frac{y^2}{2}}, \tag{1.48}$$

where A_0 is a normalisation constant. Successive eigenstates are simply $a^\dagger\Psi_0 = \Psi_1$ and $a^\dagger a^\dagger\Psi_0 = \Psi_2$ *etc.* which take the general form

$$\Psi_\nu(x) = A_\nu \mathcal{H}(\alpha x) e^{-\frac{\alpha^2 x^2}{2}}, \tag{1.49}$$

where $A_\nu = \left(\frac{\alpha}{2^\nu \nu! \pi^{\frac{1}{2}}}\right)^{\frac{1}{2}}$, $\alpha = \left(\frac{\mu k}{\hbar^2}\right)^{\frac{1}{4}}$, and $\mathcal{H}(\alpha x) = (-1)^\nu e^{-\alpha^2 x^2} \frac{1}{\alpha} \frac{\mathrm{d}^\nu}{\mathrm{d}x^\nu} e^{-\alpha^2 x^2}$ are the Hermite polynomials.

The first four wavefunctions and their corresponding probability densities are shown in Figure 1.1. A particularly important feature of this system, a feature of all wavefunctions in the presence of any finite potential, is the non-zero probability of the particle in regions outside the boundary potential, the classical limit. This is known as quantum tunnelling, a pure quantum mechanical phenomenon, and can allow some classically energetically forbidden reactions to occur with finite probability. Another important observation is that E is always greater than the minimum of the potential. The lowest vibrational state, $\nu = 0$ has energy $E = \frac{1}{2}\hbar\omega$, known as the zero-point energy of the system. This is consistent with the uncertainty principle, in that the position and parallel momentum of the system cannot both be simultaneously known to arbitrary precision. The modelling of the diatomic molecule as a harmonic oscillator has allowed us to solve the Schrödinger equation and obtain the wavefunctions of the system. This allows one to calculate the various quantities that might want to known, for example the energy of any particular vibrational state. This model, however, falls short of capturing many of the important properties of more chemically relevant systems which are discussed in the following section.

1.1.3 The Morse potential solution

A failure of the quantum harmonic oscillator lies in the assumption that any displacements are small, which means chemically important processes such as bond breaking and the existence of unbound states are inadequately described. Furthermore, the symmetric potential cannot capture the anharmonicity of real chemical bonds and thus is unable to predict overtones of vibrations. Philip Morse, in 1929,[7] suggested a simple model of an anharmonic potential which approximates the treatment of diatomic species much better, now known as the Morse potential which takes the functional form

$$V(r) = D\left(1 - e^{-a(r-r_0)}\right)^2, \tag{1.50}$$

where D is an amplitude referred to as the dissociation energy, r_0 is the equilibrium position or geometry, and a is a shape parameter. The dimension r describes the internuclear separation between the two atoms. The three variable parameters together allow the Morse potential to fit various diatomic models and thus forms the foundations of modern spectroscopy, in particular its adaptations to include long-range behaviour, although this is not discussed here.[8] The Schrödinger equation for a particle diatomic system of reduced mass μ in the presence of a Morse potential, in state $\Psi(r)$ is then

$$-\frac{\hbar}{2m}\frac{\mathrm{d}^2\Psi}{\mathrm{d}r^2}+D\left(1-e^{-a(r-r_0)}\right)^2\Psi=E\Psi. \tag{1.51}$$

Using the following substitutions:

$$x=ar;\quad x_0=ar_0;\quad \lambda=\frac{\sqrt{2mD}}{a\hbar};\quad \epsilon=\frac{2m}{a^2\hbar^2}E, \tag{1.52}$$

the Schrödinger equation is written as

$$-\frac{\mathrm{d}^2\Psi}{\mathrm{d}x^2}+\lambda^2\left(1-e^{-(x-x_0)}\right)^2\Psi=\epsilon\Psi. \tag{1.53}$$

There exists an analytical solution to the above differential equation, yielding the general normalised wavefunction for the ν^{th} state (Figure 1.2)[7,9]

$$\Psi_\nu(x)=A_\nu\eta^{(\lambda-\nu-\frac{1}{2})}e^{-\frac{\eta}{2}}L_\nu^{(2\lambda-2\nu-1)}(\eta), \tag{1.54}$$

where $\eta=2\lambda e^{-(x-x_0)}$. The normalisation constant, A_ν is related to the Gamma functions, $\Gamma(\nu)=(\nu-1)!$, with $(\nu\in\mathbb{Z}_{\geq 0})$, where

$$A_\nu=\left[\frac{(2\lambda-2\nu-1)\,\Gamma(\nu+1)}{\Gamma(2\lambda-\nu)}\right]^{\frac{1}{2}}, \tag{1.55}$$

and $L_\nu^\alpha(\eta)$ are the Laguerre polynomials, with $\alpha=(2\lambda-2\nu-1)$, defined as

$$L_\nu^\alpha(\eta)=\frac{\eta^{-\alpha}e^\eta}{\nu!}\frac{\mathrm{d}^\nu}{\mathrm{d}\eta}\left(\eta^{(\eta+\alpha)}e^{-\eta}\right). \tag{1.56}$$

These wavefunctions have the corresponding energy eigenvalues

$$E_\nu=\left[\left(\nu+\frac{1}{2}\right)-\frac{1}{2\lambda}\left(\nu+\frac{1}{2}\right)^2\right]\hbar\omega. \tag{1.57}$$

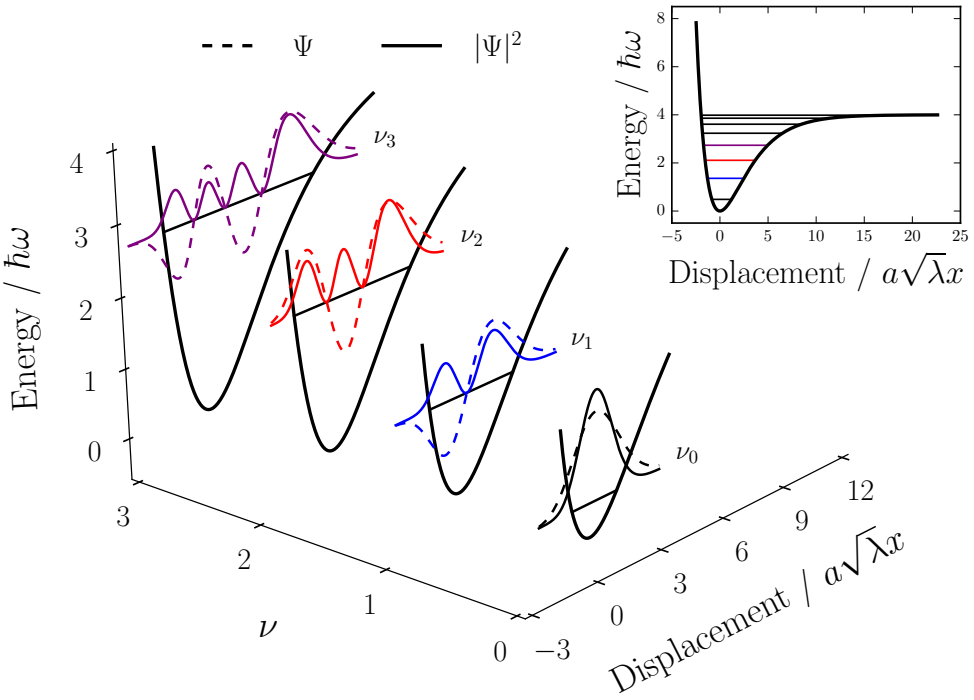

Figure 1.2 | The first four vibrational eigenstates of a diatomic species in a Morse potential. Similar observations are seen as with the quantum harmonic oscillator solutions, but with some important differences. Eigenenergies are nonlinearly spaced, converging quadratically towards the unbounded state of the potential; the probability distributions now display anharmonicity. A value of $\lambda = 8$ is used to characterise the potential.

The first four energy eigenstates of the Morse potential are shown in Figure 1.2. Once again, the vibrational energy levels are quantised but are nonlinearly spaced, quadratically converging for $\nu \to \lambda$, in contrast to the quantum harmonic oscillator. The wavefunctions display very similar nodal structure as with the quantum harmonic oscillator but are now asymmetrical, a fact which is particularly obvious in the corresponding probability distributions.

1.1.4 Hydrogenic solutions

A central problem to chemistry is the solution of the Schrödinger equation for the hydrogen atom because the solutions can be used in linear combinations to characterise more complicated molecular orbitals, something which is discussed later. Hydrogen is the simplest element with a single proton and electron. The electron 'sees' a Coulombic

(radial) electrostatic potential due to the charge of the central proton, thus the system resembles a so-called central-field problem.[1,6] Building the Hamiltonian for this system, and thus any 'hydrogen-like' system, is quite simple. The central potential, $V(r)$, is Coulombic, decaying radially from the central positive along the vector $\hat{\mathbf{r}}$ where $\mathbf{r} = x + y + z$. For a nucleus containing Z protons, the potential function is

$$V(\mathbf{r}) = -\frac{Ze^2}{4\pi\varepsilon_0 \mathbf{r}}, \tag{1.58}$$

where e is the elementary charge and ε_0 is the permittivity of free space. Treating the nucleus, with mass m_z, and electron with mass m_e, as a compound system, the reduced mass is $\mu = \frac{m_e m_z}{m_e + m_z}$ and thus the TISE takes the form

$$-\frac{\hbar}{2\mu}\nabla^2\Psi - \frac{Ze^2}{4\pi\varepsilon_0 \mathbf{r}}\Psi = E\Psi. \tag{1.59}$$

It is now useful to exploit the radial symmetry of this problem. To do this, we transform from Cartesian coordinate space into spherical polar coordinates, *i.e.* $x, y, z \to r, \theta, \varphi$, and hence $\Psi(\mathbf{r}) \to \Psi(r, \theta, \varphi)$ which leads to[‡]

$$-\frac{\hbar}{2\mu}\left(\frac{1}{r^2}\frac{\partial}{\partial r}\left(r^2\frac{\partial\Psi}{\partial r}\right) + \frac{1}{r^2\sin(\theta)}\frac{\partial}{\partial\theta}\left(\sin(\theta)\frac{\partial\Psi}{\partial\theta}\right) + \frac{1}{r^2\sin^2(\theta)}\frac{\partial^2\Psi}{\partial\varphi^2}\right) - \frac{Ze^2}{4\pi\varepsilon_0 r}\Psi = E\Psi. \tag{1.60}$$

We then assume a solution exists which separates these variables such that

$$\Psi(r, \theta, \varphi) = R(r)\Theta(\theta)\Phi(\varphi), \tag{1.61}$$

which, when substituted into Equation 1.60 yields three differential equations:

$$\frac{\partial^2\Phi}{\partial\varphi^2} = -m^2\Phi \tag{1.62}$$

$$\frac{1}{\sin(\theta)}\frac{\mathrm{d}}{\mathrm{d}\theta}\left(\sin(\theta)\frac{\mathrm{d}\Theta}{\mathrm{d}\theta}\right) - \frac{m^2}{\sin^2(\theta)}\Theta + \beta\Theta = 0 \tag{1.63}$$

$$\frac{1}{r^2}\frac{\mathrm{d}}{\mathrm{d}r}\left(r^2\frac{\mathrm{d}R}{\mathrm{d}r}\right) - \frac{\beta R}{r^2} + \frac{2\mu}{\hbar^2}\left(E + \frac{Ze^2}{4\pi\varepsilon_0 r}\right)R = 0, \tag{1.64}$$

where $-m^2$, $+\beta$ and $-\beta$ are separating constants.

[‡]Using the transformation: $r = \sqrt{x^2 + y^2 + z^2}$; $\theta = \arccos\left(\frac{z}{r}\right)$; $\varphi = \arctan\left(\frac{y}{x}\right)$, as well as the transformation of the Laplacian: $\nabla^2\Psi = \left(\frac{\partial^2\Psi}{\partial x^2} + \frac{\partial^2\Psi}{\partial y^2} + \frac{\partial^2\Psi}{\partial z^2}\right) = \frac{1}{r^2}\frac{\partial}{\partial r}\left(r^2\frac{\partial\Psi}{\partial r}\right) + \frac{1}{r^2\sin(\theta)}\frac{\partial}{\partial\theta}\left(\sin(\theta)\frac{\partial\Psi}{\partial\theta}\right) + \frac{1}{r^2\sin^2(\theta)}\frac{\partial^2\Psi}{\partial\varphi^2}$.

Solution to the zenith, $\Phi(\varphi)$, equation. The first of these differential equations, Equation 1.62, is directly integrable returning

$$\Phi_m(\varphi) = \left(\frac{1}{2\pi}\right)^{\frac{1}{2}} e^{im\varphi}; \quad m = 0, \pm 1, \pm 2 \dots \ . \tag{1.65}$$

These are also the eigenstates of the angular momentum component operator, denoted $\hat{\mathrm{L}}_z$ (Appendix 8.1), and thus m can be interpreted as the magnetic angular momentum quantum number.

Solution to the azimuth, $\Theta(\theta)$, equation. Equation 1.63 can be transformed using the substitution $z = \cos(\theta)$ into

$$\frac{\mathrm{d}}{\mathrm{d}z}\left[\left(1-z^2\right)\frac{\mathrm{d}P(z)}{\mathrm{d}z}\right] + \left[\beta - \frac{m^2}{(1-z^2)}\right]P(z) = 0, \tag{1.66}$$

which is a form of Legendre's differential equation, having solutions of the *associated Legendre polynomials*, denoted as $P_l^{|m|}(z)$, of

$$\Theta(\theta) = \left[\left(\frac{2l+1}{2}\right)\frac{(l-|m|)!}{(l+|m|)!}\right]^{\frac{1}{2}} P_l^{|m|}(z), \tag{1.67}$$

with

$$P_l^{|m|}(z) = (-1)^m (1-z^2)^{\frac{m}{2}} \frac{\mathrm{d}^m}{\mathrm{d}z^m}\left[\frac{1}{2^l l!}\frac{\mathrm{d}^l}{\mathrm{d}z^l}\left(z^2-1\right)^l\right], \tag{1.68}$$

where the term in the square bracket is the definition of the ordinary Legendre polynomials. β is found to be $l(l+1)$. Negative values of m are valid and the polynomials are given in terms of $|m|$, by

$$P_l^{-m}(Z) = (-1)^m \frac{(l-m)!}{(l+m)!} P_l^{|m|}(Z). \tag{1.69}$$

Another quantum number, $l = |m|,|m|+1, \dots$, is introduced and is referred to as the orbital angular momentum quantum number, interpreted through comparison to the eigenvalues of the total angular momentum operator, denoted $\hat{\mathrm{L}}$ (discussed in Appendix 8.1).

Given the solutions to the first two differential equations we can note a special property, one which is ubiquitous in such central-field problems, that the product of azimuth and zenith, *i.e.* $\Theta(\theta) \cdot \Phi(\varphi)$ are spherical harmonic functions (Figure 1.3),

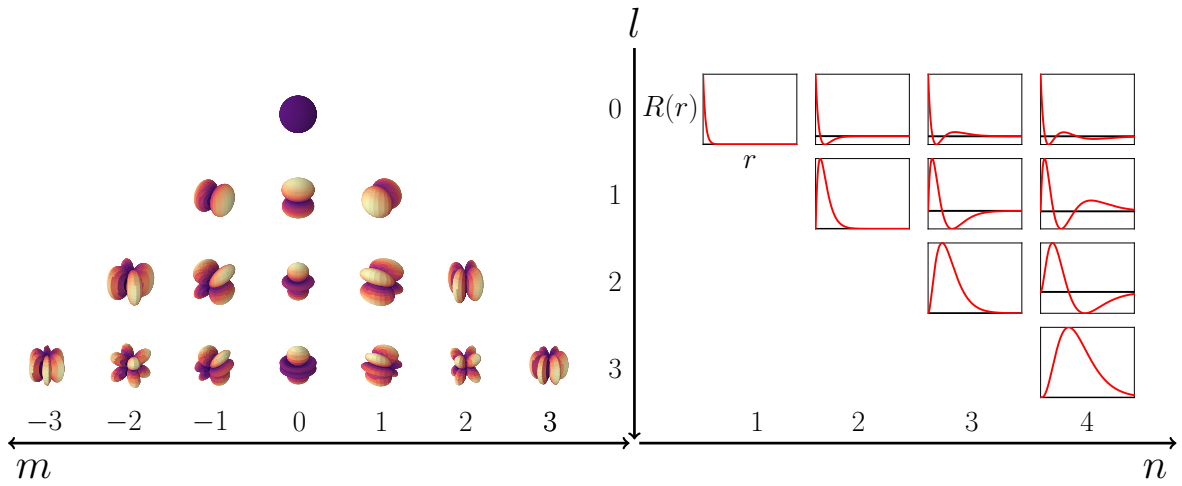

Figure 1.3 | (*left*): The first few spherical harmonics which describe the angular part of the electron wavefunction in a hydrogenic atom. (*right*): The radial (r) component of the electronic wavefunction ($R(r)$). For some orbital quantum number, l, the product of the n^{th} radial wavefunction with the m^{th} spherical harmonic gives the one-electron orbital.

denoted $Y_l^m(\theta, \varphi)$, taking the form

$$\begin{aligned} Y_l^m(\theta,\varphi) = \Theta(\theta)\Phi_m(\varphi) &= \left[\left(\frac{1}{2\pi}\right)\left(\frac{2l+1}{2}\right)\frac{(l-|m|)!}{(l+|m|)!}\right]^{\frac{1}{2}} e^{im\varphi}P_l^{|m|}(Z) \\ &= N_l^m e^{im\varphi}P_l^{|m|}(Z). \end{aligned} \tag{1.70}$$

Solution to the radial, $R(r)$, equation. Considering the final differential equation, Equation 1.64, a general solution exists which is based on the *associated Laguerre functions* [1,6]

$$R_{nl}(r) = -\left[\left(\frac{2Z}{na}\right)^3 \frac{(n-l-1)!}{2n\left[(n+l)!\right]^3}\right] \rho^l L_{n+l}^{2l+1}(\rho)e^{-\frac{\rho}{2}}, \tag{1.71}$$

where $\rho = \left(\frac{2Z}{na}\right) r$, and a third quantum number, $n = 0, 1, 2\ldots$, is introduced, referred to as the principal quantum number.

The total wavefunction for an electron in a hydrogenic atom is thus

$$\Psi(r,\theta,\varphi) = R_{nl}(r)Y_l^m(\theta,\varphi). \tag{1.72}$$

They are one-electron wavefunctions, the square of which is the probability density of finding an electron between (r, θ, φ) and $(r + \mathrm{d}r, \theta + \mathrm{d}\theta, \varphi + \mathrm{d}\varphi)$. In Figure 1.3, the first

few spherical harmonics ($Y_l^m(\theta,\varphi)$) and the radial wavefunctions (R_{nl}), are given for $n \leq 4$. If one normalises the squared radial wavefunctions by r^2, *i.e.* $r^2R_{nl}^2$ (considering the Jacobian for spherical coordinates), one recovers the familiar Radial Distribution Functions (RDFs). The extended discussion on these orbitals lies within their importance in modelling larger, more complex collection of atoms as linear combinations of these one-electron *atomic orbitals*, which are the products of spherical harmonics and radial wavefunctions. Spectroscopically, orbitals with $l = 0$ are known as 'sharp' or 's'-orbitals; $l = 1$ are called 'principal' or 'p'-orbitals; $l = 2$ are 'diffuse' or 'd'-orbitals; $l = 3$ are 'fundamental' or 'f'-orbitals, and for $l > 3$, the naming scheme follows on alphabetically from f. This nomenclature is used throughout this thesis.

1.1.5 Pauli's exclusion principle and Hund's rules

The fourth and final quantum number is *intrinsic angular momentum* called 'spin',[§] denoted m_s. It is an *ad hoc* relativistic correction to the Schrödinger equation, although falls out naturally within the Dirac equation.[10] Put simply (see literature for a more detailed discussion),[11] particles have a quantised value of spin, just as with orbital angular momentum. In fact spin angular momentum follows the same commutation relations as with orbital angular momentum (Appendix 8.1); the total spin angular momentum operator, $\hat{\mathrm{S}}^2$ and its components $\hat{\mathrm{S}}_{x,y,z}$ follow:

$$\begin{aligned}
\left[\hat{\mathrm{S}}_x, \hat{\mathrm{S}}_y\right] &= i\hbar\hat{\mathrm{S}}_z \\
\left[\hat{\mathrm{S}}_y, \hat{\mathrm{S}}_z\right] &= i\hbar\hat{\mathrm{S}}_x \\
\left[\hat{\mathrm{S}}_z, \hat{\mathrm{S}}_x\right] &= i\hbar\hat{\mathrm{S}}_y \\
\left[\hat{\mathrm{S}}^2, \hat{\mathrm{S}}_x\right] &= \left[\hat{\mathrm{S}}^2, \hat{\mathrm{S}}_y\right] = \left[\hat{\mathrm{S}}^2, \hat{\mathrm{S}}_z\right] = 0,
\end{aligned} \tag{1.73}$$

and satisfy the following eigenvalue equations:

$$\begin{aligned}
\hat{\mathrm{S}}^2 Y_l^m(\theta,\phi) &= m_s(m_s+1)\hbar^2 Y_l^m(\theta,\phi) \\
\hat{\mathrm{S}}_z Y_l^m(\theta,\phi) &= m_s\hbar Y_l^m(\theta,\phi),
\end{aligned} \tag{1.74}$$

where $m_s = \frac{1}{2}j$ for non-negative integer j, revealing the eigenvalue of the total spin angular momentum as $m_s(m_s+1)\hbar^2$ and the eigenvalue of the component is $m_s\hbar$. The salient difference is in the restriction on m_s compared to m_l, resulting in half-integer and

[§]Although this name distracts from the fact that this a pure, intrinsic quantum property of subatomic particles.

integer quantum numbers. *Fermions*, such as electrons, protons and neutrons, quarks and neutrinos, are a class of particles which all have half-integer spin quantum numbers. *Bosons*, such as photons, gauge bosons, carbon and helium nuclei, on the other hand, have integer spin. Whilst we refrain from discussing the intricacies of these classes (readers are directed to the vast literature),[10,11] the fundamental defining properties of these classes are required. Foremost, fermions obey the *Pauli exclusion principle*,[12,13] which requires the wavefunction describing the fermionic system to be antisymmetric under particle exchange. In other words, it requires that in any multi-fermionic system, fermions cannot occupy identical quantum states, *i.e.* no two fermions have the same set of four quantum numbers. The implications of this *empirical* principle are far-reaching, underpinning the very foundation of our understanding of elementary particles, and by extension, chemistry. For one of the cornerstones of modern physics, it is striking that there is still no explanation on the fundamental origin of this principle, though well-tested, it remains an open research question.[14]

A consequence of this principle is a restraint on how electrons occupy atomic orbitals. Each atomic orbital is defined by three of the four quantum numbers, n, l and m_l, thus an electron occupying such an orbital must have a matching quantum numbers to the orbital (*i.e.* the same n, l and m_l). For an electron, its spin is $\pm\frac{1}{2}\hbar$, hence for any one orbital, two electrons may occupy it, one with spin $+\frac{1}{2}\hbar$ and the other with $-\frac{1}{2}\hbar$ (often referred to as spin-up and spin-down respectively). The order with which the orbitals are occupied is governed by the empirical rules referred to as Hund's rules,[10] which predict the ground state (energetic minimum) electronic configuration of a system:

1. For a given electronic configuration, maximising the spin multiplicity, $2|S| + 1$, gives the lowest energy configuration, where $S = \max\left(\sum_i m_{s,i}\right)$.

2. For a given multiplicity, $2|S| + 1$, the configuration which maximises the total orbital angular momentum will give the lowest energy configuration, *i.e.* $L = \max\left(\sum_i m_{l,i}\right)$.

3. For an incomplete shell (of quantum number n), the total angular momentum quantum number, $J = L + S$ determines the lowest energy state. If the shell is less than half filled, the lowest energy configuration is given by $J = \min\left(|L - S|\right)$, otherwise maximise J for $J = \max\left(|L + S|\right)$.

The first rule may be understood by noting the wavefunction of a state will be more spin-symmetric if the spin multiplicity is maximised. To keep electronic wavefunctions

antisymmetric as required by the the exclusion principle, the spatial part of the wavefunction becomes more asymmetrical. In general, the more asymmetrical the spatial part of the wavefunction is, the lower the energy of that configuration. The second rule comes down to the inter-electron repulsion within orbitals. The larger the total orbital angular momentum, the smaller the average inter-electron repulsions because they, on average, experience a greater degree of separation. The final rule is a consequence of minimising the spin-orbit interaction term which arises from the interaction of an electron's spin angular momentum vector with its orbital angular momentum vector.[10]

Summary of the quantum numbers. It feels right to now summarise the set of quantum numbers in this section, and those derived from the hydrogen atom solutions. The principal quantum number n determines the energy of the orbital (or shell) for the electron, and is any non-zero, positive integer. The orbital angular momentum of an electron is given by l, restricted by n such that, $l = 0, 1, 2, \ldots, n-1$. The magnetic angular momentum quantum number, m_l, describes the projection of the orbital angular momentum onto a particular axis, and is restricted by integer values such that $-l \leq m_l \leq l$. Finally, the spin quantum number, m_s, describes the intrinsic angular momentum, which for an electron, is always $m_s = \pm\frac{1}{2}$.

1.1.6 Molecular orbital theory

Solving the Schrödinger equation for the hydrogen atom gave us the form of the wavefunction and thus the probability densities for each electronic orbital, which forms the foundation of atomic orbital theory. However, as a system grows in size, solving the Schrödinger equation becomes impossible because one is unable to correctly describe the correlation between the motion of multiple electrons, the subject of the succeeding section. Given this, approximate orbitals are chosen to describe a system, which are then optimised to minimise some quantity, usually total energy. In *molecular orbital theory*, an infinite set of atomic orbitals, χ_i, *cf.* Equation 1.72, are used as the initial approximation, each with a expansion coefficient, c_i, which together describe a molecular orbital, Ψ, known as the Linear Combination of Atomic Orbitals (LCAO),[1]

$$\Psi = \sum_{i}^{\infty} c_i \chi_i. \tag{1.75}$$

The set of the initial approximate atomic orbitals which are to describe the final molecular orbitals is known as a *basis set*.[15] Of course, in practice, such an infinite basis set is mathematically intractable, and a finite basis set is used. This means that when

working within molecular orbital theory, a prominent example being computational chemistry, a decision on where a basis set is truncated has to be taken, which will limit the accuracy of calculated properties.

The result of the LCAO is an array of molecular orbitals. A clear example of this can been seen with diatomic fluorine (Figure 1.4). On either side of the diagram, a fluorine atom, which will have atomic orbitals very close to those of hydrogenic atoms, covalently bonds to the second fluorine atom. The result is a diatomic molecular system. The corresponding molecular orbitals are shown, and are labelled as 'σ' or 'π' orbitals, their subscripts denoting the specific LCAO which form them. σ orbitals are formed from the superposition of atomic orbitals which exist in the same plane, which, for the example given in Figure 1.4, can be achieved through the superposition of two s orbitals, two p_z-orbitals, or one s and one p_z orbital. Similarly, for π orbitals, these are described by the superposition of two p_x or p_y orbitals which lie in same plane, with overlapping probability densities. Both σ and π-orbitals are referred to as 'bonding-orbitals' because they are formed through the constructive interference of atomic orbital wavefunctions. Since wavefunctions have phase, destructive interference can occur, which results in 'anti-bonding' orbitals, where additional nodes are introduced. Anti-bonding orbitals are denoted by an asterisk, *i.e.* σ^*, π^* *etc.* Finally, it is possible that the atomic orbitals from each atom in a molecule combine with zero overlap, perhaps because of symmetry, which leaves a 'non-bonding' orbital. These are most often found in molecule systems which have atoms with lone pairs of electrons, *e.g.* nitrogen. Non-bonding molecular orbitals are denoted as n. The power of the LCAO approach comes from the fact that any complicated electronic density can be described using partial amounts of s, p, d *etc.* orbitals by optimising the coefficients c_i and increasing the number of basis functions used; the iterative procedure in achieving this optimisation is discussed later.

The choice of the basis functions used to form the basis set is important if one is to describe the relevant chemistry accurately. In order to reproduce the radial wavefunction (*cf.* Figure 1.3), a sensible choice needs to be made. Intuitively, an exponential decay function would model the radial wavefunction well, such as[19]

$$R(r) = Nr^{n-1}e^{-\zeta r}, \tag{1.76}$$

known as Slater Type Orbitals (STOs), where n is the principal quantum number, N and ζ are constants. However, it was recognised that linear combinations of Gaussian functions are much more practical;[20] enormous computational savings could be achieved exploiting the Gaussian Product Theorem, where the product of two Gaussian functions

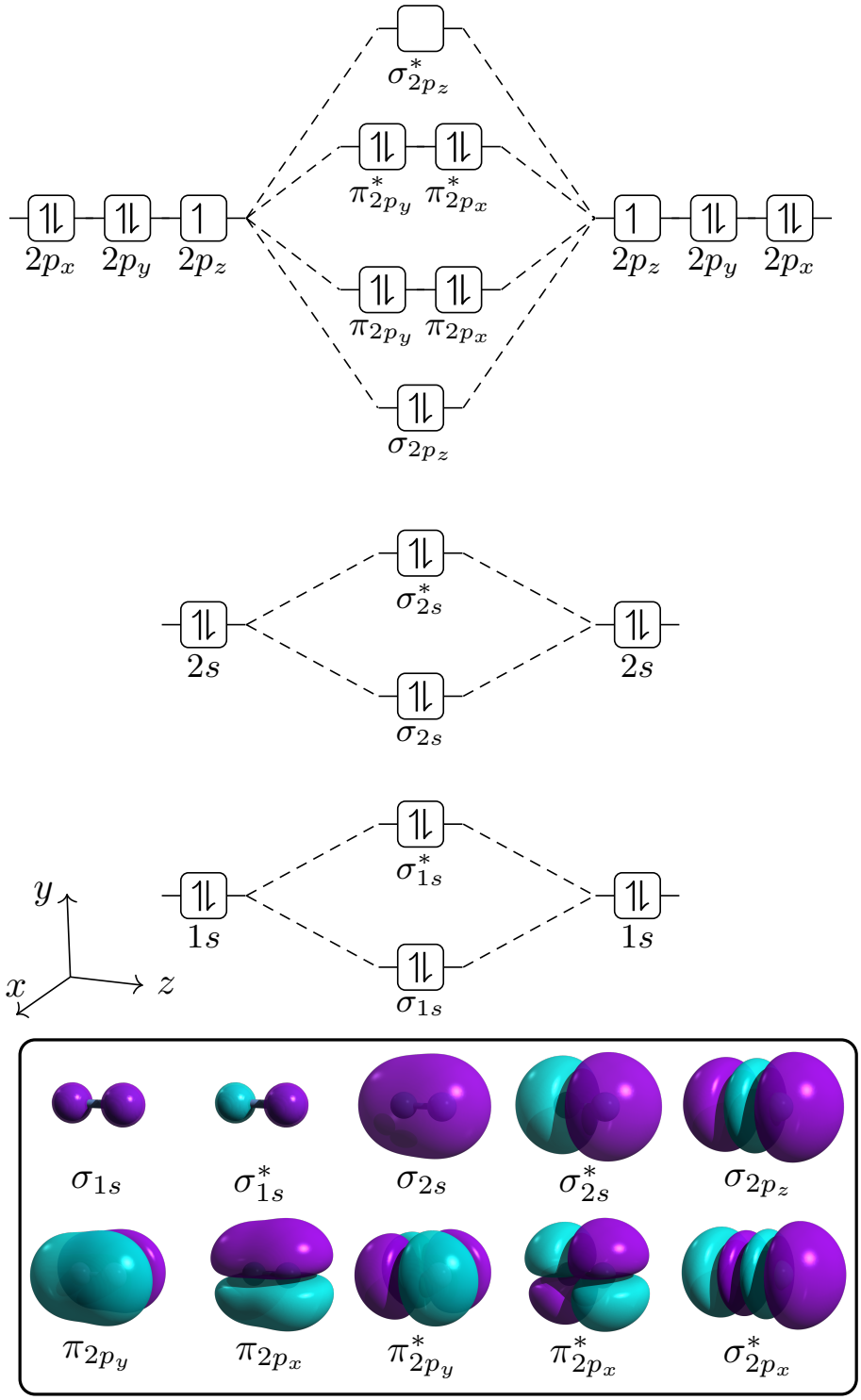

Figure 1.4 | An example of the LCAO principle used to describe the molecular orbitals for diatomic fluorine, where blue and purple represent the phase of the wavefunction.[16–18] Molecular orbitals optimised using the B3LYP functional and the 6-31G* basis set (discussed later).

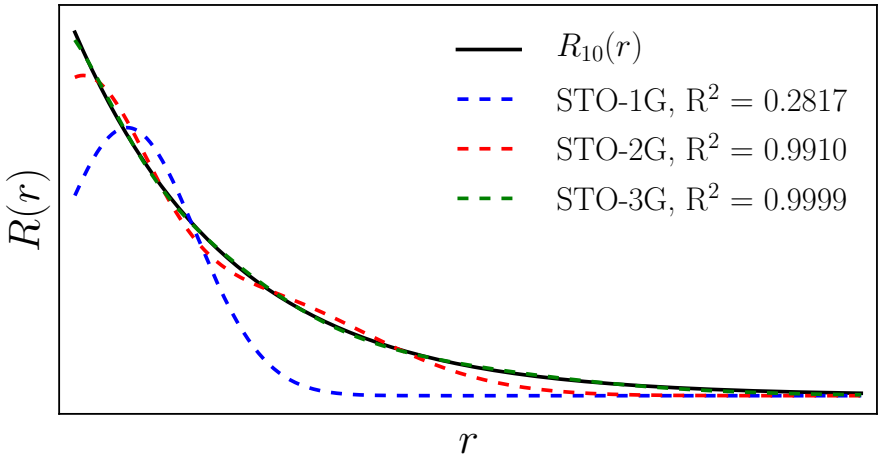

Figure 1.5 | The radial wavefunction for a hydrogen 1s orbital is very well described by the sum of three Gaussian functions ($R^2 = 0.9999$).

could be replaced by a single (weighted) Gaussian function. As such, Gaussian Type Orbitals (GTOs) have become by far the most common basis functions used in basis sets, pioneered by John Pople,[21–23] where a STO is approximated by n Gaussian functions, such that

$$R(r) \approx \sum_{i}^{n} \left(\frac{2\alpha_i}{\pi}\right)^{\frac{3}{4}} e^{-\alpha_i (r-r_i)^2} \tag{1.77}$$

where α_i and r_i are to-be-determined parameters. The applicability of these functions can be seen when compared to a typical radial wavefunction (Figure 1.5). As Figure 1.5 shows, a typical radial wavefunction can be expressed very well as the linear combination of Gaussian functions. These are so-called minimal basis sets, known as the STO-nG sets, where n is the number of Gaussian functions used to described the STO. An enormous research effort has gone into, and continues towards, generating basis sets which are more flexible, widely applicable, and better at describing a myriad of molecular states.[24–28] One of these has already been described; the use of contracted Gaussian functions has found wide-spread use, where a linear combination of Gaussian functions is used for a single basis function (such as the STO-2G and STO-3G sets). However, for polyatomic systems, such a description may been inadequate, where two atoms come close together. Instead, split-valence basis sets are used, where a valence orbital is described by more than one set of contracted Gaussian functions. For example the 6-31G basis set uses 6 contracted Gaussian functions for core orbitals, while using 3 contracted Gaussian functions and an additional 1 Gaussian function to describe

each valence electron. Another modification is the use of polarisable (often denoted with an '$*$') and diffuse functions (often denoted with a '+'), which allow orbitals to become distorted in the presence of charges or long-range interactions between different orbitals.[29,30] This is in no way a complete discussion on basis sets, rather a primer, justifying the use of many different basis sets throughout this work.[15,31–33]

1.1.7 Many-body Hamiltonians: Born-Oppenheimer approximation

So far we have solved the Schrödinger analytically for systems which contain one electron, or one electron and one proton, the latter yielding a set of hydrogenic solutions to atomic hydrogen. The problem which remains, one which underpins all quantum chemistry research, is that *all* other systems contain three or more bodies, and thus the Schrödinger equation cannot be solved analytically. Instead, a number of approximations must be made in order to progress. The first approximation is known as the Born-Oppenhiemer (BO) approximation.[1,3,6] This approximation makes use of the fact that the mass of a proton, m_p is significantly larger than that of the electron, m_e, where $\frac{m_p}{m_e}$ $\sim$1836. Within this framework, one can consider the response of electrons to changes in the nuclear geometry as instantaneous. Thus at any one particular nuclear geometry, the nuclei are fixed and the Schrödinger equations for the electrons and the nuclei are decoupled and solved separately. The simplest example which introduces the BO approximation, is the Potential Energy Surface (PES) of the three-body molecular system for a diatomic hydrogen ion, H_2^+ (Figure 1.6).

The two nuclei (protons) are positioned at z_1 and z_2, and the shared electrons at z. The total Hamiltonian for this system is

$$\hat{\mathrm{H}} = -\frac{\hbar^2}{2m_e}\frac{\partial^2}{\partial z^2} - \sum_{i=1}^{2}\frac{\hbar^2}{2m_p}\frac{\partial^2}{\partial z_i^2} + V\left(z, z_1, z_2\right) = T_e + T_n + V, \tag{1.78}$$

where T_e, T_n are the kinetic energies of the electron and nuclei respectively, and V the potential energy of the system. The Schrödinger equation is

$$\hat{\mathrm{H}}\Psi(z_1, z_2) = E\Psi(z, z_1, z_2), \tag{1.79}$$

but we assume a solution exists of the form

$$\Psi(z, z_1, z_2) = \psi_e(z; z_1, z_2)\psi_n(z_1, z_2), \tag{1.80}$$

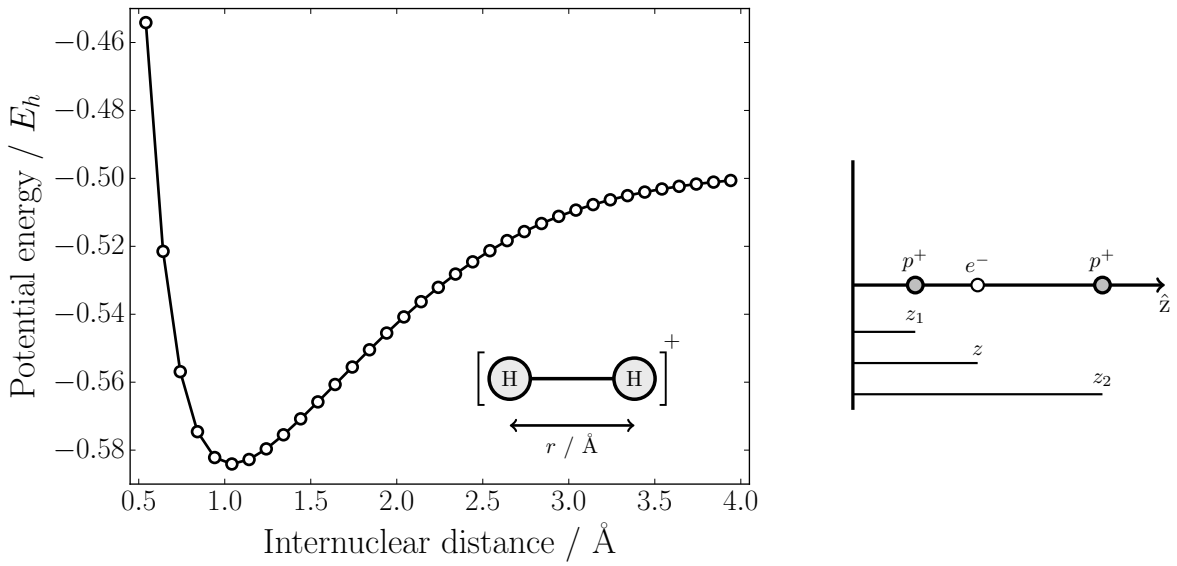

Figure 1.6 | (*left*): The PES for H_2^+ (calculated at the Hartree-Fock level of theory, with a 6-31G basis set, discussed later).[17,22] Each point on the curve represents a different nuclear geometry, in this case, an increasing internuclear distance. At each point the total energy is calculated, under the assumption the nuclei positions are fixed. The equilibrium geometry is found at the energy minimum, around 1 Å. (*right*): A 1-dimensional analogue of the three body H_2^+ problem, as used to illustrate the BO approximation.[1]

where $\psi_e(z; z_1, z_2)$ is the electronic wavefunction which depends parametrically on the nuclear coordinates, and $\psi_n(z_1, z_2)$ is the nuclear wavefunction. On substitution into Equation 1.79, we find

$$\hat{\mathrm{H}}\psi_e\psi_n = \psi_n T_e\psi_e + \psi_e T_n\psi_n + V\psi_e\psi_n - \sum_{i=1}^{2}\frac{\hbar^2}{2m_{p,i}}\left(2\frac{\partial\psi_e}{\partial z_i}\frac{\partial\psi_n}{\partial z_i} + \frac{\partial^2\psi_e}{\partial z_i^2}\psi_n\right) = E\psi_e\psi_n. \tag{1.81}$$

The final term on the left hand side, the summation over the nuclei, contains a denominator of m_p which, under the BO approximation, we can assume is small compared to the other terms. Of course, this term depends on both the electronic and nuclear wavefunctions, and as such, if a discontinuity exists, it renders the derivative of the electronic wavefunction with respect to the nuclear coordinates ill-defined, and the BO approximation breaks down. The breakdown of the BO approximation is well-known and presents a serious issue for modern day electronic structure calculations. Other methods, some of which are discussed later, can work around regions of potential energy curves or surfaces where the dependency of the electronic wavefunction on the

nuclear geometry is too large to be neglected, perhaps the most notable example of this is at conical intersections (discussed in Section 2.1).[34] Continuing with the BO approximation by neglecting the small terms, Equation 1.81 becomes

$$\psi_e T_n \psi_n + \left(T_e \psi_e + V\psi_e\right)\psi_n = E\psi_e\psi_n. \tag{1.82}$$

The terms in the parentheses give the Schrödinger equation for the electronic sub-system only, which has the form

$$T_e\psi_e + V\psi_e = E_e(z_1, z_2)\psi_e, \tag{1.83}$$

i.e. an electron in a potential V, which depends on the nuclear coordinates. This can be substituted into Equation 1.82 to give

$$\psi_e T_n \psi_n + E_e\psi_e\psi_n = E\psi_e\psi_n, \tag{1.84}$$

which, left multiplying by ψ_e and integrating, noting $\langle\psi_e|\psi_e\rangle = 1$ for a normalised wavefunction, yields

$$T_n\psi_n + E_e\psi_n = E\psi_n, \tag{1.85}$$

which is the Schrödinger equation for the nuclear wavefunction but with the nuclear potential energy written in terms of the electronic energy as calculated by Equation 1.84. The BO approximation only solves the hydrogen ion exactly; its use in other molecular species introduces an inherent approximation. However, despite this, it remains almost universally used and any deviation from the true energy is essentially negligible if the electronic states of a system are not strongly coupled.

For the work presented in this thesis, we are most concerned with the electronic Schrödinger equation, Equation 1.83 since this is required to calculate any electronic structure properties. The general electronic Hamiltonian for any molecular system describing N_e electrons at positions $\mathbf{r}$, and N_n nuclei of charge Z at positions R, and its corresponding electronic Schrödinger equation under the BO approximation is therefore

$$\hat{\mathrm{H}} = -\frac{\hbar^2}{2m_e}\sum_i^{N_e}\nabla_i^2 - \sum_i^{N_e}\sum_j^{N_n}\frac{Z_j e^2}{4\pi\epsilon_0 r_{ij}} + \frac{e^2}{4\pi\epsilon_0}\sum_{i>j}^{N_e}\frac{1}{r_{ij}} + \sum_{i>j}^{N_n}\frac{Z_i Z_j}{4\pi\epsilon_0 R_{ij}} \tag{1.86}$$

and

$$\hat{\mathrm{H}}\psi(\mathbf{r};\mathbf{R}) = E(\mathbf{R})\psi(\mathbf{r};\mathbf{R}). \tag{1.87}$$

The final term, the nuclear-nuclear repulsion term is usually accounted for as a classical correction to the total energy, and thus is easy to calculate. However, the problem that

remains is in trying to correctly describe the electron repulsion term, r_{ij}, which is the subject of the next section.

1.1.8 Many-body Hamiltonians: Hartree-Fock

The first step to providing a model to account for electron repulsion, and thus solving the Schrödinger equation, is to assume each electron experiences a repulsion of the mean Coulombic field of the $N_e - 1$ remaining electrons, *i.e.* reducing the system to a central field problem. This model was suggested by Hartree[35,36] and later improved upon by Fock to include exchange effects,[37] known as Hartree-Fock (HF), and its implementation is known as the Hartree-Fock Self-Consistent Field (HF-SCF) method.[1,38]

In this model, the exact N_e wavefunction, Ψ, is written as the product of N_e one-electron wavefunctions, $\psi_m(i)$, where $\psi_m(i)$ implicitly represents the i^{th} electron in orbital m at position r_i, and is parametrically dependent on nuclear coordinates, $\mathbf{R}$. It is also assumed that such a wavefunction is a solution of the TISE, analogous to the N_e wavefunction in Equation 1.87

$$\hat{\mathrm{h}}_i \psi_m(i) = E_m \psi_m(i), \tag{1.88}$$

where the total Hamiltonian is constructed from the sum of the N_e one electron Hamiltonians, *i.e.* $\hat{\mathrm{H}}_i = \sum_i^{N_e} \hat{\mathrm{h}}_i$. As stated, the overall wavefunction can be written as the product of the one-electron wavefunctions

$$\Psi = \prod_{i,m}^{N_e} \psi_m(i). \tag{1.89}$$

However, such a wavefunction is not necessarily antisymmetric, an absolute requirement of the Pauli exclusion principle. A solution to this is to introduce the concept of the spinorbital, denoted $\phi_m(i)$ which, as the name suggests, is a product of both orbital and spin functions, with each spinorbital orthonormal to one another. To ensure adherence to the Pauli exclusion principle, a Slater determinant is used

$$\Psi = \frac{1}{(N_e!)^{\frac{1}{2}}} |\phi_1(i)\phi_2(i)\dots\phi_{N_e}(i)|, \tag{1.90}$$

where only the principal diagonal is given. Applying the variational theorem (Appendix 8.2) with the constraint that spinorbitals must be orthonormal allows their optimisation,[1] which, for a closed-shell system with doubly occupied orbitals, leads to the HF

equation for individual orbital wavefunctions

$$\hat{\mathrm{f}}_1\phi_m(1) = \epsilon_m\phi_m(i), \tag{1.91}$$

where $\hat{\mathrm{f}}_1$ is the Fock operator, and ϵ_m the electronic energy of orbital m. The Fock operator is defined by two operators, the Coulomb operator, $\hat{\mathrm{J}}_m$, and the exchange operator, $\hat{\mathrm{K}}_m$:[1,39]

$$\hat{\mathrm{f}}_1 = \hat{\mathrm{h}}_1 + \sum_{m'}\left[2\hat{\mathrm{J}}_{m'}(1) - \hat{\mathrm{K}}_{m'}(1)\right] \tag{1.92}$$

$$\hat{\mathrm{J}}_{m'}(1)\psi_m(1) = \frac{e^2}{4\pi\epsilon_0}\int \psi^*_{m'}(2)\frac{1}{r_{12}}\psi_m(1)\psi_{m'}(2)d\tau_2 \tag{1.93}$$

$$\hat{\mathrm{K}}_{m'}(1)\psi_m(1) = \frac{e^2}{4\pi\epsilon_0}\int \psi^*_{m'}(2)\frac{1}{r_{12}}\psi_{m'}(1)\psi_m(2)d\tau_2. \tag{1.94}$$

The Coulomb term originates from the electrostatic repulsion between the electron in orbital m, and the average electrostatic field of the remaining $N_e - 1$ electrons in orbitals m'. The exchange term on the other hand originates from the constraint on the wavefunction that it is antisymmetric, arising from the ability to interchange the indistinguishable electrons between the same spin states. In an iterative fashion, the trial wavefunction can be optimised in order to minimise the total energy of the system with respect to a variational restraint. This is a so-called Self-Consistent Field (SCF) method.[1] A problem, however, emerges when one tries to apply this HF-SCF procedure to many-body molecular systems because they no longer possess the spherical symmetry that isolated atoms do. Roothaan and Hall proposed a solution to this which has now become the standard procedure for modern day HF-SCF procedures.[40,41] Using the LCAO to express molecular orbitals is much more convenient and flexible. As stated in Equation 1.75, a wavefunction can be described by the linear combination of N_b basis functions, *i.e.* $\psi_m = \sum_i^{N_b} c_i^m\chi_i$. Substituting this into Equation 1.91 gives

$$\hat{\mathrm{f}}_1\sum_i^{N_b} c_i^m\chi_i(1) = \epsilon_m\sum_i^{N_b} c_i^m\chi_i(1). \tag{1.95}$$

Left multiplying by $\chi^*_{i'}$ and integrating over all space gives

$$\sum_i^{N_b} c_i^m \underbrace{\int \chi^*_{i'}\hat{\mathrm{f}}_1\chi_i(1)d\tau}_{\hat{\mathrm{F}}_{i',i}} = \epsilon_m\sum_i^{N_b} c_i^m \underbrace{\int \chi^*_{i'}\chi_i(1)d\tau}_{\hat{\mathrm{S}}_{i',i}}, \tag{1.96}$$

where two new matrix elements are introduced for convenience. The first is the Fock

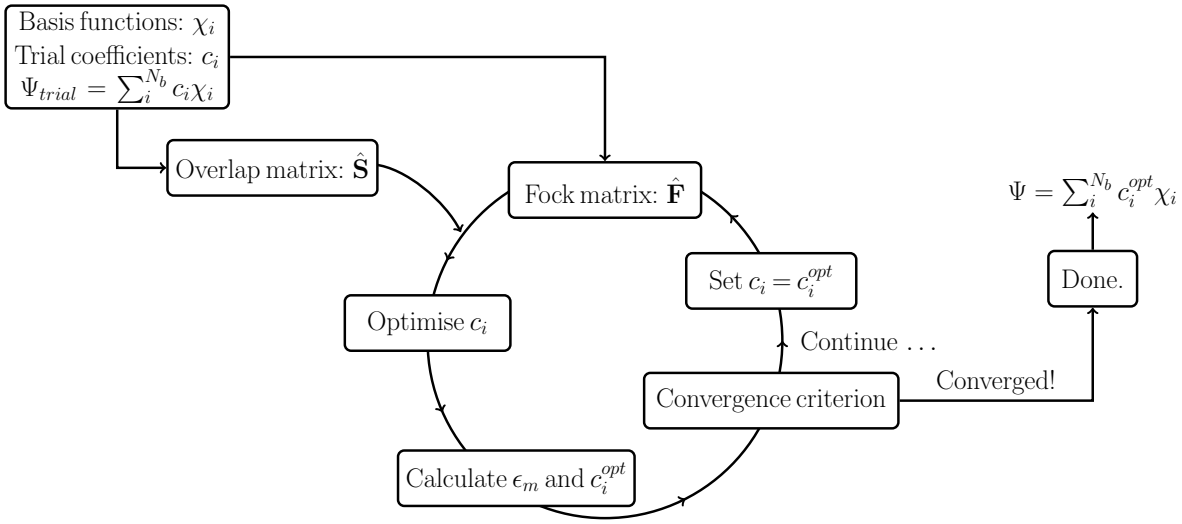

Figure 1.7 | Overview of the HF-SCF procedure. The basis functions are selected and do not change during iterations. A set of trial coefficients are selected and thus a trial wavefunction is defined. The overlap matrix, $\hat{\mathbf{S}}$, is calculated and does not change since it only depends on the basis functions. The Fock matrix, $\hat{\mathbf{F}}$, is built as described in the text. The coefficients are then varied in some manner, *via* the variational principle (Appendix 8.2). A set of one-electron orbital energies and basis function coefficients are obtained. Some metric is calculated and compared to a predefined convergence criterion, often the total energy and gradient of the system. If these criteria are met, the final wavefunction is obtained and used to calculate the properties required. If the criteria are not met, the new coefficients are set as the trial coefficients and the cycle repeats until convergence is achieved.

matrix, $\hat{\mathrm{F}}_{i',i}$, which is the expectation value of the Fock operator $\hat{\mathrm{f}}_1$, and the second is the overlap matrix, $\hat{\mathrm{S}}_{i',i}$, a measure of the spatial overlap between pairs of basis functions. The set of equations given in Equation 1.96 can be compactly written as the matrix equation

$$\hat{\mathbf{F}}\mathbf{c} = \boldsymbol{\epsilon}\hat{\mathbf{S}}\mathbf{c}. \tag{1.97}$$

Here $\mathbf{c}$ is an N_b by N_b matrix of c_i^m coefficients, and $\boldsymbol{\epsilon}$ is a vector of one-electron orbital energies. This equation has a non trivial solution if the determinant of its corresponding secular equation is zero, thus $\left|\hat{\mathbf{F}} - \boldsymbol{\epsilon}\hat{\mathbf{S}}\right| = 0$. The problem however is that both the Fock matrix and the orbital energies depend on the coefficients, c_i^m, which themselves need to be optimised, hence an iterative self consistent field approach is needed, as summarised in Figure 1.7.

Unfortunately, whilst this HF implementation of HF-SCF shows an important result, the ability to solve this complicated equation to obtain the wavefunction, the approximation taken at the start that the electrons see a mean field Coulomb repulsion

turns out to be an enormous approximation. The energy calculated within the HF framework, E_{HF}, is too high. The reason for this is that electrons are correlated, in that (*i*), the position of one electron spatially changes the Coulomb repulsion felt on all other electrons, *i.e.* the instantaneous Coulomb interactions between electrons and (*ii*), it neglects all quantum mechanical effects originating from electron distribution of the remaining $N_e - 1$ electrons. The vast majority of quantum chemistry method development is spent on trying to improve how electron correlation is accounted for. In the following section we introduce some of the common ways this done.

1.1.9 Post-Hartree-Fock *ab initio* methods: Accounting for electron correlation

Configuration interaction. Even at the HF limit, where an infinite basis set is used, the HF wavefunction is still not the exact ground state wavefunction since it does not account for electron correlation, where more than one electron is present. Instead, one can express the ground state wavefunction, Ψ, as a linear combination of all the N_e possible Slater determinants for all possible electronic excitations. For example, after a set of HF orbitals have been established, the Slater determinant with one electron in spinorbital ϕ_l is promoted to a higher-energy orbital $\psi_{l'}$, which is denoted by $\Psi_l^{l'}$ with a coefficient $c_l^{l'}$. Similarly for a double excitation, one electron in spinorbital ϕ_l is promoted to $\phi_{l'}$ and another in spinorbital ϕ_m is promoted to $\phi_{m'}$, denoted by the modified wavefunction $\Psi_{l,m}^{l',m'}$. This expression is continued to include the entire unique combinatorial space of single excitations, double excitations, triple excitations *etc.* Thus the exact ground state wavefunction can be written as

$$\Psi = c_0\Psi_0 + \sum_{l,l'} c_l^{l'}\Psi_l^{l'} + \sum_{\substack{l<m \\ l'<m'}} c_{l,m}^{l',m'}\Psi_{l,m}^{l',m'} + \sum_{\substack{l<m<n \\ l'<m'<n'}} c_{l,m,n}^{l',m',n'}\Psi_{l,m,n}^{l',m',n'} \ldots \,. \tag{1.98}$$

This wavefunction model is known as (full) Configuration Interaction (CfI).[1] The calculated energy with this model, E_{CI} is the exact ground state energy of the system within the framework of the BO approximation, and of course, excluding relativistic corrections. The electron correlation energy, E_{ec} can be defined as

$$E_{ec} = E_{\mathrm{CI}} - E_{\mathrm{HF}}, \tag{1.99}$$

i.e. the difference between the exact HF energy (using an infinite basis set) and the full-CfI energy. In practice, a finite basis set is used, and thus the calculated energy

difference between these two *ab initio* methods using the same sized basis set is know as the *basis-set correlation energy*, hence practically, a full-CfI calculation is one which involves all the combinatorial excitations for a given basis set. The CfI wavefunction in Equation 1.98 can be written as

$$\Psi = \sum_{i=1} C_i \Psi_i, \tag{1.100}$$

where C_i are expansion coefficients about the number of excitations, i. The C_i coefficients can be determined *via* the variational principle. Thus the total procedure for a CfI calculation is an initial HF-SCF calculation, which is then augmented by the CfI calculation. A full-CfI calculation is usually too computationally expensive for even reasonably small systems with moderate basis sets, and as such if some of C_i coefficients are not included in the wavefunction expansion, we get a *limited*-CfI wavefunction model. This is generally fine so long as the calculation remains *size-consistent*, that is, the energy of many-electron system is proportional to the number of electrons in the system, something which is not general to limited-CfI.¶

Multiconfiguration self-consistent field. A popular compromise between CfI and HF calculations is Multiconfigurational Self-Consistent Field (MCSCF). MCSCF methods use the procedure of limited-CI calculations but with a salient difference; both the coefficients of the orbital basis functions, c_i, and the expansion CfI coefficients, C_i, are optimised during the SCF procedure. Though this method is more computationally expensive, because two sets of parameters are optimised during each cycle of the SCF routine, results are more accurate even with a truncated set of expansion coefficients. These methods are extensively used in excited state calculations, where the electronically excited-state wavefunction is wanted, important for many chemical processes such as bond dissociation, and spectroscopy in general. The most widely used scheme is probably the Complete Active-Space Self-Consistent Field (CASSCF) method (Figure 1.8).[42] As with all MCSCF methods, both the basis coefficients and expansion coefficients are optimised during each SCF cycle. However, because such calculations are very computationally demanding as a system's size grows, in CASSCF, the set of spatial wavefunctions are split into three sub-sets (Figure 1.8).[1]

(*i*) The first is a set of *inactive orbitals* which comprise of doubly occupied orbitals with the lowest spatial energy. (*ii*) The second is a set of *virtual orbitals*, none of which are occupied, and in general are of much higher energy than the inactive orbitals.

¶A system XY is size-consistent if the calculated energy of the XY system is the sum of the energies of the isolated systems, X and Y, *i.e.* $E(\mathrm{XY}) = E(\mathrm{X}) + E(\mathrm{Y})$.[1]

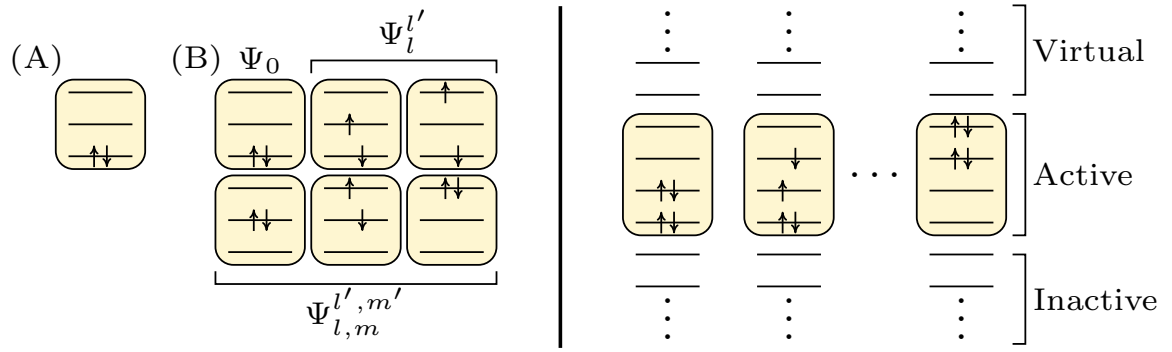

Figure 1.8 | (*left*): (A) The HF ground state configuration for an example molecular system described in the basis of three molecular orbitals. (B) The full-CfI wavefunction for this example system (*cf.* Equation 1.98). (*right*): A similar example, instead using the CASSCF procedure, for a larger molecular system, involving a choice of inactive, active and virtual orbitals, as described in the main text.[42]

(*iii*) The final set, the *active orbitals*, are found in the energetic intermediate between inactive and virtual orbitals. This active space is a set of orbitals in which N electrons are distributed in all possible combinations, *i.e.* a full-CfI within the active space. However, CASSCF will only give reliable results if a good (chemical) choice of orbitals is chosen. The set of active orbitals and virtual orbitals is often referred to colloquially as the 'CAS-space'. The biggest issue with CASSCF is picking a CAS-space which describes the chemistry well enough, whilst minimising the size of the space to make it computationally feasible.

A further methodology which reduces the computational expense is that of the Restricted Active-Space SCF (RASSCF) scheme. Here the set of active orbitals is divided further into three sets. (*i*) Specified orbitals which are doubly occupied, except for some defined maximum number of excitations allowed in this sub-set. (*ii*) Specified orbitals where any combinatorial excitation is allowed (*i.e.* CASSCF). (*iii*) Specified orbitals which are unoccupied except for a defined number of allowed electrons allowed in this sub-set. This scheme of work reduces the number of calculations which would have otherwise been done in CASSCF if one is confident certain orbitals are weakly correlated with others in the active space.

Møller-Plesset many-body perturbation theory. As an alternative to the CfI methods discussed above, Perturbation Theory (PT) is a size-consistent method which can systematically correct for the correlation energy. PT is not variational and therefore does not necessarily give an upper bound to the total energy instead, increasingly higher

order terms are included with the sum assumed to converge to the exact energy.[43,44] Applied to quantum chemistry, the implementation of PT to approximate the correction of electron correlation to the HF energy is known as *Møller-Plesset many-body perturbation theory.*[45] The perturbation applied, $\hat{\mathrm{H}}^{(1)}$, is the difference between the exact many-body Hamiltonian (Equation 1.86) and the HF Hamiltonian (the sum of one-electron Fock operators; Equation 1.92), known as the correlation potential

$$\hat{\mathrm{H}}^{(1)} = \hat{\mathrm{H}} - \hat{\mathrm{H}}^{(0)}, \tag{1.101}$$

where

$$\hat{\mathrm{H}}^{(0)} = \sum_{i=1}^{N_e} \hat{\mathrm{f}}_i. \tag{1.102}$$

This choice of perturbation comes from the fact that one is interested in the electron correlation for the ground state, and is the choice in its original formulation in 1934.[45] As such, the perturbing Hamiltonian for electron i is

$$\hat{\mathrm{H}}^{(1)}(i) = \frac{e^2}{4\pi\epsilon_0} \sum_{i \neq j} \frac{1}{r_{ij}} - \sum_m \left(2\hat{\mathrm{J}}_m(i) - \hat{\mathrm{K}}_m(i) \right), \tag{1.103}$$

where m is the sum over occupied orbitals (*cf.* Equation 1.92). Considering the lowest eigenstate of the Fock operator, ϕ_0, the perturbation corrections to the energy (up to the second order) are[1]

$$\begin{aligned} E^{(0)} &= \langle \phi_0 | \, \hat{\mathrm{H}}^{(0)} \, | \phi_0 \rangle = E_{\mathrm{HF}} \\ E^{(1)} &= \langle \phi_0 | \, \hat{\mathrm{H}}^{(1)} \, | \phi_0 \rangle = 0 \\ E^{(2)} &= \sum_{j \neq 0} \frac{\langle \phi_j | \, \hat{\mathrm{H}}^{(1)} \, | \phi_0 \rangle \, \langle \phi_0 | \, \hat{\mathrm{H}}^{(1)} \, | \phi_j \rangle}{E_0^{(0)} - E_j^{(0)}}. \end{aligned} \tag{1.104}$$

The first energy term is simply the expectation value of the unperturbed Hamiltonian, *i.e.* the HF energy. The first perturbation correction is zero under this construction of the perturbation Hamiltonian, hence the first correction which accounts for any electron correlation is the second perturbation term and is referred to as the Møller-Plesset 2nd-Order Perturbation Theory (MP2) correction. Thus, the energy calculated, with some of the electron correlation accounted for, is

$$E \approx E_{\mathrm{HF}} + E^{(2)}. \tag{1.105}$$

This method is widely employed in quantum chemistry calculations, and higher order corrections can be used, such as MP3 or MP4, but these often do not improve the calculated molecular properties enough to justify the increased computational cost.[46]

Coupled-cluster method. A related method to the CfI wavefunction model discussed above is the Coupled-Cluster (CC) method.[1] This method is not variational, although it is size-consistent. Here the exact wavefunction, Ψ, is related to the HF wavefunction, Ψ_0, by the exponentiated cluster operator, $\hat{\mathrm{C}}$,

$$\Psi = e^{\hat{\mathrm{C}}}\Psi_0 = \sum_{i=0}^{\infty} \frac{\hat{\mathrm{C}}_i}{i!}\Psi_0, \tag{1.106}$$

where

$$\hat{\mathrm{C}} = \sum_{i=0}^{N_e} \hat{\mathrm{C}}_i. \tag{1.107}$$

The terms of the cluster operator are not known, but each operator pulls out the sum of one-electron effects ($\hat{\mathrm{C}}_1$) and two-electron effects ($\hat{\mathrm{C}}_2$) *etc.* In this formulation, $\hat{\mathrm{C}}_0$ is of course unity, returning only the HF wavefunction and is omitted in the succeeding discussion. These work similarly to the CfI expansion coefficients (Equation 1.100) with

$$\begin{aligned} \hat{\mathrm{C}}_0\Psi_0 &= \Psi_0 \\ \hat{\mathrm{C}}_1\Psi_0 &= \sum_{n,n'} c_n^{n'}\Psi_n^{n'} \\ \hat{\mathrm{C}}_2\Psi_0 &= \sum_{n,n',m,m'} c_{n,m}^{n',m'}\Psi_{n,m}^{n',m'}, \end{aligned} \tag{1.108}$$

where $c_n^{n'}$ is the amplitude of the singly excited Slater determinant, $\Psi_n^{n'}$, and $c_{n,m}^{n',m'}$ is the amplitude of the doubly excited Slater determinant, $\Psi_{n,m}^{n',m'}$, *etc.*, *cf.* the notation used for the discussion on CI. Substituting the form of the cluster operator into the Schrödinger equation, left multiplying by Ψ_0^* and integrating over all-space leads to a set of (nonlinear) equations which can be solved in an iterative fashion to find the energy of the system. Obviously, the limitation in this method is that CC uses an infinite series of the cluster operator and thus must be truncated to be useful, just like CfI. Common use of the CC method truncate the operator to:

$$\begin{aligned} \hat{\mathrm{C}} &= \hat{\mathrm{C}}_1 \longrightarrow \mathrm{CCS} \\ \hat{\mathrm{C}} &= \hat{\mathrm{C}}_1 + \hat{\mathrm{C}}_2 \longrightarrow \mathrm{CCSD} \\ \hat{\mathrm{C}} &= \hat{\mathrm{C}}_1 + \hat{\mathrm{C}}_2 + \hat{\mathrm{C}}_3 \longrightarrow \mathrm{CCSDT}, \end{aligned} \tag{1.109}$$

where CCX denotes CC singles (X = S), singles and doubles (X = SD), and singles, doubles and triples (X = SDT) and so on for higher order terms. As with CfI, the more terms used, the better the approximation of the wavefunction and energies, but, of course, the computational costs rise quickly. Typically CCSD and CCSDT are used in computational chemistry, noting that like with MP2, X = D is the first correction to include correlation effects.[47] An expansion to this which has also proven popular is to use CC, and then treat the next higher correction *via* PT which is denoted by parentheses. For example, CCSD(T),[47] will treat all single and double excitations with the CC method, after which a perturbation correction term is added to approximate triplet excitations. Though less accurate than treating triple excitations explicitly, it can prove to be a useful compromise between accuracy and computational costs.

1.1.10 Density functional theory

An entirely different approach can be taken to tackle the problem of electron correlation if one forgets about explicitly representing the N-electron wavefunction denoted as $\Psi(x_1, x_2, \ldots, x_N)$, and instead considers electrons collectively as a charge density, $\rho(\mathbf{r})$.[1,48] For electron 1 at position r_1,

$$\rho(r_1) = N \int |\Psi(x_1, x_2, \ldots, x_N)|^2 \mathrm{d}s_1 \mathrm{d}x_2 \ldots \mathrm{d}x_N, \tag{1.110}$$

considering any of the N electrons in the volume element dr_1; dx_i are space-spin coordinates and ds_1 is the spin coordinate of electron 1. Within this context, the central idea is to express the electronic energy as a functional of the electron density, and thus this framework is known as Density Functional Theory (DFT). The energy contributions are identical to those discussed within the HF framework: nuclear-electron attraction, classical electron-electron repulsion, electron kinetic energy, and electron exchange energy. The former two are easy since they are already explicit functionals of the $\rho(\mathbf{r})$, the latter two however are much more difficult and remain the subject of the rest of this discussion.

Early functional models for the kinetic ($T[\rho]$) and exchange energies ($E_X[\rho]$) were suggested, notably as[48–50]

$$T[\rho] \propto \int \rho^{\frac{5}{3}}(\mathbf{r}) \mathrm{d}\mathbf{r} \tag{1.111}$$

$$E_X[\rho] \propto \int \rho^{\frac{4}{3}}(\mathbf{r}) \mathrm{d}\mathbf{r}. \tag{1.112}$$

As is known from virial theorem, the kinetic energy is of the order of total energy. Hence

errors in the kinetic term will propagate and render the entire model quantitatively useless.[48] This ultimately is the failing of these early models.

From here modern DFT takes hold. First, Hohenberg and Kohn provided a rigorous proof that electronic energy ($E[\rho]$) can be expressed as a functional of $\rho(\mathbf{r})$,[51] such that

$$E[\rho] = \int \rho(\mathbf{r}) v(\mathbf{r}) \mathrm{d}\mathbf{r} + F[\rho], \tag{1.113}$$

where

$$F[\rho] = T[\rho] + V_{ee}[\rho] = \langle \Psi | \, \hat{\mathrm{T}} + \hat{\mathrm{V}}_{ee} \, | \Psi \rangle \, . \tag{1.114}$$

$v(\mathbf{r})$ is the external potential arising from the electrons, $F[\rho]$ is a universal functional determined by the kinetic energy ($T[\rho]$) and potential energy ($V_{ee}[\rho]$; classical electron repulsion and electron exchange) operators for electrons and electron-electron interactions respectively. This therefore retroactively justifies the early attempts for finding a functional form for electronic energy in terms of electron density. In the same work, Hohenberg and Kohn provided a practical methodology for calculating Equation 1.113 by establishing a variational principle based on $\rho(\mathbf{r})$.[51] In essence this involves minimising[52] the total electronic energy subject to the constraint that

$$\int \rho(\mathbf{r}) d(\mathbf{r}) = N, \tag{1.115}$$

which is simply the number of electrons in the system.[48] So far, so good, but the initial failing of the early models has not been solved; this all still relies on having a good representative functional for $T[\rho]$ and $V_{ee}[\rho]$. Kohn and Sham in 1965 provided a solution.[53] Their idea was to introduce electron orbitals (basis functions) as with HF theory, which allows a good calculation of kinetic energy. It assumes that the system is a non-interacting electron gas ($T[\rho]$), which introduces a small error compared to the real system ($T_s[\rho]$); the difference in kinetic energy between these two system is therefore $T[\rho] - T_s[\rho]$. Within this framework, Equation 1.113 is written as

$$E[\rho] = \int \rho(\mathbf{r}) v(\mathbf{r}) \mathrm{d}\mathbf{r} + F[\rho] = \int \rho(\mathbf{r}) v(\mathbf{r}) \mathrm{d}\mathbf{r} + T_s[\rho] + J[\rho] + E_X[\rho], \tag{1.116}$$

where $J[\rho]$ is the classical electron-electron repulsion given by

$$J[\rho] = \frac{1}{2} \int \int \frac{\rho(r_1)\rho(r_2)}{r_{12}} \mathrm{d}r_1 \mathrm{d}r_2. \tag{1.117}$$

This now allows a formal definition of the electron exchange-correlation energy,

$$E_{XC}[\rho] = T[\rho] - T_s[\rho] + V_{ee}[\rho] - J[\rho], \tag{1.118}$$

and hence the central quantity which remains the focus of the DFT community,

$$E = \int \rho(\mathbf{r}) v(\mathbf{r}) \mathrm{d}\mathbf{r} + T_s[\rho] + J[\rho] + E_{XC}[\rho]. \tag{1.119}$$

'All' that remains is to determine the exchange-correlation functional. Practically, this Kohn-Sham formalism then follows an almost identical SCF procedure as with HF (*cf.* Figure 1.7), except that instead of the exchange contribution in the Fock-matrix, an equivalent exchange-correlation term is used instead.

This is in no way a comprehensive summary of DFT, but rather a phenomenological overview of one of the most widely used methods for calculating molecular properties of medium to large systems.[54] In stark contrast to the *ab initio* methods discussed in previous sections which often are restricted to small (tens) of atoms; DFT is routinely used for 100s of atoms. As exchange-correlation functionals are developed which reproduce important chemical properties, there is no doubt interest in DFT will continue to grow. Interested readers are directed towards the vast detailed literature for more information on the development of such functionals and the practicalities of performing DFT calculations.[55–63]

1.1.11 Excited states methods and quantum dynamics

All of the methods discussed so far are used to calculate the ground state wavefunction and thus ground state properties. However, excited state properties are of particular interest to molecular studies, *e.g.*, photochemistry. Many of the aforementioned methods (specifically not HF) can take a ground state configuration and represent an excited state in a sensible way which can be optimised. The most obvious way of generating an excited state would be to take a ground state configuration and optimised orbitals, place an electron in a virtual orbital and calculate the energy, however, this assumes that the orbitals are representative of this excited state configuration - which may or may not be true. Thus, the orbitals will have to be optimised for the excited state (against some convergence criterion), but a simple energy minimisation is useless since it will always just lead to the ground state - which is why the implementation of excited state methods does vary from their ground state counterparts. The commonplace methods for wavefunction and DFT excited state electronic structure calculations are listed and relevant litera-

ture given: CASSCF,[64,65] Complete Active-Space Second-Order Pertubation Theory (CASPT2)[66–68] and Multi-Reference Configuration Interaction (MRCI),[69] Equation-of-Motion Coupled-Cluster (EOM-CC),[70] Second-Order Approximate Coupled-Cluster (CC2),[71] Second-Order Algebraic Diagrammatic Construction (ADC(2)),[72] and Time-Dependent Density Functional Theory (TD-DFT).[51,73] An important point, which is particularly important for larger, more complex systems, is that these methods can all be used in conjunction with classical theories such as Molecular Mechanics (MM). Such cases are referred to as Quantum Mechanics/Molecular Mechanics (QM/MM); it involves treating the parts of a systems which require an accurate quantum mechanical description with high-level QM, and treating everything else, such as a protein environment or solvent molecules with a MM force-field, and has shown marked success in a number of problems related to photochemistry and photobiology.[74–77] Since MM calculations are significantly computational cheaper than QM counterparts, this can often provide the perfect balance between computational costs and accuracy.

To date, there are numerous electronic structure and MM programs where many of these methods and algorithms have been efficiently implemented, making them appealing to a broad range of problems throughout the physical and biological sciences.[17,78–96]

1.1.12 Quantum dynamics and surface hopping

Everything up to now has involved solving the TISE within the BO approximation (*i.e.* at selected fixed nuclear geometries). As such there is no explicit information about dynamical processes commonly encountered in nature. This information is obtained by simulating the nuclear dynamics of the system of interest, *i.e.* solving the TDSE.[97–99] This, however, is somewhat an idealised procedure for the systems which are studied in this thesis; such simulations are incredibly computationally demanding, traditionally they employ approximations such as a reduced dimensionality,[97,100] or are restricted to a short total simulation time, typically 100 fs or less. Such limitations, particularly the limitation on simulation time, make such methodologies impractical for the processes likely to be found in photochemistry (described in the next section). Much longer, >1 ps simulations would be desirable. To this end, semi-classical methods are usually employed (Figure 1.9).[101–105] These methods involve numerically integrating the TDSE for electronic coordinates, whilst nuclear coordinates are driven by solving Newton's classical equations of motion; the most common method which utilises this is Tully's Fewest-Switches Surface Hopping (FSSH) (Figure 1.10).[106–108]

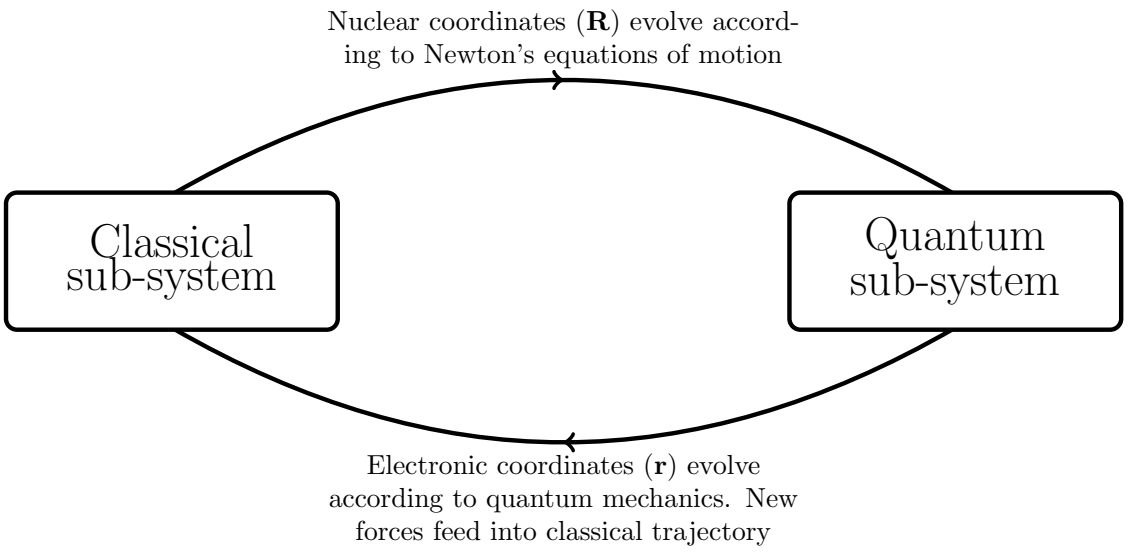

Figure 1.9 | One common option to simulate longer scale simulations (>ps) is to split the molecule into a classical (the nuclei) and quantum sub-system (the electrons). The quantum system is treated with one of the methods described so far such as DFT or ADC(2), returning the PES for some nuclear geometry at positions, $\mathbf{R}$. The PES is then used to calculate the forces acting on each of the nuclei, which are then evolved according to Newton's equations of motion for some (small) time-interval. This new nuclear geometry is used to recalculate the PES and the cycle continues until the trajectory reaches a user defined threshold, such as energy gap or total simulation time.

Here the total Hamiltonian $\hat{\mathrm{H}}$ of the quantum and classical subsystems is given by[106]

$$\hat{\mathrm{H}} = \hat{\mathrm{T}}_{\mathbf{R}} + \hat{\mathrm{H}}_0(\mathbf{r}; \mathbf{R}), \tag{1.120}$$

where $\hat{\mathrm{T}}_{\mathbf{R}}$ is the kinetic energy operator for atomic motions, and $\hat{\mathrm{H}}_0(\mathbf{r}; \mathbf{R})$ is the electronic Hamiltonian for fixed atomic positions, $\mathbf{R}$. As before, working within the BO approximation, we can select some set of (orthonormal) electronic basis functions, $\psi_i(\mathbf{r}, \mathbf{R})$, which depend on the electronic coordinates and parametrically on the nuclear coordinates. Matrix elements of the electronic Hamiltonian are then simply

$$V_{ij} = \langle \psi_i(\mathbf{r}; \mathbf{R}) | \, \hat{\mathrm{H}}_0(\mathbf{r}, \mathbf{R}) \, | \psi_j(\mathbf{r}; \mathbf{R}) \rangle \,, \tag{1.121}$$

integrating over electronic coordinates only. Furthermore, a so-called 'nonadiabatic coupling' vector is defined as[106]

$$d_{ij}(\mathbf{R}) = \langle \psi_i(\mathbf{r}; \mathbf{R}) | \nabla_{\mathbf{R}} \psi_j(\mathbf{r}; \mathbf{R}) \rangle \,, \tag{1.122}$$

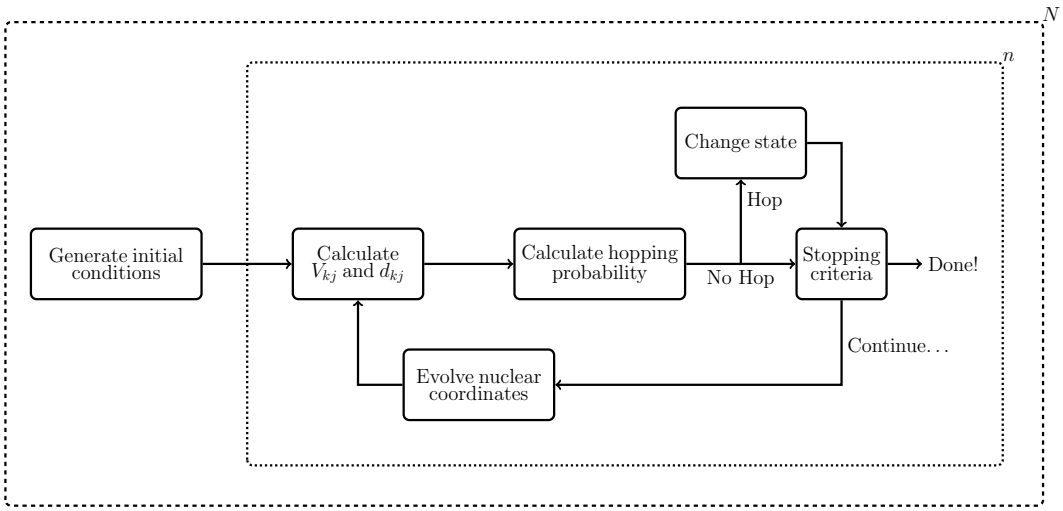

Figure 1.10 | A typical simulation using Tully's FSSH algorithm. The stopping criteria is often a maximum user defined simulation time, and/or when a trajectory reaches a state of interest. Because of the stochastic nature of determining if a hop takes place, n repeats of the same trajectory should be averaged together, although this is often not used in practice due to computational costs involving large systems. Furthermore, N trajectories should be taken each with different initial conditions to sufficiently sample phase space.

This term arises from the Schrödinger equation, but has up to now been ignored within the BO approximation. As alluded to, the atomic coordinates will be propagated in time thus, $\mathbf{R} = \mathbf{R}(t)$; there are many choices one could use to integrate the nuclear equations-of-motion, most commonly a velocity-Verlet algorithm is used.[109] A system wavefunction ($\Psi(\mathbf{r}, \mathbf{R}, t)$) can be defined in terms of the electronic basis functions and expansion coefficients, $c_i(t)$,

$$\Psi(\mathbf{r}, \mathbf{R}, t) = \sum_i c_i(t)\psi_i(\mathbf{r}, \mathbf{R}). \tag{1.123}$$

Substituting this into the TDSE, left multiplying by $\psi_k(\mathbf{r}, \mathbf{R})$, and integrating over electronic coordinates gives the differential equation[106]

$$i\hbar\frac{dc_k}{dt} = \sum_j c_j \left(V_{kj} - i\hbar\frac{d\mathbf{R}}{dt} \cdot d_{kl} \right). \tag{1.124}$$

Solving this differential equation allows one to determine the time-dependence of the coefficients. In turn, these coefficients determine the population of excited states on any PES. Now, population is allowed to flow between different PESs which is deter-

mined by (*i*) the derivative coupling between the two PESs (d_{kl}) and (*ii*) the energy difference between the two PES surfaces (V_{kl}). Together, these terms are used as a 'hopping' threshold; as the population propagates on a PES, the V and d terms are re-evaluated between all pairs of surfaces. This probability is compared to a random uniformly distributed number between 0 and 1. If the probability is higher than the random number, the population 'hops' to the corresponding PES. The greatest hopping probabilities are therefore achieved when electronic states are close in energy and/or the curvature between them is large (*cf.* Equation 1.124; Figure 1.10).

Now the algorithm has been established, the final part of the FSSH is to evolve the nuclear coordinates ($\mathbf{R}(t)$). This is computationally the cheapest part of the simulation, classical equations of motion are solved using the potential energy calculated in the *ab initio* step. This is used to determine the forces acting on each atom, then the atoms are accelerated over one time-step along the direction of the force. After this, another *ab initio* calculation is performed to recalculate the electronic energy at this new nuclear geometry. The entire surface hopping procedure is then repeated until a stopping criterion is met, for example, when the population reaches a particular PES or after the simulation has propagated to a maximum allowed time. Of course, this procedure only considers one possible set of initial conditions (trajectory) and would need to be repeated and averaged over to get statistically reliable results, typically 10s to 100s of trajectories depending on the rarity of the processes to be observed (Figure 1.10). On top of this, because the decision on whether to hop is stochastic, repeats of each trajectory should be performed, although in practice this is not performed to reduce computational effort.

Chapter 2

Introduction: Photochemistry and photoprotection

Parts of this chapter have been published by the author:

---

1. **Lewis A. Baker** and Vasilios G. Stavros. Observing and understanding the ultrafast photochemistry in small molecules: Applications to sunscreens. *Sci. Prog.*, **2016**, 99(*3*):282–311.

2. **Lewis A. Baker**, Simon E. Greenough, and Vasilios G. Stavros. A perspective on the ultrafast photochemistry of solution-phase sunscreen molecules. *J. Phys. Chem. Lett.*, **2016**, 7(*23*):4655–4665.

3. **Lewis A. Baker**, Barbara Marchetti, Tolga N. V. Karsili, Vasilios G. Stavros, and Michael N. R. Ashfold. Photoprotection: Extending lessons learned from studying natural sunscreens to the design of artificial sunscreen constituents. *Chem. Soc. Rev.*, **2017**, 46(*2*):3770–3791.

2.1 Photochemistry: The fate of electronic excited states

2.1.1 Paradigm of photochemistry

Where the first chapter of this thesis has developed a narrative for treating the electrons in molecular systems quantum mechanically, and how this is achieved in practice, this chapter instead takes on the perspective of molecular (electronic) interactions with electromagnetic radiation, namely, photochemistry. Generally speaking, a reactant (R) is photoexcited (R*) to some electronic excited state. In an effort to stabilise this high-energy system there are a number of possible processes the excited state molecule may undergo, creating intermediate structures (I) of various energetics (I*) in order to form a 'stable' product (P). The term stable is somewhat ambiguous, entirely depending on the timescale of the experiment and relative to other processes occurring in some deactivation mechanism; typically stable suggests (at least) meta-stable states with lifetimes well beyond 10s of ns. Indeed, this product could well be the original reactant, many examples of which are observed in this thesis. A 'global paradigm' for photochemical reactions captures all the typical questions photochemistry tries to answer (Figure 2.1):[110]

1. What are the *plausible structures* of the reactive and intermediate species in the process (*i.e.* R*, I, I*, P, and P*)?
2. What are the most *probable photochemical processes* which drive the reaction of R* → P?
3. What are the *plausible competing processes* for the reaction of R* → P?
4. What are the *rates* and kinetics for the reactions and processes observed?

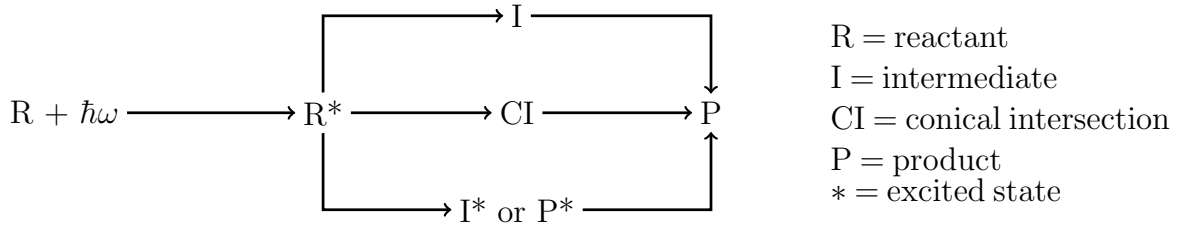

Figure 2.1 | A 'global paradigm', as suggested by Turro *et al.*[110] for the photochemical reactions which may occur after a molecule is photoexcited.

These types of questions, as will be discussed in detail in the next section, are at the heart of results in this thesis; understanding how molecules found in photoprotective applications respond to photoexcitation. Importantly, both experiments and theory (*ab initio* electronic structure calculations and/or quantum dynamics simulations) are required to fully answer all these questions.

2.1.2 Framework of light-matter interactions and the origin of photochemical processes

The most intuitive place to begin in building the working framework of photochemistry is with one of the electronic properties of a molecule, its (molecular) electric dipole moment, $\boldsymbol{\mu}$. This quantity captures the distributions of charges (electrons and nuclei) within a system as

$$\boldsymbol{\mu} = \boldsymbol{\mu}_e + \boldsymbol{\mu}_n = -e\sum_{i}^{n} \mathbf{r}_i + e\sum_{j}^{N} Z_j \mathbf{R}_j, \tag{2.1}$$

where $\boldsymbol{\mu}_e$ and $\boldsymbol{\mu}_n$ are the electronic and nuclear dipoles due to n electrons at positions $\mathbf{r}_i$ and N nuclei at $\mathbf{R}_j$ with nuclear charge Z_j. respectively. The issue is as with HF, where are the electrons? Since they are not localised, a quantum mechanical framework is most appropriate, utilising our previous discussion of wavefunctions and their linear expansions of basis functions. Furthermore, the subsequent calculation of electronic properties are only accurately determined by post-HF methods.

When radiation of a specific wavelength is incident on the molecule, the molecular dipole moment may resonate with the oscillating electromagnetic field of the radiation, triggering the absorption of that quantum of radiation, and promoting an electron to a higher-lying energy orbital; the molecule goes from being in its molecular ground state, Ψ_i into a electronically excited state, Ψ_j. This process is usually adequately captured by treating this 'light-matter' interaction as a weak perturbation. The first-order result *via* time-dependent perturbation theory is known as Fermi's golden rule,[1,3,111] which models the probability ($P_{j\leftarrow i}$) of the transition from state Ψ_i to Ψ_j as

$$P_{j\leftarrow i} = \frac{2\pi}{\hbar} |\left\langle \Psi_j \right| \boldsymbol{\mu}\cdot\hat{\boldsymbol{\epsilon}} \left| \Psi_i \right\rangle|^2 \delta(E_j - E_i \pm \hbar\omega), \tag{2.2}$$

for radiation of frequency ω, with electric field in direction $\hat{\boldsymbol{\epsilon}}$. Immediately it is obvious that if a change of electronic state occurs, it must be accompanied by the absorption ($+\hbar\omega$) or the emission ($-\hbar\omega$) of radiation equal to the energy gap between the two states involved ($E_j - E_i$), justifying the usual phenomenological interpretation of absorption

and emission.

This can be taken further by first invoking the BO approximation as before; one can write the wavefunction as a product of electronic, vibrational, and spin wavefunctions, *i.e.* $\Psi = \psi_e\psi_v\psi_s$. Substituting this into Equation 2.2 yields

$$P_{j\leftarrow i} = \frac{2\pi}{\hbar}|\left\langle\psi_{j,e}\psi_{j,v}\psi_{j,s}\right|\boldsymbol{\mu}\cdot\hat{\boldsymbol{\epsilon}}\left|\psi_{i,e}\psi_{i,v}\psi_{i,s}\right\rangle|^2\delta(E_j - E_i \pm \hbar\omega). \tag{2.3}$$

Using $\boldsymbol{\mu} = \boldsymbol{\mu}_e + \boldsymbol{\mu}_n$, these integrals can be split up within the BO approximation as

$$\begin{aligned} P_{j\leftarrow i} = \frac{2\pi}{\hbar}|&\left\langle\psi_{j,e}\right|\boldsymbol{\mu}_e\cdot\hat{\boldsymbol{\epsilon}}\left|\psi_{i,e}\right\rangle\left\langle\psi_{j,v}|\psi_{i,v}\right\rangle\left\langle\psi_{j,s}|\psi_{i,s}\right\rangle + \ldots \\ &\ldots\left\langle\psi_{j,e}|\psi_{i,e}\right\rangle\left\langle\psi_{j,v}\right|\boldsymbol{\mu}_n\cdot\hat{\boldsymbol{\epsilon}}\left|\psi_{i,v}\right\rangle\left\langle\psi_{j,s}|\psi_{i,s}\right\rangle|^2\delta(E_j - E_i \pm \hbar\omega). \end{aligned} \tag{2.4}$$

Since electronic wavefunctions are orthogonal, $\langle\psi_{j,e}|\psi_{i,e}\rangle = 0$ and the above expression reduces to

$$P_{j\leftarrow i} = \frac{2\pi}{\hbar}|\left\langle\psi_{j,e}\right|\boldsymbol{\mu}_e\cdot\hat{\boldsymbol{\epsilon}}\left|\psi_{i,e}\right\rangle\left\langle\psi_{j,v}|\psi_{i,v}\right\rangle\left\langle\psi_{j,s}|\psi_{i,s}\right\rangle|^2\delta(E_j - E_i \pm \hbar\omega). \tag{2.5}$$

Putting the conservation of energy term aside for a moment, and concentrating on the three integrals in this expression, this expression highlights the components of the probability amplitude which determines how likely a transition ($j \rightarrow i$) is to occur. A summary of the possible photochemical and photophysical transitions a molecule may undergo is given in a Jablonski diagram (Figure 2.2).[110,112] The origins of these processes are discussed below.

$\langle\psi_{j,e}|\boldsymbol{\mu}_e\cdot\hat{\boldsymbol{\epsilon}}|\psi_{i,e}\rangle$. This integral forms the so-called 'orbital-selection rules'.[1] These place restrictions on the change in quantum numbers (l, m_l) when an electronic transition takes place (*cf.* Section 1.1.4). This integral is non-zero only when there is a parity change between orbitals ($(-1)^l$, for orbital angular momentum quantum number l). Similarly, orbital angular momentum must be conserved, since a photon (which is a boson) has $l = 1$, thus a change of state which involves a photon being absorbed or emitted must be accompanied with an electron changing orbital by $\Delta l = \pm 1$. Finally, a selection rule involving the magnetic orbital angular moment quantum number (m_l) is deduced from noting photons have the intrinsic property of helicity (σ_h; the projection of spin onto linear momentum) which is a conserved physical quantity. Photons have $\sigma_h = \pm 1$, which is conserved if a transition involves a change in magnetic orbital angular momentum of $\Delta m_l = 0, \pm 1$.[1] Many of these selection rules which are formally forbidden (the integral is zero), can be observed if the perturbation of the electric field is large enough to distort orbital symmetry. Furthermore, the magnetic field of a photon

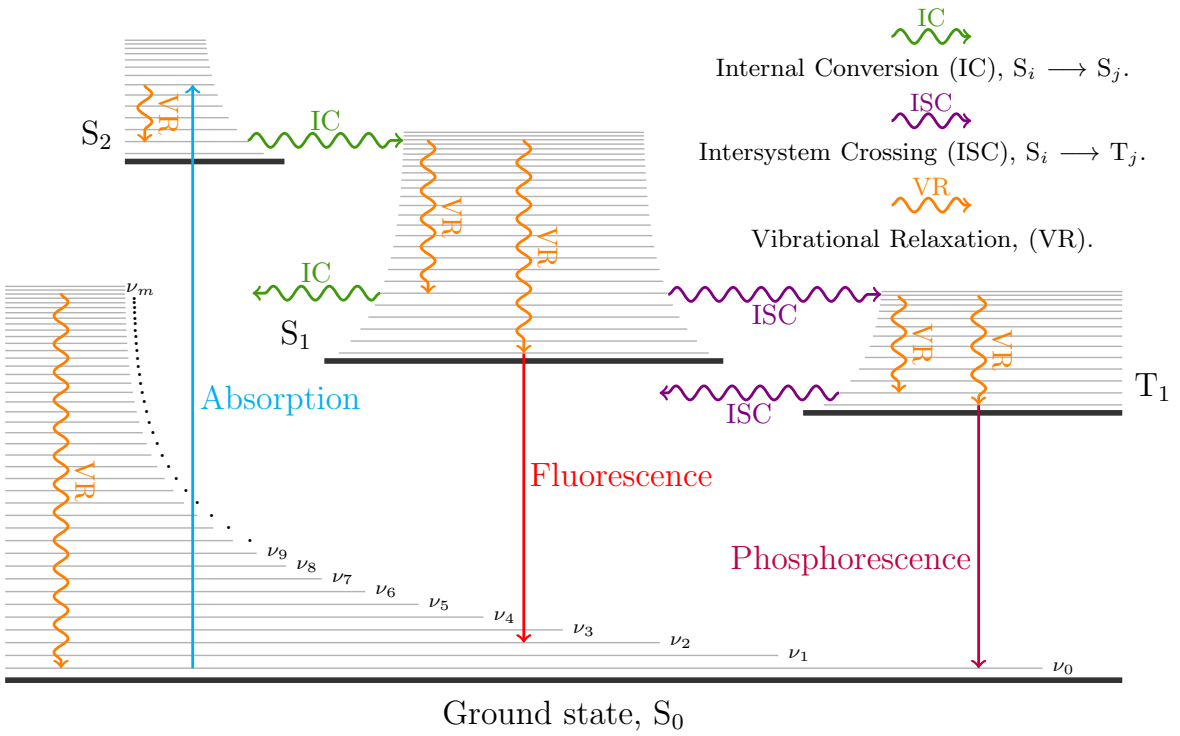

Figure 2.2 | A summary of the important photophysical processes which occur after a molecule is photoexcited from its electronic ground state, S_0, and vibrational ground state, ν_0, to an excited vibronic state, *i.e.* excited electronic (S_n; $n \geq 1$) and vibrational state (ν_m; $m \geq 1$). Following this, there are a number of radiative ($\rightarrow$) and nonradiative ($\rightsquigarrow$) processes a molecule may undergo to dissipate its excess energy. Photodissociation, ionisation, and isomerisation are not shown.

can induce a magnetic dipole transition and in turn open up some of these previously forbidden transitions. Such a discussion on the orbital-selection rule is valid for atoms; molecules on the other hand become more complicated since l is no longer a 'good' quantum number. In such cases, composite quantum numbers are instead used to predict allowed transitions, the result being the molecular *point groups* used throughout chemistry and physics.[3]

$\langle\psi_{j,v}|\psi_{i,v}\rangle$. This integral is known as the Franck-Condon (FC) factor.[113–115] It is the overlap integral of the vibrational modes between the electronic states $|i\rangle$ and $|j\rangle$. In other words, the probability of an electronic transition is proportional to the degree of overlap between the initial and final vibrational state wavefunctions, perfect overlap ($\langle\psi_{j,v}|\psi_{i,v}\rangle = 1$) results in the most intense (probable) transitions (Figure 2.3). This has come to be known as the FC principle and hence the integral's name. Importantly,

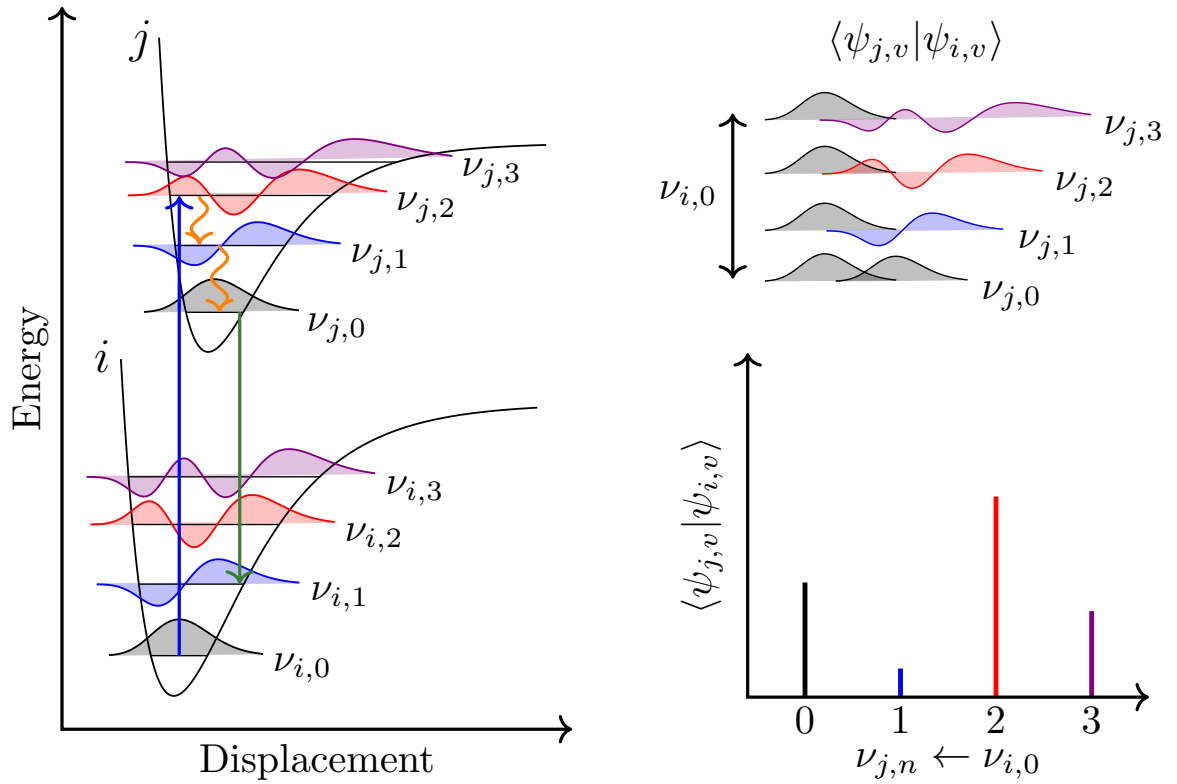

Figure 2.3 | (*left*): A pictorial analogue of the FC principle for a given transition from electronic state $|i\rangle$ to electronic state $|j\rangle$. (*top-right*): For two representative anharmonic states, the overlap ($\langle\psi_{j,v}|\psi_{i,v}\rangle$) between the ground vibration state $\nu_{i,0}$ and the energetically accessible vibrational states of $|j\rangle$ determines how probable each possible transition is. (*bottom-right*): The result is an absorption spectrum shown as delta functions. The blue arrow between $\nu_{i,0}$ and $\nu_{j,2}$ depicts a vertical transition (electronic transition with no change in nuclear geometry), which, given the vibrational wavefunctions of these two states have greatest spatial overlap, this transition is most intense. The FC principle can also be applied to transitions between vibrational modes, where the probability of transitioning between two modes depends on how similar the vibrational wavefunctions are (their overlap) and how similar the nuclear geometry is between the modes. As such, the energy difference between the initial vibronic state (depicted as $\nu_{j,2}$) and $\nu_{j,0}$ means emitted photons are red-shifted compared to absorbed photons, known as a Stokes shift.

Figure 2.3 depicts vertical transitions, an electronic transition without an accompanying change in nuclear geometry (*i.e.* a transition within the BO approximation). These transitions are most probable given the nuclear geometry between initial and final states is the same, hence the corresponding vibrational wavefunctions exhibit a large FC factor.

The concept of the FC factor also qualitatively describes how radiationless energy

loss of an excited state may occur, a fundamentally important process in photochemistry. Whilst in an excited vibronic state (both electronically and vibrationally excited state), a molecule may release excess vibrational energy as heat, known as Vibrational Energy Transfer (VET). The molecule may distribute excess vibrational energy to the environment, known an Intermolecular Energy Transfer (IET), which, for example, will decrease its vibrational state by conserving energy through transferring heat to a solvent bath. Alternatively, or indeed concurrently, it may redistribute vibrational energy throughout the normal mode space available to it, known as Intramolecular Vibrational Energy Transfer (IVR), noting an N-atom polyatomic molecule has 3N - 6 vibrational modes. Such processes are responsible for the Stokes shift in emissions such as with fluorescence. As depicted in the Jablonski diagram, absorption usually results in an excited vibronic state. Once in the emitting electronic state, VET ensues to occupy the ground vibrational state, where fluorescence takes place. Indeed, this sequence of events is more probable than emitting from an excited vibrational state because of the large FC overlap between vibrational states at some nuclear geometry. The result of this is the (often considerable) red-shift of fluorescence profile for a molecule, relative to its absorption spectrum. In fact, fluorescence generally occurs from the first excited state since higher excited states are closer in energy to one another, making non-adiabatic couplings between electronic states more probable. This is known as Kasha's rule.[116]

Nuclear vibrations can also initiate electronic transitions. During vibrations, the nuclear geometry may couple (mix) two vibrational modes between two electronic states. The FC factor once again captures this. An electronic state may change if the vibrational wavefunctions between two energy-degenerate vibrational modes, of the two different electronic states, display significant overlap. The probability of this transition is multiplied by the density of states accessible for this transition. This vibrationally initiated change of electronic state is know as Internal Conversion (IC). Importantly, there is no change in vibrational energy.

$\langle\psi_{j,s}|\psi_{i,s}\rangle$. This is referred to as the spin-selection rule, being an overlap integral of spin wavefunctions between the two states involved in a transition. As briefly discussed with Hund's rules for predicting the ground state electronic configuration of a molecular system (Section 1.1.5), the lowest energy configuration for a stable molecular system will have paired electrons in all orbitals (Figure 2.4). The spin multiplicity, M, is defined as $M = \sum_n 2m_{s,n} + 1$; for a molecular system with all paired electrons, the sum of the spin quantum numbers will be zero, and thus $M = 1$, as such these are referred to as singlet states, S_n ($n \geq 0$), where $n = 0$ denotes the ground state configuration. In excited state configurations, an electron may be promoted and access higher energy

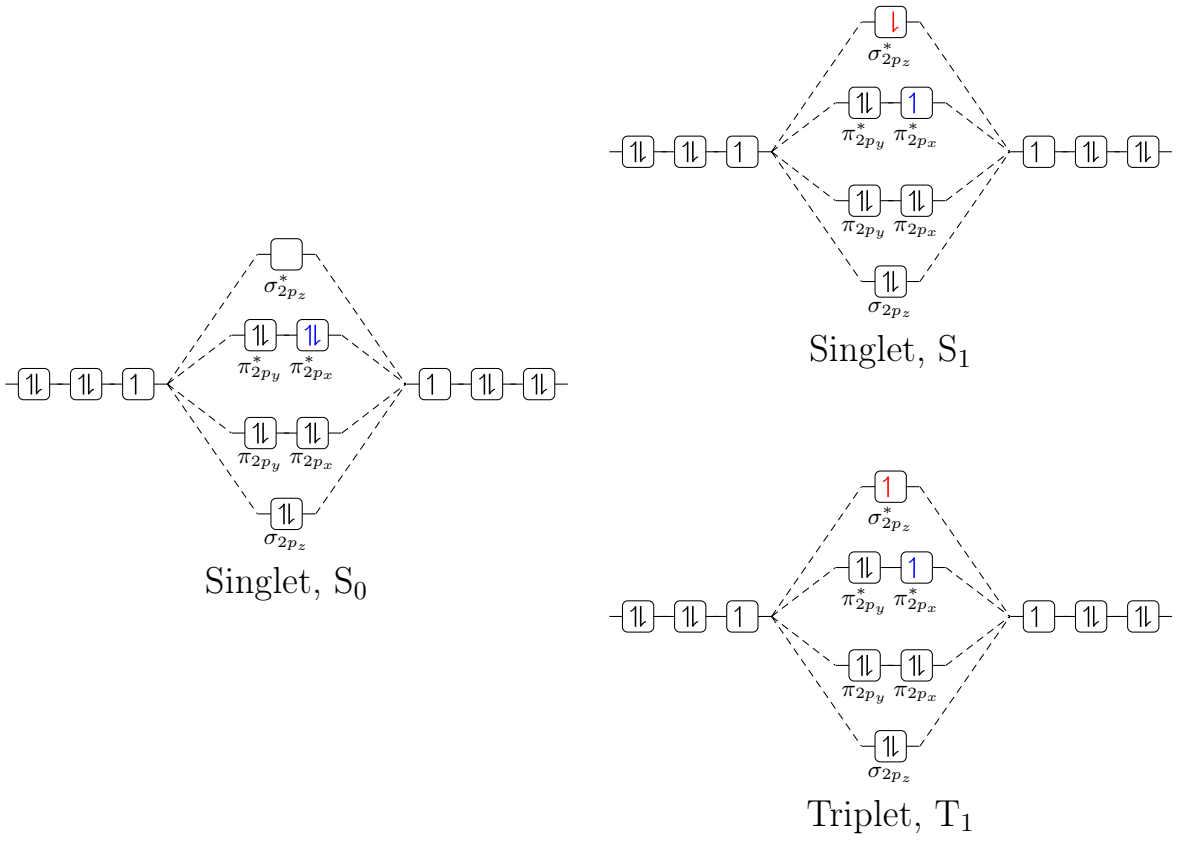

Figure 2.4 | The ground singlet state (S_0), the first excited singlet state (S_1), and the first excited triplet state T_1 electronic configuration for F_2 ($n = 1$ electrons are omitted for clarity, *cf.* Figure 1.4).

singlet states for example the first excited singlet state, S_1. Triplet states on the other hand have a set of unpaired spins, the sum of the spins are 1, and thus $M = 3$ and hence the name triplet states. These are denoted as T_m ($m \geq 1$), where the lowest energy triplet state is T_1. A representative example of this is given for F_2 (Figure 2.4). As such, if there is no change in spin multiplicity (*e.g.* singlet to singlet or triplet to triplet transition) in a transition, $\langle \psi_{j,s} | \psi_{i,s} \rangle = 1$. Thus, a transition which results in a change in spin multiplicity is formally forbidden. In practice, magnetic interactions involving an electron's spin can lift this restriction making some transitions possible.

The magnetic interactions (couplings) involving electron spin can occur from: (*i*) coupling to the orbital angular momentum of the electron known as spin-orbit coupling; (*ii*) coupling to an external magnetic field, such as an applied laboratory field, *e.g.* the Zeeman effect; (*iii*) coupling to the magnetic moment of nuclear spin known as hyperfine coupling. Thus, if a transition involves the change of spin multiplicity, it

may only occur if one of these sources of magnetic interaction is available to conserve magnetic energy. Such a transition is known as Intersystem Crossing (ISC). In terms of organic photochemistry, spin-orbit coupling is by far the strongest (and therefore dominant) source of magnetic interaction, and remains the subject of this discussion. ISC is commonplace in photochemistry, perhaps most notably through the observation of phosphorescence, an analogue of fluorescence which involves a change of spin multiplicity (Figure 2.2).

Since ISC to the zeroth order is forbidden, the probability of ISC compared to other radiationless relaxation processes (IC and VET) is significantly smaller, and thus is often out-competed. However, within a molecular ensemble, there will be a statistical distribution of molecules undergoing any one competitive pathway, based on their probability. In the case of spin-orbit coupling, increasing the magnetic interaction will increase the probability amplitude of ISC, P_{ISC}

$$P_{\mathrm{ISC}} = \langle \Psi_j | \, \hat{\mathrm{H}}_{so} \, | \Psi_i \rangle \,, \tag{2.6}$$

where $\hat{\mathrm{H}}_{so}$ is the spin-orbit coupling operator, which is approximately the product of the spin and orbital angular momentum dipole moments, $\boldsymbol{\mu}_s$ and $\boldsymbol{\mu}_l$ respectively,

$$P_{\mathrm{ISC}} = \langle \Psi_j | \, \eta_{so} \boldsymbol{\mu}_s \boldsymbol{\mu}_l \, | \Psi_i \rangle \,, \tag{2.7}$$

where η_{so} is known as the spin-orbit coupling constant, which is the effective nuclear charge coupling to the electron spin. This constant is atom-dependent, where heavy atoms (atomic number Z) contribute more greatly to η_{so}, thus inducing a higher rate of ISC. For hydrogenic atoms,[110,117] $\eta_{so} \sim Z^4$, although for molecules this effect will be smaller given the electron will observe a screened nuclear charge from the rest of the molecule. However, in both cases, atom or molecule, the closer the electron is to the heavy atom (small l quantum numbers), the larger the spin-orbit interaction. Finally, a transition which involves a change in orbital angular momentum, analogous to fluorescence, but involves a change in spin multiplicity, may occur, known as phosphorescence. Generally, these undergo a greater Stokes shift than with fluorescence since they will occur from the lowest triplet state, which is lower in energy than the first excited singlet state (Hund's first rule).

The take-home message from this discussion is that an electronic transition initiated by the interaction of its electric dipole moment with radiation (and indeed radiationless transitions) is determined by a series of probabilistic integrals which depend on the electric dipole moment (orbital selection rules), and are proportional to the spatial overlap

Table 2.1: The typical times for the processes discussed thus far.[118]

Process	Time taken / s
Absorption	10^{-18} – 10^{-15}
Intersystem Crossing	10^{-14} to 10^{-8}
Vibrational Relaxation	10^{-12} to 10^{-10}
Internal Conversion	10^{-11} to 10^{-9}
Fluorescence ($S_1 \rightarrow S_0$)	10^{-7} to 10^{-1}
Phosphorescence ($T_1 \rightarrow S_0$)	10^{-6} to 1

of involved wavefunctions (FC factor), and the overlap of spin states (spin-selection rule). Importantly, many of these are zeroth-order rules, which means some formally forbidden transitions are possible under certain higher order interactions. Perhaps most notably the magnetic field of the radiation, and the magnetic properties of electrons have been ignored since they are not included in the perturbation term which was used to derive Equation 2.2. When considered, transitions between formally forbidden states, such as those of different spin multiplicities, are possible.

In general, a particular transition will have a finite probability of occurring; in essence all allowed relaxation mechanisms are in competition with one another where the 'winning' transition is that with the greatest probability amplitude (for an ensemble, as previously stated, a distribution of mechanisms will occur drawn from each probability amplitude). Such amplitudes are generally sufficiently well described (with the given addenda) within Fermi's golden rule (Equation 2.2). On the macroscale, these probabilities are observed as timescales; an unlikely event will take longer to happen (in terms of sampling phase space) and thus have a longer 'lifetime' (Table 2.1), the core measurement of ultrafast photochemistry.

2.1.3 Photochemistry and potential energy surfaces

A discussion on the breakdown of the BO approximation in Section 1.1.7 ended prematurely with the conical intersection as a notable example of when the BO approximation no longer remains valid. Conical Intersections (CIs) are configurations of a molecule's nuclear geometry (and by extension PES) which couples two electronic states so strongly that there is a point of degeneracy (or near degeneracy) in the PES. Whilst the subject

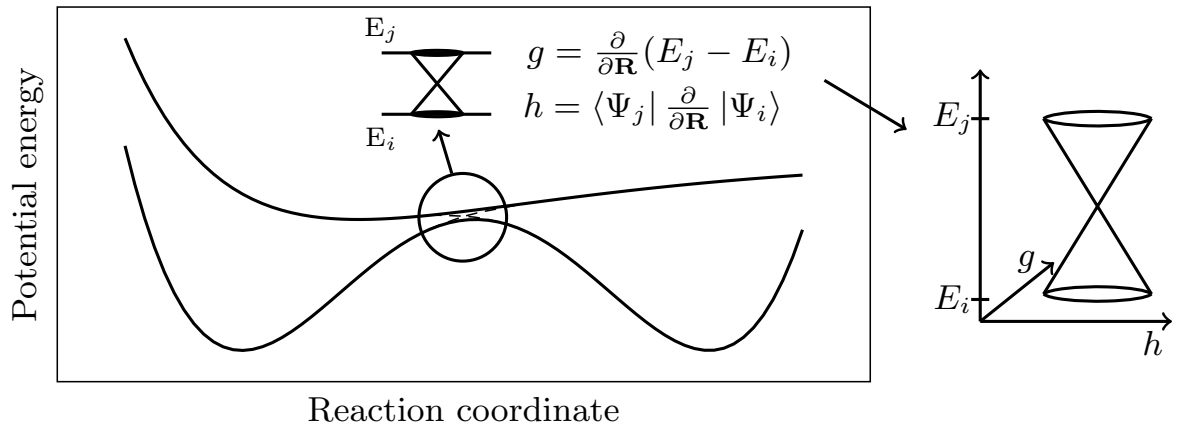

Figure 2.5 | An idealised CI between two (adiabatic) PESs. For some particular nuclear geometry, two PESs may couple (become degenerate) and excited state population may internally convert through the intersection. The strength of this coupling is understood through the g and h vectors which span a two dimensional space around the CI geometry.

of CIs is of great research interest, and many of the details beyond the scope of this thesis,[119,120] it suffices to appreciate that CIs between PES in many organic molecules are essential in providing an efficient route for transitions (IC) between the electronic states involved. IC through a CI is referred to as nonadiabatic dynamics since the coupling between PES due to the nuclear degrees of freedom can no longer be considered separable from electronic motion (thus the BO approximation is no longer valid). The probability (rate) of transition through a CI depends on the strength of the coupling between the involved electronic states. For the driving reaction coordinate which allows the molecule to reach this specific nuclear geometry, creating the CI, one or more of the normal modes is favourable for facilitating IC through the CI. The dominant mode which facilitates IC through the CI is known as the gradient difference (g) vector,

$$g = \frac{\partial}{\partial \mathbf{R}}(E_b - E_a), \tag{2.8}$$

where E_a and E_b are the potential energies for the wavefunctions (Ψ_a and Ψ_b) at the CI nuclear geometry (Figure 2.5). At the CI, another normal mode is required which couples the electronic states together, ultimately allowing IC to take place, known as the derivative coupling vector (h), orthogonal to the g vector,

$$h = \langle \Psi_b | \frac{\partial}{\partial \mathbf{R}} | \Psi_a \rangle . \tag{2.9}$$

These g and h vectors lie along the 'double-cone' topography for which a CI is imagined (Figure 2.5). In particular, this h vector is of the form of the aforementioned nonadiabatic coupling vector, used to define the hopping probability in FSSH (*cf.* Section 1.1.11).

2.1.4 The link to experimentally observable quantities

Up to here the physical origins of the dominant photophysical processes have been discussed, and the major factors which determine their rates, qualitatively justifying why one process may outcompete another process. It is however important to respect the fact that in an experiment, one is instead measuring the expectation values for an ensemble of a molecular species. Radiative rates are measured through the exponential decay of observed signals, where the lifetime of the radiative processes is the reciprocal of the decay time.

Absorption is considered experimentally as a sample cell of cross-sectional area a, containing an absorbing species with effective cross-sectional absorption area σ (Figure 2.6). A portion of the incident light of intensity $I_0(\lambda)$ is absorbed and the remainder is transmitted through the cell, resulting in a transmitted intensity of $I(\lambda)$. Absorbance ($A(\lambda)$) is defined as the logarithmic quotient of these intensities,

$$A(\lambda) = -\log\left(\frac{I(\lambda)}{I_0(\lambda)}\right). \tag{2.10}$$

Considering for a moment an infinitesimally small portion of the pathlength of the cell,

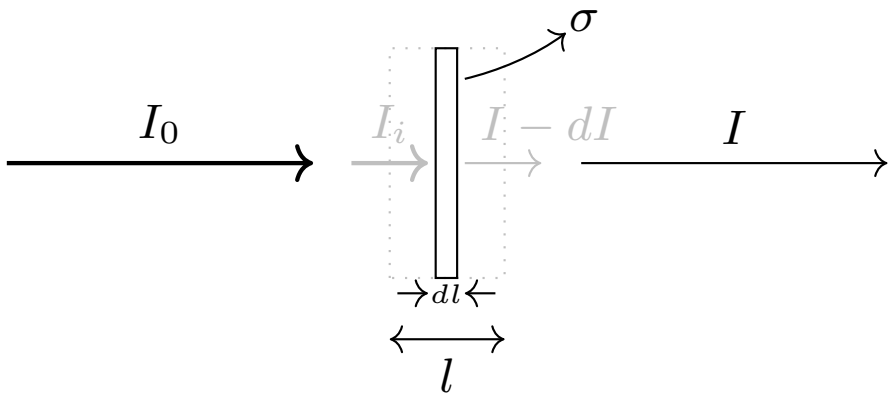

Figure 2.6 | A simple schematic of absorption in a sample cell with pathlength l. The absorbing species has an effective cross-sectional area of σ.

the rate of change of intensity for incident light (I_{dl}) is

$$\int \frac{dI}{I_i} = -\int_0^l \sigma N dl, \tag{2.11}$$

since the fraction of photons absorbed is $\frac{\sigma N a \cdot dl}{a}$, hence independent of cell cross-sectional area, and where N is the number of absorbing molecules over the volume element $a \cdot dl$. This has the simple solution

$$-\frac{\ln(I)}{\ln(I_0)} = \sigma N l. \tag{2.12}$$

Transforming into the $\log_{10}$ basis, and defining a molar absorptivity, ε as

$$\varepsilon(\lambda) = \frac{N_A}{2303}\sigma(\lambda) \quad [\mathrm{M}^{-1}\mathrm{cm}^{-1}], \tag{2.13}$$

where N_A is Avogadro's constant. Finally, defining the concentration of absorptive species as $c = \frac{1000N}{N_A}$, returns the familiar Beer-Lambert law for absorption

$$A = \varepsilon c l. \tag{2.14}$$

Radiation (within a classical theory) is considered to be an oscillating electromagnetic wave, and the negatively charged (bound) electrons of a molecule to be harmonic oscillators, which resonate for specific frequencies of radiation. Within this framework the concept of an oscillator strength, denoted f, is viewed as the ratio of radiation absorbed (or emitted) by a molecule, compared to an ideal harmonic oscillator. The oscillator strength is defined as[110]

$$f = 4.3 \times 10^{-9} \int \varepsilon d\nu, \tag{2.15}$$

expressed in terms of wavenumber (ν); $f = 1$ indicates the molecule is an ideal harmonic oscillator. Thus, the area of a plot of ε *vs.* ν returns the oscillator strength. The final remark is that the oscillator strength is proportional to the square of the transition dipole moment discussed at the beginning of this section. Combining this classical expression of oscillator strength with the quantisation of the transition dipole moment, the oscillator strength is brought together with quantum mechanical transition dipole moment by

$$f = \left(\frac{4 m_e \nu}{3\hbar e^2}\right) |\, \langle \Psi_j |\, \boldsymbol{\mu} \cdot \hat{\boldsymbol{\epsilon}}\, | \Psi_i \rangle \,|^2, \tag{2.16}$$

thus bringing this brief overview of photochemistry to a close.

2.2 Biological photoprotection

2.2.1 UV selective pressures and the development of an oxygenated atmosphere

Ultraviolet (UV) Radiation (UVR), ∼400–100 nm, is the most energetic component of the solar spectrum which reaches the Earth, typically subdivided into the UV-A region (400–315 nm), the UV-B (315–280 nm) region, and the most energetic region, UV-C (280–100 nm). These high energy components can cause major disruptions to the biochemistry of life, often in the form of chemical bond breaking or free radical generation. Throughout the development of Earth's atmosphere, the radiation which bombards the Earth's surface has changed dramatically. Around 3 billion years ago in the Archean era of Earth's history, when the earliest lifeforms on Earth are known to have existed, the atmosphere likely consisted predominately of: methane, ammonia, water vapour, carbon dioxide, nitrogen, hydrogen, hydrogen sulphide and various Noble gases, which together, at the theorised total surface pressure of 100 kPa are transparent to electromagnetic radiation of wavelengths beyond ∼220 nm.[121] Thus the solar spectrum reaching the Earth's surface consisted of much UV-C radiation. As such, these early organisms were forced to migrate away from the surface, or develop other mechanisms in order to reduce exposure in order to survive.[122]

One such example is extant cyanobacterium, a phylum of bacteria, and one of the Earth's earliest phototrophs, suggested to exist from at least ∼3 Giga-annum (Ga) ago.[123] This organism has exhibited numerous mechanisms to strike a balance between obtaining sunlight for photosynthesis, whilst mitigating UV-C damage (Figure 2.7). (*i*) In the early 'primordial soup' water would have served as a UV-C attenuator, though several 10s of meters would be required for adequate protection, and thus would not be considered a surface habitat.[121,124,128] (*ii*) Sedimentation in water certainly can attenuate UV-C significantly, reducing the depth of water required. For example, inorganic salts such as sodium nitrate and sodium nitrite dissolved in water provide an attenuating environment, and have been demonstrated to mitigate such damage for cyanobacteria,[129] although the concentrations of such salts available during this period of Earth's history are not well-known leaving this open to speculation. The presence of iron in such sediments has also been suggested as a likely candidate for early UV-C protection given only a small, ∼0.1%, of dopant in sediments would be required for significant UV-C attenuation.[124,125] (*iii*) Fossil remains as well as present-day observations, for example at Chilean high-altitude hot-springs,[130] have shown matting communities of cyanobacteria can help a population survive through the sacrifice of a small portion of the population.

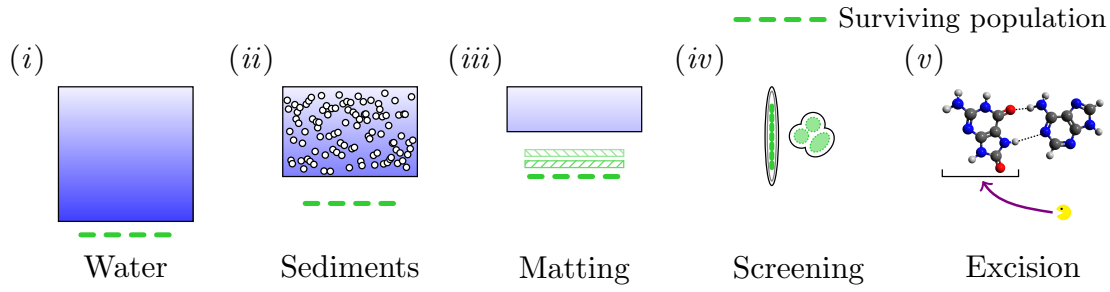

Figure 2.7 | Suggested mechanisms of early photoprotection from UV-C radiation likely utilised by cyanobacteria.[124] (*i*) Tens of meters of water could provide protection for UV-C radiation,[121] (*ii*) with the addition of sediments such as salts and iron, the depth required would be significantly reduced.[124,125] (*iii*) Matting habitats are known to afford protection; the top layers (green hashes) are damaged or destroyed but provide protection to the lower lying population.[126,127] (*iv*) Screening molecules, *e.g.* pigmentation, have been identified which attenuate UV-C forming sheaths around a population.[124] (*v*) In the event of UV-induced damage, to DNA for example, there exist enzyme controlled mechanisms which identify and repair damage, such as base excision (shown, oxidised guanine with adenine; a Hoogsteen base pair) and nucleotide excision.[124]

Here, upper layers reside in the path of UV-C radiation, blocking it for lower lying layers. Even in death, these upper layers of cells continue to provide photoprotection to those below until they lyse, and then need to be replaced.[124,126,127] (*iv*) Organic screening compounds, akin to present day skin pigmentation (discussed in Section 2.2.2), have been observed. Cyanobacteria can form protective sheaths with screening compounds such as scytonemin,[131,132] mycosporines,[132] flavonoids and carotenoids,[133] all of which can display strong absorption cross-sections in the UV-A and UV-B regions in present-day cyanobacteria, thus it is a tangible extrapolation that such pigmentation might have existed in the UV-C region during this period of Earth's history.[124] (*v*) In the event that UV-induced damage occurs, for example in Deoxyribonucleic Acid (DNA) where dimerisation or base-pair mismatch are known to occur *via* UV irradiation (UV-A, UV-B and UV-C), sophisticated enzyme controlled identification and repair mechanisms, such as base-excision and nucleotide-excision, attempt to rectify the damage.[132] It comes as no surprise that a number of these mechanisms were likely used together to strike a balance of meeting metabolic requirements, but reducing UV damage, to not only survive, but to *thrive*.

Moving forward in time, more complicated organisms and ecosystems such as large plant life on land masses, required a broad, efficient, and geographical photoprotection to thrive. This was, and still is, provided by today's ozone rich stratosphere. Impor-

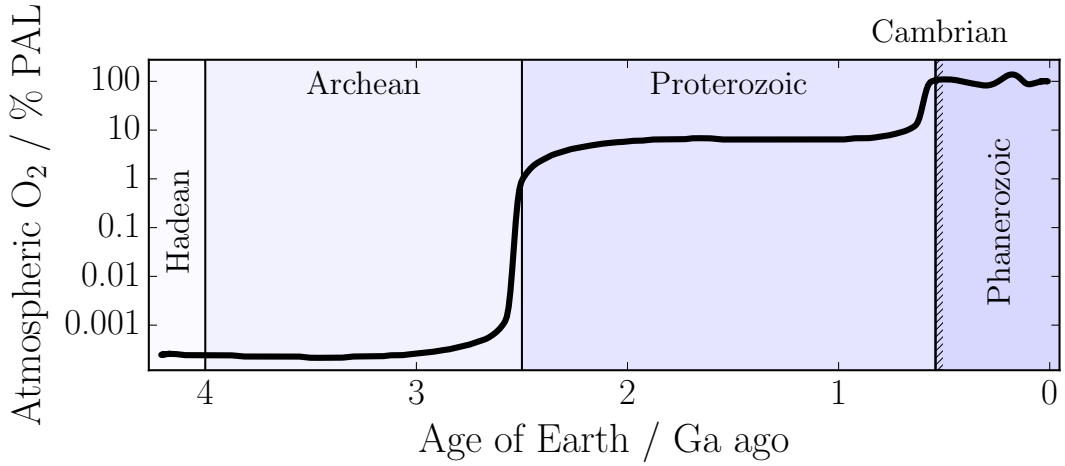

Figure 2.8 | The development of an oxygen rich atmosphere happened after the GOE *c.* 2.45 Ga ago, the exact cause of which still remains elusive.[138] Data reconstructed from Kump, *figure 2*.[135]

tantly however, it is only recently in Earth's history that the oxygen content of the atmosphere could support such life, *c.* 500 Ma ago, let alone provide UV photoprotection in the form of ozone (Figure 2.8). In the Archean era, oxygen levels were $\sim 10^{-5}$ of Present O_2 Atmosphere Levels (PAL).[134,135] There is evidence that oxygenic respiration predates oxygenic photosynthesis, suggested from the phylogenetic reconstructions of cytochrome oxidase molecular sequences.[136] This might be counter-intuitive but a reconciliation is found through the use of catalase enzymes which convert atmospheric hydrogen peroxide to water and oxygen.[136] Despite this, the trace amounts of oxygen certainly point to early life being dominated by anoxygenic respiration, utilising sulphur-based energy sources like hydrogen sulphide, as well as oxidative-iron or UV mediated processes as electron donors for respiration.[136] Cyanobacteria are suggested to have evolved oxygenic photosynthesis, *i.e.* utilising oxygen as an electron donor as most life does today (a significantly more energy rich pathway), around 2.7 Ga ago.[135–137] The summary of this is that atmospheric O_2 levels remained essentially constant for well over a Ga, before the Great Oxidation Event (GOE).

The GOE marks a 'boom' in atmospheric O_2 levels, from $\sim$0.001 % PAL to $\sim$1 % PAL in as little as 30 Ma, beginning some 2.45 Ga ago, see Figure 2.8.[135] The exact cause of this event remain uncertain,[138] but the time frame of this event has been well established through the measurement of $^{33}S/^{32}S$ isotopic ratios in ancient rock formations.[135,137] Some suggestions have been made; given this was around the time large

land masses likely formed,[135] a new selective pressure towards oxygenic photosynthesis for cyanobacteria might have occurred,[139,140] or perhaps geological changes in plate tectonics led to a decrease in oxygen demand *via* subsequent oxygen reactions with volcanic or metamorphic out-gassings.[141,142] After the GOE, O_2 levels varied minimally, staying steady at ∼10 % PAL for over a Ga, sometimes dubbed the 'boring billion',[143] where evolution appeared to stagnate, before another, smaller oxygen boom occurred marking the Cambrian era, during which an explosion in diversity of life and the development of complicated multicellular eukaryotic organisms persisted throughout the Phanerozoic era for another 500 Ma, and O_2 atmospheric levels slowly reached 100% PAL.[144,145] After the GOE, atmospheric O_2 levels would have been high enough for an effective ozone layer, shielding subsequent organisms from harsh UV-C radiation, and thus the selective pressure of UV radiation is reduced, but not negligible given UV-A and UV-B radiation are only attenuated, rather than completely blocked by ozone.[146] This has important consequences for present day organisms including both humans and plants, as is discussed in the next section.

2.2.2 Solar irradiation and its impact on the present day biosphere

Today, the ozone rich stratospheric layer of the Earth's atmosphere absorbs all the UV-C wavelengths, and much of the UV-B, and as a result the solar spectrum reaching Earth's surface comprises less than 8% UVR (Figure 2.9; data simulated using the Simple Model of the Atmospheric Radiative Transfer of Sunshine (SMARTS) modelling suite).[147] Though this is a small proportion of the total solar spectrum (especially compared to the early Earth atmosphere), these high energy components still have an extensive impact on the Earth's biosphere. Most notably, more than 90% of the vitamin-D requirements of the human body are met through UV-B photocatalytic reactions.[148] On the other hand, the negative attributes of UV-B exposure are extensive; DNA nucleotides and protein manifolds for example can absorb UV-B radiation which can lead to mutations in cells or the disruption of vital biochemical pathways like photosynthesis.[149] Thus exposure to UVR remains in an equilibrium of the so-called *burden of disease*; too little UV-B exposure, and important biochemical processes are not active, too much, and the prevalence of adverse effects increase, depicted in Figure 2.10. At the heart of this burden of disease is the ability of an organism to adapt to varied levels of exposure. Such biological dependencies, consequences and adaptations are first discussed in the context of humans, followed by a review of the analogies for higher order plant life.

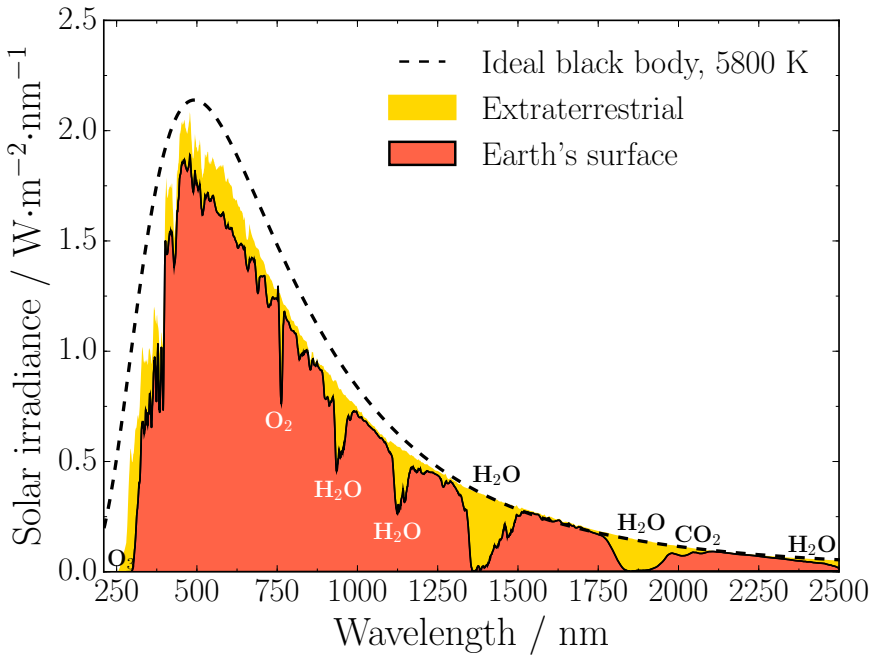

Figure 2.9 | The solar irradiance spectrum from the Sun at the top of Earth's atmosphere (extraterrestrial; yellow) and at sea level (Earth's surface; red), simulated using the SMARTS modelling suite. The theoretical irradiation of the Sun is an ideal black body with temperature ~5800 K (black line).*

Humans; negative attributes of UVR exposure. The negative attributes of UVR exposure to humans are extensive and still remain an active area of research. Broadly speaking, one can group ailments and conditions into three physiological groups: the skin, the eyes, and the immune system, all of which display acute and chronic effects depending on the duration of exposure. Probably the most well known consequence of UV-B overexposure is skin cancer. Both non-melanoma *e.g.* basal and squamous cell carcinomas, and malignant melanomas, of which there are estimated 2-3 million and 130,000 cases per annum respectively, world-wide, contribute to the ~65,000 fatalities from skin cancers every year.[150–152] These are without doubt the most publicised consequences of UVR overexposure, often forming the basis of various 'Sun safety' cam-

*Irradiance ($I(\lambda)$) from a black body at temperature, T, is calculated as the integration of Planck's law over spectral components, λ, *i.e.*

$$I(\lambda,T) = \int \frac{2\pi hc^2}{\lambda^5} \cdot \frac{1}{\exp\left(\frac{hc}{\lambda kT}\right) - 1} d\lambda.$$

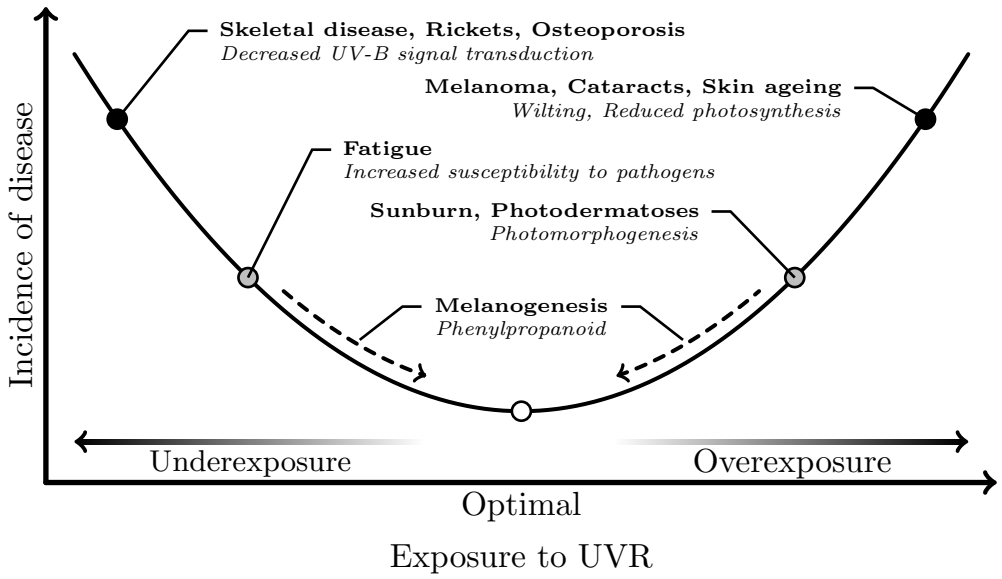

Figure 2.10 | A burden of disease curve exhibited by **humans** and *plants* in response to UVR exposure. There are a number of ailments due to acute and chronic under or overexposure to UVR. Gene-regulated pathways (dashed arrows) exist in response to changing UVR exposure in order to perturb the incidence of disease to a minimum.

paigns. Perhaps less well known examples of UV-induced skin damage include degenerative changes in the cells of the skin, fibrous tissues and blood vessels, all of which have been associated with premature skin-ageing and photodermatoses, and of course, erythema solare (sunburn), most of which are acute effects of UVR overexposure. For the eyes, acute effects range from conjunctivitis, photokeratitis and retinopathy, to chronic effects including pinguecula (which itself is usually benign, but can lead to pingueculitis), pterygium, macular degeneration, ocular melanoma and cataracts, the latter of these is responsible for around ∼3 million cases per year globally,[152] contributing a significant global disease burden. The immune system can also become disrupted by UVR overexposure where cell-mediated immunity can become suppressed leading to an increased susceptibility to infections. Furthermore, overexposure has been associated with the activation of latent viral infections, *herpes labialis* (cold sores) for example.[150]

Positive attributes of UVR exposure. On the face of it there appear to be a myriad of reasons to avoid UV exposure, but UVR plays an important role in many biological processes making use of the high energy components which can penetrate the surface of the skin. Most prevalently, UV-B radiation initiates the conversion of 7-dehydrocholesterol

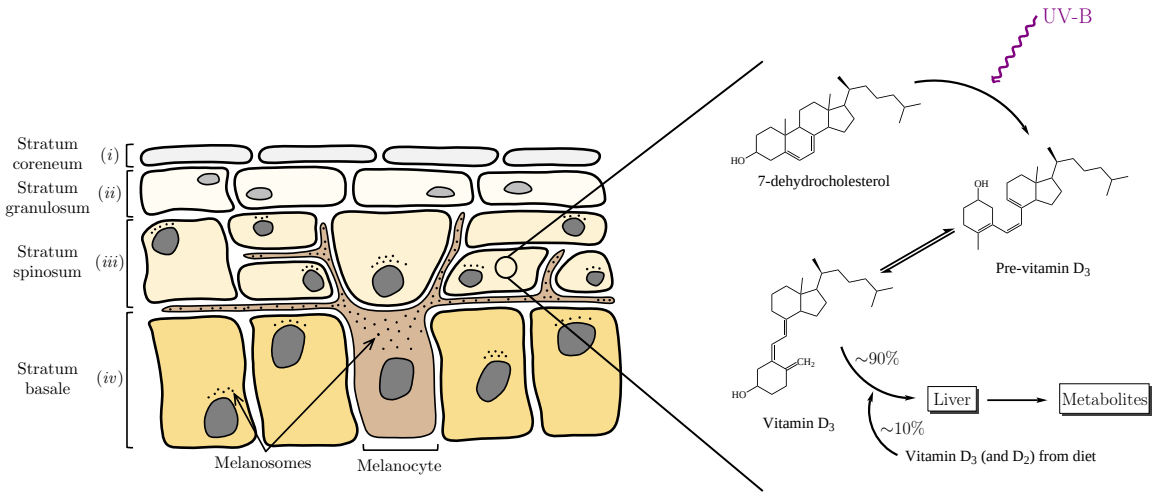

Figure 2.11 | Schematic diagram of the layers found in the skin epidermis. (*i*) The first layer of the epidermis is the stratum coreneum, which consists of a protective layer of dead keratinocytes. This protective layer is by no means negligible; eye and lip tissues are particularly susceptible for the very reason living cells lie close to the surface of those tissues.[156] (*ii*) The stratum granulosum is a layer of keratinocytes migrating towards the stratum coreneum, which, in the process, lose their nucleus and organelles. (*iii*) The stratum spinosum is the thickest layer of the epidermis, packed with keratinocytes. (*iv*) The bottom layer of the epidermis is the stratum basale layer. This layer consists of keratinocytes and melanocytes. The melanocytes produce melanosomes, which are packed with the UV absorbing pigment melanin. These melanosomes are distributed throughout the keratinocytes within the basale and spinosum layers and reside predominately in a supranuclear cap above the cell's nucleus, in the path of incoming UVR. Also shown are the early steps of vitamin D_3 synthesis. 7-Dehydrocholesterol in the skin is converted to previtamin D_3 *via* UV-B radiation. Isomerisation occurs forming vitamin D_3 which is subsequently processed in the liver (along with any vitamin D_3 from one's diet) to form metabolites for various biological processes, discussed in the main text.

to previtamin D_3,[153] an early step in the synthesis of vitamin D (Figure 2.11).[†,‡] In fact, UV-B mediated production of vitamin D constitutes more than 90% of the total vitamin D requirements of the body, with less than 10% being provided through diet.[148] Furthermore, in an almost idyllic equilibrium, UV-B also destroys previtamin D_3 on long exposures which means vitamin D overdose through sun exposure is essentially impossible.[157,158] Thus UV-B underexposure can lead to a deficiency in vitamin D, which has a range of far-reaching consequences on the body. Early development of bones (*in*

[†]Vitamin D is not a vitamin, it is a hormone.[154]

[‡]For clarity, the natural form of vitamin D synthesised in the body, vitamin D_3, is used synonymously with vitamin D throughout this thesis. Vitamin D_2 on the other hand is synthesised in yeast *via* UVR, and is often used as a vitamin D supplement (Figure 2.11).[155]

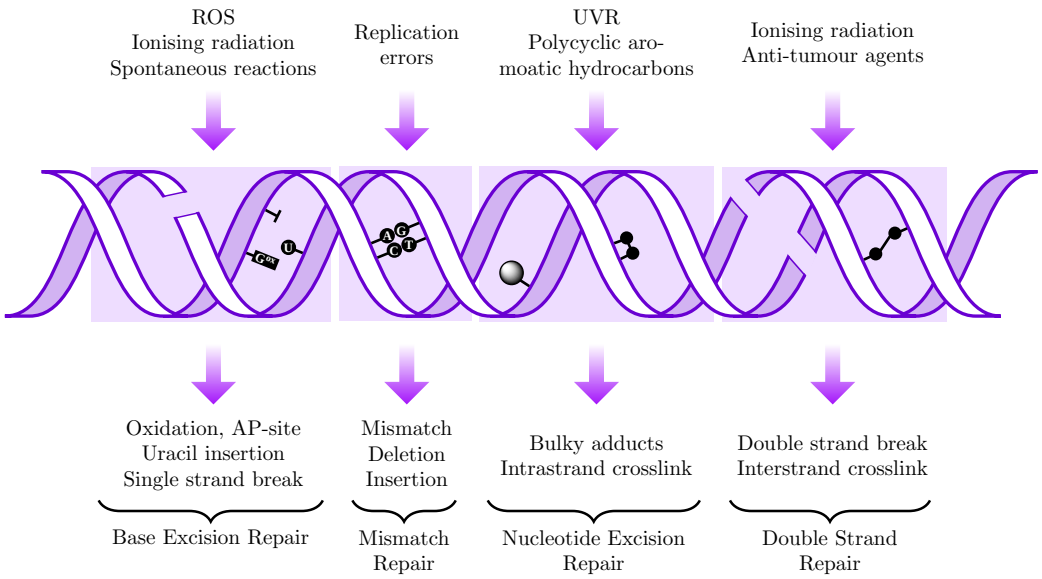

Figure 2.12 | Summary of the typical sources and consequences of DNA damage.[161]

utero or childhood) for example requires vitamin D which otherwise can lead to rickets and skeletal disease.[148,153] Even in adulthood, a deficiency in vitamin D can contribute to osteopenia and osteoporosis. These conditions are linked to vitamin D because of its role in calcium and phosphorus uptake. For example, 1,25-dihydroxyvitamin D, a metabolite of vitamin D stimulates the uptake of calcium and phosphorus in the intestine by ∼40% and ∼80% respectively.[153,159] Other beneficial effects of adequate UVR exposure include a possible lower incidence of many conditions and illnesses.[160] For example some cancers, *e.g.* non-Hodgkins lymphoma, prostate, breast and colon cancers has been suggested.[150] Conditions such as hypertension, and psychiatric disorders such as seasonal affective disorder and schizophrenia have been suggested to benefit from adequate UVR exposure.[150] The moral of this is that a balance, or equilibrium, needs to be struck between UVR under- and overexposure.

Maintaining an equilibrium in the burden of disease. The human body has a number of mechanisms at its disposal in order to prevent, protect, and repair damage from the adverse effects of UVR under- or overexposure. An overview of the typical sources and biochemical consequences of DNA damage is given in Figure 2.12. We restrict our discussions to damage induced either by direct, or indirect interaction with UVR.[161] Direct damage is the result of UVR interacting with electrons localised on nucleotides which can result in the formation of nucleotide dimers (such as inter- or intrastrand crosslinks), breaks in either single or double strands of DNA, as well as the oxidation

of existing bases such as guanine (*cf.* Figure 2.7).

Indirect damage on the other hand is caused by the secondary reactions a chemical species undergoes with DNA, formed as the result of UVR exposure. Perhaps the most well known examples of this are the generation of Reactive Oxygen Species (ROS),[162] such as superoxide ions ($O_2^{\bullet -}$), which are produced through ionising radiation like UV as well as exogenous chemical species. They go on to interact with DNA and other vital structures like protein manifolds which disrupts their job, or in the case of DNA, alters the bases leading to errors in the sequences. This example of UV-induced DNA damage is capable of being fixed through various means, predominantly through enzyme controlled base excision or nucleotide excision repair mechanisms. These mechanisms utilise a complex set of check-pointing processes which spot different DNA damage,[163] and initiate the appropriate response. In the worst case, where damage cannot be repaired, 'programmed cell death' or apoptosis is triggered preventing the replication of a damaged genome.[164]

These mechanisms are reserved as a 'last resort' to DNA damage; skin pigmentation is the primary photoprotective mechanism found in humans. Skin pigmentation works by absorbing harmful UVR before it has had chance to interact with DNA or other UV sensitive constituents of a cell.[§] This pigmentation is made up of melanins, a class of UV absorbing molecules which polymerise into chains and are deposited inside a cell above its nucleus, in the path of incoming UVR.[166] There are four types of melanin: eumelanin, a black-brown pigment, pheomelanin, a reddish-yellow pigment, mixed melanin, a combination of eumelanin and pheomelanin, and finally neuromelanin, a dark brown pigment found only in the brain.[165,167] Of these different melanin pigments, eumelanin and pheomelanin are singled out to be the ones dominantly responsible for UVR photoprotection, and thus we restrict our discussion to these pigments henceforth. Eumelanin and pheomelanin are synthesised through a tyrosine-driven biochemical pathway, summarised in Figure 2.13. First, tyrosine is converted to dopaquinone enzymatically. If no cysteine is present, dopaquinone can be converted to 5,6-Dihydroxyindole (DHI) or 5,6-Dihydroxyindole-2-Carboxylic Acid (DHICA), which polymerise together to form

[§]A point of consideration is that pigmentation is indeed required for photoprotection but may have arisen for entirely other selective pressure. For example, as the brains of early humans developed, blood flow to the brain needed to be increased, at the expense of increased heat generation. In turn this would require more effective heat dissipation mechanism, such as shedding coats of hair, where the skin becomes more susceptible to UVR damage. An interesting, counter-intuitive question is raised, why does the scalp continue to have thick coats of hair? This might be addressed by noting that melanins have a strong propensity to bind to heavy transition metals, and given evidence ancestors would have likely consumed a heavy fish-based diet, this would have been an important selective pressure on maintaining scalp hair.[165] In this thesis however, we restrict our consideration of melanin to a photoprotective pigment.

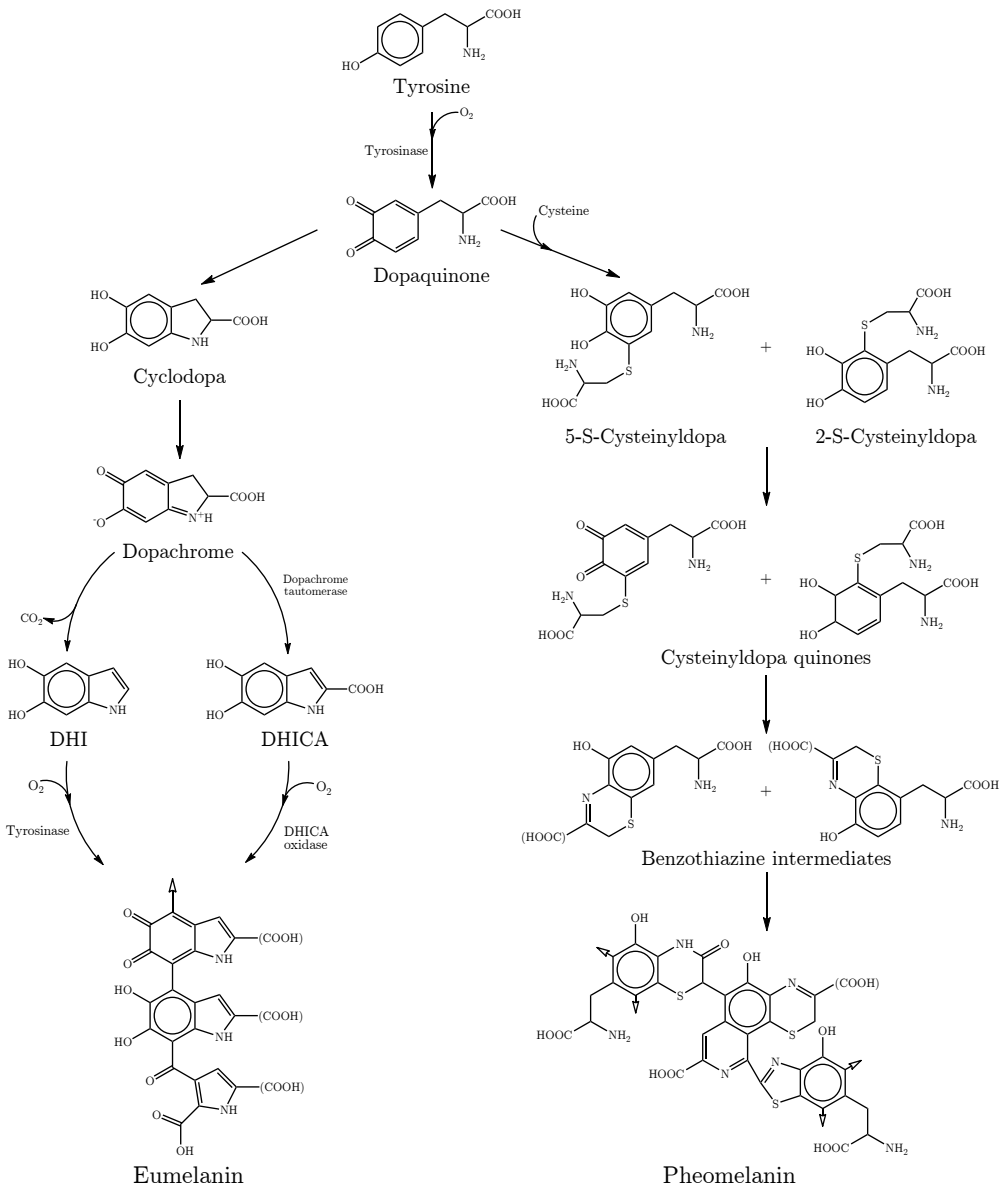

Figure 2.13 | Overview of the biochemical synthesis of eumelanin and pheomelanin inside melanosomes.[168] For both eumelanin and pheomelanin, the first step is the hydroxylation and enzymatic conversion of tyrosine to dopaquinone. If no cysteine is present, dopaquinone converts to cyclodopa and then dopachrome. Here DHI and DHICA form, which polymerise together to form eumelanin. If cysteine is present, then dopaquinone can form cysteinyldopa isomers which convert to cysteinyldopa quinones and finally benzothiazine intermediates. These intermediates polymerise together to form pheomelanin. (COOH) can be COOH or H. Hollow arrows indicates the direction of further polymerisation.[169]

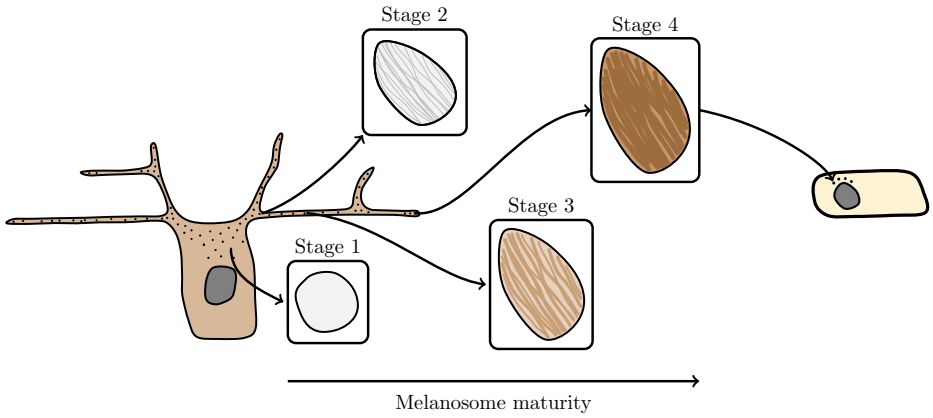

Figure 2.14 | An overview of melanosome maturity inside melanocytes as they journey towards the end of a dendrite.[166] Stage 1: An approximately spherical organelle forms with an amorphous matrix and essentially no structure, called a premelanosome. Stage 2: A structured protein fibrillar matrix forms; tyrosinase is present. Stage 3: Melanin production begins and is deposited onto the fibrils. Stage 4: Melanosomes become fully melanised and now lose tyrosinase activity, they are then transported to the host keratinocyte through a number of suggested processes.[170]

eumelanin. On the other hand, in the presence of cysteine, dopaquinone is converted to isomers of cysteinyldopa before forming benzothiazine intermediates, which polymerise together to form pheomelanin.

This synthesis takes place inside specialised cells called *melanocytes*.[166] They synthesise vesicles termed *melanosomes* which in turn synthesise melanin as described in Figure 2.13.[166,171] Melanocytes form long projections (dendrites) out to surrounding skin keratinocytes in the stratum basale and stratum spinosum layers; typically one melanocyte reaches upwards of forty keratinocytes.[170] Melanosome mature and become fully melanised as they are transferred to the ends of the dendrites through cytoskeletal assisted processes (Figure 2.14), and then to surrounding keratinocytes through a number of suggested mechanisms.[170,172] Once the melanosomes are inside their host keratinocyte, they are positioned around the nucleus forming a supranuclear cap in the path of incident UVR. The overall photoprotection provided will depend on the concentration and distribution of melanocytes, their size and morphology, as well as the concentration of melanin inside melanosomes, properties which are regulated by a set of genes, collectively known as the process of *melanogenesis*.[164,166,173]

Melanogenesis turns a static picture of photoprotection into a dynamic, adaptive photoprotective process. For example, when skin is subjected to high levels of UVR, which the current level of skin pigmentation is not protected against, signalling path-

ways up-regulate melanogenesis which can increase the number of melanocytes and melanosome production, the result is facultative skin colour, often referred to as tanning.[174] Conversely, if UVR exposure is too low, melanogenesis is down-regulated to decrease eumelanin distribution so that sufficient vitamin D can be synthesised. Melanogenesis therefore provides the ability for the body to respond to changing levels of UVR as well as metabolic requirements, which helps to maintain an optimal position in the burden of disease, *cf.* Figure 2.10.

An issue remains; although there is a regulated pathway to respond to changes in incident UVR, it is a delayed response (∼3-5 days after UVR overexposure), after which photodamage could have already occurred, with any intermediate tanning affording almost no additional protection.[175,176] Thus photodamage may have already occurred by the time the body has begun to respond to damaging UVR levels. In the proceeding text, we provide an analogous overview of the photobiology exhibited by plants through UVR exposure.

Plants; negative attributes of UVR exposure. Plant life has achieved phenomenal resilience to a variety of living conditions and an ability to adapt to dynamic changes in its habitat, of which UVR exposure is just one example. Like humans however, overexposure to UVR, and in particular UV-B radiation can have detrimental effects on a plant's ability to survive. Perhaps the most profound effect is once again through damage to DNA either by direct photodamage, or indirectly *via* the generation of ROS which subsequently interact with DNA nucleotides.[177,178] This can lead to genetic mutations which, unless repaired (the probability of which decreases with increased UVR exposure) will cause cells to either replicate a damaged genome or to undergo apoptosis and die. UVR is also known to damage photosynthetic machinery, specifically enzymatic control of photosystem II which can dramatically reduce photosynthetic efficiency. Similarly a reduction in pollen fertility is known to occur in some plants.[178] Another noticeable change brought on by UVR overexposure is photomorphogenesis, whereby a plant's leaves change morphology due to UVR *e.g.* the epidermis may become thicker, increased auxiliary branching, leaf length and leaf area,[179–182] some of these might be useful for survival, but some do increase susceptibility to invading pathogens, clearly some 'trade-off' is met.[177,178]

Positive attributes of UVR exposure. UVR, in particular UV-B radiation behaves as a signal transducer for an enormous array of processes; some, as described above, are degenerative to a plant's survival but many initiate or regulate gene responses which are vital for correct functioning.[177] UV-B radiation stimulates the expression of genes responsible for DNA repair, a noteworthy example is the use of UV-A and enzymatic

control for the repair of photodamaged DNA nucleotides. Contrary to the negative attributes of photomorphogenesis described above, some changes to leaf morphology can deter pests, significantly increasing survival rates.[177,178] An excellent review of UV-B signal transduction can be found in Jenkins, *Annu. Rev. Plant Biol.*, 60:407-431, 2009.[177]

Maintaining an equilibrium. Like with humans, plants are continuously trying to maintain a balance in the burden of disease *cf.* Figure 2.10. They require sunlight to carry out photosynthesis and thus have to be subjected to some UVR in the daily solar spectrum, but clearly too much UVR can be damaging. Analogous to melanogenesis in humans, plants have a regulated biochemical pathway which can be up-regulated and down-regulated in response to UVR exposure, called the *phenylpropanoid pathway.*[183] This pathway is responsible for the synthesis of a rich source of metabolites used in a myriad of biochemical processes throughout a plant. The keys to this pathway are aromatic amino acids and their derivative metabolites. Early plant life, such as aquatic algae, simply used aromatic amino acids as UV-B filters, similarly to early cyanobacterium screening agents as discussed. More complex plant life evolved on the Earth's surface, and phenolic acids and polyphenolic molecules were utilised for both filtering properties as well as the regulation and transduction of UV-B signals for defence against micro-organisms.[179,184] Beyond this, with the evolution of terrestrial vascular plants (*i.e.* those which exhibit a system of xylem and phloem), these plants use such polyphenolic molecules as precursors for the synthesise of a number of compounds, most notably: tannins for defence against predation; lignin for defence against micro-organisms as well as mechanical strength for a vascular system; flavonoids, which among many functions, provide UV-B filtering, signal transduction, flower colour and allelopathy.

With respect to photoprotection in many of present day plants, studies on the model plant organism *arabidopsis thaliana*,[183,185] have suggested that the most prominent photoprotective metabolites are sinapate esters (a class of phenolic acids) such as sinapoyl malate which are deposited in the vacuoles of cells in the upper epidermis of leaves (Figure 2.16). These behave as UV-B filters, absorbing and subsequently dissipating UV energy before it reaches sensitive cells in the mesophyll palisade layers. Thus, mirroring melanogenesis in humans cells, in environments of high UVR, the phenylpropanoid pathway is up-regulated to synthesise more sinapate esters to deposit in the upper epidermis.[183] The full pathway for the synthesis of sinapoyl malate has been omitted in this discussion but is widely discussed in the literature,[183,184,187,188] we however present a simple overview (Figure 2.15). Sinapoyl malate is a secondary metabolite synthesised in plants following carbohydrate precursors (phosphoenolpyru-

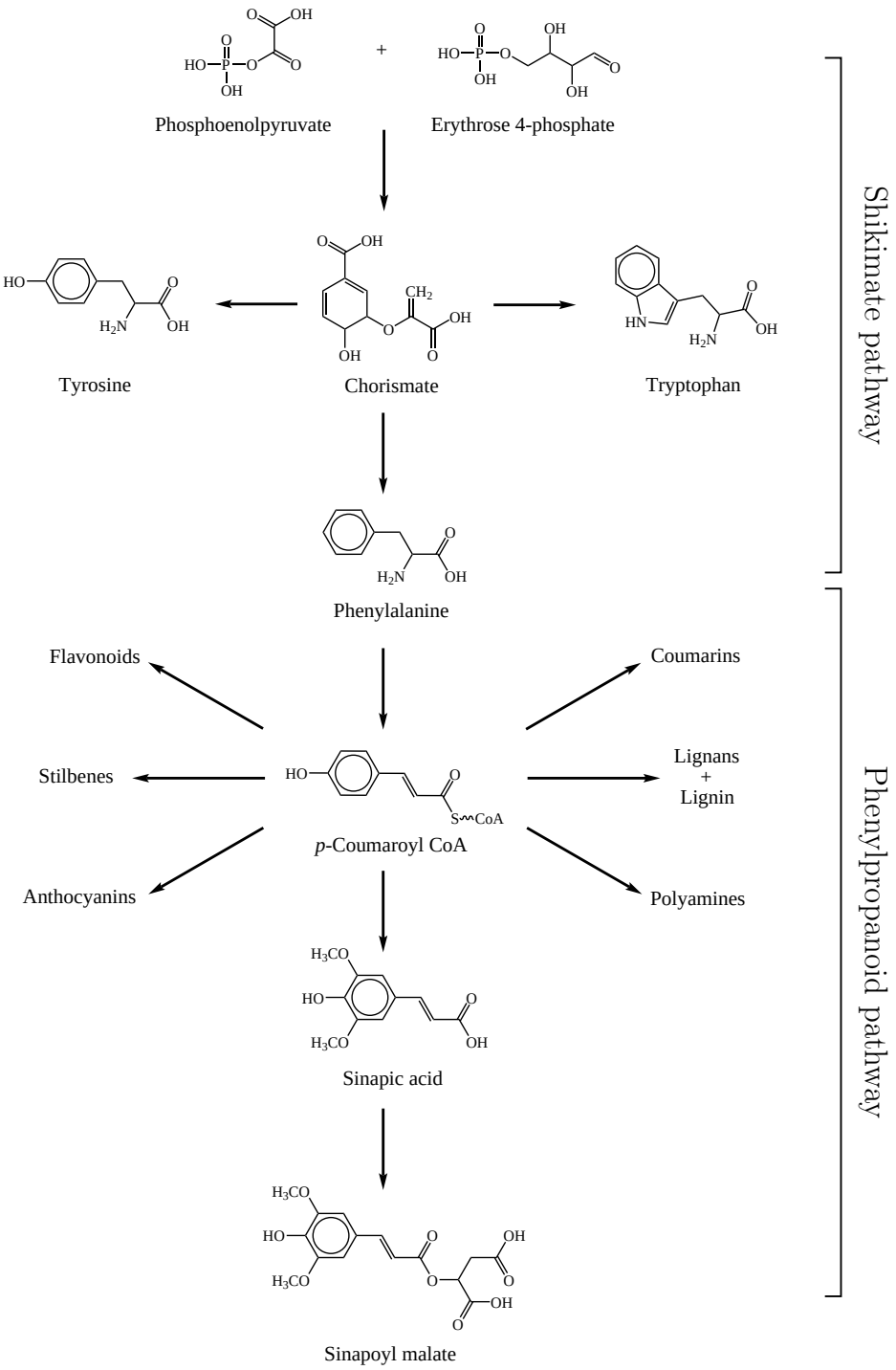

Figure 2.15 | Overview of the synthesis of sinapoyl malate. The Shikimate pathway takes phosphoenolpyruvate and erythrose 4-phosphate as precursor to synthesise tyrosine, tryptophan and phenylalanine. The latter of these is the precursors of the phenylpropanoid pathway which produces *p*-coumaroyl coenzyme A (CoA), the precursor to an array of important secondary metabolites, including sinapic acid which is used to synthesis sinapoyl malate *cf.* Figure 2.16.

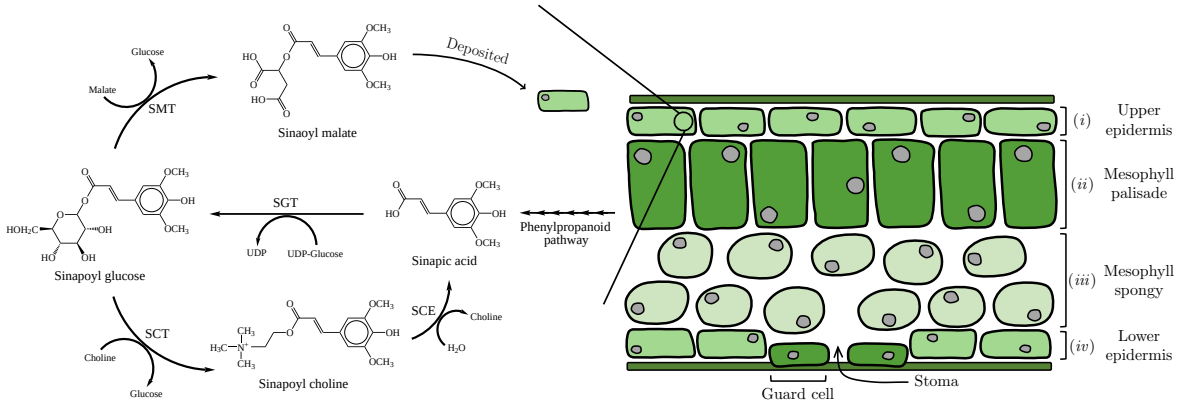

Figure 2.16 | (*right*): Schematic diagram of the layers found in a typical plant leaf. (*i*) The upper epidermis consists of cells with UV-absorbing metabolites, synthesised *via* the phenylpropanoid pathway, providing photoprotection to lower lying layers. (*ii*) The mesophyll palisade layer contains a high proportion of chlorophyll, responsible for the majority of light harvesting from the Sun for photosynthesis. (*iii*) The mesophyll spongy is a dispersed layer of cells allowing room for the exchange of gases required for photosynthesis. (*iv*) The lower epidermis contains cell-regulated openings (stoma) in the leaves by guard cells, allowing photosynthetic gases to be imported (CO_2) or exported (O_2). (*left*): Synthesis of sinapoyl malate from sinapic acid. Sinapic acid is converted to sinapoyl glucose *via* the enzyme sinapoyl glucosetransferase (SGT) metabolising uridine diphosphate glucose (UDP; a sugar-based nucleotide). Sinapoyl glucose is converted to sinapoyl malate *via* sinapoyl malatetransferase (SMT) utilising a malate substrate. This is then deposited in the vacuoles of cells in the upper epidermis.[183,186,¶]

vate and erythrose 4-phosphate) through the *Shikimate pathway*,[187] which produces the three key amino acids, tryptophan, tyrosine and phenylalanine.[‖] The latter of these, phenylalanine, is the sole precursor for the phenylpropanoid pathway previously discussed. Phenylalanine is used to synthesise *p*-coumaroyl acid coenzyme A, a precursor to an enormous array of molecules including flavonoids, coumarins, lignans and lignin, stilbenes, polyamines, anthocyanins, and importantly for photoprotection, sinapic acid and thus sinapoyl malate *cf.* Figure 2.16.

It should come as no surprise that if humans (and indeed some bacteria) have complicated DNA repair mechanisms in the event that primary photoprotective processes fail, then plant life has also developed equally diverse and effective repair processes. They are essentially analogous to those given in Figure 2.12 with a few salient caveats.

¶Sinapoyl glucose can be converted into sinapoyl choline using sinapoyl cholinetransferase and a choline substrate. This is used to form a stock of sinapoyl choline in seeds which upon germination, convert these stores into a supply of sinapic acid *via* hydrolysis with sinapoyl cholinesterase.[183,186]

‖This pathway exits in various bacteria, fungi, algae and plants, but not animals, the latter obtaining these three essential amino acids purely from diet.

For example, plants have retained a repair pathway in evolution utilising multiple photolyases to repair DNA-dimers, humans on the other hand have lost this pathway, perhaps due to adaptive phenotypes like hair or adaptive behaviour characteristics like seeking shelter, which means that humans and mammals in general resort to nucleotide excision repair.[156] Overall however, biologically relevant UV-B exposure does not cause plants to undergo apoptosis nor for plants to develop cancers, implying that the synthesised compounds and repair mechanisms provide extremely efficient photoprotection; there is much to learn from plants.

Global effects. To conclude this section on UVR effects on the biosphere, we highlight the impact to Earth's organisms indirectly, something often taken for granted. This has become an increasingly studied area in the context of climate change;[189] as the ozone layer is depleted by pollution, incidence UVR increases, particularly for UV-B, and more worryingly, eventually, UV-C wavelengths. In the first instance, this of course means that the incidence of the negative effects on humans and plants, *e.g.* skin cancer rates, and environmental stress on plants will becomes an increased disease burden. For example, for each 1°C rise in surface temperature, it is suggested that the incidence of basal and squamous cell carcinomas increase by 3% and 6% respectively.[190,191] Moving away from species-specific UVR-overexposure consequences, concerns have been raised about the survival of aquatic life,[192,193] for example, phytoplankton. They are the main producers of the ocean, using photosynthesis to produce organic matter, responsible for about half of all ocean organic matter! Increases in UVR exposure have been shown to be detrimental to specific species of phytoplankton, indicating disruption to the global ocean food-web where some species can adapt, and some will die off.[194] Biochemical cycling, for example, carbon fixation, nutrient cycling, trace metal micronutrient cycling are all affected by variations in solar UVR, particularly detrimental for aquatic ecosystems. Given the effects of UVR on plant life, increased UVR is suggested to pose a threat to the global food supply,[180,195] although the degree to which this might occur still remains unclear.[196]

2.2.3 The rise of artificial photoprotection

Up until now we have discussed the biological implication for UVR under- or overexposure and how the body pre-emptively protects against UVR, or repairs UV-induced damage. As briefly mentioned, tanning is the response to protecting the skin against UVR levels that the body is not phenotypically predisposed for. However, tanning is a delayed response, it can take between 3 and 5 days for initial UVR over exposure to induce measurable additional photoprotection even if there is intermediate tanning. This

is because any intermediate tanning is simply the oxidation of pre-existing melanin, and thus does not provide additional photoprotection.[175,176] This has become increasingly important given today's availability of tourism,[197] and attitudes towards tanning,[176] meaning tourists for example, are increasingly subjected to UVR levels well beyond their skin's current photoprotection. Of course, this is not an issue for plants, as they build up the required photoprotection for their environmental UVR levels and maintain them.

So what are the options available for humans to satisfy the behaviour exhibited? The simplest is of course to avoid UVR by seeking shade or shelter through various means *e.g.* avoiding direct sunlight around the solar meridian or using parasols. Clothing (shirts, trousers, hats *etc.*) can provide sufficient photoprotection, but it is subject to the fabric type, its construction (weave *etc.*), the dyes used, as well as how worn it is.[198–201] What is particularly effective about clothes as a photoprotective measure is that they provide essentially uniform UV-A and UV-B protection, are waterproof, they don't need reapplying, and essentially cannot be used incorrectly. These, however, are not convenient for people who want to sunbathe or swim without restriction, which of course limits their use for these activities. Sunglasses are an important measure given the particular sensitivity eye tissue has compared to the skin, and adequate sunglasses can provide essentially complete UVR protection for the eyes.[202,203] In addition to these readily available photoprotective measures, sunscreen products have become an almost universally adopted method of providing on-demand additional photoprotection for many reasons, most of which stem from facilitating the various holiday activities people wish to partake in. Sunscreen products will be the focus of this thesis and are discussed in detail in the next section.

So far we have described the options available for additional photoprotection in a qualitative manner. In an effort to standardise a quantitative measure on the effectiveness of sunscreens in providing photoprotection, the Australian scientist Franz Greiter in 1974 proposed a methodology which has now been adopted by the pharmaceutical, cosmetic, and textile industries globally. The Sun Protection Factor (SPF) is used in assessing the protection of sunscreen products;[204] the Ultraviolet Protection Factor (UPF) is used in assessing the protection of textiles. SPF and UPF are identically calculated, and differ only by the experimental conditions used to acquire the data used for the calculation. For UPF, a spectrophotometer is usually employed to measure the photon flux with and without the textile present.[205] For SPF, 2 $mg \cdot cm^{-2}$ sunscreen is used on skin samples (or human participants), and the time to the onset of erythema is detected with and without the sunscreen applied.[206] These measures are

Table 2.2: The UPF for some common textiles and items of clothing.[210,211] The rating is based on current European Union guidelines.[206] The important lesson with this is that the variability in photoprotection for the same material depends heavily on the % coverage the clothing provides, and the type of weave and dye used to make the item.

Material / Garment	UPF	% UVR Transmission	Rating
Cotton	3–13	7.7–33.3	Low–Medium
Nylon	5–77	1.3–5.0	Low–Very high
Wool	8–139	0.7–12.5	Low–Very high
Linen	5–9	11.1–20	Low
Acrylic	6–104	1.0–16.7	Low–Very high
Acetate	4-5	20.0–25.0	Low
Polyester	7-77	1.3–14.3	Low–Very high
Summer dress	137	0.7	Very high
100% cotton T-shirt	41–49	2.0–2.4	High
Polo T-shirt	71-114	0.9–1.4	Very high

therefore *the ratio of UVR transmitted with and without some photoprotective measure*, or formally[206,207]

$$\mathrm{SPF} = \mathrm{UPF} = \frac{\int \mathrm{I}(\lambda)\mathrm{E}(\lambda)d\lambda}{\int \mathrm{I}(\lambda)\mathrm{E}(\lambda)\mathrm{T}(\lambda)d\lambda}, \tag{2.17}$$

where $\mathrm{I}(\lambda)$ is the irradiance spectrum used in the experiment, perhaps the solar irradiance *cf.* Figure 2.9 or an artificial solar spectrum like a UV lamp, $\mathrm{E}(\lambda)$ is the erythemal action spectrum,[208,209] *i.e.* the absorption coefficient for wavelength λ by the skin, and $\mathrm{T}(\lambda)$ is the transmittance of wavelength λ through the photoprotective measure (sunscreen or textile *etc.*). The UPF for some common textiles as calculated from Equation 2.17 are provided in Table 2.2. The result is a single number which tries to capture the photoprotection of the item. Whilst it is debated whether or not this is a truly useful labelling mechanism for a consumer,[205,212] it remains the most widely used quantitative labelling system for all commercial sunscreen products and specialised UV-protective textiles.

2.2.4 Photoprotection through the use of sunscreens

The causal link between excessive sun exposure and the development of skin erythema and tanning has been known for thousands of years, even if the reason for this link has only begun to be understood over last century or so. Ancient civilisations, such as the Egyptians and Greeks, took steps to protect the skin with varying success; rice bran, jasmine and olive oil were applied to the skin, often for cosmetic reasons, but

they provided additional photoprotection making them some of the earliest recorded sunscreens.[213,214] It was not until 1801 when Johann Ritter discovered UVR, and a series of experiments in 1889 by Erik Widmark, who proved erythema solare (sunburn) was caused by UVR, which led to the suggestion of using chemical sunscreens in order to protect the skin by the end of the 19th century.[215]

One of the first successful commercial sunscreen products was developed by Eugene Schueller in 1935/6, who went onto found the company now known as L'Oreal.[204] The sunscreen was called 'Ambre Solaire', an oily substance which contained the UV absorber benzylsalicylate. Over the following decades, many compounds were studied spectroscopically and led to the widespread use of para-aminobenzoic acid,[215–219] later benzonphenones,[220] and today's many 10s of UV absorbing molecules which are regularly used in commercial products, many of the widely used popular filters are given in Table 2.3.[204,221,222] The use of sunscreens has exploded since their first inception, leading to a multi-billion-pound global industry, which is now largely regulated with the inclusion of specific UV absorbing molecules approved at limited concentrations for use in commercial products.

Sunscreen products are applied to the upper epidermis of the skin and work in a complementary manner to the natural photoprotection provided by skin pigmentation. They contain components which are responsible for intercepting UVR and dissipating the energy through safe processes. Generally speaking, there are two classes of such components, *organic filters* and *inorganic particulate filters* (Figure 2.17).[204,264,265] Organic filters are typically aromatic molecules which have a high degree of charge conjugation. They absorb broadly at UV-A and/or UV-B wavelengths often through $^1\pi\pi^*$ transitions which are accessible at these energies. They dissipate the energy through a variety of nondestructive pathways,[267] for example as heat to the surroundings. Inorganic particulate filters are usually nano-sized particles that display broad absorption across UV-A and UV-B wavelengths. They also have the ability to scatter incoming radiation away from the skin (Figure 2.17(B)), where the ratio of absorption and scattering cross-sections depends on the properties of the particulate,[268] *e.g.* diameter and coating. As such, these components are sometimes referred to as inorganic scatterers. Thus, a combination of organic and inorganic particulate filters can provide a broad spectral coverage for sunscreen products, which serves as the defining property of any good sunscreen product. However, there are a number of other considerations in designing a commercial sunscreen product: the texture, ease of application, degree of water-resistance, frequency of application required, suitability for a broad range of skin types and conditions, smell and production costs, all weigh in when designing the final

Table 2.3: 54 of the popular UV filters used as sunscreen components authorised around the world, and a non-exhaustive list of related studies regarding: photostability (PS), allergies (photo or contact; PA), endocrine absorption (AB). Regions: European Union (1), United states of America (2), Australia and New Zealand (3), Canada (4), Japan (5), South Africa (6). Parts of this table have been reproduced from Shaath, *Table 1.*[223]

Name	Authorisation	Suitability studies
Benzophenone-1	5, 6	–
Benzophenone-2	3, 5, 6	–
Benzophenone-3 (Oxybenzone)	1–6	PS,[224] PA,[225] AB[226–230]
Benzophenone-4	1–5	PA[221,231–233]
Benzophenone-5 (Sulibenzone)	1, 3, 5, 6	PS,[234] PA,[235] AB[226]
Benzophenone-6	5, 6	–
Benzophenone-8	2, 3, 4, 6	PA[232]
Benzophenone-9	5, 6	–
3-Benzylidene camphor	1, 6	PS[234]
Benzylidene camphor sulfonic acid	1, 3, 5, 6	PS[236]
Beta-2-Glucopyranoxy propyl hydroxy benzophenone	5, 6	–
Bis-ethylhexyloxyphenol methoxyphenyl triazine (Bemotrizinol)	1, 3, 6	PS[237]
Butyl methoxydibenzoylmethane (Avobenzone)	1–6	PS,[238–240] PA[241]
Camphor benzalkonium methosulfate	1, 3, 6	–
Cinoxate (2-ethoxyethyl-p-methoxycinnamate)	2, 3, 4, 5, 6	PS,[219] PA[242]
DEA methoxycinnamate	4, 6	–
Diethylamino hydroxybenzoyl hexyl benzoate	1, 3, 5, 6	–
Diethylhexyl butamido triazone	1, 6	–
Digalloyl trioleate	6	PS[243]
Diisopropyl methyl cinnamate	5, 6	–
Dimethoxyphenyl-[1-(3,4)]-4,4-dimethyl 1,3-pentanedione	5, 6	–
Disodium phenyl dibenzylimidazole tetrasulfonate	1, 3, 6	–
Drometrizole	5	–
Drometrizole trisiloxane	1, 3, 5, 6	PA[244,245]
Ethyl dihydroxypropyl PABA	4, 6	PA[246]
Ethylhexyl dimethoxy benzylidene dioxoimidazoline propionate	5, 6	–
Ethylhexyl dimethyl PABA	1–6	PS,[224] PA[231]
Ethylhexyl methoxycinnamate (Octyl methoxycinnamate)	1–6	PS,[224,237] AB[227]
Ethylhexyl salicylate	1–6	PS[234]
Ethylhexyl triazone (Octyl triazone)	1, 3, 5, 6	PS,[234,237,247] PA[231]
Ferulic acid	5, 6	PS[248]
Glyceryl ethylhexanoate dimethoxycinnamate	5, 6	–
Glyceryl PABA	4, 5, 6	PA[232,246]
Homosalate	1–6	PS,[234] PA[235]
Isoamyl *p*-methoxycinnamate	1, 3, 5, 6	PS,[234] PA[233]
Isopentyl trimethoxycinnamate trisiloxane	5, 6	–
Isopropyl benzyl salicylate	3, 5	–
Isopropyl methoxycinnamate	5, 6	–
Menthyl anthranilate	2–6	PS[249]
4-Methylbenzylidene camphor	1, 3, 4, 6	PS,[234] PA[235,250]
Methylene bis-benzotriazolyl tetramethylbutylphenol	1, 3, 5, 6	PS[234], PA[231]
Octocrylene	1–6	PS,[234,237,251] PA[252–254]
PABA	1–6	PS,[239,255,256] PA[256]
PEG-25 PABA	1, 3, 5	PS[234]
Pentyl dimethyl PABA	5	PA[257]
Phenyl benzimidazole sulfonic acid	1–6	PS,[224,234] PA[250]
Polyacrylamido methylbenzylidene camphor	1, 6	PA,[258] AB[259]
Polysilicone-15	1, 3, 5, 6	PS,[234] PA[260]
Salicylic acid	3	PA,[261] AB[261]
TEA salicylate	2, 3, 4, 6	–
Terephthalylidene dicamphor sulfonic acid	1, 3, 4, 5, 6	PS,[247] PA[250]
Titanium dioxide	1–6	PS,[247,262] AB[263]
Zinc oxide	2–6	PS,[247] AB[263]

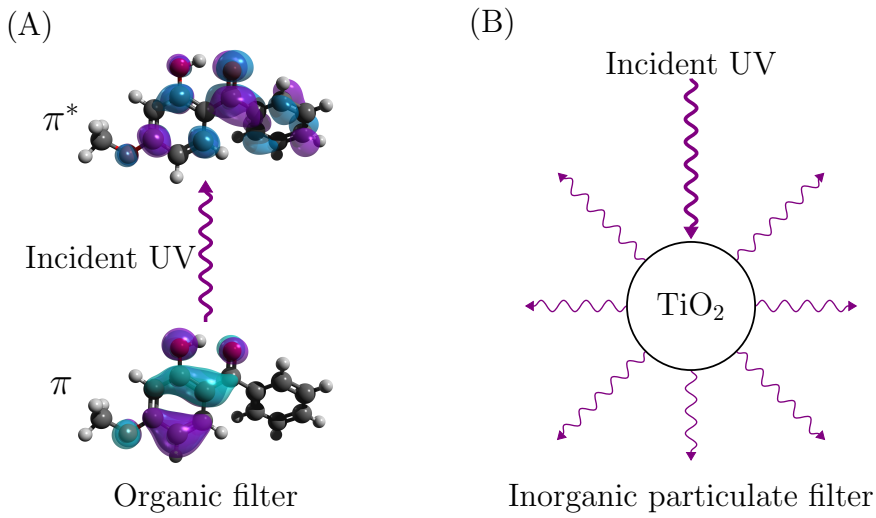

Figure 2.17 | (A) Oxybenzone, a common organic filter used in commercial sunscreens exhibits a strong $\pi^* \leftarrow \pi$ transition when excited by UV radiation, responsible for its broadband absorption profile across the UV region.[16,17,266] In general, organic filters absorb UVR and dissipate it before it can reach sensitive skin cells. (B) An extensively used inorganic particulate filter in commercial sunscreens, titanium dioxide (TiO_2). Unlike organic filters, inorganic particulate filters also provide photoprotection through scattering and reflecting UVR away from the skin, as well as absorbing incident UVR.

product.

Another consideration that needs to be taken when selecting a molecule for a sunscreen is the speed at which energy dissipation occurs with. Any good filtering sunscreen molecule needs to not only absorb harmful UVR, but also needs to dissipate the energy on ultrafast timescales faster than any potentially destructive pathways. One can assume the faster the better, pointing towards ultrafast timescales (picoseconds, 1 ps $= 10^{-12}$ seconds; femtoseconds, 1 fs $= 10^{-15}$ seconds), such that it is ready to absorb another UV photon, otherwise the sunscreen would not provide photoprotection for any tangible time, or, many layers of sunscreen would be required for any photoprotection which would not be consumer friendly. The result of this is a product which contains many 10's of individual components in order to satisfy as many of these requirements as possible (Figure 2.18).

A point of contention remains in commercial sunscreen products in that even with these design criteria, sunscreen products are not necessarily safe for the skin. For instance, if any of the components are absorbed into the blood stream, questions about the effect of the component on the human physiology will clearly be of concern,[271] *cf.*

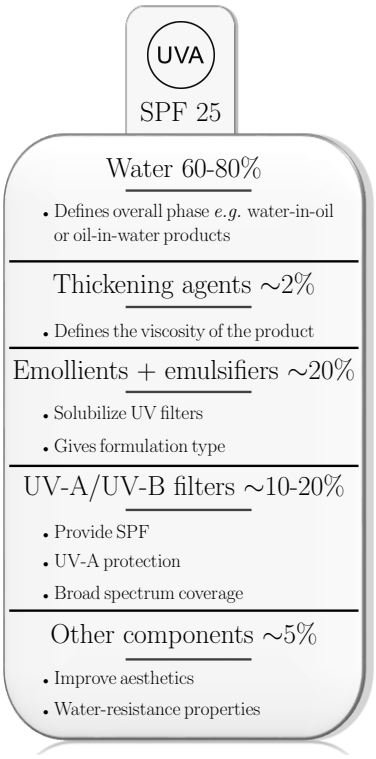

Figure 2.18 | The typical formulation of commercial sunscreen products is the combination of many individual components to make an effective and consumer friendly product.[269] The European symbol of UV-A protection is shown.[270]

Table 2.3. Generally speaking, this contention point is referred to as the "sunscreen controversy", which essentially asks the question, *do the products used to protect the skin from UVR have adverse physiological effects?* This controversy has grown given incidences of skin cancers are rising,[272] coupled with studies which have raised concerns for some commonly used filters (such as skin sensitisation), many of which have been highlighted in Table 2.3.[222,239,273–275] To gain perspective however, it is important to note that even with these potential avenues for adverse effects, the photoprotective role sunscreens play cannot be disputed. For example, a landmark study by Green *et al.*[276] clearly showed that melanoma risk can be cut in half through regular sunscreen use.[277] Such perspective is particularly important given some of the perpetuated myths and misinformed allegations regarding sunscreen use which can be dangerous to the public perception of sunscreens.[278]

Ultrafast photochemistry might contribute somewhat to the resolution of the sunscreen controversy, from a photophysical perspective. By understanding the detailed photophysical and photochemical processes a sunscreen component undergoes at the

molecular level, and ultrafast timescales, an evaluation on its photo-suitability can be made. Furthermore, solution-phase measurements of these components, as opposed to isolated gas-phase measurements, are a step closer to mimicking the environment of a commercial sunscreen. Indeed, this technique has proven remarkably successful in understanding many molecular systems (vision, light-harvesting), including sunscreen molecules, and as such, a review of the current literature is given in the following section.

2.2.5 Current state of the ultrafast photochemistry of sunscreens

Studies have essentially focussed on single molecular systems of many of the popular sunscreen given in Table 2.3, the structures of which are shown in Figure 2.19. Specific details of the experimental techniques which are at the heart of many of these studies are given in the next section, this however places the rest of the thesis on a firm foundation and where the results have contributed to this field.

Benzophenones and derivatives. These are a class of molecules which contain two aromatic rings connected by a carbonyl group see Figure 2.19(A). They are used widely as organic UV-A and UV-B filters due to their strong absorption in these regions, usually *via* strong absorbing $^1\pi\pi^*$ transitions. (*i*) *Avobenzone* has been widely used in commercial sunscreens since the 1970s and as such, has been the subject of numerous studies. It exhibits a broadband absorption maximum in the UV-A region, *c.* 350

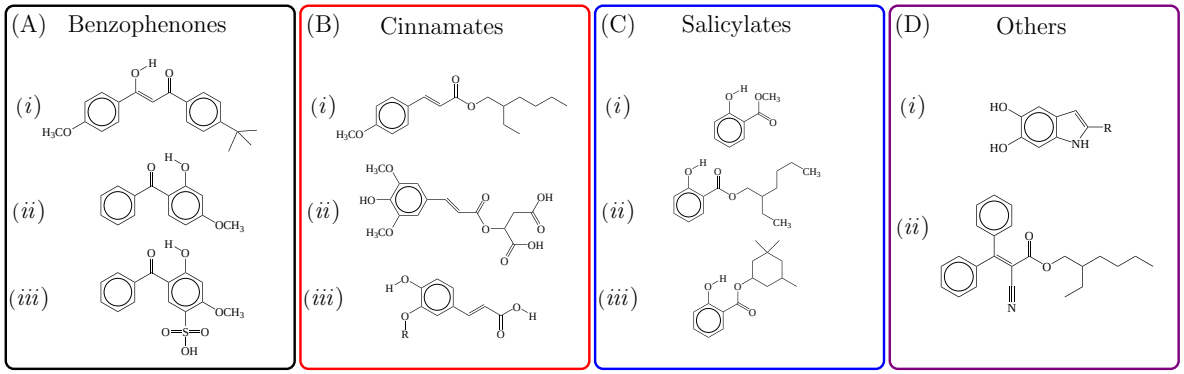

Figure 2.19 | Common sunscreen organic filters. (A) Benzophenones: (*i*) avobenzone, (*ii*) oxybenzone and (*iii*) sulisobenzone. (B) Cinnamates: (*i*) octyl methoxycinnamate, (*ii*) sinapoyl malate and (*iii*) ferulic acid (R=CH_3) and caffeic acid (R=H). (C) Salicylates: (*i*) methyl salicylate, (*ii*) octyl salicylate, (*iii*) homomethyl salicylate. (D) Others: (*i*) 5,6-dihydroxyindole (R=H), 5,6-dihydroxyindole-2-carboxylic acid (R=CO_2H) and (*ii*) octocrylene.

nm, which extends into the UV-B region, peaking again around 270 nm,[279] and exists in an energetically preferable *enol*-tautomer, as shown in Figure 2.19(A)(*i*).[238,280] Through nanosecond flash photolysis experiments, avobenzone has been shown to relax through an *enol-keto* tautomerisation.[279,281] Recently, Dunkelberger *et al.* have performed transient electronic absorption measurements on avobenzone in a series of solvents to understand the relaxation mechanism on the ultrafast timescale.[282] Exciting avobenzone at 350 nm populates the first excited state, S_1, which promptly decays over ∼0.4–1.4 ps depending on the polarity of the solvent, and forms an ensemble of energetic populations; a chelated *enol*-avobenzone and three distinct non-chelated *enol*-avobenzone isomers,[282,283] the relative proportions of which depend on the solvent, in the ground electronic state, S_0.[284] The vibrationally hot chelated *enol*-avobenzone reforms the ground state *enol*-avobenzone state by ∼6 ps, through VET to the surrounding solvent. The non-chelated structures have quite different relaxation timescales, one reforms the ground *enol*-avobenzone by ∼1 ps, the second remains for ∼20-80 ps whilst the third extends beyond the time-duration of the experiment. The incomplete recovery of the ground state bleach suggests that some of *enol*-avobenzone transforms into the *keto*-isomer as inferred from other measurements.[279]

(*ii*) *Oxybenzone*, for similar reasons to avobenzone, has found wide spread use in commercial sunscreens due to a strong absorption cross-section across the UV-A and UV-B regions, exhibiting broad peaks at *c.* 325 nm and 287 nm respectively. There have now been several studies focussed on understanding the ultrafast photochemistry oxybenzone displays after UV excitation.[285–289] Ultrafast (electronic and vibrational) transient absorption measurements have been able to suggest an almost complete relaxation mechanism.[286,287] Oxybenzone exists in an energetically more stable *enol*-isomer which after 325 nm photoexcitation, predominately populates the $S_2(1^1\pi\pi^*)$ state. This relaxes by IC to the $S_1(1^1n\pi^*)$ state and then undergoes an Excited State Hydrogen Atom Transfer (ESHT) to form a *keto*-isomer, together taking ∼100 fs. A rotation around its aliphatic C-C bond occurs which allows oxybenzone to couple to its S_0 state through a $1^1n\pi^*/S_0$ CI on a timescale of ∼400 fs. A Ground State Hydrogen Atom Transfer (GSHT) and VET to the surrounding solvent reforms the *enol*-isomer, on the timescale of ∼5-8 ps depending on degree of hydrogen bonding to the solvent bath. An incomplete ground state recovery suggests that a small portion of the excited state populations form a photoproduct, which transient vibrational absorption studies attribute to a trans *keto*-isomer from extended C-C rotation,[286] although other studies have suggested this could be attributed to the formation of a phenoxyl radical.[288] (*iii*) *Sulisobenzone*, similar to oxybenzone, was also studied by Ignasiak *et al.*,[288] to reveal a

$\sim$700 fs and a $\sim$3-4 ps relaxation component which may be understood through a radical formation pathway mechanism, similar to one of pathways suggested for oxybenzone.

Cinnamates and their derivatives. These are a class of molecules which are derived from cinnamic acid, an aromatic, unsaturated carboxylic acid, which are prevalent as sunscreen molecules in commercial products[290] as well as naturally synthesised in some plants for photoprotection, *e.g.* sinapic acid and sinapoyl malate.[183,291,292] (*i*) *Octyl methoxycinnamate* has been used extensively in commercial sunscreen products, though surprisingly, literature on its relaxation mechanism from a ultrafast photochemical perspective remains sparse; studies have focused on its stability as an organic filter.[293–295] Studies have suggested that after UV-B irradiation, octyl methoxycinnamate undergoes an isomerisation from the more stable *trans*-isomer to the less energetically stable *cis*-isomer in both polar and nonpolar solvents.[296,297] Tan *et al.*,[298] have taken further important steps to understanding the ultrafast dynamics of this molecule. Here they used resonance two-photon ionisation to study isolated octyl methoxycinnamate molecules in the gas-phase reporting relaxation lifetimes in the ns regime attributed to the population of a long-lived $1^1n\pi^*$ state. Building on this they use microsolvation with water in order to approximate a solution-phase environment. Interestingly, the addition of this water microsolvation increases the relaxation efficiency remarkably to the ps regime due to a destabilisation of the $1^1n\pi^*$ state, which might otherwise be accessible in the gas-phase environment, although more work remains to be done in order to conclude this.[299] This work laid the foundations of solution-phase studies by Peperstraete *et al.*,[300] which model octyl methoxycinnamate a step closer to a sunscreen environment. The results indeed suggest that a *trans-cis* isomerisation is central to the observed photoprotective properties, in contrast to gas-phase measurements.

(*ii*) *Sinapoyl malate* is a naturally synthesised molecule in many plants from sinapic acid as part of the phenylpropanoid pathway,[183,291] the plant's equivalent of melanogenesis. This molecule has been suggested to fulfil the role of a sunscreen in plants, where UV-B plays a central role to survival but too much can be damaging.[177,178,195,267] Whilst this molecule is not explicitly used in commercial sunscreen products, it remains a point of interest which might help with the rationale of designing commercial products. Vibrationally resolved gas-phase UV spectroscopy experiments along with steady-state fluorescence measurements by Dean *et al.*[301] have laid the foundations of understanding the sinapoyl malate by chemically deconstructing it into a series of sinapate esters. Their results show that sinapoyl malate is unique in having an inherently broad absorption spectrum even under such jet expansion-cooled gas-phase conditions, and likely exhibits an efficient and nonradiative energy dissipation mecha-

nism. Building upon this, solution-phase transient absorption measurements have been able to identify the likely underlying relaxation mechanism in a more closely matched environment to how sinapoyl malate is found.[302] After UV excitation (*c.* 330 nm), the ground state *trans*-isomer populates an excited electronic state which begins to relax. Three components are identified, a short ∼50-600 fs component, a ∼1-5 ps component and a longer ∼20-30 ps component, depending on the solvent. The study suggests two possibilities for the excited states involved: (I) photoexcitation to an $1^1\pi\pi^*$ state, followed by IC mediated by an $1^1\pi\pi^*/2^1\pi\pi^*$ CI to the $2^1\pi\pi^*$ state. Next IC along the *trans-cis* isomerisation coordinate follows, which couples to the ground state mediated by a second CI, $2^1\pi\pi^*/S_0$, followed by VET to the solvent bath. (II) Photoexcitation to the $1^1\pi\pi^*$ state which couples to the ground state *via* an $1^1\pi\pi^*/S_0$ CI. For both of these mechanisms, it is suggested that the dynamics occur along a *trans-cis* isomerisation coordinate. (*iii*) Ferulic and caffeic acids are also naturally synthesised molecules which also exhibit antioxidant properties,[303] with ferulic acid an already approved organic filter in some countries.[223] The photodynamics have been elucidated and follow closely those discussed for sinapoyl malate.[304] Thus sinapoyl malate and its derivatives are worthy research candidates for commercial sunscreen products.

Salicylates and their derivatives. Salicylates are a group of aromatic esters which have been shown to exhibit an *enol-keto* tautomerisation *via* an ESHT, providing an efficient non-radiative relaxation pathway after UV photoexcitation. Despite their commercial use, many of these have received little attention with respect to their ultrafast dissipation mechanisms. (*i*) The most well-studied example is methyl salicylate, a subunit of the larger salicylates found in commercial products and thus an ideal model for a 'bottom-up' approach to understanding the photodynamics of the more complex molecules. Methyl salicylate has been suggested to undergo an ESHT after UV photoexcitation in a number of studies over the years, with particular attention on fluorescence properties.[305–314] Herek *et al.* provided ultrafast measurements in the isolated gas-phase which identified the ESHT occurring within 60 fs, as well as a longer decay channel of 120 ps.[315] Solution-phase studies would be an important extension given fluorescence lifetimes show solvent dependence.[314,316] (*ii*) Octyl salicylate,[317] and (*iii*) homomethyl salicylate are often used in sunscreen products but the literature on their relaxation mechanism remains sparse.[318]

'Others'. (*i*) *Indoles*, DHI, R=H, and DHICA, R=CO_2H, are naturally synthesised subunits of the polymeric eumelanin, responsible for skin pigmentation and thus natural photoprotection.[173,319,320] There has been significant focus on these subunits (and indeed further subunits such as phenol,[321–323] and derivatives[324,325]) in an attempt

to provide a bottom-up approach to understanding the photoprotective properties of eumelanin. Sundström and co-workers,[326–330] among others,[331–333] have made significant progress in elucidating the relaxation mechanism for DHI and DHICA. Ultrafast measurements have suggested that photoexcited molecules might deactivate through ESIPT in ∼100-200 ps. Furthermore, it has been shown that polymerised units of these molecules deactivate faster which might contribute to why eumelanin displays such efficient photoprotection.[334] Eumelanin itself has been studied to some extent but much of its photodynamics still remains to be understood.[334–337] (*ii*) *Octocrylene* is a remarkably popular sunscreen component used around the world,[253] it has found use as an organic filter due to its broadband absorption profile across the UV-A/UV-B regions,[253] its photostability,[251,253] as well as its properties as a photostabilser for other molecules such as avobenzone.[237,251,264,338] Transient electronic absorption studies have recently been reported.[339] This study highlights the efficacy with which octocrylene absorbs UV-B radiation and deactivates through non-radiative pathways, the majority of which happens by ∼2 ps after photoexcitation. Whilst the exact electronic states which participate in this relaxation pathway remains ambiguous, the dynamical lifetimes extracted are very encouraging for such a widely used sunscreen molecule.

Sunscreen controversy. There remain many unanswered questions surrounding the use of sunscreens, and the current state of the sunscreen controversy appears heightened given its prominence in the current literature.[204,221,222,273,340,341] Many of the sunscreen filters discussed here have been subject to various studies specifically to evaluate their photostability or effect on the body (*cf.* Table 2.3).[238–240,253,342,343] For example, oxybenzone, as discussed, predominately relaxes back to its original ground state on ultrafast timescales, but around ∼10 % forms a long-lived photoproduct, where current literature suggests a trans *keto*-tautomer or a phenoxyl radical are likely candidates.[286,288] These photoproducts, in particular the latter, might go on to cause damage to surrounding cells. Furthermore, the oxybenzone molecules themselves might affect the body through absorption into the blood stream, or even other organisms through sunscreens washing off the skin causing water pollution.[229,230,344–346] Knowing detailed spectroscopy about oxybenzone (and indeed other UV filters) has already shown such adverse effects can begin to be reduced, for example through microencapsulation where a filter is embedded inside a particulate carrier, or through lipid nanoparticles, both of which can reduce the filter-skin interaction and generally improve long-term photostability.[256,347–352]

Chapter 3

Experimental methodology

Parts of this chapter have been published by the author:

---

1. **Lewis A. Baker** and Vasilios G. Stavros. Observing and understanding the ultrafast photochemistry in small molecules: Applications to sunscreens. *Sci. Prog.*, **2016**, 99(*3*):282–311.

Declarations:

- The solution-phase transient absorption spectroscopy experimental table was set-up by Dr Simon E. Greenough (University of Warwick, U.K.). The *LabView* program which controls the experimental procedure was written by Dr Simon E. Greenough with contributions from Dr Michael D. Horbury (University of Warwick, U.K.).
- The global fitting script was provided by Dr Adam Chatterly (University of California, Berkeley), which was edited by the author, and used as discussed in Chapters 4 and 5.

3.1 Transient absorption spectroscopy

The historic measurements by Ahmed Zewail's group in 1985,[353] (and later refined in 1987)[354] of the bond breaking reaction, $ICN^* \rightarrow I + CN$, is widely attributed to the birth of femtochemistry,[355] where for the first time, reaction dynamics (*i.e.* the formation of the I and CN fragments) could be observed on a femtosecond timescale. Since then, this pioneering technique used to study simple dissociation reactions has been applied to a plethora of physical, chemical and biological systems, with examples ranging from understanding fundamental quantum dynamics[356] to energy transfer in photosynthetic antennas[357] and porphyrin biomimics.[358] The key in all these experiments is the use of ultrashort lasers pulses, which typically have a duration of <100 fs,[359,360] in what is known as a *pump-probe* scheme.

One laser pulse is used to photoexcite a molecule at a particular wavelength, called the *pump* pulse. In the case of sunscreens molecules, this wavelength will be in the UV region to simulate the conditions sunscreens are used in. Another laser pulse, drawn from a White Light Continuum (WLC) consisting of wavelengths across the UV and visible regions (∼300–800 nm), is used to measure the UV-visible excited state absorption profile of the photoexcited molecule, called the *probe* pulse. The result is essentially a UV visible absorption spectrum of the excited state molecule. By altering the time at which the probe pulse arrives at the molecule relative to the pump pulse, 'snapshots' of the *static* excited state absorption profile can be recorded and used to produce a *dynamic* absorption profile (analogous to the many single pictures used to make a video). The difference in arrival times of the pump and probe is termed the *time delay*, Δt, where $\Delta t = 0$ describes perfect temporal arrival synchronisation, also referred to as 'time zero', and $\Delta t > 0$ describes the probe pulse arriving *after* the pump pulse. Typically, time delays up to many nanoseconds (1 ns = 10^{-9} seconds) in increments as small as 10 fs are used to capture snapshots of the excited state absorption profile across the entire ultrafast timescale.

Ultrashort pulse generation. As briefly described, to resolve ultrafast processes, ultrashort laser pulses are required; the generation of ultrashort pulses has received considerable attention given the inherent requirement of time resolution.[267] A common method for ultrashort pulse generation is through the use of Ti:sapphire lasers which exhibit strong lasing transitions around 800 nm, illustrated in Figure 3.1(A).[357,364] Typically, a green seed laser optically pumps a Ti:sapphire oscillator. This oscillator is mode-locked[365] around 800 nm and releases pulses at a repetition rate of ∼80 MHz *via* an optical switch.[366] Typically, one in 80,000 of these pulses is selected as a 800

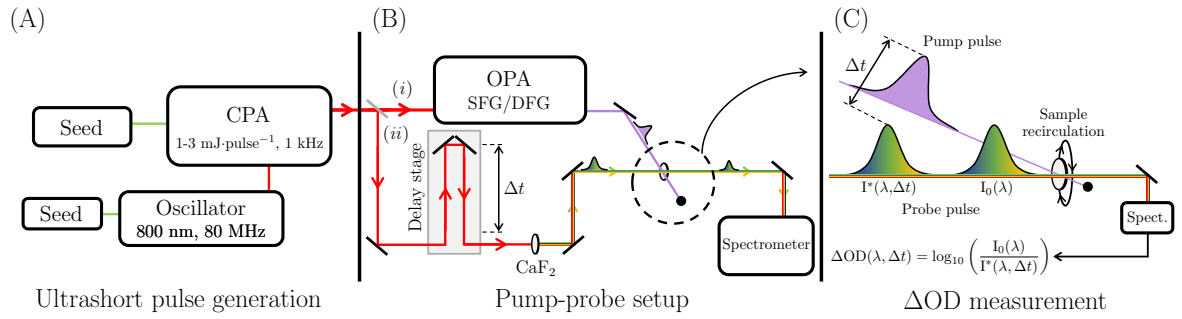

Figure 3.1 | Schematic representation of a typical transient absorption spectroscopy experimental set-up.[267,361,362] (A) A mode-locked Ti:sapphire laser outputs 800 nm pulses with a repetition rate of ∼80 MHz. These are energetically weak (∼1-3 nJ per pulse) so they are used to seed a Ti:sapphire CPA. The CPA amplifies and compresses one in 80,000 seed pulses and outputs 800 nm, ∼1-3 mJ per pulse at a repetition rate of 1 kHz, with a pulse duration of ∼45 fs. (B) The 800 nm output is split into two beams. (*i*) The majority of the output from the CPA seeds either optical parametric amplification (OPA), sum frequency generation (SFG) or difference frequency generation (DFG), discussed in Appendix 8.4.3, which is used for the pump pulses. (*ii*) A small portion of the output of the CPA is focussed inside a CaF_2 crystal for WLG[363] to be used as the probe-pulse for transient electronic absorption spectroscopy. For transient vibrational absorption spectroscopy, broadband infrared pulses can be generated *via* a suitable nonlinear medium which are used as the probe pulses.[363] A delay stage is used to change the pathlength of the probe relative to the pump to introduce a specific time delay, Δt, between them. Both pump and probe are overlapped inside a flow-through cell where the sample is recirculated. A polariser is often used in the probe path to rotate the polarisation of the probe relative to the pump for magic angle (∼54.7°) spectroscopy. (C) The transmission of the probe-pulse is recorded for both a pumped ($I^*(\lambda, \Delta t)$) and unpumped sample ($I_0(\lambda)$), for a range of pump-probe time delays. From these measurements the change in optical density, ΔOD, is calculated for each wavelength at every time delay, the result is the commonly reported transient absorption spectra.

nm seed for amplification (*i.e.* a repetition rate of 1 kHz). Inside the amplifier (*e.g.* a Ti:sapphire Chirp Regenerative Amplifier (CPA), optically pumped by another green seed laser) this 800 nm seed pulse is amplified by factor of $\sim 10^6$ and compressed to about ∼45 fs in duration.[366–368] A full description of ultrashort pulse generation used in this thesis is given in Appendix 8.3.

The power of ultrashort pulses lies with their ability the resolve temporal features, however, the trade-off with temporal resolution is an intrinsic decrease in spectral resolution. This is referred to as the *time-bandwidth product*, a statement of Fourier-limited pulses. A pulse with a Full-Width at Half-Maximum (FWHM) duration Δt and a

Table 3.1: Fourier transform limit (K) for the FWHM of different pulse shapes.[369] The temporal profile for each pulse shape is also given (A)–(F). For the rectangle pulse, $(a+b)/2 = t_0$.

Shape	Functional form	K
(A) Gaussian	$\exp\left[-(t/\sqrt{2}t_0)^2\right]$	0.441
(B) Lorentzian	$[1+(t/t_0)^2]^{-1}$	0.142
(C) Exponential	$\exp[-(\lvert t\rvert/t_0)]$	0.140
(D) Secant	$\mathrm{sech}(t/t_0)$	0.315
(E) Rectangle	$\theta(t-a)\theta(b-t)$	0.892
(F) Sinc	$\sin^2(t/t_0)/(t/t_0)^2$	0.336

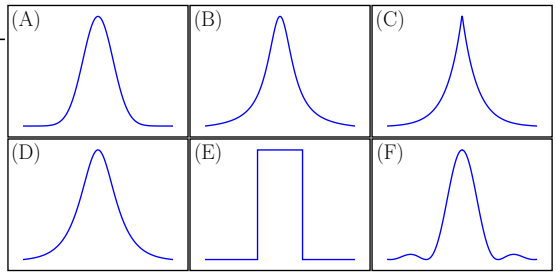

FWHM spectral width of $\Delta\omega$ obeys the inequality

$$\Delta t \Delta\omega \geq K, \tag{3.1}$$

where K is a constant that depends on the pulse shape, see Table 3.1. Clearly this is a statement of the uncertainty principle (*cf.* Equation 1.24) and thus is a universal equation which governs laser pulses, although one must be careful in the interpretation of Δt since a 'time-operator' is ill-defined.[370,371] Instead, we continue to only deal with these experimentally measureable quantities. In the case of Gaussian pulse shapes ($K = 0.441$) which are the only ones used in this thesis, a 10 fs pulse ($\Delta t = 10$ fs) corresponds to a *minimum* spectral window of 80 nm if the pulse has a central wavelength of 800 nm. Thus, as discussed in Section 2.1, the shortest pulses may end up populating an ensemble of excited states which lie within $\pm\frac{1}{2}\hbar\Delta\omega$. As such, the measured transient signal will be the convolution of the photochemistry of multiple excited states, making assignment more difficult.

Pump-probe set-up. The ultrashort 800 nm pulses are used to generate both the pump and probe pulses (Figure 3.1(B)) by splitting them into two beams (*i*) and (*ii*) for the pump and probe-pulse generation respectively. (*i*) To generate the pump pulses, the 800 nm pulses seed an Optical Parametric Amplifier (OPA) which can generate tunable laser pulses of a variety of wavelengths (in particular for sunscreens, across the UV regions).[372] Another option is to use sum frequency generation or difference frequency generation to produce specific wavelengths (*e.g.* the second harmonic, 400 nm, or the third harmonic, 267 nm; discussed in Appendix 8.4).[373] The result of either of these options is a consistent source of pump pulses at the wavelength required for photoexci-

tation. These processes are also used in OPA to generate the higher frequencies such as UV. (*ii*) The probe pulses on the other hand are generated by focussing 800 nm pulses into a suitable nonlinear medium,[363,374] *e.g.* CaF_2,[375,376] which produces pulses with a broad bandwidth referred to as White Light Generation (WLG), typically consisting of wavelengths between ∼300–1000 nm which are subsequently used as probe pulses (Figure 3.2(A)). In practice, only probe wavelengths between ∼300–700 nm are used since these correspond to electronic transitions, furthermore, the CaF_2 crystal is translated to avoid damage and to maintain a consistent source of probe pulses. Because of the use of UV-visible wavelengths this technique is often referred to as Transient Electronic Absorption Spectroscopy (TEAS).[362] Importantly, broadband Infrared (IR) pulses may be used in place of white light pulses which probe the vibrational modes of the molecule,[377] called Transient Vibrational Absorption Spectroscopy (TVAS).[362,378] Within this line, before WLG, the 800 nm pulses travel along a delay stage which consists of a motorised retro-reflector that introduces a specified Δt into the probe path. Equivalently of course, the delay stage can in principle be introduced in either the pump or probe beam path, with the latter being used here. A polariser can be placed in this path for magic angle (54.7°) pump-probe spectroscopy. Both pump and probe pulses are focussed into the sample with any pump pulses not absorbed by the sample collected in a beam dump, whereas residual probe pulses are collimated and coupled into a spectrometer.

Sample delivery. As with most spectroscopy measurements, the sample to be studied is placed within a transparent cuvette (flow-through cuvette; Demountable Liquid Cell, Harrick Scientific; Figure 3.2(B)). However there are a few additional details which make it worthwhile discussing. Firstly, unlike most steady-state measurements, the sample is recirculated from a reservoir to ensure each pump-probe measurement receives a fresh sample, ensuring subsequent measurements do not contain excited state species from the previous pump-pulse. Polytetrafluoroethylene (PTFE) spacers, 100 μm thick unless stated otherwise, are used to define the absorption pathlength between two transparent windows (CaF_2). The rest of the flow-through cuvette: O-rings (Kalrez), the compression ring, and retaining nut, are to ensure a fluid-tight fit within the cell body, where the entire cuvette is mounted onto a translation stage.

ΔOD *measurement.* The actual reported measurements from these experiments are the changes in optical density ΔOD, which for *all* probe wavelengths and *all* Δt, are collectively referred to as Transient Absorption Spectra (TAS), see Figure 3.1(C). The calculation of ΔOD is as follows. The spectral absorption of the probe by a molecule *without any photoexcitation* results in a transmitted intensity for each probe

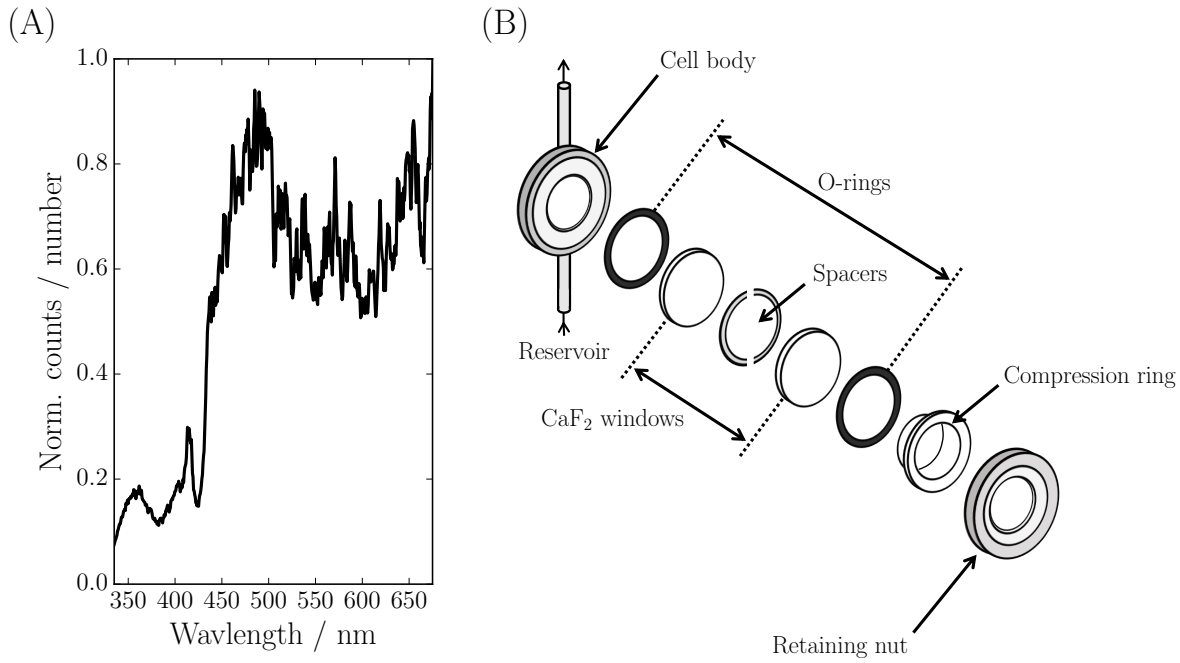

Figure 3.2 | (A) A typical WLC generated from high-order nonlinear optical processes in a 2 mm CaF_2 crystal (335–675 nm shown only). (B) A 'blown-up' schematic of the commercially available[379] Demountable Liquid Cell used in this thesis. The spacers define the absorption pathlength, the rest of the components ensure a fluid-tight fitting.

wavelength, λ, of $I_0(\lambda)$. The molecule is then photoexcited with a pump-pulse. After a time Δt another probe-pulse is absorbed by the *photoexcited molecule*, which results in a transmitted intensity for each probe wavelength, for the given Δt, of $I^*(\lambda, \Delta t)$. The logarithmic quotient of these measurements is a dimensionless, instrument independent quantity known as the aforementioned change in optical density, ΔOD,

$$\Delta\mathrm{OD}(\lambda, \Delta t) = \log_{10}\left(\frac{I_0(\lambda)}{I^*(\lambda, \Delta t)}\right). \tag{3.2}$$

The recorded TAS is the total signal from the photoexcited molecule, *i.e.* a convolution of all possible sources of a ΔOD. There are four main processes which manifest themselves as a change in optical density in a typical experiment,[357] illustrated in Figure 3.3.

- - - Ground State Bleach (GSB). The pump pulse photoexcites a fraction of the molecules in a sample to an excited state, thus the number of molecules in the ground state decreases (Figure 3.3(A)). This leads to a decrease in the ground state absorption compared the absorption of a unpumped sample. Therefore, the transmission intensity

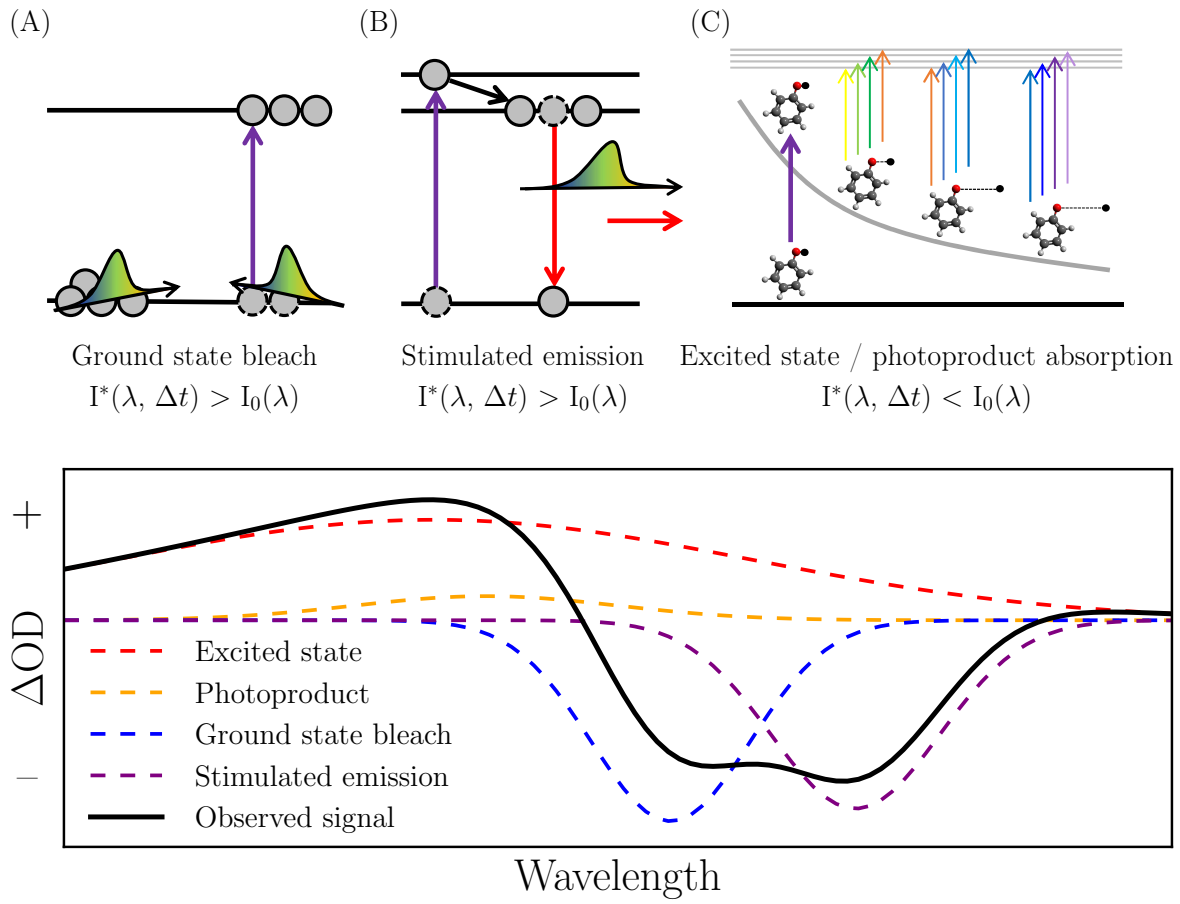

Figure 3.3 | (*top*): A physical interpretation of the common transient absorption signals measured. (A) A GSB manifests as negative signal; after the pump excites a portion of the ground state, less of the probe is absorbed relative to the ground state thus Equation 3.2 is < 0. (B) SE similarly manifests as a negative signal; SE can *only* happen with an excited state population, thus the measured intensity will always be greater than with a ground state population. (C) Both ESA and photoproduct absorption will always manifest as a positive signal; these populations are *only* present after a pump event (photoexcitation), thus the measured intensity probe will always be smaller (since it is absorbed) than a ground state population. (*bottom*): Schematic of the typical components which contribute to the measured TAS, for a particular Δt.

of the probe in the pumped sample is greater than the unpumped sample, *i.e.* $I^*(\lambda, \Delta t) > I_0(\lambda)$ so the quotient in Equation 3.2 is < 0. Thus, a GSB signal manifests as a *negative* ΔOD signal.

- - - Stimulated Emission (SE). One probe photon may initiate the SE of an additional photon from an excited state (Figure 3.3(B)). In the pumped sample, there are more molecules in an excited state which may undergo SE compared to the unpumped

sample. Thus the intensity detected from SE is greater in the pumped sample than the unpumped sample hence SE manifests as a *negative* ΔOD signal.

- - - Excited State Absorption (ESA). In the pumped sample, the molecules will absorb wavelengths of the probe pulse corresponding to optically allowed transitions to higher electronic states (S_n), thus will decrease the transmission intensity of the probe-pulse (Figure 3.3(C)). In the unpumped sample, these same transitions will not be accessible thus the transmission intensity of the unpumped sample will be greater than in the pumped sample, *i.e.* $I^*(\lambda, \Delta t) < I_0(\lambda)$ so the quotient in Equation 3.2 is > 0. Thus an ESA signal manifests as a *positive* ΔOD signal.

- - - Photoproduct absorption. After photoexcitation, a molecule may relax through a mechanism which does not result in its original state forming a photoproduct, for example, long-lived triplet states, fragmentation into two or more fragments or isomerisation to a stable state (Figure 3.3(C)). In this case, photoproducts may absorb probe wavelengths, reducing the transmission intensity compared to the unpumped sample where there are no photoproducts. Hence photoproduct absorption also manifests as a *positive* ΔOD signal.

Thus the final output of the experiment is TAS, which gives the temporal information; as spectral features appear or disappear, information about what processes are taking place, and on what timescales, can be garnered. A note on terminology used in this thesis; Transient Electronic Absorption (TEA) and Transient Vibrational Absorption (TVA) refers to the probe pulse wavelength range for the acquired spectrum, both being examples of TAS. A final point to mention is this experiment is controlled with *LabView* programming suite.[380] Details pertaining to the use of *LabView* can be found in Dr Simon Greenough's PhD thesis.[381]

3.2 Post-processing of transient absorption spectra

Typically in each acquisition of TAS, a series of background measurements are taken to account for contributions to the measured ΔOD which does not originate from the sample. For the pump-path, the probe-path is blocked, and only the pump passes through the sample, where the absorption is recorded, I_{pu}^{bkg}. This measurement captures any additional light from pump scattering or sample fluorescence and/or phosphorescence which will affect the measurement of $I^*(\lambda, \Delta t)$. Background absorption from the dark charge of the Charge-Coupled Device (CCD) array, fibre coupling response and any scattered light are accounted for by measuring the absorption when both the pump and probe beams are blocked, I^{bkg}. A final background measurement is taken when

both pump and probe pulses are sent through the sample, referred to as baseline artefacts. The subtraction of baseline artefacts is simple, the most negative time delay of the TAS, *i.e.* well before any temporal overlap between pump and probe, typically taken to be $\Delta t = -1$ ps, I^{bl}, is subtracted off all absorbance values. This subtraction accounts for any probe-pump dynamics, that is, when the probe excites the sample, which is subsequently probed by the pump-pulse. Thus the experimentally measured, and post-processed TAS is:

$$\Delta\mathrm{OD}(\lambda, \Delta t) = \log\left(\frac{\mathrm{I}_0(\lambda)}{\mathrm{I}^*(\lambda, \Delta t)}\right) = \log\left(\frac{\mathrm{I}_0(\lambda) - \mathrm{I}^{bkg}}{\mathrm{I}^*(\lambda, \Delta t) - \mathrm{I}^{bkg}_{pu}} - \mathrm{I}^{bl}\right). \tag{3.3}$$

In addition to these baseline measurements, it is important to note that the use of a broadband probe continuum introduces time-dependent artefacts into all experimentally recorded TAS. The phenomena is referred to as 'chirp', where different wavelengths of light travel with different group velocities in a medium which manifests in time-delay dependent absorption signals for each wavelength.[382–384] In other words, the wavevector of an electromagnetic wave travelling in some medium experiences a frequency dependence. Overall, this causes the time zero for each wavelength to be slightly different. Chirp, or Group Velocity Dispersion (GVD),[369] is an important nonlinear optical process which becomes significant in this work due to the intensity of the laser beams used. Particularly, the CaF_2 crystal for supercontinuum generation introduces positive chirp.[385] The important nonlinear optical phenomena to this thesis are described in Appendix 8.4. To correct for chirp, we use an available piece of software, Kinetics Observed After Light Absorption (KOALA),[386] but fundamentally this just uses an approximate expansion of the wavevector.[369,387] Consider first the Taylor series expansion about ω_0 of the wavevector of an electromagnetic wave, $k(\omega)$, truncating the series at the second order,

$$k(\omega) = \sum_{n=0}^{\infty} k^{(n)}(\omega_0)\frac{\omega^n}{n!} \approx k_0 + k'(\omega_0)(\omega - \omega_0) + \frac{1}{2}k''(\omega_0)(\omega - \omega_0)^2 + \ldots. \tag{3.4}$$

Taking the derivative of $k(\omega)$ (the inverse of the group velocity of the pulse), and multiplying through by an arbitrary length of (dispersive) medium, L, the time zero at a particular frequency ($t_0(\omega)$), and its dependence on angular frequency can be expressed as[386]

$$t_0(\omega) = L\frac{dk(\omega)}{d\omega} = \mathrm{ABP} + \mathrm{GDD}\omega + \frac{1}{2}\mathrm{TOD}\omega^2, \tag{3.5}$$

where we have defined three new terms which are coefficients of a general quadratic

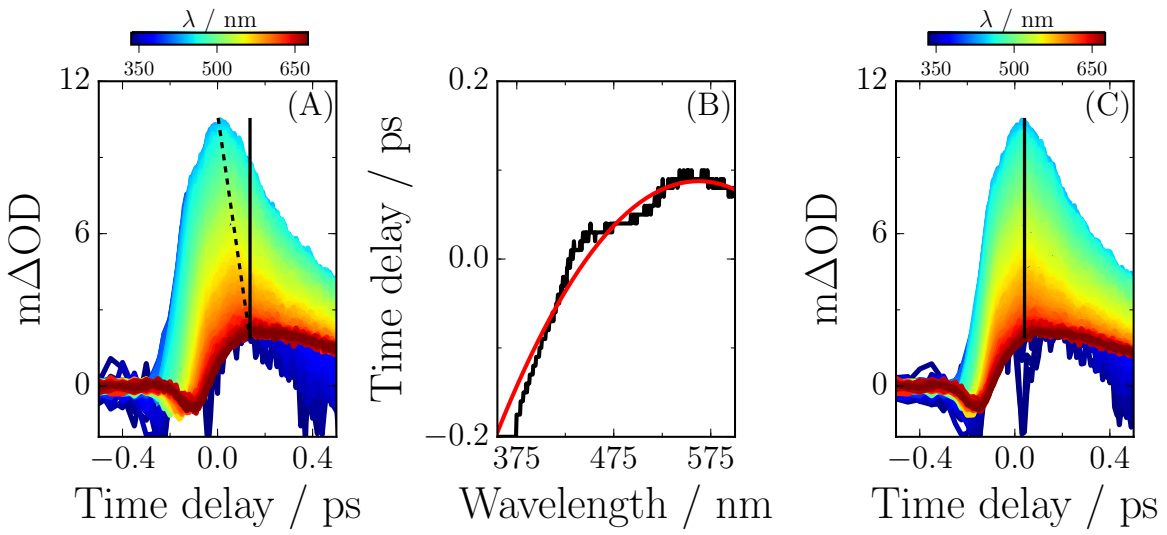

Figure 3.4 | (A) The raw TAS (shown as an exhaustive set of transients) displays significant chirp, as depicted by the angle between the bold and dashed lines. (B) Choosing a threshold (here 1 mΔOD is used) and recording the time delay each wavelength reaches it, a simple nonlinear regression (red line) is used to generate the translation coefficients ($t_0(\lambda)$). (C) After applying the chirp correction, the angle between the two lines is reduced to essentially zero, and the TAS is considered 'chirp-corrected'.

polynomial, Absolute Phase (ABP), Group Delay Dispersion (GDD) and Third-Order Disperion (TOD). A user defined absorption threshold is set and the first unique time delay for each wavelength to reach the threshold absorption determined to be $t_0(\omega)$, see Figure 3.4(A). This is calculated for all wavelengths, and Equation (3.5) is used in nonlinear regression where the coefficients ABP, GDD and TOD are determined (Figure 3.4(B)). Once these coefficients are determined, each transient is translated by $-t_0(\omega)$ and the result is a chirp corrected TAS (Figure 3.4(C)).

3.3 Analysis of transient absorption spectra

Knowing what each contribution to the ΔOD makes to the resulting TAS helps to assign spectral features to specific processes. For example, the very existence of processes themselves are very informative, *e.g.* if a GSB does not fully recover, it suggests the original molecule is not reforming on the timescale of the experiment. Quantitatively TAS are typically analysed under two models, (*i*) *simultaneous dynamics* or (*ii*) *sequential dynamics*.[388,389]

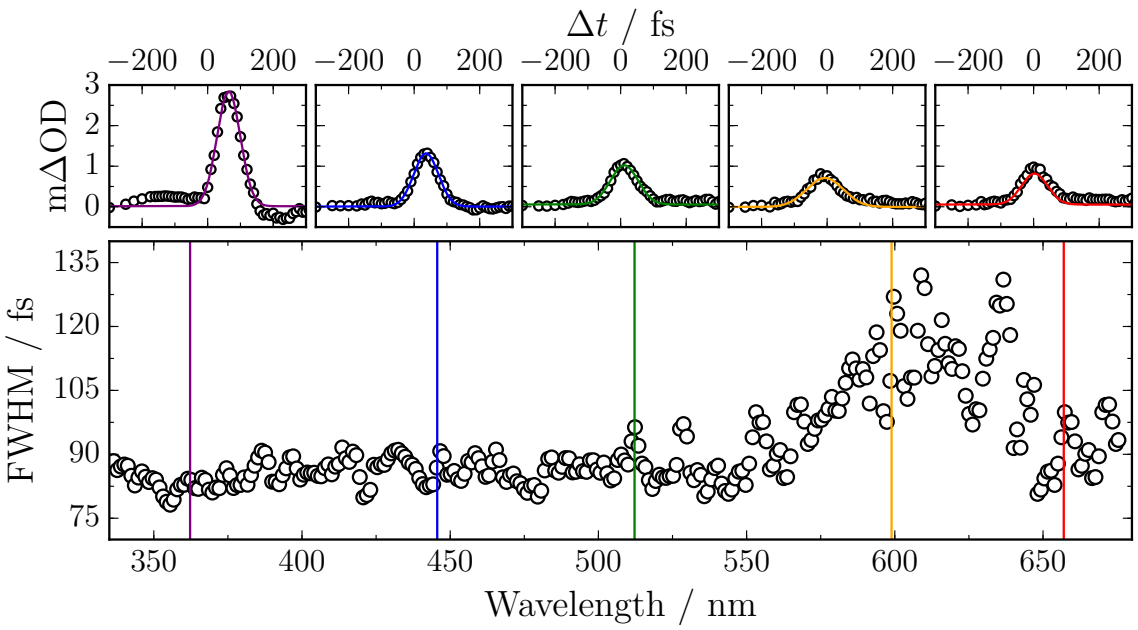

Figure 3.5 | An example of a cross correlation study as a function of wavelength; shown is methanol photoexcited at 325 nm. The IRF is dependent on wavelength, although it typically remains around 80–120 fs.

(*i*) Most dynamical processes occurring during the relaxation of a molecule can be adequately described through first-order kinetics. This means a single exponential decay with some characteristic *lifetime* describes one process. Experimentally things are a bit more complicated because of nonlinear (polarisation) processes occurring around pump-probe overlap (time zero), *e.g.* multiphoton effects in the sample cell,[382,384] referred to as the Instrument Response Function (IRF). This is typically well modelled by a Gaussian function with a FWHM in the region of ∼100 fs which ultimately limits the time resolution of the experiment (Figure 3.5). Together, this means a general TAS under simultaneous dynamics can be modelled as the sum of n exponential decay functions with lifetimes τ_n, convoluted with a Gaussian IRF $\mathrm{G}(\lambda, \Delta t)$,

$$\mathrm{TAS}_{model}(\lambda, \Delta t) = \sum_{i}^{n} \mathrm{G}(\lambda, \Delta t) \otimes \mathrm{A}_i(\lambda) e^{\frac{-(\Delta t - t_0)}{\tau_i}}, \tag{3.6}$$

where $\mathrm{A}_i(\lambda)$ is referred to as the Decay Associated Spectrum (DAS) for the corresponding exponential decay function with lifetime τ_i, and t_0 denotes time zero. Nonlinear regression can minimise the residuals between the experimental TAS and TAS_{model},

for a particular wavelength. This analysis can be extended to include all wavelengths of the TAS simultaneously, so-called *global fitting*, the result of which is the 'average' dynamics across the entire TAS. This is the modelling procedure used throughout this thesis; the basis of the global fitting routine was written in *MATLAB*,[390] and can be found in Dr Adam Chatterly's PhD thesis.[391] One potential issue with this analysis is that the model intrinsically assumes that *all* dynamics start at the same time. If the processes within a relaxation mechanism are far removed from one another, *i.e.* occur on different timescales this assumption is adequate. However, for dynamical processes very close in magnitude this assumption breaks down and sequential dynamics become important.

Uncertainties at the 95% level are assigned to the determined lifetimes using either an Asymptotic Standard Error (ASE) technique, or Support Plane Analysis (SPA).[392] In the latter, the 'goodness-of-fit', χ^2, of the lifetimes reported (τ_i) which together parametrise the raw TAS, is a global minimum with value χ^2_{min}. The lifetimes used in the global fit are varied in a systematic manner to sample the goodness of fit in the local parameter space surrounding this minimum, which return the values $\chi^2(\tau_1, \tau_2, \ldots, \tau_n)$. The ratio $\frac{\chi^2(\tau_1,\tau_2,\ldots,\tau_n)}{\chi^2_{min}}$ is then determined. The global minimum is given by $\frac{\chi^2(\tau_1,\tau_2,\ldots,\tau_n)}{\chi^2_{min}}$ = 1. For all fitting values which are not a global minimum, the ratio is always >1. A confidence interval at the N level (N = [0,1]; N = 0.95 throughout this thesis) is defined as

$$\frac{\chi^2(\tau_1, \tau_2, \ldots, \tau_n)}{\chi^2_{min}} = 1 + \frac{p}{\nu}\mathrm{F}\left(N, p, \nu\right), \tag{3.7}$$

where p is the number of parameters in the global fit, ν is the number of degrees of freedom and F, is the inverse cumulative F-distribution function. Thus, the upper bound on the uncertainty for each varied parameter is the value which results in the largest deviation from the global fitted values whilst satisfying Equation 3.7.

ASE are simply the limit of SPA where only one lifetime (τ) is varied in a systematic manner whilst keeping all other lifetimes fixed. The global fit optimisation proceeds as before and a new goodness-of-fit is calculated denoted by $\chi^2(\tau)$. A 95% confidence interval for the value of the lifetime τ is then defined by

$$\frac{\chi^2(\tau)}{\chi^2_{min}} = 1 + \frac{p}{\nu}\mathrm{F}^{-1}\left(0.95, p, \nu\right). \tag{3.8}$$

This is then repeated for each lifetime.

(*ii*) Sequential dynamics use a kinetic model for the TAS where each process leads onto the next. This solves the problem of two or more dynamical processes being close in magnitude but requires the formation of a suitable model, where complexity rapidly

increases when one process may 'branch' into multiple processes, something that has to be known before fitting of the TAS can be achieved. Often these models are formed on chemical intuition or following *ab initio* electronic structure calculations to inform on the likely model.

Either of these fitting methods can model a TAS and thus extract the lifetimes of the processes occurring following photoexcitation of the molecule of interest. Choosing a method of fitting will depend on the situation; whilst simultaneous dynamics can reveal very useful information, if sequential dynamic fitting is possible, it is ultimately always more representative of the actual relaxation mechanism. This experiment and subsequent analysis can reveal processes with lifetimes as short as ∼100 fs. The issue remains in assigning lifetimes to physical processes *e.g.* IC, ISC, photoproduct formation *etc.* With sensible assignment (sometimes easier said than done), the relaxation mechanism of a molecule and the timescale it occurs on may be deduced, which is essentially the subject of majority of the work presented in this thesis.

A final note regarding the assignment of the photophysical processes is that a number of steady-state techniques are used throughout the analysis of the measurements reported in this thesis, such as UV-visible spectroscopy, infrared spectroscopy and nuclear magnetic resonance. In particular, they are most often used to interpret long-lived components such as photoproducts given they appear static within the temporal resolution of TEAS and TVAS. However, there are no specialised customisation to the use of these techniques and thus details are given in the relevant methodology sections of appropriate chapters.

3.4 *In vacuo* transient absorption spectroscopy

In addition to the experimental methodology discussed thus far, which is indicative of solution-phase measurements, *in vacuo* or gas-phase measurements are often highly complementary to solution-phase measurements;[300,325] the exclusion of solvent perturbations significantly decreases the convolution of the transient signals measured. Whilst the vast majority of measurements taken and discussed in this thesis are indeed in the solution-phase, many of the relaxation mechanisms are justified from gas-phase measurements reported in the literature, thus justifying a short-discussion, although the reader is directed to the vast literature for further details.[393–396]

Pump-pulses are generated in an identical way as with solution-phase measurements, either through higher harmonic generation or the use of a OPA. Probe-pulses on the other hand are not drawn from a supercontinuum, instead, higher harmonics or OPAs

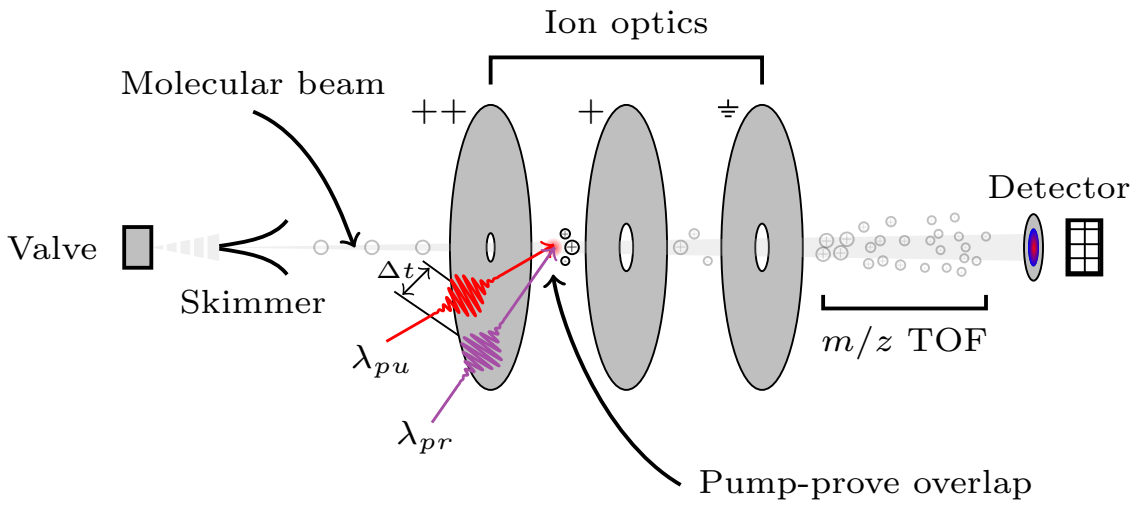

Figure 3.6 | The key features of *in vacuo* transient absorption. A pulsed valve produces a molecular beam which is collimated by the skimmer. The beam enters the ion optics (charged plates) into the interaction zone where pump-probe overlap is achieved. The pump excites the molecular beam, and some time later (Δt), the probe ionises and/or fragments the excited state species. The charged particles are accelerated (proportional to their mass to charge ratio; m/z) by the optics, entering the time-of-flight (TOF) spectrometer. The ions are detected by a spatial-temporal plate which is recorded by a charged-coupled-device camera, together forming the detection unit.

are used for reasons which will become apparent. The general technique is referred to as Time-Resolved Mass-Spectroscopy (TR-MS). A collimated molecular beam of the sample of interest is generated by heating and injecting into a vacuum chamber by a seeding inert (buffer) gas (*e.g.* helium or argon; Figure 3.6).

By pulsing the injection of the molecular beam in synchronisation with the arrival of the pump-probe pulses, the sample is photoexcited and probed in a similar way as for solution-phase measurements. Pump pulses arrive and cause a photoexcitation (defined to be time zero, t_0). Delaying the arrival of the probe-pulse allows the collection of snapshots of the photophysical and photochemical processes happening. Probe wavelengths are selected to ensure the generation of ionisation of the sample. As such, the generated ions are accelerated out of the interaction region, down the time-of-flight drift region, and impact onto a spatial-temporal sensitive detector.

Whilst each ion will have the same kinetic energy due to the accelerator voltage plate, their velocity will depend on their mass-to-charge (m/z) ratio. Thus, the time-of-flight drift region will ensure ions of different m/z can be resolved by their arrival time at the detector. The dynamics of the photoexcited sample can be tracked and

understood by recording how the yield of an associated ion varies with pump-probe time delay.[397,398] With these measurements, the experimental data can then be fitted with an appropriate kinetic model to extract the number of unique processes present, as well as the lifetimes of each process. Such analysis is similar to the aforementioned simultaneous dynamics and sequential dynamics; since a quasi-monochromatic probe is used (contrary to the supercontinuum in solution-phase measurements), a global analysis is not required, and a simultaneous dynamics kinetic fit is usually described by a set of n exponential decays and m exponential rises, all of which are convoluted with an appropriate IRF ($\mathrm{G}(\lambda, \Delta t)$) such that[395]

$$\begin{aligned} \mathrm{TAS}(\lambda, \Delta t) = \sum_{i}^{n} \mathrm{G}(\lambda, \Delta t) \otimes \mathrm{A}_i \left(e^{\frac{-(\Delta t - t_0)}{\tau_i}} \right) \ldots \\ + \sum_{j}^{m} \mathrm{G}(\lambda, \Delta t) \otimes \mathrm{B}_j \left(1 - e^{\frac{-(\Delta t - t_0)}{\tau_j}} \right). \end{aligned} \tag{3.9}$$

From this, the number of processes ($n+m$) required to model the measurement is determined as well as the associated lifetimes. One again, as with solution-phase measurements, the difficulty is assigning these processes to plausible photophysical processes. *Ab initio* calculations are particularly powerful here as solvent/environmental terms are not required, making the calculations significantly more tractable. Indeed in much of the work discussed in this thesis, *ab initio* calculations are performed to support much of the work within a gas-phase framework, which can provide important insight into the solution-phase measurements.

Chapter 4

Artificial sunscreen constituents

Parts of this chapter have been published by the author:

---

1. **Lewis A. Baker**, Michael D. Horbury, Simon E. Greenough, Philip M. Coulter, Tolga N. V. Karsili, Gareth M. Roberts, Andrew J. Orr-Ewing, Michael N. R. Ashfold, and Vasilios G. Stavros. Probing the ultrafast energy dissipation mechanism of the sunscreen oxybenzone after UVA irradiation. *J. Phys. Chem. Lett.*, **2015**, 6(*8*):1363–1368.

2. **Lewis A. Baker**, Michael D. Horbury, Simon E. Greenough, Michael N. R. Ashfold, and Vasilios G. Stavros. Broadband ultrafast photoprotection by oxybenzone across the UVB and UVC spectral regions. *Photochem. Photobiol. Sci.*, **2015**, 14(*10*):1814–1820.

3. **Lewis A. Baker**, Lucy C. Grosvenor, Michael N. R. Ashfold, and Vasilios G. Stavros. Ultrafast photophysical studies of a multicomponent sunscreen: Oxybenzone – titanium dioxide mixtures. *Chem. Phys. Lett.*, **2016**, 664:39–43.

4. **Lewis A. Baker**, Michael D. Horbury, and Vasilios G. Stavros. Ultrafast photoprotective properties of the sunscreening agent octocrylene. *Opt. Express*, **2016**, 24(*10*):10700–10709.

5. **Lewis A. Baker**, Sarah L. Clark, Scott Habershon, and Vasilios G. Stavros. Ultrafast transient absorption spectroscopy of the sunscreen constituent ethylhexyl triazone. *J. Phys. Chem. Lett.*, **2017**, 8(*10*):2113–2118.

Declarations:

- In Section 4.1, the transient vibrational absorption spectroscopy measurements were performed in the lab of Prof. Andrew Orr-Ewing FRS, and analysed by Mr Philip M. Coulter and Dr Gareth M. Roberts (University of Bristol, U.K.). The *ab initio* electronic structure calculations were performed by Dr Gareth M. Roberts.

4.1 Oxybenzone

4.1.1 Introduction

Oxybenzone (OB), or benzophenone-3 (2-hydroxy-4-methoxyphenyl)-phenylmethanone), is an active ingredient present in many commercially-available sunscreens products. It belongs to the benzophenone family, a class of organic molecules which contain two aromatic rings covalently bonded by a carbonyl group. OB displays broadband UV absorption, spanning the UV-A, UV-B and UV-C regions, making it well suited to provide broadband UV photoprotection (Figure 4.1). Given the propensity of OB use, it is perhaps no surprise it has been the subject of numerous prior studies, most of which have focussed on its steady-state photobiological and photochemical properties. For example, OB has been shown to have great photostability even after many hours of UV-irradiation.[224] There are however concerns with its use in regards to both human skin use,[221,273,290,347] endocrine disruption,[230,285] and its possible role in disrupting

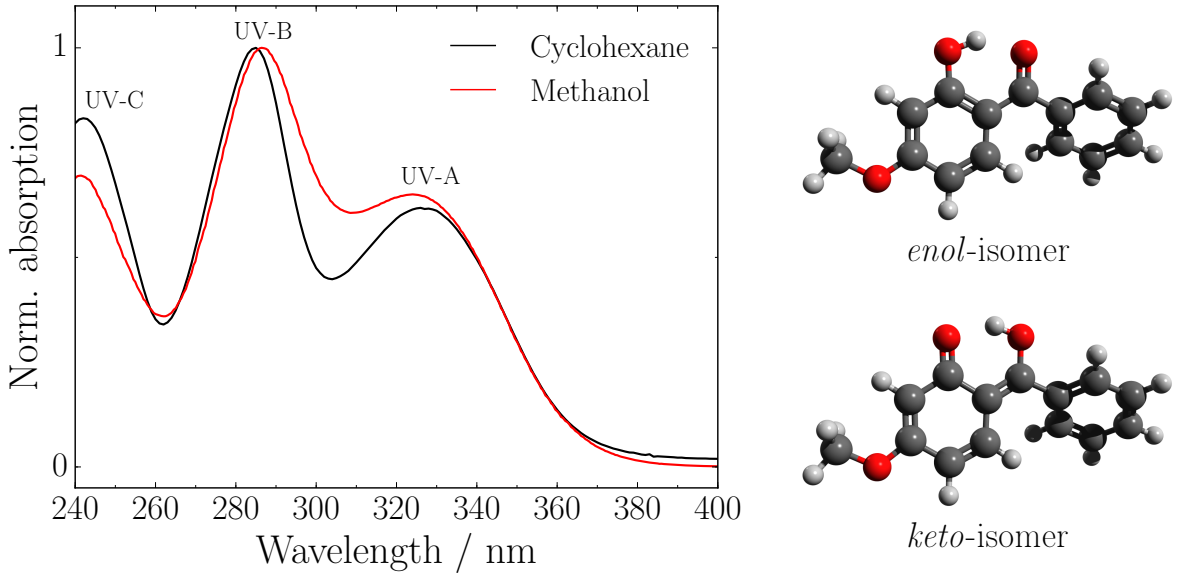

Figure 4.1 | (*left*): The UV-visible absorption spectrum of OB in cyclohexane (black) and methanol (red). There are three clear absorption peaks, one in each of the UV regions: 325 nm (UV-A), 287 nm (UV-B) and 243 nm (UV-C). These wavelengths are selected as the pump wavelengths for TEAS and TVAS experiments. (*right*): The molecular arrangement of OB in its two isomers,[16,17] the *enol*- and *keto*-isomer, calculated at the DFT level of theory using the B3LYP functional,[399,400] and a 6-31G* basis set,[22] the *enol*-isomer is much more energetically favourable and thus OB preferentially resides in the *enol*-isomer. A schematic of OB is shown in Figure 2.19(B).

aquatic ecosystems,[344] leading to its general regulation throughout Europe, the United States, Australia and Japan, where each regulatory body sets a maximum allowed concentration, typically between 5–10% (wt/wt), depending on the region.[221,269,290] One issue at the heart of these studies is that the mechanism by which OB absorbs and dissipates its energy remains unknown, thus elucidating the mechanism within OB might aid in the selection and design of more effective and/or safer sunscreens,[401] or suggest improvements in the use of OB itself. This last point in particular has shown promise where, for example, recent studies have demonstrated that the adverse effects of skin-OB contact can be reduced through the use of zeolite encapsulation.[256,264]

Recent *ab initio* electronic structure calculations suggest that ultrafast dynamics may be key to understanding the efficiency of OB as a sunscreen.[285] In particular, these studies identify IC *via* an electron-driven ESHT mechanism as a plausible energy relaxation pathway, in concordance with studies in similar species containing hydrogen donor (OH)-acceptor (CO) sites in close proximity,[402–407] as well as the related systems such as 2-(2'-Hydroxyphenyl)benzothiazole (HBT).[408–410] Recent studies have also suggested some probability of excited state OB molecules undergoing ISC to long-lived triplet states[411] and homolytic O–H bond fission to yield phenoxyl radicals.[288] The current evidence thus concludes that OB is photostable under UV irradiation (notwithstanding any undesirable minor ISC and purported O–H bond fission channels), but this cannot be confirmed while the OB excited state decay mechanism remains in question.

We therefore seek to fill this gap in the literature utilising TEAS and TVAS to understand the relaxation mechanism OB exhibits after UV-A irradiation,[286] and following on from these results, we further investigate the effect of the pump wavelength, namely, UV excitation in both the UV-B and UV-C regions with TEAS.[287]

4.1.2 Methodology

(*i*) *UV-A studies.* For all TEAS measurements, 10 mM solutions of OB (98%, Sigma-Aldrich), in either cyclohexane (≥99%, VWR) or methanol (≥99.6%, Sigma-Aldrich), are recirculated and delivered using a flow-through cell (Harrick Scientific), equipped with two CaF_2 windows separated by a 100 μm thick PTFE spacer. The sample is photoexcited with 325 nm, ∼50 fs pump-pulses, *i.e.* the UV-A peak absorbance in the UV-visible spectrum (Figure 4.1), with fluences in the region of 1–2 $mJ{\cdot}cm^{-2}$. Probe pulses are derived from a broadband WLC (340 to 675 nm) generated *via* nonlinear optical processes of the 800 nm fundamental inside a 2 mm CaF_2 crystal, and set to a time delay, Δt, of up to $\Delta t = 2$ ns relative to the pump pulse. Furthermore, the probe pulse polarisation is held at the magic angle (54.7°) relative to the pump

polarisation. All TAS are chirp corrected using the KOALA package[386] and reported lifetimes are determined using a global fitting procedure across a probe window of 355 nm $\leq \lambda_{pr} \leq$ 415 nm, with uncertainties reported to a 95% confidence interval (2σ) using SPA.[286,412–414] All steady-state UV-visible spectroscopic measurements were taken using a Cary 50 UV-visible spectrophotometer using a 1 cm pathlength quartz cuvette, and $\sim\mu$M OB-cyclohexane and OB-methanol solutions.

For all TVAS measurements, 10 mM solutions of OB (98%, Sigma-Aldrich), in either cyclohexane (≥99%, VWR) or deuterated methanol (methanol-d_4, ≥99.8%, Sigma-Aldrich) were made. Photoexcitation used 325 nm, ∼2 mJ·cm^{-2} pump-pulses with infrared probe-pulses centred on 1580 cm^{-1} and pump-probe time delays up to 50 ps. Details pertaining to the specifics of University of Bristol's TVAS experimental set-up are described elsewhere,[377] but follow the general description presented in Chapter 3. *Ab initio* calculations on possible photoproducts were performed using DFT to support both TEAS and TVAS studies. The B3LYP functional[399,400] with the 6-311+G** basis set were employed,[415] and the specific calculations are discussed in text.

(*ii*) *UV-B and UV-C studies.* Sample preparation, TEAS measurement methodology, and data analysis follow the same protocol as the aforementioned UV-A study, with the following addenda: (1) Pump wavelengths were selected to be 287 nm (UV-B) and 243 nm (UV-C), *cf.* peak absorbances in Figure 4.1; (2) The maximum Δt is 1.7 ns; (3) No TVAS measurements were taken, nor any further *ab initio* calculations performed.

4.1.3 TEAS and TVAS measurements for UV-A photoexcitation

Considering the TEAS measurements first; recording ΔOD for probe wavelengths between ∼335–675 nm over a range of pump-probe time delays up to $\Delta t = 2$ ns, the TEA spectrum of OB-cyclohexane was obtained (Figure 4.2). There are four clear features observed which are labelled (*i*)–(*iv*). A note on terminology here, TEA spectra and the vibrational analogue, TVA spectra, are both examples of the more general TAS introduced in Chapter 3. A distinction however is made here for the subsequent discussion where both TEA and TVA spectra are discussed and need to be discriminated.

(*i*) A negative feature is observed below probe wavelengths of ∼350 nm. From the UV-visible absorption spectrum of OB (Figure 4.1), OB displays a large absorption cross-section below ∼350 nm, which means that upon photoexcitation, there will be fewer molecules to absorb probe-pulses in this spectral region leading to a negative ΔOD, thus this feature is assigned to a GSB (*cf.* Figure 3.3). This feature persists out to

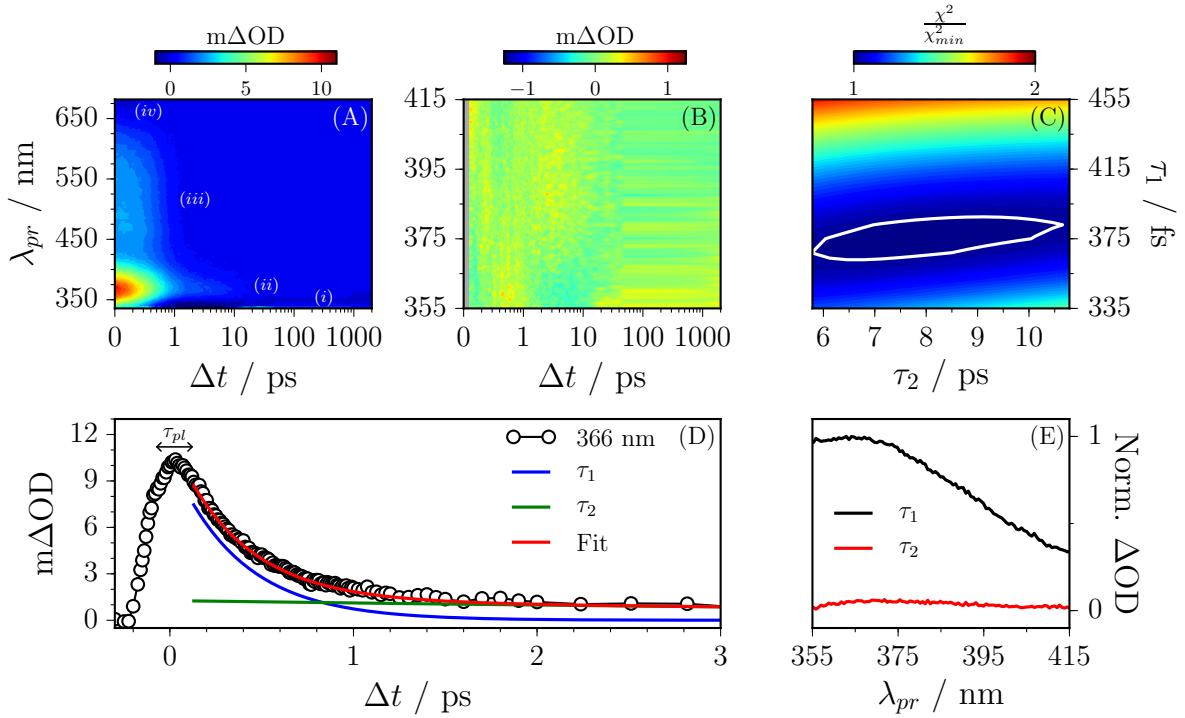

Figure 4.2 | (A) TEA spectra of OB in cyclohexane following an initial photoexcitation at ∼325 nm, in the form of a colourmap indicating the change in optical density. There are four main features observed in the TEA spectra which have been labelled. (*i*) A negative feature below ∼350 nm which remains out to the maximum available pump-probe delay time of $\Delta t =$ 2 ns. (*ii*) A localised, intense absorption feature centred on ∼366 nm which decays away by Δt ∼20 ps. (*iii*) A flat broad absorption feature which spans the probe window from ∼425–650 nm which decays away by $\Delta t = 2$ ps. (*iv*) A small negative feature beyond ∼650 nm. All of these features are described in the main text. (B) The residuals between the global fitted TEA spectra and the experimental spectra. (C) SPA of the uncertainties on the two lifetimes. (D) Representative example of the global fitting results, the ∼366 nm probe absorption transient is shown up to $\Delta t = 3$ ps. Two exponential decay functions with lifetimes, τ_1 (blue line) and τ_2 (green line) summed together (red line) describe the experimental data (black circles). (E) The DAS for the extracted lifetimes.

the maximum available pump-probe time delay, $\Delta t = 2$ ns, which suggests that within this experimental set-up, OB does not completely reform its *enol*-isomeric ground state. (*ii*) A localised, intense absorption peak is observed centred on ∼366 nm which persists out to Δt ∼20 ps. Recent *ab initio* electronic structure calculations guide the interpretation of this signal,[285] where it is suggested that an initial photoexcitation leads to the population of the higher lying electronic state, S_2, from which this absorption feature likely originates. Therefore, this feature is attributed to an ESA (*cf.* Figure 3.3). (*iii*) A flat, broad absorption across the probe spectral region ∼425–650 nm is observed

which decays away to the baseline by $\Delta t = 2$ ps. With a similar interpretation of *ab initio* calculations[285] this feature too is attributed to an ESA. (*iv*) A negative feature is observed beyond the probe spectral region of ~650 nm for early time delays (<1 ps) which might originate from the SE of an excited electronic state, predominately the S_1. This is suggested given that this feature does not persist past ~1 ps, by which time IC to the S_0 would have taken place, and hence this feature would decay away (discussed later).

Qualitatively, the observation of features in the TEA spectra are quite informative, particularly if GSB or SE signals are observed, giving insight into the excited state PES or long-time fate of a molecule. In the case of OB, a conclusion can already be drawn from the incomplete recovery of the GSB, signalling the possible formation of a photoproduct. Quantitatively, the dynamical processes which occur in the TEA spectra may be modelled in order to extract the lifetime (or timescales) of each process. Two exponential decay functions were required in the global fitting procedure to fully describe the TEA spectra (*cf.* residual spectrum in Figure 4.2(B)). The probe spectral region between 355–415 nm is only considered, *i.e.* focussing only on the localised absorption peak (*ii*). Furthermore, no convolution with a Gaussian IRF was included since the fitting was only considered for $\Delta t \geq$130 fs, *i.e.* sufficiently far away from the IRF, *cf.* Figure 4.2(D). The result of this fitting is two dynamical lifetimes, $\tau_1 = 375 \pm 13$ fs and $\tau_2 = 7.8 \pm 2.8$ ps.

A third dynamical lifetime is *inferred* from a signal plateau at very short time delays (τ_{pl} ~100 fs) which would be heavily convoluted with any IRF in this experiment.[287] Figure 4.2(D) also shows a representative example of the resulting fitting procedure for the ~366 nm transient of the TEA spectra, the two decay components, τ_1 and τ_2 as well as their sum are shown.

Considering next the analogous measurements for OB-methanol, the TEA spectrum and global fitting results are given in Figure 4.3. Similar dynamics are found for OB-methanol as with OB-cyclohexane, with only a slight blue shifting of the observed features. A similar global fitting procedure is used, where time delays below 160 fs are not included in the fit. The result of this fitting is two dynamical lifetimes, $\tau_1 = 368 \pm 13$ fs and $\tau_2 = 4.9 \pm 1.9$ ps, with a similar third lifetime τ_{pl} ~100 fs which manifests as a signal plateau, see Figure 4.3(D).

4.1.4 TVAS measurements after UV-A photoexcitation

In support of the TEAS measurements and the assignment of photophysical processes, TVAS measurements were also taken. The subtle, but important difference, is that the

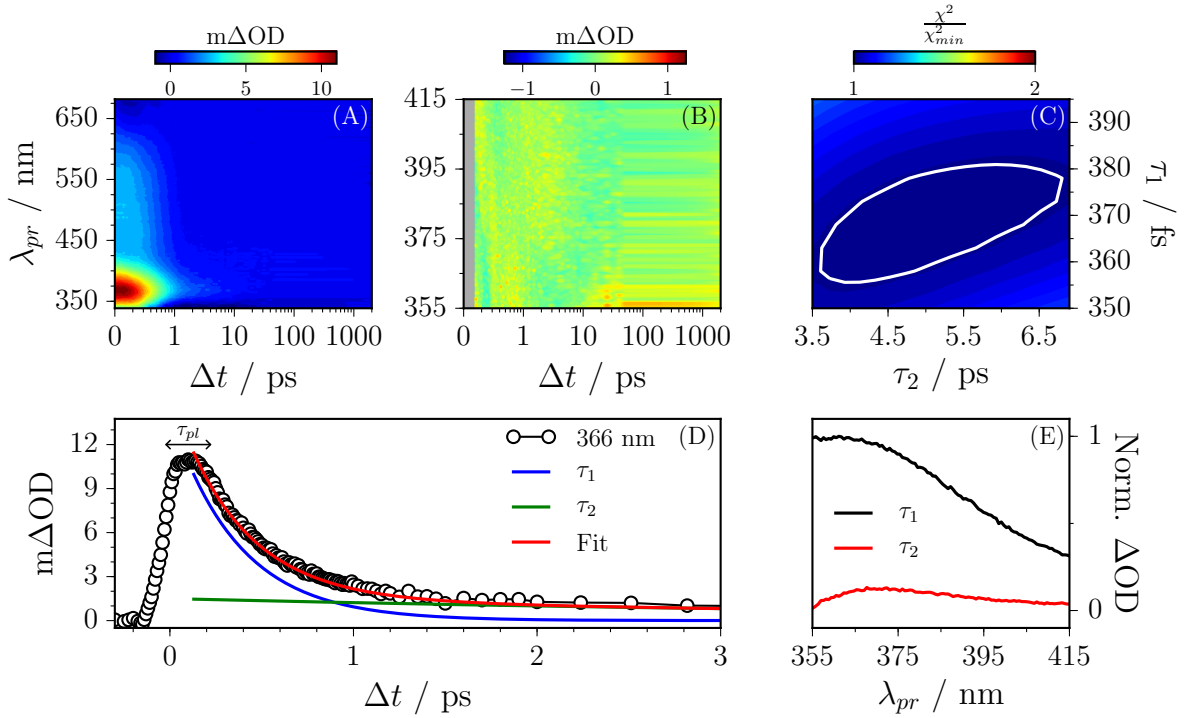

Figure 4.3 | (A) TEA spectrum of OB in methanol following an initial photoexcitation at 325 nm. The same four spectral features are seen as with cyclohexane *cf.* Figure 4.2. (B) The residuals between the global fitted TEA spectrum and the experimental spectrum. (C) SPA of the uncertainties on the two lifetimes. (D) Representative example of the global fitting results, the ∼366 nm probe absorption transient is shown up to $\Delta t = 3$ ps. (E) The DAS for the extracted lifetimes.

probe pulses are in the infrared region, ∼5.9–6.7 μm (∼1700–1500 cm^{-1}), *cf.* ∼335–675 nm in TEAS measurements, which excite vibrational modes within OB. The advantage of this technique over TEAS is that the formation or destruction of bonds can be tracked, whereas in TEAS only the changes in electronic states are observed. The result of these measurements are TVA spectra for OB-cyclohexane and OB-methanol given in Figure 4.4(A) and 4.4(B) respectively. Considering OB-cyclohexane first, Figure 4.4(A), the spectrum is dominated by several GSB features from the earliest pump-probe time delays (Δt <1 ps), and matches the steady-state Fourier Transform Infrared (FTIR) spectrum (black line; the UV-visible spectrum is equivalent in TEAS measurements). The most intense GSB contribution is observed at ∼1620 cm^{-1} labelled (*i*). This feature shifts to shorter wavelengths for increased time delay (Figure 4.4(A), dashed line). *Ab initio* calculations for the chelated *enol*-isomer, discussed below, return a number of vibrations in the relevant wavenumber range, the strongest of which is not

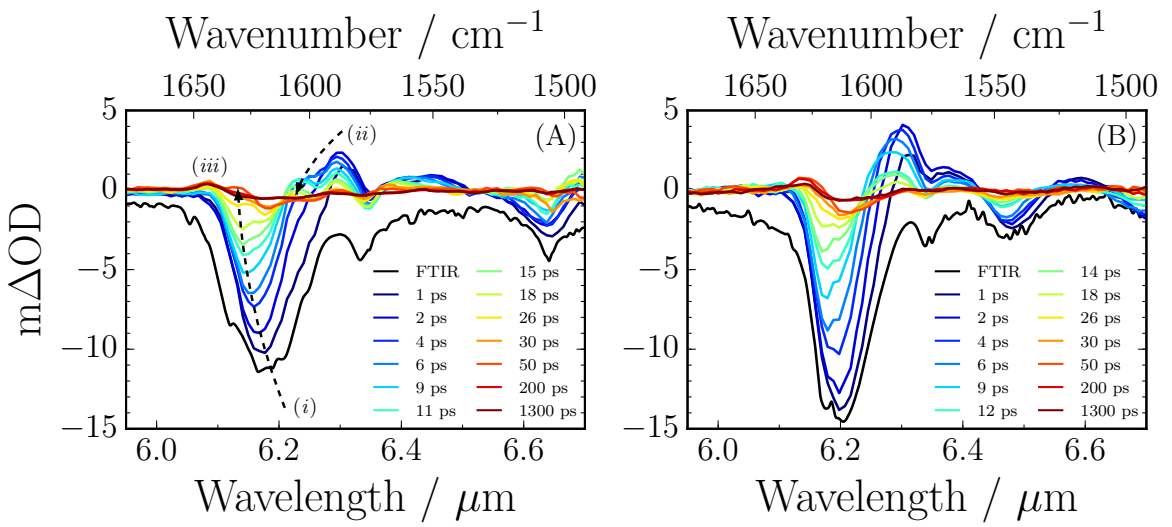

Figure 4.4 | TVA spectra for a range of pump-probe time delays up to $\Delta t = 1.3$ ns. (A) For OB-cyclohexane, the TVA spectra is dominated by three features. (*i*) An intense GSB feature centred around 1620 cm^{-1} (∼6.2 μm), which decays and shifts to shorter wavelengths with increasing Δt, but does not fully recover by $\Delta t = 1.3$ ns. (*ii*) A positive absorption centred around 1580 cm^{-1} (∼6.3 μm). (*iii*) Another positive absorption feature is observed centred around 1640 cm^{-1} (∼6.1 μm). (B) Similar features are observed in the TVA spectrum of OB-methanol-d_4.

the C=O stretch but a ring stretch mode of the methoxyphenol moiety (1668 cm^{-1}), which is responsible for the GSB observed in the TVA spectra in both solvents. A positive absorption feature is also seen to the longer wavelength side of this GSB feature, labelled (*ii*), centred at ∼1580 cm^{-1}. Similarly this feature can be seen to shift towards shorter wavelengths for an increased time delay up to $\Delta t = 10$ ps. Qualitatively, the temporal behaviour of this feature is characteristic of a vibrationally energetic molecule transferring excess energy to a surrounding solvent, consistent with the last step observed in TEAS measurements (*cf.* τ_2).[377] Similar features are observed for OB-methanol, see Figure 4.4(B).

Quantitatively, feature (*i*) can be analysed by numerical integration of the peak at each time delay.[377] The resultant fitting of this is the kinetic trace given in Figure 4.5. The kinetic traces for both OB-cyclohexane and OB-methanol are well described by a single exponential decay function, with lifetime, $\tau = 8.0 \pm 0.2$ ps and $\tau = 5.2 \pm 0.2$ ps respectively suggesting the time taken for the overall relaxation process is in very good agreement with the τ_2 lifetime determined by the TEAS measurements. Finally, the GSB feature (*i*) does not fully recover at the maximum available time delay, Δt

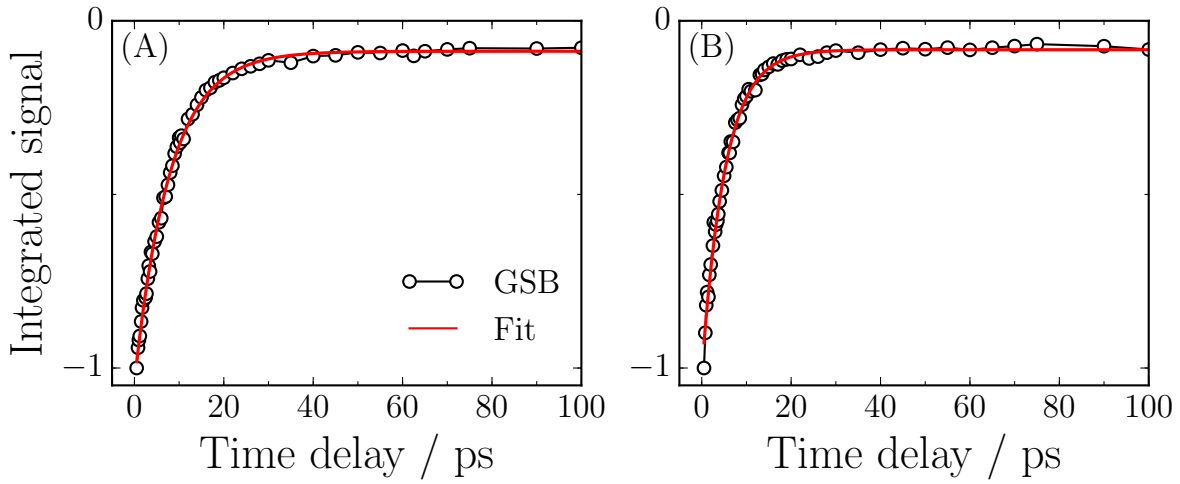

Figure 4.5 | The kinetic trace of the integrated peak centred at ∼1620 cm^{-1} for increasing pump-probe time delay (black circles) of (A), OB-cyclohexane and (B) OB-methanol-d_4. The kinetic traces are well described by a single exponential decay (blue line) with lifetime τ = 8.0 ± 0.2 ps and τ = 5.2 ± 0.2 ps for OB-cyclohexane and OB-methanol respectively.

= 1.3 ns, suggesting a quantum yield for the photoproduct of ϕ ∼10%, based on the numerical integration.

4.1.5 *Ab initio* calculations of photoproducts

The long-lived photoproduct is investigated through *ab initio* calculations of the harmonic frequencies of the likely candidates which are compared to the experimental TVA spectra of OB-cyclohexane, see Figures 4.6 and 4.7. The likely candidates are considered from previous *ab initio* studies of OB,[285,416] an oxetane derivative of OB has been suggested, as well as various isomers of OB given rotation around its aliphatic C–C bond. For each candidate, the sum of its absorption spectrum with the calculated bleach spectrum of the chelated *enol*-OB structure yields a *difference spectrum*. The harmonic wavenumbers of the chelated *enol*-OB isomer are scaled by 0.97 to best fit the experimental FTIR spectrum (*cf.* Figure 4.4). This scaling is applied to all calculated spectra of the candidates of interest. Band intensities and their corresponding line-widths are derived from the calculated IR transition intensities, with an associated 20 cm^{-1} Gaussian line shape applied to each spectral component. These calculations assume that all photoexcited chelated *enol*-OB molecules form the photoproduct, thus intensities are normalised, and only the shapes or presence of particular spectral features are considered in the proceeding analysis. The difference spectra for the candidates of

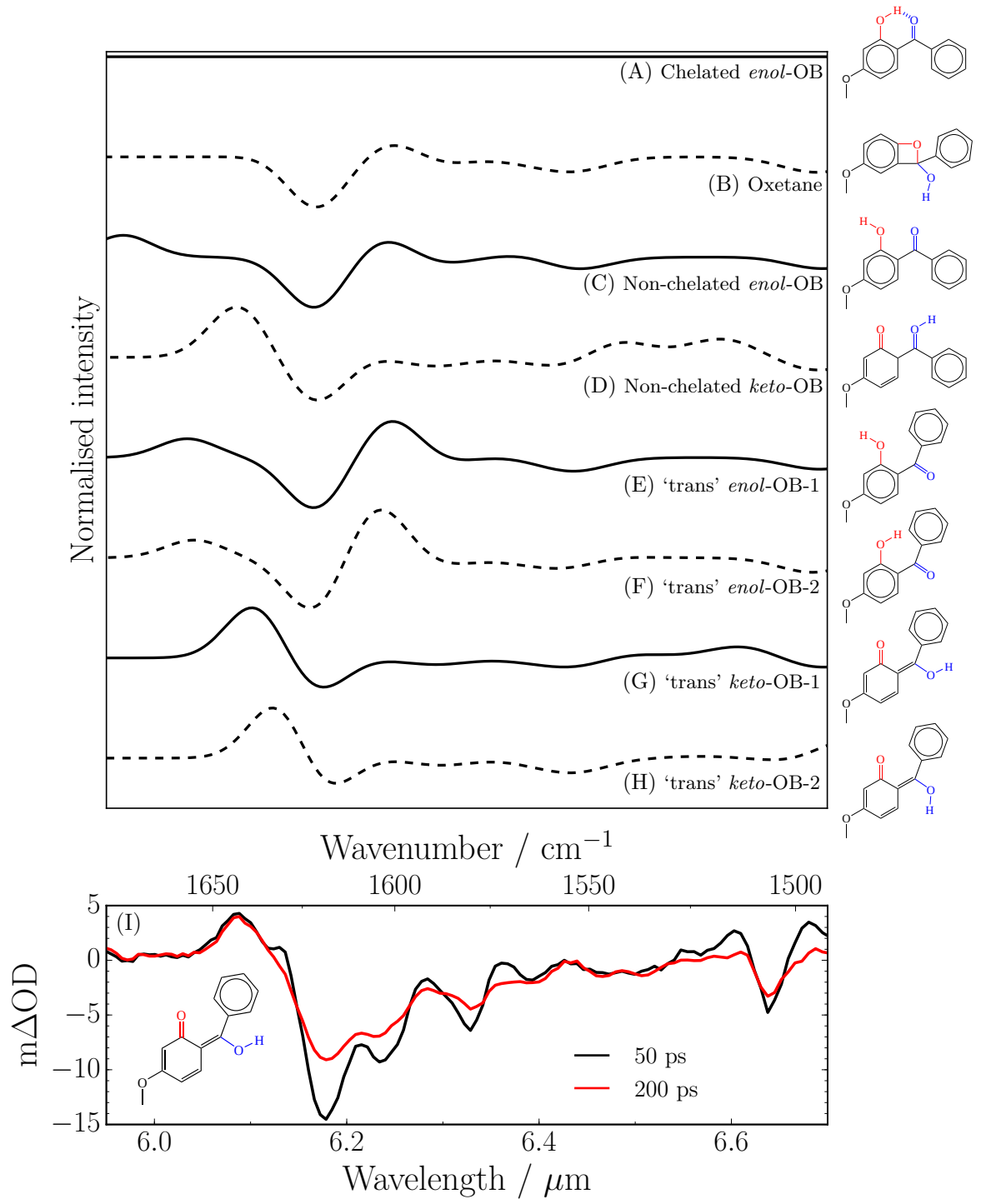

Figure 4.6 | (A-H) Calculated difference spectra for candidate photoproducts, as labelled. (I) The experimental OB-cyclohexane TVAS spectrum at time delays $\Delta t = 50$ ps and $\Delta t = 200$ ps. On comparison of the difference spectra and the experimental spectrum, the trans *keto*-OB isomers appearing the most likely candidates, with the trans *keto*-OB-1 isomer, shown, fitting particular well.

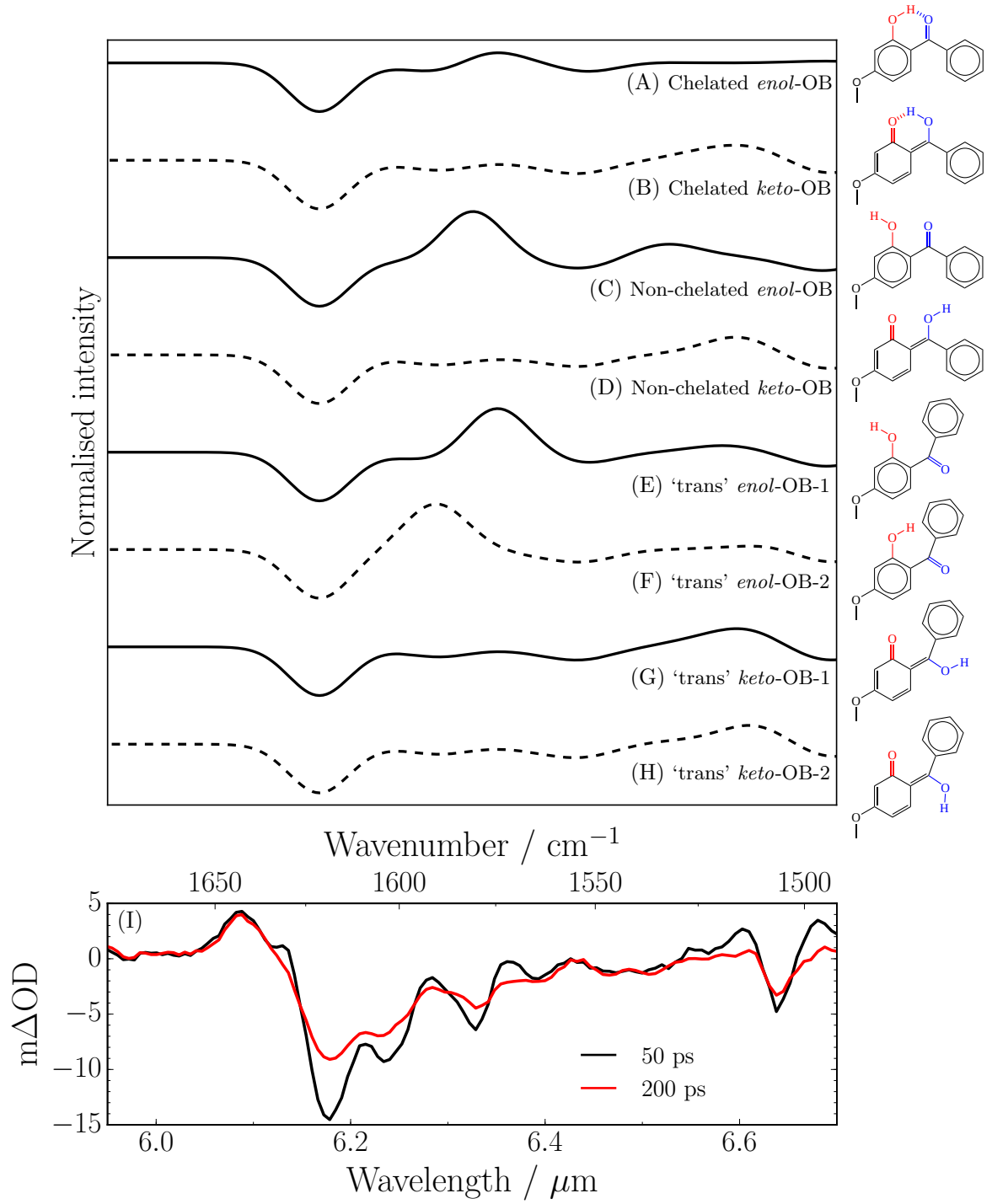

Figure 4.7 | (A-H) Calculated difference spectra for candidate triplet state photoproducts, as labelled. (I) The experimental OB-cyclohexane TVAS spectrum at time delays $\Delta t = 50$ ps and $\Delta t = 200$ ps. On comparison with the difference spectra and the experimental spectrum, triplet state photoproducts are unlikely to contribute to the incomplete recovery of the GSB significantly.

interest are given in Figure 4.6.

Following an identical procedure, analogous calculations of candidate triplet states are performed and the results shown in Figure 4.7. Of particular interest, we computed difference spectra for the chelated *enol*-OB and chelated *keto*-OB triplet state photoproducts, along with the non-chelated *enol*-OB and *keto*-OB triplet photoproducts, and finally the trans *enol*-OB and *keto*-OB triplet photoproducts. All calculated harmonic wavenumbers were again scaled (by multiplying by 0.97) on the basis of matching the calculated wavenumbers for the chelated *enol*-OB with the experimental FTIR spectrum.

4.1.6 Discussion and conclusions

Reviewing recent *ab initio* calculations aids in the interpretation of the dynamical processes occurring on both the TEAS and TVAS measurements.[285] The calculations produce cuts through the PESs for the S_0, $S_1(1^1n\pi^*)$, $S_2(1^1\pi\pi^*)$, and $S_3(2^1\pi\pi^*)$ states of OB and reveal the availability of CIs by which population in the optically "bright" S_2 state (formed as a result of 325 nm photoexcitation of the chelated *enol*-isomer) can be funnelled to the S_1 state (which is optically "dark"). Following radiationless transfer to the S_1 state, the calculations identify a barrierless ESHT pathway (along O–H), involving necessary rotation about the central aliphatic C–C bond, that links the S_1 state to a CI with the S_0 state. However, the resultant twisted chelated *keto*-isomer is not a stable species on S_0, and the local topography of the S_0 PES likely provides a driving force to regenerate the original stable chelated *enol*-isomer through GSHT, which is cooled *via* VET to the solvent bath. The following discussion of the results presented thus far is given in reference to a summary mechanism which is justified in the proceeding text, see Figure 4.8.

TEAS and TVAS measurements. Firstly, given the similarity of the TAS measured in both cyclohexane and methanol, we conclude that the intramolecular hydrogen bond in OB is preserved in both solvents, in both the ground[285] and excited states[285], as depicted in Figures 4.6 and 4.7. Further support for this conclusion is provided by previous studies of HBT[417] and 4-*tert*-Butylcatechol[325] for example. Both show markedly different dynamics when photoexcited in polar and non-polar solvents, consistent with loss of a intramolecular hydrogen bond in suitably polar solvents. The TEAS measurements identify three dynamical features. The TEA spectra highlight two of these, which as briefly discussed, from the global fitting of the 366 nm-centred absorption feature, referred to as feature (*ii*), reveals a short (τ_1) and a longer-time (τ_2) process. The third feature is an apparent flat maximum close to time zero in the transients shown in Figures

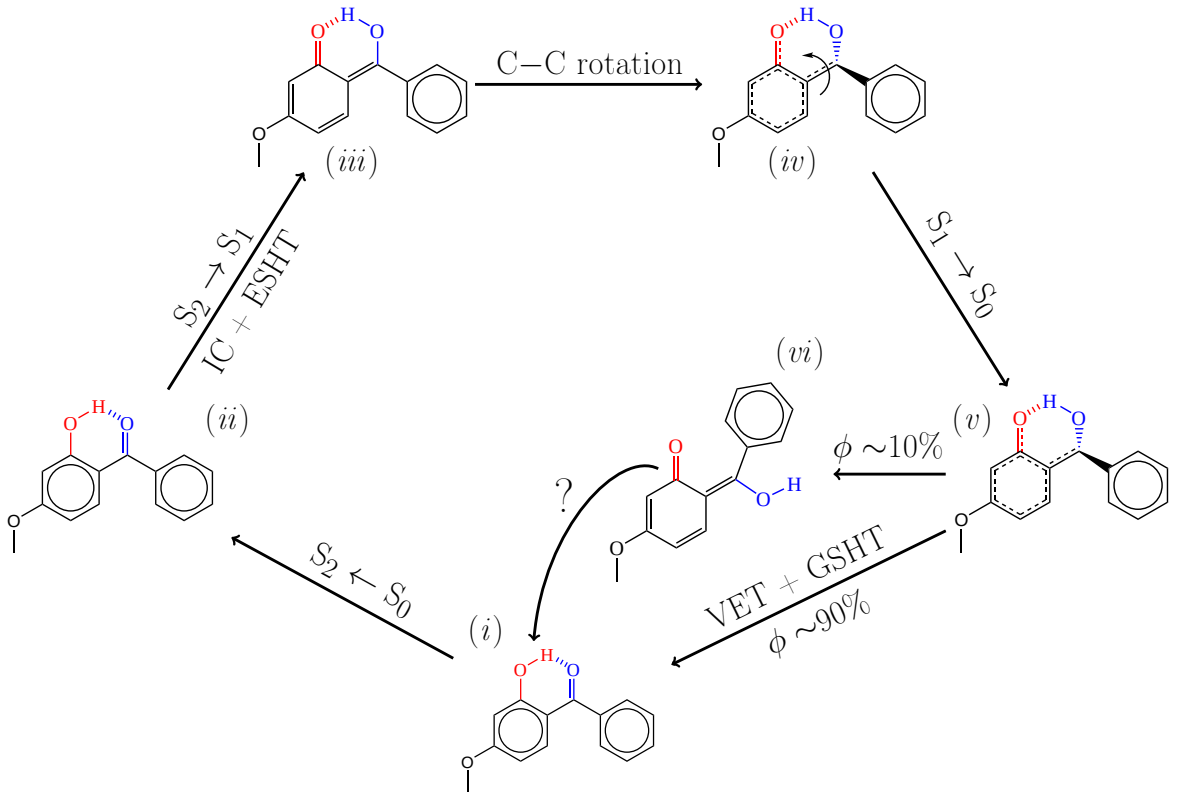

Figure 4.8 | Overall proposed relaxation mechanism of UV photoexcited OB. (*i*) Initial UV photoexcitation populates the $S_2(1^1\pi\pi^*)$ state. (*ii*) ESHT to the *keto*-tautomer and IC couple OB to the $S_1(1^1n\pi^*)$ state. (*iii*) Rotation about the aliphatic C−C bond (*iv*) couples the S_1 back to the ground S_0 state (*v*) where VET to the surrounding solvent and GSHT reforms the original *enol*-tautomer, or (*vi*) extended rotation can lead to a trans *keto*-tautomer photoproduct, with an estimated yield of ~10% based on TVAS measurements, which might then reform the original ground state.

4.2(D) and 4.3(D), which persists for ~100 fs. Guided by the *ab initio* calculations,[285] we try to rationalise these features. The signal plateau around time zero, which we are unable to resolve within our IRF (which is on the order of 100 fs), is attributed to a combination of ultrafast IC from the photoexcited S_2 state to S_1, and ballistic ESHT on the S_1 state. After ESHT to form the chelated *keto* species, slower rotation about the central C–C bond can occur, enabling IC back to the S_0 state through an S_1/S_0 CI at the twisted chelated *keto* structure (Figure 4.8). We associate τ_1 with this subsequent twisting and IC process; the timescale is sensibly consistent with that derived for *enol* → *keto* tautomerism in similar systems that require a twisted ESHT.[283,418,419] Two caveats are in order here. First, we cannot rule out the alternative possibility that τ_1 represents simultaneous (or concerted) H-atom transfer and C–C twisting, prior to

IC from S_1 to S_0, in which case the short-lived, flat absorption transient would most likely be attributable to IC from S_2 to S_1. Second, given the low frequency of the torsional mode, some fraction of the molecular ensemble will already be in the correct (or a more correct) geometry to pass through the S_1/S_0 CI. τ_1 reflects the dynamics of the overall molecular ensemble. After IC to form hot S_0 molecules, GSHT can regenerate the original chelated *enol* structure, which is then quenched by VET to the solvent. We associate τ_2 with this final VET-mediated cooling process. Support for this assignment comes from the evident small redshift of the UV-A absorption maximum of OB (*cf.* the steady-state UV absorption of OB; Figure 4.1), the expected characteristic of vibrationally hot S_0 OB molecules.[420] The TVAS measurements support this conclusion: given the ultrashort (τ_1) lifetime of photoexcited OB molecules in both solvents, the recovery of the GSB features in TVAS will report the rate of vibrational cooling of hot S_0 OB molecules, as described for other systems.[377] Importantly, the GSB recovery timescales from TVAS (τ) mirror closely the τ_2 values assigned to VET-driven cooling in TEAS. Furthermore, both τ and τ_2 are solvent dependent; the extracted lifetimes for methanol are consistently shorter than in cyclohexane, implying higher VET efficiencies in OB-methanol than in OB-cyclohexane. Such is fully consistent with prior expectations that the interaction of OB with a more strongly interacting (polar) solvent will promote a higher rate of VET.[421]

Identifying the photoproduct. As noted above, a small fraction (∼10%) of the GSB does not recover in either solvent, which is a tell-tale sign of some form of extended dynamics or photoproduct formation. Such a conclusion is reinforced by the appearance of a new absorption feature centred at 1640 cm^{-1} in cyclohexane (1630 cm^{-1} in methanol-d_4) in the TVA spectra recorded at extended time delays. Both the residual GSB and this new absorption feature are evident in the TVA spectra shown in Figure 4.6(I) for the case of OB in cyclohexane at Δt = 50 and 200 ps. Even though both the TEAS and TVAS measurements agree on the *presence* of a photoproduct, the *ab initio* calculations shown in Figures 4.6 and 4.7 are required to understand what the photoproduct *actually* is. Inspecting the differences in spectral features between the calculated difference spectrum and the experimental TVA spectrum, immediately the absence of a positive going signal at ∼1640 cm^{-1} in the difference spectrum for the oxetane is obvious (Figure 4.6(B), *cf.* the experiment Figure 4.6(I)) which suggests that the oxetane is not a significant photoproduct. Likewise, the spectral mismatch of the positive going signal in the experiment (∼1640 cm^{-1}) and calculated difference spectrum of the non-chelated *enol*-OB tautomer (∼1675 cm^{-1}) also suggests it to is an unlikely photoproduct (Figure 4.6(C)), as is the 'trans' *enol*-OB isomers due to the positive going

signal at ∼1650 cm^{-1} (Figures 4.6(E) and 4.6(F)). These results instead point towards the non-chelated *keto*-OB tautomer (Figure 4.6)(D)) or the 'trans' *keto*-OB isomers (Figures 4.6(G) and 4.6(H)) as the most likely products. Importantly, we are unable to rule out the non-chelated *keto*-OB isomer based on this work alone, however, drawing on studies involving related systems[418,419] lead us to favour the 'trans' *keto*-conformers as the more likely photoproducts, but, without additional experimental studies, we cannot discriminate between the two 'trans' *keto*-OB species (Figures 4.6(G) and 4.6(H)). We however choose to compare the experimental TVA spectra with that involving trans *keto*-OB-1 on account of its slightly better overall fit. Considering next the candidate triplet state photoproducts as given in Figure 4.7. The absence of a increasing signal at ∼1640 cm^{-1} in all difference spectra leads us to rule out significant triplet product formation, which is reinforced by the fact that none of the experimental TVA spectra show an increasing signal in the 1575–1625 cm^{-1} region, a predicted characteristic of all *enol*-OB triplet state photoproducts.[411]

We now revisit the possible importance of excited state O–H bond fission and phenoxyl radical formation, which Ignasiak *et al.*[288] suggested as a possible explanation for the incomplete signal recovery in their TEA spectra. The present study corroborates other aspects of their recent study, but careful inspection of the present TEA data (*e.g.* Figures 4.2 and 4.3) at wavelengths of ∼400 nm, where such phenoxyl radicals show a well-documented absorption,[422,423] reveals no such signature. The present measurements thus suggest that O–H bond fission is an insignificant photoproduct channel (at least within our signal-to-noise) and that the incomplete signal recovery might more likely be attributable to a trans *keto*-tautomer photoproduct. However, we also note differences in the pulse energy and photoexcitation wavelengths used in the two studies (10 μJ/pulse, 340 nm,[288] *cf.* < 1 μJ/pulse and 325 nm in this work) and suggest that additional pulse energy and/or wavelength studies might be necessary to check that such factors do not affect the detailed excited state dynamics of OB.

To conclude, we have determined two ultrafast relaxation processes by which photoexcited OB molecules revert to (predominantly) the ground state, where they are available to continue to absorb UV radiation. We suggest that the mechanism by which OB dissipates energy following UV excitation involves ultrafast excited state *enol* $\rightarrow$ *keto* tautomerisation, followed by two (IC and VET) relaxation processes to reform the original chelated *enol*-tautomer.

4.1.7 TEAS measurements after UV-B and UV-C photoexcitation

We extend the TEAS UV-A studies of OB to include higher pump excitations, namely the UV-B at 287 nm and the UV-C at 243 nm. The reasons for this are simple. The first is that OB is used as a broadband filter, thus its photochemical properties should be evaluated at all relevant regions, and the UV-visible spectrum of OB (Figure 4.1) displays three maxima, the UV-A and UV-B are of interest to sunscreen applications, and the UV-C might provide useful information for industrial applications where high energy UV is used, *e.g.* food security or polymer chemistry. The second reason lies in the interest of understanding the possible photolytic properties of OB; a higher photoexcitation would likely make such a process proceed with higher probability.

Considering UV-B photoexcitation first using a wavelength of 287 nm, the TAS of OB-cyclohexane and OB-methanol for a range of pump-probe time delays are shown in Figure 4.9(A). We consider OB-cyclohexane first. At early pump-probe time delays (<500 fs) the TAS are dominated by two features. There is an intense absorption peak centred on ∼366 nm and a broad absorption extending out to ∼650 nm. Based on the analysis of similar absorption features observed after UV-A excitation, and guided by *ab initio* calculations, this broad absorption is assigned to the OB ESA,[285,286,288] likely to originate from a transition to a dense manifold of high-lying electronic states *i.e.* $S_n \leftarrow S_1$.[321,364] By 2 ps, the majority of the broad ESA feature has decayed away, leaving the ∼366 nm absorption peak. A negative feature between 340 and 350 nm is also present which we assign, through comparison with the steady-state UV-visible of OB (Figure 4.1), to a GSB. By 50 ps, the 366 nm feature has almost decayed to the baseline, without full recovery of the GSB up to the maximum available pump-probe time delay of 1.7 ns. Similar dynamics are found for OB-methanol with a small observed blue-shift in the features discussed thus far.

Quantitative insight into the dynamical processes observed in the TAS is obtained by employing a global fitting procedure.[412,413] To recover the dynamics observed in the TAS, two exponential fitting functions are required over the spectral range of $355 \leq \lambda \leq 415$ nm. This short wavelength limit is once again required to avoid the GSB, and includes only the 366 nm absorption peak. Furthermore, for all UV-B measurements, a broad feature around time zero, unresolvable within our IRF (∼100 fs) and which shifts by ∼50 fs to longer time delays for UV-C measurements (*vide infra*), is excluded by the omission of very early delay times (<250 fs). For OB-cyclohexane, the transient signal is fitted using two lifetimes, $\tau_1 = 391 \pm 12$ fs and $\tau_2 = 8.6 \pm 2.7$ ps, with DAS

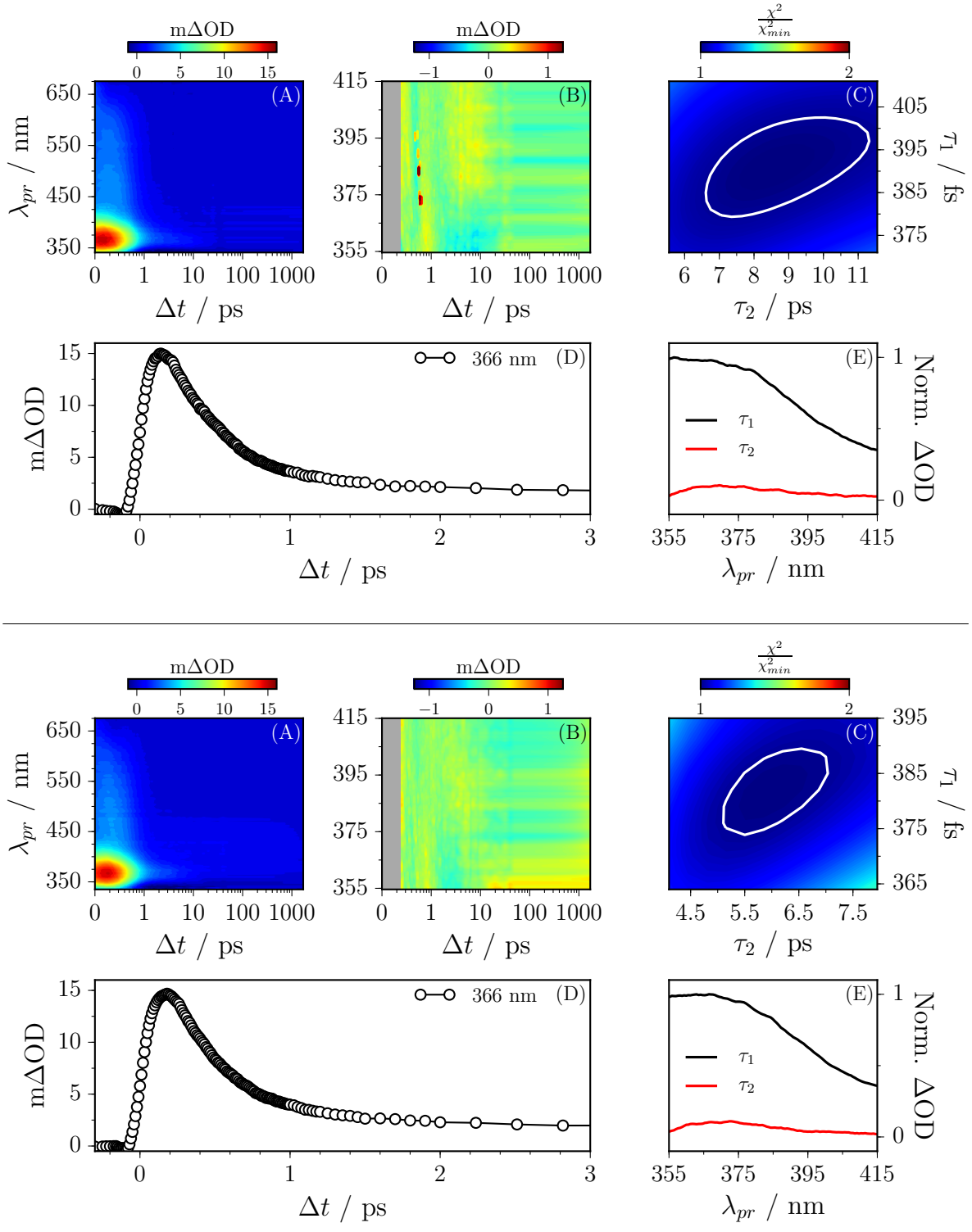

Figure 4.9 | (*top*): (A) Raw TAS following 287 nm photoexcitation of OB-cyclohexane. (B) Residual of the global fitting and the raw data. (C) SPA of the extracted lifetimes. (D) Early time 366 nm transient. (E) Corresponding DAS. (*bottom*): (A)-(E) Similarly for 287 nm photoexcitation of OB-methanol.

Table 4.1: Summary of the lifetimes of observed, dynamical processes of OB when photoexcited at $\lambda = 325$ nm, 287 nm and 243 nm radiation. The time delay Δt_{start} is given, below which time delays were not included in the global fit.

	Cyclohexane			Methanol		
λ / nm	Δt_{start} / fs	τ_1 / fs	τ_2 / ps	Δt_{start}	τ_1 / fs	τ_2 / ps
325	130	375 ± 13	7.8 ± 2.8	150	368 ± 13	4.9 ± 1.9
287	250	391 ± 12	8.6 ± 2.7	300	382 ± 8	6.0 ± 1.0
243	250	392 ± 10	11.0 ± 4.4	300	371 ± 9	7.8 ± 1.8

as shown in Figure 4.9(E). Similarly, for OB-methanol, the corresponding lifetimes are $\tau_1 = 382 \pm 8$ fs and $\tau_2 = 6.0 \pm 1.0$ ps, with corresponding DAS as shown in Figure 4.9(E).

Analogous experiments were performed for photoexcitation at 243 nm. TAS of OB-cyclohexane and OB-methanol are shown in Figure 4.10(A). We observe similar spectral features as described in the above UV-B case. Again, quantitative insight into the prevailing dynamical processes is obtained through global fitting. In the case of the UV-C measurements, time delays <300 fs were excluded in order to avoid the broad feature at very early time delays (*vide infra*). To recover the dynamics of the TAS over the spectral range of $355 \leq \lambda \leq 415$ nm, three exponential functions are required; one of which is a long-lived solvent response with a lifetime ∼400 ps for cyclohexane and ∼3 ns for methanol, predetermined from fitted solvent-only TAS (see Appendix 8.5).

The lifetimes of the other two processes are determined analogously to the UV-B case. These are determined to be $\tau_1 = 392 \pm 10$ fs and $\tau_2 = 11.0 \pm 4.4$ ps for OB-cyclohexane and $\tau_1 = 371 \pm 9$ fs and $\tau_2 = 7.8 \pm 1.8$ ps for OB-methanol. The corresponding DAS are shown in Figure 4.10(E). The lifetimes are summarised in Table 4.1 for all photoexcitation wavelengths.

4.1.8 Discussion and conclusions

For all pump excitation wavelengths, TEAS measurements identify three dynamical features (excluding any solvent responses) which closely match those previously seen for OB photoexcited at 325 nm.[286] Two of these processes, a short lived process τ_1 and a longer lived process τ_2, are extracted from the TAS by the global fitting of the 366 nm absorption maxima. The third feature is that previously described; a broad feature

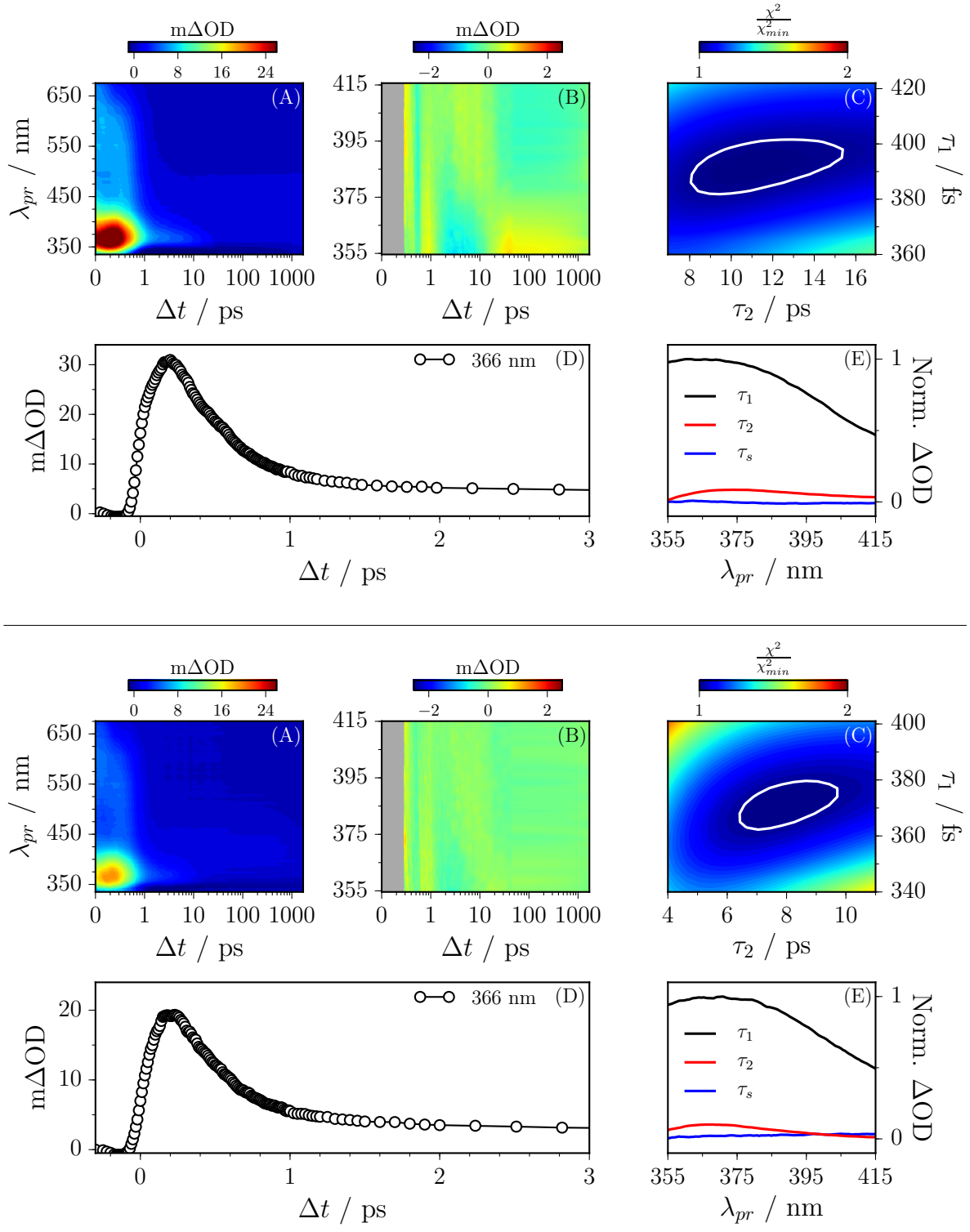

Figure 4.10 | (*top*): (A) Raw TAS following 243 nm photoexcitation of OB-cyclohexane. (B) Residual of the global fitting and the raw data. (C) SPA of the extracted lifetimes. (D) Early time 366 nm transient. (E) Corresponding DAS. (*bottom*): (A)–(E) Similarly for 243 nm photoexcitation of OB-methanol.

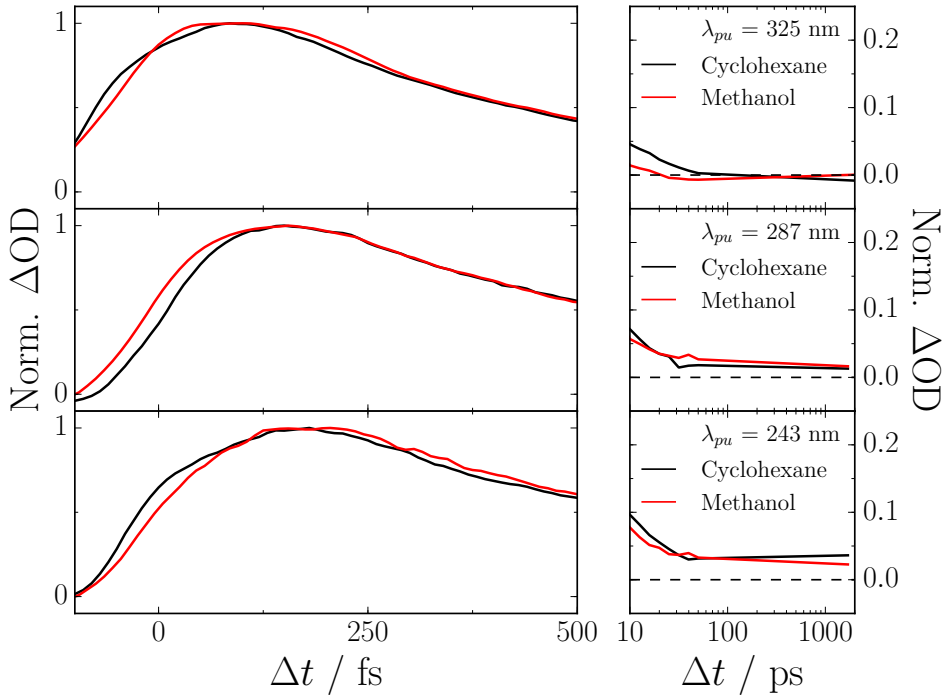

Figure 4.11 | (*left*): 366 nm transients displaying early time dynamics of OB-cyclohexane (black line) and OB-methanol (red line) after 325 nm (*top*) 287 nm (*middle*) and 243 nm (*bottom*) excitation. Increasing photoexcitation energy appears to shift the 366 nm peak to longer time delays. (*right*): The corresponding plots show the late-time dynamics, where a positive signal remains up to the maximum available time delay, most clearly seen for 287 nm and 243 nm photoexcitation, *n.b.* the S/N is ∼2% making such a conclusion for 325 nm photoexcitation difficult.

which persists over time delays $100 < \Delta t < 200$ fs, and which appears to shift ∼50 fs to longer time delays with increasing excitation energy (*cf.* Figures 4.2(D), 4.3(D), 4.9(D) and 4.10(D); see Figure 4.11). In the case of 243 nm photoexcitation, there is a suspicion of the emergence of a 'double hump' structure in this broad feature, that is not evident in the corresponding data obtained when exciting in the UV-A or UV-B regions.[286] Furthermore, for all excitation wavelengths, we note that the GSB has not fully recovered, seen from the non-zero baseline out to the maximum delay time of our experiment (1.7 ns; Figure 4.11).

We can begin to rationalise these features drawing on *ab initio* calculations performed in previous studies.[285,286] Firstly, given the similarity of the TAS measured in both cyclohexane and methanol, we conclude that the intramolecular hydrogen bond in OB is preserved in both solvents as observed with UV-A photoexcitation. The signal broadening for higher energy excitations observed in Figure 4.11, may be understood

as IC from a photoexcited $S_3(2^1\pi\pi^*)$ state to S_1 in the case of UV-B excitation,[285] or, in the case of UV-C excitation, from a higher lying S_n state ($n \geq 4$) to S_1; followed by ballistic ESHT on the S_1 PES. Once again, we are unable to say whether ESHT occurs before IC or indeed concomitantly. This mechanism fits well with the observed shift of the very early time feature (Figure 4.11) given that IC from higher electronic states will take longer to relax to the S_1 *enol*-OB tautomer before ESHT occurs. In such cases, one might speculate the appearance of a double hump, as these processes begin to emerge from our experimental temporal resolution of ∼100 fs. From here the dynamics which occur accord identically with those discussed for UV-A excitation: ESHT, which drives *enol* → *keto* tautomerisation, preceded by a slower rotation about the C–C bond which facilitates IC back to the S_0 state through a S_1/S_0 CI (nonadiabatic transfer). Following IC and formation of vibrationally hot S_0 *keto* molecules, GSHT allows *keto* → *enol* tautomerisation, which subsequently cools *via* VET with the surrounding solvent. The lifetimes are summarised in Table 4.1.

There is agreement in the τ_1 lifetimes when OB is excited by either a UV-A, UV-B or UV-C pump pulse. As τ_1 represents the rotation around the C–C bond, this lack of change suggests that rotational motion about the C–C bond is unaffected by the increase in vibrational energy in the S_1 molecules. One might anticipate that, following $S_1 \rightarrow S_0$ nonadiabatic transfer, the extra vibrational energy in the vibrationally hot S_0 *keto*-tautomer would lead to an increase in VET lifetime (τ_2). However, within a 2σ uncertainty, our measurements of τ_2 remain constant over different excitation energies, *cf.* 7.8 ± 2.8 ps to 8.6 ± 2.7 ps to 11.0 ± 4.4 ps after UV-A, UV-B and UV-C excitation respectively (OB-cyclohexane), indicating an insensitivity to this extra vibrational energy. Once again the τ_2 lifetime is solvent dependent in that the extracted lifetimes for OB-methanol are consistently shorter than the OB-cyclohexane counterparts, implying higher VET efficiencies for OB-methanol than OB-cyclohexane, consistent with a more strongly (polar) interacting (hydrogen bonding) solvent.[421]

4.2 Titanium dioxide

4.2.1 Introduction

Where OB is an exemplar of popular organic filters used in commercial sunscreen products, titanium dioxide (TiO_2) is without doubt currently the most widely used inorganic particulate filter in commercial products, followed by zinc oxide (Figure 4.12).[274,424] TiO_2, in particular, is also attracting widespread interest in terms of TiO_2-dye photophysics.[426,427] Most studies of the photoprotection properties of these sunscreen components have focused on individual filters in isolation, but commercial sunscreen products, as discussed in Section 2.2.4, typically contain tens of components in order to produce an efficient, broadband photoprotective and aesthetically pleasing product (*cf.* Figure 2.18). In this study we focus on OB *and* TiO_2, two sunscreen constituents which are often combined to provide broad spectral coverage and efficient photoprotection, to understand if the previously observed photodynamics in OB are changed by the presence of the inorganic particulate filter.[286–288] Multi-molecular compositions have already been shown to display photodynamics different to that of the individual constituents, for example, octocrylene (introduced later) is known to behave as a photostabiliser to avobenzone when in solution together.[264] Here we explore the photophysical interdependency (or otherwise) of the individual components within an organic molecule/inorganic particulate filter blend.

In commercial products TiO_2 nanoparticles are used since their absorption and scattering coefficients of incident UVR are dependent on the diameter of the nanoparticles.[268] Typically nanoparticles with diameter ∼10s of nm will suitably scatter and

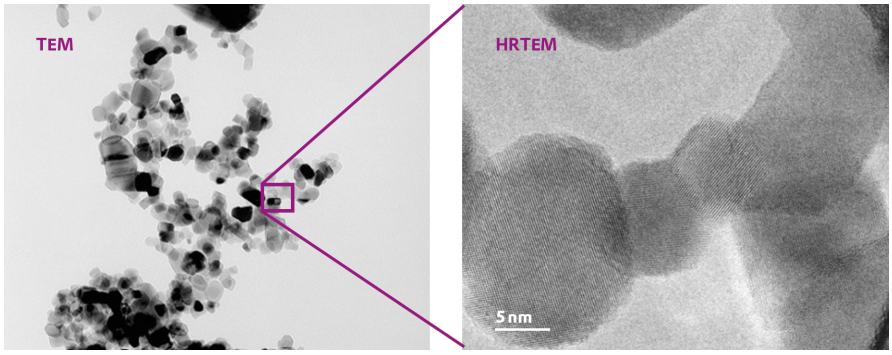

Figure 4.12 | (*left*): Transmission Electron Micrograph (TEM) and (*right*): High-Resolution TEM (HRTEM) images of TiO_2 nanoparticles (Titania, *P*25). Images taken from *Evonik inductries*.[425]

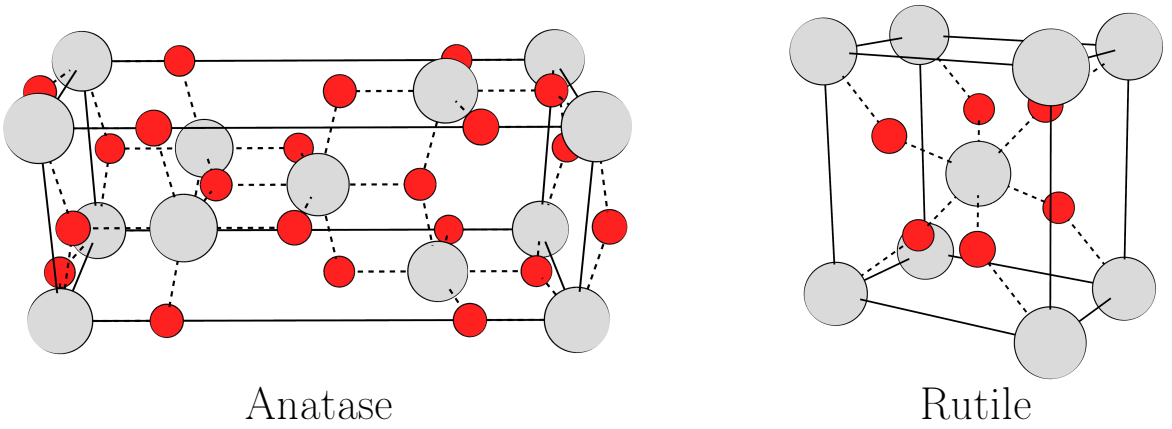

Figure 4.13 | The two crystalline structure of TiO_2 applicable for use in sunscreen products. (*left*): Anatase (lattice parameters: A = 3.785 Å, B = 3.785 Å, C = 9.514 Å, $\alpha = \beta = \gamma = 90°$).[433,434] (*right*): Rutile (lattice parameters: A = 2.958 Å, B = 4.594 Å, C = 4.954 Å, $\alpha = \beta = \gamma = 90°$).[433,435,436]

absorb in the UV-A and UV-B regions and thus are selected for use in sunscreen products (Figure 4.12). From a commercial aspect, control of the absorption (and scattering) profile of the nanoparticles can lead to a translucent visible absorption spectrum making the product colourless upon application, an important aesthetic factor in the manufacturing of sunscreen.[271] Furthermore, there has been concerns regarding the use of such nanoparticles with respect to the generation of ROS, specifically in the case of deep skin penetration, although the literature on this subject remains somewhat sceptical.[271,428–431] TiO_2 comes in three crystalline forms, *anatase*, *rutile*, and *brookite*, see Figure 4.13.[263] Brookite absorbs outside the relevant UVR window making it unsuitable for use as a sunscreen and thus is not considered further. Whilst either anatase or rutile can be used in sunscreens, commercial TiO_2 compositions are often mixtures of the two structure and will often include a coating to enhance UV absorption or other properties such as solubility.[432] One example is the widely available Titania (Aeroxide *P*25)[425] which is a mixture of anatase and rutile (∼80:20 wt/wt) with a diameter of ∼21 nm and exhibits hydrophilic character due to the presence of hydroxyl groups on the surface. This formulation is used throughout this chapter.

4.2.2 Methodology

Sample preparation of the multicomponent mixtures used OB, TiO_2 nanoparticles (>99%, ∼21 nm diameter, *P25*, Sigma-Aldrich) and the combination of the two, TiO_2:OB

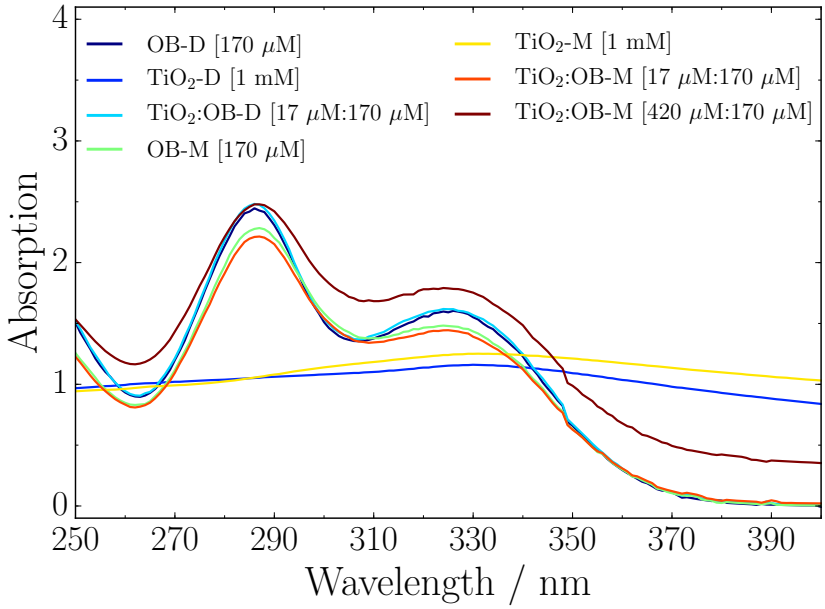

Figure 4.14 | UV-visible spectra of OB, TiO_2 and combinations of them in dioxane and methanol. Specific concentrations were used to highlight the additivity of the absorption spectra and are given in the square brackets. The TiO_2 profiles are convolutions of both absorption and scattering contributions.[268] A schematic, qualitative picture of these systems is given in Figure 0.1(B).

in dioxane (≥99%, Fisher Scientific) or methanol. For all solutions containing OB, 10 mM was used. For dispersions containing TiO_2, 1 mM and 25 mM (for full saturation) in methanol were used. In dioxane, 1 mM was sufficient for saturation. These ratios were chosen for the extreme ends of what might exist in a commercial product.[221] Samples are from hereon referred to as; OB-D (10 mM OB in dioxane), TiO_2:OB-D (1 mM TiO_2 with 10 mM OB in dioxane), 1 mM-TiO_2:OB-M (1 mM TiO_2 with 10 mM OB in methanol) and 25 mM-TiO_2:OB-M (25 mM TiO_2 with 10 mM OB in methanol). All steady-state UV-visible spectra are taken with either a Cary 50 (TiO_2-only samples) or Cary 1E UV-visible spectrophotometer (all other samples), with a 1 cm path length quartz cuvette, the spectra of which are given in Figure 4.14. Samples containing OB were photoexcited at 325 nm, while those containing TiO_2 only were photoexcited at 330 nm (*cf.* Figure 4.14). The pump-pulses, probe-pulses, polarisation, and sample delivery details are the same as described above for the TEAS measurements of OB.

4.2.3 TEAS measurements of TiO_2

Measurements of TiO_2 only in methanol (both concentrations) and in dioxane following photoexcitation at the UV-visible absorption maximum (330 nm, *cf.* Figure 4.14) are given in Figure 4.15. Minimal dynamics are seen, all of which occur within the temporal resolution of the experimental IRF (∼100 fs), except for when using 25mM-TiO_2-M where a strong negative signal is observed which does not fully recover by the maximum available pump-probe time delay of 2 ns. Comparing the spectral location of the negative signal to the UV-visible spectrum of TiO_2, this signal can be attributed to a GSB.

4.2.4 TEAS measurements of oxybenzone and TiO_2 suspensions

TAS for OB-D following photoexcitation at 325 nm is given in Figure 4.16(A). The TAS shows three features. (*i*) A negative signal below 355 nm which, through comparison with the UV-visible spectrum of OB (Figure 4.14) is assigned to a GSB. (*ii*) An intense positive signal centred ∼365 nm, which decays to the baseline by ∼20 ps. (*iii*) A broad positive signal spanning the probe spectral region ∼425–650 nm which decays within ∼2 ps. Both positive signals are assigned to ESAs through comparison to previous measurements,[286,287] and *ab initio* calculations of similar systems[285] which

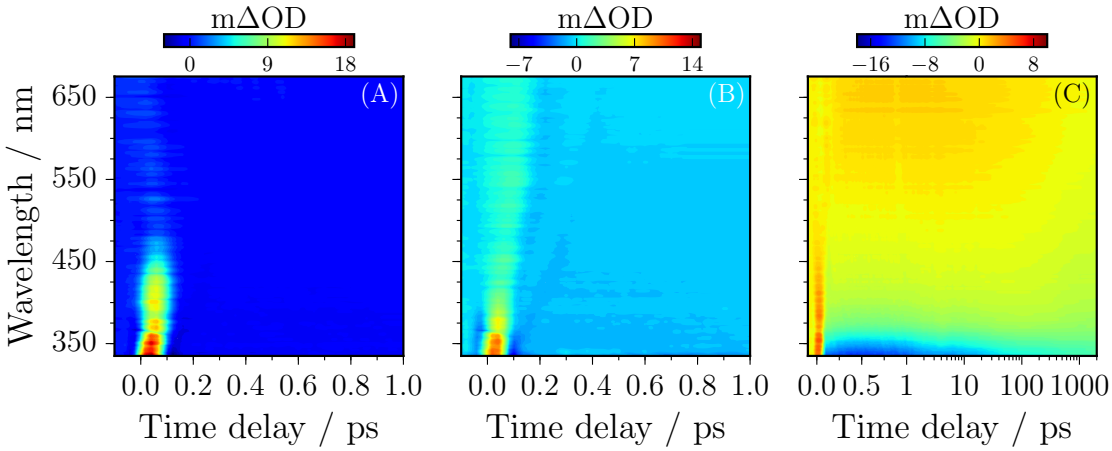

Figure 4.15 | Raw TAS of (A) TiO_2-dioxane, (B) 1 mM-TiO_2 methanol, and (C) 25 mM TiO_2-methanol. The latter uses a linear scale to represent time delays below 1 ps, beyond this, a logarithmic scale is used.

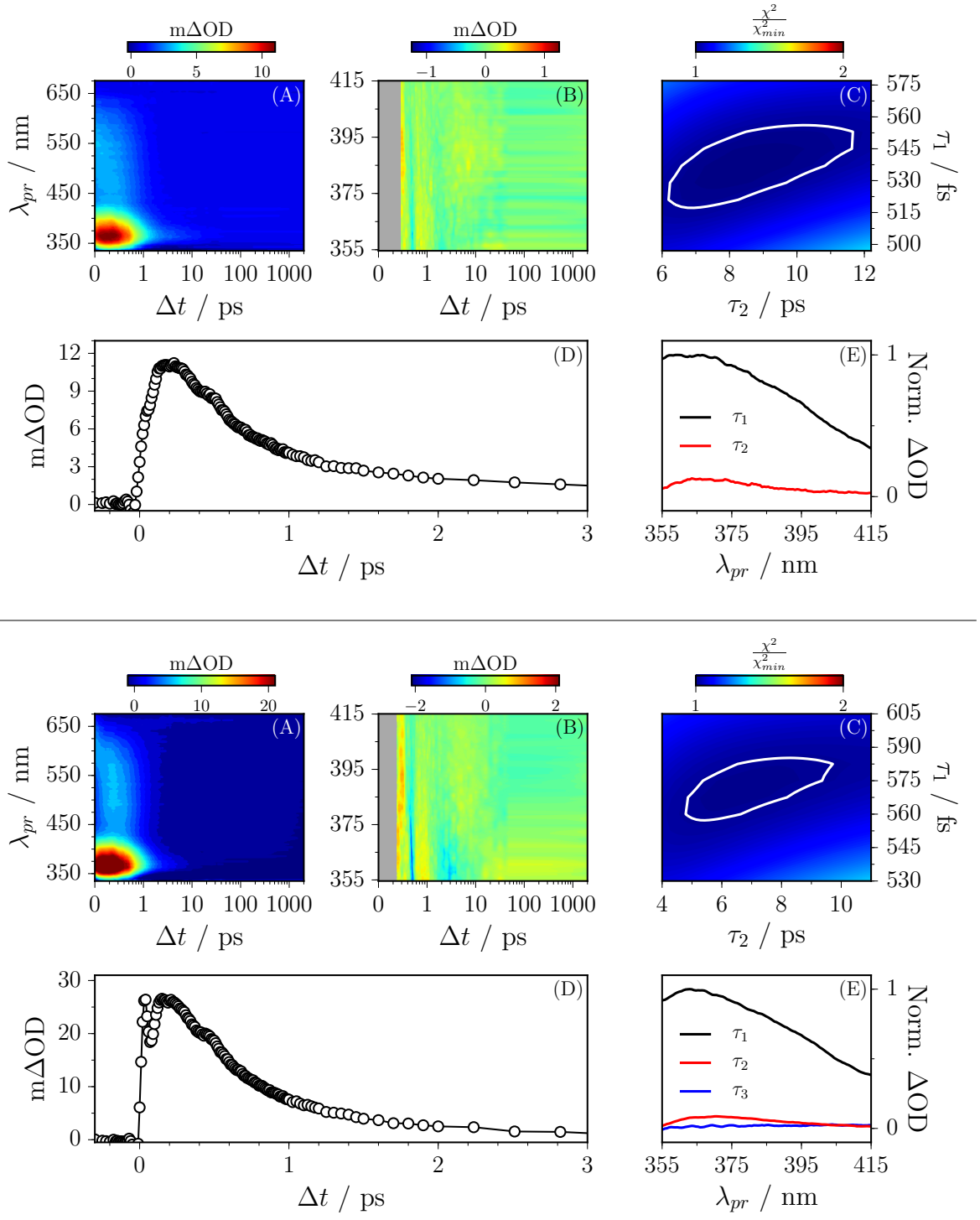

Figure 4.16 | (*top*): (A) TAS OB in dioxane following an initial photoexcitation at ∼325 nm. (B) The residuals between the global fitted TEA spectrum and the experimental spectrum. (C) SPA of the uncertainties on the two lifetimes. (D) The 366 nm probe absorption transient is shown up to $\Delta t = 3$ ps. (E) The DAS for the extracted lifetimes. (*bottom*): (A)–(E) Similarly for TiO_2 and OB in dioxane.

likely originate from transitions to a myriad of electronics states *i.e.* $S_n \leftarrow S_1$.

Global fitting is employed in order to quantify the dynamical processes revealed in the TAS. Two exponential decay functions were required to describe the TAS over the probe spectral region of 355–415 nm, which centres on the intense absorption feature (*ii*). Very early time delays (<250 fs) were omitted to avoid convolution with our IRF as well as a broad feature around time zero (*cf.* Figure 4.15). This analysis reveals two dynamical lifetimes $\tau_1 = 537 \pm 20$ fs and $\tau_2 = 8.3 \pm 3.3$ ps with corresponding DAS shown in Figure 4.16(E), which agree well with previous studies of OB in the nonpolar solvent cyclohexane ($\tau_1 = 375 \pm 13$ fs and $\tau_2 = 7.8 \pm 2.8$ ps).[286] The difference in τ_1 between dioxane measurements and the previously reported cyclohexane and methanol measurements[286] may be understood by the differences in solvent viscosity, discussed later.

Similar features are observed for the TAS of TiO_2:OB-D, Figure 4.16 with the negative feature (*i*) appearing more strongly and spectrally broadened. This apparent broadening is consistent with the addition of the TiO_2, most clearly seen for the 25 mM-TiO_2 measurements in Figure 4.15(C). The TAS for TiO_2:OB-D shown in Figure 4.16(A) displays the same features as for OB-D with this addendum. A third lifetime, attributed to the additional negative contribution from the presence of the TiO_2 (*cf.* Figure 4.15), was required to describe these TAS. This has the effect of creating a long-lived baseline offset which this third lifetime (≥2 ns) captures, labelled τ_3. Once again omitting early delay times (Δt <250 fs), the other lifetimes are determined to be $\tau_1 = 575 \pm 18$ fs and $\tau_2 = 6.9 \pm 2.8$ ps which correspond very closely to the OB-D measurements.

Next we consider the solvent methanol. Previous measurements determined that OB-M displays two dynamical features, analogous to those discussed for OB-D, with lifetimes $\tau_1 = 368 \pm 13$ fs and $\tau_2 = 4.9 \pm 1.9$ ps,[286] and thus provides a point of comparison when TiO_2 is included. For low concentrations, 1 mM-TiO_2:OB-M, Figure 4.17, similar spectral features are seen in the TAS as in the dioxane measurements. Global fitting reveals three dynamical lifetimes, $\tau_1 = 357 \pm 9$ fs, $\tau_2 = 4.8 \pm 1.8$ ps and the long lifetime τ_3 ≥2 ns. The corresponding DAS are given in Figure 4.17(E). For saturated concentrations, 25 mM-TiO_2:OB-M, Figure 4.17, the dynamics of TiO_2 are much more clearly observed, whereby the long-time recovery of the GSB persists for the duration of the experiment. Global fitting reveals three lifetimes, $\tau_1 = 363 \pm 11$ fs, $\tau_2 = 3.0 \pm 1.4$ ps and τ_3 ≥2 ns. For both measurements including TiO_2, other than the appearance of the long-lived recovery of the TiO_2 which requires the third lifetime, τ_1 and τ_2 compare very closely with OB-M measurements *cf.* Table 4.2.

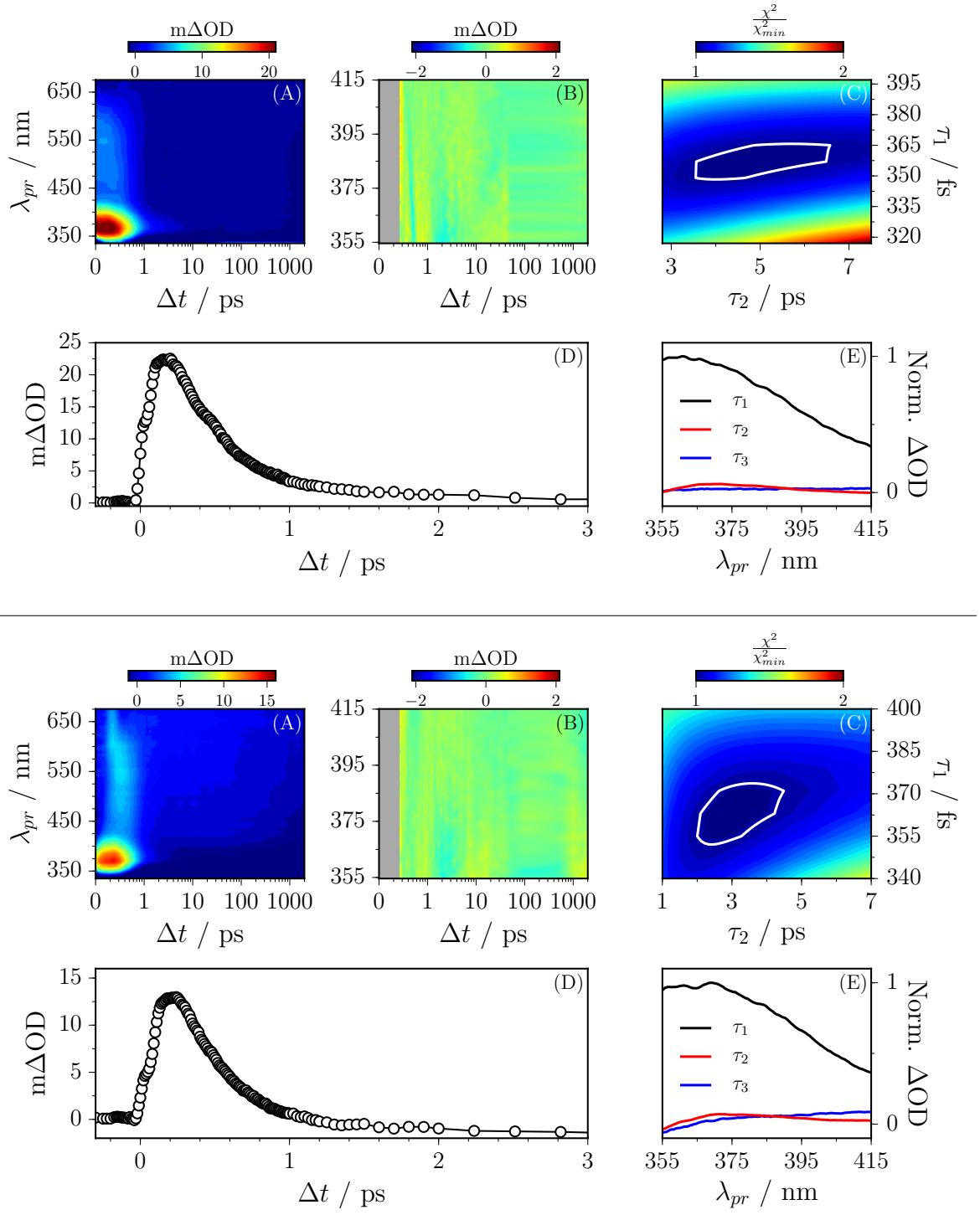

Figure 4.17 | (*top*): (A) TAS of 1 mM-TiO_2:OB in methanol following an initial photoexcitation at ∼325 nm. (B) The residuals between the global fitted TEA spectrum and the experimental spectrum. (C) SPA of the uncertainties on the two lifetimes. (D) The 366 nm probe absorption transient is shown up to $\Delta t = 3$ ps. (E) The DAS for the extracted lifetimes. (*bottom*): (A)–(E) Similarly for 25 mM-TiO_2:OB in methanol.

Table 4.2: Summary of the dynamical lifetimes as determined from the global fitting for all samples (D = dioxane, M = methanol).

Sample	Δt_{start}	τ_1 / fs	τ_2 / ps	τ_3 / ns
OB-D	300	537 ± 20	8.3 ± 3.3	–
1 mM-TiO_2:OB-D	250	575 ± 18	6.9 ± 2.8	≥2 ns
1 mM-TiO_2:OB-M	280	357 ± 9	4.8 ± 1.8	≥2 ns
25 mM-TiO_2:OB-M	280	363 ± 11	3.0 ± 1.4	≥2 ns

4.2.5 Discussion and conclusions

We can begin to rationalise the features in our measured TAS and assign dynamical processes to the lifetimes determined from global fitting of the TAS by drawing on both *ab initio* calculations and previous ultrafast measurements.[285–287] Considering OB-D first, the dynamics observed follow closely those of OB-M and OB-cyclohexane;[286] initial 325 nm photoexcitation populates the S_2 state from the ground state, S_0. Following this, OB undergoes IC to the S_1 state, followed by an ESHT along the O−H stretch, forming the *keto*-tautomer. This cascade of processes is captured by the broad absorption feature which is not considered in the global fit, and resides, heavily convoluted, within the IRF of the experiment of ∼100 fs, which is in accord with other *enol-keto* driven systems[437] and has been supported recently *via* trajectory surface hopping calculations.[289] Rotation about the aliphatic C−C bond is required in order to couple the S_1/S_0 states, resulting in a twisted *keto* geometry and enables population transfer through a CI between the S_1 and S_0 PES (*cf.* summarised mechanism of OB in Figure 4.8). These processes are captured by the lifetime τ_1. This assignment also accounts for the difference in the τ_1 lifetime between solvents, which may be understood through differences in the solvent viscosity, η. Dioxane exhibits a greater viscosity compared to cyclohexane or methanol (η = 1.19, 0.897 and 0.551 mPa·s respectively[438]) and is therefore likely to offer greatest friction to the geometry change required before OB can couple to its S_0 state.[439]

The twisted *keto* species is not stable on the S_0 PES, and there are two routes *via* which it may relax. (*i*) The ground state may recover through a reverse tautomerisation involving a GSHT reforming the *enol*-tautomer, which further relaxes by VET to the surrounding solvent molecules. (*ii*) Formation of a long-lived photoproduct, most likely

through extended C−C bond rotation forming a non-chelated, trans *keto*-tautomer as previously discussed.[286] However, a possibility remains that the photoproduct might be a phenoxyl radical.[288] The first of these routes appears dominant, given that the majority of the GSB recovers on the timescale of the experiment; the incomplete recovery is therefore attributed to the formation of a photoproduct which does not recover by the maximum time delay available of 2 ns. These processes are captured by the lifetime τ_2. This lifetime also displays a solvent dependence; τ_2 is consistently shorter in the more strongly interacting (polar) solvent methanol, which is in agreement with VET driven cooling where a greater degree of hydrogen bonding enhances VET.[286,421] That being said, it could also indicate that methanol promotes the GSHT but remains convoluted with the VET.

Considering next the TiO_2 measurements only, minimal dynamics are observed, the results of which are given in Figure 4.15. For low concentrations (1 mM), any dynamics are within the IRF or are well within the signal to noise of the experiment (<0.5 mΔOD). In methanol (Figure 4.15(C)), where higher concentrations are achieved (25 mM), there are clear dynamics which persist to the maximum pump-probe time delays. These observations are consistent with previous studies on isolated TiO_2 nanoparticles in solution.[440–442] In the low concentration regime, TiO_2 displays ultrafast relaxation, likely through the generation and subsequent trapping of surface electrons.[443,444] At higher concentrations, TiO_2 begins to behave more like a thin film, where deep trapping of electrons equilibrating between surface and shallow trapping sites occurs over 100's of ps.[442]

Having characterised the dynamics displayed by each component, individually, we now discuss the measurements for the multicomponent systems. For 1 mM TiO_2:OB-D, the TAS (Figure 4.16(A)) appears to be a simple weighted sum of the isolated OB and TiO_2 systems, with the requirement of the third lifetime accounting for the long-lived dynamics of TiO_2. This is further evidenced by similar τ_1 and τ_2 lifetimes for the individual and multicomponent systems (within 2σ of each other). Very similar conclusions are reached for both the 1 mM-TiO_2:OB-M and 25 mM-TiO_2:OB-M systems (Figure 4.17(A)) where all lifetimes are again within 2σ of their OB-M counterparts. The effect of the presence of TiO_2 in low (or saturated) concentrations on the overall dynamics is simply additive; the presence of one appears not to affect the relaxation dynamics of the other component.

A simple but representative example of the additive effect of TiO_2 with OB in dioxane is shown in Figure 4.18. Here the TAS of the isolated components, *i.e.* 1 mM TiO_2 (Figure 4.18(A)) and 10 mM OB (Figure 4.18(B)) are added together and the

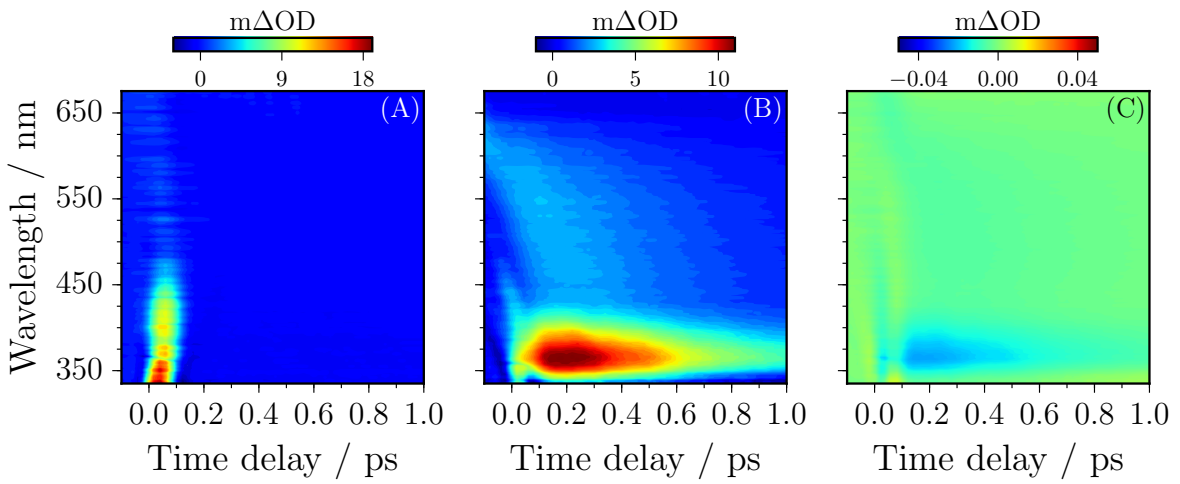

Figure 4.18 | (A) 1 mM TiO_2-D TAS, (B) 10 mM OB-D TAS and (C) the residual between the 1 mM-TiO_2:OB-D TAS and the isolated components (*i.e.* (A) and (B)).

result normalised. Then the TAS of the combined system (Figure 4.16(A)) is normalised and subtracted, which we refer to as the residual, *i.e.*

$$\text{Residual} = Norm.\left[(\text{TAS}_{\text{TiO}_2} + \text{TAS}_{\text{OB}})\right] - Norm.\left[(\text{TAS}_{\text{TiO}_2+\text{OB}})\right]. \qquad (4.1)$$

All residual points are very small (*cf.* Figure 4.18(C)), and thus even with this reasonably crude estimate, the TAS of the mixed system can be described sufficiently well by the sum of the individual components. We stress however that this is an approximate analysis, where several experimental conditions which are not easily controlled ultimately limit this description of additivity. For example, differences in pump-probe intensities, pump-probe overlap, the difference in pump wavelength (*i.e.* 330 nm *vs.* 325 nm for TiO_2 and OB respectively), and any difference in chirp correction,[386] will of course affect the residual.

To conclude, the relaxation dynamics of the popular organic filter OB in commercial sunscreens appear unaltered by the presence of the widely utilised scattering (and absorptive) additive TiO_2. Unlike other additives such as photostabilisers which are known to enhance the photostability of an organic filter, TiO_2 is shown to have minimal impact on the dynamics displayed by the organic filter. This implies, at the very least, little or no interaction between the two species. This is an important result given the widespread use of TiO_2 in commercial sunscreen products and may justify the inclusion of both components in order to provide efficient broadband protection.

4.3 Octocrylene

4.3.1 Introduction

Octocrylene (OC), also known as 2-ethylhexyl 2-cyano-3,3-diphenylprop-2-enoate, *cf.* Figure 4.19, as briefly discussed in Section 2.2.5 is an organic filter, closely related to the cinnamate family, whose prevalence is remarkably high amongst commercial sunscreens.[253] It displays broadband absorption of UV-B and high energy components of UV-A radiation, as shown from its UV-visible absorption spectrum in Figure 4.19. It notably has also been shown to act as a stabiliser to other sunscreen constituents, such as avobenzone.[264] In general there remains much ongoing research to understand the potential adverse dermatological and physiological effects resulting from the use of sunscreens, including OC.[221,252,273] Given its widespread use, there has also been interest in understanding the wider-reaching consequences such as water pollution, where water-based activities wash sunscreen off a person, or, untreated water allows these products to propagate into the wider aquatic ecosystem.[345,346]

OC shows no significant fluorescence or phosphorescence, hinting that ultrafast processes may be occurring that out-compete any spontaneous emission pathways.[338] Closely related molecules, ethylhexylmethoxycrylene and octylmethoxycinnamate have been shown to undergo isomerisation as the dominant relaxation pathway after UV

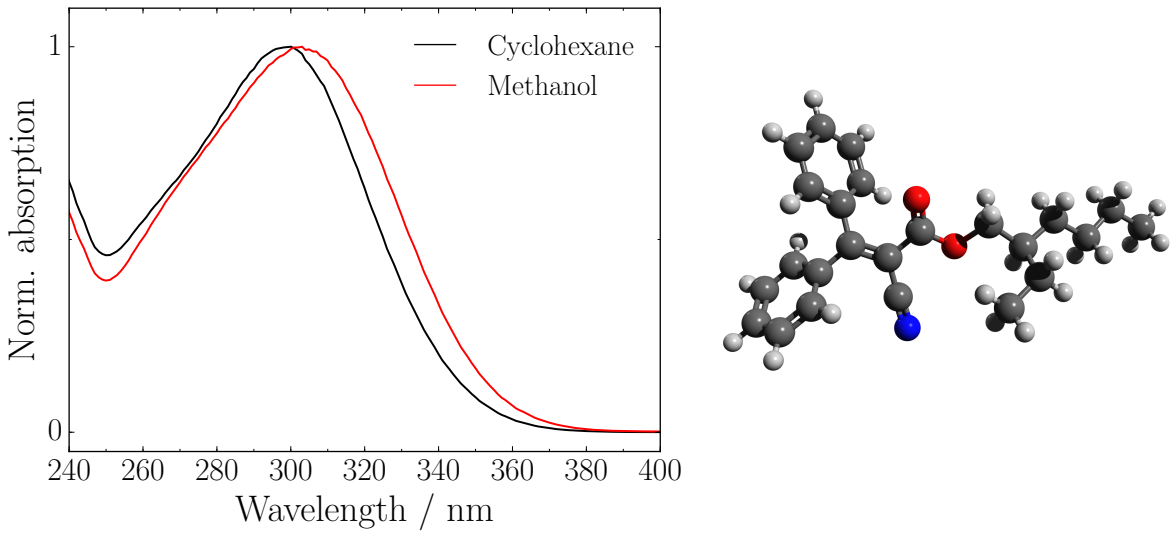

Figure 4.19 | (*left*): The UV-visible spectrum of OC in cyclohexane (black) and methanol (red). (*right*): The optimised geometry at the DFT level of theory, using the B3LYP functional[399,400] and a 6-311G+** basis set.[29,415] A schematic of OC is given in Figure 0.1(C).

photoexcitation with high efficiency leading to the idea that OC will relax *via* similar processes.[296,300,338] The latter of these has also been recently studied by our group using TEAS and has indeed been shown to display ultrafast relaxation in the solution phase *via* nonradiative transitions along an *trans-cis* isomerism reaction coordinate.[300]

4.3.2 Methodology

A stock sample of 97% OC was purchased from Sigma-Aldrich and used without further purification. For all reported TEAS measurements, 10 mM solutions of OC in either cyclohexane (>99%, VWR) or methanol (≥99.6%, Sigma-Aldrich), referred to as OC-cyclohexane and OC-methanol respectively, are recirculated between two CaF_2 windows with 100 μm PTFE spacers *via* a flow-through cell (Harrick Scientific). The samples are photoexcited by 300 nm pump pulses with fluences of ∼1–2 mJ cm^{-2} produced by a commercially available OPA (TOPAS-C, Light Conversion) seeded by a 1 kHz pulse train (1 W, 800 nm) from a Ti:sapphire CPA (Spitfire Pro XP, Spectra Physics). A small portion of the 800 nm fundamental (∼5 mW) is focussed into a 1 mm thick CaF_2 window producing a broadband WLC (∼335–675 nm) used as the probe pulses. A half-wave plate is used to hold probe polarisation at the magic angle (54.7°) relative to the pump polarisation. All measured TAS are chirp corrected using the KOALA package.[386]

Both the TAS of OC-cyclohexane and OC-methanol were analysed using a global fitting procedure.[302,412] The experimental TAS are modelled by the sum of n exponential functions convoluted with a Gaussian IRF, G(Δt). For both OC-cyclohexane and OC-methanol, four exponential functions are required to fully describe the experimental TAS and the G(Δt) is taken to be ∼100 fs.[287] All confidence intervals assigned to lifetimes are reported to the 95% level using ASE, as described in Section 3.3.

All steady-state UV-visible spectroscopic measurements were taken using a Cary 50 UV-visible spectrophotometer with a 1 cm path length quartz cuvette, and ∼μM OC-cyclohexane and OC-methanol solutions. To investigate evidence of long-lived photoproducts, continuous wave UV irradiation studies were performed on OC using the following procedure. First, a steady-state UV-visible spectrum of each sample was taken (Cary 300 spectrometer), to obtain a '*before*' spectrum. Samples were then irradiated with continuous wave radiation, ∼3 W, from an arc lamp (OBB, Tunable KiloArc) for 10 minutes using the a central wavelength of 300 nm and bandwidth of ∼20 nm. A second UV-visible spectrum was taken (Cary 300 spectrometer) following irradiation, referred to as the '*after*' spectrum. A subtraction of the before spectrum from the after spectrum results in the reported '*difference spectrum*'.

All *ab initio* electronic structure calculations of OC were performed with the Gaussian 09 suite of programs.[78] The ground state geometry energy minimum is determined using DFT with the B3LYP functional[399,400] and the 6-311+G** basis set.[29,415] The likely excited states were characterised using TD-DFT with the B3LYP functional and 6-311+G** basis set. Calculations were also performed with the M05-2X functional for comparison.[445]

4.3.3 TEAS measurements of octocrylene

The TAS of OC-cyclohexane were recorded for a range of pump-probe time delays, Δt, and are shown in Figure 4.20. We start by considering the early time ($\Delta t < 2$ ps) OC-cyclohexane. The TAS is dominated by two positive absorption features: (*i*) a broad, intense absorption across probe wavelengths ∼335–475 nm, and (*ii*) a weaker absorption signal which extends out to, and decays towards the baseline by, ∼675 nm (the limit of our probe spectral window). Both of these positive signals are attributed to the ESA of OC, based on subsequent analysis, discussed later. In particular, absorption feature (*i*) changes significantly for increasing Δt, up to 2 ps, see Figure 4.20(D). The absorption signal displays an intense peak at Δt ∼150 fs with a short-lived negative signal also observed beyond ∼550 nm for ∼250 $< \Delta t <$ 500 fs which we attribute to SE. As this SE signal decays, another absorption peak grows in by Δt ∼500 fs, which is most clearly seen at probe wavelengths of λ ∼500 nm, see Figure 4.20(A). By 2 ps, the ESA has almost completely returned to the baseline, with no further spectral features observed up to the maximum available pump-probe time delay of $\Delta t = 600$ ps ($\Delta t \leq$ 16 ps shown in TAS). Similar features are observed in the TAS of OC-methanol shown in Figure 4.20.

Quantitative insight into the dynamical processes observed in the TAS is gleaned from global fitting, where four exponential functions convoluted with a Gaussian IRF are required to fully describe the TAS (Figure 4.20(A)). For OC-cyclohexane, global fitting reveals four lifetimes (τ_1, τ_2, τ_3 and τ_4) as summarised in Table 4.3, which are characterised by the corresponding DAS given in Figure 4.20(E). The shapes of the DAS are valuable in aiding in the interpretation of the corresponding TAS. Positive components of the DAS indicate the decay of population from a particular state whereas negative components indicate a rise in the population of a state. In particular, a negative going component (an exponential rise) concomitant with a positive component (an exponential decay) can be interpreted as a flow of population from the positive region into the negative region, which can be induced by a change in electronic state or by VET within a single electronic state.[446] The DAS of τ_1, τ_3 and τ_4 are positive indicating

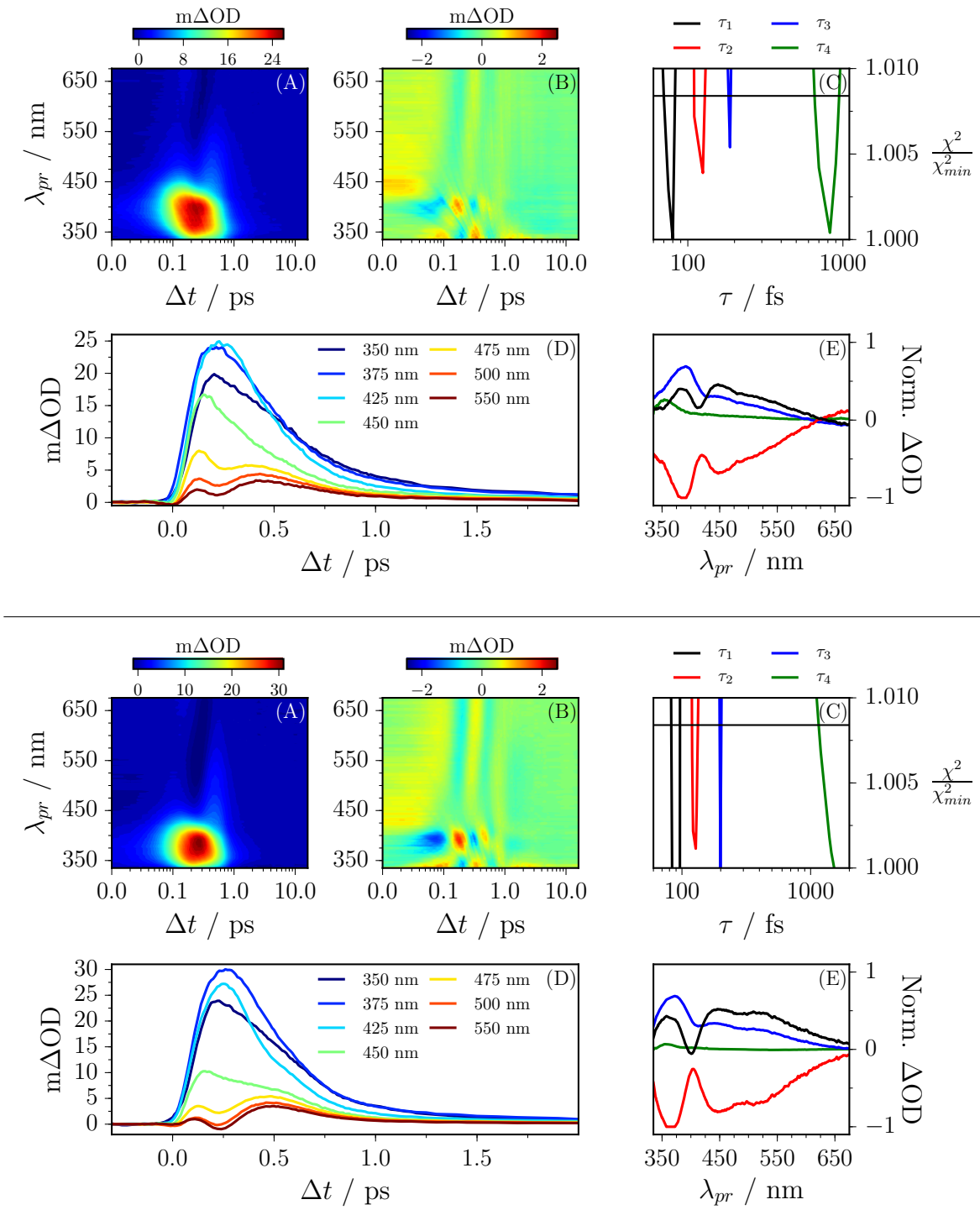

Figure 4.20 | (*top*): (A) The TAS of OC-cyclohexane. The vast majority of the dynamics appear to be over within the first few ps. (B) The residuals between the experimental TAS and the global fitted TAS. (C) ASE analysis returning the uncertainties on the lifetimes. (D) Selected transients which shows the quickly varying spectral features seen in the TAS. (E) The corresponding DAS of the global fitted lifetimes. (*bottom*): (A)–(E) Similarly for OC-methanol.

Table 4.3: Summary of the lifetimes of dynamical processes observed in OC.

Lifetime / fs	Cyclohexane	Methanol
τ_1	80 ± 10	90 ± 10
τ_2	120 ± 10	130 ± 10
τ_3	180 ± 10	200 ± 10
τ_4	810 ± 140	1520 ± 360[a]

[a]Lower limit of unbounded interval used.

a decaying absorption signal whilst τ_2 is negative indicating a growing absorption or SE feature which agrees qualitatively with the observed absorption features (*i*) and (*ii*) of the TAS (Figures 4.20(A) and 4.20(E)). Following an identical procedure, global fitting of the OC-methanol TAS (Figure 4.20(A)) reveals four dynamical processes with lifetimes summarised in Table 4.3, and are characterised by the corresponding DAS given in Figure 4.20(E), which display similar features to those discussed for OC-cyclohexane. The confidence interval of the lifetime τ_4 for OC-methanol is unbounded on the positive limit. We suggest this is because of the convolution with an increased photoproduct absorption signal compared to OC-cyclohexane (Figure 4.21, discussed later), as such, the lower limit is used (Table 4.3).[302]

The presence of a GSB is not observed which is likely due to the convolution with the strong positive ESA as well as the limit of the probe window being at the tail end of OC's absorption profile (Figure 4.19). Continuous wave irradiation studies were used to investigate any long-lived photoproducts which would typically be signalled by an incomplete GSB recovery. Following the procedure described in Section 4.3.2, the resulting difference spectra for OC-cyclohexane and OC-methanol are shown in Figure 4.21. There are small discrepancies between the OC-cyclohexane difference spectrum with the corresponding TAS (Figure 4.21(A)) whereby the difference spectrum displays a more prominent negative absorption. A similar observation is made for OC-methanol (Figure 4.21(B)), where a pronounced offset between the difference spectrum and the Δt = 600 ps spectrum around ∼350 nm is seen. These features may indicate the presence of a long-lived photoproduct which contributes a minor channel to the relaxation mechanism of OC. Additionally, a broad absorption spans the probe window in both OC-cyclohexane and OC-methanol TAS at Δt = 600 ps. For OC-methanol, there is an emergence of a defined peak centred at ∼375 nm. There is no evidence

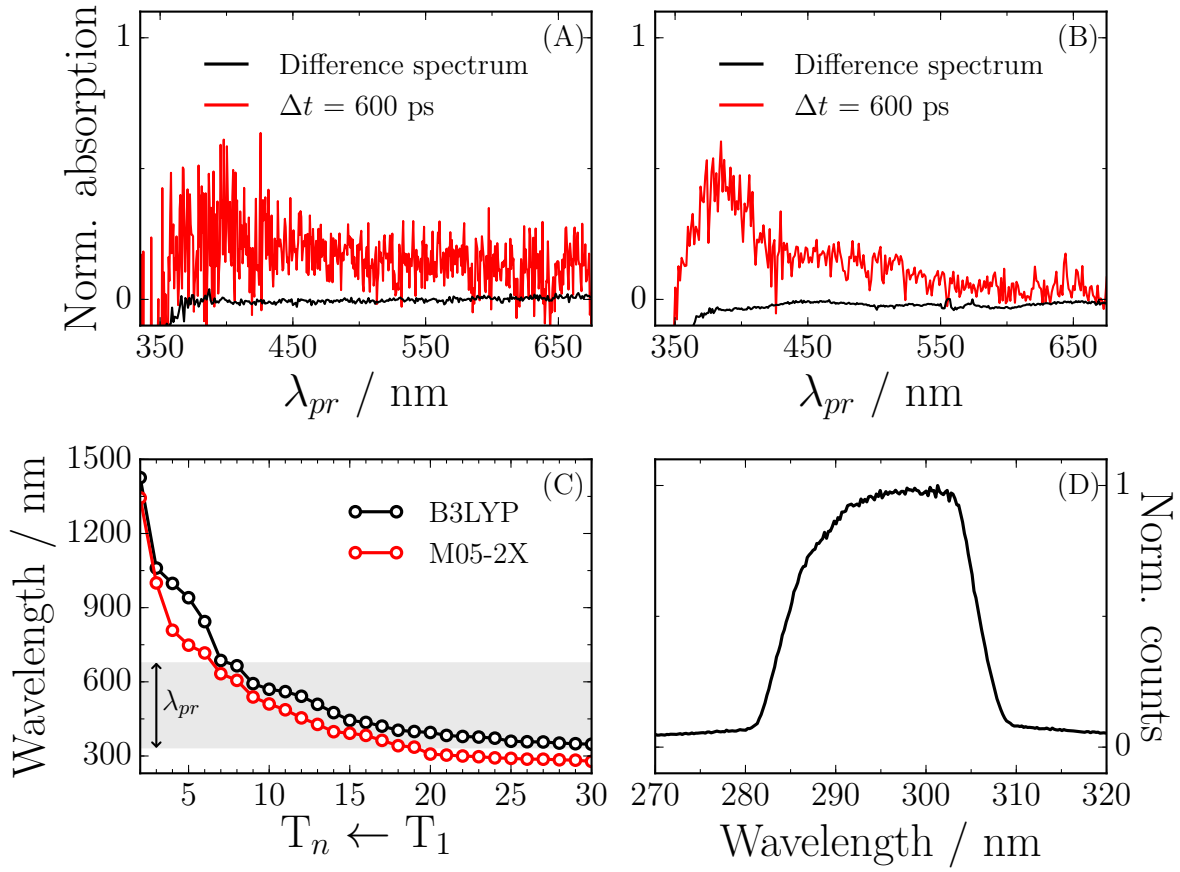

Figure 4.21 | (A) For OC-cyclohexane, continuous wave irradiation results in the difference spectrum (black line) using the procedure described in the main text. Overlaid is a Δt = 600 ps spectrum (red line). (B) Similarly for OC-methanol. Absorption signals have been normalised with respect to the most negative going signals. (C) Calculated transition energies between triplet states, $T_n \leftarrow T_1$. The accessible wavelengths by the probe is highlighted in grey. (D) The output of the KiloArc lamp used for irradiation experiments.

for either of these features in the corresponding difference spectra which suggests that these features may originate from long-lived triplet state absorption.[264,338]

4.3.4 Discussion and conclusions

We now begin to discuss the implications to the photoprotective properties of OC drawing on the different experimental results presented here. Firstly, the continuous wave irradiation measurements indicate an incomplete recovery of the original OC molecule. This (minor) pathway could be caused by photodegradation, a scenario that has been previously reported, forming predominately ethyl 2-cyano-3,3-diphenyl acrylate, and in

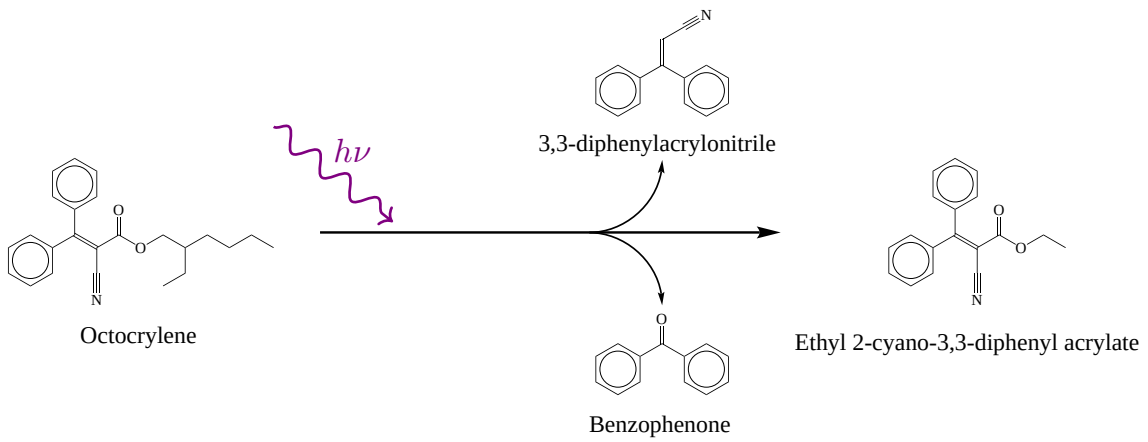

Figure 4.22 | The identity of photoproducts UV-photoexcited (300–400 nm) OC might form.[254]

smaller amounts, 3,3-diphenylacrylonitrile and benzophenone (Figure 4.22).[251,254]

When compared to the TAS of OC for $\Delta t = 600$ ps, we observe a weak absorption ($\sim$100 μOD) across the probe window, which is clearly not present in the difference spectrum obtained from continuous wave irradiation measurements. *Ab initio* calculations of triplet-triplet transition energies, as described in the methodology, are shown in Figure 4.21(C). These suggest there are a number of triplet states accessible within the probe window (335–675 nm). We therefore suggest this feature can be attributed to triplet state absorption, which is known to be accessible under these conditions, and a property that has been exploited in mixtures with avobenzone to improve its photostability.[223,264,338] The spectrum at $\Delta t = 600$ ps shows a clear positive peak centred around $\lambda \sim$375 nm for OC-methanol compared to OC-cyclohexane. This might indicate that the rate of ISC to the triplet state, and/or the absorption cross-section between this triplet state and higher lying states increases in the more polar solvent methanol, which may be explained by an increase in solvent perturbations on the excited state energy levels. These observations have an important consequence of OC's use in sunscreens; the relaxation mechanism of OC only has an apparently minor contribution that involves triplet state absorption or photodegradation, which means there may be a lower probability of OC-containing sunscreens causing adverse dermatological effects, a finding which complements the current literature.[251,253,254] Another possibility remains, given the presence of a CN substituent in OC, namely IC to a long-lived charge transfer state.

Table 4.4: First five electronic transitions determined at the TD-DFT//B3LYP/6-311+G** level of theory, with corresponding oscillator strengths. Results using the M05-2X functional are given in parentheses.

Transition, $S_n \leftarrow S_0$			Wavelength / nm	Osc. strength
$S_1 \leftarrow S_0$	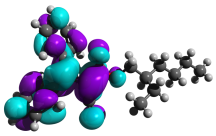	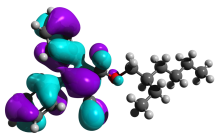	336 (295)	0.649 (0.687)
$S_2 \leftarrow S_0$	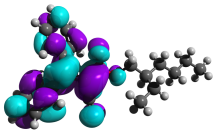	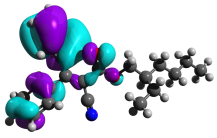	315 (268)	0.657 (0.437)
$S_3 \leftarrow S_0$	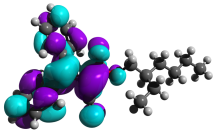	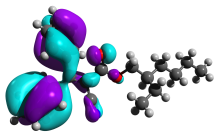	307 (257)	0.675 (0.477)
$S_4 \leftarrow S_0$	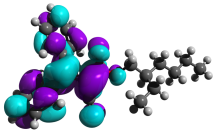	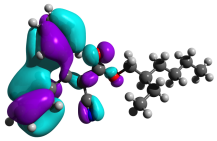	298 (251)	0.658 (0.480)
$S_5 \leftarrow S_0$	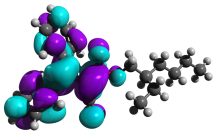	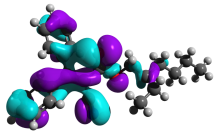	279 (240)	0.643 (0.412)

Considering next the dynamical processes extracted from the global fitting of the TAS we can attempt to rationalise the dynamics operating in OC after UV-B photoexcitation, although, as we reiterate below, we acknowledge that further work is essential; this discussion however serves as an important starting point. Precedence in the mechanism comes from simple excited state calculations of OC. We found that the likely first excited state, initially populated through excitation by the pump pulse is a $\pi\pi^* \leftarrow S_0$ transition, see Table 4.4 (for molecular orbitals (TD-DFT//B3LYP/6-311+G** shown), transition wavelengths and oscillator strengths) and the steady-state absorption spectra shown in Figure 4.19. We also note that both OC-cyclohexane and OC-methanol display similar lifetimes and DAS, suggesting that the proposed dynamics are very similar in both, hence the dynamics discussed are applicable to both systems.

We propose that an initial photoexcitation likely populates an ensemble of similar

energy $n^1\pi\pi^*$ states ($n \geq 1$). The subsequent decay of this population to a lower lying excited state is assigned the lifetime τ_1. We suggest this in turn populates another excited $m^1\pi\pi^*$ state ($n \neq m$) with lifetime τ_2. We draw confidence in the assignment of τ_1 and τ_2 by considering the DAS associated with these similar lifetimes (*cf.* Figure 4.20(E) and Table 4.3). The positive DAS associated with τ_1 closely mirrors the negative DAS associated with τ_2 which might imply a population flow between two states. Furthermore, the negative feature in the TAS assigned to SE onsets from ∼250 fs (see Figures 4.20(A) and 4.20(D)) suggest that it may originate from a state other than the initially populated one(s). Thus τ_2 predominately captures the population flowing between these two states by IC, likely *via* a $n^1\pi\pi^*/m^1\pi\pi^*$ CI given the efficiency this occurs with. We suggest the population on this second state subsequently relaxes with the lifetime of τ_3. Since photoexcited OC appears to almost completely recover its ground state, we suggest this state will couple back to the ground state *via* a $m^1\pi\pi^*/S_0$ CI and subsequently will relax to the ground vibrational state by VET, likely mediated by a combination of IVR and VET to the surrounding solvent molecules.[325,447] This last step is captured by the lifetime τ_4, especially the IC to the ground state. An interesting possibility remains in that this relaxation may occur *via* the isomerisation around the aliphatic C=C bond, a process suggested to occur in the closely related molecule ethylhexylmethoxycrylene,[338] however, confirmation of this would require further theoretical and experimental studies; for example, one could envisage aromatic ring substitution as one possible technique, but this is beyond the scope of this work.

There are two important caveats here. First, since the lifetimes of the dynamical processes described are similar in magnitude and are very fast, the underlying assumption of the global fitting procedure, that the processes are not sequential, begins to break down. This has the effect of clouding the onset of one process with that of another. Ultimately, this means each lifetime will also capture some of the preceding and/or proceeding dynamics, making the absolute assignment of a lifetime with any one process unrealistic.[448] Second, there will likely be a contribution to the lifetime(s) (in particular τ_1, τ_2 and τ_3) from an evolution out of the FC window, as well as any solvent rearrangement. These processes typically persist for comparable timescales as the extracted lifetimes, meaning the absolute assignment of population decay from one state to another is highly complex. Furthermore, any spectral shift in the positive absorption signal would likely affect τ_1 and τ_2. In this case, τ_1 and τ_2 may describe a spectral shift (on a single PES), which is consistent with the closely mirrored DAS (Figure 4.20(E)). This would mean that the likely relaxation mechanism would be *via* an $n^1\pi\pi^*/S_0$ CI on the timescale τ_3 followed by vibrational relaxation in the S_0 state

captured by τ_4. However, the overall picture of the relaxation dynamics observed in OC is clear; UV-B photoexcited OC undergoes ultrafast nonradiative relaxation which repopulates the ground state with high efficiency. The vast majority of the dynamics are over in the first ∼5 ps after photoexcitation, with most of the processes over within the first 2 ps of photoexcitation (Figure 4.20(A)). This has major implications for OC's role as a sunscreening agent since the ability to dissipate energy from UV-B photoexcitation through ultrafast nonradiative processes is vital for a safe and efficient organic filter.[264]

Further experimental studies are required to fully understand the states likely to be involved in OC. Specifically, we suggest sequential kinetic studies would provide valuable insight into the observed population flow in both OC-cyclohexane and OC-methanol, a limitation of both our IRF (∼100 fs) and our global fitting procedure,[448] which will likely prove useful in the deconvolution of the τ_1, τ_2 and τ_3 lifetimes. Theoretical studies will be invaluable in understanding the states involved in the relaxation mechanism observed in our TAS and indicate if such an isomerisation provides an energetically favourable route to couple back to the ground state. We hope this work will provide a stimulus for further studies along both experimental and theoretical directions.

In summary we have provided early ultrafast measurements of the commonly used sunscreen molecule OC, which is shown to exhibit an ultrafast relaxation mechanism predominately *via* nonradiative pathways, with high efficiency. Furthermore, non-polar and polar solvents show little effect on the predominant dynamics, but with some noticeable effects on potential triplet state formation. These measurements highlight the efficiency of OC used as a sunscreen molecule and suggest there is minimal triplet state absorption and photodegradation, important properties for sunscreens.

4.4 Ethylhexyl triazone

4.4.1 Introduction

In this study we focus on the organic filter, Ethylhexyl Triazone (EHT),[449] also known as octyl triazone, see Figure 4.23.[449] It is one of many organic filters authorised for use across Europe, Australia, New Zealand, Japan and South Africa (*cf.* Table 2.3),[223] and resembles a group of large aromatic organic filters which are also used in sunscreens such as bis-ethylhexyloxyphenol methoxyphenyl triazine (Bemotrizinol) and diethylhexyl butamido triazone (Iscotrizinol).[223] A particularly interesting property of EHT (and the family in general) is its large molecular weight (823.07 g·mol^{-1}); such filters are unlikely to penetrate the skin, thereby reducing effects associated with skin penetration.[452] It displays a broad absorption profile across the UV-B region, with a maximum absorption at ∼311 nm and ∼313 nm for EHT-dioxane and EHT-methanol respectively (Figure 4.23). Much work has been focussed on EHT from a photostability viewpoint, where it is generally regarded as photostable,[237,453] although under certain conditions can photodegrade.[237] Other work has investigated the role EHT plays as a photostabiliser on other organic filters such as avobenzone.[237]

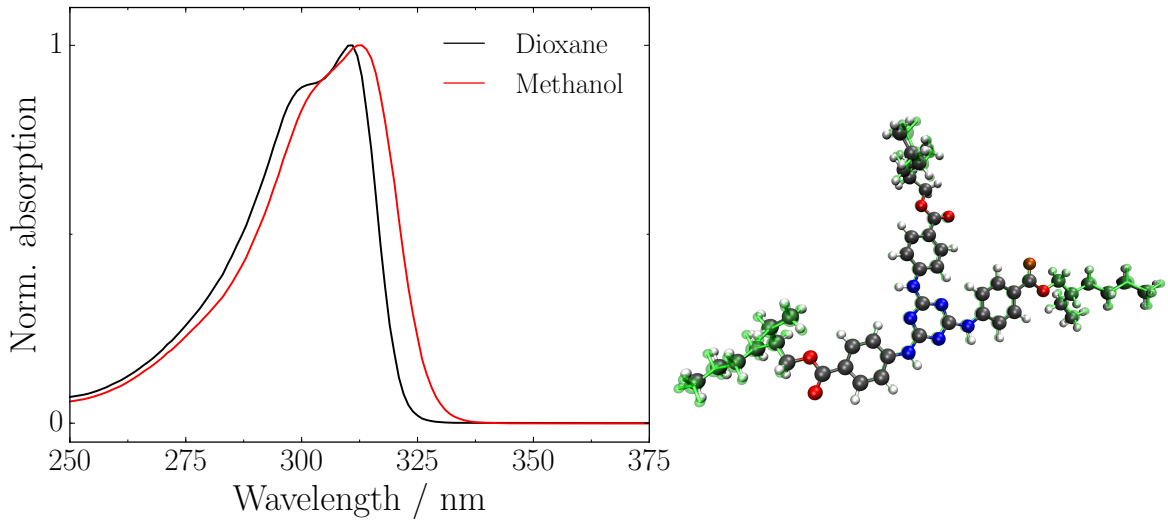

Figure 4.23 | (*left*): The UV-visible absorption spectrum of EHT-dioxane and EHT-methanol.[450] (*right*): The ground state optimised geometry of EHT, with (opaque) and without (translucent green) an implicit methanol solvent field, at the DFT level of theory using the BP-86 functional[451] and an aug-cc-pVDZ basis set.[24,25] A schematic of EHT is given in Figure 0.1(D).

To date, the literature on the ultrafast photochemistry of EHT remains sparse compared to other common organic filters,[361] with most studies involving EHT focussing on its photostability[237,453] and photoallergy properties.[454] Recent work by Tsuchiya *et al.*[455] has examined the excited states of EHT (and a close derivative diethylhexylbutamido triazone) primarily through the use of steady-state techniques including fluorescence and phosphorescence. The reported fluorescence and phosphorescence quantum yields at room temperature suggest that IC is the dominant deactivation mechanism after UV photoexcitation. The decay of the fluorescence profile returns a lifetime which is resolution-limited, below 0.6 ns; phosphorescence on the other hand, decays with a lifetime reported to be several seconds. These results are useful in characterising the excited states involved in the photodeactivation of EHT, however, the findings also point toward ultrafast processes being involved, something beyond the experimental resolution of the reported study.[455]

It is here where ultrafast spectroscopy can once again begin to unravel these processes.[361] We utilise solution-phase TEAS to probe the photodeactivation mechanism of EHT in the non-polar solvent dioxane, and the polar solvent methanol. Our results agree with previous work,[455] that IC is the likely dominant deactivation mechanism of UV-excited EHT. Initial UV-B photoexcitation to high-lying electronic states results in IC to the first excited electronic state, and occurs within ∼400 fs. Following this, a geometry change concomitant with VET occurs over ∼20 ps, allows population to flow through a CI and thus repopulates the ground vibrational state of EHT. We also observe the presence of long-lived photoproducts which accord closely with microsecond transient absorption measurements,[455] further evidenced by UV absorption measurements pre- and post UV-B irradiation, confirming that ISC to a low-lying triplet state is a likely (competing) pathway. The experimental findings observed herein are supported by electronic structure calculations of these photoproducts.

4.4.2 Methodology

A stock sample of ≥98% EHT was purchased from Sigma-Aldrich and used without further purification. For all reported TAS measurements, 1 mM solutions of EHT in either dioxane (EHT-dioxane) or methanol (EHT-methanol) are recirculated *via* a flow-through cell, between two CaF_2 windows separated by 100 μm PTFE spacers. Samples are photoexcited by 311 nm or 313 nm pump-pulses for EHT-dioxane and EHT-methanol, at their respective UV-B absorption maxima, *cf.* Figure 4.23. Pump-pulses with fluences of ∼1–2 mJ·cm^{-2} are produced by a commercially available OPA (TOPAS-C, Light Conversion) seeded by a 1 kHz pulse train (1 W, 800 nm) from a

Ti:sapphire CPA (Spectra-Physics Spitfire Pro XP, 3 W, ∼40 fs). Probe-pulses are derived from a broadband (∼340–670 nm) WLC by focussing a small portion of the 800 nm fundamental (∼5 mW) into a CaF_2 crystal. TAS are collected with the probe-pulse held at the magic angle (54.7°) relative to the pump-pulse. All TAS are chirp corrected using the KOALA package.[386]

All steady-state UV-visible spectroscopic measurements are taken using a Cary 60 UV-visible spectrophotometer with a 1 cm path length quartz cuvette, and ∼μM EHT-dioxane and EHT-methanol solutions. Continuous wave UV irradiation studies are performed on EHT to investigate the nature of any long-lived photoproducts using the following procedure. First, a steady-state UV-visible spectrum of each sample is taken to obtain a '*before*' spectrum. Samples are then irradiated with continuous wave radiation, ∼50 mW, from an arc lamp (Flurolog, HORBIA scientific) for 10 minutes using a central wavelength of 311 or 313 nm (EHT-dioxane and EHT-methanol respectively) with a bandwidth of 5 nm. A second UV-visible spectrum is taken, referred to as the '*after*' spectrum. Finally, subtraction of the before spectrum from the after spectrum results in the reported '*difference spectrum*'.

All electronic structure calculations is performed using the TURBOMOLE package.[82,83,456] DFT and TD-DFT theory is used with the BP-86 functional,[451] the augmented Dunning aug-cc-pVDZ basis set,[24,25] the resolution of the identity[457] and multipole accelerated resolution of the identity approximations,[458] with the corresponding auxiliary basis set.[459] The use of the BP-86 function is justified for its successful use as a 'general chemistry' functional,[460,461] and its efficient implementation in the TURBOMOLE program making calculations on EHT feasible.

4.4.3 TEAS measurements of ethylhexyl triazone

Perhaps the most natural place to start is considering the UV-visible spectrum given in Figure 4.23. The broad, essentially featureless, nature of the spectrum indicates that a multitude of excited states are accessible in the UV-A, and in particular, the UV-B region. Indeed, even at cryogenic temperatures, this spectrum remains mostly unchanged.[455] This is further confirmed through DFT (*vide infra*) where ∼20 singlet excited states reside within this broad peak (Appendix 8.6).

TAS for EHT-dioxane and EHT-methanol photoexcited at 311 nm and 313 nm respectively are shown in Figure 4.24. Considering the TAS of EHT-dioxane first, see Figure 4.24(A), the TAS display two main features. The first is an intense absorption centred around probe wavelengths of ∼350 nm. It almost completely decays away by the maximum available pump-probe time delay of 2 ns, indicating that the overall re-

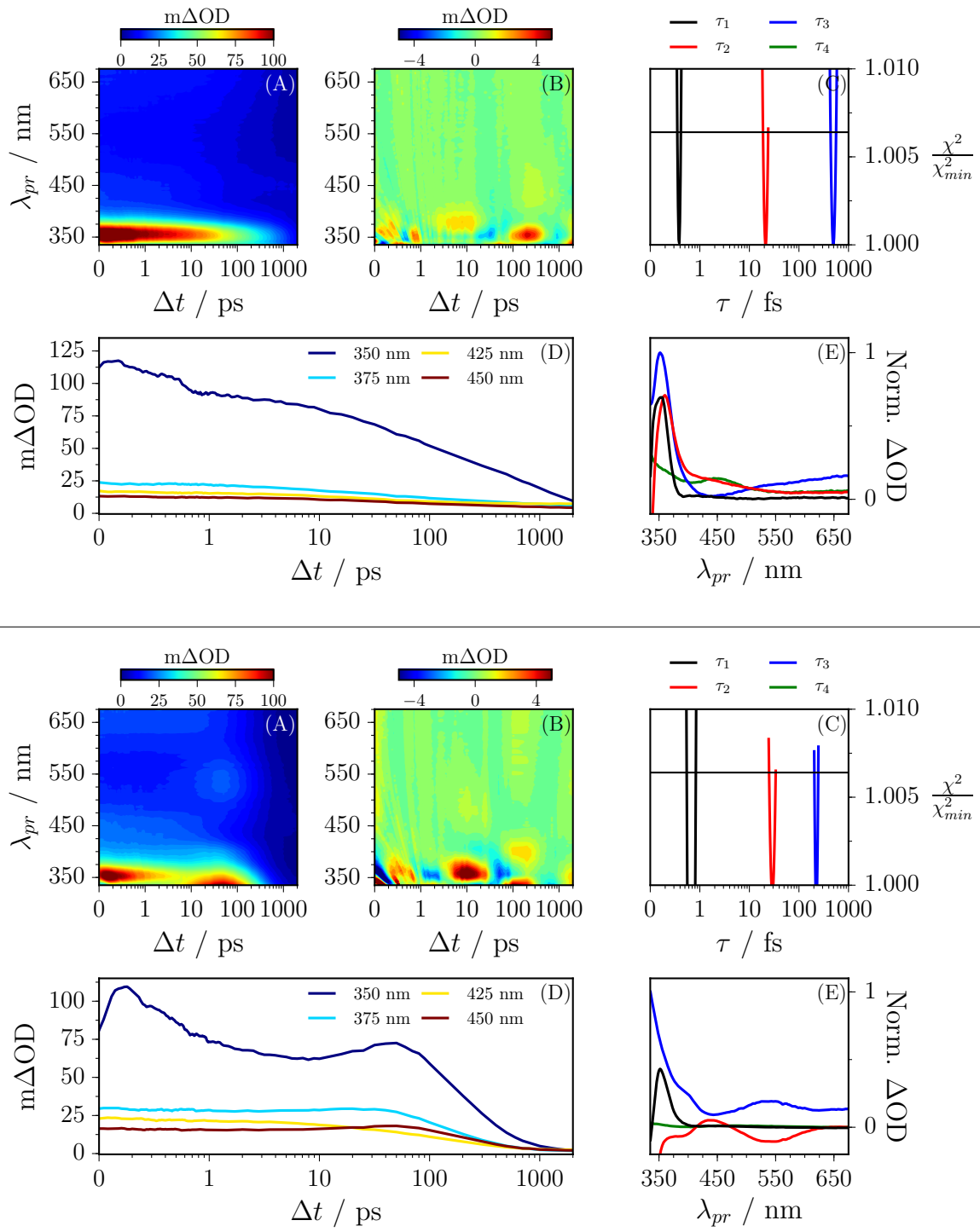

Figure 4.24 | (*top*): (A) The TAS of EHT-dioxane. The vast majority of dynamics appear to be over within the first few picoseconds. (B) The residuals between the experimental TAS and the global fitted TAS. (C) ASE analysis returning the uncertainties on the lifetimes. (D) Selected transients which shows the early time decay and the much slower decay component. (E) The corresponding DAS of the global fitted lifetimes. (*bottom*): (A)–(E) Similarly for EHT-methanol.

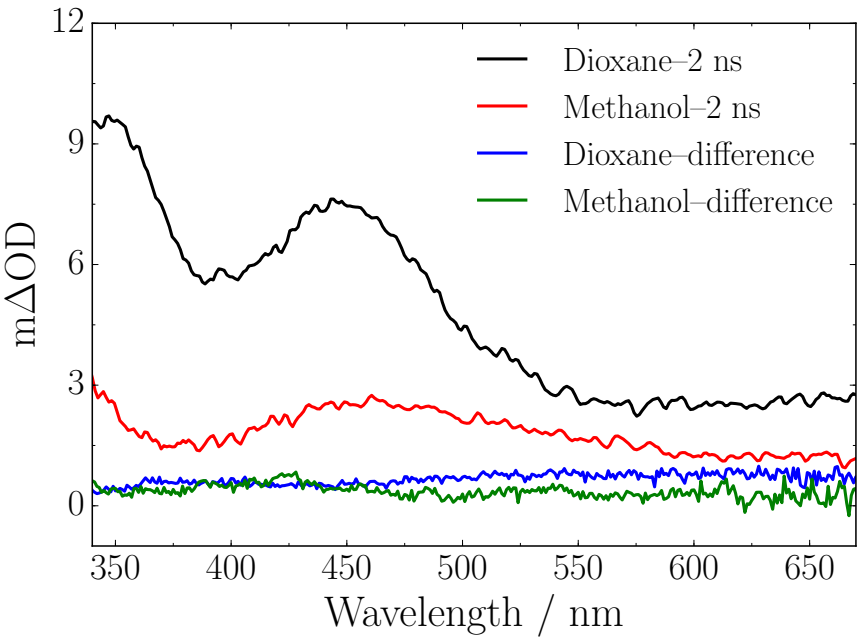

Figure 4.25 | The long-lived signals observed at the maximum pump-probe time delay of 2 ns for EHT-dioxane (black) and EHT-methanol (red). For both systems, very similar spectral features are observed with a peak centred ∼350 nm and ∼450 nm. Continuous wave irradiation studies of EHT resulting in difference spectra (EHT-dioxane, blue; EHT-methanol, green) show flat featureless profiles in contrast to the $\Delta t = 2$ ns spectra.

laxation mechanism in EHT-dioxane predominately is ultrafast, as has been previously suggested.[455] The second is a broad absorption across the rest of the probe window (up to ∼675 nm), which decays towards the baseline, however not completely, where a clear, broad absorption remains across the probe spectral window, as indicated in Figure 4.25 (black line).

Quantitative insight into the ultrafast photodeactivation mechanism may be understood by employing a global fitting procedure, as described earlier.[412] Four exponential functions, convoluted with a Gaussian IRF, are required to describe (Figure 4.24(B)) the experimental TAS given in Figure 4.24(A). The extracted lifetime for each of these functions is given in Table 4.5, characterised by its DAS, shown in Figure 4.24(E). The (almost completely) positive nature of each DAS indicates that all extracted lifetimes are associated with decaying features in the TAS.

Similar features are observed for EHT-methanol, see Figure 4.24(A), with two differences. The TAS show a signal growing in around 330 nm after ∼10 ps, which then decays away. A broad positive signal is also observed centred around ∼550 nm which

Table 4.5: Summary of the lifetimes extracted from global fitting analysis of the measured TAS of EHT-dioxane and EHT-methanol after UV-B photoexcitation.

Lifetime	Dioxane	Methanol
τ_1 / fs	382 ± 33	556 ± 276
τ_2 / ps	21.2 ± 2.7	27.9 ± 6.0
τ_3 / ps	493.6 ± 68.0	216.0 ± 29.0
τ_4	$\gg$ ns	$\gg$ ns

grows in with the signal centred around 350 nm after Δt ∼10 ps. We return to discuss both of these features below. The characteristics of the corresponding DAS corroborate this, where the τ_2 DAS is negative below 350 nm, as well as around 550 nm. This also changes the τ_3 DAS in these regions too, given that each lifetime is not sequential in this fitting procedure; each lifetime will capture some of the preceding and proceeding dynamical processes.[339,448] A similar long-lived excited state profile as seen for EHT-dioxane is observed at the maximum available pump-probe time delay of 2 ns, see Figure 4.25 (red line).

4.4.4 Discussion and conclusions

We first begin discussing these results with reference to the observed long-lived signals in the EHT-dioxane and EHT-methanol TAS at Δt = 2 ns. The observation of the long-lived feature in both EHT-dioxane and EHT-methanol TAS is explored through the use of continuous UV-irradiation. The resulting difference spectrum for each sample is given in Figure 4.25, calculated after 10 minutes of irradiation, with the pump wavelength centred on that used in the TEAS studies. Both samples show a flat, almost featureless profile indicating that there is minimal photoproduct formation; the long-lived signals observed in the TAS must therefore be attributed to metastable transient states. Previous work has shown that photoexcited EHT undergoes both fluorescence and phosphorescence.[455] This work suggested the peak centred around 350 nm might be attributed to excited state population trapped on the S_1 state, based on fluorescence measurements. Similarly, the peak centred around 450 nm may be attributed to excited state population trapped in a triplet state based on phosphorescence and microsecond transient absorption measurements. These of course are metastable, and the population

would return to the ground S_0 state, the majority of which however will be well-beyond our maximum experimental pump-probe time delay of 2 ns, but before the effective 10 minute 'time delay' in the continuous wave measurements.

In an effort to confirm this, electronic structure calculations were performed, although we note that these calculations can only provide qualitative support for the experimental results discussed herein. To confirm the structures discussed are sensible, we initially performed the ground state optimisation of EHT with and without an implicit methanol field using the Conductor-Like Screening Model (COSMO) model,[462] see Figure 4.23. Very little difference between the two geometries are seen. The largest differences are observed in the tails of EHT, which we have shown are not involved in the photodynamics (discussed below), thus the gas-phase calculations are likely a reasonable representation of the lowest energy conformer of EHT. Given the size of EHT, such a gas-phase description is much less computationally demanding. In fact, in some cases, such as excited state geometry optimisations, the COSMO module has not been implemented thus restricting the breath of calculations which can be performed at present.

First, the ground state EHT structure is optimised, from which vertical excitations suggest UV-B photoexcitation populates an excited $n^1\pi\pi^*$ state ($n > 1$) where the electronic density remains localised near the central core of EHT, see Figure 4.26 and Appendix 8.6. We calculate the absorption spectrum of the possible excited state species (Figure 4.27). EHT is optimised in its first triplet state, and an array of vertical excitations calculated. The corresponding oscillator strength ($f(\lambda_\mathbf{0})$) for each vertical excitation ($\lambda_\mathbf{0}$) is broadened through convolution ($\otimes$) with a Gaussian function, to generate the absorption spectrum ($I(\lambda)$), where:

$$I(\lambda) = f(\lambda_\mathbf{0}) \otimes e^{-\frac{(\lambda-\lambda_\mathbf{0})^2}{2\sigma^2}}. \tag{4.2}$$

A value of $\sigma = 15$ nm is used which broadens the spectra similarly to the broadening observed in the experimental data (Figure 4.27). This spectrum is red shifted by ∼70 nm (∼0.52 eV) in order to overlap with the experimental absorption signal observed at ∼450 nm, suspected to be from the T_1 population.[455] An identical procedure is followed after EHT is optimised in its first singlet excited state, which is similarly red shifted by ∼70 nm. These calculated spectra support the assignment of ESA in the S_1 state (centred on ∼350 nm) and triplet state absorption in the T_1 state (centred on ∼450 nm).

From this investigation, assignment of the dynamical processes responsible for the

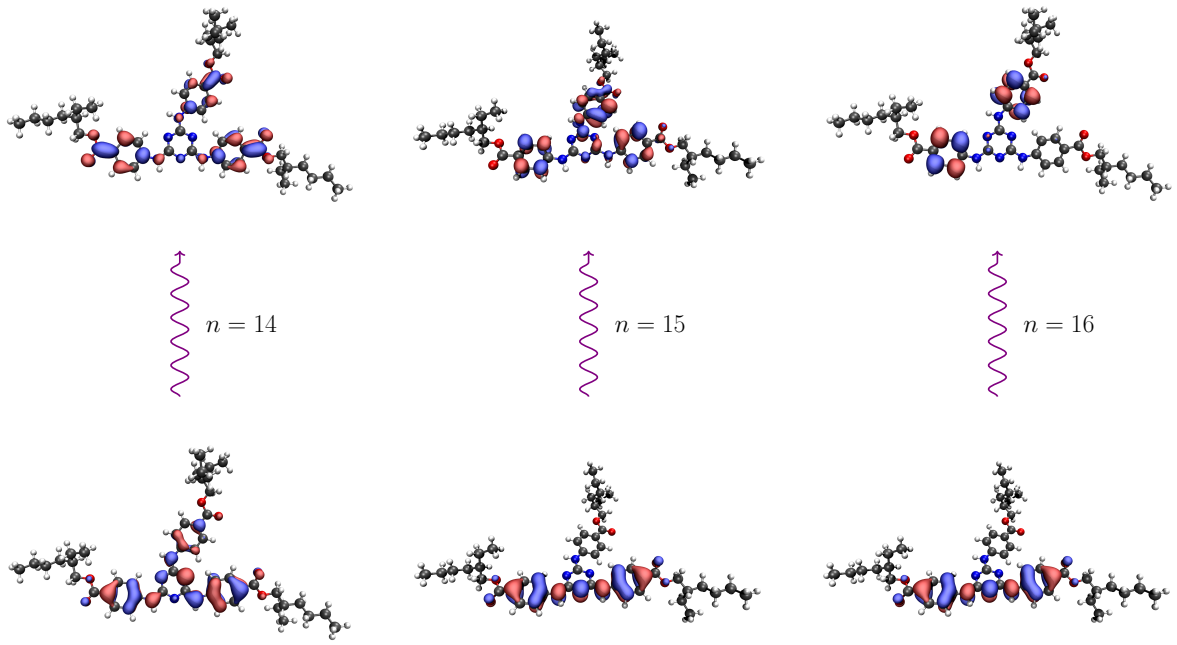

Figure 4.26 | Representative examples of the likely initial photoexcitations which populates a $n^1\pi\pi^*$ state ($n > 1$, where n refers to the n^{th} singlet excited state; *cf.* Appendix 8.6).[463]

extracted lifetimes in the global fitting procedure can be suggested. After photoexcitation to a high-lying $n^1\pi\pi^*$ state, EHT will undergo IC to populate a vibrationally hot $S_1(1^1\pi\pi^*)$ state (in keeping with Kasha's rule,[116] and faithfully accords with similar studies of the sunscreen constituent OB[287]) which we attribute to lifetime τ_1. We make two important remarks here: (1) initial population of higher lying S_n states will likely lead to IC within the IRF to populate lower lying electronic states (or even S_1 directly). What τ_1 then captures will be the latter parts of the IC to populate S_1 from neighbouring S_n states, along with any evolution from the initial FC window and accompanying solvent re-arrangement. (2) The similarity in the DAS (τ_{1-3}) <400 nm obtained in dioxane encourages the view that the origins of τ_1 originate principally from S_1 (or nearby states). We note such a similar comparison for the DAS extracted in methanol cannot be made owing to the positive signal around 350 (and 550 nm, see below). From here we suggest the geometry will continue to rearrange as it undergoes IVR within the S_1 state given the observed distorted/bent nature of the optimised structure in this excited state *cf.* Figure 4.27. Indeed, a linear interpolation over this distortion clearly shows that the ESA spectrum depends heavily on the geometry over the course of the distortion, see Figure 4.28. This distortion then couples the S_1 surface to the ground S_0 state through a $1^1\pi\pi^*/S_0$ CI. Here the vibrationally hot EHT molecule cools *via* VET

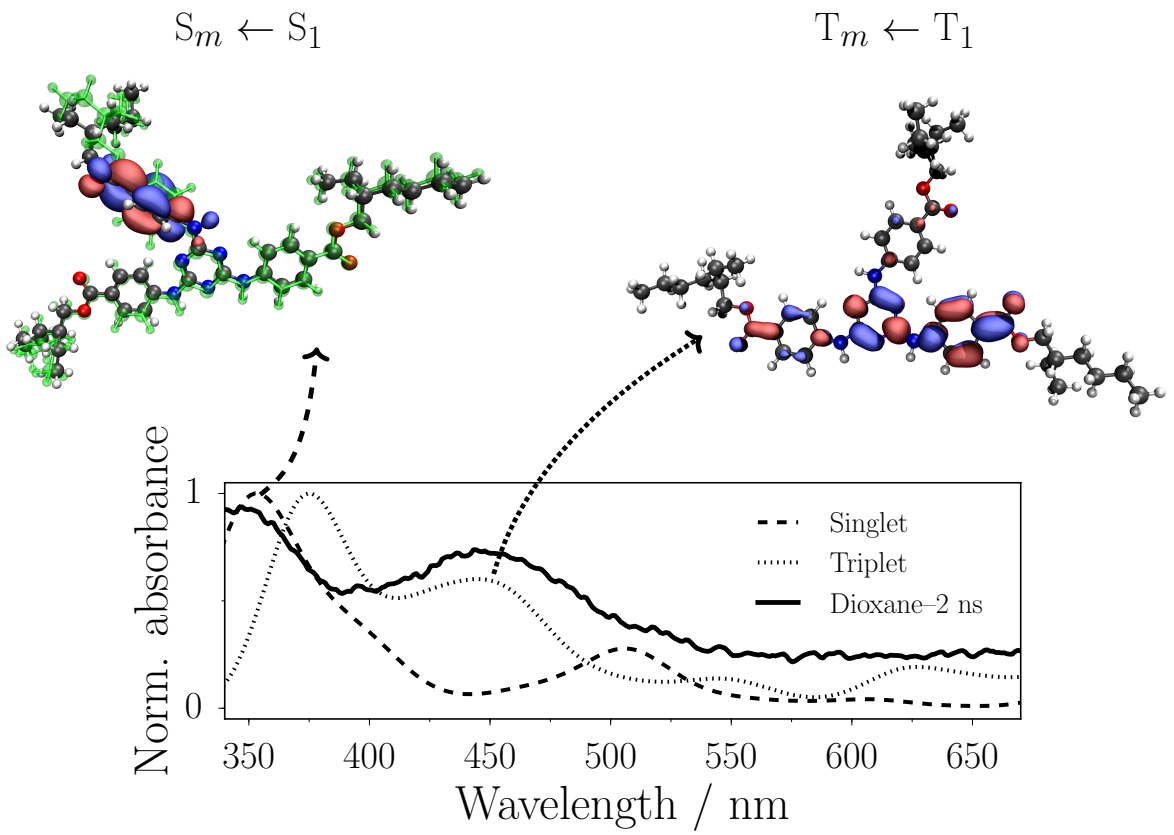

Figure 4.27 | The long-lived signal observed for EHT-dioxane at $\Delta t = 2$ ns (black line, *cf.* Figure 4.25), the calculated absorption spectrum of the first excited singlet state (dashed line; excited state geometry shown (opaque) against the ground state geometry (translucent green)) and the first triplet state (dotted line; excited state geometry shown). The calculated spectra have been red-shifted by 70 nm given the assignment of the experimental ∼450 nm peak to triplet state absorption.[455] Both these states display significant π character, and lead to broad absorption features suggesting there is a manifold of accessible excited states ($m \geq 2$) at the probe wavelengths.

to the surrounding solvent. These processes (IVR, passage through the CI and VET) are captured by the lifetime τ_2. Contrary to what might be expected,[421] the more polar solvent methanol does not appear to contribute to a greater rate of vibrational relaxation. This can be explained by the size of EHT (126 atoms; 372 vibrational modes); even with the non-polar dioxane, EHT will likely exhibit efficient VET to the solvent given the high number of modes available. Another contribution will be the observation that EHT-methanol shows a decaying signal (centred around ∼350 nm) which rises again before decaying towards the baseline (*cf.* EHT-methanol TAS in Figure 4.24(D)). This feature is discussed below.

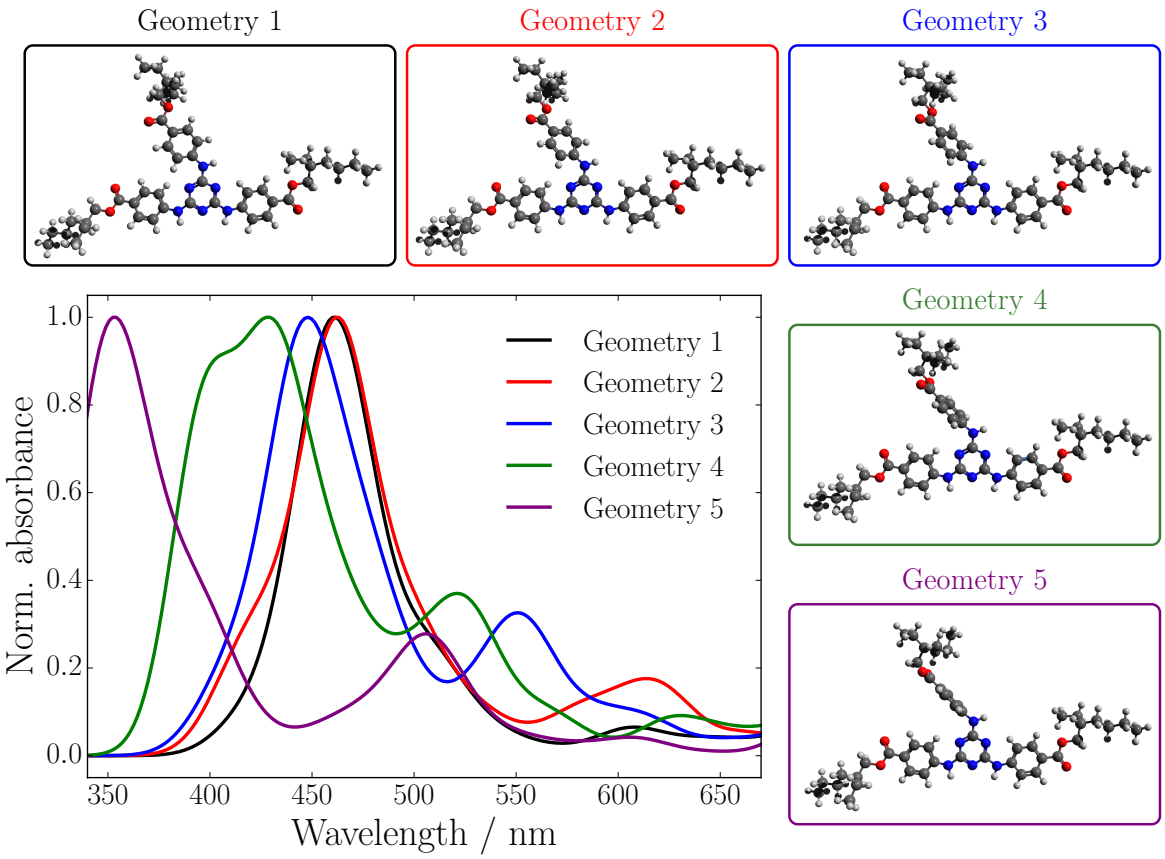

Figure 4.28 | The evolution of the absorption profile of EHT along the S_1 PES. Linearly interpolated coordinates are used between the initial geometry (Geometry 1) and the optimised S_1 geometry (Geometry 5). Geometries are equally spaced in their interpolations.

Given the observation of the long-lived absorption signals discussed (Figure 4.25), some of the population will become trapped on the S_1 surface, likely due to a significant geometry mismatch restricting any direct coupling to the S_0 state *via* the $1^1\pi\pi^*/S_0$. Instead, this population will revert to the ground state *via* fluorescence, suggested to be sub-600 ps from previous work.[455] Unfortunately, this fluorescence signal (which will manifest as SE) is not directly observed in the TAS, as it is likely to be buried under the convoluted triplet state absorption and the ESA of the remaining S_1 population. In competition with the fluorescence relaxation pathway is ISC to a triplet state, which is attributed to the observed signal at ∼450 nm at $\Delta t = 2$ ns. These processes are captured by the lifetime τ_3, a timescale which would sensibly compete with the proposed fluorescence, and thus populate the triplet state. Any population in this triplet state will undergo phosphorescence over a much longer timescale, and thus on the timescale

of this experiment, manifests as a baseline offset. The lifetime given by τ_4 captures this long-lived nature of this triplet state. The broad absorption signals observed at $\Delta t = 2$ ns are also supported by these calculations, where both the S_1 and T_1 show absorption features between 450 nm and 670 nm respectively.

Two further observations are made for EHT-methanol which are not seen in EHT-dioxane. (*i*) The first is a signal observed centred at ∼550 nm in the TAS (Figure 4.24(A)) which appears concomitant with the growing signal centred around ∼350 nm. We suggest this might be attributed to trapped S_1 population which will inevitably adopt a different minimum energy geometry in the presence of the more strongly perturbing solvent methanol. Thus, as the excited state geometry evolves, the PES of EHT-methanol and EHT-dioxane begins to diverge due to the differences in solvent perturbation resulting in a different transient absorption signal, as evidenced in Figure 4.24. As EHT-methanol approaches its minimum energy geometry in the S_1 it absorbs probe wavelengths centred around 525 nm. It is important to note these calculations remain qualitative given solvent effects are not included, evidently resulting in optically dark transitions for geometries (*cf.* Figure 4.28) until EHT reaches the minimum energy geometry in the S_1. Furthermore, geometries are generated from a linear interpolation between the initial excited geometry and the minimum energy S_1 geometry thus will not follow the minimal energy pathway along the S_1 surface (noting this pathway will also be perturbed by the solvent). These caveats might reconcile the absence of such a signal in the EHT-dioxane TAS (Figure 4.24(A)), with its presence in EHT-methanol. This signal assignment is further supported by the timescale of its appearance, much shorter than the timescale for ISC (τ_3) making triplet state absorption an unlikely candidate for this signal. Furthermore, this feature will cause the τ_2 lifetime to extend thus masking any increased rate of VET in methanol (*vide supra*). (*ii*) The second observation is a shorter τ_3 lifetime at ∼220 ps compared to ∼490 ps, for methanol and dioxane respectively. Given the previous assignment, (*i*), of ESA from the S_1 minimum geometry of EHT-methanol, this observation may be explained by a potentially stronger spin-orbit coupling to the nearby triplet states(s), accelerating ISC.

To conclude, we have suggested the first complete mechanism for the photodeactivation of UV-B excited EHT, simulating its possible role in a sunscreen product. Combining ultrafast pump-probe TEAS and electronic structure calculations, we have built upon previous work investigating the photophysical properties of EHT (and its analogues).[455] Given that the deactivation mechanism involves the conjugated π system at the centre of EHT, this molecule in particular provides a stepping stone for future studies. For example, one might envision functionalising the alkane-chains of each

branch of EHT to improve its chemical properties such as solubility, with little effect to its photophysical properties. On the other hand, one could alter the photophysical properties by functionalising only the conjugated part of EHT, thereby enhancing its photostability. We hope this work serves as a stimulus for further work along both experimental and theoretical directions, which would no doubt prove fruitful.

Chapter 5

Natural sunscreen constituents

Parts of this chapter have been published by the author:

---

1. **Lewis A. Baker**, Michael D. Horbury, Simon E. Greenough, Florent Allais, Patrick S. Walsh, Scott Habershon, and Vasilios G. Stavros. Ultrafast photoprotecting sunscreens in natural plants. *J. Phys. Chem. Lett.*, **2016**, 7(*1*):56–61.

Declarations:

- Florent Allais (AgroParisTech, France) synthesised the methyl sinapate and sinapoyl malate compounds.

5.1 Sinapic acid, methyl sinapate, sinapoyl malate

5.1.1 Introduction

As discussed in the introduction, UVR acts as a signal transducer for numerous processes including immune response, plant morphology and the phenylpropanoid pathway in plants.[149,177] Deleterious effects of this radiation exposure to organisms are widely known *e.g.* reduction of photosynthesis, growth inhibition, and an increased susceptibility to pathogens.[178,195] As such, plants synthesise and deposit UV-absorbing phenolic compounds in epidermal tissues *via* the phenylpropanoid pathway to protect against overexposure to UV radiation.[149,177]

Specifically, studies of gene mutations in the plant *Arabidopsis thaliana*, a member of the *Brassicaceae* family, have found that the phenylpropanoid pathway could be disrupted such that the concentrations of sinapate esters present in the epidermal layers of the plant are reduced, rendering the plant hypersensitive to UVR exposure.[183,291,292,464–466] Such experiments therefore point to sinapate esters as being the likely class of UVR screening molecules used by *Brassicaceae* plants. Sinapate esters are derivatives of Sinapic acid (SA), the precursor to Sinapoyl malate (SM), which has been identified to be the dominant constituent deposited in the upper epidermis of *Arabidopsis* plant leaves (Figure 5.1).[183,291,292] The interesting question raised in light of this is, *how* do these molecules provide UVR photoprotection?

Previous work in characterising the photophysical properties of cinnamates,[294,467–473] a set of molecules closely related to the sinapates, identified a variety of relaxation pathways after an initial photoexcitation to a $1^1\pi\pi^*$ state. In particular, relaxation through IC, mediated by *trans–cis* isomerisation,[294,467–470] or IC to a long-lived $1^1n\pi^*$ state[298,471,474–477] have been suggested as viable relaxation mechanisms. In SA, similar studies suggest IC along an aborted *trans–cis* isomerisation of the aliphatic C=C bond couples the excited state to the ground state.[439] Recent vibrationally resolved UV spectroscopy measurements of SA, SM and the simplest derivative, Methyl sinapate (MS), suggest that along this series, SM is unique in having an inherently broad absorption spectrum even under jet-cooled gas phase conditions exhibiting an efficient, nonradiative energy dissipation mechanism that may be responsible for the biological selectivity of SM as a UVR photoprotective sunscreen molecule in plants.[301] These studies provide a solid foundation to build upon in understanding the underlying photodynamics of the sinapate ester derivatives presented here.

This section focusses on the use of TEAS to probe the ultrafast energy relaxation mechanisms of SA, MS and SM in the solution-phase. We complement these measure-

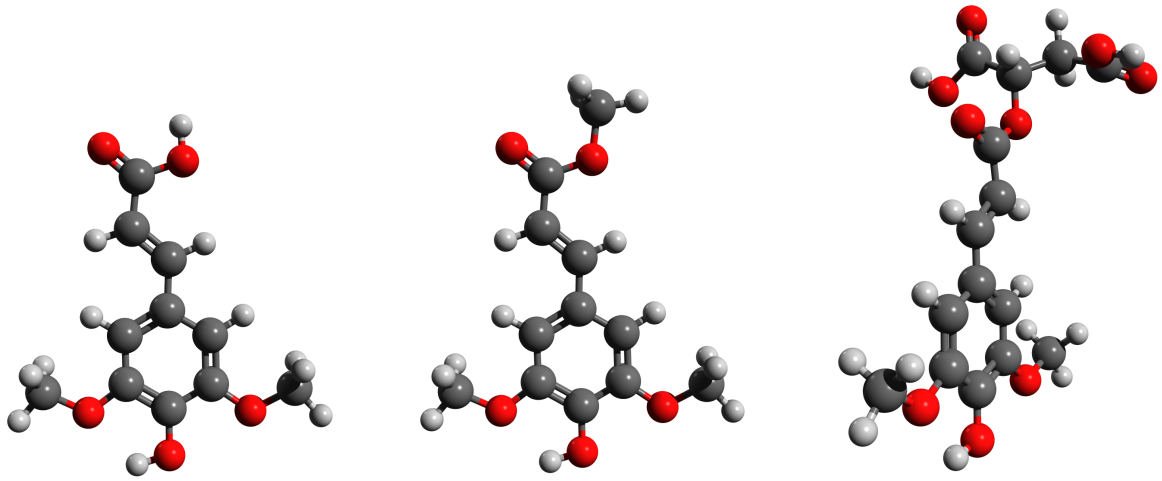

Sinapic acid (SA) Methyl sinapate (MS) Sinapoyl malate (SM)

Figure 5.1 | Structures of SA, MS and SM. All structures optimised at the DFT level of theory with the B3LYP functional[399,400] and the cc-pVDZ basis set.[24]

ments with continuous wave UV irradiation studies to elucidate long-lived photoproducts. We present evidence to suggest that photoexcited SA, MS and SM relax by IC to the ground electronic state *via* a *trans–cis* isomerisation of the aliphatic C=C bond.

5.1.2 Methodology

The TEAS set up[286,364] used throughout this work employs ∼320–330 nm, 1–2 mJ cm^{-2} pump pulses with probe pulses drawn from a broadband WLC (335–675 nm), with polarisation set to the magic angle (54.7°) relative to the pump pulses. TAS are taken of 1 mM SA (≥98%, Sigma-Aldrich), MS and SM (synthesised as described previously[478,479]), in solution with either the non-polar aprotic solvent dioxane (≥99%, Fisher Scientific), the polar aprotic solvent Acetonitrile (ACN), ≥99%, Sigma-Aldrich, or the polar protic solvent methanol (≥99.6%, Sigma-Aldrich) for a range of pump-probe time delays, Δt, up to a maximum of 2 ns. Each molecule is excited at its UVR absorption maximum (Figure 5.2). Spectra are acquired with a Cary 50 UV-vis spectrophotometer using a 1 cm path length cuvette. The peak maxima for each molecule in each solvent is used as the pump wavelength for all TEAS and continuous wave irradiation studies, as determined from the UV-visible spectra shown in Figure 5.2. For SA, the peak absorbance wavelengths are determined to be 325 nm, 323 nm and 318 nm for dioxane, ACN and methanol respectively. For MS, peak absorbance

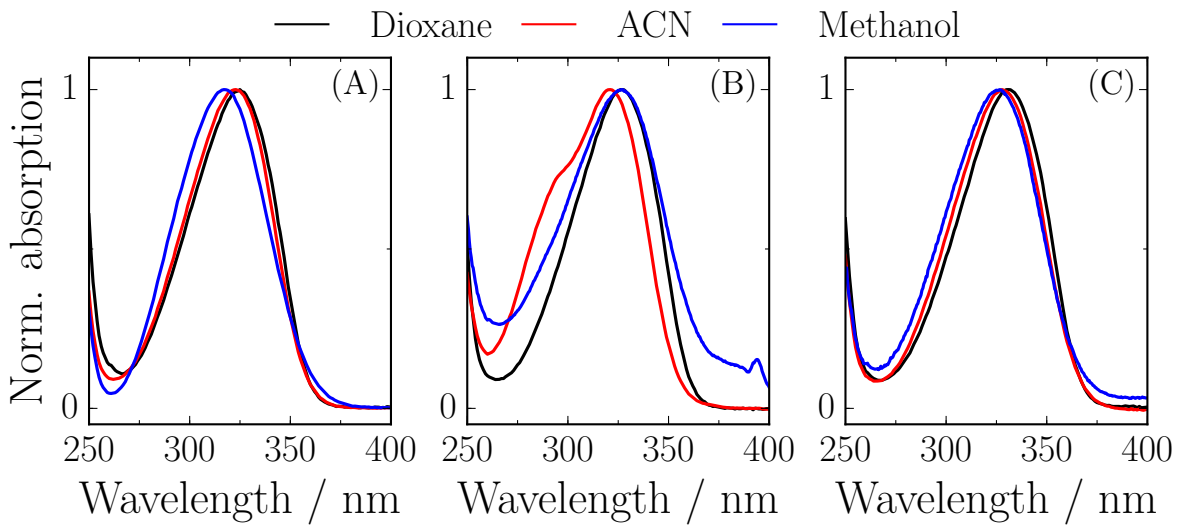

Figure 5.2 | Steady-state UV-visible spectra of: (A) SA, (B) MS, (C) SM in dioxane (black line), ACN (red line) or methanol (blue line).

wavelengths are determined to be: 327 nm, 322 nm and 328 nm in dioxane, ACN and methanol respectively. Similarly, for SM, the peak absorbance is determined to be, 329 nm, 328 nm and 326 nm in dioxane, ACN and methanol respectively. All TAS are chirp corrected using the KOALA package[386] and reported lifetimes are determined using a global fitting procedure[286,412] with uncertainties reported to a 95% confidence interval (2σ) using ASE, as discussed in Section 3.3.

Continuous wave UV irradiation studies are performed on all molecules using the following procedure. A steady-state UV-visible spectrum of each sample is taken (Cary 300 spectrometer), to obtain a '*before*' spectrum. Samples are then irradiated with continuous wave radiation from an arc lamp (OBB, Tunable KiloArc) for 10 minutes. The central wavelength used for irradiation is the same as the pump wavelength used in the TEAS measurements. The bandwidth is set to 10 nm with a power of 3 W. A second UV-visible spectrum was taken following irradiation, referred to as the '*after*' spectrum. The before spectrum is subtracted from the after spectrum resulting in the reported '*difference spectrum*'.

5.1.3 Results

Considering first the biological precursor, SA, in solution with dioxane, ACN or methanol, the TAS are shown in Figure 5.3 for photoexcitation at 325, 323 and 318 nm respec-

tively (SA-ACN shown in Appendix 8.7). For SA-dioxane (Figure 5.3(A)), the TAS is dominated by three features. The first is an intense absorption centred at ∼420 nm that decays away to the baseline by ∼50 ps. Secondly there is a broad absorption spanning the spectral region ∼420–650 nm. Finally, a negative signal is observed below ∼350 nm. Since photoexcitation around ∼320 nm (∼4 eV) promotes a $1^1\pi\pi^* \leftarrow S_0$ transition,[301] the first two features are attributed to ESA of the $1^1\pi\pi^*$ state (*i.e.* $S_n \leftarrow 1^1\pi\pi^*$). The negative feature, which grows in with increasing pump-probe time delays, with the decay of the ESA, is assigned to a GSB, through comparison with the steady-state UV-visible absorption (Figure 5.2), which does not fully recover at the maximum available pump-probe time delay of 2 ns. The TAS for SA-ACN and SA-methanol (Figure 8.11(A) and Figure 5.3(A) respectively) are also dominated by the three features seen in the SA-dioxane TAS with these addenda: the intense absorption of the $1^1\pi\pi^*$ ESA is blue shifted, centred instead on ∼370 nm, and an additional feature is observed; a strong negative signal centred around ∼460 nm which we attribute to SE.[301,480]

Quantitative insight into the dynamical processes observed in the TAS can be obtained by employing a global fitting procedure.[286,412] The lifetimes of the available processes are summarised in Table 5.1 for all the systems studied herein, and we return to this Table throughout our ensuing discussion. Following this, continuous wave irradiation was used to investigate the incomplete GSB recovery and assist in our analysis of these dynamical processes (Figure 5.4; black lines). A representative spectrum is overlaid with the absorption spectrum obtained for $\Delta t = 2$ ns from the corresponding TAS (red lines). For SA-dioxane the difference spectrum and the $\Delta t = 2$ ns spectrum (Figure 5.4(A)) match closely, with a positive absorption appearing at ∼370 nm in both spectra. This ∼370 nm absorption is also seen in SA-ACN and its red-wavelength shoulder is spectrally broadened (Figure 5.4(B)). Finally, for SA-methanol, there are large discrepancies between the difference spectrum and the absorption spectrum obtained for $\Delta t = 2$ ns (Figure 5.4(C)). A ∼20 nm '*gap*' between the two absorption maxima is observed. Once again, there is a shoulder to the red of the absorption feature in the $\Delta t = 2$ ns spectrum, which appears broader than seen in SA-dioxane and SA-ACN.

The simplest sinapate derivative, MS is analysed using an identical treatment as described for SA in the main text. The TAS for MS-dioxane and MS-methanol are shown in Figure 5.5(A) for photoexcitation at 327 and 328 nm respectively (MS-ACN after photoexcitation at 322 nm is shown in Appendix 8.8). We observe very similar spectral features as seen in SA-dioxane, *i.e.* an intense absorption centred at ∼420 nm which decays away to the baseline by ∼50 ps, a broad absorption spanning the spectral region ∼420–650 nm and a negative signal observed below ∼350 nm. As with SA, a

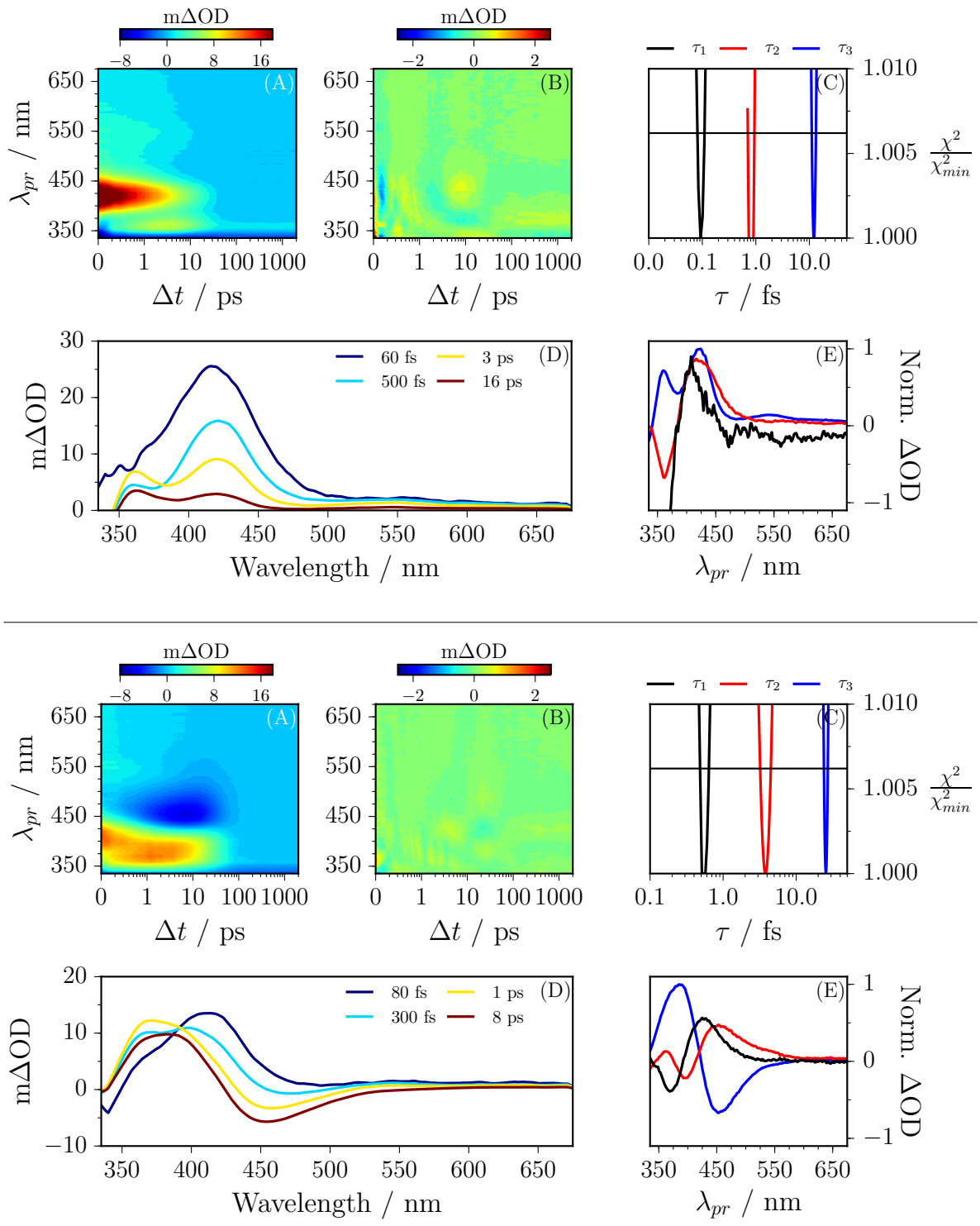

Figure 5.3 | (*top*): (A) Raw TAS following 325 nm photoexcitation of SA-dioxane. (B) Residual of the global fitting and the raw data. (C) ASE of extracted lifetimes. (D) Selected spectra at given Δt. (E) Corresponding DAS. (*bottom*): (A)–(E) Similarly for SA-methanol photoexcited at 318 nm.

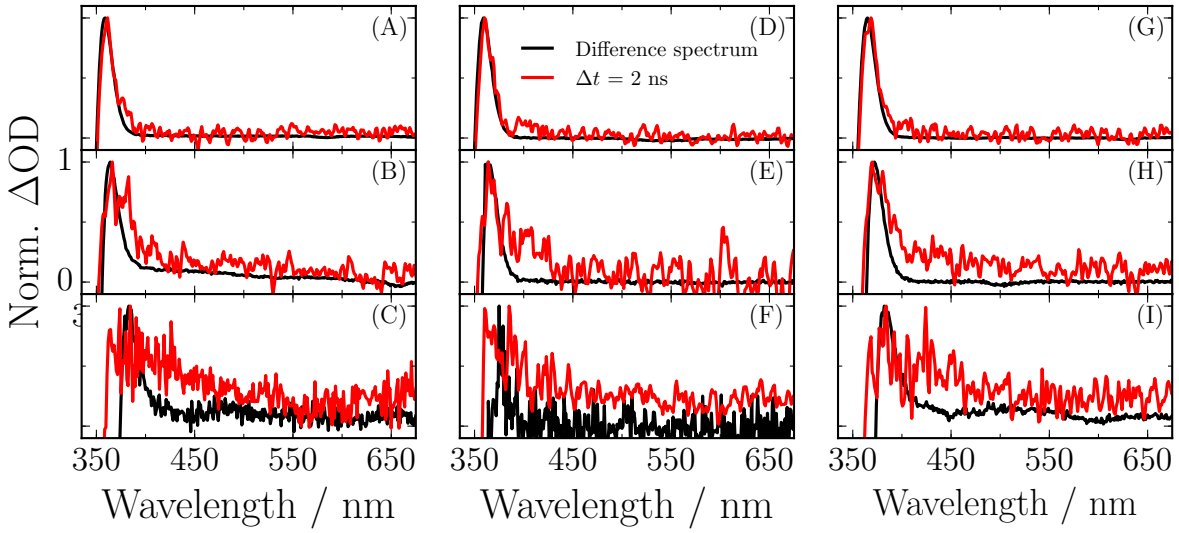

Figure 5.4 | UV irradiation difference spectra for SA-dioxane (A), SA-ACN (B) and SA-methanol (C) are shown (black line) in comparison to the absorption spectrum at the maximum available pump-probe time delay of 2 ns (red line). Similarly for MS-dioxane, MS-ACN, MS-methanol (D–F), and SM-dioxane, SM-ACN, and SM-methanol (G–I).

blue-shift of this first feature to ∼370 nm and a strong negative signal centred around ∼460 nm are observed in the TAS of MS-ACN and MS-methanol. Employing the global fitting procedure reveals the dynamical lifetimes as summarised in Table 5.1. As before, continuous wave irradiation studies are conducted to understand the long-lived nature of the incomplete GSB (Figure 5.4(D–F)). A similar solvent dependence is observed; the more protic and hydrogen bonding solvents display an increasing shoulder appearing to the red of the absorption feature at ∼370 nm. Thus the observed dynamics in MS closely accord with those discussed for SA.

We now consider the biological sunscreen deposited in the upper epidermis of plant leaves, SM. The TAS are shown in Figure 5.6(A) for SM-dioxane and SM-methanol for photoexcitation at 329 and 326 nm respectively (SM-ACN after 328 photoexcited is shown in Appendix 8.9)). As described for both SA and MS studies, similar solvent dependent spectral features are observed in the TAS. Once again employing a global fitting procedure we determine the lifetimes of the dynamical processes and these are summarised in Table 5.1. Continuous wave studies also reveal similar patterns as observed for SA and MS (Figure 5.4(G–I)), specifically, an increasing shoulder appearing to the red of the absorption feature at ∼370 nm in the more protic and hydrogen bonding solvent methanol.

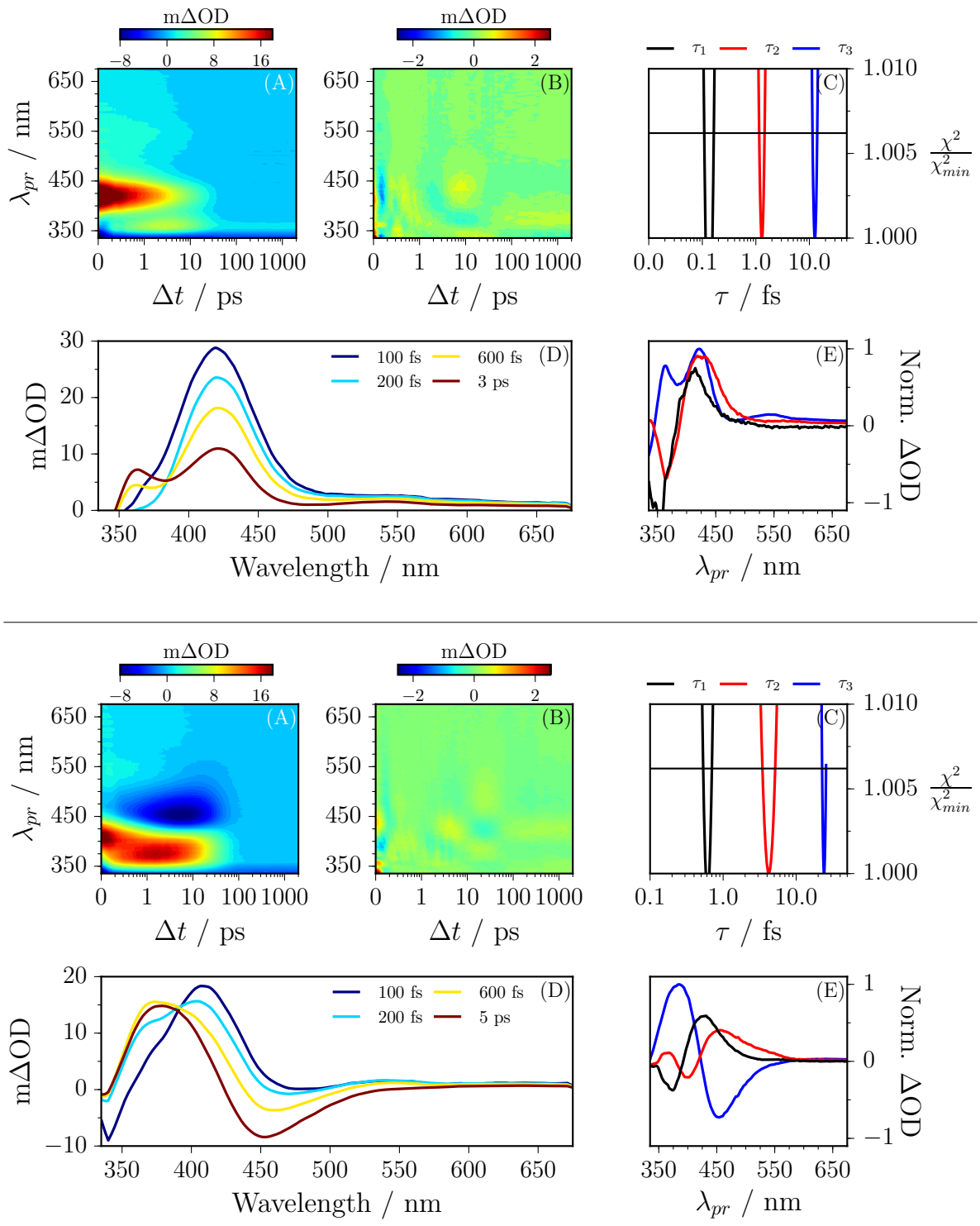

Figure 5.5 | (*top*): (A) Raw TAS following 327 nm photoexcitation of MS-dioxane. (B) Residual of the global fitting and the raw data. (C) ASE of extracted lifetimes. (D) Selected spectra at given Δt. (E) Corresponding DAS. (*bottom*): (A)–(E) Similarly for MS-methanol photoexcited at 328 nm.

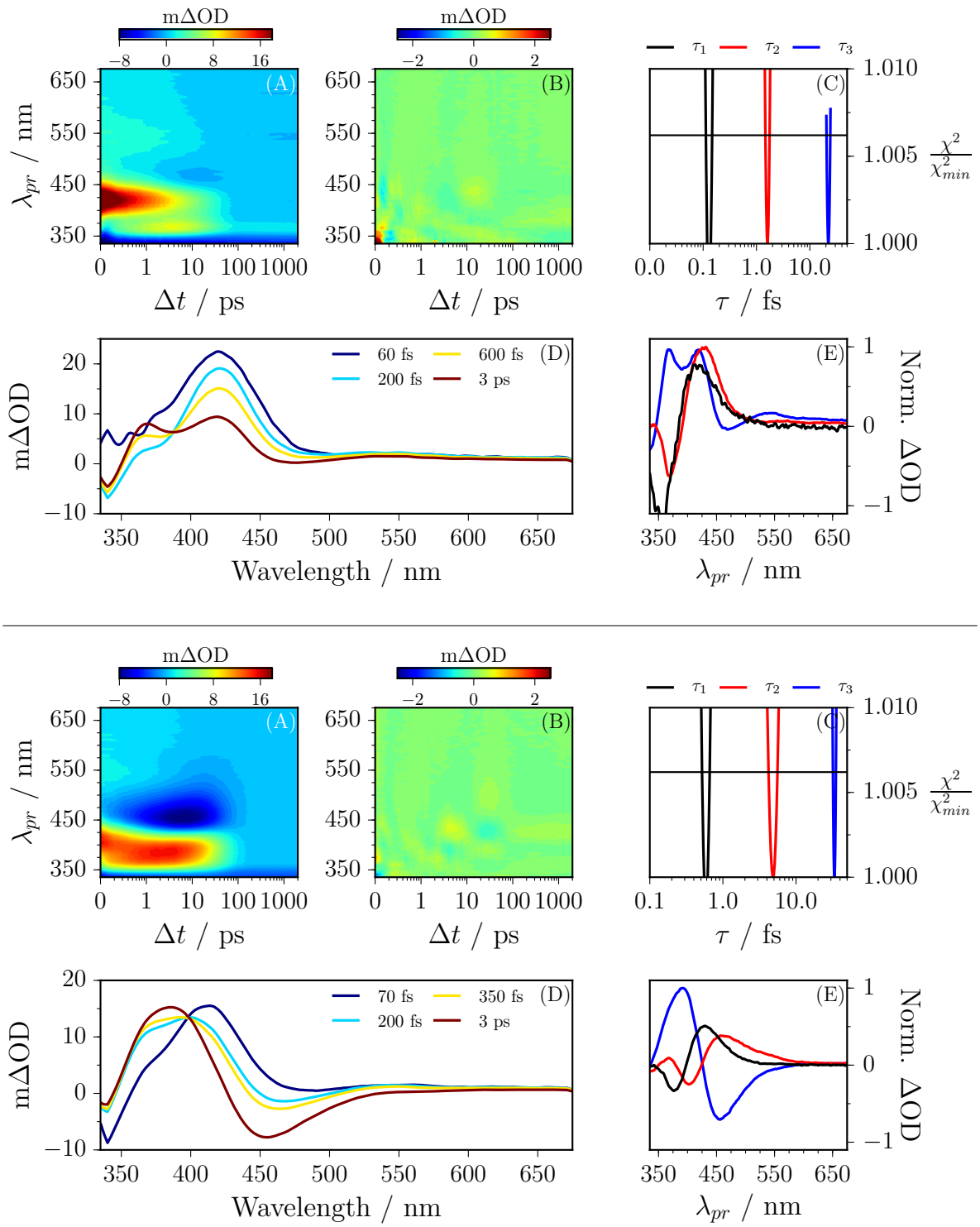

Figure 5.6 | (*top*): (A) Raw TAS following 329 nm photoexcitation of SM-dioxane. (B) Residual of the global fitting and the raw data. (C) ASE of extracted lifetimes. (D) Selected spectra at given Δt. (E) Corresponding DAS. (*bottom*): (A)–(E) Similarly for SM-methanol photoexcited at 326 nm.

Table 5.1: Summary of the lifetimes of dynamical processes of sinapic acid (SA), methyl sinapate (MS) and sinapoyl malate (SM).

SA	Dioxane	ACN	Methanol
τ_1 / fs	93 ± 17	52 ± 5	572 ± 87
τ_2 / ps	0.90 ± 0.19	0.57 ± 0.04	3.79 ± 0.72
τ_3 / ps	12.2 ± 1.1	17.0 ± 0.66	25.5 ± 1.6
MS	Dioxane	ACN	Methanol
τ_1 / fs	115 ± 49	53 ± 5	647 ± 114
τ_2 / ps	1.32 ± 0.16	0.54 ± 0.05	4.26 ± 0.90
τ_3 / ps	12.8 ± 1.3	18.0 ± 0.8	24.2 ± 1.5
SM	Dioxane	ACN	Methanol
τ_1 / fs	119 ± 28	51 ± 4	619 ± 101
τ_2 / ps	1.62 ± 0.15	0.63 ± 0.04	4.81 ± 0.77
τ_3 / ps	22.4 ± 1.9	27.3 ± 0.77	33.5 ± 1.7

5.1.4 Discussion and conclusions

We now discuss the implications with regards to photoprotection, drawing on the different aspects of the experimental results. First, considering the continuous wave irradiation studies, we note very good agreement between the difference spectrum and the Δt = 2 ns spectrum for SA, MS, and SM in the aprotic, weakly hydrogen bonding solvent dioxane. In these measurements, the *trans*-isomer and any photoproduct will have different steady-state UV-visible spectra and as such, any appreciable formation of photoproducts can be identified. An intense positive peak centred at ∼370 nm is attributed to a long-lived photoproduct, which we assign to be the *cis*-isomer of each molecule drawing confidence from the observation of photoisomerisation in similar molecules.[470,471] This feature is also seen for SA, MS and SM, in ACN and, to a lesser extent, methanol. In addition, a weak absorption is observed, convoluted with the ∼370 nm peak, which we have referred to as the red-wavelength shoulder. In ACN, an aprotic, mild hydrogen bonding solvent, for all three molecules we observe a broadening of this red-wavelength shoulder. In methanol, a protic strongly hydrogen bonding solvent, the three molecules display this signal broadening as with ACN, but the absorption feature of the difference spectrum is spectrally red-shifted ∼20 nm relative to the Δt = 2 ns

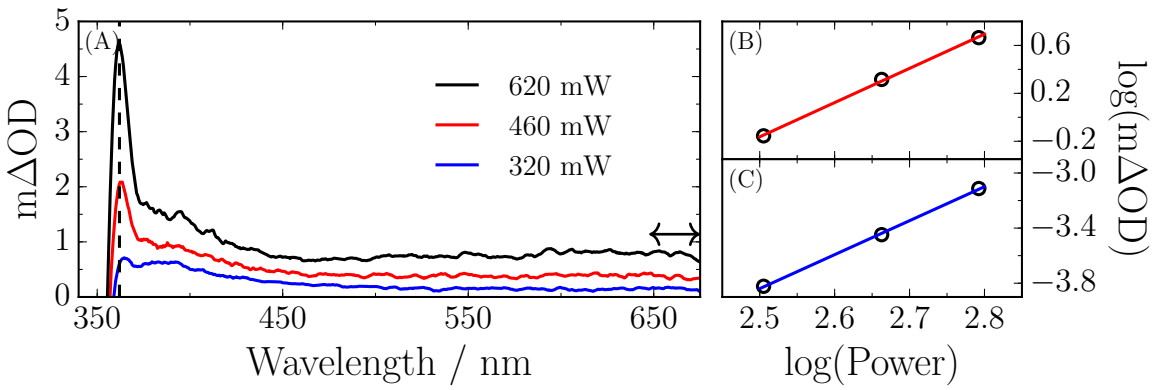

Figure 5.7 | (A) $\Delta t = 2$ ns spectrum of SA-methanol with changing incident pump power. Vertical dashed line and horizontal arrow indicates the 362 nm and 650 nm slices respectively, taken to compare signal intensities for the power dependency study. (B) For the 362 nm slice, a linear relationship between logarithmic power and logarithmic ΔOD is observed with a gradient of 2.84 ± 0.08, thus this signal is attributed to a (at least) two-photon absorption event (C) Once again, but instead for a 650–675 nm averaged slice, a linear relationship is observed, with gradient 2.47 ± 0.06, thus this signal is attributed to a solvated electron. Similar measurement for SA-dioxane and SA-ACN display a linear relationship with gradients 0.91 ± 0.01 and 1.09 ± 0.03 respectively, shown in Appendix 8.10

spectrum for all three molecules. The absorption feature in the $\Delta t = 2$ ns spectrum has characteristics similar to the UV-visible absorption spectrum of the SA radical.[439] We attribute the disparity seen for *all* methanol measurements (and to some extent in ACN), between the $\Delta t = 2$ ns absorption spectrum and the difference spectrum to two processes: (1) a two-photon (at least) ionisation process which generates the radical,[481–483] and (2), possible triplet state absorption given the characteristic 'tail' in the absorption towards the red end of the TAS.[325] We suggest (1) arises due to methanol's (and again, to some extent ACN) apparent propensity to alter the electronic structure of the molecules through perturbative interactions. In an effort to confirm (1), power dependent measurements of SA in dioxane, ACN and methanol are performed (Figure 5.7), which evidence that the feature observed at ∼360 nm can be attributed to a (at least) two-photon ionisation in methanol, convoluted with the *cis*-isomer signal (in all solvents). Taking a slice of the TAS at the signal maxima at ∼360 nm, which corresponds to the absorption maximum of the radical signature,[481] the SA-dioxane and SA-ACN signals display a linear relationship to the incident pump power (log(Power) *vs* log(mΔOD)) whereas SA-methanol displays a nonlinear relationship, see Figure 5.7. For all measurements, the TOPAS output was optimised for the wavelength used (*i.e.*

325, 323 or 318 nm for dioxane, ACN or methanol) and a sample pathlength of 950 μm was used to increased the signal strength of the long-lived features shown in the 2 ns spectra. Furthermore, each spectrum has been smoothed by a $\sim$3 nm integration.

Through due consideration of the data provided by the TEAS measurements, drawing on *ab initio* calculations on isolated gas-phase hydroxycinnamic acids,[285] and experimental results on related systems,[301,481] we attempt to rationalise the dynamical processes in operation. We do however note that additional theory is required to fully comprehend the dynamical processes evidently in operation. Following excitation to the $1^1\pi\pi^*$ state by the pump pulse, we propose that SA, MS and SM undergo numerous processes which are convoluted together, and described by the lifetimes τ_1 and τ_2, thus making distinct assignment of any one process with a lifetime difficult. In particular, we suggest that a coherent artefact of the IRF and an evolution out of the FC window contribute to τ_1. Along with any solvent rearrangement, IC ensues from this state to the intermediary $2^1\pi\pi^*$ state, *via* a $1^1\pi\pi^*/2^1\pi\pi^*$ CI which we suggest contributes to the lifetime τ_2. The timescale for these processes sensibly compares with previous dynamical studies in related molecular systems.[325,421,439,447,480,482,484] Both these lifetimes will inevitably be affected by the formation of the radical species (*cf.* Table 5.1). From here, isomerisation may occur along the $2^1\pi\pi^*$ state to generate the *cis*-isomer in S_0, mediated through an $2^1\pi\pi^*/S_0$ CI, with the remaining population reverting back to the original ground state *trans*-isomer. These final steps account for the lifetime τ_3. The overall relaxation dynamics are depicted in the schematic shown in Figure 5.8(A). Furthermore, an equally plausible alternative relaxation mechanism to that proposed in Figure 5.8(B), consistent with the data presented should be noted. The dynamics may ensue from the $1^1\pi\pi^*$ to the S_0 without the $2^1\pi\pi^*$ intermediary state. In this case, τ_1 and τ_2 would be considered relaxation along a single PES (which likely will be convoluted with numerous processes, see above) before coupling back to the S_0 *via* a $1^1\pi\pi^*/S_0$ CI on the timescale of τ_3.[439]

We suggest the SE observed for SA, MS and SM in ACN and methanol is likely to originate from population on the $2^1\pi\pi^*$ (or $1^1\pi\pi^*$ considering the alternative mechanism). This assignment is given for the following reasons. The onset of the SE signals are from Δt $\sim$100 fs onwards and last beyond $\Delta t > 30$ ps, which is on the timescale of τ_3 (Figure 5.6D). The signals are spectrally broad,[439] which is consistent with a disperse excited state population along the plateau of the $2^1\pi\pi^*$ (or $1^1\pi\pi^*$) PES. No SE is observed for dioxane measurements which we suggest is due to the much larger, increasing, ESA convoluted with any SE. Finally we note the very good agreement between spectral location of the SE in SA and SM with previous fluorescence measurements.[301]

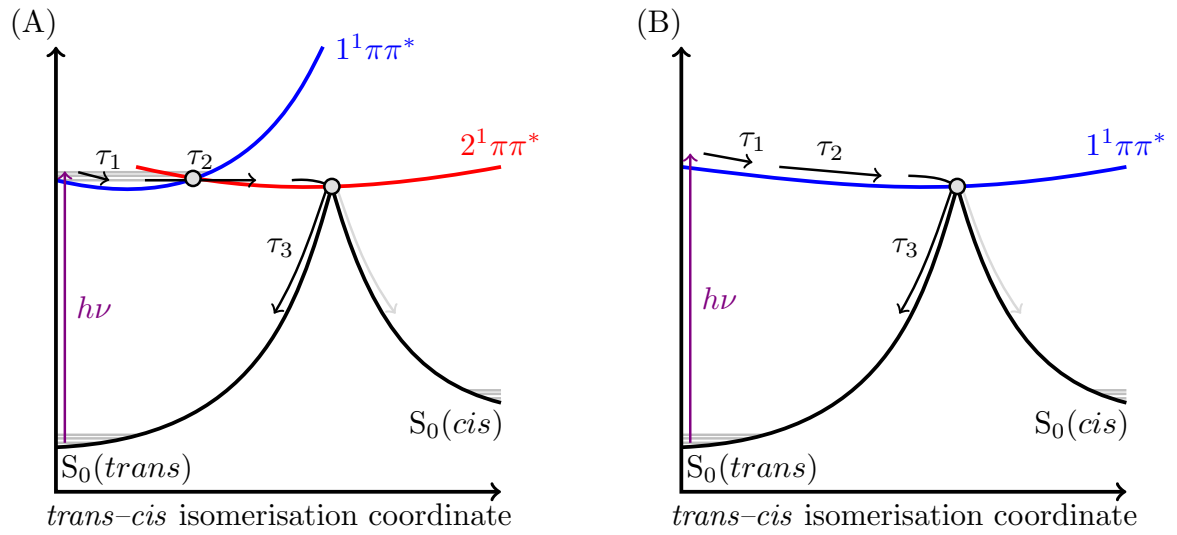

Figure 5.8 | A schematic diagram of the relaxation schemes proposed in this work adapted from the calculated PES for similar systems.[285] (A) A vertical excitation to the $1^1\pi\pi^*$ state and IC to a $2^1\pi\pi^*$ state in the adiabatic limit before non-adiabatic transfer to the ground electronic (S_0) state, with associated timescales τ_1, τ_2 and τ_3 as discussed in text. CIs between states are shown as grey circles. The $1^1n\pi^*$ state has been omitted for simplicity. (B) An equally plausible alternative relaxation mechanism instead involves dynamics along a single excited ($1^1\pi\pi^*$) state as discussed in the text.

Some general remarks are needed regarding the lifetimes of the dynamical processes given in Table 5.1, and how these are influenced by additional factors not included in the scheme of Figure 5.8. Firstly, it is a limitation of the global fitting procedure that all lifetimes correspond to processes that start instantaneously (*i.e.* non-sequential dynamics). This has the effect of 'blurring' the onset of one process with the onset of another (as, notably discussed for OC in Section 4.3). Ultimately, this means each lifetime will also capture some of the preceding and/or proceeding dynamics, making the absolute assignment of a lifetime with any one process very difficult.[412,448] Secondly, it is evident that all the lifetimes measured for methanol are appreciably longer than those measured in dioxane and ACN, which we attribute to the formation of the radical (and associated solvated electron; Figure 5.7).

We close with a comparison between the present solution-phase measurements and those recently obtained in the gas-phase, focussing on SA, as this system demonstrates quite notable differences.[301] Sharp features in the resonant two-photon ionisation spectrum for SA imply an initial excited state lifetime of the order of ps, in stark contrast to the SA-dioxane results obtained herein of ∼100 fs. One would anticipate observing

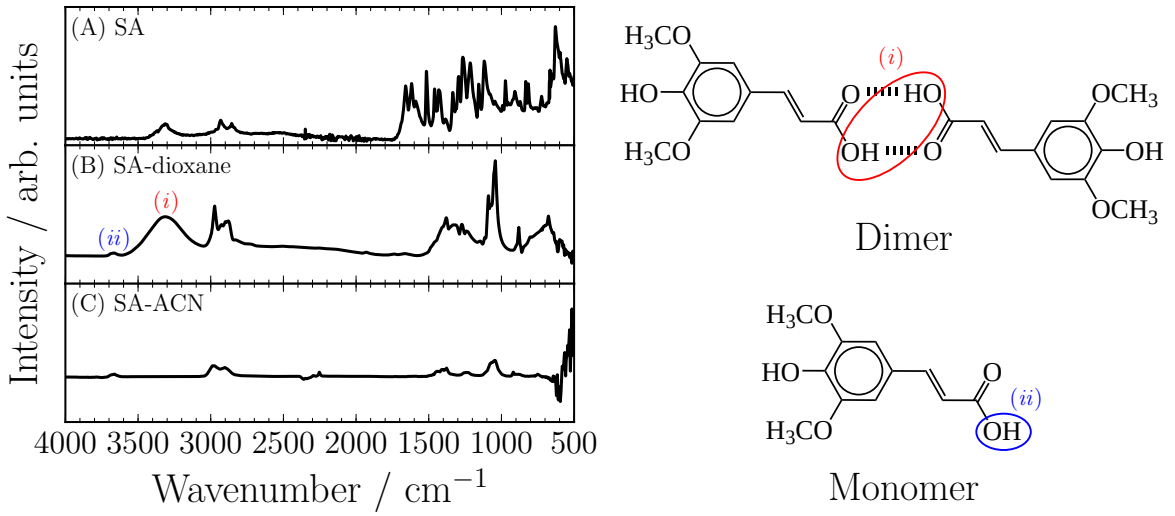

Figure 5.9 | Steady-state IR spectra of SA in: (A) the solid state, (B) 1 mM SA in dioxane, and (C) 1 mM SA in ACN. Two of the characteristic absorption bands relating to the hydroxyl moiety of the carboxylic acid are given:[302] (*i*) O−H of the dimer and (*ii*) O−H of the monomeric species. Assignments agree with previous studies of SA.[485,486]

similar timescales between the weakly perturbing non-polar dioxane solvent and the gas-phase. However, in addition to the mild perturbations induced by the solvent, SA exists as a dimer in dioxane, as confirmed by steady-state IR spectroscopy, which will of course influence its electronic structure.[485,486] To confirm the presence of dimers in dioxane, steady-state IR absorption spectra of 1 mM SA-dioxane and SA-ACN were recorded using a Jasco FTIR 4200 spectrometer in addition to a complementary solid state spectrum (to aid spectral assignment) recorded using a Bruker alpha spectrometer (Figure 5.9). A characteristic broad absorption from the hydrogen bonded O−H group on the SA carboxylic acid is observed across the range ∼3500–1750 cm^{-1} (highlighted in red in Figure 5.9) indicating the presence of SA dimers, in both the solid state and in dioxane. In ACN, this broad absorption, and the absorption centred on ∼3400 cm^{-1} in both solid state and dioxane are absent. This supports the assignment of SA dimers in these conditions, which are not present in ACN due to the increased polarity of the solvent, serving to disrupt the intermolecular hydrogen bonding between monomers. Assignments of the absorption bands are given in Figure 5.9, taken from similar studies.[485,486]

In ACN and methanol, the hydrogen bonds between dimers are broken, however the strong perturbations to the electronic structure by these solvents (*vide supra*) will inevitably lead to larger deviations between the gas- and solution-phase studies. Im-

portantly, the differences between these two phases serve to highlight the crucial role of both solvent-dynamics and structure-dynamics-function relationships. For example, if either the $1^1n\pi^*$ (as suggested to be involved in the gas-phase[301]) or $2^1\pi\pi^*$ state has charge transfer character, it will further influence the energy difference between these two states, and hence the excited state dynamics, due to solvent stabilisation.[301]

In summary, we have explored the photoprotection mechanisms in operation in SA, MS, and the plant sunscreen SM. In all three systems, excited state relaxation occurs on an ultrafast timescale, involving, in part, IC from $1^1\pi\pi^* \rightarrow 2^1\pi\pi^* \rightarrow S_0$, mediated by the appropriate $1^1\pi\pi^*/2^1\pi\pi^*$ and $2^1\pi\pi^*/S_0$ CIs. Importantly, at the $2^1\pi\pi^*/S_0$ CI, the photoexcited molecule can either reform the original ground state *trans*-isomer or generate the *cis*-isomer. We also suggest a combination of other processes in operation, notably the formation of a radical species and possibly ISC. Crucially however, and with the exception of the radical species which is generated through consequence of the experiment itself (at least a two-photon absorption process which is unlikely to occur in nature), the present work serves to highlight the efficiency in which the plant sunscreen, SM, is able to undergo ultrafast relaxation in order to bypass the deleterious effects of UV radiation in the biosphere. This study also further highlights that there may be other reasons why SM is selected as a sunscreen molecule in plants, given that there is little difference in the excited state dynamics between the biological precursor (SA) through to plant sunscreen (SM) in the solution phase.

Chapter 6

Network-based analysis of pigment-protein complexes

Parts of this chapter have been published by the author:

---

1. **Lewis A. Baker** and Scott Habershon. Robustness, efficiency, and optimality in the Fenna-Matthews-Olson photosynthetic pigment-protein complex. *J. Chem. Phys.*, **2015**, 143(*10*):105101.

2. **Lewis A. Baker** and Scott Habershon. Photosynthetic pigment-protein complexes as highly-connected networks: Implications for robust energy transport. *Proc. R. Soc. A*, **2017**, 20170112.

3. **Lewis A. Baker** and Scott Habershon. Photosynthesis, pigment-protein complexes and electronic energy transport - simple models for complicated processes. *Sci. Prog.*, **2017**, 100(*3*):313–330..

6.1 Common functionality in photosynthetic processes

Essentially all the accessible energy for life in the Earth's biosphere is made available through the process of photosynthesis, the conversion of light energy from the Sun into storable chemical energy for metabolism.[487,488] The process itself has been the subject of remarkable evolution throughout Earth's history. The early Archean Earth atmosphere was without oxygen, meaning photosynthetic life was predominantly anoxygenic; indeed fossil records suggest the presence of anoxygenic bacteria some 3 Ga ago (1 Ga = 10^9 years).[489] Somewhat paradoxically, it has been suggested that before the great oxidation event (*c.* 2.45 Ga ago)[135] which gave oxygen prevalence in the atmosphere as observed today, some bacteria evolved oxygenic photosynthetic machinery (*c.* 2.7 Ga ago),[136,489] likely making use of trace amounts of oxygen derived from atmospheric hydrogen peroxide (H_2O_2).[136] Today, our oxygen-rich atmosphere means oxygenic photosynthesis is by far the dominant form of photosynthesis, as evidenced in a wide variety of photosynthetic organisms including green plants, algae, and many bacteria. Photosynthetic machinery has continued to evolve, with each organism striving to achieve photosynthesis with greater efficiency. This efficiency, in particular, is the focal point of this chapter; for decades the applications of the knowledge gleaned from a deep understanding of not just photosynthesis, but the integral photosynthetic machinery, has been a significant driving force within the research and industrial communities. For example, mimicking the capture of solar energy as an untapped renewable energy source for electrical power generation on a mass scale could constitute a resolution to the energy crises.[490–493] Another application is the bioengineering of common crops to increase harvest yield thus increasing food security, which has recently reported successful proof-of-concept studies.[494] The work in this chapter focusses on understanding how organisms have managed to utilise photosynthesis with great efficiency. Specifically, modelling important photosynthetic machinery as a network of interacting sub-units provides a broadly applicable methodology to begin to contribute to some of these topical research directions.

All photosynthetic systems broadly operate on the same basic principles,[495,496] (Figure 6.1). The first step in any photosynthetic process is the absorption of light energy, most dominantly in the visible region (∼400–700 nm, often with a notable absence in the green region).[497] This is known as light-harvesting, and is achieved using a collection of densely-packed light-absorbing pigments (chromophores) in a structure referred to as the chlorosome. Such pigments often bear homology to porphyrin and chlorin

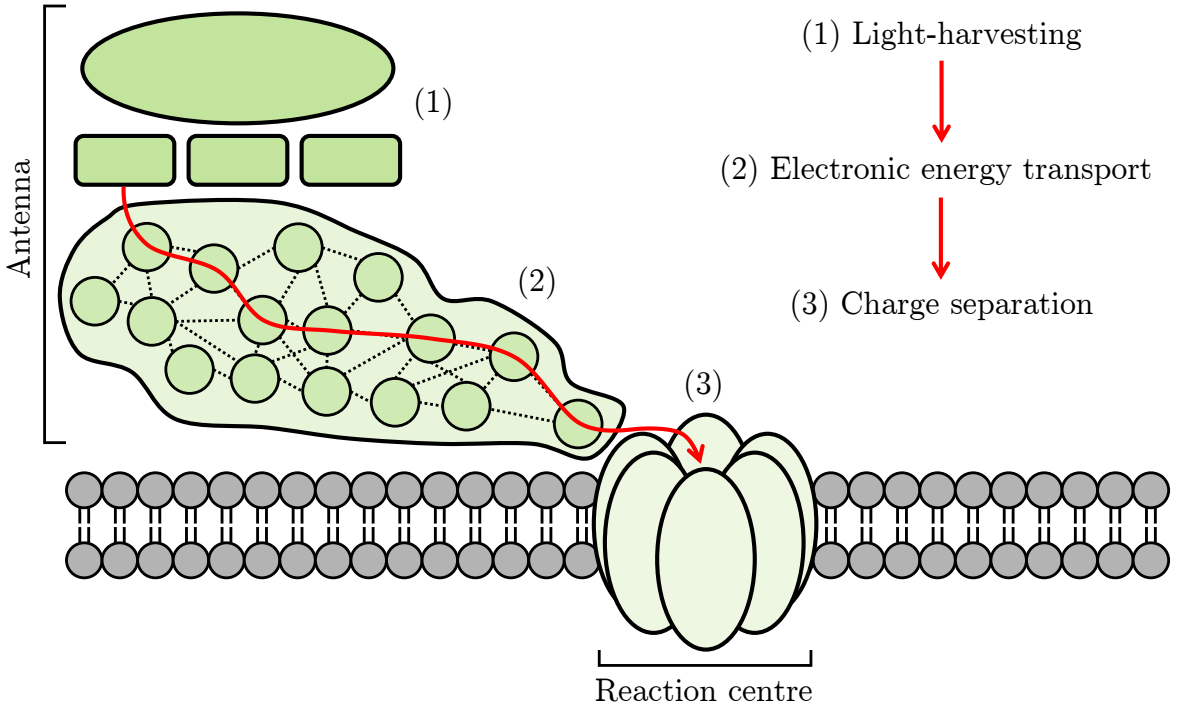

Figure 6.1 | A general overview of photosynthesis. The chlorosome consists of densely packed pigments which absorb light energy (1, light-harvesting) to create electronic excited states. This energy is passed to pigments inside the pigment-protein complex which funnels it towards the reaction centre (2, electronic energy transport). The reaction centre creates a chemical gradient through charge separation across the lipid membrane, which drives energy synthesis (3, charge separation).

(Figure 6.2), with variations in pigment structures occurring as ring substitutions on the head group and/or the ligand chain.[498,499] Carotenoids on the other hand, are another group of pigments which are derivatives (*via* cyclic additions or oxidation) of tetraterpene (long hydrocarbons of molecular formula $C_{40}H_{64}$).[500] Each type of pigment absorbs radiation in a specific spectral region;[497] the adoption of several types of pigment, each in different pigment-protein environments, thus generally ensures a large spectral coverage.[501] Light-absorption promotes formation of an electronically excited state, and Electronic Energy Transport (EET)[502] subsequently passes this excitation energy through a Pigment-Protein Complex (PPC), which is comprised of a set of pigments that are held in a specific spatial arrangement. The PPC's function is to funnel this electronic energy towards the Reaction Centre (RC). Once electronic energy reaches the RC, a chemical gradient is established through charge separation which is used to drive chemical energy storage.[503]

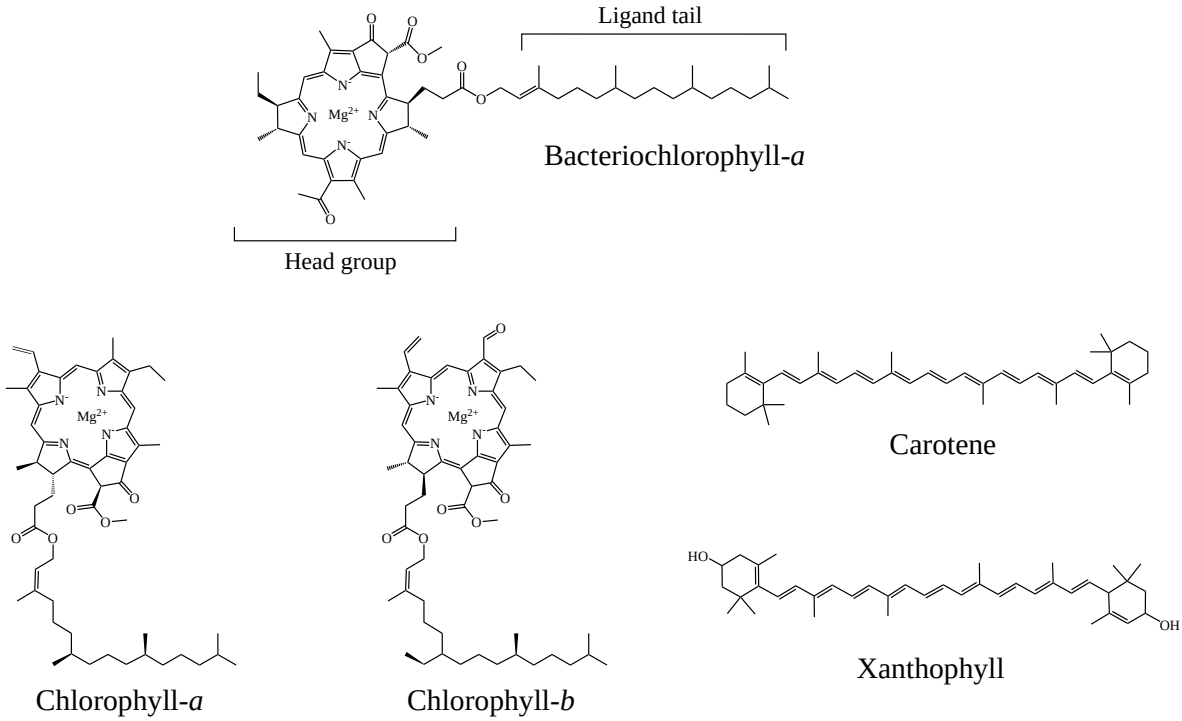

Figure 6.2 | Light-absorbing pigments all have similar structures based around porphyrin and chlorin. Variations include ring substitutions on the head group as well as the chain length in the ligand. Shown are Bchl-*a*, found in many photosynthetic bacteria, and the main pigments found in higher green plants: chlorophyll-*a* and chlorophyll-*b*, and the carotenoids, carotene and xanthophyll.[498,499]

This rather complicated set-up may at first appear inefficient; instead, pigments around the RC could simply absorb light and pass the excitation energy straight to the RC, which might be expected to increase the rate of EET. However, having a large density of pigments in the chlorosome amplifies light-absorption such that even weak sources of light prove sufficient for photosynthetic life to thrive. An excellent example of this so-called *absorption amplification* occurs in a species of green sulphur bacterium which contain bacteriochlorophyll-*e*. The bacterium can reside at depths of up to 80 m in the Black Sea, such that the intensity of light reaching this depth is ∼10,000 times smaller than that on the surface of the Earth.[496,504]

This is, of course, a broad overview, and there is a wide range of chemical mechanisms which contribute to any one of the processes mentioned,[503,505] including water splitting, chemiosmosis and Adenosine Triphosphate (ATP) synthesis. However, this overview serves as a precursor to highlight the role PPCs play in photosynthesis, which is the focal point for the remainder of this chapter.[506]

6.2 The role of pigment-protein complexes

After light-harvesting takes place in the periphery of the antenna complex, EET to the RC is facilitated by the PPC. It is this process which is understood to be the origin of unique photosynthetic efficiency; PPCs exhibit outstanding light-to-charge efficiencies close to 100% with highly directional EET towards the RC.[507] As stated above, PPCs are made up of a collection of pigment molecules, such as Bacteriochlorophyll (Bchl) or chlorophyll (Figure 6.2), which are held in a well-defined spatial arrangement by a protein scaffold. The number of pigments in a PPC varies greatly between organisms;[497,498] for example, Green Sulphur Bacteria (GrSB) utilise eight Bchl units in each monomer of a trimeric structure, known as the Fenna-Matthews-Olson (FMO) complex, while the Light-Harvesting Complex II (LHC-II) found in green plants and algae has scores of pigments, namely chlorophyll-a and chlorophyll-b pigments (the spinach plant has 42 for example; Figure 6.3). EET through PPC structures typically occurs over 10-100s of ps.[495,496] Given the timescales over which these PPCs have evolved, one might ask are they in some way optimised for their EET properties,[510] or are they instead optimised to exhibit a robustness to some environmental variable such as temperature fluctuations,[511,512] or even some balance between these factors? Answers to such ques-

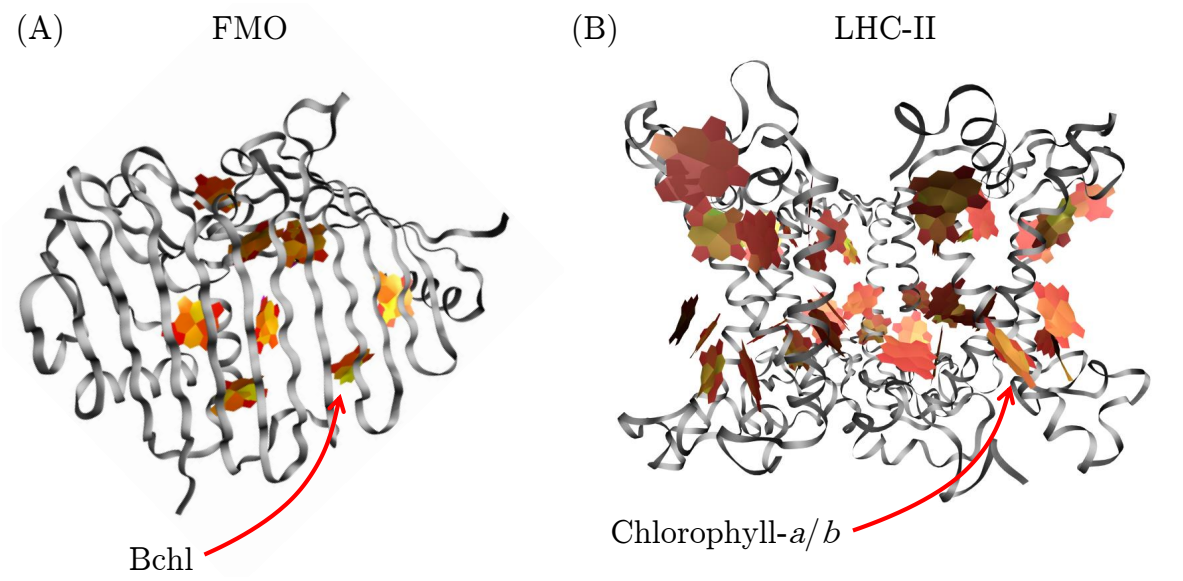

Figure 6.3 | Commonly studied PPC complexes. (A) The FMO complex found in GrSB. It consists of a trimeric structure where each monomer (as shown) contains eight Bchl-a pigments.[508] (B) The LHC-II as found in the majority of green plants; shown is the complex from the spinach plant.[509]

tions are likely to provide valuable insight into the design of artificial light-harvesting systems.[513,514]

A further area of focus which has received considerable attention is in understanding the role of quantum mechanics in EET within biological PPCs. Because the magnitude of the electronic couplings between pigments is comparable to temperature fluctuations at room temperature, one might expect that such quantum mechanical effects would be 'washed out' by the environment. However, seminal experiments at both cryogenic[515] and room temperatures[516] have observed coherent 'quantum beats' in the EET between the pigments of FMO, demonstrating electronic coherence within the first few hundred fs of EET. These observations have since been supported by a large literature of computational studies utilising a range of methods from density matrix propagation[517,518] (which is the subject of this chapter) to atomistic simulations.[519,520] Additionally, the concept of Environmentally-Assisted Quantum Transport (ENAQT) has also been extensively investigated both theoretically and through experiments (predominantly coherent 2D spectroscopy[521]),[522–528] exploring how the protein environment surrounding the pigments might support EET. The role of quantum mechanics therefore must not be overlooked in the design of the model used to answer questions concerning EET in biological PPCs and artificial light-harvesting systems.

6.3 Methodology

When it comes to building a model to describe EET in a PPC there are many choices one must make, balancing the accuracy of the model to sufficiently answer the questions of interest, whilst minimising the computational expense of the model.[529] Obviously, treating an entire PPC with a high level of theory, particularly accounting for the quantum-mechanical aspects of electron structure, would be ideal, but one quickly runs into the scaling problems inherent in quantum calculations. Linear scaling DFT can begin to address this problem,[92] allowing calculation of electronic properties for systems containing up to a few thousand atoms, but a full description of an explicitly solvated PPC is still too large to be computationally tractable. QM/MM is a powerful method which treats the most important part of the system (the pigments, for example) within a quantum mechanical model,[74] and the rest of the system (the protein and solvent) with a classical force-field. These certainly can be much more efficient than approaches treating the entire system quantum mechanically, but one must be careful to select the correct sub-system to treat with quantum mechanics while also accurately accounting for interactions between the two different regions. These methods can, and have been

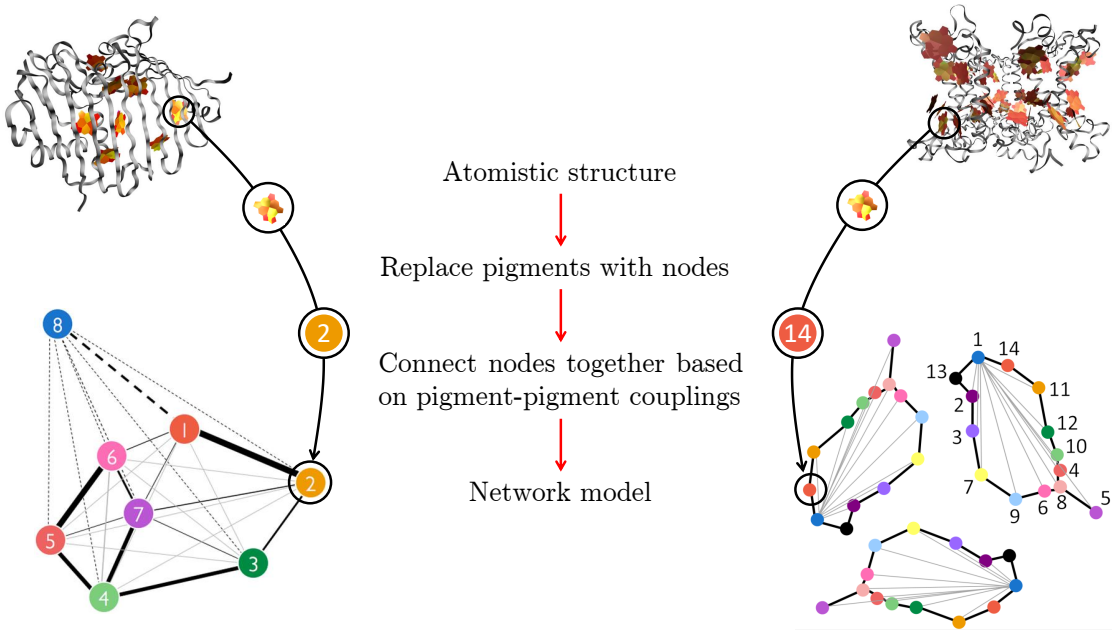

Figure 6.4 | An entire PPC can often be reduced to a simple system of interconnected nodes with the protein environment included as a pure dephasing effect which acts on each node. Each node represents a pigment, and the connections between nodes represent the electronic coupling between the two relevant pigments. (*left*): This model reduction is shown for the FMO monomer; the labelling scheme follows that of Fenna, Matthews and Olson. (*right*): Similar model reduction for LHC-II.

applied successfully to some PPCs, most notably the FMO complex shown in Figure 6.3(A).[530,531] However, they are computationally demanding and are not suitable for systematic studies of structural and electronic trends, as studied here.

Instead, in the present work, as with many other related studies,[532–536] the PPC is viewed as a system of interconnected 'nodes' or 'vertices' (the pigments) and 'edges' (the electronic couplings between pigments), which together form the electronic sub-system of the PPC (Figure 6.4). The Hamiltonian of this electronic sub-system is analogous to a typical tight-binding model of n pigments which, in the basis of molecular excited states, is given by[518,523,537,538]

$$\hat{\mathrm{H}}_{ex} = \sum_{i=1}^{n} \epsilon_i \left|i\right\rangle \left\langle i\right| + \sum_{i<j} J_{ij} \left(\left|i\right\rangle \left\langle j\right| + \left|j\right\rangle \left\langle i\right|\right), \tag{6.1}$$

where ϵ_i is the electronic excitation energy of the i^{th} pigment and J_{ij} is the electronic coupling between the i^{th} and j^{th} pigment (Figure 6.5). $|i\rangle$ denotes molecular state i in

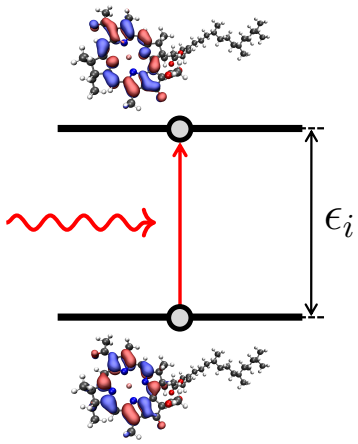

Electronic excitation

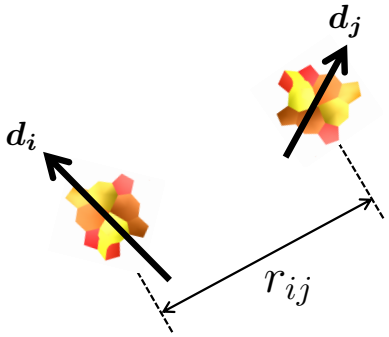

Electronic dipole-dipole coupling

Figure 6.5 | (*left*): The first term of the electronic Hamiltonian captures the excitation energy of each pigment.[82,463] (*right*): The second term models the electronic couplings of the electric dipoles between pairs of pigments.

standard bra-ket notation. The values of ϵ_i are obtained from fluorescence studies, the fitting of optical spectra[498,539,540] or direct *ab initio* calculations,[541,542] whereas the J_{ij} are most commonly determined from the magnitude and separation of the excited state transition dipole moments for each pigment according to

$$J_{ij} \propto \left(\frac{\mathbf{d}_i \cdot \mathbf{d}_j}{|r_{ij}|^3} - 3\frac{(\mathbf{d}_i \cdot \mathbf{r}_{ij})\,(\mathbf{d}_j \cdot \mathbf{r}_{ij})}{|r_{ij}|^5} \right), \tag{6.2}$$

where $\mathbf{d}_i$ and $\mathbf{d}_j$ are unit vectors for the dipole of pigment i and j respectively, and r_{ij} is the magnitude of the distance between pigment i and j. This approximation of the electronic dipole-dipole coupling is known as the *transition dipole-dipole cube method*;[517] other approximations exist, such as the inclusion of a dielectric medium to better model the *in vivo* conditions PPCs reside in,[543] but are not further considered here.

The *electronic* Hamiltonian above is augmented to include the effects of (*i*) exciton recombination, whereby the exciton created by light absorption recombines before reaching the 'exit' from the PPC, and (*ii*) energy trapping, whereby electronic energy reaching the sink pigment in the PPC subsequently flows out of the PPC and towards the RC. These two effects are typically included in the electronic Hamiltonian through the addition of anti-Hermitian operators, namely a recombination operator $\hat{\mathrm{H}}_{rec}$, and a

trapping operator $\hat{\mathrm{H}}_{trap}$:

$$\hat{\mathrm{H}}_{rec} = -i\hbar\Gamma \sum_{i=1}^{n} |i\rangle \langle i| , \tag{6.3}$$

$$\hat{\mathrm{H}}_{trap} = -i\hbar\kappa |k\rangle \langle k| . \tag{6.4}$$

The recombination operator acts on all pigments with an exciton recombination rate Γ; a typical value is $\Gamma = 1$ ns^{-1}, which is in line with *in vivo* systems.[522,523] In contrast, the trapping operator only acts on pigment k, the PPC sink site which must be identified for each PPC. As a result of $\hat{\mathrm{H}}_{trap}$, when electronic energy reaches the trapping site, it is funnelled out of the PPC with rate κ, with typical values for this rate being $\kappa = 1$ ps^{-1}.[522,523] The full electronic Hamiltonian for describing an n pigment PPC, within the model described above, can therefore be written as

$$\hat{\mathrm{H}} = \hat{\mathrm{H}}_{ex} + \hat{\mathrm{H}}_{rec} + \hat{\mathrm{H}}_{trap}. \tag{6.5}$$

In our work, the protein environment of the PPC is considered separately from the electronic sub-system described above. We assume that the environment induces Markovian fluctuations in all the pigment excitation energies, leading to a pure dephasing effect at each pigment node. This description allows the simulation of EET dynamics to include both the electronic sub-system and the protein environment within a simple quantum master equation approach known as the Haken-Strobl model.[518,523,537,538] Instead of working with a wavefunction model, Ψ as in quantum chemical calculations, the density matrix, ρ is used as the object of interest. In the basis of pigment excited-states, the density operator is given by

$$\hat{\rho}(t) = \sum_{i}^{n} \sum_{j}^{n} p_{ij}(t) |i\rangle \langle j| , \tag{6.6}$$

where p_{ij} is the density matrix element for state i, j. Within the Haken-Strobl approach, the equation-of-motion for the density matrix is

$$\frac{d\rho_{ij}}{dt} = \mathcal{H}[\hat{\rho}]_{ij} + \mathcal{L}[\hat{\rho}]_{ij}, \tag{6.7}$$

where ρ_{ij} denotes the matrix element ij. Here, $\mathcal{H}[\hat{\rho}]_{ij}$ is the standard density matrix propagation equation for the electronic Hamiltonian (as given in Equation 6.5) which is given by

$$\mathcal{H}[\hat{\rho}]_{ij} = -\frac{i}{\hbar} \left[\hat{\mathrm{H}}, \hat{\rho}\right]_{ij} . \tag{6.8}$$

On the other hand, $\mathcal{L}[\rho]_{ij}$ describes the interaction between the protein environment and the electronic sub-system as a pure dephasing effect, and is given by

$$\mathcal{L}[\hat{\rho}]_{ij} = -\left(\frac{1}{2}\left(\gamma_i + \gamma_j\right) - \sqrt{(\gamma_i\gamma_j)}\delta_{ij}\right)\rho_{ij}, \tag{6.9}$$

where the dephasing rate at pigment i is γ_i. Typical values for γ_i can vary quite considerably since previous work[544,545] has shown that comparable EET efficiency is maintained over a range of values; however, $\gamma_i = 100$ cm^{-1} is used throughout unless stated otherwise, given it lies within typically physiological temperatures that the PPCs studied here reside in.

Integration of Equation 6.7 provides the time dependent density matrix, $\rho(t)$, from which time-dependent observables may be calculated. The diagonal elements of this $n \times n$ matrix give the site populations at each chromophore,

$$p_{ii}(t) = \langle i|\,\hat{\rho}(t)\,|i\rangle\,. \tag{6.10}$$

The last thing required is a metric which can be used to assess EET. Here, we define the EET efficiency,[523] η, as the time-integral of the population on the trapping site over some maximum simulation time, t_{max}. In other words, we have

$$\eta = 2\kappa \int_0^{t_{max}} p_{kk}(t)\ dt, \tag{6.11}$$

where $p_{kk}(t)$ is the population on the trapping site k. Thus, calculating η in response to perturbations of the PPC Hamiltonian will indicate how such perturbations modify the overall EET within the PPC; this gives us a direct method of interrogating the role of the PPC structure, *via* the Hamiltonian matrix elements, on EET properties. All simulations in this work employ $t_{max} = 10$ ps, which is sufficiently long to capture the vast majority of population transfer (discussed later).

It is worth pointing out that our simulation approach, comprising of Hamiltonian and dynamics, is just one such approach that can be used. As discussed at the start of this section, the model by which the electronic Hamiltonian is built is a choice which one must make. So too, is the choice of how to model environmental effects. Here we have highlighted the use of the Haken-Strobl model where the environment (protein and solvent bath) are introduced as a pure dephasing effect through Markovian fluctuations in the pigment excitation energies; explicit correlations between the electronic Hamiltonian and the protein environment are not incorporated. Although, as

will be shown, this model works quite well in reproducing the qualitative results of more complicated models, better approximations clearly exist. For example, another popular method is treating the environment as a collection of harmonic oscillators derived from a physically-motivated spectrum of frequencies and coupling strengths.[517,546] This, along with the interaction with the electronic sub-system can be included in the total Hamiltonian (Equation 6.5). In this model, the bath (environment) is represented by a set of f-harmonic oscillators drawn from a frequency spectrum which is chosen (or calculated through the selection of an appropriate spectral density,[517,547,548] or classical molecular dynamics simulations)[520,549] to model the PPC environment subject to the relevant physiological conditions (*e.g.* temperature). In this manner, the bath Hamiltonian, $\hat{\mathrm{H}}_b$ takes the form

$$\hat{\mathrm{H}}_b = \sum_{k=1}^{f} \frac{1}{2} m_k \omega_k^2 \hat{q}_k^2, \tag{6.12}$$

where ω_k is the vibrational frequency of normal mode operator $\hat{q}_k$, and m_k is the associated mass. In addition to this, each pigment site can be given a specific 'localised' bath which has been shown to impact the EET dynamics significantly.[548] The final term to be included in this approach is then a system-bath coupling which captures the interaction between the electronic sub-system and the vibrational bath denoted $\hat{\mathrm{H}}_{sb}$. Once again a choice is required here, the most common being a linear coupling such that

$$\hat{\mathrm{H}}_{sb} = \sum_{i=1}^{n} \sum_{k=1}^{f} c_k^i \hat{q}_k |i\rangle\langle i|. \tag{6.13}$$

Unlike parametrising the bath Hamiltonian (either through electronic structure or molecular dynamics calculations), the coupling parameters, c_k^i, are more difficult to determine and are usually selected to be physically-reasonable, treated as variables or are optimised to agree with experimental optical spectra.[550]

6.4 The Fenna-Mathews-Olson complex

Turning our attention to a specific example of how this network picture can be used to rationalise EET properties in common PPCs. Our first example is the FMO complex,[551] as shown in Figure 6.6. The FMO complex has been extensively studied from many perspectives under a myriad of models varying in complexity. Recent crystal structures of the FMO complex shows it consists of three monomers, each of which contains eight Bchl-a pigments.[508,552,553] Each FMO monomer is assumed to be an isolated system, such that there are no inter-monomer interactions, an approach which is known to

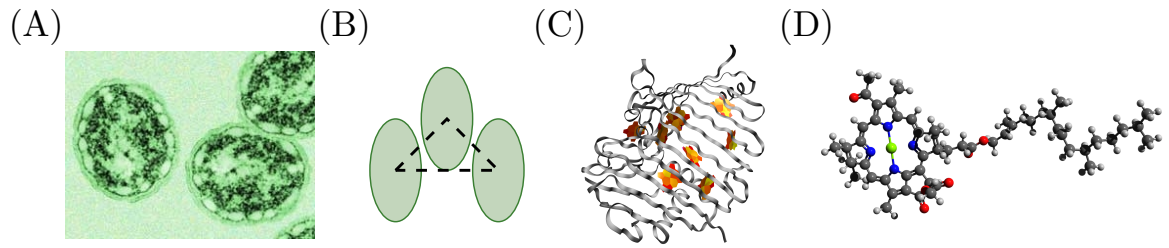

Figure 6.6 | The different length-scales involved in the FMO complex. (A) GrSB, typically a few microns in length.[554] Image retrieved from *digitaluniverse.net*.[555] (B) The FMO complex consists of three identical monomers, the so-called 'eighth' Bchl-*a* of each monomer is positioned towards the centre of the trimeric complex. (C) Each of the monomers consists of eight Bchl-*a* pigments. (D) The Bchl-*a* pigment.[16,266]

be a reasonable assumption with regards to energy transport in FMO,[523,556] although the trimeric system has been studied and shown to exhibit some differences.[557] Initial electronic excitation is suggested to occur at pigment 1, pigment 6, or pigment 8 because of their proximity to the chlorosome baseplate (*cf.* Figure 6.3(A)). These pigments (1, 6 and 8; Figure 6.4) are referred to hereafter as the *source* pigments (sites). The excitation energies of each pigment are calculated from the fitting of optical spectra,[540,550] which reveals the lowest energy pigment is site 3.[556] This is, therefore, suggested to be the *sink* site, where electronic energy is trapped and passed to the RC. Constructing the total Hamiltonian as described in the previous section (and explicitly given in Appendix 8.11) allows each possible initial excitation scenario to be simulated using the Haken-Strobl model for EET.

At this point, it is worth summarising some of the most relevant work which has focussed on FMO in terms of a 'network' and examined some of the properties of its EET pathways. Amongst the myriad research focussing on FMO, the simulation parameters have been extensively studied including temperature (related to the dephasing), and exciton trapping and recombination,[517,523,544,545,558,559] which have helped choose a set of reasonable simulation parameters,[556] as discussed. Furthermore, the consequences from the removal of a single pigment from the network have been explored which has revealed such networks exhibit a degree of robustness for EET even when the network is broken.[517,533,560–562] Finally, as briefly discussed, FMO has received considerable attention from the perspective of ENAQT, where it has been cemented as a prototypical example of biological quantum coherence, exploring how the protein environment surrounding the pigments might support EET.[522–525,527,528,563,564] In contrast to these previous inves-

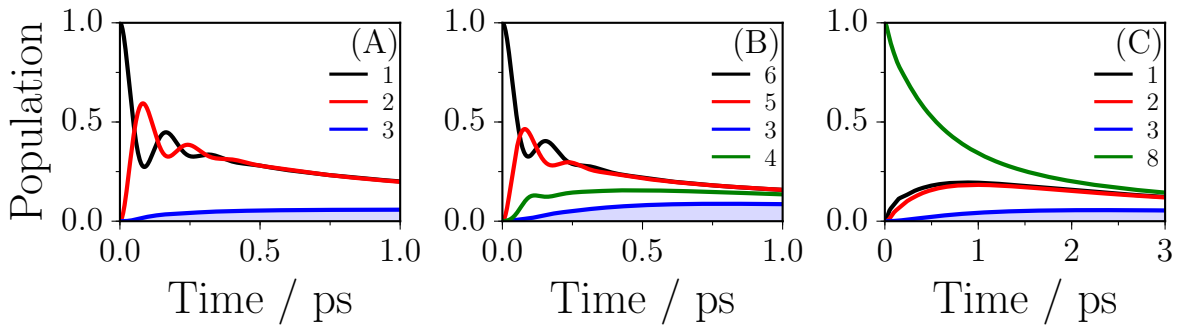

Figure 6.7 | (A) The time-dependent populations at each pigment site after the FMO PPC is initially excited at pigment 1. (B) Similarly for initial excitation at pigment 6, and (C) for initial excitation at pigment 8. The population at the sink site (pigment 3) is shown in blue. The shaded area indicates the calculated EET efficiency as given by Equation 6.11. The legend refers to pigment number. Weakly coupled pigments to the initially excited pigment are omitted for clarity, however, they are given in Appendix 8.13, up to $t_{max} = 10$ ps.

tigations, this chapter focuses on evaluating EET and its associated pathways from the perspective of robustness and optimality. Specifically, by employing the computationally tractable Haken-Strobl model, we simulate the electronic Hamiltonian of FMO in a variety of scenarios which may occur in nature, in order to evaluate how EET changes.

The simplest and most natural starting point, is calculating the time-dependent populations for each of the pigment sites over the total simulation time of 10 ps. These 'population curves', which are the graphical representation of the quantity given in Equation 6.10, are shown in Figure 6.7 for initial excitation at pigment 1, 6 and 8. For initial excitations at pigments 1 and 6, the population on the source pigment quickly flows to other strongly, electronically-coupled pigments. Some of the initial population is recovered as energy flows back and forth between strongly coupled pairs of pigments such as pigments 1 and 2 (Figure 6.7(A)), and pigments 5 and 6 (Figure 6.7(B)). In contrast, for initial excitation at pigment 8 (Figure 6.7(C)), the population flows much more slowly, as evidenced by the much shallower gradient of the initial population decay. Furthermore, there is no pronounced oscillation in the populations observed. These differences, in the time-dependent populations between the three possible initial excitation sites, are easily reconciled by the fact that the pigment 8 is only strongly coupled to pigment 1; after population flows to pigment 1, it quickly moves to other strongly coupled pigments (*i.e.* the population dynamics then follows that of Figure 6.7(A)). These populations curves accord very well with more complicated treatments of the environment which lends justification for the use of the simple Haken-Strobl model

for qualitative insight.[517,520,565–569] Integrating over the pigment 3 population returns the EET efficiency (shown by the blue shaded area of Figure 6.7(A–C)) returns, $\eta_1 = 0.770$ and $\eta_6 = 0.804$, $\eta_8 = 0.748$ for initial excitation at pigment 1, 6 and 8 respectively.

6.4.1 Robustness to network disruption

Now a benchmark has been established for this model, we move towards a more interesting question with regards to EET properties in FMO: what happens if we break up, or perturb, the network of EET pigments or couplings? For example, one can imagine removing or altering a pigment, which might represent an error in protein transcription or a larger (destructive) environmental perturbation; evaluating how EET is modified by such changes gives direct insight into core properties of EET networks like FMO, such as relating to the inherent robustness of EET. Indeed, such questions can be experimentally probed through the selective mutation of a wild type FMO complex.[570–573] Within the network-based picture adopted here, such questions are relatively simple to address; pigments can be systematically removed from the network (*i.e.* all elements of the Hamiltonian set equal to zero for the pigment in question) and the EET efficiency can be recalculated.

In our simulations of FMO, the full combinatorial space of possible pigment removals is considered, *i.e.* all single, pairs, triplets... of pigments are removed and the average EET is calculated (Figure 6.8). This procedure leads to an interesting observation; for

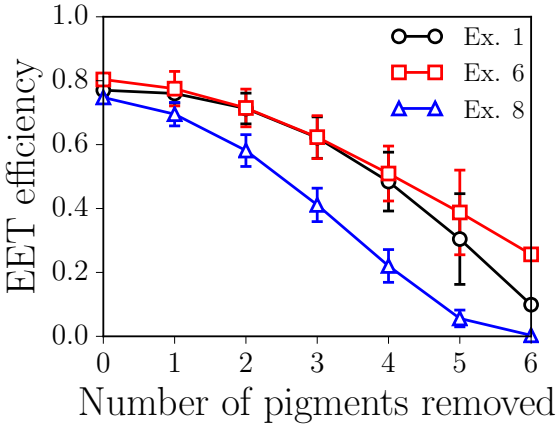

Input : Electronic Hamiltonian, $\hat{H}_{ex}$
Output: Average EET efficiency for removing i pigments
initialisation
$k = 1$
P = set of removable pigments
for $i \leftarrow 1$ **to** *length(P)* **do**
  Combinations $\leftarrow$ choose set of i elements from P
  for $j \leftarrow 1$ **to** *length(Combinations)* **do**
    $NewH \leftarrow \hat{H}_{ex}$
    $NewH \leftarrow$ delete elements resembling $Combinations[j]$
    EET$[k] \leftarrow$ calculate EET for network $NewH$
    $k = k + 1$
  end
  Calculate and store the average EET for i pigment removal
end

Figure 6.8 | (*left*): EET efficiency of FMO for a series of pigment removals. All possible unique combinations of removing pigments (singles, triples *etc.*) are considered. The source and sink pigments are never removed. (*right*): Pseudo-code for this pigment 'knock-out' procedure.

initial excitation at pigments 1 or 6, even when three pigments are removed out of the possible six (source and sink pigments are never removed), representing a loss of 50% of available pigments, EET only drops by around 20%, showing that FMO is remarkably robust to the loss of pigments. The origin of this robustness is easily explained by the presence of multiple EET pathways between the source and sink pigments, which provide an enormous redundancy in transport pathways which can be exploited in the event of pigment removal. Even when multiple pigments are removed, the interconnectivity between pigments means that EET can still continue, albeit with reduced efficiency. For initial excitation at pigment 8, EET is disrupted to a greater degree than for other initial excitations, the reason for this comes from the weak pigment-pigment couplings between pigment 8 and all other pigments, aside from pigment 1. When the strong coupling between pigment 1 and 8 is disrupted, all other pathways lead to a significantly reduced EET efficiency. The average EET efficiency therefore drops more quickly for pigment removal than for initial excitation at pigment 1 or 6. The idea of multiple pathways has already been well established,[517,566,574] however in this network-based picture employing simple and efficient quantum dynamics methods, the full extent of the robustness can be evaluated and rationalised.

Taking this 'knock-out' approach further proves useful in identifying the key EET pathways within the FMO complex. Specifically, instead of removing pigments (*i.e.* network vertices), we now consider the removal of inter-site Hamiltonian coupling elements (*i.e.* network edges). Again, this scenario can be viewed as representing fluctuations in the structure of complex, where, for example, two pigments move further away from each other and thus the coupling (*cf.* Figure 6.5) is reduced. There are 28 ($N = n(n-1)/2$; $n = 8$ pigments) couplings which can be removed. We could once again consider the combinatorial removal of couplings (*i.e.* all single removals, doubles, triples...) up to the one combination of all 28 couplings being removed, where EET efficiency drops to zero; however, because the number of possible combinations rapidly increases beyond millions of possible unique combinations, we instead choose to average our results over 1000 independent simulations where a given number (X) of couplings are randomly removed (Figure 6.9). The presence of multiple EET pathways becomes clear with these results. First, with regards to the magnitude of EET efficiency, we note that the removal of three pigments is comparable of removal of 18 coupling elements. However, we find that the removal of 18 coupling elements causes a drop in EET by $\sim$75%, and is therefore much more disruptive to EET. This finding can be explained by the presence of multiple pathways. The removal of couplings, rather than pigments, will disrupt several EET pathways simultaneously, causing a more significant drop in

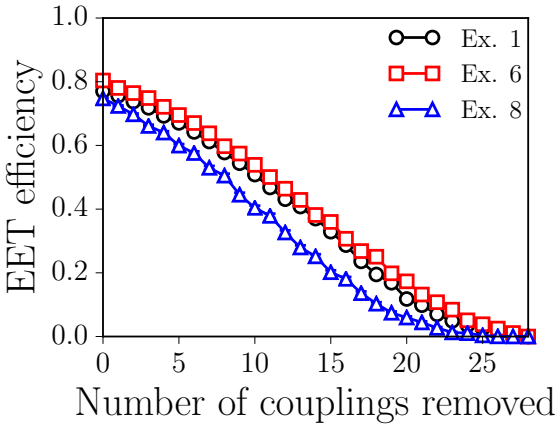

Input : Electronic Hamiltonian, $\hat{H}_{ex}$
Output: Average EET efficiency for removing i couplings
initialisation
$k = 1$
$R = 1000$ /* Number of realisations */
$N = 28$ /* Number of couplings */
$X = 7$ /* Number of couplings to remove */
for $i \leftarrow 1$ **to** R **do**
  $NewH \leftarrow \hat{H}_{ex}$
  $C \leftarrow$ [1,2,3...N]
  for $j \leftarrow 1$ **to** X **do**
    $ele \leftarrow$ choose random element from C
    $NewH \leftarrow$ set off-diagonal ele to zero
    $C \leftarrow$ remove element ele
  end
  EET[k] $\leftarrow$ calculate EET for network $NewH$
  $k = k + 1$
end
Calculate and return the average EET for N coupling removal

Figure 6.9 | (*left*): The average EET efficiency for the combinatorial removal of pigment-pigment couplings. The legend refers to the initially excited pigment. (*right*): Pseudo-code for this pigment-pigment coupling 'knock-out' procedure.

EET efficiency than if a localised pigment (and its coupling elements) was removed. Considering, as an example, the case where one coupling has been removed, specific EET pathways can be identified when the EET efficiency changes significantly from the unperturbed FMO network (Figure 6.10). For initial excitations at pigments 1 and 6, two dominant EET pathways are clearly identifiable which contribute strongly to the EET efficiency, consistent with previous work which has similarly identified at least two major EET pathways.[517] Since pigment 8 is weakly coupled to all pigments, other than pigment 1, the dominant EET pathway for initial excitation at pigment 8 follow closely those pathways identified for initial excitation at pigment 1.

A network-based approach also lends itself naturally to many network or 'graph' based analytical tools which can be used to analyse complex systems.[575,576] Perhaps the most relevant in regards to robustness and EET is the calculation of the *average pathlength* and the *network diameter*, both are standard measures of node connectivity, and are defined in the following text. Here, if two pigment sites are strongly coupled, they can be viewed as exhibiting an effective shorter pathlength between them, while weakly coupled sites can be viewed as exhibiting a longer effective pathlength. In this way, the average pathlength as well as the network diameter become indicators for the expected EET efficiency; smaller average pathlengths and network diameters of a given electronic Hamiltonian should equate to greater EET efficiency. Firstly, we transform the electronic Hamiltonian of the PPC in question to a weighted-connectivity matrix,

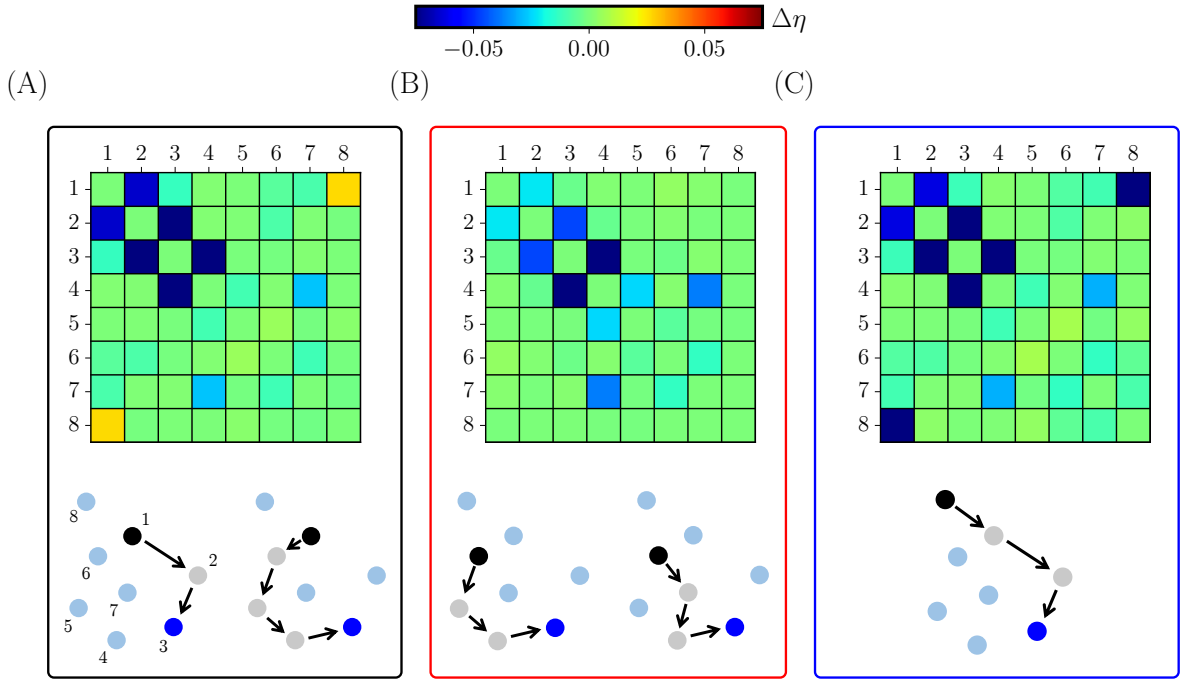

Figure 6.10 | For the case where only one coupling is removed, the coupling removed is identified and the change in EET efficiency, $\Delta\eta$, compared to the unperturbed FMO network is calculated. The axes labels correspond to the pigment-pigment coupling, *i.e.* 1 and 8 (top right of colourmap) corresponds to the coupling between pigment 1 and pigment 8. The dominant EET pathways can be identified from the specific increases (warm colours) or decreases (cold colours) in EET efficiency compared to the unperturbed FMO network, revealing different dominant pathways for each initial excitation scenario: (A) initial excitation at pigment 1; (B) pigment 6; (C) pigment 8.

where the effective distance between pigments i and j is given by

$$d_{ij} = \frac{1}{|J_{ij}|}. \tag{6.14}$$

With this definition of effective distances, the Floyd-Warshall algorithm[577,578] can then be employed to evaluate the shortest path between any two nodes (*i.e.* pigments). Applying this tool to FMO, pigments can then be removed in a combinatorial way as before; the set of shortest paths can then be calculated, and the average of these shortest paths for each set of pigment removals (singles, doubles, triples *etc.*) can be determined, referred to as the 'average pathlength' (Figure 6.11). Similarly, the longest pathway from source to sink pigment, is referred to as the 'network diameter'.

Considering initial excitations at pigment 1 and 6 first, it is immediately obvious

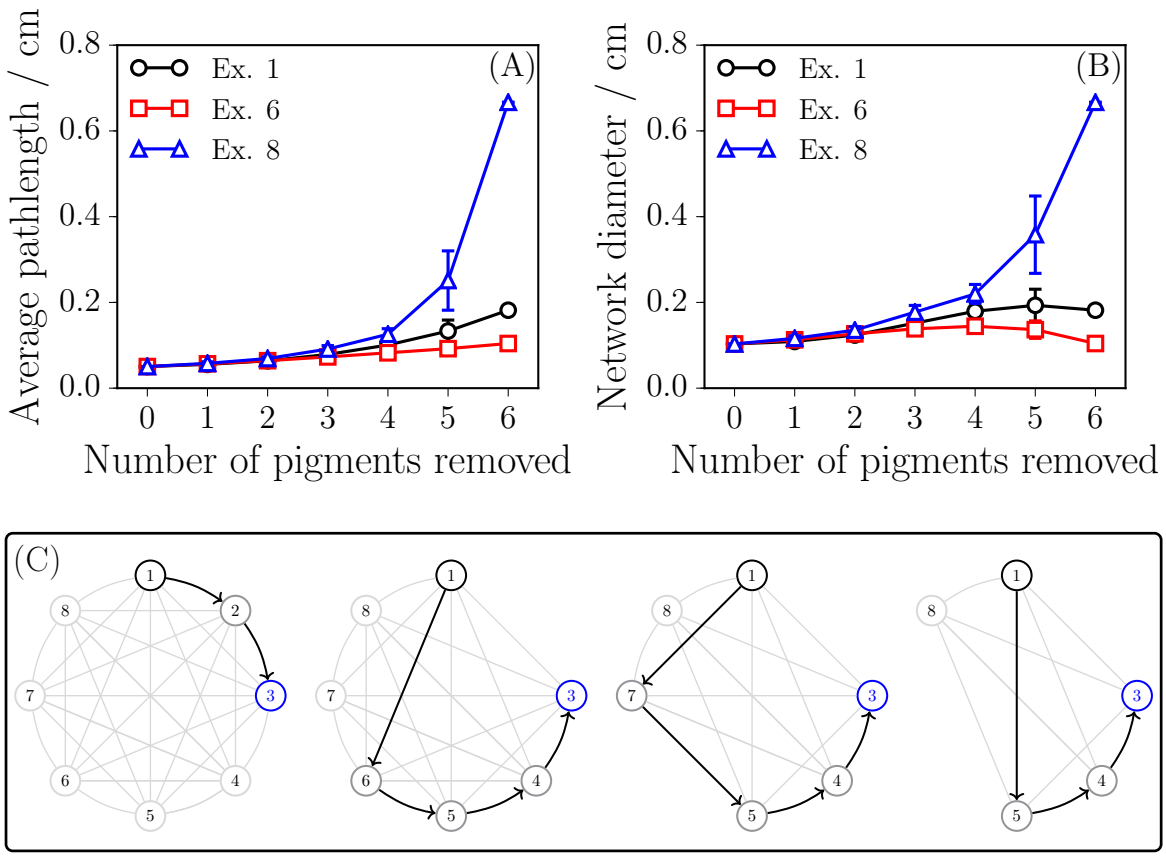

Figure 6.11 | (A) The average pathlength of the FMO network as pigments are removed from the network. (B) Similarly for the network diameter of FMO. (C) Reconstructing the shortest pathways (*i.e.* those with greatest EET efficiency) supports the identification of the dominant pathways discussed in Figure 6.10. Shown are the shortest pathways for initial excitation at pigment 1. From *left* to *right*, the first intermediate pigment (*i.e.* the most strongly coupled pigment to source pigment) is removed, and the new shortest path calculated. This procedure leads to the dominant pathways previously discussed.

that the average pathlength appears essentially unaffected when multiple pigments are removed from the FMO network. This is, once again, explained by the high degree of connectivity within the FMO network. When one path becomes unavailable there are others which have a similar pathlength; in other words, FMO consists of multiple strongly coupled pathways to the energy sink. Reconstructing the shortest path agrees with the dominant pathways observed in the coupling removal simulations (Figure 6.9). For excitation at pigment 1, the shortest path is *via* the pigments: $1 \rightarrow 2 \rightarrow 3$. Removing the intermediate pigment 2, the next shortest path is *via* the pigments: $1 \rightarrow 6 \rightarrow 5 \rightarrow 4 \rightarrow 3$. Removing pigment 6 reveals the next shortest path *via* pigments: $1 \rightarrow 7 \rightarrow 5$

$\rightarrow 4 \rightarrow 3$. Finally, removing pigment 7 reveals the next shortest path *via* pigments: 1 $\rightarrow 5 \rightarrow 4 \rightarrow 3$. The network diameter shows an equivalent trend; it remains insensitive to the loss of pigments showing there are multiple pathways which display similar EET efficiency, so when one (or more) are disrupted, EET remains viable. For initial excitation at pigment 8, the average pathlength and network diameter are much more sensitive to the loss of pigments. This comes as no surprise given that pigment 8 is weakly coupled to most pigments other than pigment 1. As such, there are fewer pathways which exhibit efficient EET.

The conclusion of these simulations is that the FMO network is generally robust to changes in the connectivity of the electronic Hamiltonian. For example, removing 50% of the pigments in the network has a relativity small impact on the overall EET efficiency. Essentially, this is a consequence of heterogeneity; several efficient EET pathways exist between source and sink pigments. The network-based picture of FMO lends itself particularly well for identifying the dominant EET pathways, where both coupling removal simulations and the application of the Floyd-Warshall algorithm help to identify the specific pathways which contribute to the observed EET in FMO.

6.4.2 Robustness to environment

EET efficiency for a global dephasing rate. The results in the previous section indicate that FMO displays a strong robustness to changes in the network, but what about the environment? The motivation from this question arises since GrSB species are well known to be thermophilic. For example, the species *Chlorobium tepidum* is found in hot springs at temperatures up to 52°C.[579] The crystal structures of such species are shown to be very similar to non-thermophilic species,[512,580,581] suggesting the FMO is robust to the environment given no special genetic adaptations are observed across the species. To investigate the effect of the environment within our simple density matrix formalism, we alter the dephasing rate, γ (*cf.* Equation 6.9). Large dephasing rates approximate the effect of a strongly interacting environment with the pigments, such as would be expected in high temperature environments for example. We continue to consider a global dephasing rate, where γ is the same for each pigment. In other words, we assume the interaction between the environment and pigments is identical, *i.e.* $\gamma = \gamma_i$, for all pigments. The contrary to this, a local dephasing rate, is considered later in this section.

Figure 6.12 shows the effect of changing the global dephasing rate of FMO. It is clear from this that for initial excitations at pigments 1 and 6, EET remains efficient over two orders of magnitude from $\sim$40 cm^{-1} to $\sim$3000 cm^{-1}, outside of this range,

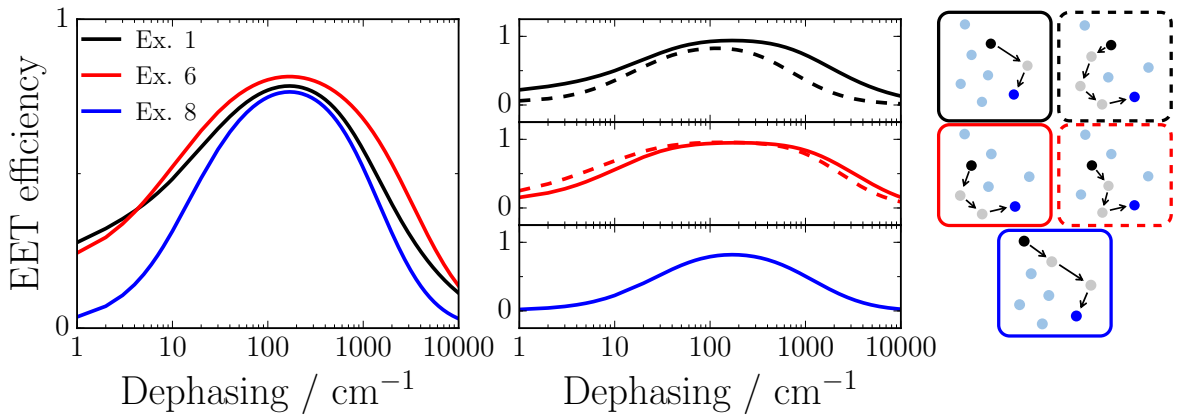

Figure 6.12 | (*left*): The response curves of EET efficiency for a changing environmental dephasing rate applied to all pigments. The legend refers to the initial excitation. (*right*): The environment response curve for each initial excitation is shown to be the addition of unique response curves from the dominant EET pathways identified in Figures 6.10 and 6.11.

EET efficiency quickly drops off. This so-called ENAQT, discussed in this chapter, has been noted for the seven-site FMO model.[523] Here, a weak dephasing is shown to increase the rate of EET, whilst the extreme of high dephasing results in the loss of exciton localisation, and thus decreased EET efficiency. Excitation at pigment 8 shows a similar behaviour. However, the range of which ENAQT remains constructive to EET efficiency is reduced.

An interesting result of these environment-response curves is that they are the superposition of the response curves for the individual dominant pathways observed for each initial excitation (Figure 6.10 and Figure 6.11). Considering the environmental dephasing on networks which comprise only of the source, sink and the intermediate pigments of each dominant pathway observed in Figures 6.10 and 6.11,* shows that each pathway exhibits its own unique environment response curve, spectrally shifted from one another, resulting in a broader overall response. Since there are two dominant pathways observed for initial excitation at pigments 1 and 6, the overall robustness to environmental dephasing is much greater than for initial excitation at pigment 8 which only has one dominant pathway.

We conclude that, as was shown for the robustness to network changes, that the heterogeneity of the network is a major factor which is responsible for FMO's resilience to environmental conditions such as temperature.[508,579,582]

*For example, for the dominant pathway $1 \rightarrow 2 \rightarrow 3$, pigments 4, 5, 6, 7 and 8 are removed for the network, and the environmental response curve is calculated.

EET efficiency for a local dephasing rate. So far we have shown that FMO displays robustness to changes in the environment on a global scale, *i.e.*, when the environment interacts with each pigment equally. Next we investigate the effect of different dephasing rates on pigments. Considering first the general role of heterogeneous dephasing rates on EET efficiency, we simulate the FMO Hamiltonian in the presence of different dephasing rates for each pigment. Each dephasing rate is sampled from a log-uniform probability distribution in the range $\gamma_i \in [1\ \text{cm}^{-1}, 10\ 000\ \text{cm}^{-1}]$ and then the EET efficiency calculated for initial excitations at pigment 1, 6 and 8. Figure 6.13(A) shows the histogram of EET efficiencies calculated for the set of 2000 randomly generated Hamiltonians. For all initial excitations (pigment 1 and 6 in particular) show a skew towards lower EET efficiencies. In light of the finding from the previous robustness simulations (Figure 6.12), it is perhaps not surprising this is the case given there are a range of dephasing values which lead to a lower EET within the distribution they are drawn from. In particular we find that the Hamiltonians which display a significant drop in EET efficiency compared to the FMO Hamiltonian with a global dephasing rate of 100 cm^{-1}, tend to have a 'poor' dephasing rate (in terms of the region of optimised EET efficiency in Figure 6.12, *i.e.* $100\ \text{cm}^{-1} > \gamma_i > 3000\ \text{cm}^{-1}$) on the pigments which contribute to the dominant EET pathways. Clearly, local dephasing effects can contribute significantly to the overall EET efficiency, echoing the conclusions from previous work.[545]

The second investigation of the role of local dephasing was to systematically assign a 'poor' dephasing rate to pigments to assess the change in EET efficiency. Specifically we selected a 'poor' dephasing value of 10 cm^{-1} for the chosen pigments; for all other pigments we continued to use a dephasing of 100 cm^{-1}. What follows is an identical procedure to that set out for the 'knock-out' studies described in the previous section. For each combination of singles, doubles, triples, *etc.* of pigments, those pigments are given the 'poor' dephasing rate, all others are given the standard dephasing. One addendum to the previous combinatorial studies is that both source and sink pigments are now also considered, whereas previously they were excluded from the combinatorials. Figure 6.13(B) demonstrates the conclusion reached with Figure 6.13(A); the probability of generating a Hamiltonian which exhibits a reduced EET efficiency (compared to original simulated FMO Hamiltonian) is high.

Finally, the last set of local dephasing simulations involved considering the local dephasing rate acting on only the source and sink pigments. The rationale for this is that these pigments lie close to the chlorosome baseplate and RC respectively. As such one might expect the local dephasing rate at these pigments to vary significantly

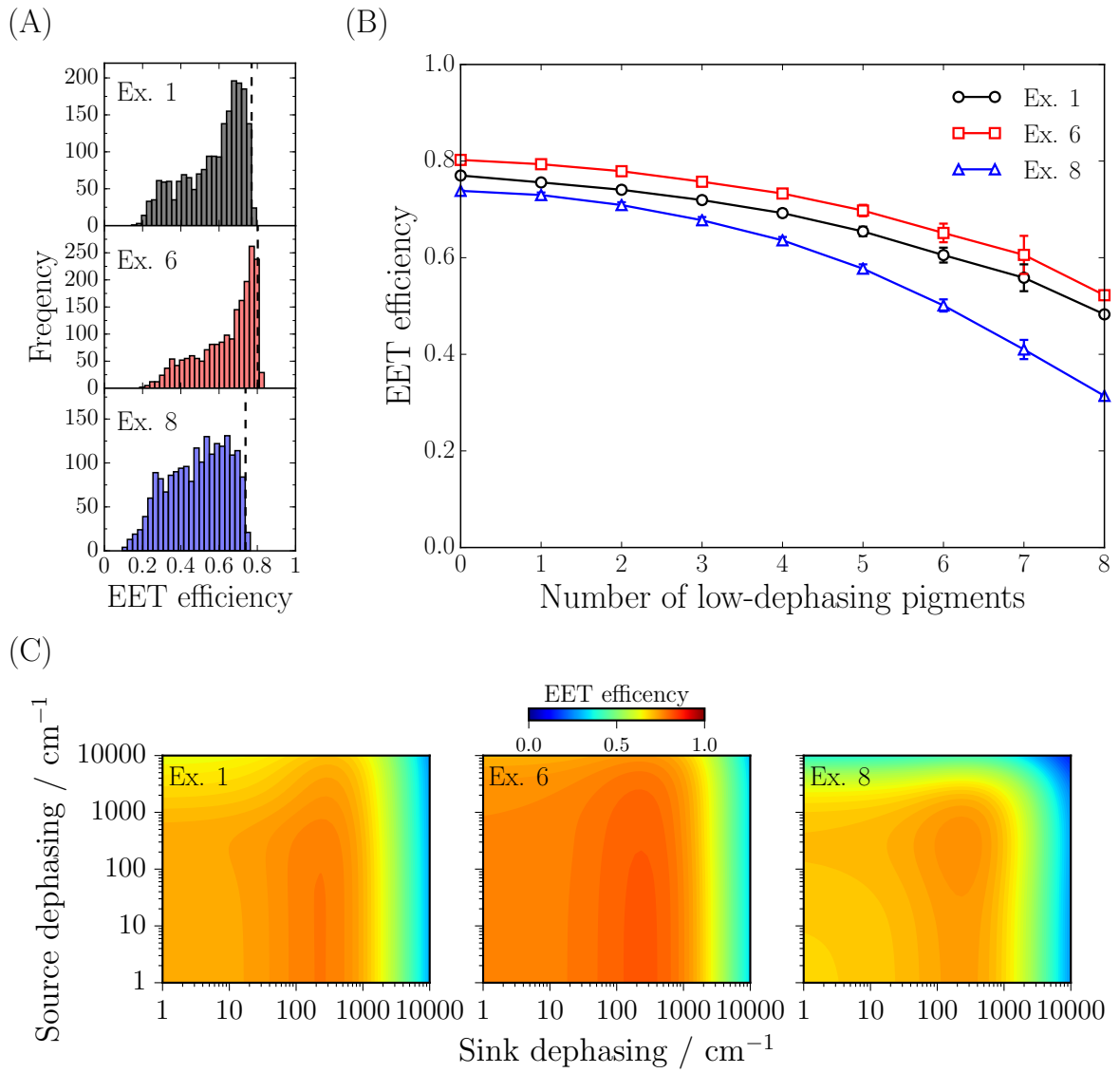

Figure 6.13 | (A) Histograms of EET efficiency for the 2000 generated Hamiltonians which are given randomly sampled local dephasing rates. The dashed line represents the EET efficiency of the original FMO Hamiltonian with dephasing rate of $\gamma_i = 100$ cm^{-1}. (B) EET efficiencies calculated in simulations where increasing numbers of pigments are given the 'poor' dephasing rate of $\gamma = 10$ cm^{-1}. (C) EET efficiency as a function of local dephasing rate applied only to the source and sink pigments; all other pigments are given a dephasing rate of $\gamma = 100$ cm^{-1}. Ex. 1, Ex. 6 and Ex. 8 refer to the initial excitation pigments.

compared to the intermediate pigments involved in EET. For these simulations, all intermediate pigments are given a dephasing rate of $\gamma = 100$ cm^{-1}, whilst source and sink pigments vary between $\gamma \in [1\text{ cm}^{-1}, 10\,000\text{ cm}^{-1}]$; the resultant EET efficiencies are shown in Figure 6.13(C). We find that initial excitation at pigment 1 and 6 display little

sensitivity to the local dephasing rates at source or sink pigments. Initial excitation on pigment 8 on the other hand shows a much greater sensitivity to local dephasing rates. The origins of these observations are found in the population decay curves (Figure 6.7). For initial excitation at pigments 1 and 6, population quickly decays away from the source pigment, whereas this decay of source pigment 8 is significantly slower. As such, the longer the time the population spends on the source pigment, the greater the effect the local dephasing rate will have.

6.4.3 Efficiency of EET in FMO-like networks

Up to now, the simulations we have performed only highlight the extent to which FMO is robust to changes in the network (the electronic sub-system) and the environment (global and local protein interactions with the pigments). The final investigation of FMO is to attempt to answer the question whether FMO as a whole is in any way optimised for EET efficiency. Indeed, it has been shown FMO is remarkably efficient as well as robust to perturbations in the network and environment. Of course, the most efficient system would resemble a simple, one-dimensional molecular wire where pigments are positioned closely together with a large excited state transition dipole-dipole interaction. However, such a low-dimensional molecular wire would not exhibit the same robustness as seen so far in FMO. Furthermore, while rapid EET is clearly beneficial for energy synthesis in the RC, the RC performs charge separation at a rate of $\sim$1 ps^{-1}, thus EET at a faster rate than this provides no evolutionary advantage, and, instead, could lead to the damage of photosynthetic machinery.[583–585]

With this in mind, along with the observation that the FMO structure is so well conserved across different GrSB species,[512,539,579,580] we limit ourselves to assessing EET efficiency in FMO-like Hamiltonians. To generate FMO-like Hamiltonians, Gaussian random noise is added to all elements of the electronic Hamiltonians. The Gaussian distribution for off-diagonal elements used was $\mathcal{G}(0, \sigma_{ij})$ and the Gaussian distribution for diagonal elements (pigment electronic excitation energies) was $\mathcal{G}(0, \sigma_{ii})$. The standard deviations for these distributions were determined as follows. For the off-diagonal elements, the mean difference in coupling strengths from different GrSB species (*Chlorobium tepidum* and *Prosthecochloris aestuarii*),[550] was taken giving an average value of 3.5 cm^{-1}. For the site energies, the standard deviations were determined by empirical analysis of FMO optical spectra;[539] specifically, the values were: $\sigma_{11} = \sigma_{33} = \sigma_{44} =$ 25.5 cm^{-1}, $\sigma_{22} = 42.5$ cm^{-1}, $\sigma_{55} = \sigma_{66} = \sigma_{77} = \sigma_{88} = 51.0$ cm^{-1}.[†] These standard de-

[†]Note that, because the previous work studied the seven-site FMO model, we have assumed that $\sigma_{88} = 51.0$ cm^{-1}.

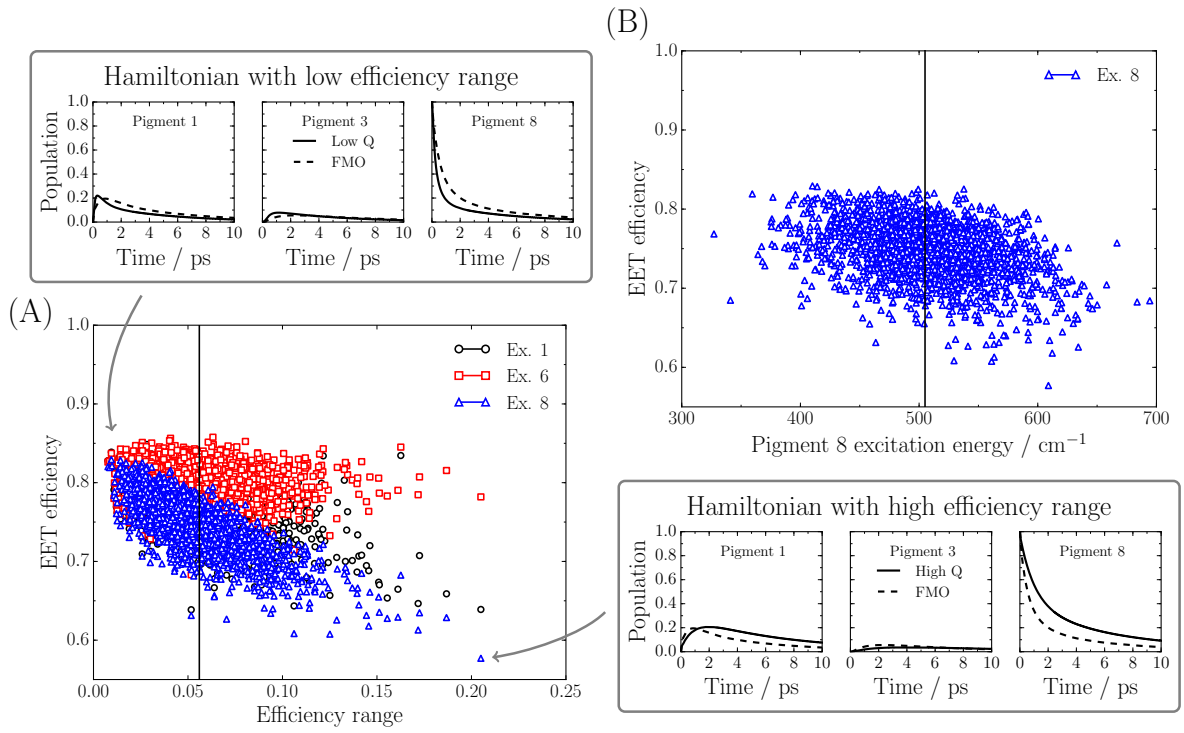

Figure 6.14 | (A) EET efficiency of the 2000 generated FMO-like Hamiltonians, using Gaussian random noise applied to all elements of the electronic Hamiltonian. The efficiency range (Q) is used as a measure of how similar the EET efficiencies of the three initial excitations are. The vertical line denotes the efficiency range of the unperturbed FMO network ($Q_{\mathrm{FMO}} = 0.056$). An example of the population dynamics for FMO-like Hamiltonians which display a low efficiency range, and an example of high efficiency range, show how sensitive pigment 8 is to the addition of this Gaussian noise. (B) EET efficiency as a function of the excitation energy of pigment 8.

viation values were used to generate new FMO-like Hamiltonians to assess the impact of network changes on the EET efficiency. In total 2000 new FMO-like Hamiltonians were generated and used throughout the proceeding investigations. It is important to note that this procedure may lead to some physically unrealistic Hamiltonians, but the majority will have modified site energies and pigment spatial distributions which still resemble the unperturbed FMO Hamiltonian.

Firstly, for each generated Hamiltonian, we calculated the EET efficiency for initial excitations at pigment 1, 6 and 8, see Figure 6.14(A). Here we use the statistical range of the calculated EET efficiencies for different initial excitations, Q, as our measure. This captures information about the whole network as it is a function of all three initial excitations, which we can easily compare to the unperturbed FMO which has a range of

$Q_{\mathrm{FMO}} = 0.056$. We observe some clear trends in the EET efficiencies for the generated Hamiltonians. Firstly, for those which display the largest EET efficiencies, they do so for initial excitations at pigment 1 and 6, at the expense of a reduced EET efficiency for initial excitation at pigment 8. Indeed, further analysis of the generated Hamiltonians show that many of these Hamiltonians are characterised by a large excitation energy for pigment 8, see Figure 6.14(B). As demonstrated in Figure 6.7(C), the population dynamics of EET after excitation at pigment 8 is characterised by a slow, incoherent decay which is slower for large excitation site energies. For low Q values, the EET efficiency for excitation at pigment 8 is faster resulting is a greater EET efficiency. Both of these cases are shown in Figure 6.14.

This analysis highlights an interesting feature of the unperturbed FMO network. The efficiency range is $Q_{\mathrm{FMO}} = 0.056$, where EET efficiency remains similar for all three initial excitations scenarios. This suggests that while clearly it is possible to generate FMO-like Hamiltonians which display a better EET efficiency for any one initial excitation, the FMO network appears to favour less efficient individual pathways, but each pathway having a similar efficiency, a marker for robustness highlighted in the previous two sections.

6.5 The light-harvesting complex II

A network-based view of EET can be trivially extended to larger PPCs,[586] as long as the electronic Hamiltonian can be constructed. LHC-II, as found in green plants, is another well-studied PPC for which an electronic Hamiltonian is available. The specific LHC-II we consider is from the spinach plant (*Spinacia oleracea*), and consists of a trimer of 14 chlorophyll pigments (both chlorophyll-*a* and chlorophyll-b pigments) distributed in ring-like structures embedded inside a protein scaffold (Figure 6.15(A) and 6.15(B)).[587] Here, the pigment excitation energies were determined through DFT electronic structure calculations, and the pigment-pigment electronic couplings were determined based on the known LHC-II crystal structure.[587] The total electronic Hamiltonian can then be represented in the same way as in FMO (Equation 6.1). Overall, our approach to simulating EET dynamics in LHC-II is then identical to that employed above to study FMO. The only difference is that the source pigment is now considered to be either pigment 1 or pigment 8 in LHC-II, and the energy sink is pigment 4 (Figure 6.15(C–D)). These assignments are made based on the pigment excitation energies and their positions relative to the RC. In what follows only the monomer of the LHC-II trimer is considered.

As with FMO, the first simulation is to determine the time-dependent populations for each pigment (Figure 6.16). Compared to the population curves for FMO, the first observation is that the decay of the initial excited pigment is much slower. We

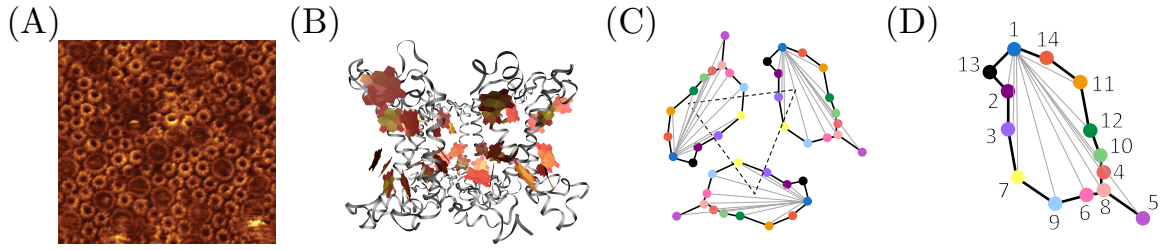

Figure 6.15 | The different length-scales involved in the LHC-II complex. (A) Atomic force microscope image of photosynthetic complexes within the membrane of *Rhodospirillum photometricum*.[588] The small circles of diameter ∼2 nm are the LHC-II complexes, whilst the large circles with diameter ∼5 nm are the LHC-II photosystems. Image adapted from Scholes *et al. Nature*, 2011.[496] (B) The LHC-II complex consists of three (almost) identical monomers. (C) Both the monomeric and trimeric structures are considered. The network-view of the entire LHC-II trimer. (D) A single monomer of the LHC-II complex, consisting of 14 pigments, with the number scheme used throughout this work.

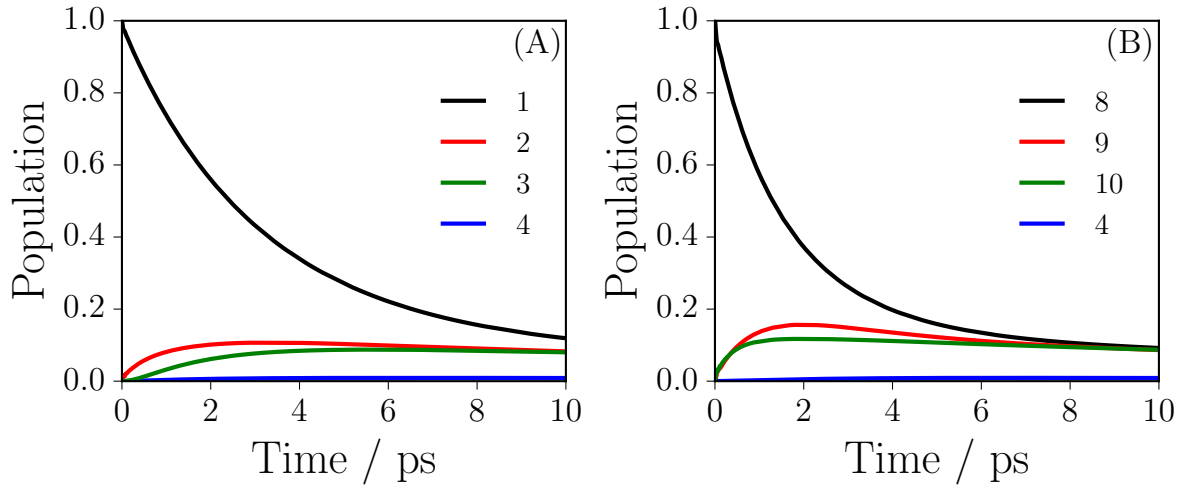

Figure 6.16 | (A) The time-dependent populations at each pigment site (only strongly coupled pigments shown, see Appendix 8.14 for all pigment populations) after LHC-II is initially excited at pigment 1. (B) Similarly for initial excitation at pigment site 8. The population at sink site (pigment 4) is shown in blue.

find that it takes several ps for the majority of the population to move off the initial pigment. This observation may be explained by the generally weaker pigment-pigment couplings in LHC-II compared to FMO ($|J_{ij}|$ ~8 cm^{-1} *vs.* $|J_{ij}|$ ~24 cm^{-1}), meaning that EET is generally slower in LHC-II. This is also highlighted in the calculated EET efficiencies, found to be $\eta_1 = 0.153$ and $\eta_8 = 0.148$ for initial excitation and pigment 1 and 8, respectively, compared to FMO's $\eta_1 = 0.770$, $\eta_6 = 0.804$ and $\eta_8 = 0.748$ for initial excitations at pigment 1, 6 and 8, respectively. In general, this result is unsurprising; the LHC-II monomer is much larger than the FMO monomer, while the pigments are very similar in structure, resulting in smaller average electronic couplings between pigments, and thus an overall lower rate of EET.

6.5.1 Robustness to network disruption

As with FMO, a systematic approach of removing pigments from the network, removing pigment-pigment couplings, and recalculating the resulting EET efficiency can be applied (Figure 6.17). For both initial excitation sites, LHC-II shows a high degree of robustness to the loss of pigments, as was found in the case of FMO. Notably, initial excitation at pigment 1 shows a greater degree of robustness; for example, the loss of 50% of the available pigments results in a drop in EET by around 10% whereas the drop in EET for initial excitation at pigment 8 is around 30%. First, the overall robustness

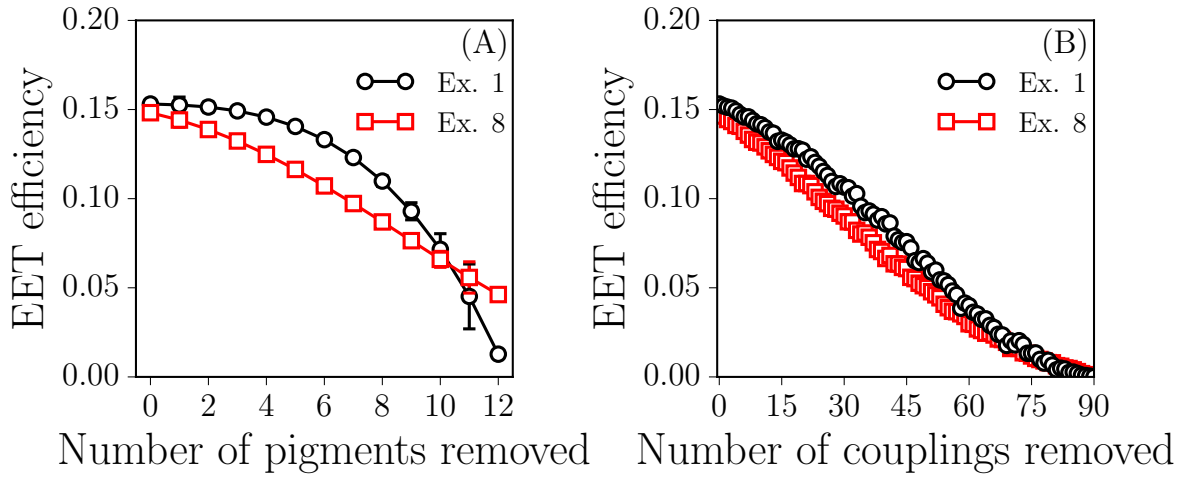

Figure 6.17 | (A) The average EET efficiency for the combinatorial removal of pigments (except for source and sink pigments) from the LHC-II complex. (B) The average EET efficiency for the combinatorial removal of pigment-pigment couplings. The legends refer to the initially excited pigment.

can once again be attributed to the presence of multiple pathways which support EET in the event of the loss of pigments. The greater degree of robustness observed for initial excitation at pigment 1 can be explained by the position of pigment 8 relative to the sink pigment 4 (Figure 6.15(D)). Pigment 8 resides close to pigment 4 and has weak electronic couplings to its surrounding pigments. This results in fewer efficient EET pathways, manifesting in a quicker drop in EET as pigments are removed from the network. The removal of coupling elements, on the other hand, shows little difference and follows a similar trend to FMO, whereby the PPC appears much less robust to the removal of couplings than the pigments themselves. For example, removal of 63 couplings (equivalent to the loss of 6 pigments) shows a reduction in EET by around 60%. Once again, this trend may be attributed to the disruption of multiple pathways simultaneously.

We once again exploit the network-based view of the LHC-II PPC to calculate the average pathlength and network diameter. Consider the average pathlength first (Figure 6.18(A)). As with the FMO monomer, we see that this measure is reasonably insensitive to the removal of pigments for both excitation sites considered; many sites must be removed before any significant change in the average network pathlength is observed. This observation is consistent with several strongly-coupled EET pathways in the PPC, just as was seen for FMO (Figure 6.11); as a result, removing a few network nodes will 'turn off' some EET pathways, but other strongly coupled paths remain,

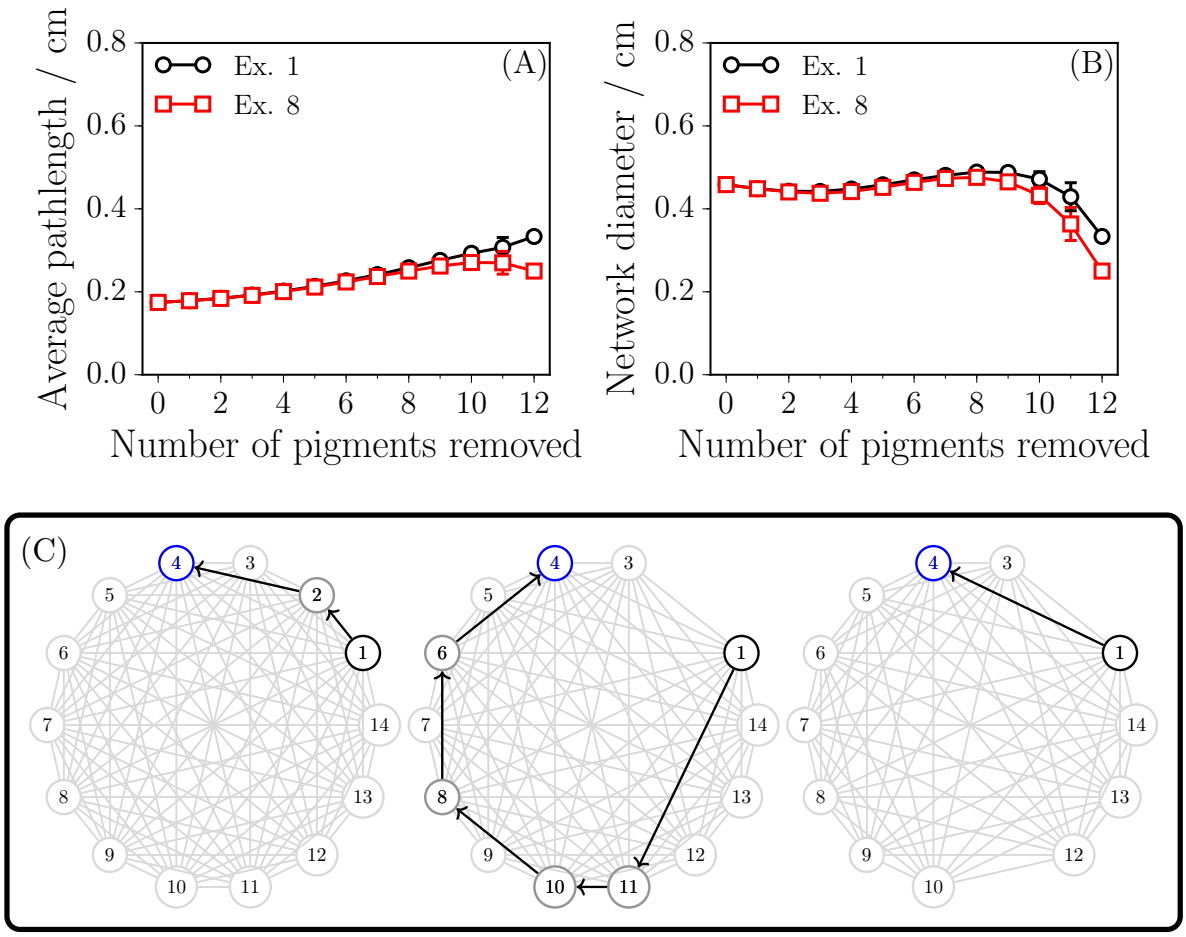

Figure 6.18 | (A) The average pathlength of the LHC-II network as pigments are removed from the network. (B) The weaker pigment couplings present in the LHC-II monomer display a greater sensitivity for chromophore knock-out beyond the removal of 9 pigments. (C) Shown are the shortest pathways for initial excitation at pigment 1. From *left* to *right*, the first intermediate pigment (*i.e.* the most strongly coupled pigment to source pigment) is removed, and the new shortest path calculated.

leading to inherent robustness, as observed in Figure 6.17. We note, however, that the mean pathlength for the LHC-II monomer is always greater than FMO, which implies EET is generally less efficient according to Equation 6.10. Reconstructing the route of the shortest path reveals two dominant EET pathways (Figure 6.18(C)): the first is the shortest path of the unperturbed LHC-II; the second is the shortest path after pigment 2 has been removed from the network; the third is the shortest path after pigment 11 is removed. It is worth noting that the average pathlength for LHC-II is larger than that of FMO, consistent with the generally weaker electronic couplings between pigments,

and thus the slower rate of EET observed throughout these simulations.

A similar observation can be made for the network diameters up to the removal of 9 pigments. Beyond the removal of 9 pigments, the LHC-II monomer shows marked sensitivity, an observation which may be understood based on the weak average inter-pigment couplings in LHC-II displays compared to those in FMO. The network diameter, like the mean pathlength, highlights the presence of less strongly coupled pigments in LHC-II compared to FMO; in particular, LHC-II always has a larger network diameter than FMO. However, the conclusion from all of these sets of simulations is quite transferable; the average pathlength and network diameter of both PPCs considered in this work are found to be reasonably insensitive to the removal of pigments, up to a certain point. This relatively constant nature of EET paths through the network emphasises the existence of multiple EET paths with comparable couplings; in short, our results reinforce the idea of inherent network redundancy in both PPCs considered here. A final point is the scalability of these network tools. The identification of dominant pathways through the coupling knock-outs for FMO (Figure 6.10) would be much more difficult in this case and indeed quickly scales in number of computations for the number of pigments. Instead these network tools can be trivially applied to very large systems with essentially no modification.

6.5.2 Robustness to environment

Once again, these simulations have, so far, only considered changes to the network itself, through the loss of pigments or pigment-pigment coupling. We now consider environmental perturbations, investigated through changing the global dephasing rate and subsequently recalculating the EET efficiency. The results of these simulations are shown in Figure 6.19. Notably, the width of the EET response curves for LHC-II are much narrower than that of the FMO complex (Figure 6.12). This can once again be explained by the average coupling strength of FMO being much stronger than in the LHC-II monomer. Both FMO and LHC-II, in general, display broad response curves to a changing environmental dephasing rate; this response, which arises due to the interaction between exciton transport and trapping, as noted previously, demonstrates that these PPCs exhibit efficient EET across a broad range of dephasing rates, again demonstrating an inherent robustness to environmental fluctuations. Notably, the typical range of dephasing rates over which efficient EET is observed is consistent with the experimentally-observed dephasing rates of typically 100 cm^{-1}. Like FMO, the broad nature of the response curves indicate LHC-II is robust across a range of thermal environments.

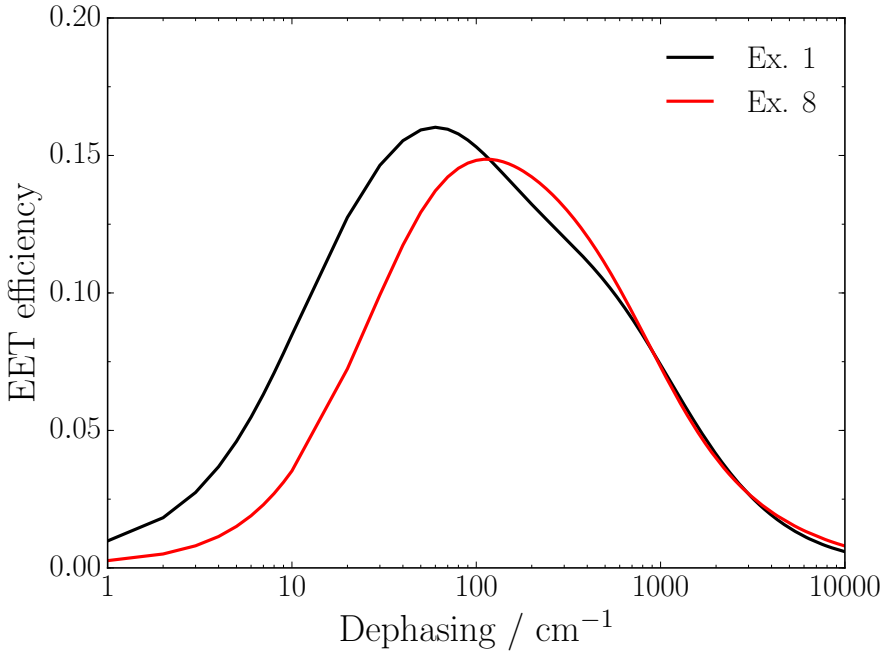

Figure 6.19 | The response curves of EET efficiency for a changing environmental dephasing rate applied to all pigments. The legend refers to the initial excitation.

6.5.3 Including inter-monomer effects: The LHC-II trimer

The entire LHC-II trimer can be simulated by including the inter-monomer couplings in the electronic Hamiltonian. Adding in the other two monomers to form the native LHC-II trimer shows a pronounced change to the network. For excitation at pigment 1 (Figure 6.20(A)), the population decays much faster than the isolated monomer (*cf.* Figure 6.16(A)), a feature which can be understood by noting the introduction of an additional strong couplings to pigment 9 of neighbouring monomers (Figure 6.20(A), purple dashed line). In contrast, for initial excitation at pigment 8 (Figure 6.20(B)), the additional inter-monomer couplings are generally smaller than the intra-monomer couplings and so the dynamics appear essentially unchanged relative to the LHC-II monomer.

We can extend these studies of the LHC-II monomer to consider the effect of the additional EET pathways available when other LHC-II monomers are available, as in the LHC-II trimer. Here, we assume that initial excitation still takes place on either pigment 1 or pigment 8, on just one of the monomers. However, *each* LHC-II monomer has an energy sink at pigment 4 with identical trapping rates. Thus population is allowed to flow from the initially excited monomer, to the other two monomers, which

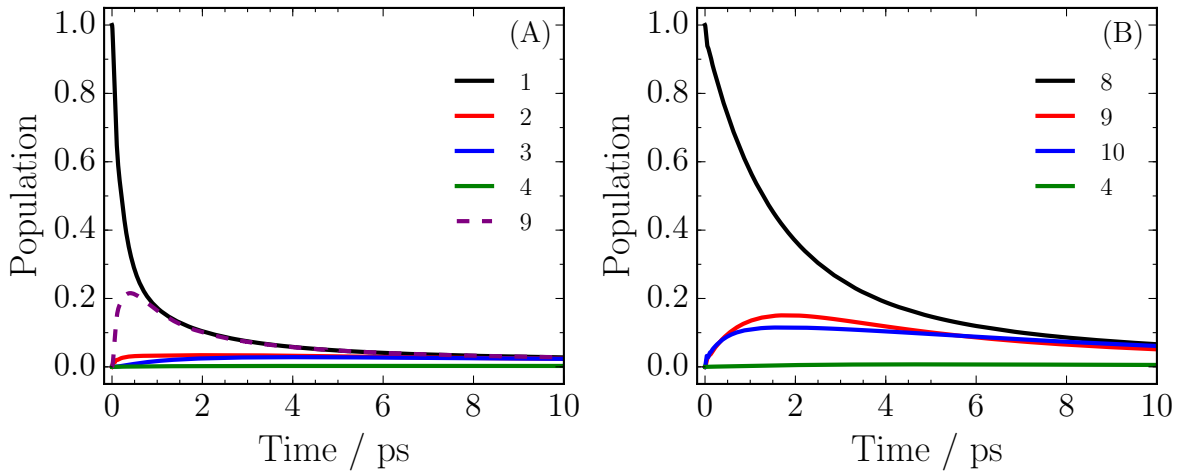

Figure 6.20 | LHC-II trimer with excitation on one monomer at pigment 1 and pigment 8 respectively. For this system, a large inter-monomer coupling allows energy to flow from pigment 1 of one monomer to pigment 9 of a neighbouring monomer (purple dashed line).

can trap population at their respective pigment 4 sinks (*i.e.* the trimer has one source and three identical sinks). The reported EET efficiency is calculated as the sum of the individual EET efficiencies of each monomer. Here, an increasing number of couplings (N) are removed from the full LHC-II trimer electronic network, and the EET efficiency is recalculated, as in our previous investigations of FMO and the LHC-II monomer. However, instead of averaging 1000 simulations of randomly removed edges to sample the total combinatorial space, we apply an additional restriction. In particular, the largest coupling is removed first, followed by the two largest and then the three largest, and so on, continuing up to the N largest couplings. The results of these simulations are shown in Figure 6.21.

Specific increases and decreases in the EET efficiency are observed for the particular removal of couplings between the pigment of one monomer and the pigment of another, for example when $N = 1$, 6, 25 or 41 highlighted in Figure 6.21. In these simulations the effect of removing specific strong coupling elements on the EET efficiency can be directly mapped onto the LHC-II trimer structure. In the case of the removal of the largest coupling (*i.e.* $N = 1$) from the electronic Hamiltonian matrix which couples two of the LHC-II monomers ($\hat{\mathrm{H}}_{cp}^{12}$) we see that EET increases. We find that the removed coupling element connects pigment 1, the initial excitation pigment on one monomer, and pigment 9 of the third monomer (consistent with the fast population decay shown in Figure 6.20(A)); when removing this coupling element, EET efficiency increases because

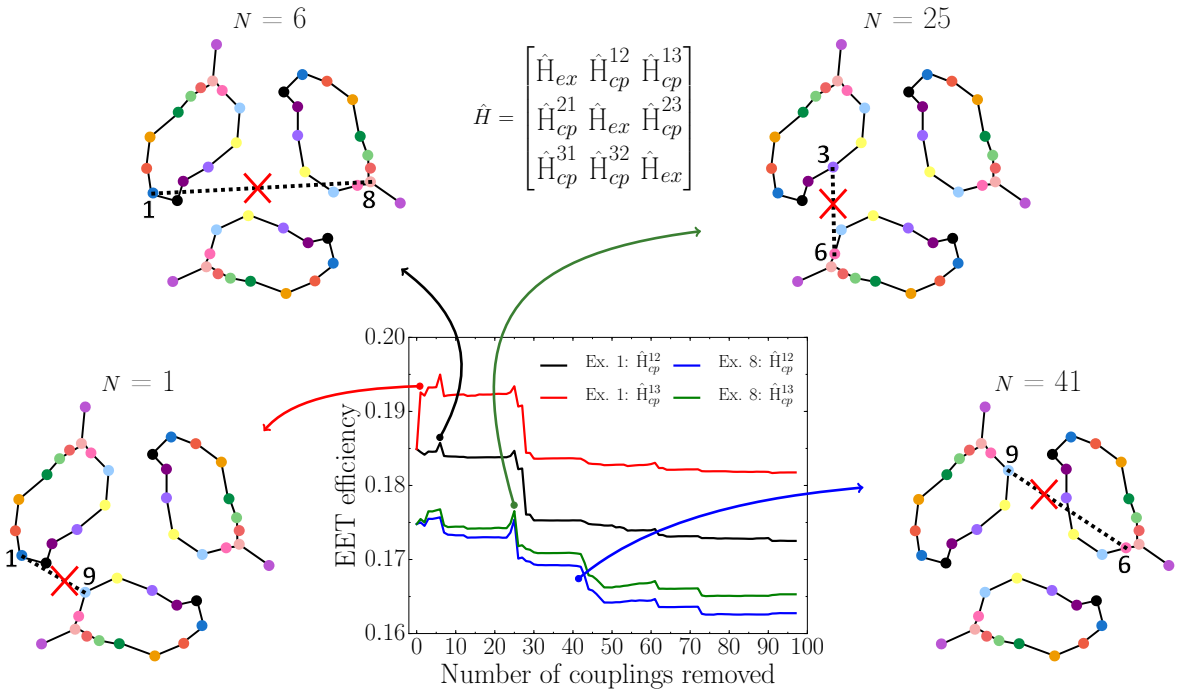

Figure 6.21 | EET efficiency for LHC-II trimer networks with an increasing number of the largest couplings between pigments in different monomers removed; in other words, increasing numbers of vertices (N) are removed from the inter-monomer Hamiltonian matrices $\hat{H}_{cp}$ (superscripts denote monomer number). Specific cases of increases or decreases in EET efficiency for initial excitation at pigment 1 or pigment 8 are highlighted; we also highlight the coupling element responsible in the cartoon schematics of the LHC-II trimer system. The total EET is the sum of the EET calculated for each LHC-II monomer.

the removed pathway is less efficient, given that it is further from the sink site of the first monomer (and no closer to the sink of the third monomer in terms of coupling strength). On the other hand, for excitation at pigment 8, the removal of the 41 largest couplings ($N = 41$), results in a large drop in EET (blue line in Figure 6.21). This decrease in EET efficiency is traced to the removal of the coupling between pigment 9 of the first monomer and pigment 6 of the second monomer. This pathway provides a route to the sink site of the third monomer, so its removal reduces EET efficiency. Similar observations are seen for other values of N, as illustrated in Figure 6.21.

6.6 Discussion and conclusions

This chapter began with a brief overview of photosynthesis and its evolution into the highly efficient and specialised biochemical pathway we observe today. The role of PPCs

is highlighted for their dominant contribution to the overall efficiency of the transfer of electronic energy to the RC, where electronic energy is converted into chemical energy; this is clearly one of the most fundamental processes required for life on Earth. PPCs consist of a set of light-absorbing pigments, held within a protein scaffold, which are electronically excited after absorption of light within the photosynthetic supercomplex. We have discussed EET in two of the most widely studied PPCs, namely the FMO complex and LHC-II. We have also outlined the mathematical description of these biological complexes as a simple network of vertices (the pigments) and edges (the electronic coupling between pigments). The protein scaffold is accounted for through a simple Markovian 'white noise' approach which reproduces the qualitative dynamical behaviour of these complexes. Within this network picture, it is possible to identify several attributes of the complexes which provide the robustness to network disruption, predominantly through the systematic deletion of pigments and their corresponding electronic couplings.

For the first time, the full extent of FMO robustness has been investigated by combining quantum dynamics simulations within a network-based view of EET. Importantly, we have demonstrated several features of FMO which lead to efficient and robust EET. Firstly, the extent to which FMO is robust to disruption in its network shows remarkable resilience to the removal of pigments. Up to 50% of the available pigments can be removed and EET remains highly efficient. The origin of this robustness is found to come from the existence of multiple efficient EET pathways which provides redundancy in the event of the loss of pigments. We have also shown that FMO displays robustness to environmental fluctuations, understood once again through the multiple available EET pathways, each of which contribute to the overall robustness. The final set of investigations were to assess the optimality of FMO with respect to EET. Surprisingly, we found that there are a number of FMO-like networks which display better efficiency, but these have the drawback of a decreased robustness. FMO instead displays, while not optimal, good efficiencies across multiple pathways, which could be considered redundancy measures, hence increased robustness.

We then considered the more complicated PPC, LHC-II. Both its monomers and its trimer were considered. A number of robustness simulations conclude that, as with FMO, LHC-II displays a surprising robustness to network disruption and environmental perturbations. We note that it appears less robust to such scenarios compared to FMO, predominately as a consequence of the weaker pigment-pigment couplings in this larger (spatially) PPC.

Overall, these studies highlight the power of this network analysis of biological

complexes, where a large variety of a system properties can be assessed with a very tractable computational model. Although this approach provides interesting insights into the EET features of biological complexes, this type of analysis can easily be imagined as a 'screening' test to aid in the design of any related networks of chromophores such as those found in artificial solar cells or photoinduced catalytic systems.[589] The results of this simple model are qualitative yet computationally tractable; this approach therefore enables a large number of quantum dynamics simulations to be performed quickly, as required if one is interested in addressing questions relating to construction of large EET networks. Going beyond this simple effective-environment approach, including explicit correlation between the electronic Hamiltonian and the environment in a computationally-simple manner, is the next step in modelling these systems.

Finally, we note that there are many questions relating to biological PPCs which simple modelling studies, such as that considered here, cannot address in a broader biological context. For example, why are the complexes highly conserved across species as found with FMO in GrSB which are found at very different levels of environmental stress?[582] Are these complexes optimised for any one particular characteristic such as the rate of EET or robustness to damage, or is it optimised for some compromise between these requirements? It seems likely that such broader questions can only be fully addressed by a coherent strategy, incorporating both experimental biological and spectroscopic studies, as well as computation.

Chapter 7

Conclusions and outlook

7.1 Scope of thesis

This thesis introduced two subject areas of study, biological photoprotection and photosynthetic pigment-protein complexes. Both these areas may be understood from the perspective of electronic energy transport. In biological photoprotection, this involves the dissipation of electronic energy through a range of photochemical pathways in order to deactivate a photoexcited molecule. For pigment-protein complexes, electronic energy is transported through directed pathways to provide energy to the reaction centre quickly and efficiently.

Specifically, with regards to biological photoprotection, sunscreens are introduced as the almost universal method of providing additional photoprotection at time of increased UVR levels. Applying femtosecond pump-probe transient absorption spectroscopy, the deactivation of excited state sunscreen molecules are measured and analysed through a global fitting analysis procedure, revealing the lifetime of the processes occurring. In complement to this, *ab initio* electronic structure calculations are often performed to understand the likely electronic states involved in the overall deactivation mechanism. To this end, a series of popular sunscreen constituents found in commercial products are investigated. Furthermore, the biologically relevant naturally synthesised sunscreening molecules found in many plants are studied.

Pigment-protein complexes on the other hand present an interesting topic of study given the current trend in research towards artificially mimicking the processes and machinery involved in natural photosynthesis. Quantum dynamics simulations are performed on model pigment-protein complexes found in green sulphur bacteria and in higher-order green plants. Introducing appropriate approximations in 'coarse-graining' the complex, and in the treatment of its environment, allows the entire system to be

simulated over many picoseconds, encompassing the entire electronic energy transport process. Overall, two distinct pigment-protein complexes are studied, and a wide-variety of properties pertaining to robustness and efficiency of electronic energy transport networks are investigated.

7.2 Overview of results and contribution to field

The current landscape of ultrafast photochemistry, with respect to sunscreens, and the photophysics of pigment-protein complexes have been set out in their respective chapter introductions. A comprehensive discussion and conclusion of the work presented in this thesis has been given in the relevant results chapters, it is however summarised here. We consider the artificial sunscreen constituents first.

From the work involving the sunscreen constituent oxybenzone, we determined that there are two dominant relaxation pathways which allow UV-A photoexcited molecules to revert back to the ground state, namely *enol-keto* (∼400 fs) isomerisation followed a back isomerisation and vibrational energy transfer to the surrounding solvent (together, ∼5–8 ps).[286] We also found that not all the photoexcited molecules reverted back to the ground state, instead, we determined that they likely form a long-lived trans *keto*-isomer of oxybenzone, lasting beyond the maximum experimental time delay of ∼1.3 ns. Furthermore, identical conclusions were reached for the case where oxybenzone is photoexcited within the UV-B and UV-C regions, highlighting from a photochemical perspective, the broadband applicability of this sunscreen filter.[287]

Titanium dioxide was considered next, where we confirmed an ultrafast relaxation within our experimental resolution (<100 fs), attributed to surface electron recombination. When suspended with oxybenzone in various mixtures, resembling a first approximation of a sunscreen product, we observed no changes to the dynamics of either molecule, and the total dynamics could be treated separately.[590]

Literature involving the photoprotective properties of octocrylene remains rather sparse, particularly given its wide-spread use. We have now provided, to our knowledge, the first reported measurements of the ultrafast photoprotective properties of octocrylene. We found that octocrylene relaxes predominantly through nonradiative pathways with incredible efficiency; the majority of dynamics are over within ∼2 ps and are assigned to various internal conversion pathways through conical intersections. Importantly, these are early measurements; there is no doubt that computational studies will be key to understanding the nature of the excited states involved in this relaxation mechanism.

The final artificial sunscreen constituent considered in this thesis was ethylhexyl triazone. Again, the literature involving this molecule remains sparse, with a notable exception of the work by Tsuchiya *et al.*[455] We provided an in-depth follow-up to this work, with an experimental resolution of ∼100 fs and various density functional theory electronic structure calculations to identify the likely excited states involved, and the structure of the molecule at important points of the measured transient absorption signal. We measured ultrafast processes, between ∼400 fs, ∼20 ps, and ∼200 ps, where deactivation involves fast internal conversion from excited singlet states, before reverting to the ground electronic state. A portion of the excited state is suggested to undergo intersystem crossing to triplet states, which increases the lifetime of the deactivation mechanism significantly for these molecules. We also identify that electron density involved in the deactivation mechanism is localised to the centre of the molecule, thus the photodynamics may be altered through selective substitutions, or conversely, other properties such as solubility can be altered through changes to the triazone edges, without affecting the photodynamics.

Considering next the natural sunscreen constituents, specifically those found in many plant leaves. We explored the photoprotective mechanisms of sinapoyl malate, and its precursor sinapic acid along with its simplest derivative methyl sinapate. We find that all molecules relax *via* ultrafast internal conversion (∼10–30 ps) mediated by appropriate conical intersections, although the exact nature of excited states remains ambiguous, leading us to suggest two plausible relaxation mechanism, although ultimately, it does not change the lessons learnt from the molecules. We find that all systems also can undergo *trans–cis* isomerisms to form a long-lived, stable *cis*-isomer. These results are in stark contrast to those observed for gas-phase measurements,[301] making this a new result, and complements much of the work conducted on the cinnamate family of molecules.

The final part of this thesis focused on the electronic transport properties of Fenna-Matthews-Olson and light-harvesting complex II pigment-protein complexes found in the green sulphur bacteria and higher-order green plants respectively. Considering the Fenna-Matthews-Olson; for the first time the full extent of robustness has been investigated revealing that up to 50% of the available pigments may be completely removed from the pigment-network and the electronic energy transport efficiency drop by as little as 20%, meaning even after significant network disruption, electronic energy can still reach the reaction centre to support photosynthesis. We also identify the dominant transport pathways and show how each pathway contributes to the overall efficiency and robustness observed.[538] Considering how optimal this complex is, we

generate a vast number of perturbed Hamiltonians and show that the natural occurring complex is not optimised for transport efficiency, but rather for redundancy in providing electronic energy fast *enough*. We applied similar quantum dynamics simulations for the light-harvesting complex II where similar observations were made.[586]

7.3 Outlook: Where does this work fit in?

Biological photoprotection. This thesis began with a broad overview of the natural adaptive photoprotective mechanisms humans exhibit towards changing levels of UV exposure. In particular, it was highlighted when such mechanisms are inadequate and the burden-of-disease increases. Sunscreens are introduced as today's almost universal solution to pre-empting UV overexposure. Given the prevalence of sunscreen use it is perhaps no surprise they have come under increasing scrutiny. Specifically, scrutiny has been paid to the adverse effects of sunscreens; whether or not they contribute to the disease burden, referred to as the "sunscreen controversy". This thesis focuses on how the detailed mechanistic properties, gleaned from ultrafast photochemistry, can reveal the complete photodeactivation pathway of a sunscreen constituent. Gas-phase measurements and *ab initio* electronic structure calculations often provide the fundamental photodeactivation pathway without any perturbation on the excited state involved in the pathway. A step closer to the environment a sunscreen constituent is used in, is the solution-phase. As has been suggested by the literature review and the introduction to each of the molecules studied in this thesis, moving from the gas- to the solution-phase can prove highly informative since photodeactivation pathways can vary greatly. Knowing the complete pathway allows an assessment of the photophysical applicability of the filter. Of particular interest is the efficacy with which the deactivation pathway occurs, as well as whether or not photoproducts are formed as a result of UV exposure. The latter is particularly important given photoproducts are often the root cause of adverse effects. This thesis has highlighted the extent of information which can be obtained and understood through the use of common gas- and solution-phase spectroscopy techniques, as well as computational studies. The latter of these is particularly important given there is great interest in the transient signals which lie within the temporal resolution of many of these experiments (typically <100 fs), something which quantum dynamics studies can reveal.[107,289,337,591,592] When extended to include solvent effects, for example using a continuum solvation model or QM/MM approach,[337,593] these studies can complement solution-phase experiments even more closely. After considering the above, there are perhaps three main questions which remain from the work discussed

in this thesis.

(*i*) Given that sunscreen products contain many tens of individual components, how do the dynamics of one component change in the presence of another? This question is not necessarily new; many components are included in particular combinations because of the way they interact, avobenzone and octocrylene being a prime example,[237,251,264] but any interaction is not necessarily synergistic, thus examining one component in the presence of others is important in understanding its behaviour in a commercial product. Extending the experimental work discussed here to include two or more components is relatively simple if the signals from each are far removed,[590] either spectrally or temporally, otherwise different analytical procedures or protocols would have to be implemented.

(*ii*) Is any observed photoproduct safe? Many studies observe the presence of a photoproduct but identifying that photoproduct can be more difficult. Nuclear magnetic resonance and gas chromatography mass spectrometry have shown success in identifying photoproducts after photoexcitation,[300,594] but this alone does not always allow an adequate evaluation on the safety of the component in a sunscreen product. Understanding the photoreactive excited states of such photoproducts, for example a radical species and its subsequent reactions, would likely lead to a much improved evaluation of their safety, or can be protected against using a suitable scavenger species for example.

(*iii*) If the dynamics of a filter changes from the gas-phase to the solution-phase, what happens in an actual sunscreen product? Whilst the solution-phase is a closer environment to a sunscreen than the gas-phase, it is still quite far from the actual commercial product which ranges from an oil to a paste, in the presence of many different components. Whilst such multimolecular systems have been discussed in (*i*), the fact that the solution-phase is still far away from the native environment of a commercial product needs to be addressed. Thin-film studies would likely be the next intuitive step.[361,595] Moving on from here, clinical trials involving skin samples would be one way to evaluate the safety and efficacy of a product in ways not accessible by the techniques discussed thus far.

Using such a bottom-up approach to evaluating a filter for use as a sunscreen, provides an excellent opportunity to optimise and rationally design improved or novel sunscreen filters which can be tested for suitability and find use in commercial products. What is being described is a work-flow for designing better sunscreens using a bottom-up process, see Figure 7.1.

There is still the reservation to be had with what has been discussed on sunscreen thus far, in that whilst there is clearly a route to developing improved sunscreens, this

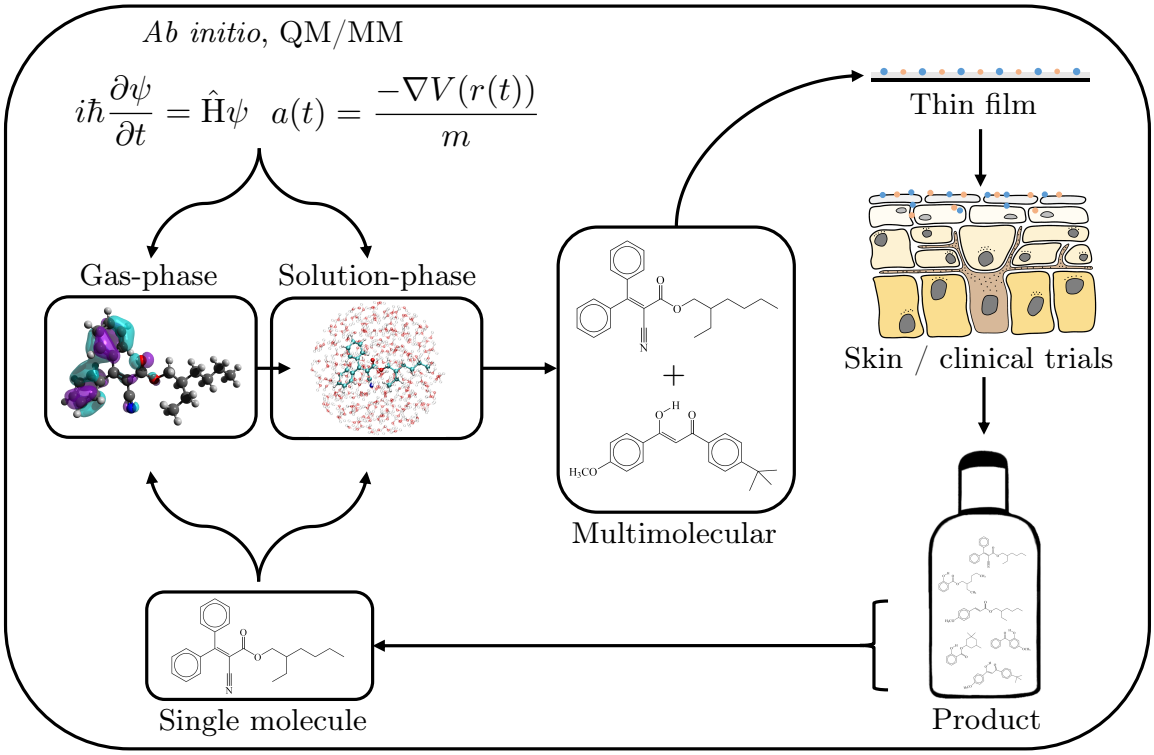

Figure 7.1 | An overview of the proposed process of designing good sunscreen products from a bottom-up approach.[463,596]

is of little use if the end-user does not use them, or uses them incorrectly. Numerous studies have concluded that one of the biggest factors in sun-related ailments lies with the end-user's sun-behaviour.[597–601] I leave it to the reader to decide, but one must ask, *would so much research effort in designing and optimising sunscreens be required if users were better educated?* One could posit that if the cost of sunscreens were reduced, and that advertising, education, and sun-behaviour minimises misinformation, and maximises safe sun-exposure, then a 'next-generation' of sunscreens might not even be required.

Pigment-protein complexes. The second part of this thesis began with a brief overview of photosynthesis and its evolution into the highly efficient and specialised biochemical pathway we observe today. The role of protein-pigment complexes has been highlighted for their dominant contribution to the overall efficiency of the transfer of electronic energy to the reaction centre, where electronic energy is converted into chemical energy; this is clearly one of the most fundamental processes required for life on Earth. Pigment-protein complexes consist of a set of light-absorbing molecules

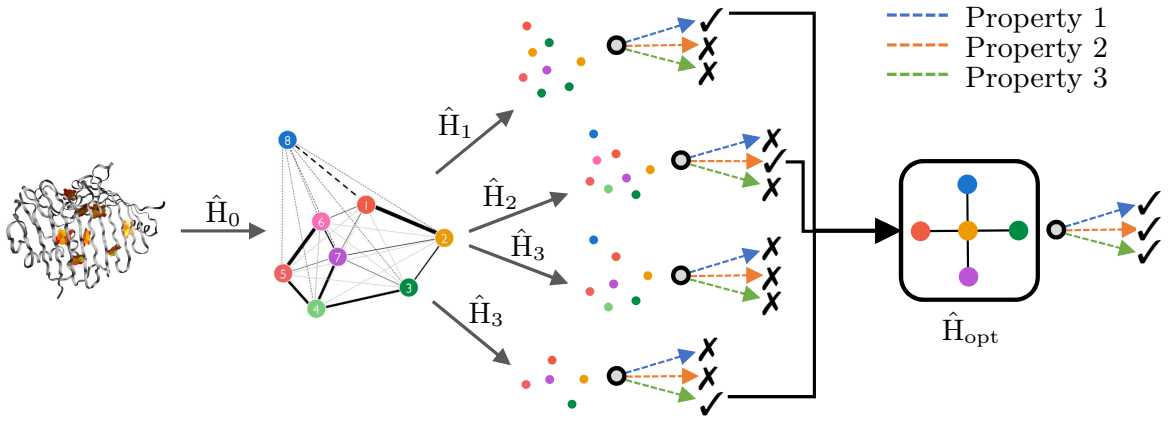

Figure 7.2 | A representative work-flow for using a pigment-protein complex to understand particular properties of electronic energy transport. The pigment-protein complex ($\hat{H}_0$) can be perturbed, producing a number of other structures ($\hat{H}_n$; $n \geq 1$). Each of these can be tested against a number of criteria, such as robustness, optimality, or efficiency. Those which display desirable properties can be used to inform on the construction of artificial chromophore networks, $\hat{H}_{opt}$.

(pigments), held within a protein scaffold, which are electronically excited after absorption of light within the photosynthetic supercomplex. We have discussed electronic energy transport in two of the most widely studied pigment-protein complexes, namely the Fenna-Matthews-Olson complex and light-harvesting complex-II. We have also outlined the mathematical description of these biological complexes as a simple network of vertices (the pigments) and edges (the electronic coupling between pigments). The protein scaffold is accounted for through a simple Markovian 'white noise' approach which reproduces the qualitative dynamical behaviour of these complexes. Within this network picture, it is possible to identify several attributes of the complexes which provide the robustness to network disruption, predominantly through the systematic deletion of pigments and their corresponding electronic couplings.

The main purpose in this work has been to highlight the power of this network analysis of biological complexes, where a large variety of system properties can be assessed with a very tractable computational model. Although this approach provides interesting insights into the electronic energy transport features of biological complexes, this type of analysis can easily be imagined as a 'screening' test to aid in the design of any related networks of chromophores such as those found in artificial solar cells or photoinduced catalytic systems (Figure 7.2). The results of this simple model are

qualitative yet computationally tractable; this approach therefore enables a large number of quantum dynamics simulations to be performed quickly, as required if one is interested in addressing questions relating to construction of large electronic energy transport networks. Going beyond this simple effective-environment approach, including explicit correlation between the electronic Hamiltonian and the environment in a computationally-simple manner, is a challenge we are now seeking to address.

Finally, we note that there are many questions relating to biological protein-pigment complexes which simple modelling studies, such as that considered here, cannot address in a broader biological context. For example, why are the complexes highly conserved across species as found with Fenna-Matthews-Olson in green sulphur bacteria which are found at very different levels of environmental stress? Are these complexes optimised for any one particular characteristic such as the rate of electronic energy transport or robustness to damage, or are they optimised for some compromise between these requirements? It seems likely that such broader questions can only be fully addressed by a coherent strategy, incorporating both experimental biological and spectroscopic studies, as well as computation.

7.4 Immediate research directions

Some of the (many) remaining questions involving the work reported in this thesis have already been outlined, but, in general, these allude to some of the more far-reaching, general questions being addressed. On more acute timescales, there are a number of research directions currently being pursued, or likely to be pursued in the near-future. Currently, there remains a gap in the literature regarding the plant sunscreen constituents discussed in this thesis. Time-resolved gas-phase measurements remain somewhat sparse, where resonant-two photon ionisation has revealed many properties of these molecules,[301] but there remains more work to be done. We have recently performed time-resolved gas-phase measurements on the constituent methyl sinapate using procedures proven successful with similar molecular systems,[300,602] which, with the addition of TEAS measurements in cyclohexane, and complementary *ab initio* electronic structure calculations, we hope to fill the gap in the literature.

Following on from this, we have conducted experiments to probe the suspected *trans–cis* isomerism observed in sinapoyl malate. These experiments have taken novel substituted sinapoyl malate molecules (Figure 7.3) which should increase the steric hindrance around the aliphatic C=C bond, which in turn, should cause a significant change in the observed dynamics. Preliminary results however suggest that there is little

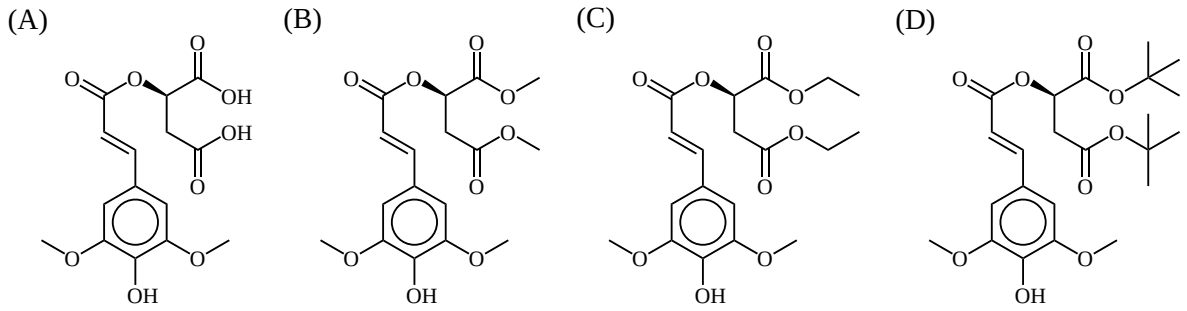

Figure 7.3 | Sinapoyl malate derivatives selected for study: (A) sinapoyl malate, (B) sinapoyl L-dimethyl malate, (C) sinapoyl L-diethyl malate, and (D) sinapoyl L-ditertbutyl malate.

change to the lifetimes of the excited state processes, indicating that the isomerisation pathway remains accessible, and competitive even with an increased steric hindrance about the isomerisation dihedral reaction coordinate.

Chapter 8

Appendices

8.1 Angular momentum

Two quantum numbers were introduced in Chapter 1, the magnetic angular momentum, m_l, and the orbital angular momentum, l. In this appendix, we formally introduce angular momentum and quantise it to justify the label of angular momentum with respect to these quantum numbers.[11] Classically, the angular momentum, $\mathbf{L}$, of a particle is the vector multiplication of its position, $\mathbf{r}$, and momentum, $\mathbf{p}$,

$$\mathbf{L} = \mathbf{r} \times \mathbf{p}. \tag{8.1}$$

Replacing each classical term with a corresponding quantum operator gives $\hat{\mathbf{L}} = \hat{\mathbf{r}} \times \hat{\mathbf{p}}$ which means angular momentum can be expressed in terms of its Cartesian components such that

$$\hat{\mathrm{L}}^2 = \hat{\mathrm{L}}_x^2 + \hat{\mathrm{L}}_y^2 + \hat{\mathrm{L}}_z^2 \quad \hat{\mathrm{L}}_x = \hat{y}\hat{\mathrm{p}}_z - \hat{z}\hat{\mathrm{p}}_y \quad \hat{\mathrm{L}}_y = \hat{z}\hat{\mathrm{p}}_x - \hat{x}\hat{\mathrm{p}}_z \quad \hat{\mathrm{L}}_z = \hat{x}\hat{\mathrm{p}}_y - \hat{y}\hat{\mathrm{p}}_x. \tag{8.2}$$

Writing these in component form gives a set of cyclic commutation relations

$$\begin{aligned}
\left[\hat{\mathrm{L}}_x, \hat{\mathrm{L}}_y\right] &= \hat{\mathrm{L}}_x\hat{\mathrm{L}}_y - \hat{\mathrm{L}}_y\hat{\mathrm{L}}_x \\
&= \left(\hat{y}\hat{\mathrm{p}}_z - \hat{z}\hat{\mathrm{p}}_y\right)\left(\hat{z}\hat{\mathrm{p}}_x - \hat{x}\hat{\mathrm{p}}_z\right) - \left(\hat{z}\hat{\mathrm{p}}_x - \hat{x}\hat{\mathrm{p}}_z\right)\left(\hat{y}\hat{\mathrm{p}}_z - \hat{z}\hat{\mathrm{p}}_y\right) \\
&= \hat{y}\hat{\mathrm{p}}_z\hat{z}\hat{\mathrm{p}}_x - \cancel{\hat{y}\hat{\mathrm{p}}_z\hat{x}\hat{\mathrm{p}}_z} - \cancel{\hat{z}\hat{\mathrm{p}}_y\hat{z}\hat{\mathrm{p}}_x} + \hat{z}\hat{\mathrm{p}}_y\hat{x}\hat{\mathrm{p}}_z - \hat{z}\hat{\mathrm{p}}_x\hat{y}\hat{\mathrm{p}}_z + \cancel{\hat{z}\hat{\mathrm{p}}_x\hat{z}\hat{\mathrm{p}}_y} + \cancel{\hat{x}\hat{\mathrm{p}}_z\hat{y}\hat{\mathrm{p}}_z} - \hat{x}\hat{\mathrm{p}}_z\hat{z}\hat{\mathrm{p}}_y \\
&= \hat{y}\hat{\mathrm{p}}_z\hat{z}\hat{\mathrm{p}}_x + \hat{z}\hat{\mathrm{p}}_y\hat{x}\hat{\mathrm{p}}_z - \hat{z}\hat{\mathrm{p}}_x\hat{y}\hat{\mathrm{p}}_z - \hat{x}\hat{\mathrm{p}}_z\hat{z}\hat{\mathrm{p}}_y \\
&= \hat{y}\hat{\mathrm{p}}_x\left(\hat{\mathrm{p}}_z\hat{z} - \hat{z}\hat{\mathrm{p}}_z\right) + \hat{x}\hat{\mathrm{p}}_y\left(\hat{z}\hat{\mathrm{p}}_z - \hat{\mathrm{p}}_z\hat{z}\right) \\
&= \underbrace{\left(\hat{x}\hat{\mathrm{p}}_y - \hat{y}\hat{\mathrm{p}}_x\right)}_{\hat{\mathrm{L}}_z}\underbrace{\left(\hat{z}\hat{\mathrm{p}}_z - \hat{\mathrm{p}}_z\hat{z}\right)}_{i\hbar} \\
&= i\hbar\hat{\mathrm{L}}_z.
\end{aligned} \tag{8.3}$$

Where we have used the commutation relations in Equation 1.4. Similarly, for each set of possible commutation relation we can complete the set

$$\begin{aligned}
\left[\hat{\mathrm{L}}_x, \hat{\mathrm{L}}_y\right] &= i\hbar\hat{\mathrm{L}}_z \\
\left[\hat{\mathrm{L}}_y, \hat{\mathrm{L}}_z\right] &= i\hbar\hat{\mathrm{L}}_x \\
\left[\hat{\mathrm{L}}_z, \hat{\mathrm{L}}_x\right] &= i\hbar\hat{\mathrm{L}}_y.
\end{aligned} \tag{8.4}$$

The other possible set of commutation relations surround that of total angular momentum with its components. Consider first the commutation of total angular momentum and the angular momentum in the z- direction

$$\left[\hat{\mathrm{L}}^2, \hat{\mathrm{L}}_z\right] = \left[\hat{\mathrm{L}}_x^2, \hat{\mathrm{L}}_z\right] + \left[\hat{\mathrm{L}}_y^2, \hat{\mathrm{L}}_z\right] + \left[\hat{\mathrm{L}}_z^2, \hat{\mathrm{L}}_z\right]. \tag{8.5}$$

Considering first the $\left[\hat{\mathrm{L}}_x^2, \hat{\mathrm{L}}_z\right]$ term

$$\begin{aligned}
\left[\hat{\mathrm{L}}_x^2, \hat{\mathrm{L}}_z\right] &= \hat{\mathrm{L}}_x\hat{\mathrm{L}}_x\hat{\mathrm{L}}_z - \hat{\mathrm{L}}_z\hat{\mathrm{L}}_x\hat{\mathrm{L}}_x \\
&= \hat{\mathrm{L}}_x\left(-i\hbar\hat{\mathrm{L}}_y + \hat{\mathrm{L}}_z\hat{\mathrm{L}}_x\right) - \left(i\hbar\hat{\mathrm{L}}_y + \hat{\mathrm{L}}_x\hat{\mathrm{L}}_z\right)\hat{\mathrm{L}}_x \\
&= -i\hbar\left(\hat{\mathrm{L}}_x\hat{\mathrm{L}}_y + \hat{\mathrm{L}}_y\hat{\mathrm{L}}_x\right).
\end{aligned} \tag{8.6}$$

In a similar fashion one can show

$$\begin{aligned}
\left[\hat{\mathrm{L}}_y^2, \hat{\mathrm{L}}_z\right] &= i\hbar\left(\hat{\mathrm{L}}_x\hat{\mathrm{L}}_y + \hat{\mathrm{L}}_y\hat{\mathrm{L}}_x\right) \\
\left[\hat{\mathrm{L}}_z^2, \hat{\mathrm{L}}_z\right] &= \hat{\mathrm{L}}_z^2 - \hat{\mathrm{L}}_z^2 = 0,
\end{aligned} \tag{8.7}$$

which substituted into Equation 8.5 yields the result

$$\left[\hat{\mathrm{L}}^2, \hat{\mathrm{L}}_x\right] = \left[\hat{\mathrm{L}}^2, \hat{\mathrm{L}}_y\right] = \left[\hat{\mathrm{L}}^2, \hat{\mathrm{L}}_z\right] = 0. \tag{8.8}$$

Since only commuting operators allow a system to be simultaneously eigenstates of both operators, this leads to two important results. The first is that two components of angular momentum cannot be simultaneously known. However, one component, and the total angular momentum can be known simultaneously.* Moving to understand the eigenvalues and eigenfunctions of angular momentum, we revisit the classical equation of angular momentum Equation 8.1. Replacing these classical terms for their quantum mechanical operators (*cf.* postulate 3 and Equations 1.26 and 1.27), the angular momentum operator is written as

$$\hat{\mathbf{L}} = -i\hbar\mathbf{r} \times \nabla. \tag{8.9}$$

This problem lends itself to spherical polar coordinates just as with the hydrogen atom, using the same transformations, the angular momentum operator is†

$$\hat{\mathbf{L}} = -i\hbar\left(\hat{\phi}\frac{\partial}{\partial\theta} - \frac{1}{\sin(\theta)}\hat{\theta}\frac{\partial}{\partial\phi}\right), \tag{8.10}$$

where $\hat{r}$, $\hat{\psi}$ and $\hat{\theta}$ are unit vectors in those coordinates. If one chooses the polar axis to be along the z-direction, the $\hat{z}$ unit vector is $\hat{z} = \cos(\theta)\hat{r} - \sin(\theta)\hat{\theta}$ which means the z-component of angular momentum is simply

$$\hat{\mathrm{L}}_z = \hat{z} \cdot \hat{\mathbf{L}} = -i\hbar\frac{\partial}{\partial\phi}. \tag{8.11}$$

Turning attention to the total angular momentum, standard vector identities yield

$$\hat{\mathrm{L}}^2 = -\hbar^2\hat{\mathbf{r}} \cdot \left[\nabla \times (\hat{\mathbf{r}} \times \nabla)\right], \tag{8.12}$$

which is

$$\hat{\mathrm{L}}^2 = -\hbar^2\left[\frac{1}{\sin(\theta)}\frac{\partial}{\partial\theta}\left(\sin(\theta)\frac{\partial}{\partial\theta}\right) + \frac{1}{\sin^2(\theta)}\frac{\partial^2}{\partial\phi^2}\right]. \tag{8.13}$$

The similarities of the functional form of this operator should become obvious when compared to the azimuth equation for the hydrogen atom, *cf.* Equation 1.63. The

*As a convention, take the z-component with total angular momentum.

†For unit vectors $\hat{r}$, $\hat{\theta}$ and $\hat{\phi}$, $\nabla = \hat{r}\frac{\partial}{\partial r} + \frac{1}{r}\hat{\theta}\frac{\partial}{\partial\theta} + \frac{1}{\sin(\theta)}\hat{\phi}\frac{\partial}{\partial\phi}$

operator satisfies the following eigenvalue equation

$$\hat{\mathrm{L}}^2 Y_l^m(\theta,\phi) = l(l+1)\hbar^2 Y_l^m(\theta,\phi), \tag{8.14}$$

where $Y_l^m(\theta,\phi)$ are the aforementioned spherical harmonics, the eigenfunctions of $\hat{\mathrm{L}}^2$, yielding the eigenvalue of the total angular momentum operator $l(l+1)\hbar^2$. Similarly for the z-component of angular momentum

$$\hat{\mathrm{L}}_z Y_l^m(\theta,\phi) = m\hbar Y_l^m(\theta,\phi), \tag{8.15}$$

thus $Y_l^m(\theta,\phi)$ are simultaneous eigenfunctions of $\hat{\mathrm{L}}^2$ and $\hat{\mathrm{L}}_z$, and the eigenvalue of $\hat{\mathrm{L}}_z$ is $m\hbar$ where $-l \leq m \leq l$, as described for the solution to the zenith equation (*cf.* Equation 1.65). This angular momentum, described by l and m quantum numbers is referred to as *orbital angular momentum*, in order to differentiate it from spin angular momentum, as discussed in Chapter 1.

8.2 Variational theorem

One of the most widely used methods for estimating the energy of a system by approximating its wavefunction is using variational theory, specifically the Rayleigh-Ritz method.[1,3] The variational theorem states that for any trial wavefunction, Ψ, the expectation value, E, of the Hamiltonian, $\hat{\mathrm{H}}$, is always greater than, or equal to, the lowest energy eigenvalue of the Hamiltonian, E_0,

$$E = \frac{\langle \Psi | \, \hat{\mathrm{H}} \, | \Psi \rangle}{\langle \Psi | \Psi \rangle} \geq E_0. \tag{8.16}$$

This inequality only holds for the case where the trial wavefunction is identical to the ground state wavefunction. This is quickly deduced by first considering the linear expansion of the eigenstates of the Hamiltonian, Ψ_n,

$$\Psi = \sum_n c_n \Psi_n, \tag{8.17}$$

where c_n are the usual expansion coefficients. Substituting this expansion into Equation 8.16, yields

$$\sum_{m,n} \langle c_m^* \Psi_m^* | \, \hat{\mathrm{H}} \, | c_n \Psi_n \rangle - E_0 \sum_{m,n} \langle c_m^* \Psi_m^* | c_n \Psi_n \rangle \geq 0, \tag{8.18}$$

which, given the eigenstates are orthonormal (and are normalised), the inequality becomes

$$\sum_n c_n^* c_n \left(E_n - E_0 \right) \geq 0. \tag{8.19}$$

Since $E_n \geq E_0$ and $|c_n|^2 \geq 0$, then

$$\langle \Psi | \, \hat{\mathrm{H}} - E_0 \, | \Psi \rangle \geq 0, \tag{8.20}$$

and the variational theorem is recovered. Practically, quantum chemistry expands the wavefunction using a basis set, with variable basis coefficients, exactly like Equation 8.17, except that Ψ_n are now the basis functions, and the coefficients c_n, are now variational, which are optimised as such. This implementation of the variational theorem is known as the Rayleigh-Ritz method. The solution to Equation 8.16 within this framework satisfies

$$|\mathrm{H}_{ij} - E S_{ij}| = 0 \tag{8.21}$$

and

$$\sum_i c_i \left(\mathrm{H}_{ij} - E S_{ij} \right) = 0 \tag{8.22}$$

where H_{ij} and S_{ij} are the Hamiltonian and overlap matrix elements respectively. Thus, during an optimisation, Equation 8.21 returns a set of n energy eigenvalues, the lowest of which is used in Equation 8.22 to calculate the basis set coefficients.

8.3 Ultrashort pulse generation

A 40 W continuous wave water cooled, gallium-aluminium-arsenide (GaAlAs) semiconductor diode (*Millennia Pro s-Series*, Spectra-Physics, henceforth referred to as 'Millennia') is used as an optical pump to the laser oscillator (*Tsunami*, Spectra-Physics, henceforth referred to as 'Tsunami'). The diode produces a 808 nm continuous wave which optically pumps a neodymium-doped yttrium vanadate (Nd^{3+}:YVO_4) gain medium to the first excited state of a four-level population inversion. The Nd^{3+}:YVO_4 crystal is thermally isolated from the rest of the laser head and is situated in the middle of the lasing cavity, and is water cooled. The most probable lasing transition of this gain medium is the ejection of a 1064 nm photon. The 1064 nm photons remain trapped in a cavity between two high reflectivity cavity mirrors. Most the 1064 nm photons are frequency doubled using a non-critically phased matched Lithium Triborate (LBO), LiB_3O_5, crystal, producing 532 nm photons. The LBO crystal is situated in a temperature regulated oven which maintains optimum conditions for the required phase matching. The 532 nm photon passes through a dichroic mirror and exits the laser cavity, whilst reflecting any 1064 nm photons and thus retaining them in the cavity to initiate further SE. The final dichroic mirror also functions as an output coupler which feeds back information about the uniformity of the laser output to the diode electronics to regulate a consistent laser beam. A polariser is placed between the LBO crystal and the output coupler to ensure the output laser beam is vertically polarised.

The 532 nm output of the Millennia is used to seed the Tsunami. The 532 nm beam is transmitted through a Brewster window to ensure maximum transmission of a single polarisation of light only whilst reflecting residual 1064 nm since it has the opposite polarisation. A Ti:sapphire (Ti^{3+}:Al_2O_3) crystal is situated between two spherical mirrors, the first of which functions to focus and pump the crystal with 532 nm, whereby Ti:sapphire's dominant transitions radiate a continuum of modes between 670 nm and 1000 nm, of which wavelengths around 800 nm are the most intense contribution. The second spherical mirror focusses the continuum of modes back into the crystal to initiate SE. The continuum passes through a GVD compensation prism and is reflected into a wavelength selector construction, using two dispersion prisms with a wavelength selection slit in between. The central selected wavelength, 800 nm, passes a final GVD compensation prism and travels through the Acousto-Optic Modulator (AOM) which utilises a piezo-electric crystal modulated with a pure sine wave to reflect signals of different wavelengths, such that the 800 nm transmission is maximised. This helps the cavity to be primarily composed of 800 nm photons with a small bandwidth, typically

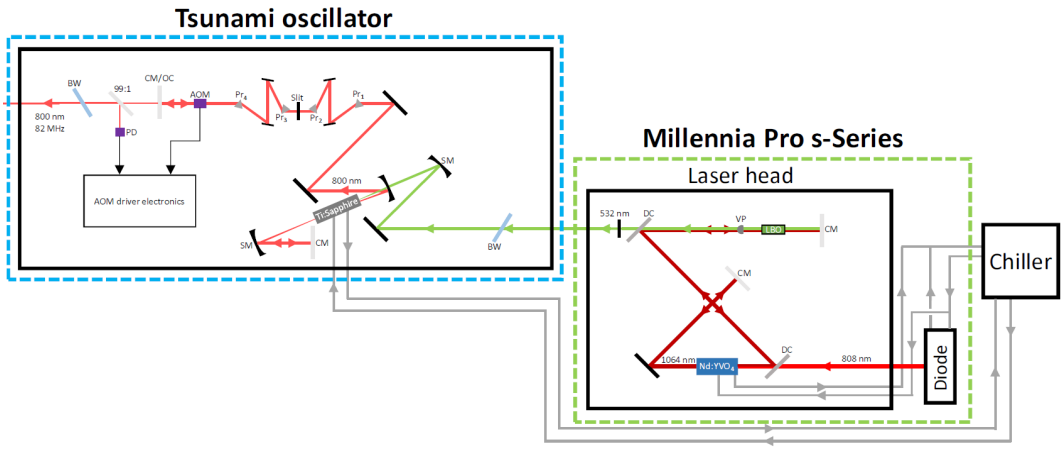

Figure 8.1 | Schematic of the Millennia pump laser and Tsunami oscillator. The Millennia produces 532 nm photons which optically pump the Ti:sapphire gain medium in the Tsunami. The Tsunami produces 800 nm photons which seed the Spitfire CPA. See text for details.

a 40-50 nm FWHM. A cavity mirror reflects all light back into the cavity, with the exception of a small percentage allowed to transmit through modulation by an optical coupling element. A small fraction of this transmitted light is fed into a photodiode through the use of a beam splitter. Together, the photodiode and AOM feed back into the AOM driver electronics to optimise the mode locking in the laser cavity. The rest of the transmitted light passes a final Brewster window ensuring the only output is the 800 nm pulses and no residual 532 nm. The repetition rate of the output train of pulses is 82 MHz, controlled by the length of the cavity and the Kerr lens effect of the optical coupling element leading to an output power of ∼300 mW.

A second pump laser (*Empower-15*, Spectra-Physics, henceforth referred to as 'Empower') optically pumps the Ti:sapphire crystal of the CPA (*Spitfire Pro XP*, Spectra-Physics, henceforth referred to as 'Spitfire'). The operation of the Empower is similar to that of the Millennia with some subtle variations. A 15 W GaAlAs semiconductor diode produces a 808 nm continuous wave which optically pumps a neodymium-doped yttrium lithium fluoride (Nd^{3+}:$YLiF_4$) gain medium through a four-level population inversion with two intense transitions, 1047 and 1053 nm, the latter is chosen as the fundamental mode given its reduced tendency to exhibit thermal lensing. Nd^{3+}:$YLiF_4$ is chosen as the gain medium over Nd^{3+}:YVO_4 because it can produce higher powered pulses at low repetition rates (<2 kHz), which, as described below, is required. Frequency doubling to 527 nm is provided through the use of a LBO crystal. An AOM is used to *Q-switch* pulses out of the laser cavity, that is, essentially ejecting a pulse with

a defined repetition rate, set to 1 kHz. Q-switching allows the generation of intense pulses by allowing the gain medium to be saturated before SE of 1053 nm photons is induced, the AOM is then turned off, and the 1053 nm photons are allowed to transverse the laser cavity and initiate SE in the saturated gain medium. The final variation on the Millennia design is the addition of water cooling for the AOM and LBO crystal as well as the Nd^{3+}:$YLiF_4$ crystal and the GaAlAs diode. The requirement for this comes from the intense pulse energies in the Empower compared to those produced by the Millennia.

The Spitfire's Ti:sapphire gain medium is pumped by the 527 nm output of the Empower. The 800 nm, 82 MHz, 300 mW output of the Tsunami is also fed into the Spitfire. The 800 nm pulses are stretched temporally (chirped) using a splitting grating (GVD+), reducing the peak intensity of each pulse. The reason for the introduction of addition chirp is to protect the Ti:sapphire gain medium from the possible self focussing effects of high peak intensity pulses, which would otherwise damage the crystal. The pulses pass through a twisted periscope which rotates the polarisation of the pulses to vertical. It is then reflected into the first Pockel cell (PC1) after passing a polarised periscope. PC1 allows pulses to enter the cavity at a rate of 1 kHz, thus, 1 in every 8200 pulses enters the cavity per second. Upon the injection of one of these pulses, after being horizontally polarised by PC1, it is transmitted through a Thin Film Polariser (TFP) and a second Pockel cell, PC2, remains inactive and allows the pulse to pass through to a quarter-wave plate ($WP_{\lambda/4}$), circularly polarising it. It reflects off the cavity mirror and passes the $WP_{\lambda/4}$ leaving the pulses vertically polarised and are therefore reflected off the TFP. PC2 is now turned on so that on each pass, the pulse will remain vertically polarised since PC2 behaves as a $WP_{\lambda/4}$. The pulse makes 12-15 passes of the cavity to reach optimal amplification. Just before returning to PC2, a signal is sent to deactivate both PC1 and PC2. When the amplified pulse reaches the now inactive PC2, it is circularly polarised by the $WP_{\lambda/4}$, reflected by the cavity mirror, and passes $WP_{\lambda/4}$ once more resulting in a horizontally polarised pulse, which can be transmitted through the TFP. Since PC1 is now inactive, the amplified pulse remains horizontally polarised, and these enters the regenerative stage via the TFP. In the regenerative stage the amplified pulses are recompressed into $\sim$35 fs pulses using a compression grating (GVD–). The output of the Spitfire is a 1 kHz, 800 nm pulse train with a power of $\sim$3 W. For our use, 1 W of this output is used to seed an OPA, 1 W is sent into the solution phase table for WLG and, if required, second harmonic generation of 400 nm pulses and third harmonic generation of 267 nm pulses which can be used as a pump source. If other wavelengths are required for the pump pulses the

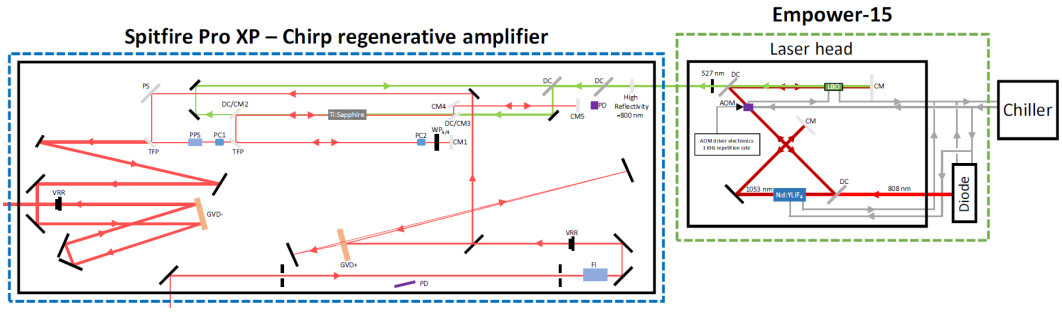

Figure 8.2 | Schematic diagram of the Empower pump laser and Spitfire CPA. The Empower produces 527 nm pulses which optically pumps the Ti:sapphire gain medium of the Spitfire. 800 nm seed pulses from the Tsunami are amplified in the Spitfire's optical cavity and are expelled at a repetition rate of 1 kHz. See text for details.

use of an OPA is usually required where high-order mixing is utilised.

Collinear travelling-wave OPA of WLC (*TOPAS-C*, Light Conversion, henceforth referred to as 'TOPAS') is a commerical OPA used to produce laser pulses of variable wavelengths (∼230–2100 nm) which can be used as a pump pulse for TAS experiments. It is seeded by 1 W, 800 nm laser pulses output from the Spitfire. The 800 nm pulses are horizontally polarised upon entering the TOPAS and are split by the BS, ∼90% is directed towards the second power amplifier (PA2) stage as an amplifier, and the rest is taken as a seed for the PA2 stage. The latter beam goes through two telescopic lenses, two Brewster windows, an iris, and finally a lens before hitting a second beam splitter. All optics between the two beam splitters are required to cut the beam to an

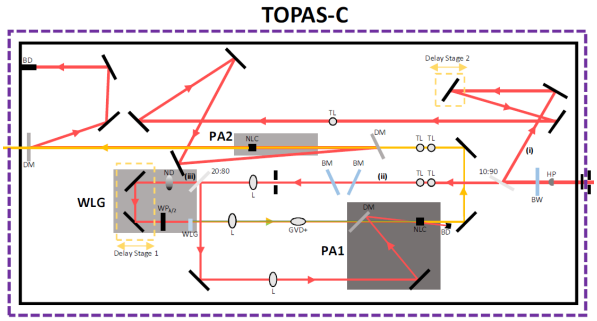

Figure 8.3 | Schematic diagram of the OPA, TOPAS, used to produce pulses of wavelengths between ∼230–2100 nm. It is seeded by the 800 nm pulses from the Spitfire which are used to produce a WLC and subsequently used to amplify the required wavelength. See text for details.

acceptable size for later non-linear optical processes. The lens has two functions; the first is to focus the beam for WLG, the second is that it behaves as the first lens of another telescope for the first power amplifier stage (PA1). The second beam splitter directs ∼80% of the beam towards the far end of a dichroic mirror which reflects it into a nonlinear crystal (Sapphire). The other ∼20% enters a computer controlled retro reflector, called *delay stage 1*, passes a half wave plate ($WP_{\lambda/2}$) into a sapphire window for WLG. The WLC is focused and then stretched temporally by a lens and a dispersive plate (GVD+) into the nonlinear crystal. Coupled with delay stage 1, this allows the selection of a particular wavelength in the WLC to be amplified. PA1 occurs in the nonlinear crystal with spatial overlap of the 800 nm split from the second BS. This first amplified beam is left spatially dispersed and requires collimating which is achieved using two telescopic lenses. Another dichroic mirror is used to transmit the PA1 beam and reflect the PA2 800 nm seed into another nonlinear crystal which performs the final amplification step. A second delay stage, *delay stage 2* is present in the PA2 seed path to allow optimal spatial overlap of the seed and the PA1 beam inside the nonlinear crystal.

This concludes the generation of the 800 nm fundamental, used as the seed for the WLC probe pulses and when required, higher-harmonic generation of the 800 nm pulses can be used as the pump. The TOPAS can be used to produce pulses of wavelengths between the range ∼230–2100 nm. All pulses have a duration of ∼50 fs. The 800 nm beam and, when required, the TOPAS beam, enter the solution phase table where the TEAS actually takes place.

8.4 Electromagnetic radiation and its interaction with media

8.4.1 Electromagnetic radiation in free space

The postulates of special relativity are:[603,604]

(i) The laws of physics remain unchanged in *all* inertial frames of reference.

(ii) The speed of light in a vacuum, c, is constant for *all* observers in *any* inertial frame of reference.

Under the second postulate and working within a Minkowski space-time, and with a standard metric signature of $(+,-,-,-)$, the space-time interval, ds, can be written as

$$(ds)^2 = ct^2 - x^2 - y^2 - z^2 = \eta_{\alpha\beta} dx^\alpha dx^\beta. \tag{8.23}$$

An arbitrary set of space-time coordinates is described by the four-position contravariant vector, $x^\alpha = (ct, x, y, z)$, where standard tensor notation has been used *e.g.* $\alpha = 0, 1, 2, 3$; $x^0 = ct$, $x^1 = x$, $x^2 = y$ and $x^3 = z$, the speed of light in a vacuum is denoted by c, and the Minkowski metric, $\eta^{\alpha\beta}$, has been introduced and given by[604]

$$\eta^{\alpha\beta} = \begin{pmatrix} 1 & 0 & 0 & 0 \\ 0 & -1 & 0 & 0 \\ 0 & 0 & -1 & 0 \\ 0 & 0 & 0 & -1 \end{pmatrix}. \tag{8.24}$$

This is an equivalent analogue of the 3–D Euclidean distance in classical mechanics and serves as an example of how other physical laws can be written within this framework. Of particular importance are Maxwell's equations of electromagnetism, which can be elegantly derived in this formalism.

Any electric field, denoted $\mathbf{E}(\mathbf{r},\, t)$, can be written in terms of a electric scalar potential, ϕ, and a magnetic vector potential, $\mathbf{A}(\mathbf{r},\, t)$, together written as the four-potential $A^\mu \doteq (\phi/c,\, \mathbf{A})$ and defining the electric and magnetic fields as:

$$\mathbf{E}(\mathbf{r},\, t) = -\nabla\phi - \frac{\partial \mathbf{A}}{\partial t} = \sum_{i=0}^{3} -\partial_i A_0 + \partial_0 A_i, \tag{8.25}$$

where the four-gradient operator, $\partial_\alpha = \left(\dfrac{\partial}{\partial(ct)}, \dfrac{\partial}{\partial x}, \dfrac{\partial}{\partial y}, \dfrac{\partial}{\partial z}\right) = \left(\dfrac{\partial}{\partial x^0}, \dfrac{\partial}{\partial x^1}, \dfrac{\partial}{\partial x^2}, \dfrac{\partial}{\partial x^3}\right)$,

follows from the definition of the four-position. Similarly, for an arbitrary magnetic field, $\mathbf{B}(\mathbf{r}, t)$, one can write:

$$\mathbf{B}(\mathbf{r}, t) = \nabla \times \mathbf{A}, \tag{8.26}$$

which satisfies the Lorentz invariance condition:[605]

$$\nabla \cdot \mathbf{A} + \frac{1}{c^2}\frac{\partial \phi}{\partial t} = 0. \tag{8.27}$$

A new four-vector is now introduced, the four-current, $J^\alpha = (c\rho, \mathrm{J}_x, \mathrm{J}_y, \mathrm{J}_z)$, simply describing how some current varies spatially and temporally within the framework of special relativity, specifically, that the equations which will be derived below, conform to postulate (i). Given only these definitions, along with the condition that ϕ and $\mathbf{A}$(**r**, t) satisfy the Lorentz condition, the electromagnetic (Faraday) tensor, $F^{\alpha\beta}$, is defined to be

$$F^{\alpha\beta} \doteq \partial_\alpha A_\beta - \partial_\beta A_\alpha = -F^{\beta\alpha}, \tag{8.28}$$

which, along with its dual contravariant tensor $\mathcal{F}^{\alpha\beta}$, take the respective form

$$F^{\alpha\beta} = \begin{pmatrix} 0 & -\mathrm{E}_x/c & -\mathrm{E}_y/c & -\mathrm{E}_z/c \\ \mathrm{E}_x/c & 0 & -\mathrm{B}_z & \mathrm{B}_y \\ \mathrm{E}_y/c & \mathrm{B}_z & 0 & -\mathrm{B}_x \\ \mathrm{E}_z/c & -\mathrm{B}_y & \mathrm{B}_x & 0 \end{pmatrix}, \tag{8.29}$$

and

$$\mathcal{F}^{\alpha\beta} = \begin{pmatrix} 0 & -\mathrm{B}_x & -\mathrm{B}_y & -\mathrm{B}_z \\ \mathrm{B}_x & 0 & \mathrm{E}_z/c & -\mathrm{E}_y/c \\ \mathrm{B}_y & -\mathrm{E}_z/c & 0 & \mathrm{E}_x/c \\ \mathrm{B}_z & \mathrm{E}_y/c & -\mathrm{E}_x/c & 0 \end{pmatrix}, \tag{8.30}$$

where E_x, E_y and E_z are the vector components of $\mathbf{E}$(**r**,t) in the x, y and z dimensions respectively, similarly for $\mathbf{B}$(**r**,t). Given the electromagnetic tensor, Maxwell's laws for electromagnetic fields in free space can be obtained from the following tensor equations:

$$\partial_\alpha F^{\alpha\beta} = \mu_0 J^\alpha \tag{8.31}$$

$$\partial_\alpha \mathcal{F}^{\alpha\beta} = 0. \tag{8.32}$$

Considering Equation 8.31 first. Letting $\beta = 0$, and summing over the dummy index

α, one obtains:

$$\partial_\alpha F^{\alpha 0} = \frac{\cancel{\partial(0)}}{\cancel{\partial(ct)}} + \frac{\partial(\mathrm{E}_x/c)}{\partial x} + \frac{\partial(\mathrm{E}_y/c)}{\partial y} + \frac{\partial(\mathrm{E}_z/c)}{\partial z} = \mu_0 c\rho$$

$$\frac{\partial(\mathrm{E}_x)}{\partial x} + \frac{\partial(\mathrm{E}_y)}{\partial y} + \frac{\partial(\mathrm{E}_z)}{\partial z} = \mu_0 c^2 \rho$$

$$\boxed{\nabla \cdot \mathbf{E} = \frac{\rho}{\epsilon_0},} \tag{8.33}$$

which is Gauss' Law for electric fields, also known as Maxwell's first law. The relation, $c = \frac{1}{\sqrt{(\mu_0 \epsilon_0)}}$ is also used in this derivation, a relation which is later shown to originate from the wave equation, where μ_0 is the permeability of free space and ϵ_0 is the permittivity of free space. This law states that the *net* flux through a closed surface is proportional to the *net* electric charged enclosed in that surface.

Letting $\beta = 1, 2, 3$ and once again summing over the dummy index α, Equation 8.31 leads to:

$$\begin{aligned}
\beta = 1: &\quad \frac{\partial(-\mathrm{E}_x)/c}{\partial(ct)} + \frac{\cancel{\partial(0)}}{\cancel{\partial(x)}} + \frac{\partial(\mathrm{B}_z)}{\partial(y)} + \frac{\partial(-\mathrm{B}_y)}{\partial(z)} + \ldots \\
\beta = 2: \ldots &\frac{\partial(-\mathrm{E}_y)/c}{\partial(ct)} + \frac{\partial(-\mathrm{B}_z)}{\partial(x)} + \frac{\cancel{\partial(0)}}{\cancel{\partial(y)}} + \frac{\partial(\mathrm{B}_x)}{\partial(z)} + \ldots \\
\beta = 3: \ldots &\frac{\partial(-\mathrm{E}_z)/c}{\partial(ct)} + \frac{\partial(\mathrm{B}_y)}{\partial(x)} + \frac{\partial(-\mathrm{B}_x)}{\partial(y)} + \frac{\cancel{\partial(0)}}{\cancel{\partial(z)}} = \mu_0 \mathrm{J}_x + \mu_0 \mathrm{J}_y + \mu_0 \mathrm{J}_z
\end{aligned}$$

$$\left(\frac{\partial \mathrm{B}_z}{\partial y} - \frac{\partial \mathrm{B}_y}{\partial z}\right)\hat{x} + \left(\frac{\partial \mathrm{B}_x}{\partial z} - \frac{\partial \mathrm{B}_z}{\partial x}\right)\hat{y} + \left(\frac{\partial \mathrm{B}_y}{\partial x} - \frac{\partial \mathrm{B}_x}{\partial y}\right)\hat{z} = \mu_0 \mathbf{J} + \frac{1}{c^2}\frac{\partial \mathbf{E}}{\partial t}$$

$$\boxed{\nabla \times \mathbf{B} = \mu_0 \mathbf{J} + \mu_0 \epsilon_0 \frac{\partial \mathbf{E}}{\partial t},} \tag{8.34}$$

where $\hat{x}$, $\hat{y}$ and $\hat{z}$ are unit vectors in the x, y and z dimensions respectively. This is the Ampère-Maxwell law, also referred to Maxwell's third law.

Now turning to the second tensor equation, Equation 8.32, taking $\beta = 0$ and summing over α:

$$\frac{\cancel{\partial(0)}}{\cancel{\partial(ct)}} + \frac{\partial \mathrm{B}_x}{\partial x} + \frac{\partial \mathrm{B}_y}{\partial y} + \frac{\partial \mathrm{B}_z}{\partial z} = 0 \tag{8.35}$$

$$\boxed{\nabla \cdot \mathbf{B} = 0,} \tag{8.36}$$

which is Gauss' Law for magnetic fields, also referred to Maxwell's second law. Analogously to Maxwell's first law, this law states that the *net* magnetic flux through a closed

surface is always zero, which, with the absence of evidence of magnetic monopoles remains zero.[‡] Analogously for the derivation of Maxwell's third law, consider Equation 8.32 with $\beta = 1, 2, 3$:

$$\begin{aligned}
\beta = 1: \quad & \frac{\partial(-\mathrm{B}_x)}{\partial(ct)} + \cancel{\frac{\partial(0)}{\partial(x)}} + \frac{\partial(-\mathrm{E}_z/c)}{\partial(y)} + \frac{\partial(\mathrm{E}_y/c)}{\partial(z)} + \ldots \\
\beta = 2: \ldots & \frac{\partial(-\mathrm{B}_y)}{\partial(ct)} + \frac{\partial(\mathrm{E}_z/c)}{\partial(x)} + \cancel{\frac{\partial(0)}{\partial(y)}} + \frac{\partial(-\mathrm{E}_x/c)}{\partial(z)} + \ldots \\
\beta = 3: \ldots & \frac{\partial(-\mathrm{B}_z)}{\partial(ct)} + \frac{\partial(-\mathrm{E}_y/c)}{\partial(x)} + \frac{\partial(\mathrm{E}_x/c)}{\partial(y)} + \cancel{\frac{\partial(0)}{\partial(z)}} = 0,
\end{aligned}$$

$$-\left(\frac{\partial \mathrm{E}_y}{\partial z} - \frac{\partial \mathrm{E}_z}{\partial y}\right)\hat{x} - \left(\frac{\partial \mathrm{E}_z}{\partial x} - \frac{\partial \mathrm{E}_x}{\partial z}\right)\hat{y} - \left(\frac{\partial \mathrm{E}_x}{\partial y} - \frac{\partial \mathrm{E}_y}{\partial x}\right)\hat{z} = \left(\frac{\partial \mathrm{B}_x}{\partial t} + \frac{\partial \mathrm{B}_y}{\partial t} + \frac{\partial \mathrm{B}_z}{\partial t}\right)$$

$$\boxed{\nabla \times \mathbf{E} = -\frac{\partial \mathbf{B}}{\partial t},} \tag{8.37}$$

which is Faraday's Law of electromagnetic induction, referred to as Maxwell's fourth Law. This law states that a time-varying magnetic field can produce an electric field and *vice versa*.[§]

Taking the curl of Equation 8.34 and Equation 8.37 for a vacuum (*i.e.* $\rho = \mathbf{J} = 0$):

$$\nabla^2 \mathbf{E} = \mu_0 \epsilon_0 \frac{\partial^2 \mathbf{E}}{\partial t^2} \longrightarrow \mathbf{E}(\mathbf{r}, t) = \mathrm{E}_0 e^{i(\boldsymbol{k}\cdot\mathbf{r} - \omega t)} + c.c, \tag{8.38}$$

and,

$$\nabla^2 \mathbf{B} = \mu_0 \epsilon_0 \frac{\partial^2 \mathbf{B}}{\partial t^2} \longrightarrow \mathbf{B}(\mathbf{r}, t) = \mathrm{B}_0 e^{i(\boldsymbol{k}\cdot\mathbf{r} - \omega t)} + c.c, \tag{8.39}$$

which are solutions to the general wave equation,[605] which therefore means that the quantity $\mu_0\epsilon_0$ is equal to the reciprocal speed the fields travel at, denoted as c, *i.e.* $c = \frac{1}{\sqrt{(\mu_0\epsilon_0)}}$, thus justifying the use of this relation used in the derivation of Equation 8.33. Solutions to these wave equations take the form of plane waves, where $c.c$ denotes the complex conjugate, and E_0 and B_0 are the electric and magnetic field amplitudes respectively. k is the wave number defined in terms of a wave's wavelength λ where $k = \dfrac{2\pi}{\lambda}$ and ω is related to the wave's frequency ν, where $\omega = 2\pi\nu$, called the angular frequency. These solutions demonstrate fundamental properties of the waves governed

[‡]Indeed, if magnetic monopoles are discovered, Maxwell's second law can be written as $\nabla \cdot \mathbf{B} = \mu_0 \eta$, where η is the total magnetic charge density in the closed surface.

[§]Similarly, this law can be modified to include the contribution to the generated electric field from the presence of a magnetic current density η such that $\nabla \times \mathbf{E} = -\mu_0\eta - \dfrac{\partial \mathbf{B}}{\partial t}$. For completeness, the Lorentz force experienced on a electrically charged, q_e, and magnetically charged, q_m particle with velocity, v is $\mathbf{F} = q_e\left(\mathbf{E} + v \times \mathbf{B}\right) + q_m\left(\mathbf{B} - v \times \frac{\mathbf{E}}{c^2}\right)$.

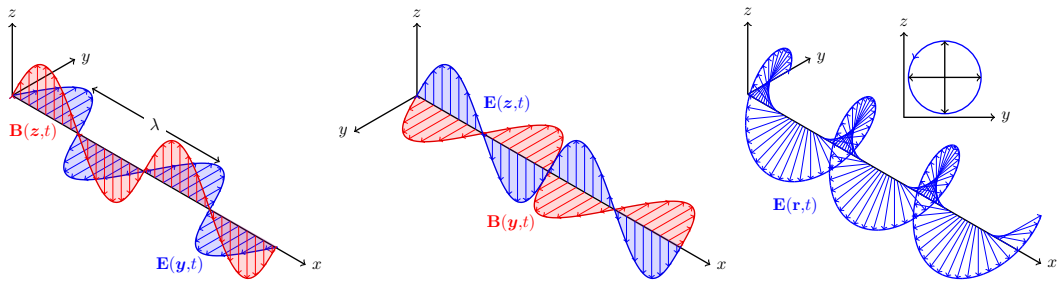

Figure 8.4 | The solutions of Maxwell's equations for free space are plane waves. Both the electric field $\mathbf{E}(\boldsymbol{y},t)$ and the magnetic field $\mathbf{B}(\boldsymbol{z},t)$ are orthogonal to the direction of propagation $\boldsymbol{x}$ as well as being orthogonal to one another. The wavelength has also been defined as λ. (*left*): A linear-horizontally polarised, $\mathbf{E}(\boldsymbol{y},t)$ waveform. (*middle*): A linear-vertically polarised waveform, $\mathbf{E}(\boldsymbol{z},t)$. (*right*): A circularly polarised waveform from the superposition of two linearly polarised waves, $\mathbf{E}(\mathbf{r},t)$.

by the wave equation. The first is that substituting the solutions into the respective Maxwell equation for divergence in free space, *i.e.* $\nabla \cdot \mathbf{E} = 0$ and $\nabla \cdot \mathbf{B} = 0$ are only simultaneously satisfied for all positions at all times if and only if $\boldsymbol{k} \cdot \mathrm{E} = \boldsymbol{k} \cdot \mathrm{B} = 0$ which is true only if *electric and magnetic fields exist in perpendicular planes to the direction of propagation.* From Maxwell's third and fourth laws, the curl of one field is equal to the time derivative of the other field which demonstrates that *electric and magnetic fields exist in orthongonal planes to one another.* Finally, these solutions obey the superposition principle allowing linear combination of solutions also satisfy the wave equation, and thus, are also solutions to Maxwell's equations.[¶] The solutions to Maxwell's equation are depicted in Figure 8.4.

The above holds true for electromagnetic fields in free space, *i.e.* a vacuum, as there are no atoms in the medium to interact with an applied electric or magnetic field. When there are atoms present *i.e. any* media other than a vacuum, charges are perturbed by an external field such as a propagating electromagnetic field which modifies the local electric and magnetic fields inside the medium. Since all measurements, at some point, will not be *in vacuo*, whether there are mirrors and lenses, a spectrometer and fibre optics, or even air, Maxwell's equations as given above will not hold in general and must be modified to account for the type of propagation medium.

[¶]In general, one or more waves $(F(x_1), F(x_2) \ldots F(x_n))$ satisfy the superposition principle if:

$$F(x_1) + F(x_2) = F(x_1 + x_2) \quad \text{Principle of additivity} \tag{8.40}$$

$$F(ax) = aF(x) \quad \text{Principle of homogeneity.} \tag{8.41}$$

8.4.2 Electromagnetic radiation in media

For any medium which contains atoms, there will be some electric and magnetic field associated with them. These fields become perturbed when a electromagnetic wave propagates through the medium, which in turn, alters the propagation of the wave. Often these perturbations are linearly proportional to the applied field with nonlinear effects being negligible for most radiation, but for laser pulses whose $\mathbf{E}(\mathbf{r},t)$ and $\mathbf{B}(\mathbf{r},t)$ fields are very intense, nonlinear effects become important. Throughout this thesis, we only consider nonlinear perturbations with respect to electric fields. The reason for this is that the nonlinear magnetic susceptibility of the materials utilised in this work are negligible and thus any perturbations are essentially zero.

We introduce a new vector, $\mathbf{P}(\mathbf{r},t)$, the polarisation of a medium. This is defined as the infinitesimally small change in the electric dipole moment, d$\mathbf{p}$, per unit volume of medium, dV, *i.e.*

$$\mathbf{P}(\mathbf{r},t) \doteq \frac{\mathrm{d}\mathbf{p}}{\mathrm{d}V}. \tag{8.42}$$

The first constitutive equation can now be defined; the displacement field $\mathbf{D}(\mathbf{r},t)$ for a polarisable medium is given by

$$\mathbf{D}(\mathbf{r},t) \doteq \epsilon_0 \mathbf{E}(\mathbf{r},t) + \mathbf{P}(\mathbf{r},t), \tag{8.43}$$

which captures the effects of local changes in the electric field of a medium in response to the applied external electric field, $\mathbf{E}(\mathbf{r},t)$. The second constitutive equation may be defined in a similar fashion using a magnetising field, $\mathbf{H}(\mathbf{r},t)$,

$$\mathbf{H}(\mathbf{r},t) \doteq \frac{1}{\mu_0}\mathbf{B}(\mathbf{r},t) + \mathbf{M}(\mathbf{r},t), \tag{8.44}$$

where $\mathbf{M}(\mathbf{r},\mathrm{t})$ is the magnetisation of the medium. For a nonmagnetic material, $\mathbf{M}(\mathbf{r},t)$ $= 0$ resulting in the simple linear relationship of $\mathbf{H}(\mathbf{r},t) = \frac{1}{\mu_0}\mathbf{B}(\mathbf{r},t)$. These constitutive relations can be substituted into Maxwell equations for electromagnetic radiation in free space to describe the propagation of radiation in a medium, *cf.* Equation 8.33, Equation

8.36, Equation 8.34 and Equation 8.37,

$$\nabla \cdot \mathbf{D} = \rho \tag{8.45}$$

$$\nabla \cdot \mathbf{H} = 0 \tag{8.46}$$

$$\nabla \times \mathbf{E} = -\mu_0 \frac{\partial \mathbf{H}}{\partial t} \tag{8.47}$$

$$\nabla \times \mathbf{H} = \frac{\partial \mathbf{D}}{\partial t} + \mathbf{J}, \tag{8.48}$$

which describes radiation propagating through polarisable, nonmagnetic media as

$$\nabla^2 \mathbf{E} + \frac{1}{c^2}\frac{\partial^2 \mathbf{E}}{\partial t^2} = -\frac{1}{\epsilon_0 c^2}\frac{\partial^2 \mathbf{P}}{\partial t^2}, \tag{8.49}$$

with a corresponding magnetic field related *via* Equation 8.47. The functional form of a material's polarisation vector can lead to a myriad of optical phenomena and needs to be calculated in order to solve the wave equation given in Equation 8.49. Generally, the polarisation vector can be written as a Taylor expansion about the linear relationship between the polarisation vector and the applied electric field strength, $\mathbf{P}(\mathbf{r},t) = \epsilon_0 \chi^{(1)} \mathbf{E}(\mathbf{r},t)$, where $\chi^{(1)}$ is the electric susceptibility of the material. This assumption holds if the nonlinear effects of the applied electric field weakly perturbs the material's polarisation away from a linear response, which is usually a reasonable approximation, even for ultrashort laser pulses. Therefore, $\mathbf{P}(\mathbf{r},t)$ can be written as

$$\mathbf{P}(\mathbf{r},t) = \underbrace{\epsilon_0 \chi^{(1)} \mathbf{E}}_{\mathbf{P}^{(1)}} + \underbrace{\epsilon_0 \chi^{(2)} \mathbf{E}^2}_{\mathbf{P}^{(2)}} + \underbrace{\epsilon_0 \chi^{(3)} \mathbf{E}^3}_{\mathbf{P}^{(3)}} + \cdots = \sum_{n=1}^{\infty} \underbrace{\epsilon_0 \chi^{(n)} \mathbf{E}^n}_{\mathbf{P}^{(n)}}, \tag{8.50}$$

where $\chi^{(n)}$ is the n^{th} order electric susceptibility and $\mathbf{P}^{(n)}$ is the n^{th} order contribution to the total polarisation vector.[‖] Thus electromagnetic radiation propagating in a polarisable medium can be readily approximated by Equation 8.50 and the resulting nonlinear optical processes can be derived.

[‖]It should be noted that this is true only when $\mathbf{P}(\mathbf{r},t)$ and $\mathbf{E}(\mathbf{r},t)$ are taken to be scalar quantities which is sufficient for the characterisation of the optical phenomena discussed in this thesis. In reality however, $\chi^{(n)}$ is a tensor $(n+1)$-rank tensor giving

$$\mathbf{P}(\mathbf{r},t) = \epsilon_0 \sum_{i=1}^{n} \left(\sum_j \boldsymbol{\chi}^{(1)}_{ij} \mathbf{E}_j + \sum_{jk} \boldsymbol{\chi}^{(2)}_{ijk} \mathbf{E}_j \mathbf{E}_k + \sum_{jkl} \boldsymbol{\chi}^{(3)}_{ijkl} \mathbf{E}_j \mathbf{E}_k \mathbf{E}_l + \dots \right).$$

8.4.3 Nonlinear optical phenomena

For an electromagnetic wave of the form Equation 8.38 which comprises of two distinct frequencies, propagating through a medium which responds quadratically to the wave's electric field, *i.e.* $\mathbf{P}^{(2)}$, the polarisation vector for some medium can be written as

$$\mathbf{P}^{(2)} = \epsilon_0 \chi^{(2)} \left(\mathrm{E}_1 e^{i(\boldsymbol{k_1}\cdot\mathbf{r} - \omega_1 t)} + \mathrm{E}_2 e^{i(\boldsymbol{k_2}\cdot\mathbf{r} - \omega_2 t)} + c.c \right)^2, \tag{8.51}$$

which simplifies to:

$$\begin{aligned} \mathbf{P}^{(2)} = \epsilon_0 \chi^{(2)} \Big[& \overbrace{\mathrm{E}_1^2 e^{-i2\omega_1 t} e^{i2\mathbf{k}_1\cdot\mathbf{r}}}^{\text{SHG}} + \overbrace{\mathrm{E}_2^2 e^{-i2\omega_2 t} e^{i2\mathbf{k}_2\cdot\mathbf{r}}}^{\text{SHG}} + \overbrace{2\mathrm{E}_1\mathrm{E}_2 e^{-i(\omega_1+\omega_2)t} e^{i(\mathbf{k}_1+\mathbf{k}_2)\cdot\mathbf{r}}}^{\text{SFG}} \ldots \\ & + \underbrace{2\mathrm{E}_1\mathrm{E}_2^* e^{-i(\omega_1-\omega_2)t} e^{i(\mathbf{k}_1-\mathbf{k}_2)\cdot\mathbf{r}}}_{\text{DFG}} + \underbrace{2\left(\mathrm{E}_1\mathrm{E}_1^* + \mathrm{E}_2\mathrm{E}_2^*\right)}_{\text{OR}} \Big]. \end{aligned} \tag{8.52}$$

Each of the labelled contributions to the quadratic polarisation vector correspond to specific optical phenomena (SHG, SFG, DFG and OR).

Second Harmonic Generation (SHG). The contribution to the nonlinear polarisation of $\mathrm{E}_1^2 e^{-i2\omega_1 t} e^{i2\mathbf{k}_1\cdot\mathbf{r}}$ describes a frequency component oscillating at twice the rate of the ω_1 component of the incident wave. Identically this is seen for the ω_2 component contributing $\mathrm{E}_2^2 e^{-i2\omega_2 t} e^{i2\mathbf{k}_2\cdot\mathbf{r}}$ to the polarisation vector. These terms therefore describe the generation of radiation with frequency components of $2\omega_1$ and $2\omega_2$ *cf.* Equation 8.51, which are the second harmonics on the incident frequency components ω_1 and ω_2 respectively.

Sum Frequency Generation (SFG). The contribution of $2\mathrm{E}_1\mathrm{E}_2 e^{-i(\omega_1+\omega_2)t} e^{i(\mathbf{k}_1+\mathbf{k}_2)\cdot\mathbf{r}}$ to the nonlinear polarisation describes the generation of a frequency component oscillating at the sum of the two distinct incident frequency components *i.e.* $\omega_1 + \omega_2$. Therefore SHG described above is simply a special case of SFG with the condition $\omega_1 = \omega_2$. A similar phenomena is described as the time reversal of SFG, so called Optical Parametric Generation (OPG), see Figure 8.5. In OPG, one photon is converted into two photons of lower frequency, with energy conserved.

Difference Frequency Generation (DFG). The contribution of $2\mathrm{E}_1\mathrm{E}_2^* e^{-i(\omega_1-\omega_2)t} e^{i(\mathbf{k}_1-\mathbf{k}_2)\cdot\mathbf{r}}$ to the nonlinear polarisation describes the generation of a frequency component oscillating at the difference of two distinct incident frequency components *i.e.* $\omega_1 - \omega_2$.

Optical Rectification (OR). The final contribution $2\left(\mathrm{E}_1\mathrm{E}_1^* + \mathrm{E}_2\mathrm{E}_2^*\right)$ to the nonlinear polarisation corresponds to a static polarisation density which sets up a direct current voltage across the surface of the nonlinear medium, perpendicular to the propagation of the radiation. This optical phenomena is often exploited in terahertz pulse generation,

but is not used in this work.

Using an identical procedure for the cubic response to an propagating electromagnetic wave, *i.e.* $\mathbf{P}^{(3)}$, with three distinct frequency components, ω_1, ω_2 and ω_3, the polarisation vector may be calculated to be

$$\mathbf{P}^{(3)} = \epsilon_0 \chi^{(3)} \left(\mathrm{E}_1 e^{i(\boldsymbol{k_1}\cdot\mathbf{r}-\omega_1 t)} + \mathrm{E}_2 e^{i(\boldsymbol{k_2}\cdot\mathbf{r}-\omega_2 t)} + \mathrm{E}_3 e^{i(\boldsymbol{k_3}\cdot\mathbf{r}-\omega_3 t)} + c.c \right)^3, \tag{8.53}$$

which, when expanded, is

$$\begin{aligned}
\mathbf{P}^{(3)} = \epsilon_0 \chi^{(3)} \Big[& (3\mathrm{E}_1\mathrm{E}_1^* + 6\mathrm{E}_2\mathrm{E}_2^* + 6\mathrm{E}_3\mathrm{E}_3^*)\,\mathrm{E}_1 e^{i(\boldsymbol{k_1}\cdot\mathbf{r}-\omega_1 t)} + (6\mathrm{E}_1\mathrm{E}_1^* + 3\mathrm{E}_2\mathrm{E}_2^* + 6\mathrm{E}_3\mathrm{E}_3^*)\,\mathrm{E}_2 e^{i(\boldsymbol{k_2}\cdot\mathbf{r}-\omega_2 t)} + \\
& (6\mathrm{E}_1\mathrm{E}_1^* + 6\mathrm{E}_2\mathrm{E}_2^* + 3\mathrm{E}_3\mathrm{E}_3^*)\,\mathrm{E}_3 e^{i(\boldsymbol{k_3}\cdot\mathbf{r}-\omega_3 t)} + \mathrm{E}_1^3 e^{3i(\boldsymbol{k_1}\cdot\mathbf{r}-\omega_1 t)} + \mathrm{E}_2^3 e^{3i(\boldsymbol{k_2}\cdot\mathbf{r}-\omega_2 t)} + \mathrm{E}_3^3 e^{3i(\boldsymbol{k_3}\cdot\mathbf{r}-\omega_3 t)} + \\
& 6\mathrm{E}_1\mathrm{E}_2\mathrm{E}_3 e^{i((\mathbf{k}_1+\mathbf{k}_2+\mathbf{k}_3)\cdot\mathbf{r}-(\omega_1+\omega_2+\omega_3)t)} + 6\mathrm{E}_1\mathrm{E}_2\mathrm{E}_3^* e^{i((\mathbf{k}_1+\mathbf{k}_2-\mathbf{k}_3)\cdot\mathbf{r}-(\omega_1+\omega_2-\omega_3)t)} + \\
& 6\mathrm{E}_1\mathrm{E}_3\mathrm{E}_2^* e^{i((\mathbf{k}_1+\mathbf{k}_3-\mathbf{k}_2)\cdot\mathbf{r}-(\omega_1+\omega_3-\omega_2)t)} + 6\mathrm{E}_2\mathrm{E}_3\mathrm{E}_1^* e^{i((\mathbf{k}_2+\mathbf{k}_3-\mathbf{k}_1)\cdot\mathbf{r}-(\omega_2+\omega_3-\omega_1)t)} + \\
& 3\mathrm{E}_1^2\mathrm{E}_2 e^{i((2\mathbf{k}_1+\mathbf{k}_2)\cdot\mathbf{r}-(2\omega_1+\omega_2)t)} + 3\mathrm{E}_1^2\mathrm{E}_3 e^{i((2\mathbf{k}_1+\mathbf{k}_3)\cdot\mathbf{r}-(2\omega_1+\omega_3)t)} + 3\mathrm{E}_2^2\mathrm{E}_1 e^{i((2\mathbf{k}_2+\mathbf{k}_1)\cdot\mathbf{r}-(2\omega_2+\omega_1)t)} + \\
& 3\mathrm{E}_2^2\mathrm{E}_3 e^{i((2\mathbf{k}_2+\mathbf{k}_3)\cdot\mathbf{r}-(2\omega_2+\omega_3)t)} + 3\mathrm{E}_3^2\mathrm{E}_1 e^{i((2\mathbf{k}_3+\mathbf{k}_1)\cdot\mathbf{r}-(2\omega_3+\omega_1)t)} + 3\mathrm{E}_3^2\mathrm{E}_2 e^{i((2\mathbf{k}_3+\mathbf{k}_2)\cdot\mathbf{r}-(2\omega_3+\omega_2)t)} + \\
& 3\mathrm{E}_1^2\mathrm{E}_2^* e^{i((2\mathbf{k}_1-\mathbf{k}_2)\cdot\mathbf{r}-(2\omega_1-\omega_2)t)} + 3\mathrm{E}_1^2\mathrm{E}_3^* e^{i((2\mathbf{k}_1-\mathbf{k}_3)\cdot\mathbf{r}-(2\omega_1-\omega_3)t)} + 3\mathrm{E}_2^2\mathrm{E}_1^* e^{i((2\mathbf{k}_2-\mathbf{k}_1)\cdot\mathbf{r}-(2\omega_2-\omega_1)t)} + \\
& 3\mathrm{E}_2^2\mathrm{E}_3^* e^{i((2\mathbf{k}_2-\mathbf{k}_3)\cdot\mathbf{r}-(2\omega_2-\omega_3)t)} + 3\mathrm{E}_3^2\mathrm{E}_1^* e^{i((2\mathbf{k}_3-\mathbf{k}_1)\cdot\mathbf{r}-(2\omega_3-\omega_1)t)} + 3\mathrm{E}_3^2\mathrm{E}_2^* e^{i((2\mathbf{k}_3-\mathbf{k}_2)\cdot\mathbf{r}-(2\omega_3-\omega_2)t)} \Big].
\end{aligned} \tag{8.54}$$

For this general case, third order nonlinear optical phenomena may be derived, four of these processes in particular are important in this thesis.**

Third Harmonic Generation (THG). The three terms highlighted in blue, for which $\omega_i = \omega_1$, ω_2 and ω_3 respectively, each contributes $\mathrm{E}_i^3 e^{3i(\boldsymbol{k_i}\cdot\mathbf{r}-\omega_i t)}$ to the polarisation vector $\mathbf{P}^{(3)}$. These terms describe a resultant wave which oscillates at three times the frequency of the distinct components of the incident wave, *i.e.* $\omega = 3\omega_1$, $\omega = 3\omega_2$ or $\omega = 3\omega_3$ respectively, referred to as third harmonic generation.

Three-wave sum frequency generation. Analogously to SFG described previously, the component of the polarisation vector highlighted in red, $6\mathrm{E}_1\mathrm{E}_2\mathrm{E}_3 e^{i((\mathbf{k}_1+\mathbf{k}_2+\mathbf{k}_3)\cdot\mathbf{r}-(\omega_1+\omega_2+\omega_3)t)}$, corresponds to a resultant wave which oscillates at the sum of the three distinct frequency components of the incident wave, *i.e.* $\omega = \omega_1 + \omega_2 + \omega_3$. Thus THG is a special case of this process with $\omega_1 = \omega_2 = \omega_3$. An important application of this process is optical parametric amplification, distinct from OPG in that an additional frequency component equal to that which is required is supplied as a weak incident wave, subsequently amplifying that component, rendering OPA an ideal alternative to OPG when applicable.

Three-wave difference frequency generation. Similarly, the contributions to $\mathbf{P}^{(3)}$,

**The terms which are not described involve the sum frequency or difference frequency generation of a wave from the second harmonic of one incident frequency with the fundamental of another, *i.e.* $3\mathrm{E}_i^2\mathrm{E}_j^* e^{i((2\mathbf{k}_i \pm \mathbf{k}_j)\cdot\mathbf{r}+(2\omega_i \pm \omega_j)t)}$, where i and $j = [1,2,3] \bigcap i \neq j; \mathrm{sgn}(\mathbf{k}_j) = \mathrm{sgn}(\omega_j)$ for which there are 12 unique permutations.

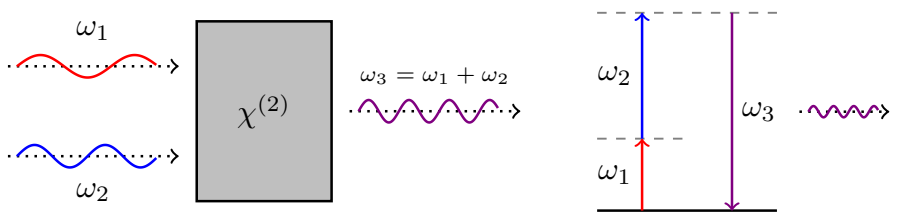

(A) Sum frequency generation

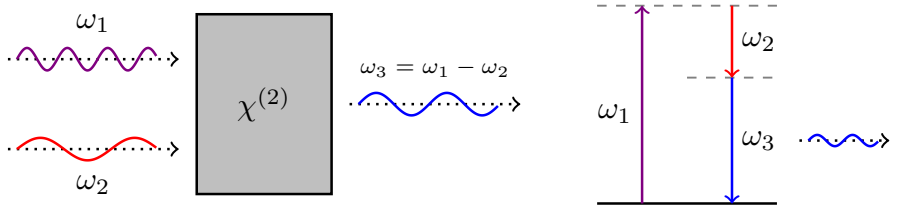

(B) Difference frequency generation

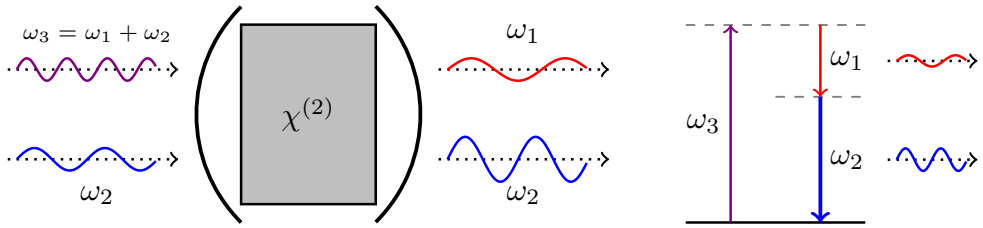

(C) Optical parametric generation, oscillation and amplification

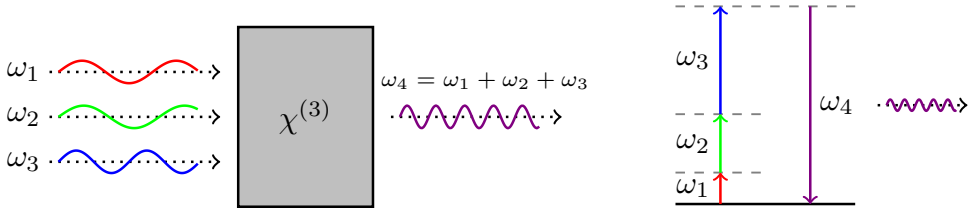

(D) Four wave mixing sum frequency generation

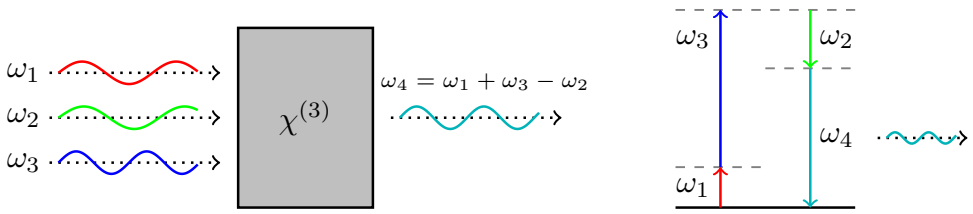

(E) Four wave mixing difference frequency generation

Figure 8.5 | (A–C) Summary of the general second order nonlinear optical phenomena. Second harmonic generation is the special case of sum frequency generation with the condition $\omega_1 = \omega_2$. Optical parametric generation can be used with resonate cavity mirrors, called optical parametric oscillation or with an addition signal pump (ω_2) to increase the gain of that frequency, called optical parametric amplification. (D–E) Two examples of four wave mixing processes from third order nonlinear susceptibility.

highlighted in violet, $6\mathrm{E}_1\mathrm{E}_2\mathrm{E}_3^* e^{i((\mathbf{k}_1+\mathbf{k}_2-\mathbf{k}_3)\cdot\mathbf{r}-(\omega_1+\omega_2-\omega_3)t)}$, $6\mathrm{E}_1\mathrm{E}_3\mathrm{E}_2^* e^{i((\mathbf{k}_1+\mathbf{k}_3-\mathbf{k}_2)\cdot\mathbf{r}-(\omega_1+\omega_3-\omega_2)t)}$ and $6\mathrm{E}_2\mathrm{E}_3\mathrm{E}_1^* e^{i((\mathbf{k}_2+\mathbf{k}_3-\mathbf{k}_1)\cdot\mathbf{r}-(\omega_2+\omega_3-\omega_1)t)}$, *i.e.* the three unique permutations of the subtraction of one frequency component from the other two, describes a resultant wave with frequency $\omega = \omega_i + \omega_j - \omega_k$, where $i = j = k = [1, 2, 3] \bigcap i \neq j \neq k$. These three third order processes are summarised in Figure 8.5.

Finally, the first three terms of Equation 8.54 which are highlighted in green, and which take the form $(a\mathrm{E}_1\mathrm{E}_1^* + b\mathrm{E}_2\mathrm{E}_2^* + c\mathrm{E}_3\mathrm{E}_3^*)\,\mathrm{E}_j e^{i(\boldsymbol{k_j}\cdot\mathbf{r}-\omega_j t)}$ with $\omega_j = \omega_1$ with $a = 3$, $b = c = 6$ or $\omega_j = \omega_2$ with $b = 3$, $a = c = 6$ or $\omega_j = \omega_3$ with $c = 3$, $a = b = 6$ describe a resultant wave with the same frequency components as the incident wave. These terms are attributed to a self focussing effect which modulates the incident wave in the medium. Self focussing is a subset of optical properties attributed to the optical Kerr effect which is discussed in the next section. All the processes described thus far are key examples of *parametric* processes, that is, there is no net change to the quantum state of the medium the process is occurring in. Conversely *nonparametric* processes do not conserve the quantum state of the medium, prominent examples being two-photon absorption (or indeed *any* multi-photon absorption event) and saturable absorption. Throughout this thesis all nonlinear optical processes utilised are parametric unless otherwise stated.

8.4.4 The optical Kerr effect and its manifestations

The optical Kerr effect is the observation that the electric field of an electromagnetic wave travelling through a medium increases the nonlinear refractive index in that medium. This occurs for *any* medium, with the magnitude of the effect depending on the intensity of the propagating electromagnetic wave, and the third order susceptibility, $\chi^{(3)}$, of the medium.

Considering the case of an electromagnetic wave with three distinct frequency components, with a electric susceptibility to the 3$^{\text{rd}}$ order,[††] *i.e.* $\chi = \chi^{(1)} + \chi^{(3)}$, and using

[††]In the ensuing description it is clear that the contribution (if any) of $\chi^{(2)}$ to the total susceptibility does not factor into the optical Kerr effect. Furthermore, since all media have a component of $\chi^{(3)}$ (albeit to varying degrees), all media can exhibit the optical Kerr effect.

the result of Equation 8.54, the polarisation vector may can be written as

$$\begin{aligned}\mathbf{P} &= \epsilon_0 \left(\chi^{(1)} + \chi^{(3)}\right) \left(\mathrm{E}_1 e^{i(\boldsymbol{k_1}\cdot\mathbf{r}-\omega_1 t)} + \mathrm{E}_2 e^{i(\boldsymbol{k_2}\cdot\mathbf{r}-\omega_2 t)} + \mathrm{E}_3 e^{i(\boldsymbol{k_3}\cdot\mathbf{r}-\omega_3 t)} + c.c\right)^3 \\ &= \epsilon_0 \chi^{(1)} \mathbf{E}(\mathbf{r},t) + \begin{pmatrix} 3\mathrm{E}_1\mathrm{E}_1^* & 6\mathrm{E}_1\mathrm{E}_1^* & 6\mathrm{E}_1\mathrm{E}_1^* \\ 6\mathrm{E}_2\mathrm{E}_2^* & 3\mathrm{E}_2\mathrm{E}_2^* & 6\mathrm{E}_2\mathrm{E}_2^* \\ 6\mathrm{E}_3\mathrm{E}_3^* & 6\mathrm{E}_3\mathrm{E}_3^* & 3\mathrm{E}_3\mathrm{E}_3^* \end{pmatrix} \cdot \begin{pmatrix} \mathrm{E}_1 e^{i(\boldsymbol{k_1}\cdot\mathbf{r}-\omega_1 t)} \\ \mathrm{E}_2 e^{i(\boldsymbol{k_2}\cdot\mathbf{r}-\omega_2 t)} \\ \mathrm{E}_3 e^{i(\boldsymbol{k_3}\cdot\mathbf{r}-\omega_3 t)} \end{pmatrix} + \ldots \\ &= \epsilon_0 \chi^{(1)} \mathbf{E}(\mathbf{r},t) + \chi^{(3)} \mathbf{I} \times \mathbf{E}(\mathbf{r},t) + \ldots \\ &= \epsilon_0 \left(\chi^{(1)} + \chi^{(3)} \mathbf{I}\right) \mathbf{E}(\mathbf{r},t) + \ldots,\end{aligned} \tag{8.55}$$

where we have introduced for simplicity a matrix $\mathbf{I}$ whose elements are simply intensities. The '...' represents the other terms of this expansion, as given in Equation 8.54, but correspond to the processes described in Figure 8.5. This shows the total susceptibility as the sum of a linear term, $\chi_{\mathrm{L}} = \chi^{(1)}$, and a nonlinear term, $\chi_{\mathrm{NL}} = \chi^{(3)}\mathbf{I}$. It is more convenient to consider the susceptibility in terms of the refractive index of the medium, n, which are related through the expression

$$n = (1+\chi)^{\frac{1}{2}} = (1 + \chi_{\mathrm{L}} + \chi_{\mathrm{NL}})^{\frac{1}{2}} \approx (1+\chi_{\mathrm{L}}) \left(1 + \frac{1}{2\,(1+\chi_{\mathrm{L}})} \chi_{\mathrm{NL}}\right), \tag{8.56}$$

by Taylor expanding under the approximation of $\chi_{\mathrm{NL}} \ll 1 + \chi_{\mathrm{L}}$, which, substituting the expressions of χ_{L} and χ_{NL} into the above yields

$$n = \left(1 + \chi^{(1)}\right) + \frac{\chi^{(3)}\mathbf{I}}{2\,(1+\chi^{(1)})} = n_0 + n_2 \mathbf{I}. \tag{8.57}$$

Thus the first three terms of the third order polarisation vector contribute to an nonlinear refractive index term which depends quadratically on the applied electric field. In general, this nonlinear refractive index is referred to as the *optical Kerr effect*. Since intensity and thus the applied electric field depends on the spatial coordinates of the wave in the medium, as well as the time-dependent amplitude, the optical Kerr effects manifests in both space and time dimensions. Such effects are typically called 'self actions' because the electromagnetic radiation causes a change in the medium's refractive index, which subsequently alters the propagation of the wave. The self actions which are most important to the concepts in this thesis are qualitatively discussed below.

Self focussing. Since the refractive index of the medium can be modulated by the intensity of the electromagnetic radiation applied, a laser pulse will create localised changes to the medium's refractive index since its intensity profile is not constant through space. As such, for a positive nonlinear refractive index, and an intensity

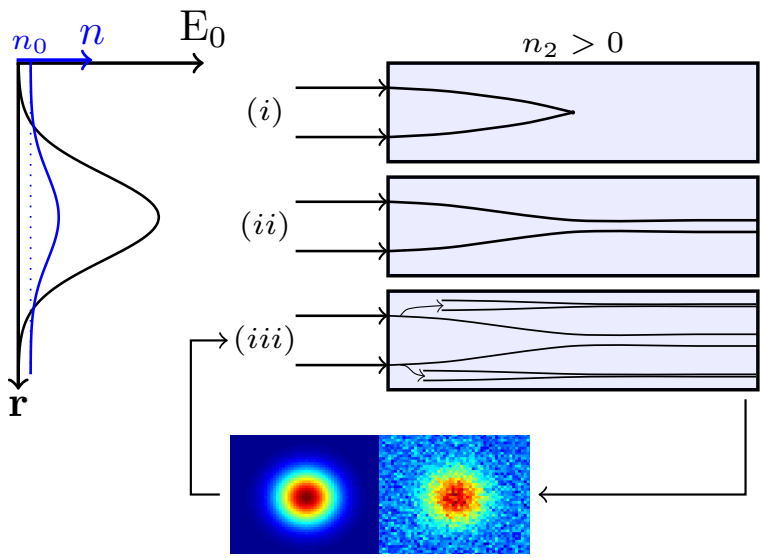

Figure 8.6 | The optical Kerr effect results from the nonlinear refractive index induced by the electric field, **E**, of an incident electromagnetic wave. For a Gaussian beam as depicted, the nonlinear refractive index (blue line) increases proportional to $|\mathbf{E}|^2$. (i) Self focussing due to a non-zero n_2 if unsuppressed leads to a single focal point for the incident wave inside of the medium. (ii) In reality, self focussing induces the production of free electrons from the medium which reduces the refractive index, in proportion to the strength of self focussing. These two processes reach an equilibrium which allows the incident waves to propagate through the medium, called self trapping. (iii) In the case of high incident power, the beam may split into multiple beams, each of which undergoes self trapping proportional to the local n_2 in that region. This processes is referred to as multi beam filamentation. The result of this process is also shown in the colour maps (bottom; colour represents intensity), left is the initial Gaussian beam, right is the resultant beam after multi beam filamentation.

profile of say a Gaussian pulse, the pulse will alter the refractive index more in regions of greater intensity, thus the beam will self focus inside the medium (Figure 8.6). This effect has important implications for the generation of supercontinua where intense, focussed light is required for initiation.

Self trapping. A pure self focussing effect will in principle cause the beam to focus into a single point. However, as self focussing increased, which causes an increased wave intensity in the medium, multi-photon effects inside the medium rapidly become more probable. This causes free electrons to be released which contribute negatively to the refractive index, thus, reduces the net self focussing effect. Self focussing and multi-photon effects eventually reach an equilibrium which allows the beam to continue propagating through the medium without being focussed into a single point, referred to as self trapping.

Multi-beam filamentation. If the power of the incident electromagnetic radiation is particular large (much larger than the power threshold for self focussing) it is possible that the incident beam will quasi-randomly split into multiple beams due to four wave mixing processes, or any inhomogeneities in the beam wave front. Each of these split beams are referred to as filaments, each of which can undergo self action processes. This has the effect of causing an inhomogeneous intensity profile across the medium. This effect is also important in the generation of supercontinua, whereby a single beam splitting into multiple beams which undergo self action processes all to varied degrees results in a larger total spectral broadening.

Self focussing, self trapping and multi-beam filamentation are all spatial manifestations of the optical Kerr effect, summarised in Figure 8.6. Temporally, the optical Kerr effect predominantly manifests as a process called self phase modulation.

Self Phase Modulation (SPM). This process describes an induced change in an incident wave's phase by the nonlinear refractive index. It is most readily understood by considering a wave of the form Equation 8.4 travelling in the x direction, which passes through some length of media, L.

$$\mathbf{E}(\mathbf{r},t) = \mathrm{E}_0 e^{i(\boldsymbol{k}\cdot\mathbf{r}-\omega_0 t)} + c.c \doteq \mathbf{E}(\mathbf{x},t) = \mathrm{E}_0 e^{i\phi_0} + c.c, \tag{8.58}$$

where we have defined a initial phase term, $\phi_0 = \boldsymbol{k}\cdot\mathbf{x} - \omega_0 t$. The forward travelling wave upon entering the medium experiences a phase change due to the time dependent wave intensity, $\mathrm{I}(t)$. If the wave travels through the medium between $x = 0$ and $x = L$, see Figure 8.7, the outgoing wave now has a phase $\phi_L = kn_oL + kn_2\mathrm{I}L - \omega_o t$, thus a change in phase occurs, $\Delta\phi = \phi_L - \phi_0$, leading to a modulated frequency:

$$\omega = -\frac{\partial(\Delta\phi)}{\partial t} = \omega_0 - n_2\frac{\omega_0}{c}L\frac{\partial \mathrm{I}}{\partial t}. \tag{8.59}$$

Thus a non-zero, positive n_2 leads the forward travelling wave to red shift in frequency, often referred to as Stokes broadening, and the trailing wave to blue shift in frequency, referred to as anti-Stokes broadening. This simple model of SPM however assumes an instantaneous response of the medium and thus of n_2 as well. This leads to the phase modulation of $\Delta\phi$ being proportional to the variation in intensity, which is generally not true. Typically a medium's finite response time can lead to an asymmetrical phase modulation resulting in an asymmetrical broadening about ω_o, thus an asymmetrical Stokes anti-Stokes shift. An important note is that this asymmetry typically favours anti-Stokes shifting, explained qualitatively by another self-action effect, self steepening.

Self steepening. This is the observation that the intensity maxima of a pulse can

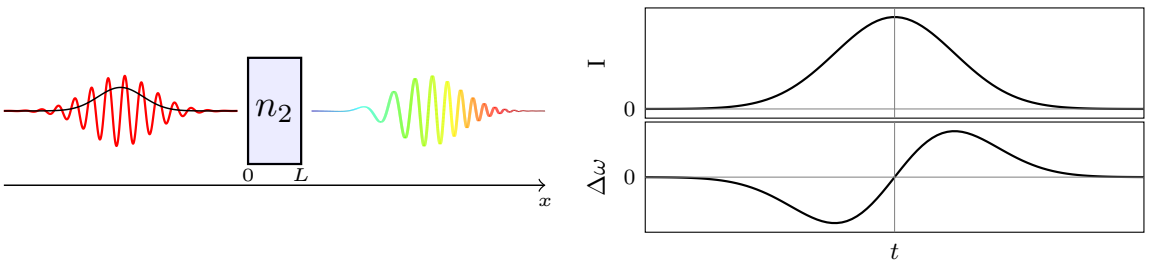

Figure 8.7 | (*left*): SPM of an incident 800 nm Gaussian pulse in a nonlinear positive n_2 medium. Above the critical power threshold for that medium, the initial beam can undergo Stokes- and anti-Stokes shifting, broadening the pulse and forming a supercontinuum. (*right*; *top*): The time-averaged intensity of the Gaussian pulse (black line of (A)). (*bottom*): The frequency shift experienced, proportional to the derivative of the intensity (Equation 8.59).

shift temporally (Figure 8.8). This reason for this is that the time dependant intensity of the incident pulse causes an intensity dependant group velocity of the pulse.

$$v_g \doteq \frac{\partial \omega}{\partial k} = \frac{c}{n(\mathbf{I}) + \omega \dfrac{\partial n}{\partial \omega}}. \tag{8.60}$$

As depicted in Figure 8.8, the high intensity regions of the pulse will result in a larger refractive index. From Equation 8.60, this means that the high intensity regions will have a lower group velocity than the rest of the pulse. For a Gaussian pulse, the intensity maxima will therefore travel slower than its 'wings'. Over time, this causes the intensity maximum to shift towards the trailing edge of the pulse, referred to as self steepening, depicted in Figure 8.7. This simple model of SPM qualitatively captures the salient phenomena required in this thesis. The most important result from this model is the broadening of the incident beam. Broadening about the initial frequency, ω_0 generates a multitude of other frequencies. In the case of this thesis, this phenomena is seen in the generation of a white light continuum, where an initial 800 nm beam is spectrally broadened to contain frequencies between ∼300 nm and ∼1000 nm.

8.4.5 Phase matching

An important consideration which has not been discussed so far is the requirement of *phase matching*. Throughout this section, the wave vector of the incident wave(s) has been left simply as k_1, $k_2 \ldots$ *etc.* since the existence of all the discussed optical phenomena can be described by considering the resultant frequency of the wave(s). In

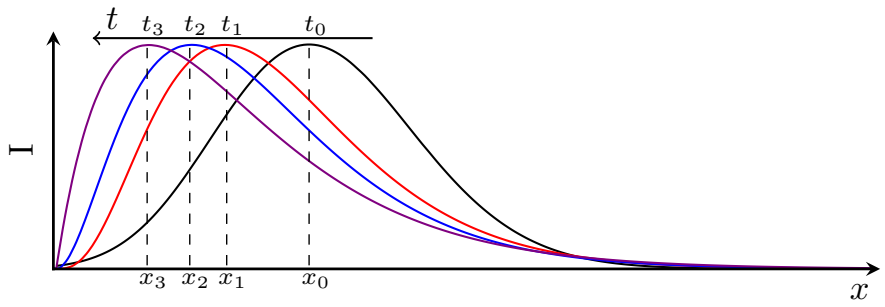

Figure 8.8 | A representative example of the self steepening effect of a Gaussian pulse in a $n_2 > 0$ medium. Over time, t_0, $t_1 \ldots t_3$, the intensity maximum moves further into the tail-end of the pulse, x_0, $x_1 \ldots x_3$.

reality, these phenomena will only occur with appreciable probability if the incident waves are phase matched, which simply means the vector sum of all the incident wave vectors (k^{in}) minus the vector sum of wave vectors of any resultant waves, k^{out}, in an optical phenomena must sum to zero, *i.e.* a statement of the conservation of momentum:

$$\Delta k = \sum_i k_i^{\text{in}} - \sum_j k_j^{\text{out}} = 0, \tag{8.61}$$

for perfect phase matching. The smaller the phase mismatch, Δk, in an optical process the more efficiently the process will occur with. Experimentally this is vital to produce intense, good quality, stable beams to use. Many OPAs use phase matching to produce tunable outputs by phase matching different parts of a supercontinuum with an amplification beam Figure 8.9.

Phase matching can be achieved in many different ways, the most common being

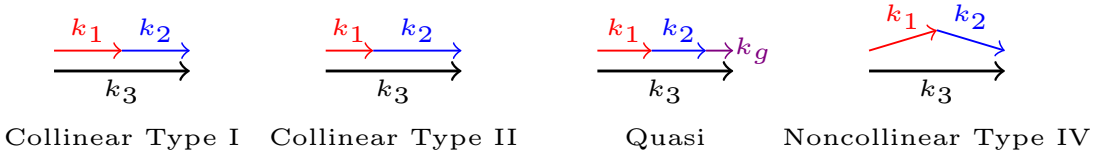

Figure 8.9 | Common phase matching schemes. The 'type' is the nomenclature that refers to the polarisation planes in which incident and resultant waves are relative to the crystal. Quasi-phase matching is achieved through the additional wave vector provided by the grating of the fabricated medium.

with the use of birefringent crystals such as β-barium borate through *angle tuning*, the rotation of the crystal relative to the polarisation of the incident wave, or through *temperature tuning*, where different crystal temperatures result in varied refractive indices. *Quasi phase matching* is another option if the birefringence of a crystal is not enough to compensate for dispersion. In this case, a medium (usually a ferromagnetic) is fabricated to contain periodic ($\sim$10 μm) inhomogeneities which can help compensate dispersion to achieve better phase matching, through the addition of a grating vector, k_g. Collinear or noncollinear beams can be used for such phase matching schemes depending on the experimental requirement, the most common of which are diagrammatically shown in Figure 8.9.

8.5 243 nm TEAS solvent-only measurements

As discussed in the main text (Section 4.1.7), three exponential fitting functions were required to describe the experimental TAS (Figure 8.10(B) and Figure 8.10(C)). One of these is attributed to the solvent response at 243 nm photoexcitation. Solvent only scans are performed and dynamics extracted through an identical global fitting procedure. The TAS (Figure 8.10(A)) reveals a lifetime of τ ∼400 ps for cyclohexane, and τ ∼3 ns for methanol.

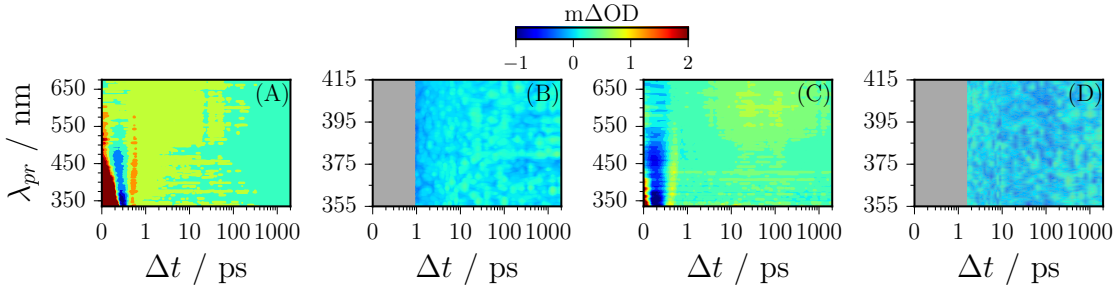

Figure 8.10 | Global fitting of the 243 nm photoexcitation solvent response. (A) Cyclohexane and residual fit (B). (C) Methanol and its residual fit (D). Lifetimes extracted are ∼400 ps and ∼3 ns for cyclohexane and methanol respectively, excluding early time delays $\Delta t < 1$ ps and $\Delta t < 1.5$ ps for cyclohexane and methanol respectively.

8.6 EHT electronic structure calculations

For all calculations, default convergence criteria were used, except for the geometry optimisation of the S_1 geometry where a relaxed criteria of 10^{-4} Hartrees in energy was used due to convergence difficulties. The first twenty-five excited states and their corresponding oscillator strengths are given for the initial photoexcitation, see Table 8.1.

Table 8.1: The first 25 singlet excited states calculated at the ground state geometry. Those in bold correspond to those considered in Figure 4.26.

n	Wavelength / nm	Oscillator Strength
1	395.10	0.00563
2	389.25	0.06531
3	383.50	0.10109
4	363.79	0.47845
5	362.94	0.22678
6	356.06	0.22312
7	335.92	0.000026
8	335.19	0.000080
9	332.35	0.03623
10	331.81	0.03242
11	331.43	0.28013
12	329.89	0.02332
13	329.57	0.00024
14	**318.89**	**1.13712**
15	**309.51**	**0.03591**
16	**306.50**	**0.02438**
17	305.12	0.00881
18	304.76	0.00359
19	303.13	0.00178
20	302.87	0.01315
21	301.19	0.000065
22	301.10	0.00022
23	300.87	0.00115
24	299.62	0.00810
25	298.11	0.00620

8.7 TEAS measurements of sinapic acid in ACN

For SA-ACN (Figure 8.11(A)), the TAS is dominated by four features. Firstly, an intense absorption centred at ∼420 nm which decays away to the baseline by ∼50 ps. Secondly there is a broad absorption spanning the spectral region ∼420–650 nm. Thirdly, a negative signal is observed below ∼350 nm. Finally, a strong negative signal centred around ∼460 nm. These features are discussed in Chapter 5.1.3.

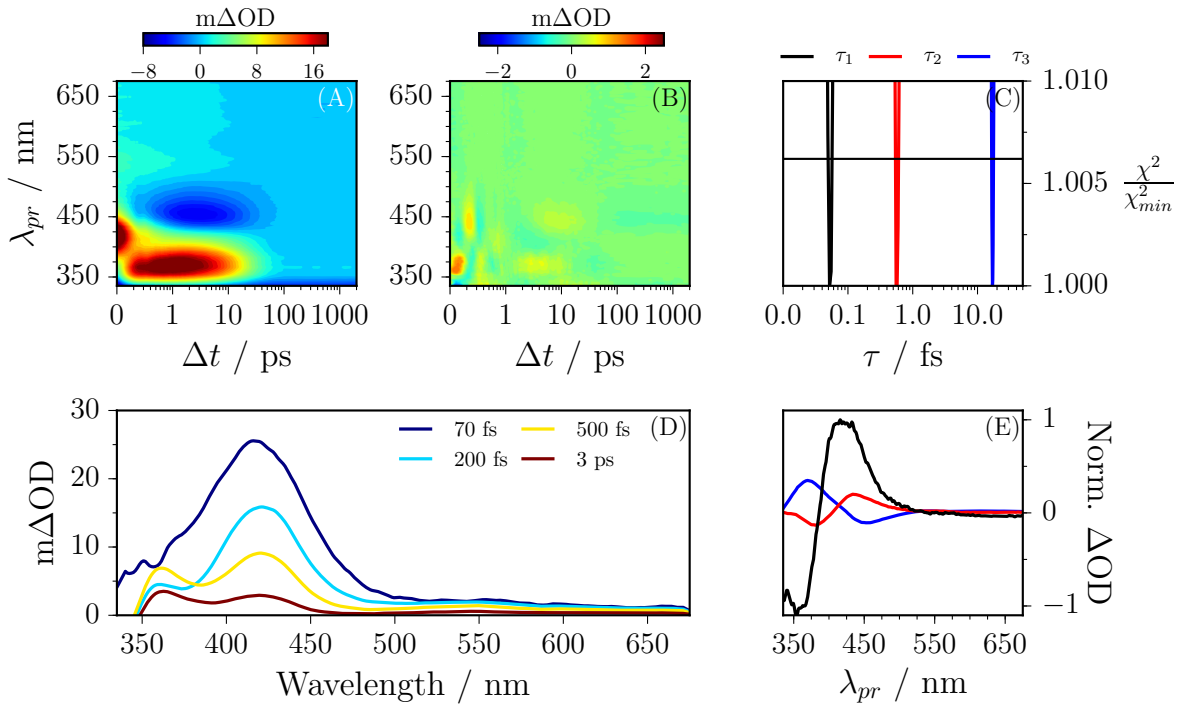

Figure 8.11 | (A) Raw TAS following 323 nm photoexcitation of SA-ACN. (B) Residual of the global fitting and the raw data. (C) ASE of extracted lifetimes. (D) Selected spectra at given Δt. (E) Corresponding DAS.

8.8 TEAS measurements of methyl sinapate in ACN

For MS-ACN (Figure 8.12(A)), the TAS is dominated by four features. Firstly, an intense absorption centred at ∼420 nm which decays away to the baseline by ∼50 ps. Secondly there is a broad absorption spanning the spectral region ∼420–650 nm. Thirdly, a negative signal is observed below ∼350 nm. Finally, a strong negative signal centred around ∼460 nm. These features are discussed in Chapter 5.1.3.

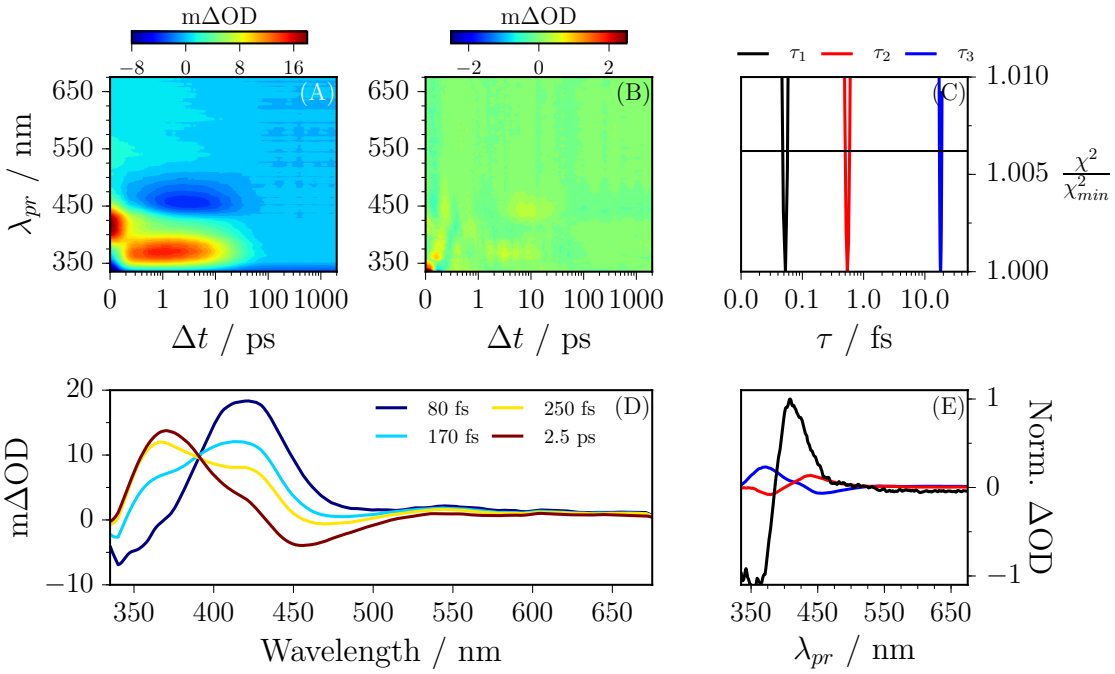

Figure 8.12 | (A) Raw TAS following 322 nm photoexcitation of MS-ACN. (B) Residual of the global fitting and the raw data. (C) ASE of extracted lifetimes. (D) Selected spectra at given Δt. (E) Corresponding DAS.

8.9 TEAS measurements of sinapoyl malate in ACN

For SM-ACN (Figure 8.13(A)), the TAS is dominated by four features. Firstly, an intense absorption centred at ∼420 nm which decays away to the baseline by ∼50 ps. Secondly there is a broad absorption spanning the spectral region ∼420–650 nm. Thirdly, a negative signal is observed below ∼350 nm. Finally, a strong negative signal centred around ∼460 nm. These features are discussed in Chapter 5.1.3.

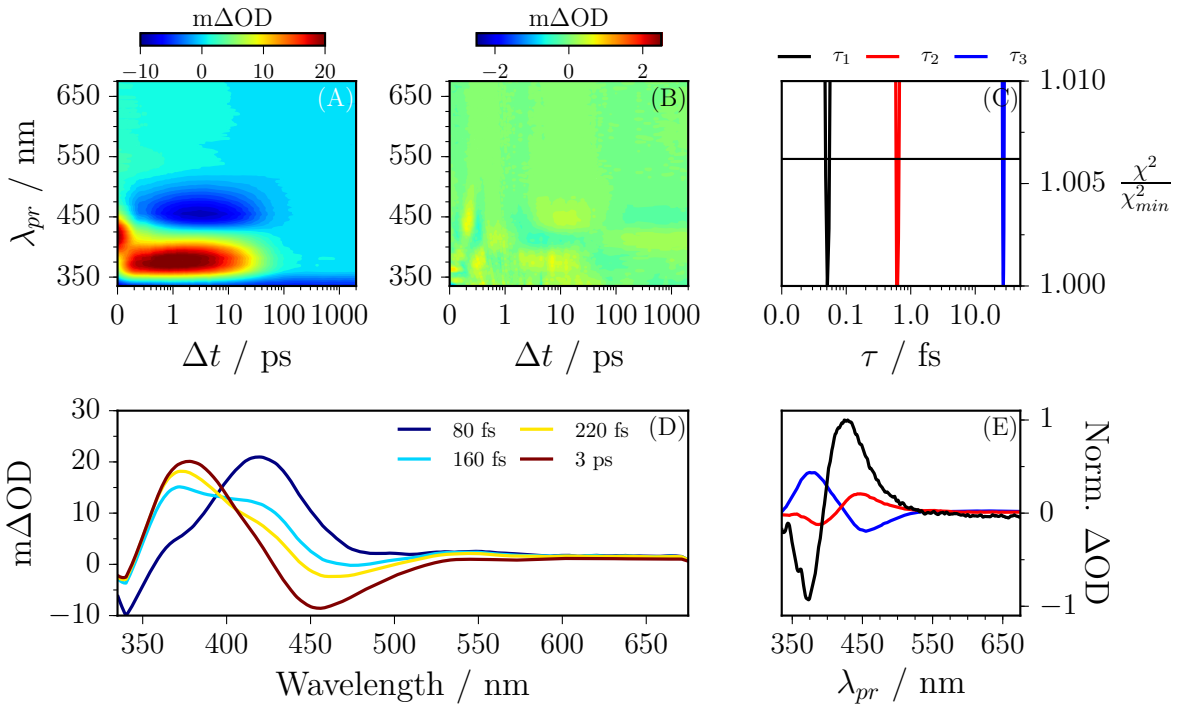

Figure 8.13 | (A) Raw TAS following 328 nm photoexcitation of SM-ACN. (B) Residual of the global fitting and the raw data. (C) ASE of extracted lifetimes. (D) Selected spectra at given Δt. (E) Corresponding DAS.

8.10 Power dependency measurements for sinapic acid in dioxane or ACN

Power dependent measurements of SA in dioxane (Figure 8.14(A)), ACN (Figure 8.14(C)) and methanol (Figure 5.7) suggest that the feature observed at ∼360 nm can be attributed to at least a two-photon ionisation in methanol, convoluted with the *cis*-isomer signal (in all solvents). Taking a slice of the TAS at the signal maxima at ∼360 nm, which corresponds to the absorption maximum of the radical signature,[481] the SA-dioxane and SA-ACN signals display a linear relationship to the incident pump power (log(signal) *vs.* log(power) plots) where as SA-methanol displays a nonlinear relationship, *cf.* Figure 5.7. For all measurements, the TOPAS output was optimised for the wavelength used (*i.e.* 325, 323 or 318 nm for dioxane, ACN or methanol) and a sample path length of 950 μm was used to increased the signal strength of the long-lived features shown in the 2 ns spectra. Each spectrum has been smoothed by a ∼3 nm integration.

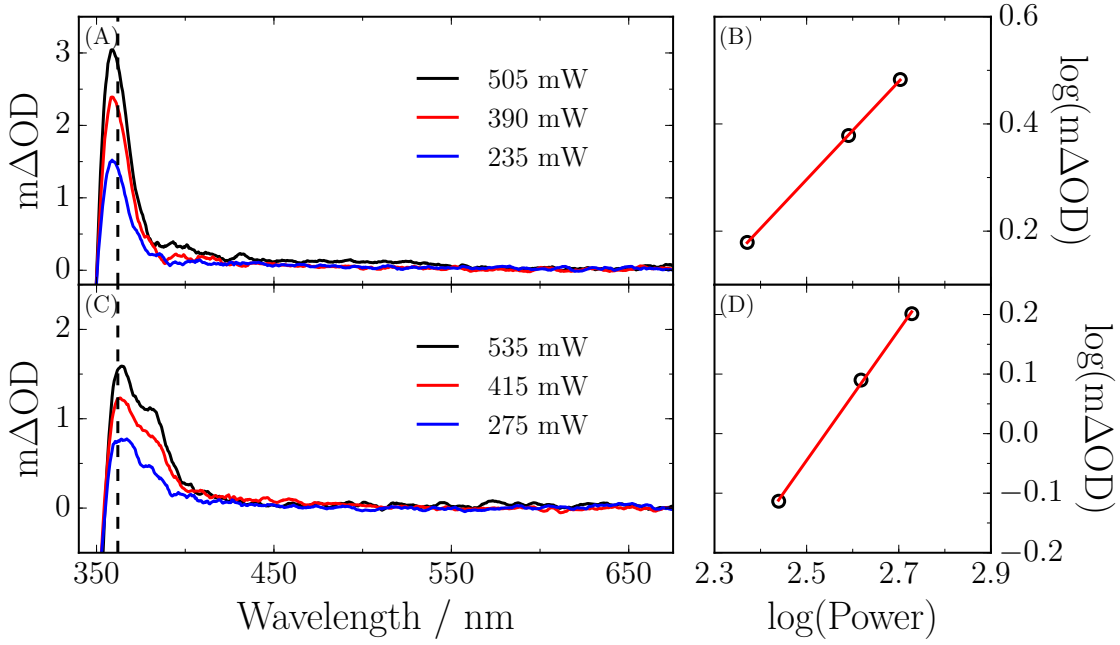

Figure 8.14 | (A) Δt = 2 ns spectrum of SA-dioxane with changing incident pump power. Vertical dashed lines indicates the 362 nm slice taken to compare signal intensities for the power dependency study, similarly for (C) SA-ACN. (B) For the 362 nm slice, a linear relationship between logarithmic power and logarithmic ΔOD is observed with a gradient of 0.91 ± 0.01, and similarly for (D) SA-ACN returns 1.09 ± 0.03.

8.11 The 8-site Fenna-Matthews-Olson Hamiltonian

Written in the basis of molecular excited states, such that $\hat{\mathrm{H}}_{ex}(i,j) = \langle i|\hat{\mathrm{H}}_{ex}|j\rangle$, the electronic sub-system Hamiltonian for the 8-site FMO complex considered here is[540,550]

$$\hat{\mathrm{H}}_{ex} = \begin{pmatrix} 310.0 & -97.9 & 5.5 & -5.8 & 6.7 & -12.1 & -10.3 & 37.5 \\ -97.9 & 230.0 & 30.1 & 7.3 & 2.0 & 11.5 & 4.8 & 7.9 \\ 5.5 & 30.1 & 0 & -58.8 & -1.5 & -9.6 & 4.7 & 1.5 \\ -5.8 & 7.3 & -58.8 & 180.0 & -64.9 & -17.4 & -64.4 & -1.7 \\ 6.7 & 2.0 & -1.5 & -64.9 & 405.0 & 89.0 & -6.4 & 4.5 \\ -12.1 & 11.5 & -9.6 & -17.4 & 89.0 & 320.0 & 31.7 & -9.7 \\ -10.3 & 4.8 & 4.7 & -64.4 & -6.4 & 31.7 & 270.0 & -11.4 \\ 37.5 & 7.9 & 1.5 & -1.7 & 4.5 & -9.7 & -11.4 & 505.0 \end{pmatrix}. \quad (8.62)$$

All elements are given in units of cm^{-1}. The site energies (the diagonal elements) are reduced such that the site 3 energy is 0 cm^{-1}.

8.12 The light-harvesting complex II Hamiltonian

Written in the basis of molecular excited states, such that $\hat{\mathrm{H}}_{ex}(i,j) = \langle i|\hat{\mathrm{H}}_{ex}|j\rangle$, the electronic sub-system Hamiltonian for the 14-site LHC-II considered here is[587]

$$\hat{\mathrm{H}}_{ex} = \begin{pmatrix} 632 & 36 & -5 & 3 & 1 & -2 & -3 & 3 & 4 & -5 & 20 & 2 & -8 & 2 \\ 36 & 77 & 15 & 6 & 0 & 5 & 6 & -6 & -24 & -5 & 1 & 8 & -2 & 0 \\ -5 & 15 & 117 & -1 & 0 & -4 & 6 & 4 & 72 & 7 & -1 & 1 & 1 & -5 \\ 3 & 6 & -1 & 133 & 4 & 71 & 24 & -4 & -2 & 0 & -3 & 3 & 2 & -3 \\ 1 & 0 & 0 & 4 & 806 & 9 & -4 & -4 & 0 & 1 & 1 & -2 & -1 & 0 \\ -2 & 5 & -4 & 71 & 9 & 691 & 16 & -5 & 2 & 0 & -2 & 2 & 2 & -2 \\ -3 & 6 & 6 & 24 & -4 & 16 & 655 & -4 & -5 & 1 & -2 & 3 & 3 & -3 \\ 3 & -6 & 4 & -4 & -4 & -5 & -4 & 471 & 24 & 43 & 5 & -1 & -2 & 1 \\ 4 & -24 & 72 & -2 & 0 & 2 & -5 & 24 & 740 & -2 & 4 & -1 & -2 & 2 \\ -5 & -5 & 7 & 0 & 1 & 0 & 1 & 43 & -2 & 0 & -26 & 13 & 6 & -1 \\ 20 & 1 & -1 & -3 & 1 & -2 & -2 & 5 & 4 & -26 & 181 & 99 & -3 & 1 \\ 2 & 8 & 1 & 3 & -2 & 2 & 3 & -1 & -1 & 13 & 99 & 206 & 0 & 0 \\ -8 & -2 & 1 & 2 & -1 & 2 & 3 & -2 & -2 & 6 & -3 & 0 & 124 & -36 \\ 2 & 0 & -5 & -3 & 0 & -2 & -3 & 1 & 2 & -1 & 1 & 0 & -36 & 195 \end{pmatrix}. \quad (8.63)$$

All elements are given in units of cm^{-1}. The site energies (the diagonal elements) are reduced such that the site 10 energy is 0 cm^{-1}. When considering the LHC-II trimer, the inter-monomer couplings matrix is[587]

$$\hat{\mathrm{H}}_{cp} = \begin{pmatrix} 0 & -1 & 3 & 2 & -1 & 2 & 0 & 5 & 34 & -3 & -1 & 1 & 1 & 0 \\ 0 & 0 & 7 & -1 & 1 & -1 & 0 & 0 & -6 & 2 & 1 & 0 & -1 & -1 \\ -1 & 4 & -4 & 2 & 0 & 2 & 2 & 0 & 0 & 0 & -1 & 1 & -1 & -1 \\ 0 & 1 & -1 & 1 & 0 & 1 & 1 & 0 & 0 & 0 & 0 & 0 & 0 & -1 \\ 0 & 0 & 0 & 0 & 0 & 0 & 0 & 0 & 0 & 0 & 0 & 0 & 0 & 0 \\ 0 & 1 & 0 & 1 & 0 & 1 & 1 & 0 & 0 & 0 & 0 & 0 & 0 & -1 \\ -1 & 1 & -1 & 1 & 0 & 1 & 1 & 0 & 0 & 0 & 0 & 0 & 0 & -1 \\ 1 & -1 & 1 & -1 & 0 & -1 & -1 & 0 & 0 & 0 & 0 & 0 & 0 & 0 \\ 1 & -2 & 2 & -1 & 0 & -1 & -1 & 1 & 0 & 0 & 1 & 0 & 0 & 0 \\ 0 & 1 & -1 & 1 & 0 & 0 & 0 & 0 & 2 & 0 & 0 & 0 & 0 & 0 \\ 0 & 0 & 0 & 0 & 0 & -1 & -1 & 2 & 4 & -1 & 0 & 0 & 0 & 0 \\ 0 & 0 & 1 & 0 & 0 & 0 & 0 & -1 & -2 & 1 & 0 & 0 & -1 & 0 \\ 0 & 0 & -4 & 0 & -1 & 0 & 8 & 1 & 3 & -1 & 0 & -1 & 2 & 1 \\ 1 & -2 & 4 & -4 & 2 & -4 & -1 & 0 & -6 & 0 & 1 & -1 & 0 & 1 \end{pmatrix}. \quad (8.64)$$

All elements are given in units of cm^{-1}. Following this, the full electronic Hamiltonian for the LHC-II trimer is

$$\hat{\mathrm{H}}_{trimer} = \begin{pmatrix} \hat{\mathrm{H}}_{ex} & \hat{\mathrm{H}}_{cp}^{12} & \hat{\mathrm{H}}_{cp}^{13} \\ \hat{\mathrm{H}}_{cp}^{21} & \hat{\mathrm{H}}_{ex} & \hat{\mathrm{H}}_{cp}^{23} \\ \hat{\mathrm{H}}_{cp}^{31} & \hat{\mathrm{H}}_{cp}^{32} & \hat{\mathrm{H}}_{ex} \end{pmatrix}. \quad (8.65)$$

8.13 Fenna-Matthews-Olson population curves

The population curves for all 8 pigments of the FMO monomer, for the total 10 ps simulation time are given in Figure 8.15.

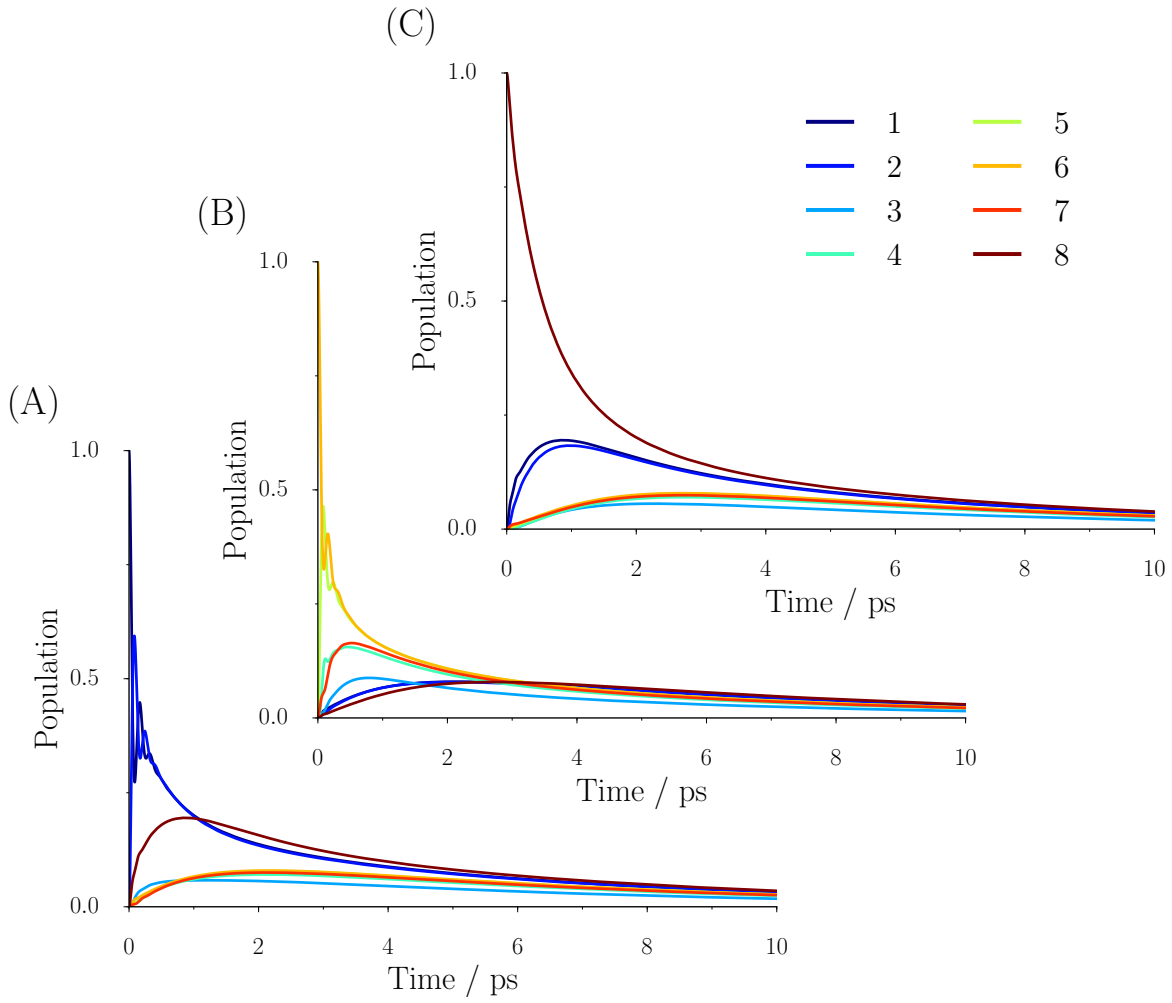

Figure 8.15 | (A) The time-dependent populations for each pigment of the FMO monomer given initial excitation on pigment 1. (B) Similarly for initial excitation on pigment 6, and (C) for initial excitation on pigment 8. The legend refers to pigment number.

8.14 Light-harvesting complex II population curves

The population curves for all 8 pigments of the LHC-II monomer, for the total 10 ps simulation time are given in Figure 8.16.

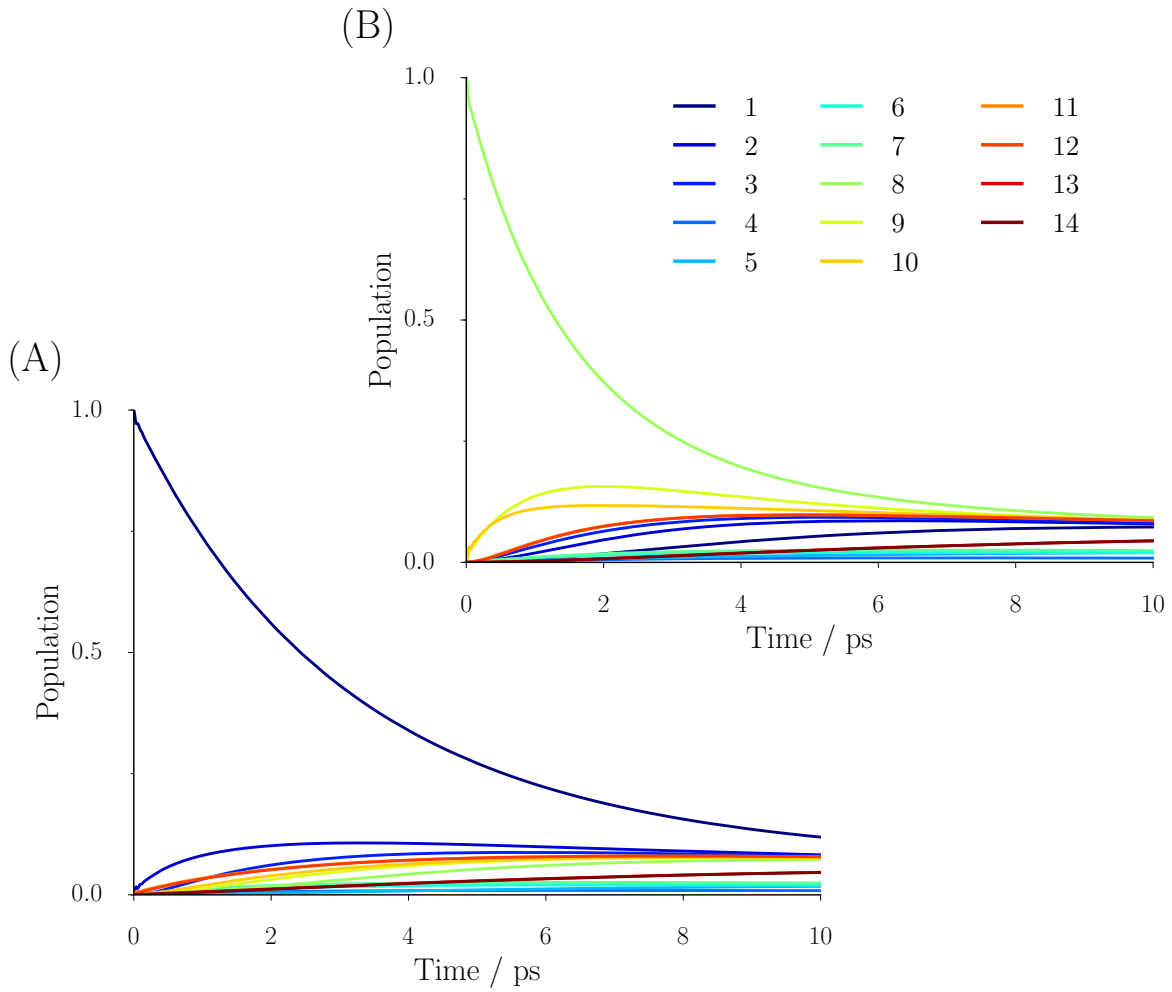

Figure 8.16 | (A) The time-dependent populations for each pigment of the LHC-II monomer given initial excitation on pigment 1 and (B) for initial excitation on pigment 8. The legend refers to pigment number.

References

[1] P. Atkins and R. Friedman. *Molecular quantum mechanics*. Oxford University Press Inc., New York, 5th edition, 2010.

[2] R. Fletcher and M. J. D. Powell. A rapidly convergent descent method for minimization. *Comput. J.*, 6(*2*):163–168, 1963.

[3] G. C. Schatz and M. A. Ratner. *Quantum mechanics in chemistry*. Prentice-Hall, Inc., New Jersey, 1st edition, 1993.

[4] D. J. Tanner. *Introduction to quantum mechanics: A time-dependent perspective*. University Science Books, Sausalito, 2007.

[5] M. D. Feit, J. A. Fleck, and A. Steiger. Solution of the Schrödinger equation by a spectral method. *J. Comput. Phys.*, 47(*3*):412–433, 1982.

[6] C. J. H. Schutte. *The theory of molecular spectroscopy*. North-Holland Publishing Company, Amsterdam, 1st edition, 1976.

[7] P. M. Morse. Diatomic molecules according to the wave mechanics. II. Vibrational levels. *Phys. Rev.*, 34(*1*):57–64, 1929.

[8] R. J. LeRoy and R. B. Bernstein. Dissociation energy and long-range potential of diatomic molecules from vibrational spacings of higher levels. *J. Chem. Phys.*, 52(*8*):3869–3879, 1970.

[9] J. P. Dahl and M. Springborg. The Morse oscillator in position space, momentum space, and phase space. *J. Chem. Phys.*, 88(*7*):4535–4547, 1988.

[10] G. Baym. *Lectures on quantum mechanics: Lecture notes and supplements in physics*. Westview Press Inc., Massachusetts, 3rd edition, 1974.

[11] A. I. Rae. *Quantum mechanics*. CRC Press, London, 5th edition, 2007.

[12] W. Pauli. Über den zusammenhang des abschlusses der elektronengruppen im atom mit der komplexstruktur der spektren. *Z. Physik*, 31(*1*):765–783, 1925.

[13] W. Pauli. The connection between spin and statistics. *Phys. Rev.*, 58(*8*):716–722, 1940.

[14] J. Marton, S. Bartalucci, S. Bertolucci, C. Berucci, M. Bragadireanu, M. Cargnelli, C. Curceanu, S. D. Matteo, J.-P. Egger, C. Guaraldo, M. Iliescu, T. Ishiwatari, M. Laubenstein, E. Milotti, D. Pietreanu, K. Piscicchia, T. Ponta, A. R. Vidal, A. Scordo, D. Sirghi, F. Sirghi, L. Sperandio, O. V. Doce, E. Widmann, and J. Zmeskal. Testing the Pauli exclusion principle for electrons. *J. Phys. Conf. Ser.*, 447(*1*):012070, 2013.

[15] E. R. Davidson and D. Feller. Basis set selection for molecular calculations. *Chem. Rev.*, 86(*4*):681–696, 1986.

[16] Persistence of Vision (TM) raytracer, 2004. Available from http://www.povray.org/.

[17] M. J. Frisch, G. W. Trucks, H. B. Schlegel, G. E. Scuseria, M. A. Robb, J. R. Cheeseman, J. A. Montgomery, Jr., T. Vreven, K. N. Kudin, J. C. Burant, J. M. Millam, S. S. Iyengar, J. Tomasi, V. Barone, B. Mennucci, M. Cossi, G. Scalmani, N. Rega, G. A. Petersson, H. Nakatsuji, M. Hada, M. Ehara, K. Toyota, R. Fukuda, J. Hasegawa, M. Ishida, T. Nakajima, Y. Honda, O. Kitao, H. Nakai, M. Klene, X. Li, J. E. Knox, H. P. Hratchian, J. B. Cross, V. Bakken, C. Adamo, J. Jaramillo, R. Gomperts, R. E. Stratmann, O. Yazyev, A. J. Austin, R. Cammi, C. Pomelli, J. W. Ochterski, P. Y. Ayala, K. Morokuma, G. A. Voth, P. Salvador, J. J. Dannenberg, V. G. Zakrzewski, S. Dapprich, A. D. Daniels, M. C. Strain, O. Farkas, D. K. Malick, A. D. Rabuck, K. Raghavachari, J. B. Foresman, J. V. Ortiz, Q. Cui, A. G. Baboul, S. Clifford, J. Cioslowski, B. B. Stefanov, G. Liu, A. Liashenko, P. Piskorz, I. Komaromi, R. L. Martin, D. J. Fox, T. Keith, M. A. Al-Laham, C. Y. Peng, A. Nanayakkara, M. Challacombe, P. M. W. Gill, B. Johnson, W. Chen, M. W. Wong, C. Gonzalez, and J. A. Pople. Gaussian 03, Revision D.01,, 2004. Gaussian, Inc., Wallingford, CT.

[18] C. Niederberger. MODIAGRAM, 2015. Avaiable from https://www.ctan.org.

[19] J. C. Slater. Atomic shielding constants. *Phys. Rev.*, 36(*1*):57–64, 1930.

[20] S. F. Boys. Electronic wave functions. *Proc. R. Soc. Lond. A*, 200(*1063*):542–554, 1950.

[21] W. J. Hehre, R. F. Stewart, and J. A. Pople. Self-consistent molecular orbital methods. I. Use of Gaussian expansions of Slater-type atomic orbitals. *J. Chem. Phys.*, 51(*6*):2657–2964, 1969.

[22] W. J. Hehre, R. Ditchfield, and J. A. Pople. Self-consistent molecular orbital methods. XII. Further extensions of Gaussian-type basis sets for use in molecular orbital studies of organic molecules. *J. Chem. Phys.*, 56(*5*):2257–2261, 1972.

[23] J. B. Collins, P. V. R. Schleyer, J. S. Binkley, and J. A. Pople. Self-consistent molecular orbital methods. XVII. Geometries and binding energies of second-row molecules. A comparison of three basis sets. *J. Chem. Phys.*, 64(*12*):5142–5141, 1976.

[24] T. H. Dunning. Gaussian basis sets for use in correlated molecular calculations. I. The atoms boron through neon and hydrogen. *J. Chem. Phys.*, 90(*2*):1007–1023, 1989.

[25] R. A. Kendall, T. H. Dunning, and R. J. Harrison. Electron affinities of the first-row atoms revisited. Systematic basis sets and wave functions. *J. Chem. Phys.*, 96(*9*):6796–6806, 1992.

[26] D. E. Woon and T. H. Dunning. Gaussian-basis sets for use in correlated molecular calculations. III. The atoms aluminum through argon. *J. Chem. Phys.*, 98(*2*): 1358–1371, 1993.

[27] A. Schaefer, H. Horn, and R. Ahlrichs. Fully optimized contracted Gaussian-basis sets for atoms Li to Kr. *J. Chem. Phys.*, 97(*4*):2571–2577, 1992.

[28] A. Schaefer, C. Huber, and R. Ahlrichs. Fully optimized contracted Gaussian-basis sets of triple zeta valence quality for atoms Li to Kr. *J. Chem. Phys.*, 100 (*8*):5829–5835, 1994.

[29] T. Clark, J. Chandrasekhar, G. W. Spitznagel, and P. V. R. Schleyer. Efficient diffuse function-augmented basis sets for anion calculations. III. The 3-21+G basis set for first-row elements, Li-F. *J. Comput. Chem.*, 4(*3*):294–301, 1983.

[30] M. J. Frisch, J. A. Pople, and J. S. Binkley. Self-consistent molecular orbital methods. XXV. Supplementary functions for Gaussian basis sets. *J. Chem. Phys.*, 80(*7*):3265–3269, 1984.

[31] F. Jensen. Atomic orbital basis sets. *WIREs Comput. Mol. Sci.*, 3(*3*):273–295, 2012.

[32] J. G. Hill. Gaussian basis sets for molecular applications. *Int. J. Quantum Chem.*, 113(*1*):21–34, 2013.

[33] B. Nagy and F. Jensen. *Basis sets in quantum chemistry*, chapter 3, pages 93–149. Reviews in Computational Chemistry. John Wiley & Sons, Hoboken, 2017.

[34] D. R. Yarkony. Diabolical conical intersections. *Rev. Mod. Phys.*, 68(*4*):985–1013, 1996.

[35] D. R. Hartree. The wave mechanics of an atom with a non-Coulomb central field. Part I. Theory and methods. *Proc. Cambridge Phil. Soc.*, 24(*1*):89–110, 1928.

[36] D. R. Hartree. The wave mechanics of an atom with a non-Coulomb central field. Part II. Some results and discussion. *Proc. Cambridge Phil. Soc.*, 24(*1*):111–132, 1928.

[37] V. Fock. Näherungsmethode zur Lösung des quantenmechanischen Mehrkörperproblems. *Z. Physik*, 61(*1*):126–148, 1930.

[38] V. Magnasco. *Methods of molecular quantum mechanics: An introduction to electronic molecular structure.* John Wiley & Sons, Chichester, 1st edition, 2009.

[39] T. Tsuneda. *Density functional theory in quantum chemistry.* Springer Science+Business Media, 1st edition, 2014.

[40] C. C. Roothaan. New developments in molecular orbital theory. *Rev. Mod. Phys.*, 23(*2*):69–89, 1951.

[41] G. G. Hall. The molecular orbital theory of chemical valency. VIII. A method of calculating ionization potentials. *Proc. R. Soc. A*, 205(*1083*):541–552, 1951.

[42] S. Gozem, F. Melaccio, H. L. Luk, S. Rinaldi, and M. Olivucci. Learning from photobiology how to design molecular devices using a computer. *Chem. Soc. Rev.*, 43(*12*):4019–4036, 2014.

[43] N. C. Handy, P. J. Knowles, and K. Somasundram. On the convergence of the Møller-Plesset perturbation series. *Theor. Chim. Acta*, 68(*1*):87–100, 1985.

[44] J. Olsen, O. Christiansen, H. Koch, and P. Jørgensen. Surprising cases of divergent behavior in Møller-Plesset perturbation theory. *J. Chem. Phys.*, 105(*12*):5082–5090, 1996.

[45] C. Møller and M. S. Plesset. Note on an approximation treatment for many-electron systems. *Phys. Rev.*, 48(*7*):618–622, 1934.

[46] J. A. Pople. Nobel lecture: Quantum chemical models. *Rev. Mod. Phys.*, 71(*5*): 1267–1274, 1999.

[47] J. F. Stanton. Why CCSD(T) works: A different perspective. *Chem. Phys. Lett.*, 281(*1–3*):130–134, 1997.

[48] D. J. Tozer. *Density functional theory*, chapter 9, pages 459–472. Euoropean Summerschool in Quantum Chemistry Book II. Lund University, 2009.

[49] L. H. Thomas. The calculation of atomic fields. *Proc. Cambridge Phil. Soc.*, 23 (*5*):542–548, 1927.

[50] P. A. M. Dirac. Note on exchange phenomena in the Thomas atom. *Proc. Cambridge Phil. Soc.*, 26(*3*):376–385, 1930.

[51] P. Hohenberg and W. Kohn. Inhomogeneous electron gas. *Phys. Rev. Lett.*, 136 (*3B*):864–871, 1964.

[52] M. Levy. Universal variational functionals of electron densities, first-order density matrices, and natural spin-orbitals and solution of the v-representability problem. *Proc. Natl. Acad. Sci. U. S. A.*, 76(*12*):6062–6065, 1979.

[53] W. K. K. J. Sham. Self-consistent equations including exchange and correlation effects. *Phys. Rev.*, 140(*4A*):1133–1138, 1965.

[54] R. O. Jones. Density functional theory: Its origins, rise to prominence, and future. *Rev. Mod. Phys.*, 87(*3*):897–923, 2015.

[55] R. G. Parr and W. Yang. *Density-functional theory of atoms and molecules*, volume 16 of *International Series of Monographs on Chemistry*. Oxford University Press Inc., 1994.

[56] W. Koch and M. C. Holthausen. *A chemist's guide to density functional theory*. John Wiley & Sons, 2nd edition, 2001.

[57] J. P. Perdew and S. Kurth. *Density functionals for non-relativistic Coulomb systems in the new century*, chapter 1, pages 1–55. A Primer in Density Functional Theory. Springer Science+Business Media, 2003.

[58] L. J. Bartolotti and K. Flurchick. *An introduction to density functional theory*, volume 7 of *Rev. Comp. Ch.*, chapter 4, pages 187–216. John Wiley & Sons, 2007.

[59] C. J. Cramer and D. G. Truhlar. Density functional theory for transition metals and transition metal chemistry. *Phys. Chem. Chem. Phys.*, 11(*46*):10757–10816, 2009.

[60] K. Burke. Perspective on density functional theory. *J. Chem. Phys.*, 136(*15*): 150901, 2012.

[61] A. D. Becke. Perspective: Fifty years of density-functional theory in chemical physics. *J. Chem. Phys.*, 140(*18*):18A301, 2014.

[62] H. S. Yu, S. L. Li, and D. G. Truhlar. Perspective: Kohn-Sham density functional theory descending a staircase. *J. Chem. Phys.*, 145(*13*):7029–7039, 2016.

[63] M. G. Medvedev, I. S. Bushmarinov, J. Sun, J. P. Perdew, and K. A. Lyssenko. Density functional theory is straying from the path toward the exact functional. *Science*, 355(*6320*):49–52, 2017.

[64] B. O. Ross and P. R. Taylor. A complete active space SCF method (CASSCF) using a density matrix formulated super-CI approach. *Chem. Phys.*, 48(*2*):157–173, 1980.

[65] L. M. Cheung, K. R. Sundberg, and K. Ruedenberg. Dimerization of carbene to ethylene. *J. Am. Chem. Soc.*, 100(*25*):8024–8025, 1978.

[66] J. Finley, P.-A. Malmqvist, B. O. Roos, and L. Serrano-Andres. The multi-state CASPT2 method. *Chem. Phys. Lett.*, 288(*2–4*):299–306, 1998.

[67] K. Andersson and B. O. Roos. *Multiconfigurational second order perturbation theory, modern electronic structure theory*, chapter 2. Advanced Series in Physical Chemistry: Modern Electronic Structure Theory. World Scientific, 1995.

[68] P. Pulay. A perspective on the CASPT2 method. *Int. J. Quantum Chem.*, 111 (*13*):3273–3279, 2011.

[69] K. Ruedenberg, M. W. Schmidt, M. M. Gildbert, and S. T. Elbert. Are atoms intrinsic to molecular electronic wavefunctions? I. The FORS model. *Chem. Phys.*, 71(*1*):41–49, 1982.

[70] J. F. Stanton and R. J. Bartlett. The equation of motion coupled-cluster method. A systematic biorthogonal approach to molecular excitation energies, transition probabilities, and excited state properties. *J. Chem. Phys.*, 98(*9*):7029, 1993.

[71] P. Baudin, J. S. Marín, I. G. Cuesta, and A. M. J. S. de Merás. Calculation of excitation energies from the CC2 linear response theory using Cholesky decomposition. *J. Chem. Phys.*, 140(*10*):104111, 2014.

[72] A. Dreuw and M. Wormit. The algebraic diagrammatic construction scheme for the polarization propagator for the calculation of excited states. *WIREs Comput. Mol. Sci.*, 5(*1*):82–95, 2015.

[73] E. Runge and E. K. U. Gross. Density-functional theory for time-dependent systems. *Phys. Rev. Lett.*, 52(*12*):997–1000, 1984.

[74] H. M. Senn and W. Thiel. QM/MM methods for biomolecular systems. *Angew. Chem. Int. Ed.*, 48(*7*):1198–1229, 2009.

[75] H. M. Senn and W. Thiel. QM/MM studies of enzymes. *Curr. Opin. Chem. Biol.*, 11(*2*):182–187, 2007.

[76] A. M. Virshup, C. Punwong, T. V. Pogorelov, B. A. Lindquist, C. Ko, and T. J. Martínez. Photodynamics in complex environments: *Ab initio* multiple spawning quantum mechanical/molecular mechanical dynamics. *J. Phys. Chem. B*, 113 (*11*):3280–3291, 2009.

[77] E. Brunk and U. Rothlisberger. Mixed quantum mechanical/molecular mechanical molecular dynamics simulations of biological systems in ground and electronically excited states. *Chem. Rev.*, 115(*12*):6217–6263, 2015.

[78] M. J. Frisch, G. W. Trucks, H. B. Schlegel, G. E. Scuseria, M. A. Robb, J. R. Cheeseman, G. Scalmani, V. Barone, B. Mennucci, G. A. Petersson, H. Nakatsuji, M. Caricato, X. Li, H. P. Hratchian, A. F. Izmaylov, J. Bloino, G. Zheng, J. L. Sonnenberg, M. Hada, M. Ehara, K. Toyota, R. Fukuda, J. Hasegawa, M. Ishida, T. Nakajima, Y. Honda, O. Kitao, H. Nakai, T. Vreven, J. A. Montgomery, Jr., J. E. Peralta, F. Ogliaro, M. Bearpark, J. J. Heyd, E. Brothers, K. N. Kudin,

V. N. Staroverov, R. Kobayashi, J. Normand, K. Raghavachari, A. Rendell, J. C. Burant, S. S. Iyengar, J. Tomasi, M. Cossi, N. Rega, J. M. Millam, M. Klene, J. E. Knox, J. B. Cross, V. Bakken, C. Adamo, J. Jaramillo, R. Gomperts, R. E. Stratmann, O. Yazyev, A. J. Austin, R. Cammi, C. Pomelli, J. W. Ochterski, R. L. Martin, K. Morokuma, V. G. Zakrzewski, G. A. Voth, P. Salvador, J. J. Dannenberg, S. Dapprich, A. D. Daniels, . Farkas, J. B. Foresman, J. V. Ortiz, J. Cioslowski, and D. J. Fox. Gaussian 09, Revision C.01, 2009. Gaussian, Inc., Wallingford, CT.

[79] M. J. Frisch, G. W. Trucks, H. B. Schlegel, G. E. Scuseria, M. A. Robb, J. R. Cheeseman, G. Scalmani, V. Barone, G. A. Petersson, H. Nakatsuji, X. Li, M. Caricato, A. V. Marenich, J. Bloino, B. G. Janesko, R. Gomperts, B. Mennucci, H. P. Hratchian, J. V. Ortiz, A. F. Izmaylov, J. L. Sonnenberg, D. Williams-Young, F. Ding, F. Lipparini, F. Egidi, J. Goings, B. Peng, A. Petrone, T. Henderson, D. Ranasinghe, V. G. Zakrzewski, J. Gao, N. Rega, G. Zheng, W. Liang, M. Hada, M. Ehara, K. Toyota, R. Fukuda, J. Hasegawa, M. Ishida, T. Nakajima, Y. Honda, O. Kitao, H. Nakai, T. Vreven, K. Throssell, J. A. Montgomery, Jr., J. E. Peralta, F. Ogliaro, M. J. Bearpark, J. J. Heyd, E. N. Brothers, K. N. Kudin, V. N. Staroverov, T. A. Keith, R. Kobayashi, J. Normand, K. Raghavachari, A. P. Rendell, J. C. Burant, S. S. Iyengar, J. Tomasi, M. Cossi, J. M. Millam, M. Klene, C. Adamo, R. Cammi, J. W. Ochterski, R. L. Martin, K. Morokuma, O. Farkas, J. B. Foresman, and D. J. Fox. Gaussian 16, Revision A.03, 2016. Gaussian Inc. Wallingford CT.

[80] H.-J. Werner, P. J. Knowles, G. Knizia, F. R. Manby, M. Schütz, P. Celani, W. Györffy, D. Kats, T. Korona, R. Lindh, A. Mitrushenkov, G. Rauhut, K. R. Shamasundar, T. B. Adler, R. D. Amos, A. Bernhardsson, A. Berning, D. L. Cooper, M. J. O. Deegan, A. J. Dobbyn, F. Eckert, E. Goll, C. Hampel, A. Hesselmann, G. Hetzer, T. Hrenar, G. Jansen, C. Köppl, Y. Liu, A. W. Lloyd, R. A. Mata, A. J. May, S. J. McNicholas, W. Meyer, M. E. Mura, A. Nicklass, D. P. O'Neill, P. Palmieri, D. Peng, K. Pflüger, R. Pitzer, M. Reiher, T. Shiozaki, H. Stoll, A. J. Stone, R. Tarroni, T. Thorsteinsson, and M. Wang. MOLPRO, version 2015.1, a package of *ab initio* programs, 2015.

[81] H.-J. Werner, P. J. Knowles, G. Knizia, F. R. Manby, and M. Schütz. Molpro: A general-purpose quantum chemistry program package. *WIREs Comput. Mol. Sci.*, 2(*2*):242–253, 2012.

[82] TURBOMOLE V7.0 2015, A development of University of Karlsruhe and Forschungszentrum Karlsruhe GmbH, 1989-2007, TURBOMOLE GmbH, since 2007. Available from http://www.turbomole.com.

[83] F. Furche, R. Ahlrichs, C. Hättig, W. Klopper, M. Sierka, and F. Weigend. Turbomole. *WIREs Comput. Mol. Sci.*, 4(*2*):91–100, 2014.

[84] F. Neese. The ORCA program system. *WIREs Comput. Mol. Sci.*, 2(*1*):73–78, 2012.

[85] M. Valiev, E. J. Bylaska, N. Govind, K. Kowalski, T. P. Straatsma, H. J. J. V. Dam, D. Wang, J. Nieplocha, E. Apra, T. L. Windus, and W. A. de Jong. NWChem: A comprehensive and scalable open-source solution for large scale molecular simulations. *Comput. Phys. Commun.*, 181(*9*):1477–1489, 2010.

[86] Y. Shao, Z. Gan, E. Epifanovsky, A. T. B. Gilbert, M. Wormit, J. Kussmann, A. W. Lange, A. Behn, J. Deng, X. Feng, D. Ghosh, M. Goldey, P. R. Horn, L. D. Jacobson, I. Kaliman, R. Z. Khaliullin, T. Kús, A. Landau, J. Liu, E. I. Proynov, Y. M. Rhee, R. M. Richard, M. A. Rohrdanz, R. P. Steele, E. J. Sundstrom, H. L. Woodcock III, P. M. Zimmerman, D. Zuev, B. Albrecht, E. Alguire, B. Austin, G. J. O. Beran, Y. A. Bernard, E. Berquist, K. Brandhorst, K. B. Bravaya, S. T. Brown, D. Casanova, C.-M. Chang, Y. Chen, S. H. Chien, K. D. Closser, D. L. Crittenden, M. Diedenhofen, R. A. DiStasio Jr., H. Dop, A. D. Dutoi, R. G. Edgar, S. Fatehi, L. Fusti-Molnar, A. Ghysels, A. Golubeva-Zadorozhnaya, J. Gomes, M. W. D. Hanson-Heine, P. H. P. Harbach, A. W. Hauser, E. G. Hohenstein, Z. C. Holden, T.-C. Jagau, H. Ji, B. Kaduk, K. Khistyaev, J. Kim, J. Kim, R. A. King, P. Klunzinger, D. Kosenkov, T. Kowalczyk, C. M. Krauter, K. U. Lao, A. Laurent, K. V. Lawler, S. V. Levchenko, C. Y. Lin, F. Liu, E. Livshits, R. C. Lochan, A. Luenser, P. Manohar, S. F. Manzer, S.-P. Mao, N. Mardirossian, A. V. Marenich, S. A. Maurer, N. J. Mayhall, C. M. Oana, R. Olivares-Amaya, D. P. O'Neill, J. A. Parkhill, T. M. Perrine, R. Peverati, P. A. Pieniazek, A. Prociuk, D. R. Rehn, E. Rosta, N. J. Russ, N. Sergueev, S. M. Sharada, S. Sharmaa, D. W. Small, A. Sodt, T. Stein, D. Stück, Y.-C. Su, A. J. W. Thom, T. Tsuchimochi, L. Vogt, O. Vydrov, T. Wang, M. A. Watson, J. Wenzel, A. White, C. F. Williams, V. Vanovschi, S. Yeganeh, S. R. Yost, Z.-Q. You, I. Y. Zhang, X. Zhang, Y. Zhou, B. R. Brooks, G. K. L. Chan, D. M. Chipman, C. J. Cramer, W. A. Goddard III, M. S. Gordon, W. J. Hehre, A. Klamt, H. F. Schaefer III, M. W. Schmidt, C. D. Sherrill, D. G. Truhlar, A. Warshel, X. Xua, A. Aspuru-Guzik, R. Baer, A. T. Bell,

N. A. Besley, J.-D. Chai, A. Dreuw, B. D. Dunietz, T. R. Furlani, S. R. Gwaltney, C.-P. Hsu, Y. Jung, J. Kong, D. S. Lambrecht, W. Liang, C. Ochsenfeld, V. A. Rassolov, L. V. Slipchenko, J. E. Subotnik, T. Van Voorhis, J. M. Herbert, A. I. Krylov, P. M. W. Gill, and M. Head-Gordon. Advances in molecular quantum chemistry contained in the Q-Chem 4 program package. *Mol. Phys.*, 113:184–215, 2015.

[87] M. W. Schmidt, K. K.Baldridge, J. A.Boatz, S. T. Elbert, M. S. Gordon, J. H. Jensen, S. Koseki, N. Matsunaga, K. A. Nguyen, S. Su, T. L. Windus, M. Dupuis, and J. A. Montgomery. General atomic and molecular electronic structure system. *J. Comput. Chem.*, 14(*11*):1347–1363, 1993.

[88] Q. Sun, T. C. Berkelbach, N. S. Blunt, G. H. Booth, S. Guo, Z. Li, J. Liu, J. McClain, E. R. Sayfutyarova, S. Sharma, S. Wouters, and G. K.-L. Chan. The Python-based Simulations of Chemistry Framework. *WIREs Comput. Mol. Sci.*, 2017. DOI: 10.1002/wcms.1340.

[89] H. Lischka, R. Shepard, I. Shavitt, R. M. Pitzer, M. Dallos, T. Müller, P. G. Szalay, F. B. Brown, R. Ahlrichs, H. J. Böhm, A. Chang, D. C. Comeau, R. Gdanitz, H. Dachsel, C. Ehrhardt, M. Ernzerhof, P. Höchtl, S. Irle, G. Kedziora, T. Kovar, V. Parasuk, M. J. M. Pepper, P. Scharf, H. Schiffer, M. Schindler, M. Schüler, M. Seth, E. A. Stahlberg, J.-G. Zhao, S. Yabushita, Z. Zhang, M. Barbatti, S. Matsika, D. R. Y. M. Schuurmann, S. R. Brozell, E. V. Beck, J.-P. Blaudeau, M. Ruckenbauer, B. Sellner, F. Plasser, and J. J. Szymczak. COLUMBUS, an *ab initio* electronic structure program, 2015. Release 7.0.

[90] H. Lischka, T. Müller, P. G. Szalay, I. Shavitt, R. M. Pitzer, and R. Shepard. COLUMBUS – a program system for advanced multireference theory calculations. *WIREs Comput. Mol. Sci.*, 1(*2*):191–199, 2011.

[91] S. J. Clark, M. D. Segall, C. J. Pickard, P. J. Hasnip, M. J. Probert, K. Refson, and M. C. Payne. First principles methods using CASTEP. *Z. Kristallogr.*, 220 (*5–6*):567–570, 2005.

[92] C.-K. Skylaris, P. D. Haynes, A. A. Mostofi, and M. C. Payne. Introducing ONETEP: Linear-scaling density functional simulations on parallel computers. *J. Chem. Phys.*, 122(*8*):084119, 2005.

[93] P. Giannozzi, S. Baroni, N. Bonini, M. Calandra, R. Car, C. Cavazzoni, D. Ceresoli, G. L. Chiarotti, M. Cococcioni, I. Dabo, A. Dal Corso, S. de Giron-

coli, S. Fabris, G. Fratesi, R. Gebauer, U. Gerstmann, C. Gougoussis, A. Kokalj, M. Lazzeri, L. Martin-Samos, N. Marzari, F. Mauri, R. Mazzarello, S. Paolini, A. Pasquarello, L. Paulatto, C. Sbraccia, S. Scandolo, G. Sclauzero, A. P. Seitsonen, A. Smogunov, P. Umari, and R. M. Wentzcovitch. QUANTUM ESPRESSO: A modular and open-source software project for quantum simulations of materials. *J. Phys.: Condens. Matter*, 21(*39*):395502, 2009. Available from http://www.quantum-espresso.org.

[94] D. A. Case, T. E. Cheatham, T. Darden, H. Gohlke, R. Luo, K. Merz, A. Onufriev, C. Simmerling, B. Wang, and R. Woods. The Amber biomolecular simulation programs. *J. Comput. Chem.*, 26(*16*):1668–1688, 2005.

[95] B. R. Brooks, R. E. Bruccoleri, B. D. Olafson, D. J. States, S. Swaminathan, and M. Karplus. CHARMM: A program for macromolecular energy, minimization, and dynamics calculations. *J. Comput. Chem.*, 4(*2*):187–217, 1983.

[96] W. Smith, C. Yong, and P. Rodger. DL_POLY: Application to molecular simulation. *Mol. Simul.*, 28(*5*):385–471, 2002.

[97] M. Beck, A. Jäckle, G. Worth, and H.-D. Meyer. The multiconfiguration time-dependent Hartree (MCTDH) method: A highly efficient algorithm for propagating wavepackets. *Phys. Rep.*, 324(*1*):1–105, 2000.

[98] H.-D. Meyer, F. Gatti, and G. A. Worth, editors. *Multidimensional quantum dynamics: MCTDH theory and applications*. Wiley-VCH Verlag GmbH & Co. KGaA, 2009.

[99] H.-D. Meyer. Studying molecular quantum dynamics with the multiconfiguration time-dependent Hartree method. *WIREs Comput. Mol. Sci.*, 2(*2*):351–374, 2012.

[100] G. W. Richings, I. Polyak, K. E. Spinlove, G. A. Worth, I. Burghardt, and B. Lasorne. Quantum dynamics simulations using Gaussian wavepackets: the vMCG method. *Int. Rev. Phys. Chem.*, 34(*2*):269–308, 2015.

[101] J. W. Snyder, B. F. E. Curchod, and T. J. Martínez. GPU-accelerated state-averaged complete active space self-consistent field interfaced with *ab initio* multiple spawning unravels the photodynamics of provitamin D_3. *J. Phys. Chem. Lett.*, 7(*13*):2444–2449, 2016.

[102] G. A. Worth, M. A. Robb, and B. Lasorne. Solving the time-dependent Schrodinger equation for nuclear motion in one step: Direct dynamics of non-adiabatic systems. *Mol. Phys.*, 106(*16–18*):2077–2091, 2008.

[103] D. V. Shalashilin. Quantum mechanics with the basis set guided by Ehrenfest trajectories: Theory and application to spin-boson model. *J. Chem. Phys.*, 130 (*24*):244101, 2009.

[104] D. V. Shalashilin. Nonadiabatic dynamics with the help of multiconfigurational Ehrenfest method: Improved theory and fully quantum 24D simulation of pyrazine. *J. Chem. Phys.*, 132(*24*):244111, 2010.

[105] P. A. Sherratt, D. V. Shalashillin, and M. S. Child. Description of multidimensional tunnelling with the help of coupled coherent states guided by classical Hamiltonians with quantum corrections. *Chem. Phys.*, 322(*1–2*):127–134, 2006.

[106] J. C. Tully. Molecular dynamics with electronic transitions. *J. Chem. Phys.*, 93 (*2*):1061–1071, 1990.

[107] J. C. Tully. Perspective: Nonadiabatic dynamics theory. *J. Chem. Phys.*, 137 (*22*):22A301, 2012.

[108] J. E. Subotnik, A. Jain, B. Landry, A. Petit, W. Ouyang, and N. Bellonzi. Understanding the surface hopping view of electronic transitions and decoherence. *Annu. Rev. Phys. Chem.*, 67:387–417, 2016.

[109] M. P. Allen and D. J. Tildesley. *Computer simulations of liquids*. Oxford University Press Inc., New York, 1st edition, 2009.

[110] N. J. Turro, V. Ramamurthy, and J. C. Scaiano. *Principles of molecular photochemistry: An introduction*. University Science Books, Sausalito, 1st edition, 2009.

[111] P. A. M. Dirac. The quantum theory of the emission and absorption of radiation. *Proc. R. Soc. A*, 114(*767*):243–265, 1927.

[112] A. Jabloński. Efficiency of anti-Stokes fluorescence in dyes. *Nature*, 131:839–840, 1933.

[113] J. Franck. Elementary processes of photochemical reactions. *Trans. Faraday Soc.*, 21:536–542, 1926.

[114] E. U. Condon. A theory of intensity dirstibution in band systems. *Phys. Rev.*, 28 (*6*):1182–1201, 1926.

[115] E. U. Condon. The Franck-Condon principle and related topics. *Am. J. Phys*, 15 (*5*):365–374, 1947.

[116] M. Kasha. Characterization of electronic transitions in complex molecules. *Discuss. Faraday Soc.*, 6:14–19, 1950.

[117] I. V. Khudyakov, Y. A. Serebrennikov, and N. J. Turro. Spin-orbit coupling in free-radical reactions: On the way to heavy elements. *Chem. Rev.*, 93(*1*):537–570, 1993.

[118] B. Valeur. *Molecular fluorescence: Principles and applications*. Wiley-VCH, Weinheim, 2nd edition, 2002.

[119] B. K. Carpenter. Electronically nonadiabatic thermal reactions of organic molecules. *Chem. Soc. Rev.*, 35(*8*):736–747, 2006.

[120] F. F. Crim. Molecular reaction dynamics across the phases: Similarities and differences. *Faraday Discuss.*, 157:9–26, 2012.

[121] C. Sagan. Ultraviolet selection pressure on the earliest organisms. *J. Theor. Biol.*, 39(*1*):195–200, 1973.

[122] D. O. Hessen. Solar radiation and the evolution of life. In E. Bjertness, editor, *Solar radiation and human health*, pages 123–136. The Norwegian Academy of Science and Letters, 2008.

[123] B. A. Whitton and M. Potts. *Introduction to the Cyanobacteria*, chapter 1, pages 1–13. Ecology of Cyanobacteria II. Springer Science+Business Media, 2012.

[124] B. K. Pierson, H. K. Mitchell, and A. L. Ruff-Roberts. *Chloroflexus aurantiacus* and ultraviolet radiation: Implications for Archean shallow-water stromatolites. *Orig. Life Evol. Biosph.*, 23(*4*):243–260, 1993.

[125] J. M. Olson and B. K. Pierson. Photosynthesis 3.5 thousand million years ago. *Photosynth. Res.*, 9(*1*):251–259, 1986.

[126] M. B. Rambler and L. Margulis. Bacterial resistance to ultraviolet irradiation under anaerobiosis: Implications for pre-Phanerozoic evolution. *Science*, 210(*4470*): 638–640, 1980.

[127] L. J. Stal. *Cyanobacterial mats and stromatolites*, chapter 4, pages 65–115. Ecology of cyanobacteria II. Springer Science+Business Media, 2012.

[128] J. M. Olson. Evolution of photosynthetic reaction centers. *Biosystems*, 14(*1*): 89–94, 1981.

[129] L. Margulis, J. C. G. Walker, and M. Rambler. Reassessment of roles of oxygen and ultraviolet light in Precambrian evolution. *Nature*, 264:620–624, 1976.

[130] V. R. Phoenix, P. C. Bennett, A. S. Engel, S. W. Tyler, and F. G. Ferris. Chilean high-altitude hot-spring sinters: A model system for UV screening mechanisms by early Precambrian cyanobacteria. *Geobiology*, 4(*1*):15–28, 2006.

[131] F. Garcia-Pichel and R. W. Castenholz. Characterization and biological implications of scytonemin, a cyanobacterial sheath pigment. *J. Phycol.*, 27(*3*):395–409, 1991.

[132] R. W. Castenholz and F. Garcia-Pichel. *Cyanobacterial responses to UV radiation*, chapter 19, pages 481–496. Ecology of Cyanobacteria II. Springer Science+Business Media, 2012.

[133] Y. ping Cen and J. F. Bornman. The response of bean plants to UV-B radiation under different irradiances of background visible light. *J. Exp. Bot.*, 41(*232*): 1489–1495, 1990.

[134] J. F. Kasting. Earth's early atmosphere. *Science*, 259(*5097*):920–926, 1993.

[135] L. R. Kump. The rise of atmospheric oxygen. *Nature*, 451:277–278, 2008.

[136] D. E. Canfield. The early history of atmospheric oxygen: Homage to Robert M. Garrels. *Annu. Rev. Earth Planet. Sci.*, 33:1–36, 2005.

[137] T. W. Lyons, C. T. Reinhard, and N. J. Planavsky. The rise of oxygen in Earth's early ocean and atmosphere. *Nature*, 506(*7488*):307–315, 2014.

[138] H. D. Holland. The oxygenation of the atmosphere and oceans. *Phil. Trans. R. Soc. B*, 361(*1470*):903–915, 2006.

[139] R. E. Kopp, J. L. Kirschvink, I. A. Hilburn, and C. Z. Nash. The Paleoproterozoic snowball Earth: A climate disaster triggered by the evolution of oxygenic photosynthesis. *Proc. Natl. Acad. Sci. U. S. A.*, 102(*32*):11131–11136, 2005.

[140] J. F. Kasting and J. L. Siefert. Life and the evolution of Earth's atmosphere. *Science*, 296(*5570*):1066–1068, 2002.

[141] L. R. Kump and M. E. Barley. Increased subaerial volcanism and the rise of atmospheric oxygen 2.5 billion years ago. *Nature*, 448:1033–1036, 2007.

[142] D. C. Catling and M. W. Claire. How Earth's atmosphere evolved to an oxic state: A status report. *Earth Planet. Sci. Lett.*, 237(*1–2*):1–20, 2005.

[143] G. M. Young. Precambrian supercontinents, glaciations, atmospheric oxygenation, metazoan evolution and an impact that may have changed the second half of Earth history. *Geosci. Front.*, 4(*3*):247–261, 2013.

[144] C. R. Marshall. Explaining the Cambrian "explosion" of animals. *Annu. Rev. Earth Planet. Sci.*, 34:355–384, 2006.

[145] D. Fox. What sparked the Cambrian explosion? *Nature*, 530(*7590*):268–270, 2016.

[146] D. B. Mills and D. E. Canfield. Oxygen and animal evolution: Did a rise of atmospheric oxygen trigger the origin of animals? *Bioessays*, 36(*12*):1145–1155, 2014.

[147] C. A. Gueymard. Parameterized transmittance model for direct beam and circumsolar spectral irradiance. *Solar Energy*, 71(*5*):325–346, 2001.

[148] M. F. Holick. Sunlight and vitamin D for bone health and prevention of autoimmune diseases, cancers, and cardiovascular disease. *Am. J. Clin. Nutr.*, 80(*6*): 1678S–1688S, 2004.

[149] M. M. Caldwell, J. F. Bornman, C. L. Ballaré, S. D. Flint, and G. Kulandaivelu. Terrestrial ecosystems, increased solar ultraviolet radiation, and interactions with other climate change factors. *Photochem. Photobiol. Sci.*, 6(*3*):252–266, 2007.

[150] R. Lucas, T. McMichael, W. Smith, and B. Armstrong. *Solar ultraviolet radiation. Global burden of disease from solar ultraviolet radiation.* Environmental Burden of Disease Series, No. 13. World Health Organization, Geneva, 2006.

[151] R. M. Lucas and A.-L. Ponsonby. Ultraviolet radiation and health: Friend and foe. *Med. J. Aust.*, 177(*11–12*):594–598, 2002.

[152] Health effects of UV radiation. World Health Organization. Accessed March 2016, http://www.who.int/uv/health/en/.

[153] M. F. Holick. Vitamin D deficiency. *N. Engl. J. Med.*, 357:266–281, 2007.

[154] H. A. Morris. Vitamin D: A hormone for all seasons - how much is enough? Understanding the new pressures. *Clin. Biochem. Rev.*, 26(*1*):21–32, 2005.

[155] M. F. Holick, R. M. Biancuzzo, T. C. Chen, E. K. Klein, A. Young, D. Bibuld, R. Reitz, W. Salameh, A. Ameri, and A. D. Tannenbaum. Vitamin D_2 is as effective as vitamin D_3 in maintaining circulating concentrations of 25-hydroxyvitamin D. *J. Clin. Endocrinol. Metab.*, 93(*3*):677–681, 2008.

[156] A. B. Britt. Repair of DNA damage induced by solar UV. *Photosynth. Res.*, 81 (*2*):105–112, 2004.

[157] A. R. Webb, B. R. Decosta, and M. F. Holick. Sunlight regulates the cutaneous production of vitamin D_3 by causing its photodegradation. *J. Clin. Endocrinol. Metab.*, 68(*5*):882–887, 1989.

[158] J. N. Hathcock, A. Shao, R. Vieth, and R. Heaney. Risk assessment for vitamin D. *Am. J. Clin. Nutr.*, 85(*1*):6–18, 2007.

[159] H. F. DeLuca. Overview of general physiologic features and functions of vitamin D. *Am. J. Clin. Nutr.*, 80(*6*):1689S–1696S, 2004.

[160] P. H. Hart, S. Gorman, and J. J. Finlay-Jones. Modulation of the immune system by UV radiation: More than just the effects of vitamin D? *Nature*, 11(*9*):584–596, 2011.

[161] T. S. Dexheimer. *DNA repair of cancer stem cells*, chapter 2, pages 19–32. Springer Netherlands, 2013.

[162] M. S. Cooke, M. D. Evans, and M. D. nd Joseph Lunec. Oxidative DNA damage: Mechanisms, mutation, and disease. *FASEB J.*, 17(*10*):1195–1214, 2003.

[163] A. Sancar, L. A. Lindsey-Boltz, K. Ünsal Kaçmaz, and S. Linn. Molecular mechanisms of mammalian DNA repair and the DNA damage checkpoints. *Annu. Rev. Biochem.*, 73:39–85, 2004.

[164] R. S. Mason and J. Reichrath. Sunlight vitamin D and skin cancer. *Anticancer Agents Med. Chem.*, 13(*1*):83–97, 2013.

[165] A. Slominski, D. J. Tobin, S. Shibahara, and J. Wortsman. Melanin pigmentation in mammalian skin and its hormonal regulation. *Physiol. Rev.*, 84(*4*):1155–1228, 2004.

[166] M. Cichorek, M. Wachulska, A. Stasiewicz, and A. Tymińska. Skin melanocytes: Biology and development. *Postępy. Dermatol. Alergol.*, 30(*1*):30–41, 2013.

[167] H. Fedorow, F. Tribl, G. Halliday, M. Gerlach, P. Riederer, and K. Double. Neuromelanin in human dopamine neurons: Comparison with peripheral melanins and relevance to Parkinsons disease. *Prog. Neurobiol.*, 75(*2*):109–124, 2005.

[168] S. Ito. A chemist's view of melanogenesis. *Pigment Cell Res.*, 16(*3*):230–236, 2003.

[169] K. Wakamatsu and S. Ito. Advanced chemical methods in melanin determination. *Pigment Cell Res.*, 15(*3*):174–183, 2002.

[170] X. Wu and J. A. Hammer. Melanosome transfer: It is best to give and receive. *Curr. Opin. Cell Biol.*, 29:1–7, 2014.

[171] M. Brenner and V. J. Hearing. The protective role of melanin against UV damage in human skin. *Photochem. Photobiol.*, 84(*3*):539–549, 2008.

[172] H. Ando, Y. Niki, M. Yoshida, M. Ito, K. Akiyama, J.-H. Kim, T.-J. Yoon, M. S. Matsui, D. B. Yarosh, and M. Ichihashi. Involvement of pigment globules containing multiple melanosomes in the transfer of melanosomes from melanocytes to keratinocytes. *Cell. Logist.*, 1(*1*):12–20, 2011.

[173] J. P. Ortonne. Photoprotective properties of skin melanin. *Br. J. Dermatol.*, 146 (*61*):7–10, 2002.

[174] H. Park, M. Kosmadaki, M. Yaar, and B. A. Gilchrest. Cellular mechanisms regulating human melanogenesis. *Cell. Mol. Life Sci.*, 66(*9*):1493–1506, 2009.

[175] M. S. Eller and B. A. Gilchrest. Tanning as part of the eukaryotic SOS response. *Pigment Cell Res.*, 13(*8*):94–97, 2000.

[176] J. A. Levine, M. Sorace, J. Spencer, and D. M. Siegel. The indoor UV tanning industry: A review of skin cancer risk, health benefit claims, and regulation. *J. Am. Acad. Dermatol.*, 53(*6*):1038–1044, 2005.

[177] G. I. Jenkins. Signal transduction in responses to UV-B radiation. *Annu. Rev. Plant Biol.*, 60:407–431, 2009.

[178] H. Frohnmeyer and D. Staiger. Ultraviolet-B radiation-mediated responses in plants. Balancing damage and protection. *Plant Physiol.*, 133(*4*):1420–1428, 2003.

[179] J. Rozema, J. van de Staaij, L. O. Björn, and M. Caldwell. UV-B as an environmental factor in plant life: Stress and regulation. *Trends Ecol. Evol.*, 12(*1*): 22–28, 1997.

[180] A. H. Teramura. Effects of ultraviolet-B radiation on the growth and yield of crop plants. *Physiol. Plant.*, 58(*3*):415–427, 1983.

[181] M. M. Caldwell, A. H. Teramura, and M. Tevini. The changing solar ultraviolet climate and the ecological consequences for higher plants. *Trends Ecol. Evol.*, 4 (*12*):363–367, 1989.

[182] A. H. Teramura and J. H. Sullivan. Effects of UV-B radiation on photosynthesis and growth of terrestrial plants. *Photosynth. Res.*, 39(*3*):463–473, 1994.

[183] C. M. Fraser and C. Chapple. The phenylpropanoid pathway in *Arabidopsis*. *Arabidopsis Book*, 9:e0152, 2011.

[184] S. M. Mandal, D. Chakraborty, and S. Dey. Phenolic acids act as signaling molecules in plant-microbe symbioses. *Plant Signaling Behav.*, 5(*4*):359–368, 2010.

[185] K. Meyer, J. C. Cusumano, C. Somerville, and C. C. S. Chapple. Ferulate-5-hydroxylase from *Arabidopsis thaliana* defines a new family of cytochrome P450-dependent monooxygenases. *Proc. Natl. Acad. Sci. U. S. A.*, 93(*14*):6869–6874, 1996.

[186] C. M. Fraser, M. G. Thompson, A. M. Shirley, J. Ralph, J. A. Schoenherr, T. Sinlapadech, M. C. Hall, and C. Chapple. Related *Arabidopsis* serine carboxypeptidase-like sinapoylglucose acyltransferases display distinct but overlapping substrate specificities. *Plant Physiol.*, 144(*2*):1986–1999, 2007.

[187] R. Bently. The Shikimate pathway - a metabolic tree with many branches. *Crit. Rev. Biochem. Mol. Biol.*, 25(*5*):307–384, 1990.

[188] T. Vogt. Phenylpropanoid biosynthesis. *Mol. Plant.*, 3(*1*):2–20, 2010.

[189] R. L. McKenzie, P. J. Aucamp, A. F. Bais, L. O. Björn, M. Ilyas, and S. Madronich. Ozone depletion and climate change: Impacts on UV radiation. *Photochem. Photobiol. Sci.*, 10(*2*):182–198, 2011.

[190] J. C. van der Leun, R. D. Piacentini, and F. R. de Gruijl. Climate change and human skin cancer. *Photochem. Photobiol. Sci.*, 7(*6*):730–733, 2008.

[191] M. Norval, R. M. Lucas, A. P. Cullen, F. R. de Gruijl, J. Longstreth, Y. Takizawa, and J. C. van der Leung. The human health effects of ozone depletion and interactions with climate change. *Photochem. Photobiol. Sci.*, 10(*2*):199–225, 2011.

[192] D.-P. Häder, E. W. Helbling, C. E. Williamson, and R. C. Worrest. Effects of UV radiation on aquatic ecosystems and interactions with climate change. *Photochem. Photobiol. Sci.*, 10(*2*):242–260, 2011.

[193] C. Corinaldesi, E. Damiani, F. Marcellini, C. Falugi, L. Tiano, F. Brugè, and R. Danovaro. Sunscreen products impair the early developmental stages of the sea urchin *Paracentrotus lividus*. *Sci. Rep.*, 7(*7815*):1–12, 2017.

[194] M. Fouqueray, J.-L. Mouget, A. Morant-Manceau, and G. Tremblin. Dynamics of short-term acclimation to UV radiation in marine diatoms. *J. Photochem. Photobiol., B*, 89(*1*):1–8, 2007.

[195] M. Tevini and A. H. Teramura. UV-B effects on terrestrial plants. *Photochem. Photobiol.*, 50(*4*):479–487, 1989.

[196] D. Olszyk, Q. Dai, P. Teng, Y. L. Hei Leung, and S. Peng. UV-B effects on crops: Response of the irrigated rice ecosystem. *J. Plant Physiol.*, 148(*1–2*):26–34, 1996.

[197] N. A. Kasparian, J. K. McLoone, and B. Meiser. Skin cancer-related prevention and screening behaviors: A review of the literature. *J. Behav. Med.*, 32(*5*):406–428, 2009.

[198] K. Hoffmann, J. Laperre, A. Avermaete, P. Altmeyer, and T. Gambichler. Defined UV protection by applied textiles. *Arch. Dermatol.*, 137(*8*):1089–1094, 2001.

[199] T. Gambichler, P. Altmeyer, and K. Hoffmann. Role of clothes in sun protection. *Recent Results Cancer Res.*, 160:15–25, 2002.

[200] W. L. Morison. Photoprotection by clothing. *Dermatol. Ther.*, 16(*1*):16–22, 2003.

[201] S. Q. Wang, Y. Balagula, and U. Osterwalder. Photoprotection: A review of the current and future technologies. *Dermatol. Ther.*, 23(*1*):31–47, 2010.

[202] D. H. Sliney. Photoprotection of the eye - UV radiation and sunglasses. *J. Photochem. Photobiol., B*, 64(*2–3*):166–175, 2001.

[203] C. Tuchinda, S. Srivannaboon, and H. W. Lim. Photoprotection by window glass, automobile glass, and sunglasses. *J. Am. Acad. Dermatol.*, 45(*5*):845–854, 2006.

[204] R. Jansen, U. Osterwalder, S. Q. Wang, M. Burnett, and H. W. Lim. Photoprotection part II. Sunscreen: Development, efficacy, and controversies. *J. Am. Acad. Dermatol.*, 69(*6*):867.e1–867.e14, 2013.

[205] B. L. Diffey. Sun protection with clothing. *Br. J. Dermatol.*, 144(*3*):449–451, 2001.

[206] U. Osterwalder and B. Herzog. Sun protection factors: World wide confusion. *Br. J. Dermatol.*, 161(*3*):13–24, 2009.

[207] S. B. Stankovic, D. Popovic, G. B. Poparic, and M. Bizjak. Ultraviolet protection factor of gray-state plain cotton knitted fabrics. *Text. Res. J.*, 79(*11*):1034–1042, 2009.

[208] J. S. Mitchell. The origin of the erythema curve and the pharmacological action of ultra-violet radiation. *Proc. R. Soc. Lond. B Biol. Sci.*, 126(*843*):241–256, 1938.

[209] A. P. Popov, A. V. Priezzhev, J. Lademann, and R. Myllylä. TiO_2 nanoparticles as an effective UV-B radiation skin-protective compound in sunscreens. *J. Phys. D: Appl. Phys.*, 38(*15*):2564–2570, 2005.

[210] S. Davis, L. Capjack, N. Kerr, and R. Fedosejevs. Clothing as protection from ultraviolet radiation: Which fabric is most effective? *Pharmacol. Ther.*, 36(*5*): 374–379, 1997.

[211] J. Aguilera, M. V. de Gálvez, C. Sánchez-Roldán, and E. Herrera-Ceballos. New advances in protection against solar ultraviolet radiation in textiles for summer clothing. *Photochem. Photobiol.*, 90(*5*):1199–1206, 2014.

[212] B. Diffey. Has the sun protection factor had its day? *Br. Med. J.*, 320(*7228*): 176–177, 2000.

[213] A. S. Aldahan, V. V. Shah, S. Mlacker, and K. Nouri. The history of sunscreen. *JAMA Dermatol.*, 151(*12*):1316, 2015.

[214] C. D. Kaur and S. Saraf. *In vitro* sun protection factor determination of herbal oils used in cosmetics. *Pharmacognosy Res.*, 2(*1*):22–25, 2010.

[215] F. Urbach. The historical aspects of sunscreens. *J. Photochem. Photobiol. B*, 64 (*2–3*):99–104, 2001.

[216] A. Bachem and B. Fantus. Evaluation of skin protection against ultraviolet rays. *Arch. Phys. Therapy*, 20:69–76, 1939.

[217] U. Henschke. Untersuchungen an lichtschutzmitteln. *Strahlentherapie*, 67:659–667, 1940.

[218] A. Giese, E. Christensen, and J. Jeppard. Absorption spectra of some sunscreens for sunburn. *J. Am. Pharm. Assoc.*, 39(*1*):30–36, 1950.

[219] N. Lowe. An overview of ultraviolet radiation, sunscreens, and photo-induced dermatoses. *Dermatol. Clin.*, 24(*1*):9–17, 2006.

[220] J. M. Knox, A. C. Griffin, and R. E. Hakim. Protection from ultaviolet carcinogenesis. *J. Invest. Dermatol.*, 34(*1*):51–58, 1960.

[221] M. Lodén, H. Beitner, H. Gonzalez, D. Edström, U. Åkerström, J. Austad, I. Buraczewska-Norin, M. Matsson, and H. Wulf. Sunscreen use: Controversies, challenges and regulatory aspects. *Br. J. Dermatol.*, 165(*2*):255–262, 2011.

[222] S. E. Mancebo, J. Y. Hu, and S. Q. Wang. Sunscreens: A review of health benefits, regulations, and controversies. *Dermatol. Clin.*, 32(*3*):427–438, 2014.

[223] N. A. Shaath. Ultraviolet filters. *Photochem. Photobiol. Sci.*, 9(*4*):464–469, 2009.

[224] N. Serpone, A. Salinaro, A. V. Emeline, S. Horikoshi, H. Hidaka, and J. Zhao. An *in vitro* systematic spectroscopic examination of the photostabilities of a random set of commercial sunscreen lotions and their chemical UVB/UVA active agents. *Photochem. Photobiol. Sci.*, 1(*12*):970–981, 2002.

[225] S. T. Nedorost. Facial erythema as a result of benzophenone allergy. *J. Am. Acad. Dermatol.*, 49(*5*):259–261, 2003.

[226] E. Kurul and S. Hekimoğlu. Skin permeation of two different benzophenone derivatives from various vehicles. *Int. J. Cosmet. Sci.*, 23(*4*):211–218, 2001.

[227] N. R. Janjua, B. Mogensen, A.-M. Andersson, J. H. Petersen, M. Henriksen, N. E. Skakkebæk, and H. C. Wulf. Systemic absorption of the sunscreens benzophenone-3, octyl-methoxycinnamate, and 3-(4-methyl-benzylidene) camphor after whole-body topical application and reproductive hormone levels in humans. *J. Invest. Dermatol.*, 123(*1*):57–61, 2004.

[228] H. Gonzalez, A. Farbrot, O. Larkö, and A.-M. Wennberg. Percutaneous absorption of the sunscreen benzophenone-3 after repeated whole-body applications, with and without ultraviolet irradiation. *Br. J. Dermatol.*, 154(*2*):337–340, 2006.

[229] I. Ozáez, J. L. Martínez-Guitarte, and G. Morcillo. The UV filter benzophenone 3 (BP-3) activates hormonal genes mimicking the action of ecdysone and alters embryo development in the insect *Chironomus riparius* (Diptera). *Environ. Pollut.*, 192:19–26, 2014.

[230] S. Kim and K. Choi. Occurrences, toxicities, and ecological risks of benzophenone-3, a common component of organic sunscreen products: A mini-review. *Environ. Int.*, 70:143–157, 2014.

[231] T. Wong and D. Orton. Sunscreen allergy and its investigation. *Clin. Dermatol.*, 29(*3*):306–310, 2011.

[232] R. M. Adams and H. L. Maibach. A five-year study of cosmetic reactions. *J. Am. Acad. Dermatol.*, 13(*6*):1062–1069, 1985.

[233] F. Journe, M. claude Marguery, J. Rakotondrazafy, F. E. Sayed, and J. Bazex. Sunscreen sensitization: A 5-year study. *Acta Derm. Venereol.*, 79(*3*):211–213, 1999.

[234] C. Couteau, A. Faure, J. Fortin, E. Paparis, and L. J. Coiffard. Study of the photostability of 18 sunscreens in creams by measuring the SPF in vitro. *J. Pharm. Biomed. Anal.*, 44(*1*):270–273, 2007.

[235] E. Rodríguez, M. C. Valbuena, M. Rey, and L. P. de Quintana. Causal agents of photoallergic contact dermatitis diagnosed in the national institute of dermatology of Colombia. *Photodermatol. Photoimmunol. Photomed.*, 22(*4*):189–192, 2006.

[236] A. Deflandre and G. Lang. Photostability assessment of sunscreens. Benzylidene camphor and dibenzoylmethane derivatives. *Int. J. Cosmet. Sci.*, 10(*2*):53–62, 1988.

[237] B. Herzog, M. Wehrle, and K. Quass. Photostability of UV absorber systems in sunscreens. *Photochem. Photobiol.*, 85(*4*):869–878, 2009.

[238] G. J. Mturi and B. S. Martincigh. Photostability of the sunscreening agent 4-*tert*-butyl-4'-methoxydibenzoylmethane (avobenzone) in solvents of different polarity and proticity. *J. Photochem. Photobiol., A*, 200(*2–3*):410–420, 2008.

[239] J. F. Nash and P. R. Tanner. Relevance of UV filter/sunscreen product photostability to human safety. *Photodermatol. Photoimmunol. Photomed.*, 30(*2–3*): 88–95, 2014.

[240] S. Afonso, K. Horita, J. P. Sousa e Silva, I. F. Almeida, M. H. Amaral, P. A. L. ao, P. C. Costa, M. S. Miranda, J. C. G. Esteves da Silva, and J. M. Sousa Lobo. Photodegradation of avobenzone: Stabilization effect of antioxidants. *J. Photochem. Photobiol., B*, 140:36–40, 2014.

[241] A. Darvay, I. R. White, R. J. G. Rycroft, A. B. Jones, J. L. M. Hawk, and J. P. Mcfadden. Photoallergic contact dermatitis is uncommon. *Br. J. Dermatol.*, 145 (*4*):597–601, 2001.

[242] G. M. Murphy and I. R. White. Photoallergic contact dermatitis to 2-ethoxyethyl-p-methoxycinnamate. *Contact Derm.*, 16(*5*):296, 1987.

[243] S. H. Dromgoole and H. L. Maibach. Sunscreening agent intolerance: Contact and photocontact sensitization and contact urticaria. *J. Am. Acad. Dermatol.*, 22(*6*):1068–1078, 1990.

[244] C. Antoniou, M. G. Kosmadaki, A. J. Stratigos, and A. D. Katsambas. Sunscreens whats important to know. *J. Eur. Acad. Dermatol. Venereol.*, 22(*9*):1110–1119, 2008.

[245] T. M. Hughes, J. A. Martin, V. J. Lewis, and N. M. Stone. Allergic contact dermatitis to drometrizole trisiloxane in a sunscreen with concomitant sensitivities to other sun screens. *Contact Derm.*, 52(*4*):226–227, 2005.

[246] S. Y. Chuah, Y. H. Leow, A. T. J. Goon, C. T. S. Theng, and W.-S. Chong. Photopatch testing in Asians: A 5-year experience in Singapore. *Photodermatol. Photoimmunol. Photomed.*, 29(*3*):116–120, 2013.

[247] H. Gonzalez, N. Tarras-Wahlberg, B. Strömdahl, A. Juzeniene, J. Moan, O. Larkö, A. Rosén, and A.-M. Wennberg. Photostability of commercial sunscreens upon sun exposure and irradiation by ultraviolet lamps. *BMC Dermatol.*, 7(*1*):1–9, 2007.

[248] M. E. Carlotti, S. Sapino, E. Ugazio, E. Peira, D. Vione, and C. Minero. Photostability of ferulic acid and its antioxidant activity against linoleic acid peroxidation. *J. Dispersion Sci. Technol.*, 29(*5*):629–640, 2008.

[249] C. Gambetta, J. Natera, W. A. Massad, and N. A. García. Methyl anthranilate as generator and quencher of reactive oxygen species: A photochemical study. *J. Photochem. Photobiol., A*, 269:27–33, 2013.

[250] S. Schauder and H. Ippen. Contact and photocontact sensitivity to sunscreens: Review of a 15-year experience and of the literature. *Contact Derm.*, 37(*5*): 221–232, 1997.

[251] L. R. Gaspar and P. M. B. G. Maia-Campos. Evaluation of the photostability of different UV filter combinations in a sunscreen. *Int. J. Pharm*, 307(*2*):123–128, 2006.

[252] M. Avenel-Audran, C. Bernier, and M. Vigan. Octocrylene, an emerging photoallergen. *Arch. Dermatol.*, 146(*7*):753–757, 2010.

[253] A. C. deGroot and D. W. Roberts. Contact and photocontact allergy to octocrylene: A review. *Contact Derm.*, 70(*4*):193–204, 2014.

[254] I. Karlsson, E. Persson, J. Mårtensson, and A. Börje. Investigation of the sunscreen octocrylene's interaction with amino acid analogs in the presence of uv radiation. *Photochem. Photobiol.*, 88(*4*):904–912, 2012.

[255] M. A. Pathak. Sunscreens: Topical and systemic approaches for protection of human skin against harmful effects of solar radiation. *J. Am. Acad. Dermatol.*, 7 (*3*):285–312, 1982.

[256] M. N. Chrétien, E. Heafey, and J. C. Scaiano. Reducing adverse effects from UV sunscreens by zeolite encapsulation: Comparison of oxybenzone in solution and in zeolites. *Photochem. Photobiol.*, 86(*1*):153–161, 2010.

[257] N. Cook and S. Freeman. Report of 19 cases of photoallergic contact dermatitis to sunscreens seen at the Skin and Cancer Foundation. *Australas. J. Dermatol.*, 42(*4*):257–259, 2001.

[258] A. C. de Groot, H. B. van der Walle, B. A. Jagtman, and J. W. Weyland. Contact allergy to 4-isopropyl dibenzoylmethane and 3-(4'-methylbenzylidene) camphor in the sunscreen Eusolex 8021. *Contact Derm.*, 16(*5*):249–254, 1987.

[259] A. Klanna, G. Levy, lka Lutz, C. Müllera, W. Kloas, and J.-P. Hildebrandt. Estrogen-like effects of ultraviolet screen 3-(4-methylbenzylidene)-camphor (Eusolex 6300) on cell proliferation and gene induction in mammalian and amphibian cells. *Environ. Res.*, 97:274–281, 2005.

[260] M. E. Sarre, M. Guérin-Moreau, J. P. Lepoittevin, L. Martin, and M. Avenel-Audran. Allergic contact cheilitis caused by polysilicone-15 (Parsol SLX) in a lipcare balm. *Contact Derm.*, 70(*2*):117–127, 2014.

[261] A. N. Lin and T. Nakatsui. Salicylic acid. *Int. J. Dermatol.*, 37(*5*):335–342, 1998.

[262] J. F. Nash. Human safety and efficacy of ultraviolet filters and sunscreen products. *Dermatol. Clin.*, 24(*1*):35–51, 2006.

[263] N. Serpone, D. Dondi, and A. Albini. Inorganic and organic UV filters: Their role and efficacy in sunscreens and suncare products. *Inorg. Chim. Acta*, 360(*3*): 794–802, 2007.

[264] S. Forestier. Rationale for sunscreen development. *J. Am. Acad. Dermatol.*, 58 (*5*):S133–S138, 2008.

[265] J. S. Adams and M. Hewison. Update in vitamin D. *J. Clin. Endocrinol. Metab.*, 95(*2*):471–478, 2010.

[266] M. D. Hanwell, D. E. Curtis, D. C. Lonie, T. Vandermeersch, E. Zurek, and G. R. Hutchison. Avogadro: An advanced semantic chemical editor, visualization, and analysis platform. *J. Cheminf.*, 4:1–17, 2012.

[267] L. A. Baker and V. G. Stavros. Observing and understanding the ultrafast photochemistry in small molecules: Applications to sunscreens. *Sci. Prog.*, 99(*3*): 282–311, 2016.

[268] M. I. Cabrera, O. M. Alfano, and A. E. Cassano. Absorption and scattering coefficients of titanium dioxide particulate suspensions in water. *J. Phys. Chem.*, 100(*51*):20043–20050, 1996.

[269] U. Osterwalder, M. Sohn, and B. Herzog. Global state of sunscreens. *Photodermatol. Photoimmunol. Photomed.*, 30(*2–3*):62–80, 2014.

[270] European comission press release database: Consumers: Be sun-smart this summer. Accessed 13 May 2017, http://europa.eu/rapid/press-release_IP-09-1057_en.htm.

[271] M. D. Newman, M. Stotland, and J. I. Ellis. The safety of nanosized particles in titanium dioxide and zinc oxide based sunscreens. *J. Am. Acad. Dermatol.*, 61 (*4*):685–692, 2009.

[272] R. L. Siegel, K. D. Miller, and A. Jemal. Cancer statistics. *CA. Cancer J. Clin.*, 66(*1*):7–30, 2016.

[273] M. E. Burnett and S. Q. Wang. Current sunscreen controversies: A critical review. *Photodermatol. Photoimmunol. Photomed.*, 27(*2*):58–67, 2011.

[274] T. G. Smijs and S. Pavel. Titanium dioxide and zinc oxide nanoparticles in sunscreens: Focus on their safety and effectiveness. *Nanotechnol. Sci. Appl.*, 4: 95–112, 2011.

[275] M. Krause, A. Klit, M. B. Jensen, T. Søeborg, H. Frederiksen, M. Schlumpf, W. Lichtensteiger, N. E. Skakkebaek, and K. T. Drzewiecki. Sunscreens: are they beneficial for health? An overview of endocrine disrupting properties of UV-filters. *Int. J. Androl.*, 35(*3*):424–436, 2012.

[276] A. C. Green, G. M. Williams, V. Logan, and G. M. Strutton. Reduced melanoma after regular sunscreen use: Randomized trial follow-up. *J. Clin. Oncol.*, 89(*3*): 257–263, 2011.

[277] J. B. Mancuso, R. Maruthi, S. Q. Wang, and H. W. Lim. Sunscreens: An update. *Am. J. Clin. Dermatol.*, 18(*5*):643–650, 2017.

[278] G. J. Nohynek and H. Schaefery. Benefit and risk of organic ultraviolet filters. *Regul. Toxicol. Pharmacol.*, 33:285–299, 2001.

[279] M. Yamaji and M. Kida. Photothermal tautomerization of a UV sunscreen (4-*tert*-butyl-f'-methoxydibenzoylmethane) in acetonitrile studies by steady-state and laser flash photolysis. *J. Phys. Chem. A*, 117(*9*):1946–1951, 2013.

[280] G. H. G. Trossini, V. G. Maltarollo, R. D. Garcia, C. A. S. O. Pinto, M. V. R. Velasco, K. M. Honorio, and A. R. Baby. Theoretical study of tautomers and photoisomers of avobenzone by DFT methods. *J. Mol. Model.*, 21(*319*):1–7, 2015.

[281] A. Cantrell and D. J. McGarvey. Photochemical studies of 4-*tert*-butyl-4'-methoxydibenzoylmethane (BM-DBM). *J. Photochem. Photobiol., B*, 64(*2–3*): 117–122, 2001.

[282] A. D. Dunkelberger, R. D. Kieda, B. M. Marsh, and F. F. Crim. Picosecond dynamics of avobenzone in solution. *J. Phys. Chem. A*, 119(*24*):6155–6161, 2015.

[283] P. K. Verma, A. Steinbacher, F. Koch, P. Nuernberger, and T. Brixner. Monitoring ultrafast intramolecular proton transfer processes in an unsymmetric β-diketone. *Phys. Chem. Chem. Phys.*, 17(*13*):8459–8466, 2015.

[284] M. Kojić, M. Petković, and M. Etinski. A new insight into the photochemistry of avobenzone in gas phase and acetonitrile from *ab initio* calculations. *Phys. Chem. Chem. Phys.*, 18(*32*):22168–22178, 2016.

[285] T. N. V. Karsili, B. Marchetti, M. N. R. Ashfold, and W. Domcke. *Ab initio* study of potential ultrafast internal conversion routes in oxybenzone, caffeic acid, and ferulic acid: Implications for sunscreens. *J. Phys. Chem. A*, 118(*51*):11999–12010, 2014.

[286] L. A. Baker, M. D. Horbury, S. E. Greenough, P. M. Coulter, T. N. V. Karsili, G. M. Roberts, A. J. Orr-Ewing, M. N. R. Ashfold, and V. G. Stavros. Probing the ultrafast energy dissipation mechanism of the sunscreen oxybenzone after UVA irradiation. *J. Phys. Chem. Lett.*, 6(*8*):1363–1368, 2015.

[287] L. A. Baker, M. D. Horbury, S. E. Greenough, M. N. R. Ashfold, and V. G. Stavros. Broadband ultrafast photoprotection by oxybenzone across the UVB and UVC spectral regions. *Photochem. Photobiol. Sci.*, 14(*10*):1814–1820, 2015.

[288] M. T. Ignasiak, C. Houée-Levin, G. Kciuk, B. Marciniak, and T. Pedzinski. A reevaluation of the photolytic properties of 2-hydroxybenzophenone-based UV sunscreens: Are chemical sunscreens inoffensive? *ChemPhysChem*, 16(*3*):628–633, 2015.

[289] C.-X. Li, W.-W. Guo, B.-B. Xie, and G. Cui. Photodynamics of oxybenzone sunscreen: Nonadiabatic dynamics simulations. *J. Chem. Phys.*, 145(*7*):074308, 2016.

[290] D. R. Sambandan and D. Ratner. Sunscreens: An overview and update. *J. Am. Acad. Dermatol.*, 64(*4*):748–758, 2011.

[291] C. C. S. Chapple, T. Vogt, B. E. Ellisy, and C. R. Somerville. An *Arabidopsis* mutant defective in the general phenylpropanoid pathway. *Plant Cell*, 4(*11*): 1413–1424, 1992.

[292] M. Ruegger and C. Chapple. Mutations that reduce sinapoylmalate accumulation in *arabidopsis thaliana* define loci with diverse roles in phenylpropanoid metabolism. *Genetics*, 159(*4*):1741–1749, 2001.

[293] J. Meijer and M. Lodén. Stability analysis of three UV-filters using HPLC. *J. Liq. Chromatogr.*, 18(*9*):1821–1832, 1995.

[294] S. Pattanaargson and P. Limphong. Stability of octyl methoxycinnamate and identification of its photo-degradation product. *Int. J. Cosmet. Sci.*, 23(*3*):153–160, 2001.

[295] S. Scalia and M. Mezzena. Photostabilization effect of quercetin on the UV filter combination, butyl methoxydibenzoylmethane-octyl methoxycinnamate. *Photochem. Photobiol.*, 86(*2*):273–278, 2010.

[296] S. Pattanaargson, T. Munhapol, P. Hirunsupachot, and P. Luangthongaram. Photoisomerization of octyl methoxycinnamate. *J. Photochem. Photobiol., A*, 161 (*2–3*):269–274, 2004.

[297] K. M. Hanson, S. Narayanan, V. M. Nichols, and C. J. Bardeen. Photochemical degradation of the UV filter octyl methoxycinnamate in solution and in aggregates. *Photochem. Photobiol. Sci.*, 14(*9*):1607–1616, 2015.

[298] E. M. M. Tan, M. Hilbers, and W. J. Buma. Excited-state dynamics of isolated and microsolvated cinnamate-based UV-B sunscreens. *J. Phys. Chem. Lett.*, 5 (*14*):2464–2468, 2014.

[299] Y. Miyazaki, K. Yamamoto, J. Aoki, T. Ikeda, Y. Inokuchi, M. Ehara, and T. Ebata. Experimental and theoretical study on the excited-state dynamics of ortho-, meta-, and para-methoxy methylcinnamate. *J. Chem. Phys.*, 141(*24*): 244313, 2014.

[300] Y. Peperstraete, M. Staniforth, L. A. Baker, N. D. N. Rodrigues, N. C. Cole-Filipiak, W.-D. Quan, and V. G. Stavros. Bottom-up excited state dynamics of two cinnamate-based sunscreen filter molecules. *Phys. Chem. Chem. Phys.*, 18 (*40*):28140–28149, 2016.

[301] J. C. Dean, R. Kusaka, P. S. Walsh, F. Allais, and T. S. Zwier. Plant sunscreens in the UV-B: Ultraviolet spectroscopy of jet-cooled sinapoyl malate, sinapic acid, and sinapate ester derivatives. *J. Am. Chem. Soc.*, 136(*42*):14780–14795, 2014.

[302] L. A. Baker, M. D. Horbury, S. E. Greenough, F. Allais, P. S. Walsh, S. Habershon, and V. G. Stavros. Ultrafast photoprotecting sunscreens in natural plants. *J. Phys. Chem. Lett.*, 7(*1*):56–61, 2016.

[303] K. Sevgi, B. Tepe, and C. Sarikurkcu. Antioxidant and DNA damage protection potentials of selected phenolic acids. *Food Chem. Toxicol.*, 77:12–21, 2015.

[304] M. D. Horbury, L. A. Baker, W.-D. Quan, S. E. Greenough, and V. G. Stavros. Photodynamics of potent antioxidants: Ferulic and caffeic acids. *Phys. Chem. Chem. Phys.*, 18(*26*):17691–17697, 2016.

[305] A. Weller. Innermolekularer protonenübergang im angeregten zustand. *Z. Elektrochem*, 60(*9-10*):1144–1147, 1956.

[306] J. Goodman and L. E. Brus. Proton transfer and tautomerism in an excited state of methyl salicylate. *J. Am. Chem. Soc.*, 100(*24*):7472–7474, 1978.

[307] L. Helmbrook, J. E. Kenny, B. E. Kohler, and G. W. Scott. Lowest excited singlet state of hydrogen-bonded methyl salicylate. *J. Phys. Chem.*, 87(*2*):280–289, 1983.

[308] P. F. Barbara and P. K. Walsh. Picosecond kinetic and vibrationally resolved spectroscopic studies of intramolecular excited-state hydrogen atom transfer. *J. Phys. Chem.*, 93(*1*):29–34, 1989.

[309] J. Catalá, J. Palomar, and J. L. G. de Paz. Intramolecular proton or hydrogen-atom transfer in the ground and excited states of 2-hydroxybenzoyl compounds. *J. Phys. Chem. A*, 101(*42*):7914–7921, 1997.

[310] A. L. Sobolewski and W. Domcke. *Ab initio* study of excited-state intramolecular proton dislocation in salicylic acid. *Chem. Phys.*, 232(*3*):257–265, 1998.

[311] A. L. Sobolewski and W. Domcke. *Ab initio* potential-energy functions for excited state intramolecular proton transfer: A comparative study of *o*-hydroxybenzaldehyde, salicylic acid and 7-hydroxy-1-indanone. *Phys*, 1(*13*): 3065–3072, 1999.

[312] R. D. Massaro, Y. Dai, and E. Blaisten-Barojas. Energetics and vibrational analysis of methyl salicylate isomers. *J. Phys. Chem. A*, 113(*38*):10385–10390, 2009.

[313] R. D. Massaro and E. Blaisten-Barojas. Theoretical investigation of the photophysics of methyl salicylate isomers. *J. Chem. Phys.*, 135(*16*):164306, 2011.

[314] P. Zhou, M. R. Hoffmann, K. Han, and G. He. New insights into the dual fluorescence of methyl salicylate: Effects of intermolecular hydrogen bonding and solvation. *J. Phys. Chem. B*, 119(*6*):2125–2131, 2015.

[315] J. L. Herek, S. Pedersen, L. B. nares, and A. H. Zewail. Femtosecond real-time probing of reactions. IX. Hydrogen-atom transfer. *J. Chem. Phys.*, 97(*12*):9046, 1992.

[316] K. K. Smith and K. J. Kaufmann. Solvent dependence of the nonradiative decay rate of methyl salicylate. *J. Phys. Chem.*, 85(*20*):2895–2897, 1981.

[317] R. Krishnan and T. M. Nordlund. Fluorescence dynamics of three UV-B sunscreens. *J. Fluoresc.*, 18(*1*):203–217, 2008.

[318] K. Sugiyama, T. Tsuchiya, A. Kikuchi, and M. Yagi. Optical and electron paramagnetic resonance studies of the excited triplet states of UV-B absorbers: 2-Ethylhexyl salicylate and homomenthyl salicylate. *Photochem. Photobiol. Sci.*, 14(*9*):1651–1659, 2015.

[319] P. Meredith and T. Sarna. The physical and chemical properties of eumelanin. *Pigment Cell Res.*, 19(*6*):572–594, 2006.

[320] A. Huijser, A. Pezzellab, and V. Sundström. Functionality of epidermal melanin pigments: Current knowledge on UV-dissipative mechanisms and research perspectives. *Phys. Chem. Chem. Phys.*, 13(*20*):9119–9127, 2011.

[321] Y. Zhang, T. A. A. Oliver, M. N. R. Ashfold, and S. E. Bradforth. Contrasting the excited state reaction pathways of phenol and *para*-methylthiophenol in the gas and liquid phases. *Faraday Discuss.*, 157:141–163, 2012.

[322] S. J. Harris, D. Murdock, Y. Zhang, T. A. A. Oliver, M. P. Grubb, A. J. Orr-Ewing, G. M. Greetham, I. P. Clark, M. Towrie, S. E. Bradforth, and M. N. R. Ashfold. Comparing molecular photofragmentation dynamics in the gas and liquid phases. *Phys. Chem. Chem. Phys.*, 15(*18*):6567–6582, 2013.

[323] T. A. A. Oliver, Y. Zhang, A. Roy, M. N. R. Ashfold, and S. E. Bradforth. Exploring autoionization and photoinduced proton-coupled electron transfer pathways of phenol in aqueous solution. *J. Phys. Chem. Lett.*, 6(*20*):4159–4164, 2015.

[324] S. E. Greenough, M. D. Horbury, J. O. F. Thompson, G. M. Roberts, T. N. V. Karsili, B. Marchetti, D. Townsend, and V. G. Stavros. Solvent induced conformer specific photochemistry of guaiacol. *Phys. Chem. Chem. Phys.*, 16(*30*):16187–16195, 2014.

[325] M. D. Horbury, L. A. Baker, W.-D. Quan, J. D. Young, M. Staniforth, S. E. Greenough, and V. G. Stavros. Bridging the gap between the gas phase and solution phase: Solvent specific photochemistry in 4-*tert*-butylcatechol. *J. Phys. Chem. A*, 119(*50*):11989–11996, 2015.

[326] M. Gauden, A. Pezzella, L. Panzella, M. T. Neves-Petersen, E. Skovsen, S. B. Petersen, K. M. Mullen, A. Napolitano, M. d'Ischia, and V. Sundström. Role of solvent, pH, and molecular size in excited-state deactivation of key eumelanin building blocks: Implications for melanin pigment photostability. *J. Am. Chem. Soc.*, 130(*50*):17038–17043, 2008.

[327] M. Gauden, A. Pezzella, L. Panzella, A. Napolitano, M. d'Ischia, and V. Sundström. Ultrafast excited state dynamics of 5,6-dihydroxyindole, a key eumelanin building block: Nonradiative decay mechanism. *J. Phys. Chem. B*, 113(*37*): 12575–12580, 2009.

[328] A. Huijser, A. Pezzella, J. K. Hannestad, L. Panzella, A. Napolitano, M. d'Ischia, and V. Sundström. UV-dissipation mechanisms in the eumelanin building block DHICA. *ChemPhysChem*, 11(*11*):2424–2431, 2010.

[329] A. Corani, A. Huijser, A. Iadonisi, A. Pezzella, V. Sundström, and M. d'Ischia. Bottom-up approach to eumelanin photoprotection: Emission dynamics in parallel sets of water-soluble 5,6-dihydroxyindole-based model systems. *J. Phys. Chem. B*, 116(*44*):13151–13158, 2012.

[330] A. Corani, A. Pezzella, T. Pascher, T. Gustavsson, D. Markovitsi, A. Huijser, M. d'Ischia, and V. Sundström. Excited-state proton-transfer processes of DHICA resolved: From sub-picoseconds to nanoseconds. *J. Phys. Chem. Lett.*, 4(*9*):1383–1388, 2013.

[331] J. Peon, G. C. Hess, J.-M. L. Pecourt, T. Yuzawa, and B. Kohler. Ultrafast photoionization dynamics of indole in water. *J. Phys. Chem. A*, 103(*14*):2460–2466, 1999.

[332] A. L. Sobolewski and W. Domcke. Photophysics of eumelanin: *Ab initio* studies on the electronic spectroscopy and photochemistry of 5,6-dihydroxyindole. *ChemPhysChem*, 8(*5*):756–762, 2007.

[333] D. N. Peles and J. D. Simon. UV-absorption spectra of melanosomes containing varying 5,6-dihydroxyindole and 5,6-dihydroxyindole-2-carboxylic acid content. *J. Phys. Chem. B*, 115(*43*):12624–12631, 2011.

[334] A. Corani, A. Huijser, T. Gustavsson, D. Markovitsi, P. Malmqvist, A. Pezzella, M. d'Ischia, and V. Sundström. Superior photoprotective motifs and mechanisms in eumelanins uncovered. *J. Am. Chem. Soc.*, 136(*33*):11626–11635, 2014.

[335] J. B. Nofsinger, T. Ye, and J. D. Simon. Ultrafast nonradiative relaxation dynamics of eumelanin. *J. Phys. Chem. B*, 105(*14*):2864–2866, 2001.

[336] T. Ye and J. D. Simon. Comparison of the ultrafast absorption dynamics of eumelanin and pheomelanin. *J. Phys. Chem. B*, 107(*40*):11240–11244, 2003.

[337] B. Marchetti and T. N. V. Karsili. Theoretical insights into the photo-protective mechanisms of natural biological sunscreens: Building blocks of eumelanin and pheomelanin. *Phys. Chem. Chem. Phys.*, 18(*5*):3644–3658, 2016.

[338] A. Kikuchi, Y. Hata, R. Kumasaka, Y. Nanbu, and M. Yagi. Photoexcited singlet and triplet states of a UV absorber ethylhexyl methoxycrylene. *Photochem. Photobiol.*, 89(*3*):523–528, 2013.

[339] L. A. Baker, M. D. Horbury, and V. G. Stavros. Ultrafast photoprotective properties of the sunscreening agent octocrylene. *Opt. Express*, 24(*10*):10700–10709, 2016.

[340] M. E. Bigby. The end of the sunscreen and melanoma controversy. *Arch. Dermatol.*, 140(*6*):745–746, 2004.

[341] J. F. Nash and P. R. Tanner. *Principles and practice of photoprotection*. Springer International Publishing, 1st edition, 2016.

[342] N. Tarras-Wahlberg, G. Stenhagen, O. Larkö, A. Rosén, A.-M. Wennberg, and O. Wennerström. Changes in ultraviolet absorption of sunscreens after ultraviolet irradiation. *J. Invest. Dermatol.*, 113(*4*):547–553, 1999.

[343] M. D. Palm and M. N. O'Donoghue. Update on photoprotection. *Dermatol. Ther.*, 20(*5*):360–376, 2007.

[344] N. Blüthgen, S. Zucchi, and K. Fent. Effects of the UV filter benzophenone-3 (oxybenzone) at low concentrations in zebrafish (*Danio rerio*). *Toxicol. Appl. Pharmacol.*, 263(*2*):184–194, 2012.

[345] H. Amine, E. Gomez, J. Halwani, C. Casellas, and H. Fenet. UV filters, ethylhexyl methoxycinnamate, octocrylene and ethylhexyl dimethyl PABA from untreated wastewater in sediment from eastern Mediterranean river transition and coastal zones. *Mar. Pollut. Bull.*, 64(*11*):2435–2442, 2012.

[346] D. Kaiser, A. Sieratowicz, H. Zielke, M. Oetken, H. Hollert, and J. Oehlmann. Ecotoxicological effect characterisation of widely used organic UV filters. *Environ. Pollut.*, 163:84–90, 2012.

[347] V. Ambrogi, L. Latterini, F. Marmottini, C. Pagano, and M. Ricci. Mesoporous silicate MCM-41 as a particulate carrier for octyl methoxycinnamate: Sunscreen release and photostability. *J. Pharm. Sci.*, 102(*5*):1468–1475, 2013.

[348] P. Blasi, A. Schoubben, S. Giovagnoli, C. Rossi, and M. Ricci. The real value of novel particulate carriers for sunscreen formulation. *Expert Rev. Dermatol.*, 6(*5*): 509–517, 2011.

[349] S. Wissing and R. Müller. The development of an improved carrier system for sunscreen formulations based on crystalline lipid nanoparticles. *Int. J. Pharm.*, 242(*1–2*):373–375, 2002.

[350] G. Yener, T. Incegül, and N. Yener. Importance of using solid lipid microspheres as carriers for UV filters on the example octyl methoxy cinnamate. *Int. J. Pharm.*, 258(*1–2*):203–207, 2003.

[351] R. Tursilli, G. Piel, L. Delattre, and S. Scalia. Solid lipid microparticles containing the sunscreen agent, octyl-dimethylaminobenzoate: Effect of the vehicle. *Eur. J. Pharm. Biopharm.*, 66(*3*):483–487, 2007.

[352] S. K. Jain and N. K. Jain. Multiparticulate carriers for sun-screening agents. *Int. J. Cosmet. Sci.*, 32(*2*):89–98, 2010.

[353] N. F. Scherer, J. L. Knee, D. D. Smith, and A. H. Zewail. Femtosecond photofragment spectroscopy: The reaction ICN → CN + I. *J. Phys. Chem.*, 89(*24*):5141–5143, 1985.

[354] M. Dantus, M. J. Rosker, and A. H. Zewail. Real-time femtosecond probing of "transition state" in chemical reactions. *J. Chem. Phys.*, 87(*4*):2395–2397, 1987.

[355] A. H. Zewail. Femtochemistry. Past, present, and future. *Pure Appl. Chem.*, 72 (*12*):2219–2231, 2000.

[356] J. D. Young, M. Staniforth, M. J. Paterson, and V. G. Stavros. Torsional motion of the chromophore catechol following the absorption of ultraviolet light. *Phys. Rev. Lett.*, 114(*23*):233001, 2015.

[357] R. Berera, R. van Grondelle, and J. T. M. Kennis. Ultrafast transient absorption spectroscopy: Principles and application to photosynthetic systems. *Photosynth. Res.*, 101(*2–3*):105–118, 2009.

[358] W.-D. Quan, A. Pitto-Barry, L. A. Baker, E. Stulz, R. Napier, R. K. O'Reilly, and V. G. Stavros. Retaining individualities: The photodynamics of self-ordering porphyrin assemblies. *Chem. Commun.*, 52(*9*):1938–1941, 2016.

[359] G. Cerullo, D. Polli, G. Lanzani, S. D. Silvestri, H. Hashimoto, and R. J. Cogdell. Photosynthetic light harvesting by carotenoids: Detection of an intermediate excited state. *Science*, 298(*5602*):2395–2398, 2002.

[360] K. Nishimura, F. S. Rondonuwu, R. Fujii, J. Akahane, Y. Koyama, and T. Kobayashi. Sequential singlet internal conversion of $1B_u^+ \rightarrow 3A_g^- \rightarrow 1B_u^- \rightarrow 2A_g^- \rightarrow (1A_g^-$ ground) in all-*trans*-spirilloxanthin revealed by two-dimensional sub-5-fs spectroscopy. *Chem. Phys. Lett.*, 392:68–73, 2004.

[361] L. A. Baker, S. E. Greenough, and V. G. Stavros. A perspective on the ultrafast photochemistry of solution-phase sunscreen molecules. *J. Phys. Chem. Lett.*, 7 (*22*):4655–4665, 2016.

[362] L. A. Baker, B. Marchetti, T. N. V. Karsili, V. G. Stavros, and M. N. R. Ashfold. Photoprotection: Extending lessons learned from studying natural sunscreens to

the design of artificial sunscreen constituents. *Chem. Soc. Rev.*, 46(*12*):3770–3791, 2017.

[363] V. P. Kandidov, O. G. Kosareva, I. S. Golubtsov, W. Liu, A. B. Becker, N. Akozbek, C. M. Bowden, and S. I. Chin. Self-transformation of a powerful femtosecond laser pulse into a white-light laser pulse in bulk optical media (or supercontinuum generation). *Appl. Phys. B*, 77(*2*):149–165, 2003.

[364] S. E. Greenough, G. M. Roberts, N. A. Smith, M. D. Horbury, R. G. McKinlay, J. M. Żurek, M. J. Paterson, P. J. Sadler, and V. G. Stavros. Ultrafast photoinduced ligand solvolysis of *cis*-[ru(bipyridine)$_2$(nicotinamide)$_2$]$^{2+}$: experimental and theoretical insight into its photoactivation mechanism. *Phys. Chem. Chem. Phys.*, 16(*36*):19141–19155, 2014.

[365] H. A. Haus. Mode-locking of lasers. *IEEE J. Sel. Top. Quantum Electon.*, 6(*6*): 1173–1185, 2000.

[366] U. Keller. Recent developments in compact ultrafast lasers. *Nature*, 424:831–838, 2003.

[367] J.-C. Diels and W. Rudolph. *Ultrashort laser pulse phenomena: Fundamentals, techniques, and applications on a femtosecond time scale*. Academic Press, London, 1st edition, 1995.

[368] S. Backus, C. G. Durfee III, M. M. Murnane, and H. C. Kapteyn. High power ultrafast lasers. *Rev. Sci. Instrum.*, 69(*3*):1207–1223, 1998.

[369] C. Hirlimann. *Pulsed optics*, chapter 2, pages 25–56. Femtosecond laser pulses: Principles and experiments. Springer-Verlag, New York, 2nd edition, 2003.

[370] J. S. Briggs. A derivation of the time-energy uncertainty relation. *J. Phys. Conf. Ser.*, 99:012002, 2008.

[371] P. Busch. *The time–energy uncertainty relation*, chapter 3, pages 73–105. Time in Quantum Mechanics. Springer Berlin Heidelberg, Berlin, Heidelberg, 2008. ISBN 978-3-540-73473-4.

[372] G. Cerullo and S. D. Silvestri. Ultrafast optical parametric amplifiers. *Rev. Sci. Instrum.*, 74(*1*):1–18, 2003.

[373] R. W. Boyd. *Nonlinear optics*. Academic Press, Burlington, 3rd edition, 2008.

[374] P. J. M. Johnson, V. I. Prokhorenko, and R. J. D. Miller. Stable UV to IR supercontinuum generation in calcium fluoride with conserved circular polarization states. *Opt. Express*, 24(*17*):21488–21496, 2009.

[375] U. Megerle, I. Pugliesi, C. Schriever, C. Sailer, and E. Riedle. Sub-50 fs broadband absorption spectroscopy with tunable excitation: Putting the analysis of ultrafast molecular dynamics on solid ground. *Appl. Phys. B*, 96(*2*):215–231, 2009.

[376] M. Bradler and E. Riedle. Temporal and spectral correlations in bulk continua and improved use in transient spectroscopy. *J. Opt. Soc. Am. B*, 31(*7*):1465–1475, 2014.

[377] G. M. Roberts, H. J. B. Marroux, M. P. Grubb, M. N. R. Ashfold, and A. J. Orr-Ewing. On the participation of photoinduced N-H bond fission in aqueous adenine at 266 and 220 nm: A combined ultrafast transient electronic and vibrational absorption spectroscopy study. *J. Phys. Chem. A*, 118(*47*):11211–11225, 2014.

[378] E. T. Nibbering, H. Fidder, and E. Pines. Ultrafast chemistry: Using time-resolved vibrational spectroscopy for interrogation of structural dynamics. *Annu. Rev. Phys. Chem.*, 56:337–367, 2005.

[379] Demountable liquid cells. Accessed 14 June 2017, http://www.harricksci.com/sites/default/files/pdf/data_sheets/Data_Sheet_Demountable_Liquid_Cell.pdf.

[380] C. Elliott, V. Vijayakumar, W. Zink, and R. Hansen. National Instruments LabVIEW: A programming environment for laboratory automation and measurement. *J. Lab. Autom.*, 12(*1*):17–24, 2007.

[381] S. E. Greenough. *Transient absorption studies of biologically relevant systems; photostability and photoactivation.* PhD thesis, University of Warwick, Department of Chemistry, 2014.

[382] S. A. Kovalenko, A. L. Dobryakov, J. Ruthmann, and N. P. Ernsting. Femtosecond spectroscopy of condensed phases with chirped supercontinuum probing. *Phys. Rev. A*, 59(*3*):2369–2384, 1999.

[383] A. Maciejewski, R. Naskrecki, M. Lorenc, M. Ziolek, J. Karolczak, J. Kubicki, M. Matysiak, and M. Szymanski. Transient absorption experimental set-up with femtosecond time resolution. Femto- and picosecond study of DCM molecule in cyclohexane and methanol solution. *J. Mol. Struct.*, 555(*1–3*):1–13, 2000.

[384] M. Lorenc, M. Ziółek, R. Naskrcki, J. Karolczak, J. Kubicki, and A. Maciejewski. Artifacts in femtosecond transient absorption spectroscopy. *Appl. Phys. B*, 74(*1*): 19–27, 2002.

[385] J. Liu and T. Kobayashi. Generation of sub-20-fs multicolor laser pulses using cascaded four-wave mixing with chirped incident pulses. *Opt. Lett.*, 34(*16*):2402–2404, 2009.

[386] M. P. Grubb, A. J. Orr-Ewing, and M. N. R. Ashfold. KOALA: A program for the processing and decomposition of transient spectra. *Rev. Sci. Instrum.*, 85(*6*): 0641024, 2014.

[387] I. Walmsley, L. Waxer, and C. Dorrer. The role of dispersion in ultrafast optics. *Rev. Sci. Instrum.*, 72(*1*):1–29, 2001.

[388] I. H. van Stokkum, D. S. Larsen, and R. van Grondelle. Global and target analysis of time-resolved spectra. *Biochim. Biophys. Acta*, 1657(*2–3*):82–104, 2004.

[389] J. J. Snellenburg, S. P. Laptenok, R. Seger, K. M. Mullen, and I. H. M. van Stokkum. Glotaran: A Java-based graphical user interface for the R package TIMP. *J. Stat. Softw.*, 49(*2*):1–22, 2012.

[390] MATLAB 2013b, 2013. Avaiable from www.mathworks.com.

[391] A. S. Chatterly. *Probing nonadiabatic dynamics in isolated molecules with ultrafast velocity map imaging*. PhD thesis, University of Warwick and University of Durham, Department of Chemistry, 2013.

[392] J. R. Lakowicz. *Principles of fluorescence spectroscopy*. Springer Science+Business Media, 3rd edition, 2006.

[393] M. Staniforth and V. G. Stavros. Recent advances in experimental techniques to probe fast excited-state dynamics in biological molecules in the gas phase: Dynamics in nucleotides, amino acids and beyond. *Proc. R. Soc. A*, 469(*2159*): 20130458, 2013.

[394] V. G. Stavros and J. R. Verlet. Gas-phase femtosecond particle spectroscopy: A bottom-up approach to nucleotide dynamics. *Annu. Rev. Phys. Chem.*, 67: 211–232, 2016.

[395] J. D. Young. *The effect of increasing molecular complexity on the dynamics of biologically relevant chromophores. From dynamic competition to wavepacket evolution*. PhD thesis, University of Warwick, Department of Chemistry, 2016.

[396] N. D. N. Rodrigues, M. Staniforth, and V. G. Stavros. Photophysics of sunscreen molecules in the gas phase: A stepwise approach towards understanding and developing next-generation sunscreens. *Proc. R. Soc. A*, 472(*2195*):0677, 2016.

[397] H. Lippert, H.-H. Ritze, I. V. Hertel, and W. Radloff. Femtosecond time-resolved hydrogen-atom elimination from photoexcited pyrrole molecules. *ChemPhysChem*, 5(*9*):1423–1427, 2004.

[398] R. Montero, Álvaro Peralta Conde, V. Ovejas, M. Fernández-Fernández, and F. C. no. Femtosecond evolution of the pyrrole molecule excited in the near part of its UV spectrum. *J. Chem. Phys.*, 137(*6*):064317, 2012.

[399] A. D. Becke. Density-functional exchange-energy approximation with correct asymptotic behavior. *Phys. Rev. A*, 38(*6*):3098–3100, 1988.

[400] C. Lee, W. Yang, and R. G. Parr. Development of the Colle-Salvetti correlation-energy formula into a functional of the electron density. *Phys. Rev. B*, 37(*2*): 785–789, 1988.

[401] V. G. Stavros. Photochemistry: A bright future for sunscreens. *Nature Chem.*, 6 (*11*):955–956, 2014.

[402] S. Perun, A. L. Sobolewski, and W. Domcke. Role of electron-driven proton-transfer processes in the excited-state deactivation of the adenine-thymine base pair. *J. Phys. Chem. A*, 110(*29*):9031–9038, 2006.

[403] A. L. Sobolewski, W. Domcke, and C. Hättig. Tautomeric selectivity of the excited-state lifetime of guanine/cytosine base pairs: The role of electron-driven proton-transfer processes. *Proc. Natl. Acad. Sci. U. S. A.*, 102(*50*):17903–17906, 2005.

[404] A. L. Sobolewski and W. Domcke. Computational studies of the photophysics of hydrogen-bonded molecular systems. *J. Phys. Chem. A*, 111(*46*):11725–11735, 2007.

[405] L. Ding, X. Chen, and W.-H. Fang. Ultrafast asynchronous concerted excited-state intramolecular proton transfer and photodecarboxylation of o-acetylphenylacetic acid explored by combined CASPT2 and CASSCF Studies. *Org. Lett.*, 11(*7*):1495–1498, 2009.

[406] D. Tuna, A. L. Sobolewski, and W. Domcke. Photochemical mechanisms of radiationless deactivation processes in urocanic acid. *J. Phys. Chem. B*, 118(*4*): 976–985, 2014.

[407] D. Tuna, N. Došlić, M. Mališ, A. L. Sobolewski, and W. Domcke. Mechanisms of photostability in kynurenines: A joint electronic-structure and dynamics study. *J. Phys. Chem. B*, 119(*6*):2112–2124, 2015.

[408] P. F. Barbara, L. E. Brus, and P. M. Rentzepis. Intramolecular proton transfer and excited-state relaxation in 2-(2-hydroxyphenyl)benzothiazole. *J. Am. Chem. Soc.*, 102(*17*):5631–5635, 1980.

[409] F. Laermer, T. Elsaesser, and W. Kaiser. Femtosecond spectroscopy of excited-state proton transfer in 2-(2'-hydroxyphenyl)benzothiazole. *Chem. Phys. Lett.*, 148(*2-3*):119–124, 1988.

[410] C. Chudoba, S. Lutgen, T. Jentzsch, E. Riedle, M. Woerner, and T. Elsaesser. Femtosecond studies of vibrationally hot molecules produced by intramolecular proton transfer in the excited state. *Chem. Phys. Lett.*, 240(*1–3*):35–41, 1995.

[411] R. Kumasaka, A. Kikuchi, and M. Yagi. Photoexcited states of UV absorbers, benzophenone derivatives. *Photochem. Photobiol.*, 90(*4*):727–733, 2014.

[412] A. S. Chatterley, C. W. West, V. G. Stavros, and J. R. R. Verlet. Time-resolved photoelectron imaging of the isolated deprotonated nucleotides. *Chem. Sci.*, 5 (*10*):3963–3975, 2014.

[413] A. S. Chatterley, C. W. West, G. M. Roberts, V. G. Stavros, and J. R. R. Verlet. Mapping the ultrafast dynamics of adenine onto its nucleotide and oligonucleotides by time-resolved photoelectron imaging. *J. Phys. Chem. Lett.*, 5(*5*): 843–848, 2014.

[414] S. C. Warren, A. Margineanu, D. Alibhai, D. J. Kelly, C. Talbot, Y. Alexandrov, I. Munro, M. Katan, C. Dunsby, and P. M. W. French. Rapid global fitting of large fluorescence lifetime imaging microscopy datasets. *PLoS One*, 8(*8*):e70687, 2013.

[415] R. Krishnan, J. S. Blinkley, R. Seeger, and J. A. Pople. Selfconsistent molecular orbital methods. XX. A basis set for correlated wave functions. *J. Chem. Phys.*, 72(*1*):650–654, 1980.

[416] A. L. Sobolewski and W. Domcke. Photophysics of intramolecularly hydrogen-bonded aromatic systems: *Ab initio* exploration of the excited-state deactivation mechanisms of salicylic acid. *Phys. Chem. Chem. Phys.*, 8(*29*):3410–3417, 2006.

[417] O. F. Mohammed, S. Luber, V. S. Batista, and E. T. J. Nibbering. Ultrafast branching of reaction pathways in 2-(2'-hydroxyphenyl)benzothiazole in polar acetonitrile solution. *J. Phys. Chem. A*, 115(*26*):7550–7558, 2011.

[418] P. K. Verma, F. Koch, A. Steinbacher, P. Nuernberger, and T. Brixner. Ultrafast UV-induced photoisomerization of intramolecularly H-bonded symmetric β-diketones. *J. Am. Chem. Soc.*, 136(*42*):14981–14989, 2014.

[419] M. Barbatti, A. J. A. Aquino, H. Lischka, C. Schriever, S. Lochbrunner, and E. Riedle. Ultrafast internal conversion pathway and mechanism in 2-(2'-hydroxyphenyl)benzothiazole: A case study for excited-state intramolecular proton transfer systems. *Phys. Chem. Chem. Phys.*, 11(*9*):1406–1415, 2009.

[420] Y. Nosenko, G.Wiosna-Sałlyga, M. Kunitski, I. Petkova, A. Singh, W. J. Buma, R. P. Thummel, B. Brutschy, and J. Waluk. Proton transfer with a twist? Femtosecond dynamics of 7-(2-pyridyl)-indole in condensed phase and in supersonic jets. *Angew. Chem., Int. Ed.*, 47(*32*):6037–6040, 2008.

[421] J. C. Owrutsky, D. Raftery, and R. M. Hochstrasser. Vibrational relaxation dynamics in solutions. *Annu. Rev. Phys. Chem.*, 45:519–555, 1994.

[422] E. J. Land, G. Porter, and E. Strachan. Primary photochemical processes in aromatic molecules. *Trans. Faraday Soc.*, 57:1885–1893, 1961.

[423] J. Lind, X. Shen, T. E. Eriksen, and G. Merényi. The one-electron reduction potential of 4-substituted phenoxyl radicals in water. *J. Am. Chem. Soc.*, 112(*2*): 479–482, 1990.

[424] J. F. Jacobs, I. van de Poel, and P. Osseweijer. Sunscreens with titanium dioxide (TiO_2) nano-particles: A societal experiment. *Nanoethics*, 4(*2*):103–113, 2010.

[425] AEROXIDE, AERODISP and AEROPERL, titanium dioxide as photocatalyst, Technical information 1243, 2015. Accessed 12 June

2017, https://www.aerosil.com/sites/lists/RE/DocumentsSI/TI-1243-Titanium-Dioxide-as-Photocatalyst-EN.pdf.

[426] U. Diebold. The surface science of titanium dioxide. *Surf. Sci. Rep.*, 48(*5–8*): 53–229, 2003.

[427] Y. Lan, Y. Lu, and Z. Ren. Mini review on photocatalysis of titanium dioxide nanoparticles and their solar applications. *Nano Energy*, 2(*5*):1031–1045, 2013.

[428] M. Trivedi and J. Murase. Titanium Dioxide in Sunscreen. In M. Janus, editor, *Application of Titanium Dioxide*, chapter 4. InTech, Rijeka, 2017.

[429] N. Serpone, A. Salinaro, and A. Emeline. Deleterious effects of sunscreen titanium dioxide nanoparticles on DNA: Efforts to limit DNA damage by particle surface modification. In C. J. Murphy, editor, *Nanoparticles and Nanostructured Surfaces: Novel Reporters with Biological Applications*, volume 4258 of *The International Symposium on Biomedical Optics*, pages 86–98, San Jose, 2001. Proceedings of SPIE.

[430] J. Lademann, H.-J. Weigmann, C. Rickmeyer, H. Barthelmes, H. Schaefer, G. Mueller, and W. Sterry. Penetration of titanium dioxide microparticles in a sunscreen formulation into the horny layer and the follicular orifice. *Skin Pharmacol. Appl. Skin Physiol.*, 12(*5*):247–256, 1999.

[431] N. Sadrieh, A. M. Wokovich, N. V. Gopee, J. Zheng, D. Haines, D. Parmiter, P. H. Siitonen, C. R. Cozart, A. K. Patri, S. E. McNeil, P. C. Howard, W. H. Doub, and L. F. Buhse. Lack of significant dermal penetration of titanium dioxide from sunscreen formulations containing nano- and submicron-size TiO_2 particles. *Toxicol. Sci.*, 115(*1*):156–166, 2010.

[432] A. Jaroenworaluck, W. Sunsaneeyametha, N. Kosachan, and R. Stevens. Characteristics of silica-coated TiO_2 and its UV absorption for sunscreen cosmetic applications. *Surf. Interface Anal.*, 38(*4*):473–477, 2006.

[433] R. W. G. Wyckoff. *Crystal structures*, volume 1, pages 239–444. Interscience Publishers, 1963.

[434] R. T. Downs and M. Hall-Wallace. The american mineralogist crystal structure database. *Am. Mineral.*, 88(*1*):247–250, 2003. AMCSD#0011418.

[435] R. T. Downs and M. Hall-Wallace. The american mineralogist crystal structure database. *Am. Mineral.*, 88(*1*):247–250, 2003. AMCSD#0011415.

[436] K. Momma and F. Izumi. VESTA 3 for three-dimensional visualization of crystal, volumetric and morphology data. *J. Appl. Crystallogr.*, 44:1272–1276, 2011.

[437] M. Ziółek, J. Kubicki, A. Maciejewski, R. Naskrcki, and A. Grabowska. Enol-keto tautomerism of aromatic photochromic Schiff base N,N'-bis(salicylidene)-p-phenylenediamine: Ground state equilibrium and excited state deactivation studied by solvatochromic measurements on ultrafast time scale. *J. Chem. Phys.*, 124(*12*):124518, 2006.

[438] G. W. Kauffman and P. C. Jurs. Prediction of surface tension, viscosity, and thermal conductivity for common organic solvents using quantitative structure-property relationships. *J. Chem. Inf. Comput. Sci.*, 41(*2*):408–418, 2001.

[439] M. Vengris, D. S. Larsen, M. A. van der Horst, O. F. A. Larsen, K. J. Hellingwerf, and R. van Grondelle. Ultrafast dynamics of isolated model photoactive yellow protein chromophores: "Chemical perturbation theory" in the laboratory. *J. Phys. Chem. B*, 109(*9*):4197–4208, 2005.

[440] D. W. Bahnemann, M. Hilgendorff, and R. Memming. Charge carrier dynamics at TiO_2 particles: Reactivity of free and trapped holes. *J. Phys. Chem. B*, 101 (*21*):4265–4275, 1997.

[441] H. N. Ghosh, J. B. Asbury, and T. Lian. Direct observation of ultrafast electron injection from coumarin 343 to TiO_2 nanoparticles by femtosecond infrared spectroscopy. *Journal of Physical Chemistry B*, 102(*34*):6482–6486, 1998.

[442] Y. Tamaki, A. Furube, M. Murai, K. Hara, R. Katoh, and M. Tachiya. Dynamics of efficient electron-hole separation in TiO_2 nanoparticles revealed by femtosecond transient absorption spectroscopy under the weak-excitation condition. *Phys. Chem. Chem. Phys.*, 9(*12*):1453–1460, 2007.

[443] A. L. Linsebigler, G. Lu, and J. T. Y. Jr. Photocatalysis on TiO_2 surfaces: Principles, mechanisms, and selected results. *Chem. Rev.*, 95(*3*):735–758, 1995.

[444] S. H. Szczepankiewicz, J. A. Moss, and M. R. Hoffmann. Slow surface charge trapping kinetics on irradiated TiO_2. *J. Phys. Chem. B*, 106(*11*):2922–2927, 2002.

[445] Y. Zhao, N. E. Schultz, and D. G. Truhlar. Design of density functionals by combining the method of constraint satisfaction with parametrization for thermochemistry, thermochemical kinetics, and noncovalent interactions. *J. Chem. Theory Comput.*, 2(*2*):364–382, 2006.

[446] C. R. S. Mooney, D. A. Horke, A. S. Chatterley, A. Simperler, H. H. Fielding, and J. R. R. Verlet. Taking the green fluorescence out of the protein: Dynamics of the isolated GFP chromophore anion. *Chem. Sci.*, 4(*3*):921–927, 2013.

[447] E. W. Castner, Jr, M. Maroncelli, and G. R. Fleming. Subpicosecond resolution studies of solvation dynamics in polar aprotic and alcohol solvents. *J. Chem. Phys.*, 86(*3*):1090–1097, 1987.

[448] P. Hockett. *Faraday Discuss.*, 163:513–543, 2013.

[449] L. A. Baker, S. L. Clark, S. Habershon, and V. G. Stavros. Ultrafast transient absorption spectroscopy of the sunscreen constituent ethylhexyl triazone. *J. Phys. Chem. Lett.*, 8(*10*):2113–2118, 2017.

[450] J. D. Hunter. Matplotlib: A 2D graphics environment. *Comput. Sci. Eng.*, 9(*3*): 90–95, 2007.

[451] J. P. Perdew. Density-functional approximation for the correlation energy of the inhomogeneous electron gas. *Phys. Rev. B*, 33(*12*):8822–8824, 1986.

[452] S. González, M. Fernaández-Lorente, and Y. Gilaberte-Calzada. The latest on skin photoprotection. *Clin. Dermatol.*, 26(*6*):614–626, 2008.

[453] V. Lhiaubet-Vallet, M. Marin, O. Jimenez, O. Gorchs, C. Trullas, and M. A. Miranda. Filter-filter interactions. Photostabilization, triplet quenching and reactivity with singlet oxygen. *Photochem. Photobiol. Sci.*, 9(*4*):552–558, 2010.

[454] S. Sommer, S. M. Wilkinson, J. S. C. English, and J. Ferguson. Photoallergic contact dermatitis from the sunscreen octyl triazone. *Contact Derm.*, 46(*5*):304–305, 2002.

[455] T. Tsuchiya, A. Kikuchi, N. Oguchi-Fujiyama, K. Miyazawa, and M. Yagi. Photoexcited triplet states of UV-B absorbers: Ethylhexyl triazone and diethylhexylbutamido triazone. *Photochem. Photobiol. Sci.*, 14(*4*):807–814, 2015.

[456] M. von Arnim and R. Ahlrichs. Performance of parallel TURBOMOLE for density functional calculations. *J. Comput. Chem.*, 19(*15*):1746–1757, 1998.

[457] K. Eichkorn, O. Treutler, H. Öhm, M. Häser, and R. Ahlrichs. Auxiliary basis sets to approximate Coulomb potentials. *Chem. Phys. Lett.*, 240(*4*):283–290, 1995.

[458] M. Sierka, A. Hogekamp, and R. Ahlrichs. Fast evaluation of the Coulomb potential for electron densities using multipole accelerated resolution of identity approximation. *J. Chem. Phys.*, 118(*30*):9136–9148, 2003.

[459] K. Eichkorn, F. Weigend, O. Treutler, and R. Ahlrichs. Auxiliary basis sets for main row atoms and transition metals and their use to approximate Coulomb potentials. *Theor. Chem. Acc.*, 97(*1*):119–124, 1997.

[460] M. Orio, D. A. Pantazis, and F. Neese. Density functional theory. *Photosynth. Res.*, 102(*2–3*):443–453, 2009.

[461] J. Kuta, S. Patchkovskii, M. Z. Zgierski, and P. M. Kozlowski. Performance of DFT in modeling electronic and structural properties of cobalamins. *J. Comput. Chem.*, 27(*12*):1429–1437, 2006.

[462] A. Klamt and G. Schüürmann. COSMO: A new approach to dielectric screening in solvents with explicit expressions for the screening energy and its gradient. *J. Chem. Soc., Perkin Trans. 2*, 2(*5*):799–805, 1993.

[463] W. Humphrey, A. Dalke, and K. Schulten. VMD – Visual Molecular Dynamics. *J. Mol. Graphics*, 14(*1*):33–38, 1996.

[464] J. Li, T.-M. Ou-Lee, R. Raba, R. G. Amundson, and R. L. Last. *Arabidopsis* flavonoid mutants are hypersensitive to UV-B lrradiation. *Plant Cell*, 5(*2*):171–179, 1993.

[465] K. Bieza and R. Lois. An *Arabidopsis* mutant tolerant to lethal ultraviolet-B levels shows constitutively elevated accumulation of flavonoids and other phenolics. *Plant Physiol.*, 126(*3*):1105–1115, 2001.

[466] C. Milkowski, A. Baumert, D. Schmidt, L. Nehlin, and D. Strack. Molecular regulation of Sinapate ester metabolism in *Brassica napus*: Expression of genes, properties of the encoded proteins and correlaion of enzyme activities with metabolite accumulation. *Plant J.*, 38(*1*):80–92, 2004.

[467] F. D. Lewis, S. L. Quillen, J. E. Elbert, S. Schneider, and P. Geiselhart. The singlet states of methyl cinnamate and methyl indenoate. *J. Photochem. Photobiol., A*, 47(*2*):173–179, 1989.

[468] M. Promkatkaew, S. Suramitr, T. M. Karpkird, S. Namuangruk, M. Ehara, and S. Hannongbua. Absorption and emission spectra of ultraviolet B blocking methoxy substituted cinnamates investigated using the symmetry-adapted cluster configuration interaction method. *J. Chem. Phys.*, 131(*22*):224306, 2009.

[469] T. S. Singh, S. Mitra, A. Chandra, N. Tamai, and S. Kar. A combined experimental and theoretical study on photoinduced intramolecular charge transfer in *trans*-ethyl *p*-(dimethylamino)cinamate. *J. Photochem. Photobiol., A*, 197(*2-3*): 295–305, 2008.

[470] Y. Miyazaki, Y. Inokuchi, N. Akai, and T. Ebata. Direct spectroscopic evidence of photoisomerization in para-methoxy methylcinnamate revealed by low-temperature matrix-isolation FTIR spectroscopy. *J. Phys. Chem. Lett.*, 6(*7*): 1134–1139, 2015.

[471] T. M. Karpkird, S. Wanichweacharungruang, and B. Albinsson. Photophysical characterization of cinnamates. *Photochem. Photobiol. Sci.*, 8(*10*):1455–1460, 2009.

[472] D. Shimada, R. Kusaka, Y. Inokuchi, M. Ehara, and T. Ebata. Nonradiative decay dynamics of methyl-4-hydroxycinnamate and its hydrated complex revealed by picosecond pump-probe spectroscopy. *Phys. Chem. Chem. Phys.*, 14(*25*):8999–9005, 2012.

[473] E. V. Gromov, I. Burghardt, H. Köppel, and L. S. Cederbaum. Impact of sulfur vs oxygen on the low-lying excited states of *trans*-*p*-coumaric acid and *trans*-*p*-coumaric thio acid. *J. Phys. Chem. A*, 109(*20*):4623–4631, 2005.

[474] H. Kuramochi, S. Takeuchi, and T. Tahara. Ultrafast structural evolution of photoactive yellow protein chromophore revealed by ultraviolet resonance femtosecond stimulated raman spectroscopy. *J. Phys. Chem. Lett.*, 3(*15*):2025–2029, 2012.

[475] M. de Groot, E. V. Gromov, H. Köppel, and W. J. Buma. High-resolution spectroscopy of methyl 4-hydroxycinnamate and its hydrogen-bonded water complex. *J. Phys. Chem. B*, 112(*14*):4427–4434, 2008.

[476] S. Smolarek, A. Vdovin, D. L. Perrier, J. P. Smit, M. Drabbels, and W. J. Buma. High-resolution excitation and absorption spectroscopy of gas-phase *p*-coumaric

acid: Unveiling an elusive chromophore. *J. Am. Chem. Soc.*, 132(*18*):6315–6317, 2010.

[477] E. M. M. Tan, S. Amirjalayer, B. H. Bakker, and W. J. Buma. Excited state dynamics of photoactive yellow protein chromophores elucidated by highresolution spectroscopy and *ab initio* calculations. *Faraday Discuss.*, 163:321–340, 2013.

[478] F. Allais, S. Martinet, and P.-H. Ducrot. Straightforward total synthesis of 2-*O*-feruloyl-L-malate, 2-*O*-sinapoyl-L-malate and 2-*O*-5-hydroxyferuloyl-L-malate. *Synthesis*, (*21*):3571–3578, 2009.

[479] M. Quentin, V. Allasia, A. Pegard, F. Allais, P.-H. Ducrot, B. Favery, C. Levis, S. Martinet, C. Masur, M. Ponchet, D. Roby, N. L. Schlaich, L. Jouanin, and H. Keller. Imbalanced lignin biosynthesis promotes the sexual reproduction of homothallic oomycete pathogens. *PLoS Pathog.*, 5(*1*):e1000264, 2009.

[480] N. Mataga, H. Chosrowjan, S. Taniguchi, N. Hamada, F. Tokunaga, Y. Imamoto, and M. Kataoka. Ultrafast photoreactions in protein nanospaces as revealed by fs fluorescence dynamics measurements on photoactive yellow protein and related systems. *Phys. Chem. Chem. Phys.*, 5(*11*):2454–2460, 2003.

[481] S. Foley, S. Navaratnam, D. J. McGarvey, E. J. Land, T. G. Truscott, and C. A. Rice-Evans. Singlet oxygen quenching and the redox properties of hydroxycinnamic acids. *Free Radical Biol. Med.*, 26(*9–10*):1202–1208, 1999.

[482] M. Vengris, I. H. M. van Stokkum, X. He, A. F. Bell, P. J. Tonge, R. van Grondelle, and D. S. Larsen. Ultrafast excited and ground-state dynamics of the green fluorescent protein chromophore in solution. *J. Phys. Chem. A*, 108(*21*):4587–4598, 2004.

[483] D. S. Larsen, H. M. van Stokkum, M. Vengris, M. A. van der Horst, F. L. de Weerd, K. J. Hellingwerf, and R. van Grondelle. Incoherent manipulation of the photoactive yellow protein photocycle with dispersed pump-dump-probe spectroscopy. *Biophys. J.*, 87(*3*):1858–1872, 2004.

[484] A. Espagne, D. H. Paik, P. Changenet-Barret, M. M. Martin, and A. H. Zewail. Ultrafast photoisomerization of photoactive yellow protein chromophore analogues in solution: Influence of the protonation state. *ChemPhysChem*, 7(*8*):1717–1726, 2006.

[485] M. Ge, H. Zhao, W. Wang, Z. Zhang, X. Yu, and W. Li. Terahertz time-domain spectroscopy of four hydroxycinnamic acid derivatives. *J. Biol. Phys.*, 32(*5*): 403–412, 2006.

[486] S.-K. Chung, T. Osawa, and S. Kawakishi. Hydroxyl radical-scavenging effects of spices and scavengers from brown mustard (*brassica nigra*). *Biosci. Biotechnol. Biochem.*, 61(*1*):118–123, 1997.

[487] P. McKendry. Energy production from biomass (part 1): Overview of biomass. *Bioresour. Technol.*, 83(*1*):37–46, 2002.

[488] B. Alberts, A. Johnson, J. Lewis, M. Raff, K. Roberts, and P. Walter. *Molecular biology of the cell*. Garland Science, New York, 4th edition, 2002.

[489] T. Cavalier-Smith. Cell evolution and Earth history: Stasis and revolution. *Phil. Trans. R. Soc. B*, 361(*1470*):969–1006, 2006.

[490] R. Razeghifard. *Artificial photosynthesis*, chapter 4, pages 121–141. Natural and Artificial Photosynthesis: Solar Power as an Energy Source. John Wiley & Sons Inc., Hoboken, New Jersey, USA., 2013.

[491] M. Grätzel. Recent advances in sensitized mesoscopic solar cells. *Acc. Chem. Res.*, 42(*11*):1788–1796, 2009.

[492] T. Hisatomi, J. Kubota, and K. Domen. Recent advances in semiconductors for photocatalytic and photoelectrochemical water splitting. *Chem. Soc. Rev.*, 43 (*22*):7520–7535, 2014.

[493] G. J. Hedley, A. Ruseckas, and I. D. W. Samuel. Light harvesting for organic photovoltaics. *Chem. Rev.*, 117(*2*):796–837, 2017.

[494] J. Kromdijk, K. Głowacka, L. Leonelli, S. T. Gabilly, M. Iwai, K. K. Niyogi, and S. P. Long. Improving photosynthesis and crop productivity by accelerating recovery from photoprotection. *Science*, 354(*6314*):857–861, 2016.

[495] Y. Cheng and G. Fleming. Dynamics of light harvesting in photosynthesis. *Annu. Rev. Phys. Chem*, 60:241–262, 2009.

[496] G. D. Scholes, G. R. Fleming, A. Olaya-Castro, and R. van Grondelle. Lessons from nature about solar light harvesting. *Nat. Chem.*, 3(*10*):763–774, 2011.

[497] G. D. Scholes. Quantum-coherent electronic energy transfer: Did nature think of it first? *J. Phys. Chem. Lett.*, 1(*1*):2–8, 2010.

[498] C. König and J. Neugebauer. Quantum chemical description of absorption properties and excited-state processes in photosynthetic systems. *ChemPhysChem*, 13 (*2*):386–425, 2012.

[499] M. Taniguchi and J. S. Lindsey. Synthetic chlorins, possible surrogates for chlorophylls, prepared by derivatization of porphyrins. *Chem. Rev.*, 117(*2*):344–535, 2017.

[500] T. W. Goodwin. Nature and distribution of carotenoids. *Food Chem.*, 5(*1*):3–13, 1980.

[501] T. Mirkovic, E. E. Ostroumov, J. M. Anna, R. van Grondelle, Govindjee, and G. D. Scholes. Light absorption and energy transfer in the antenna complexes of photosynthetic organisms. *Chem. Rev.*, 117(*2*):249–293, 2017.

[502] G. D. Scholes. Introduction: Light harvesting. *Chem. Rev.*, 117(*2*):247–248, 2017.

[503] G. Renger. *Primary processes of photosynthesis, part 1: Principles and apparatus*, volume 8 of *Comprehensive Series in Photochemical & Photobiological Sciences*, chapter 1, pages 5–35. RSC publishing, 2007.

[504] J. Overmann, H. Cypionka, and N. Pfennig. An extremely low-light adapted phototrophic sulfur bacterium from the Black Sea. *Limnol. Oceanogr.*, 37(*1*): 150–155, 1992.

[505] K. Bacon. *Photosynthesis: Photobiochemistry and photobiophysics*. Advances in Photosynthesis and Respiration. Springer Science+Business Media, 1st edition, 2001.

[506] L. A. Baker and S. Habershon. Photosynthesis, pigment-protein complexes and electronic energy transport - simple models for complicated processes. *Sci. Prog.*, 100(*3*):313–330, 2017.

[507] T. Pullerits and V. Sundström. Photosynthetic light-harvesting pigment-protein complexes: Toward understanding how and why. *Acc. Chem. Res.*, 29(*8*):381–389, 1996.

[508] D. E. Tronrud, J. Wen, L. Gay, and R. E. Blankenship. The structural basis for the difference in absorbance spectra for the FMO antenna protein from various green sulfur bacteria. *Photosynth. Res.*, 100(*2*):79–87, 2009.

[509] Z. Liu, H. Yan, K. Wang, T. Kuang, J. Zhang, L. Gui, X. An, and W. Chang. Crystal structure of spinach major lightharvesting complex at 2.72Å resolution. *Nature*, 428:287–292, 2004.

[510] S. Baghbanzadeh and I. Kassal. Geometry, supertransfer, and optimality in the light harvesting of purple bacteria. *J. Phys. Chem. Lett.*, 7(*19*):3804–3811, 2016.

[511] J. M. Olson and R. E. Blankenship. Thinking about the evolution of photosynthesis. *Photosynth. Res.*, 80(*1–3*):373–383, 2004.

[512] R. Blankenship. Early evolution of photosynthesis. *Plant Physiol.*, 154(*2*):434–438, 2010.

[513] S. Y. Reece, J. A. Hamel, K. Sung, T. D. Jarvi, A. J. Esswein, J. J. H. Pijpers, and D. G. Nocera. Wireless solar water splitting using silicon-based semiconductors and Earth-abundant catalysts. *Science*, 334(*6056*):645–648, 2011.

[514] W. E. Piers. Future trends in organometallic chemistry: Organometallic approaches to water splitting. *Organometallics*, 30(*1*):13–16, 2011.

[515] G. S. Engel, T. R. Calhoun, E. L. Read, T.-K. Ahn, T. Mančal, Y.-C. Cheng, R. E. Blankenship, and G. R. Fleming. Evidence for wavelike energy transfer through quantum coherence in photosynthetic systems. *Nature*, 446:782–786, 2007.

[516] G. Panitchayangkoon, D. Hayes, K. A. Fransted, J. R. Caram, E. Harel, J. Wen, R. E. Blankenship, and G. S. Engel. Long-lived quantum coherence in photosynthetic complexes at physiological temperature. *Proc. Natl. Acad. Sci. U. S. A.*, 107(*29*):12766–12770, 2010.

[517] J. Moix, J. Wu, P. Huo, D. Coker, and J. Cao. Efficient energy transfer in light-harvesting systems, III: The influence of the eighth bacteriochlorophyll on the dynamics and efficiency in FMO. *J. Phys. Chem. Lett.*, 2(*24*):3045–3052, 2011.

[518] A. Eisfield and J. S. Briggs. Classical master equation for excitonic transport under the influence of an environment. *Phy. Rev. E*, 85(*4*):1–8, 2012.

[519] H. W. Kim, A. Kelly, J. W. Park, and Y. M. Rhee. All-atom semiclassical dynamics study of quantum coherence in photosynthetic Fenna-Matthews-Olson complex. *J. Am. Chem. Soc.*, 134(*28*):11640–11651, 2012.

[520] S. Shim, P. Rebentrost, S. Valleau, and A. Aspuru-Guzik. Atomistic study of the long-lived quantum coherences in the Fenna-Matthews-Olson complex. *Biophys. J.*, 102(*3*):649–660, 2012.

[521] M. Cho. Coherent two-dimensional optical spectroscopy. *Chem. Rev.*, 108(*4*): 1331–1418, 2008.

[522] M. Mohseni, P. Rebentrost, S. Lloyd, and A. Aspuru-Guzik. Environment-assisted quantum walks in photosynthetic energy transfer. *J. Chem. Phys.*, 129(*17*): 174106, 2008.

[523] P. Rebentrost, M. Mohseni, I. Kassal, S. Lloyd, and A. Aspuru-Guzik. Environment-assisted quantum transport. *New. J. Phys.*, 11:053041, 2009.

[524] P. Rebentrost, M. Mohseni, and A. Aspuru-Guzik. Role of quantum coherence and environmental fluctuations in chromophoric energy transport. *J. Phys. Chem. B*, 113(*29*):9942–9947, 2009.

[525] A. W. Chin, A. Datta, F. Caruso, S. F. Huelga, and M. B. Plenio. Noise-assisted energy transfer in quantum networks and light-harvesting complexes. *New J. Phys.*, 12:065002, 2010.

[526] G. Panitchayangkoon, D. V. Voronine, D. Abramavicius, J. R. Carama, N. H. C. Lewis, S. Mukamele, and G. S. Engel. Direct evidence of quantum transport in photosynthetic light-harvesting complexes. *Proc. Natl. Acad. Sci. U. S. A.*, 108 (*52*):20908–20912, 2011.

[527] I. Kassal and A. Aspuru-Guzik. Environment-assisted quantum transport in ordered systems. *New. J. Phys.*, 14:053041, 2012.

[528] S. F. Huelga and M. B. Plenio. Vibrations, quanta and biology. *Contemp. Phys.*, 54(*4*):181–207, 2013.

[529] C. Curutchet and B. Mennucci. Quantum chemical studies of light harvesting. *Chem. Rev.*, 117(*2*):294–343, 2017.

[530] J. Gao, W.-J. Shi, J. Ye, X. Wang, H. Hirao, and Y. Zhao. QM/MM modeling of environmental effects on electronic transitions of the FMO complex. *J. Phys. Chem. B*, 117(*13*):3488–3495, 2013.

[531] X. Jia, Y. Mei, J. Z. Zhang, and Y. Mo. Hybrid QM/MM study of FMO complex with polarized proteinspecific charge. *Sci. Rep.*, 5:17096, 2015.

[532] F. Caruso, A. W. Chin, A. Datta, S. F. Huelga, and M. B. Plenio. Highly efficient energy excitation transfer in light-harvesting complexes: The fundamental role of noise-assisted transport. *J. Chem. Phys.*, 131(*10*):105106, 2009.

[533] J. Wu, F. Liu, J. Ma, R. J. Silbey, and J. Cao. Efficient energy transfer in light-harvesting systems: Quantum-classical comparison, flux network, and robustness analysis. *J. Chem. Phys.*, 137(*17*):174111, 2012.

[534] J. Ye, K. Sun, Y. Zhao, Y. Yu, C. K. Lee, and J. Cao. Excitonic energy transfer in light-harvesting complexes in purple bacteria. *J. Chem. Phys.*, 136(*24*):245104, 2012.

[535] K. Sun, J. Ye, and Y. Zhao. Path induced coherent energy transfer in light-harvesting complexes in purple bacteria. *J. Chem. Phys.*, 141(*12*):124103, 2014.

[536] J. J. J. Roden, D. I. G. Bennett, and K. B. Whaley. Long-range energy transport in photosystem II. *J. Chem. Phys.*, 144(*24*):245101, 2016.

[537] M. Yang, A. Damjanović, H. M. Vaswani, and G. R. Fleming. Energy transfer in photosystem I of cyanobacteria *Synechococcus Elongatus*: Model study with structure-based semi-empirical hamiltonian and experimental spectral density. *Biophys. J.*, 85(*1*):140–158, 2003.

[538] L. A. Baker and S. Habershon. Robustness, efficiency, and optimality in the Fenna-Matthews-Olson photosynthetic pigment-protein complex. *J. Chem. Phys.*, 143(*10*):105101, 2015.

[539] J. Adolphs, F. Müh, M. E.-A. Madjet, and T. Renger. Calculation of pigment transition energies in the FMO Protein. *Photosynth. Res.*, 95(*2–3*):197–209, 2008.

[540] M. S. am Busch, F. Müh, M. E.-A. Madjet, and T. Renger. The eighth bacteriochlorophyll completes the excitation energy funnel in the FMO protein. *J. Phys. Chem. Lett.*, 2(*2*):93–98, 2011.

[541] B. P. Krueger, G. D. Scholes, and G. R. Fleming. Calculation of couplings and energy-transfer pathways between the pigments of LH2 by the *ab initio* transition density cube method. *J. Phys. Chem. B*, 102(*27*):5375–5386, 1998.

[542] N. H. List, C. Curutchet, S. Knecht, B. Mennucci, and J. Kongsted. Toward reliable prediction of the energy ladder in multichromophoric systems: A benchmark study on the FMO light-harvesting complex. *J. Chem. Theory Comput.*, 9(*11*): 4928–4938, 2013.

[543] D. J. Cole, A. W. Chin, N. D. M. Hine, P. D. Haynes, and M. C. Payne. Toward *ab initio* optical spectroscopy of the Fenna-Matthews-Olson complex. *J. Phys. Chem. Lett.*, 4(*24*):4206–4212, 2013.

[544] J. Wu, F. Liu, Y. Shen, J. Cao, and R. J. Silbey. Efficient energy transfer in light-harvesting systems, I: Optimal temperature, reorganization energy and spatial-temporal correlations. *New. J. Phys.*, 12:105012, 2010.

[545] J. Cao and R. J. Silbey. Optimization of exciton trapping in energy transfer processes. *J. Phys. Chem. A*, 113(*50*):13825–13838, 2009.

[546] F. Vaughan, N. Linden, and F. R. Manby. How Markovian is exciton dynamics in purple bacteria? *J. Chem. Phys.*, 146(*12*):124113, 2017.

[547] S. I. E. Vulto, M. A. de Baat, S. Neerken, F. R. Nowak, H. van Amerongen, J. Amesz, and T. J. Aartsma. Excited state dynamics in FMO antenna complexes from photosynthetic green sulfur bacteria: A kinetic model. *J. Phys. Chem. B*, 103(*38*):8153–8161, 1999.

[548] E. Rivera, D. Montemayor, M. Masia, and D. F. Coker. Influence of site-dependent pigment-protein interactions on excitation energy transfer in photosynthetic light harvesting. *J. Phys. Chem. B*, 117(*18*):5510–5521, 2013.

[549] C. Olbrich and U. Kleinekathöfer. Time-dependent atomistic view on the electronic relaxation in light-harvesting system II. *J. Phys. Chem. B*, 114(*38*):12427–12437, 2010.

[550] J. Adolphs and T. Renger. How proteins trigger excitation energy transfer in the FMO complex of green sulfur bacteria. *Biophys. J.*, 91(*8*):2778–2797, 2006.

[551] J. M. Olson. *The FMO protein*, volume 20 of *Discoveries in Photosynthesis*, pages 421–427. Springer Netherlands, 2005.

[552] A. Ben-Shem, F. Frolow, and N. Nelson. Evolution of photosystem I – from symmetry through pseudosymmetry to asymmetry. *FEBS Lett.*, 564(*3*):274–280, 2004.

[553] Y. Umena, K. Kawakami, J.-R. Shen, and N. Kamiya. Crystal structure of oxygen-evolving photosystem II at a resolution of 1.9Å. *Nature*, 473:55–60, 2011.

[554] A. K. Manske, J. Glaeser, M. M. M. Kuypers, and J. Overmann. Physiology and phylogeny of green sulfur bacteria forming a monospecific phototrophic assemblage at a depth of 100 meters in the Black Sea. *Appl. Environ. Microbiol.*, 71 (*12*):8049–8060, 2005.

[555] Green sulfur bacteria, Digital Universe Directory. Accessed 26 April 2017, http://www.digitaluniverse.net/treeoflife/topics/view/51cbfc53f702fc2ba8122659/.

[556] M. T. W. Milder, B. Brüggemann, R. van Grondelle, and J. L. Herek. Revisiting the optical properties of the FMO protein. *Photosynth. Res.*, 104(*2*):257–274, 2010.

[557] C. Olbrich, T. L. C. Jansen, J. Liebers, M. Aghtar, J. Strümpfer, K. Schulten, J. Knoester, and U. Kleinekathöfer. From atomistic modeling to excitation transfer and two-dimensional spectra of the FMO light-harvesting complex. *J. Phys. Chem. B*, 115(*26*):8609–8621, 2011.

[558] T. Scholak, F. de Melo, T. Wellens, F. Mintert, and A. Buchleitner. Efficient and coherent excitation transfer across disordered molecular networks. *Phys. Rev. E*, 83(*2*):021912, 2011.

[559] M. Cho, H. M. Vaswani, T. Brixner, J. Stenger, and G. R. Fleming. Exciton analysis in 2D electronic spectroscopy. *J. Phys. Chem. B*, 109(*21*):10542–10556, 2005.

[560] J.-H. Kim and J. Cao. Optimal efficiency of self-assembling light-harvesting arrays. *J. Phys. Chem. B*, 114(*49*):16189–16197, 2010.

[561] G.-Y. Chen, N. Lambert, C.-M. Li, Y.-N. Chen, and F. Nori. Rerouting excitation transfers in the Fenna-Matthews-Olson complex. *Phys. Rev. E*, 88(*3*):032120, 2013.

[562] M. K. Sener, D. Lu, T. Ritz, S. Park, P. Fromme, and K. Schulten. Robustness and optimality of light harvesting in cyanobacterial photosystem I. *J. Phys. Chem. B*, 106(*32*):7948–7960, 2002.

[563] I. Kassal, J. Yuen-Zhou, and S. Rahimi-Keshari. Does coherence enhance transport in photosynthesis? *J. Phys. Chem. Lett.*, 4(*3*):362–367, 2013.

[564] A. Shabani, M. Mohseni, H. Rabitz, and S. Lloyd. Numerical evidence for robustness of environment-assisted quantum transport. *Phys. Rev. E*, 89(*4*):042706, 2014.

[565] A. Ishizaki and G. R. Fleming. Theoretical examination of quantum coherence in a photosynthetic system at physiological temperature. *Proc. Natl. Acad. Sci. U. S. A.*, 106(*41*):17255–17260, 2009.

[566] A. Ishizaki and G. R. Fleming. Quantum coherence in photosynthetic light harvesting. *Annu. Rev. Condens. Matter Phys.*, 3:333–361, 2012.

[567] G. Tao and W. H. Miller. Semiclassical description of electronic excitation population transfer in a model photosynthetic system. *J. Phys. Chem. Lett.*, 1(*6*): 891–894, 2010.

[568] W. H. Miller. The semiclassical initial value representation: A potentially practical way for adding quantum effects to classical molecular dynamics simulations. *J. Phys. Chem. A*, 105(*13*):2942–2955, 2001.

[569] P. Nalbach, D. Braun, and M. Thorwart. Exciton transfer dynamics and quantumness of energy transfer in the Fenna-Matthews-Olson complex. *Phy. Rev. E*, 84(*4*):041926, 2011.

[570] D. Hayes, J. Wen, G. Panitchayangkoon, R. E. Blankenship, and G. S. Engel. Robustness of electronic coherence in the Fenna-Matthews-Olson complex to vibronic and structural modifications. *Faraday Discuss.*, 150:459–469, 2011.

[571] N. C. M. Magdaong, R. G. Saer, D. M. Niedzwiedzki, and R. E. Blankenship. Ultrafast spectroscopic investigation of energy transfer in site-directed mutants of the Fenna-Matthews-Olson (FMO) antenna complex from *chlorobaculum tepidum*. *J. Phys. Chem. B*, 121(*18*):4700–4712, 2017.

[572] R. Saer, G. S. Orf, X. Lud, H. Zhang, M. J. Cuneo, D. A. Myles, and R. E. Blankenship. Perturbation of bacteriochlorophyll molecules in Fenna-Matthews-Olson protein complexes through mutagenesis of cysteine residues. *Biochim. Biophys. Acta*, 1857(*9*):1455–1463, 2016.

[573] R. G. Saer, V. Stadnytskyi, N. C. Magdaong, C. Goodson, S. Savikhin, and R. E. Blankenship. Probing the excitonic landscape of the *chlorobaculum tepidum* Fenna-Matthews-Olson (FMO) complex: A mutagenesis approach. *Biochim. Biophys. Acta*, 1858(*4*):288–296, 2017.

[574] N. Skochdopole and D. A. Mazziotti. Functional subsystems and quantum redundancy in photosynthetic light harvesting. *J. Phys. Chem. Lett.*, 2(*23*):2989–2993, 2011.

[575] R. Albert, H. Jeong, and A.-L. Barabási. Error and attack tolerance of complex networks. *Nature*, 406:378–382, 2000.

[576] M. E. J. Newman. The structure and function of complex networks. *SIAM Rev.*, 45(*2*):167–256, 2003.

[577] R. W. Floyd. Algorithm 97: Shortest path. *Commun. ACM*, 5(*6*):345, 1962.

[578] S. Warshall. A theorem on boolean matrices. *J. ACM*, 9(*1*):11–12, 1962.

[579] T. M. Wahlund, C. R. Woese, R. W. Castenholz, and M. T. Madigan. A thermophilic green sulfur bacterium from New Zealand hot springs, *chlorobium tepidum* sp. nov. *Arch. Microbiol.*, 156(*2*):81–90, 1991.

[580] A. Camara-Artigas, R. E. Blankenship, and J. P. Allen. The structure of the FMO protein from *Chlorobium tepidum* at 2.2Å resolution. *Photosynth. Res.*, 75 (*1*):49–55, 2003.

[581] C. R. Larson, C. O. Seng, L. Lauman, H. J. Matthies, J. Wen, R. E. Blankenship, and J. P. Allen. The three-dimensional structure of the FMO protein from *Pelodictyon Phaeum* and the implications for energy transfer. *Photosynth. Res.*, 107(*2*):139–150, 2011.

[582] J. M. Olson and J. Raymond. Is FMO-protein related to PscA in the reaction center of green sulfur bacteria? *Photosynth. Res.*, 75(*3*):277–285, 2003.

[583] J. Barber and B. Andersson. Too much of a good thing: Light can be bad for photosynthesis. *Trends Biochem. Sci.*, 17(*2*):61–66, 1992.

[584] S. Takahashi and N. Murata. How do environmental stresses accelerate photoinhibition? *Trends Plant Sci.*, 13(*4*):178–182, 2008.

[585] R. E. Blankenship. *Antenna complexes and energy transfer processes*, chapter 5, pages 61–94. Molecular Mechanisms of Photosynthesis. Wiley-Blackwell, 2nd edition, 2014.

[586] L. A. Baker and S. Habershon. Photosynthetic pigment-protein complexes as highly-connected networks: Implications for robust energy transport. *Proc. R. Soc. A,*, 473(*2201*):20170112, 2017.

[587] F. Müh, M. E.-A. Madjet, and T. Renger. Structure-based identification of energy sinks in plant light-harvesting complex II. *J. Phys. Chem. B*, 114(*42*):13517–13535, 2010.

[588] F. Fassioli, A. Olaya-Castro, S. Scheuring, J. N. Sturgis, and N. F. Johnson. Energy transfer in light-adapted photosynthetic membranes: From active to saturated photosynthesis. *Biophys. J.*, 97(*9*):2464–2473, 2009.

[589] G. C. Knee, P. Rowe, L. D. Smith, A. Troisi, and A. Datta. Structure-dynamics relation in physically-plausible multichromophore systems. *J. Phys. Chem. Lett.*, 8(*10*):2328–2333, 2017.

[590] L. A. Baker, L. C. Grosvenor, M. N. Ashfold, and V. G. Stavros. Ultrafast photophysical studies of a multicomponent sunscreen: Oxybenzone-titanium dioxide mixtures. *Chem. Phys. Lett.*, 664:39–43, 2016.

[591] L. Wang, A. Akimov, and O. V. Prezhdo. Recent progress in surface hopping: 2011-2015. *J. Phys. Chem. Lett.*, 7(*11*):2100–2112, 2016.

[592] M. A. C. Saller and S. Habershon. Basis set generation for quantum dynamics simulations using simple trajectory-based methods. *J. Chem. Theory Comput.*, 11(*1*):8–16, 2014.

[593] E. Dumont, M. Wibowo, D. Roca-Sanjuán, M. Garavelli, X. Assfeld, and A. Monari. Resolving the benzophenone DNA-photosensitization mechanism at QM/MM level. *J. Phys. Chem. Lett.*, 6(*4*):576–580, 2015.

[594] J. Kockler, M. Oelgemöller, S. Robertson, and B. D. Glass. Photostability of sunscreens. *J. Photochem. Photobiol., C*, 13(*1*):91–110, 2012.

[595] K. M. Hanson, E. Gratton, and C. J. Bardeen. Sunscreen enhancement of UV-induced reactive oxygen species in the skin. *Free Radical Biol. Med.*, 41(*8*): 1205–1212, 2006.

[596] L. Martínez, R. Andrade, E. G. Birgin, and J. M. Martínez. Packmol: A package for building initial configurations for molecular dynamics simulations. *J. Comput. Chem.*, 30(*13*):2157–2164, 2009.

[597] R. Marks. Two decades of the public health approach to skin cancer control in Australia: Why, how and where are we now? *Australas J. Dermatol.*, 40(*1*):1–5, 1999.

[598] D. Hill, V. White, R. Marks, and R. Borland. *Changes in sun-related attitudes and behaviors, and reduced sunburn prevalence in a population at high risk of melanoma*, chapter 10, pages 163–178. Public Health Communication Evidence for Behavior Change. Lawrence Erlbaum Associates, 2002.

[599] T. Owen, D. Fitzpatrick, O. Dolan, and A. Gavin. Knowledge, attitudes and behaviour in the sun: The barriers to behavioural change in Northern Ireland. *Ulster. Med. J.*, 73:96–104, 2004.

[600] E. Thieden, P. A. Philipsen, J. Sandby-Møller, and H. C. Wulf. Sunscreen use related to UV exposure, age, sex, and occupation based on personal dosimeter readings and sun-exposure behavior diaries. *Arch. Dermatol.*, 141(*8*):967–973, 2005.

[601] S. Lautenschlager, H. C. Wulf, and M. R. Pittelkow. Photoprotection. *The Lancet*, 370(*9586*):528–537, 2007.

[602] N. D. N. Rodrigues, M. Staniforth, J. D. Young, Y. Peperstraete, N. C. Cole-Filipiak, J. R. Gord, P. S. Walsh, D. M. Hewett, T. S. Zwier, and V. G. Stavros. Towards elucidating the photochemistry of the sunscreen filter ethyl ferulate using time-resolved gas-phase spectroscopy. *Faraday Discuss.*, 194:709–729, 2016.

[603] A. Einstein. On the electrodynamics of moving bodies. *Ann. Phys. (Berlin)*, 17: 891–921, 1905.

[604] D. Fleisch. *A student's guide to vectors and tensors*. Cambridge University Press, New York, 3rd edition, 2012.

[605] I. S. Grant and W. R. Phillips. *Electromagnetism*. John Wiley & Sons, Chichester, 2nd edition, 1990.